Technische Universität Kaiserslautern

Fachbereich Chemie

Characterization of Structures Fragmentation Pathways and Magnetism of Mononuclear and Oligonuclear Transition Metal Complexes in Isolation

Am Fachbereich Chemie der Technischen Universität Kaiserslautern zur Erlangung des akademischen Grades "Doktor der Naturwissenschaften" genehmigte

Dissertation

(D386)

vorgelegt von

Dipl.-Chem Johannes Lang

Betreuer: Prof. Dr. G. Niedner-Schatteburg

Tag der wissenschaftlichen Aussprache: 18.05.2017

Technische Universität Kaiserslautern 2017

Die vorliegende Arbeit wurde im Zeitraum von Januar 2014 bis April 2017 im Fachbereich Chemie der Technischen Universität Kaiserslautern unter Betreuung von Prof. Dr. G. Niedner-Schatteburg angefertigt.

Datum des Antrags der Eröffnung des Promotionsverfahrens: 11.01.2017

Promotionskommision:

Vorsitzender	Prof. Dr. W. R. Thiel
1. Berichterstatter	Prof. Dr. G. Niedner-Schatteburg
2. Berichterstatter	Prof. Dr. M. Gerhards

MEINER FAMILIE GEWIDMET

„BASIC RESEARCH IS WHAT I AM DOING

WHEN I DON'T KNOW WHAT I AM DOING.“

- Wernher von Braun -

Content

1 Introduction

Coordination compounds such as transition metal (TM) complexes have been utilized by humanity since antiquity[1-4]. They exhibit a broad variety of properties and features, which makes them ubiquitous in everyday life and scientific research[5, 6]. TM catalysts mediate important (industrial) chemical reactions[7-11] by homogenous catalysis and activate small molecules such as N_2 or CO_2 for subsequent functionalization[12-15]. The reactivity of TM complexes relates to their three dimensional structure. Thus, molecular structure elucidation is paramount in order to gain fundamental insight into their catalytic properties.

Unpaired electrons within TM complexes give rise to intrinsic magnetic phenomena[16] like magnetization of the complexes in the presence of an external magnetic field. "Single Molecule Magnets" (SMM) are complexes designed to remain magnetized even after the magnetic field is switched off[17]. The intrinsic molecular magnetism of SMM´s sets them apart from traditional bulk magnets and promises a variety of applications[18-20]. Archetypical SMM´s contain a small number (~4 to 30) of paramagnetic TM centers, which are linked together by bridging atoms or molecules (e.g. O^{2-}, $CH_3CO_2^-$) and stabilized by further organic ligands[21]. Optimizing magnetic properties of TM complexes demands fundamental understanding of their intermetallic magnetic couplings.

The elucidation of cooperative effects between two or more metal centers within TM complexes and clusters stands out as a very active field of research[22]. A cooperative effect in TM clusters or TM complexes is defined as a new magnetic, optical, or reactive effect or function emerging by combining two or more TM centers. This definition implies, that neither the participating TM centers nor the whole complex exhibit this function if the two TM centers are sufficiently far apart. Oligometallic systems have been investigated to elucidate how cooperative effects determine their magnetic[23], catalytic[24] as well as their optical properties[25]. Investigations on free molecules *in vacuo* exclude superimposing effects (e.g. solvent or crystal packing effects) and benefits insights into such intramolecular properties.

Soft ionization techniques like Matrix Assisted Laser Desorption/Ionization[26-28] (MALDI) and Electrospray Ionization[29-31] (ESI) enable the transfer of intact ionic TM complexes[32-35] into vacuum. Subsequent mass spectrometric analysis[36-40] determines their mass to

charge (m/z) ratios and allows for an isolation of ion ensembles by m/z selection. A low ion density in the gas phase excludes molecule characterization by classical absorption spectroscopy, since any light attenuation would be below the detection limit. An "action spectroscopy" approach[41] provides a solution to this problem: Light may cause measurable changes of the ion ensemble´s m/z ratio (e.g. by dissociation) depending on the wavelength and photon flux. Collisions of the ions with background gas molecules provide an additional source of information. The ions may cool down, heat up, and undergo dissociations or reactions along sole or competing pathways. Various experimental methods[42-46] employ action spectroscopy as well as molecular collisions to extract information on molecular properties like geometrical structure[47-49], magnetism[50, 51], reaction barriers[52, 53], binding strengths[54, 55] and fragmentation pathways[56, 57]. Such molecular properties may interdepend and modulate each other. Thus, combining several experimental methods in parallel favors a complete understanding of the TM complex. Quantum chemical calculations (e.g. density functional theory[58, 59]) support interpretations of experimental data and deepen the fundamental insight thereof.

InfraRed (Multiple) Photon Dissociation (IR-(M)PD) is an established "action spectroscopy" technique to obtain insight into binding motifs and structural compositions of isolated TM complexes[60-66]. At resonance, photons in the infrared spectral region excite molecular vibrations. An intramolecular vibration redistribution[67] (IVR) process transfers the excess energy into internal vibrational degrees of freedom (internal energy). This allows for repeated absorption of several photons by one absorber[68-70]. The trapped ions fragmentize (measured as change their m/z ratio) if their internal energy reaches the dissociation threshold[71, 72]. High dissociation thresholds and/or inefficient IVR processes may prevent fragmentation within one laser pulse, which results in undetected vibrational bands[73, 74]. "Messenger" techniques[75-79] circumvent this problem by collisional cooling of the trapped ions. At cryo temperatures the ions form adducts with background gas atoms or molecules (e.g. N_2 or He). These molecules act as "messengers" of the vibrational bands, since their low dissociation thresholds allow for dissociation by single photon absorption. A resonant 2-color (2c)-IR-MPD technique enhances fragmentation efficiency of TM complexes[80] by utilizing two IR lasers. The resulting 2c-IR-MPD spectra depend crucially on the temporal delay between the two laser pulses[81]. A detailed vibrational and structural analysis of the

IR-(M)PD spectra arises via comparison with calculated IR spectra of molecular structures with adequate geometries. Density Functional Theory (DFT) has been proven to be a capable and cost efficient approach to compute geometry optimized energy minima structures, linear absorption spectra as well as other molecular properties[82, 83].

Collisions between trapped ions and background gas atoms/molecules can increase the internal energy of the ions by thermal heating[84]. Such collisional activation results in collision induced dissociation[85, 86] (CID). Historically, CID was observed in mass spectra by diffuse fragment peaks[87, 88]. Since then it has evolved to a widely used technique in mass spectrometry, e.g. for protein sequencing[89, 90]. In the context of TM complexes, CID is very useful to investigate activation barriers of catalyst precursors[91, 92], ligand binding energies[93-95] and intramolecular fragmentation pathways[96, 97]. The experimental results are compared with accompanying geometry optimized fragment and transition state structures along the reaction coordinate. The combination of CID experiments and DFT modelling provides fundamental insight into the intramolecular fragmentation processes[98-100].

The element selective X-ray Magnetic Circular Dichroism[101] (XMCD) spectroscopy allows to investigate magnetic properties of samples such as deposited nanoparticles[102, 103]. Spin and orbital contributions to the total magnetic moment of the investigated compounds can be deconstructed by sum rule analysis[104-106]. Recently, the XMCD technique has been adopted as a gas phase “action spectroscopy” method to investigate the magnetism of isolated clusters and complexes[107-109]. XMCD spectra provide information on intrinsic magnetic properties, i.e. void of any alterations such as crystal packing or surface induced effects. The broken symmetry approach[110, 111] is useful to simulate intramolecular magnetic couplings *via* DFT modelling. The combination of XMCD experiments and Broken Symmetry/DFT modelling provides fundamental insight into the molecular magnetism in isolated complexes[112].

This thesis comprises studies on isolated mononuclear and oligonuclear TM complexes. It applies ESI in conjunction with mass spectrometry to isolate species of interest as gaseous ions. Their molecular structures, fragmentation pathways and magnetic properties are elucidated by combining several experimental and computational methods (cf. Scheme 1). The thesis contains five independent research studies (chapters

3 to 7) utilizing IR-(M)PD, CID and XMCD investigations as well as DFT modelling in various combinations depending on the nature of the investigated TM complexes and individual scientific questions. Each research study provides an independent introduction, a short description of the experimental and theoretical methods, a discussion and a conclusion.

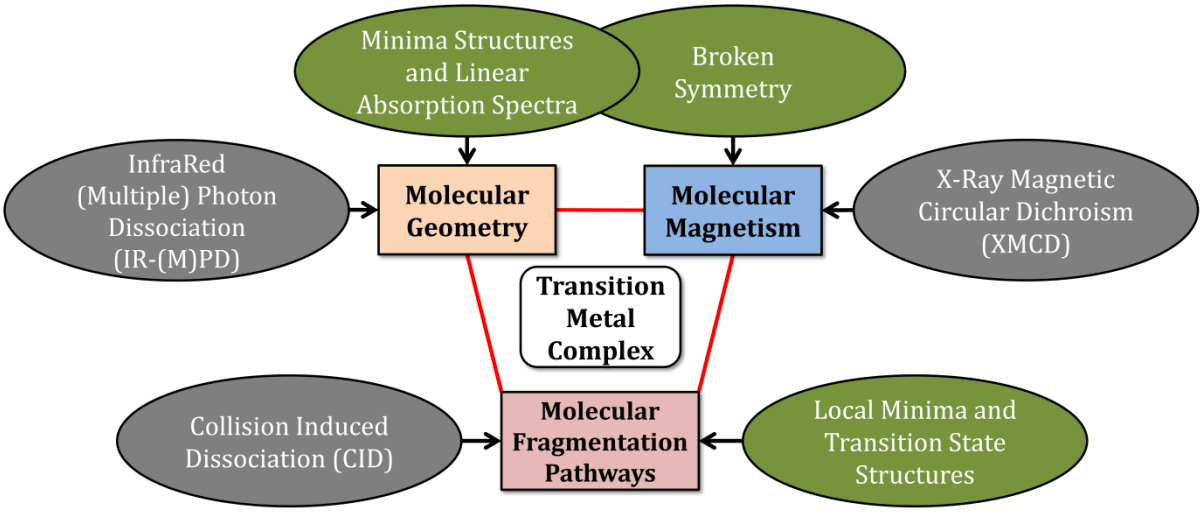

Scheme 1: Overview of the experimental methods (grey oval shapes) and associated computational modelling (green oval shapes) utilized in this thesis to investigate molecular properties of isolated TM complexes.

Chapter 3 reports on "non-classical" vibrational blue shifts of dinitrogen molecules coordinated to trinuclear iron (III) oxo acetate complexes $[Fe_3O(OAc)_6]^+$ (OAc = acetate). It presents IR-PD spectra of cryo cooled complexes in conjunction with DFT modelling. Molecular orbital analysis serves to rationalize the increasing N-N bond strength and provides insight into the nature of the N_2-Fe bonding in $[Fe_3O(OAc)_6(N_2)_n]^+$ (n = 1,2,3).

Chapter 4 elucidates the cationization of a bimetallic $[AuZnCl_3]$ complex by coordinating alkali metal ions. It characterizes structural features of the charged adducts *via* IR-MPD spectroscopy and DFT modelling. CID experiments and calculated stationary points along the fragmentation pathway reveal molecular reorganizations upon CID activation.

Chapter 5 showcases delay dependent 2c-IR-MPD spectroscopy in conjunction with DFT modelling. The investigation reveals laser induced torsional isomerization in a mononuclear silver (I) complex.

Chapter 6 establishes magnetostructural correlations in trinuclear iron (III) oxo acetate pyridine complexes $[Fe_3O(OAc)_6(Py)_n]^+$ (Py = pyridine, n = 0,1,2,3). It utilizes CID/DFT to

determine pyridine binding strengths and IR-MPD/DFT to characterize the geometrical evolution of the triangular Fe_3O core upon stepwise coordination of pyridine ligands. XMCD investigations in conjunction with Broken Symmetry/DFT modelling serve to characterize the magnetic couplings of the triangular Fe_3O core in dependence of its geometry.

Chapter 7 characterizes structural features and fragmentation pathways of mononuclear and binuclear palladium catalysts by IR-MPD and CID experiments as well as DFT modelling.

1.1 References

1. G. B. Kauffman, *Coordination Chemistry: History*, in *Encyclopedia of Inorganic Chemistry*, John Wiley & Sons, Ltd, 2006.
2. A. T. Baker and S. E. Livingstone, *Historical Sketch: The early history of coordination chemistry in Australia*, Polyhedron, 1985, **4**, 1337-1351.
3. G. A. Lawrance, in *Introduction to Coordination Chemistry*, John Wiley & Sons, Ltd, 2009, pp. 41-82.
4. K. R. Dunbar and R. A. Heintz, *Chemistry of Transition Metal Cyanide Compounds: Modern Perspectives*, in *Prog. Inorg. Chem.*, John Wiley & Sons, Inc., 2007, pp. 283-391.
5. J. E. Huheey, E. A. Keiter and R. L. Keiter, *Inorganic Chemistry: Principles of Structure and Reactivity*, Pearson Education, 2000.
6. C. Elschenbroich, *Organometallchemie*, Teubner, 2005.
7. A. Behr and P. Neubert, *Applied Homogeneous Catalysis*, Wiley, 2012.
8. E. M. Beccalli, G. Broggini, M. Martinelli and S. Sottocornola, *C–C, C–O, C–N Bond Formation on sp2 Carbon by Pd(II)-Catalyzed Reactions Involving Oxidant Agents*, Chem. Rev., 2007, **107**, 5318-5365.
9. M. Lersch and M. Tilset, *Mechanistic Aspects of C–H Activation by Pt Complexes*, Chem. Rev., 2005, **105**, 2471-2526.
10. J. A. Labinger and J. E. Bercaw, *Understanding and exploiting C-H bond activation*, Nature, 2002, **417**, 507-514.
11. V. Ritleng, C. Sirlin and M. Pfeffer, *Ru-, Rh-, and Pd-Catalyzed C–C Bond Formation Involving C–H Activation and Addition on Unsaturated Substrates: Reactions and Mechanistic Aspects*, Chem. Rev., 2002, **102**, 1731-1770.
12. H. Tanaka, K. Arashiba, S. Kuriyama, A. Sasada, K. Nakajima, K. Yoshizawa and Y. Nishibayashi, *Unique behaviour of dinitrogen-bridged dimolybdenum complexes bearing pincer ligand towards catalytic formation of ammonia*, Nat Commun, 2014, **5**.
13. C. N. Cornell and M. S. Sigman, *Molecular Oxygen Binding and Activation: Oxidation Catalysis*, in *Activation of Small Molecules*, Wiley-VCH Verlag GmbH & Co. KGaA, 2006, pp. 159-186.
14. M. Aresta, *Carbon Dioxide Reduction and Uses as a Chemical Feedstock*, in *Activation of Small Molecules*, Wiley-VCH Verlag GmbH & Co. KGaA, 2006, pp. 1-41.

15. L. M. Berreau, *Water Activation: Catalytic Hydrolysis*, in *Activation of Small Molecules*, Wiley-VCH Verlag GmbH & Co. KGaA, 2006, pp. 287-317.
16. R. S. D. Gatteschi, J. Villain *Molecular Nanomagnets*, Oxford University Press, Oxford 2006.
17. G. Christou, D. Gatteschi, D. N. Hendrickson and R. Sessoli, *Single Molecule Magnets*, MRS Bull., 2000, **25**, 66.
18. M. N. Leuenberger and D. Loss, *Quantum computing in molecular magnets*, Nature, 2001, **410**, 789-793.
19. G. Aromi, D. Aguila, P. Gamez, F. Luis and O. Roubeau, *Design of magnetic coordination complexes for quantum computing*, Chem. Soc. Rev., 2012, **41**, 537-546.
20. G. Aromí, *Single-molecule magnets and related phenomena*, Springer, Berlin, New York, 2006.
21. R. A. Layfield, *Organometallic Single-Molecule Magnets*, Organometallics, 2014, **33**, 1084-1099.
22. G. Niedner-Schatteburg, *Cooperative Effects in Clusters and Oligonuclear Complexes of Transition Metals in Isolation*, in *Clusters – Contemporary Insight in Structure and Bonding*, ed. S. Dehnen, Springer International Publishing, Cham, 2017, pp. 1-40.
23. M. Gysler, F. El Hallak, L. Ungur, R. Marx, M. Hakl, P. Neugebauer, Y. Rechkemmer, Y. Lan, I. Sheikin, M. Orlita, C. Anson, A. K. Powell, R. Sessoli, L. Chibotaru and J. van Slageren, *Multitechnique investigation of Dy3 - Implications for Coupled Lanthanide Clusters*, Chem. Sci., 2016.
24. A. Fromm, C. van Wüllen, D. Hackenberger and L. J. Gooßen, *Mechanism of Cu/Pd-Catalyzed Decarboxylative Cross-Couplings: A DFT Investigation*, J. Am. Chem. Soc., 2014, **136**, 10007-10023.
25. J. Chmela, M. E. Harding, D. Matioszek, C. E. Anson, F. Breher and W. Klopper, *Differential Many-Body Cooperativity in Electronic Spectra of Oligonuclear Transition-Metal Complexes*, Chemphyschem, 2016, **17**, 37-45.
26. K. Dreisewerd, S. Berkenkamp, A. Leisner, A. Rohlfing and C. Menzel, *Fundamentals of matrix-assisted laser desorption/ionization mass spectrometry with pulsed infrared lasers*, Int. J. Mass spectrom., 2003, **226**, 189-209.
27. M. Karas and R. Krüger, *Ion Formation in MALDI: The Cluster Ionization Mechanism*, Chem. Rev., 2003, **103**, 427-440.
28. S. Berkenkamp, F. Kirpekar and F. Hillenkamp, *Infrared MALDI Mass Spectrometry of Large Nucleic Acids*, Science, 1998, **281**, 260-262.
29. J. B. Fenn, *Electrospray Wings for Molecular Elephants (Nobel Lecture)*, Angew. Chem. Int. Ed., 2003, **42**, 3871-3894.
30. M. Yamashita and J. B. Fenn, *Negative ion production with the electrospray ion source*, J. Phys. Chem., 1984, **88**, 4671-4675.
31. M. Yamashita and J. B. Fenn, *Electrospray ion source. Another variation on the free-jet theme*, J. Phys. Chem., 1984, **88**, 4451-4459.
32. V. Katta, S. K. Chowdhury and B. T. Chait, *Electrospray ionization: a new tool for the analysis of ionic transition-metal complexes*, J. Am. Chem. Soc., 1990, **112**, 5348-5349.
33. V. B. Di Marco and G. G. Bombi, *Electrospray mass spectrometry (ESI-MS) in the study of metal–ligand solution equilibria*, Mass Spectrom. Rev., 2006, **25**, 347-379.

34. K. L. Vikse, M. P. Woods and J. S. McIndoe, *Pressurized Sample Infusion for the Continuous Analysis of Air- And Moisture-Sensitive Reactions Using Electrospray Ionization Mass Spectrometry*, Organometallics, 2010, **29**, 6615-6618.
35. J. S. McIndoe, *Mass Spectrometry and Gas-Phase Chemistry of Non-Covalent Complexes. Supramolecular Chemistry in the Gas Phase. Wiley-Interscience Series on Mass Spectrometry. By Christoph A. Schalley and Andreas Springer*, Angew. Chem. Int. Ed., 2010, **49**, 3717-3717.
36. W. N. Delgass and R. G. Cooks, *Focal Points in Mass Spectrometry*, Science, 1987, **235**, 545-553.
37. W. Paul, *Electromagnetic traps for charged and neutral particles*, Reviews of Modern Physics, 1990, **62**, 531-540.
38. R. Łobiński, D. Schaumlöffel and J. Szpunar, *Mass spectrometry in bioinorganic analytical chemistry*, Mass Spectrom. Rev., 2006, **25**, 255-289.
39. R. E. March, *Quadrupole Ion Trap Mass Spectrometer*, in *Encyclopedia of Analytical Chemistry*, John Wiley & Sons, Ltd, 2006.
40. J. S. Sampson, K. K. Murray and D. C. Muddiman, *Intact and Top-Down Characterization of Biomolecules and Direct Analysis Using Infrared Matrix-Assisted Laser Desorption Electrospray Ionization Coupled to FT-ICR Mass Spectrometry*, J. Am. Soc. Mass. Spectrom., 2009, **20**, 667-673.
41. T. Baer and R. C. Dunbar, *Ion Spectroscopy: Where Did It Come From; Where Is It Now; and Where Is It Going?*, J. Am. Soc. Mass. Spectrom., 2010, **21**, 681-693.
42. D. Scuderi, V. Lepere, G. Piani, A. Bouchet and A. Zehnacker-Rentien, *Structural Characterization of the UV-Induced Fragmentation Products in an Ion Trap by Infrared Multiple Photon Dissociation Spectroscopy*, J. Phys. Chem. Lett., 2014, **5**, 56-61.
43. A. K. Shukla and J. H. Futrell, *Tandem mass spectrometry: dissociation of ions by collisional activation*, J. Mass Spectrom., 2000, **35**, 1069-1090.
44. L. Sleno and D. A. Volmer, *Ion activation methods for tandem mass spectrometry*, J. Mass Spectrom., 2004, **39**, 1091-1112.
45. K. Eller and H. Schwarz, *Organometallic chemistry in the gas phase*, Chem. Rev., 1991, **91**, 1121-1177.
46. E. de Hoffmann, *Tandem mass spectrometry: A primer*, J. Mass Spectrom., 1996, **31**, 129-137.
47. N. Heine, M. R. Fagiani, M. Rossi, T. Wende, G. Berden, V. Blum and K. R. Asmis, *Isomer-Selective Detection of Hydrogen-Bond Vibrations in the Protonated Water Hexamer*, J. Am. Chem. Soc., 2013, **135**, 8266-8273.
48. A. Fielicke, G. Meijer and G. von Helden, *Infrared multiple photon dissociation spectroscopy of transition metal oxide cluster cations - Comparison of group Vb (V, Nb, Ta) metal oxide clusters*, EPJD, 2003, **24**, 69-72.
49. N. C. Polfer, J. Oomens, D. T. Moore, G. von Helden, G. Meijer and R. C. Dunbar, *Infrared spectroscopy of phenylalanine Ag(I) and Zn(II) complexes in the gas phase*, J. Am. Chem. Soc., 2006, **128**, 517-525.
50. V. Zamudio-Bayer, K. Hirsch, A. Langenberg, M. Kossick, A. Ławicki, A. Terasaki, B. v. Issendorff and J. T. Lau, *Direct observation of high-spin states in manganese dimer and trimer cations by x-ray magnetic circular dichroism spectroscopy in an ion trap*, J. Chem. Phys., 2015, **142**, 234301.
51. S. Peredkov, A. Savci, S. Peters, M. Neeb, W. Eberhardt, H. Kampschulte, J. Meyer, M. Tombers, B. Hofferberth, F. Menges and G. Niedner-Schatteburg, *X-ray absorption spectroscopy of mass-selected transition metal clusters using a*

cyclotron ion trap: An experimental setup for measuring XMCD spectra of free clusters, J. Electron. Spectrosc. Relat. Phenom., 2011, **184**, 113-118.

52. X.-N. Wu, H.-T. Zhao, J. Li, M. Schlangen and H. Schwarz, *Highly regioselective hydride transfer, oxidative dehydrogenation, and hydrogen-atom abstraction in the thermal gas-phase chemistry of [Zn(OH)]+/C3H8*, PCCP, 2014, **16**, 26617-26623.
53. U. Schwarz, M. Vonderach, M. Kappes, R. Kelting, K. Brendle and P. Weis, *Structural characterization of metalloporphyrin-oligomer multianions by mass spectrometry and ion mobility spectrometry—Observation of metastable species*, Int. J. Mass spectrom., 2013, **339–340**, 24-33.
54. K. M. Ervin and P. B. Armentrout, *Energy dependence, kinetic isotope effects, and thermochemistry of the nearly thermoneutral reactions N+(3P)+H2(HD,D2)→NH+(ND+)+H(D)*, J. Chem. Phys., 1987, **86**, 2659-2673.
55. P. B. Armentrout, *The Power of Accurate Energetics (or Thermochemistry: What is it Good for?)*, J. Am. Soc. Mass. Spectrom., 2013, **24**, 173-185.
56. K. Levsen and H. Schwarz, *Collisional Activation Mass Spectrometry—A New Probe for Determining the Structure of Ions in the Gas Phase*, Angew. Chem. Int. Ed., 1976, **15**, 509-519.
57. J. Lang, M. Cayir, S. P. Walg, P. Di Martino-Fumo, W. R. Thiel and G. Niedner-Schatteburg, *Intermetallic Competition in the Fragmentation of Trimetallic Au–Zn–Alkali Complexes*, Chem.-Eur. J., 2016, **22**, 2345-2355.
58. W. Koch and M. C. Holthausen, *The Kohn-Sham Approach*, in *A Chemist's Guide to Density Functional Theory*, Wiley-VCH Verlag GmbH, 2001, pp. 41-64.
59. T. Ziegler, *Approximate density functional theory as a practical tool in molecular energetics and dynamics*, Chem. Rev., 1991, **91**, 651-667.
60. J. Seo, J. Jang, S. Warnke, S. Gewinner, W. Schöllkopf and G. von Helden, *Stacking Geometries of Early Protoporphyrin IX Aggregates Revealed by Gas-Phase Infrared Spectroscopy*, J. Am. Chem. Soc., 2016, **138**, 16315-16321.
61. J. Oomens, B. G. Sartakov, G. Meijer and G. von Helden, *Gas-phase infrared multiple photon dissociation spectroscopy of mass-selected molecular ions*, Int. J. Mass spectrom., 2006, **254**, 1-19.
62. F. X. Sunahori, G. Yang, E. N. Kitova, J. S. Klassen and Y. Xu, *Chirality recognition of the protonated serine dimer and octamer by infrared multiphoton dissociation spectroscopy*, PCCP, 2013, **15**, 1873-1886.
63. J. Mohrbach, J. Lang, S. Dillinger, M. Prosenc, P. Braunstein and G. Niedner-Schatteburg, *Vibrational fingerprints of a tetranuclear cobalt carbonyl cluster within a cryo tandem ion trap*, J. Mol. Spectrosc., 2017, **332**, 103-108.
64. F. S. Menges, S. M. Craig, N. Tötsch, A. Bloomfield, S. Ghosh, H.-J. Krüger and M. A. Johnson, *Capture of CO2 by a Cationic Nickel(I) Complex in the Gas Phase and Characterization of the Bound, Activated CO2 Molecule by Cryogenic Ion Vibrational Predissociation Spectroscopy*, Angew. Chem. Int. Ed., 2015, **55**, 1282-1285.
65. N. C. Polfer and J. Oomens, *Vibrational spectroscopy of bare and solvated ionic complexes of biological relevance*, Mass Spectrom. Rev., 2009, **28**, 468-494.
66. E. M. Duffy, B. M. Marsh, J. M. Voss and E. Garand, *Characterization of the Oxygen Binding Motif in a Ruthenium Water Oxidation Catalyst by Vibrational Spectroscopy*, Angew. Chem. Int. Ed., 2016, n/a-n/a.
67. E. R. Grant, P. A. Schulz, A. S. Sudbo, Y. R. Shen and Y. T. Lee, *Is Multiphoton Dissociation of Molecules a Statistical Thermal Process?*, Physical Review Letters, 1978, **40**, 115-118.

68. J. Roithova, *Characterization of reaction intermediates by ion spectroscopy*, Chem. Soc. Rev., 2012, **41**, 547-559.
69. N. C. Polfer, *Infrared multiple photon dissociation spectroscopy of trapped ions*, Chem. Soc. Rev., 2011, **40**, 2211-2221.
70. T. D. Fridgen, *Infrared consequence spectroscopy of gaseous protonated and metal ion cationized complexes*, Mass Spectrom. Rev., 2009, **28**, 586-607.
71. D. W. Lupo and M. Quack, *IR-laser photochemistry*, Chem. Rev., 1987, **87**, 181-216.
72. S. L. Chin, *Multiphoton Ionization of Molecules*, Physical Review A, 1971, **4**, 992-996.
73. D. Schröder, H. Schwarz, P. Milko and J. Roithová, *Dissociation Routes of Protonated Toluene Probed by Infrared Spectroscopy in the Gas Phase†*, J. Phys. Chem. A, 2006, **110**, 8346-8353.
74. A. Simon, C. Joblin, N. Polfer and J. Oomens, *Infrared Spectroscopy of [XFeC24H12]+ (X = C5H5, C5(CH3)5) Complexes in the Gas Phase: Experimental and Computational Studies of Astrophysical Interest*, J. Phys. Chem. A, 2008, **112**, 8551-8560.
75. S. Dillinger, J. Mohrbach, J. Hewer, M. Gaffga and G. Niedner-Schatteburg, *Infrared spectroscopy of N2 adsorption on size selected cobalt cluster cations in isolation*, PCCP, 2015, **17**, 10358-10362.
76. J. Jašík, J. Žabka, J. Roithová and D. Gerlich, *Infrared spectroscopy of trapped molecular dications below 4K*, Int. J. Mass spectrom., 2013, **354–355**, 204-210.
77. A. B. Wolk, C. M. Leavitt, E. Garand and M. A. Johnson, *Cryogenic Ion Chemistry and Spectroscopy*, Acc. Chem. Res., 2013, **47**, 202-210.
78. C. J. Johnson, A. B. Wolk, J. A. Fournier, E. N. Sullivan, G. H. Weddle and M. A. Johnson, *Communication: He-tagged vibrational spectra of the SarGlyH+ and H+(H2O)2,3 ions: Quantifying tag effects in cryogenic ion vibrational predissociation (CIVP) spectroscopy*, J. Chem. Phys., 2014, **140**, -.
79. J. Jašík, D. Gerlich and J. Roithová, *Two-Color Infrared Predissociation Spectroscopy of C6H62+ Isomers Using Helium Tagging*, J. Phys. Chem. A, 2015, **119**, 2532-2542.
80. Y. Nosenko, F. Menges, C. Riehn and G. Niedner-Schatteburg, *Investigation by two-color IR dissociation spectroscopy of Hoogsteen-type binding in a metalated nucleobase pair mimic*, PCCP, 2013, **15**, 8171-8178.
81. J. Lang, M. Gaffga, F. Menges and G. Niedner-Schatteburg, *Two-color delay dependent IR probing of torsional isomerization in a AgL1L2 (+) complex*, PCCP, 2014, **16**, 17417-17421.
82. F. Neese, *Prediction of molecular properties and molecular spectroscopy with density functional theory: From fundamental theory to exchange-coupling*, Coord. Chem. Rev., 2009, **253**, 526-563.
83. I. Ciofini and C. A. Daul, *DFT calculations of molecular magnetic properties of coordination compounds*, Coord. Chem. Rev., 2003, **238–239**, 187-209.
84. S. A. McLuckey and D. E. Goeringer, *SPECIAL FEATURE:TUTORIAL Slow Heating Methods in Tandem Mass Spectrometry*, J. Mass Spectrom., 1997, **32**, 461-474.
85. K. Biemann and H. Scoble, *Characterization by tandem mass spectrometry of structural modifications in proteins*, Science, 1987, **237**, 992-998.
86. K. R. Jennings, *The changing impact of the collision-induced decomposition of ions on mass spectrometry*, Int. J. Mass spectrom., 2000, **200**, 479-493.
87. R. G. Cooks, *Special feature: Historical. Collision-induced dissociation: Readings and commentary*, J. Mass Spectrom., 1995, **30**, 1215-1221.

88. F. Busch and W. Paul, *Isotopentrennung mit dem elektrischen Massenfilter*, Z. Physik, 1961, **164**, 581-587.
89. K. Biemann and S. A. Martin, *Mass spectrometric determination of the amino acid sequence of peptides and proteins*, Mass Spectrom. Rev., 1987, **6**, 1-75.
90. R. Aebersold and D. R. Goodlett, *Mass Spectrometry in Proteomics*, Chem. Rev., 2001, **101**, 269-296.
91. D. Schröder, S. Shaik and H. Schwarz, *Two-State Reactivity as a New Concept in Organometallic Chemistry*, Acc. Chem. Res., 2000, **33**, 139-145.
92. C. Kerner, J. Lang, M. Gaffga, F. S. Menges, Y. Sun, G. Niedner-Schatteburg and W. R. Thiel, *Mechanistic Studies on Ruthenium(II)-Catalyzed Base-Free Transfer Hydrogenation Triggered by Roll-Over Cyclometalation*, ChemPlusChem, 2017, **82**, 212-224.
93. D. R. Carl, B. K. Chatterjee and P. B. Armentrout, *Threshold collision-induced dissociation of Sr2+(H2O)x complexes (x=1–6): An experimental and theoretical investigation of the complete inner shell hydration energies of Sr2+*, J. Chem. Phys., 2010, **132**, 044303.
94. F. Falvo, L. Fiebig, F. Dreiocker, R. Wang, P. B. Armentrout and M. Schäfer, *Fragmentation reactions of thiourea- and urea-compounds examined by tandem MS-, energy-resolved CID experiments, and theory*, Int. J. Mass spectrom., 2012, **330–332**, 124-133.
95. B. R. Bzdek, J. W. DePalma, D. P. Ridge, J. Laskin and M. V. Johnston, *Fragmentation Energetics of Clusters Relevant to Atmospheric New Particle Formation*, J. Am. Chem. Soc., 2013, **135**, 3276-3285.
96. J. Laskin, R. P. W. Kong, T. Song and I. K. Chu, *Effect of the basic residue on the energetics and dynamics of dissociation of phosphopeptides*, Int. J. Mass spectrom., 2012, **330–332**, 295-301.
97. G. E. Johnson, T. Priest and J. Laskin, *Size-dependent stability toward dissociation and ligand binding energies of phosphine ligated gold cluster ions*, Chem. Sci., 2014, **5**, 3275-3286.
98. E.-L. Zins, D. Rondeau, P. Karoyan, C. Fosse, S. Rochut and C. Pepe, *Investigations of the fragmentation pathways of benzylpyridinium ions under ESI/MS conditions*, J. Mass Spectrom., 2009, **44**, 1668-1675.
99. E.-L. Zins, C. Pepe, D. Rondeau, S. Rochut, N. Galland and J.-C. Tabet, *Theoretical and experimental study of tropylium formation from substituted benzylpyridinium species*, J. Mass Spectrom., 2009, **44**, 12-17.
100. K. V. Barylyuk, K. Chingin, R. M. Balabin and R. Zenobi, *Fragmentation of Benzylpyridinium "Thermometer" Ions and Its Effect on the Accuracy of Internal Energy Calibration*, J. Am. Soc. Mass. Spectrom., 2010, **21**, 172-177.
101. A. Scherz, H. Wende and K. Baberschke *Fine structure of X-ray magnetic circular dichroism for early 3d transition metals*, Appl. Phys. A, 2004, **78**, 843-846.
102. J. Bansmann, A. Kleibert, M. Getzlaff, A. F. Rodríguez, F. Nolting, C. Boeglin and K.-H. Meiwes-Broer, *Magnetism of 3d transition metal nanoparticles on surfaces probed with synchrotron radiation – from ensembles towards individual objects*, physica status solidi (b), 2010, **247**, 1152-1160.
103. J. T. Lau, A. Föhlisch, M. Martins, R. Nietubyc, M. Reif and W. Wurth, *Spin and orbital magnetic moments of deposited small iron clusters studied by x-ray magnetic circular dichroism spectroscopy*, New Journal of Physics, 2002, **4**, 98.
104. C. T. Chen, Y. U. Idzerda, H. J. Lin, N. V. Smith, G. Meigs, E. Chaban, G. H. Ho, E. Pellegrin and F. Sette, *Experimental Confirmation of the X-Ray Magnetic Circular*

Dichroism Sum Rules for Iron and Cobalt, Physical Review Letters, 1995, **75**, 152-155.

105. B. T. Thole, P. Carra, F. Sette and G. van der Laan, *X-ray circular dichroism as a probe of orbital magnetization*, Physical Review Letters, 1992, **68**, 1943-1946.
106. P. Carra, B. T. Thole, M. Altarelli and X. Wang, *X-ray circular dichroism and local magnetic fields*, Physical Review Letters, 1993, **70**, 694-697.
107. S. T. Akin, V. Zamudio-Bayer, K. Duanmu, G. Leistner, K. Hirsch, C. Bülow, A. Ławicki, A. Terasaki, B. v. Issendorff, D. G. Truhlar, J. T. Lau and M. A. Duncan, *Size-Dependent Ligand Quenching of Ferromagnetism in Co3(benzene)n+ Clusters Studied with X-ray Magnetic Circular Dichroism Spectroscopy*, The Journal of Physical Chemistry Letters, 2016, **7**, 4568-4575.
108. J. Meyer, M. Tombers, C. v. Wüllen, G. Niedner-Schatteburg, S. Peredkov, W. Eberhardt, M. Neeb, S. Palutke, M. Martins and W. Wurth, *The spin and orbital contributions to the total magnetic moments of free Fe, Co, and Ni clusters*, J. Chem. Phys., 2015, **143**, 104302.
109. V. Zamudio-Bayer, R. Lindblad, C. Bülow, G. Leistner, A. Terasaki, B. v. Issendorff and J. T. Lau, *Electronic ground state of Ni2+*, J. Chem. Phys., 2016, **145**, 194302.
110. S. Schmitt, *Berechnung der Magnetischen Anisotropie mit Hilfe von ein- und zweikomponentigen dichtefunktionaltheoretischen Rechnungen: Weiterentwicklung vorhandener Methoden und Anwendung auf mehrkernige Übergangsmetallkomplexe*, PhD Thesis, Technische Universität Kaiserslautern, 2015.
111. E. M. V. Kessler, S. Schmitt and C. van Wüllen, *Broken symmetry approach to density functional calculation of zero field splittings including anisotropic exchange interactions*, J. Chem. Phys., 2013, **139**, 184110.
112. M. Tombers, J. Meyer, A. Lawicki, V. Zamdio-Bayer, E. K. T. Lau, C. van Wüllen and G. Niedner-Schatteburg, *Single Molecule Magnetism in Isolation - X-Ray magnetic circular dichroism (XMCD) spectroscopy of gaseous [Mn12ac]+*, under review in Nature - Communications.

2 Experimental and Computational Methods

2.1 Electrospray Ionization (ESI)

Electrospray Ionization (ESI) is a widely used method to transfer molecular ions from solution into the gas phase[1, 2] with minimal fragmentation of the analyte ions. It has enabled mass spectrometric investigations on biomolecules[3, 4] as well as on transition metal (TM) complexes[5]. ESI ion sources have been continuously advanced in the last decades[6-8] in order to generate labile non covalent complexes[9, 10] or intermediate structures from catalytic cycles [11-13].

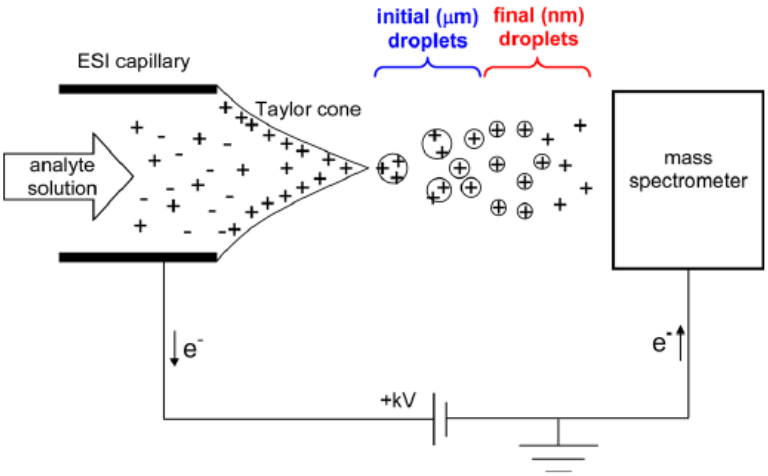

Scheme 1: Release of charged droplets and ions by the Electrospray Ionization (ESI) process[14].

On a fundamental level, ESI proceeds as follows (cf. Scheme 1): An analyte solution flows into an ESI capillary (also called spray needle). A power supply generates a strong electrostatic field between the capillary and the orifice of the mass spectrometer. This electrophoretically separates cations and anions within the solution and leads to the formation of a Taylor Cone[15, 16] at the exit of the capillary. The tip of the Taylor Cone releases charged droplets as soon as the coulomb repulsion between the ions within the solution overcomes the surface tension of the solvent. Subsequently, the droplets shrink by thermal induced desolvation. Reaching the Rayleigh limit[17] the droplets undergo Coulomb explosions. Repeating this process, the analyte ions completely desolvate and remain as bare free molecular ions *in vacuo*. ESI-Models[18] like the charge residue model[19, 20] and the ion evaporation model[21, 22] describe the desolvation mechanism on a qualitative basis. Polar solvents with low boiling points suit the ESI process since they stabilize ions and facilitate the desolvation process.

2.1.1 Apollo II ESI Source

The Bruker Apollo II ESI source (cf. Fig. 1) is used in combination with the Bruker amazon SL mass spectrometer (cf. chapter 2.2.1) and the customized FRITZ tandem mass spectrometer (cf. chapter 2.2.2). An *ESI Sprayer (1)* houses the spray needle. Hamilton™ gas tight syringes serve to inject sample solutions into the spray needle through a peek capillary (inner diameter = 0.13 mm). A syringe pump provides a constant solution flow rate of 2 µl/min. A constant flow of nitrogen gas (nebulizer pressure ~400 mbar; flowrate ~2.5 L/min) along the spray needle supports the formation of small aerosol particles in the *Spray Chamber (2)*. An electrostatic field is generated by applying a high voltage (4.5 kV – 3.5 kV) on the *Spray Shield (3)* and grounding the spray needle. The *Glass Capillary (6)* serves as the entrance to the mass spectrometer. It is metal coated on both ends (platinum coating). Nitrogen gas heated by the *Dry Gas Heater (5)* (gas temperature ~220 °C) flows in the opposite direction of the droplet stream (4 - 6 L/min) and supports the desolvation of the ions. An electrostatic potential between the *Spray Shield (3)* and the *Glass Capillary (6)* focuses the ion to the capillary entrance. An additional electrostatic gradient between the entrance and exit coatings of the *Glass Capillary (6)* guides the charged particles into the vacuum of the vacuum of the subsequent instrumentation.

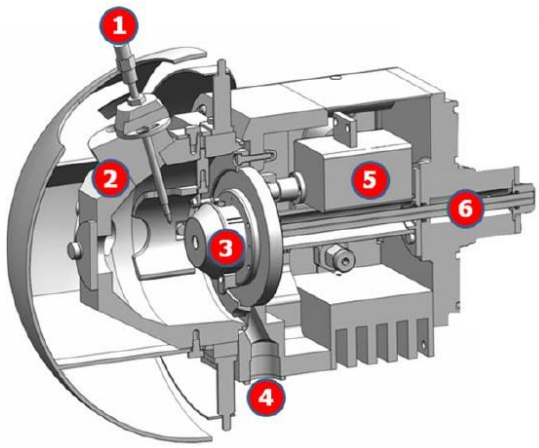

(1) ESI Sprayer
(2) Spray Chamber
(3) Spray Shield
(4) Waste
(5) Dry Gas Heater
(6) Glass Capillary

Figure 1: 3D model of the Bruker Apollo II ESI source[23].

2.1.2 Custom ESI Source

A custom ESI source[24, 25] developed by the research group of Thomas Schlathölter (University of Groningen, The Netherlands) is coupled to the NanoClusterTrap apparatus (cf. chapter 2.2.3). It consist of a stainless steel spray needle, a stainless steel transfer capillary and a home build radio frequency (RF) ion funnel[26]. Hamilton™ gas tight syringes serve to inject the sample solutions into the spray needle through a peek capillary (inner diameter = 0.13 mm). A syringe pump provides a constant solution flow rate of 2 µl/min. A x,y,z translation stage allows to optimize the position of the spray needle for maximum signal intensity. A voltage (3 - 3.5 kV) between the spray needle and the transfer capillary generates the electrostatic field needed for the ESI process. The transfer capillary is heated by an additional applied voltage of ~11 V to support desolvation. After passing the transfer capillary the ions are captured by a home build RF ion funnel consisting of 26 ion lenses with declining inner diameters. It operates at a frequency of ~250 kHz and peak to peak amplitudes of ~300 V. This alternating RF field is overlaid by a static voltage declining from the first to the last lens (120 V to 25 V). Passing the ion funnel the ions enter the vacuum of the experimental apparatus for further investigations.

2.2 Mass Spectrometric Instrumentation

Mass spectrometry is a versatile method allowing for the chemical analysis of gaseous ions[27-29]. It has as its basis the determination of mass-to-charge (m/z) ratios of these ions. A huge variety of analytical methods exploit m/z specific interactions of charged particles with electric and/or magnetic fields to extract its m/z ratios[30]. In addition, the ions can be trapped[31] within the vacuum of the instrument (ion traps). Paul type[32] traps as well as linear multipoles utilize RF voltages applied on metal rods (linear multipoles) or hyperbolic electrodes (Paul trap) to generate an alternating trapping potentials[33-37]. Wolfgang Paul has been awarded the Nobel Prize for Physics[38] in honor of this method. Fourier Transform Ion Cyclotron Resonance ion traps utilize homogenous magnetic fields[39-42] to trap the ions. The following chapters provide descriptions of the utilized mass spectrometric instrumentation of this work.

2.2.1 AmaZonSL Mass Spectrometer

The modified Bruker amaZonSL mass spectrometer serves to conduct Collision Induced Dissociation (CID) and InfraRed Multiple Photon Dissociation (IR-MPD) studies[43, 44]. It is equipped with an Apollo II ESI ion source (cf. chapter 2.1.1) and comprises several differentially pumped vacuum chambers (cf. Fig. 2). Gaseous ions exit the transfer capillary and enter the first vacuum stage (pressure ~1 mbar). A double arrangement of ion lenses with declining inner diameters forms a dual ion funnel. It focuses the voluminous ion cloud by combining radio RF and direct current (DC) voltages. The dual ion funnel is fitted "off axis", in relation to the exit of the transfer capillary. By this arrangement it blocks the flow of neutral gas molecules from the ESI source, thereby providing an optimal vacuum gradient. Two linear RF - octopoles serve to guide the focused ions to the final vacuum chamber (pressure ~ 10^{-6} mbar). A Paul type ion trap accumulates the ions and allows for their m/z determination and isolation.

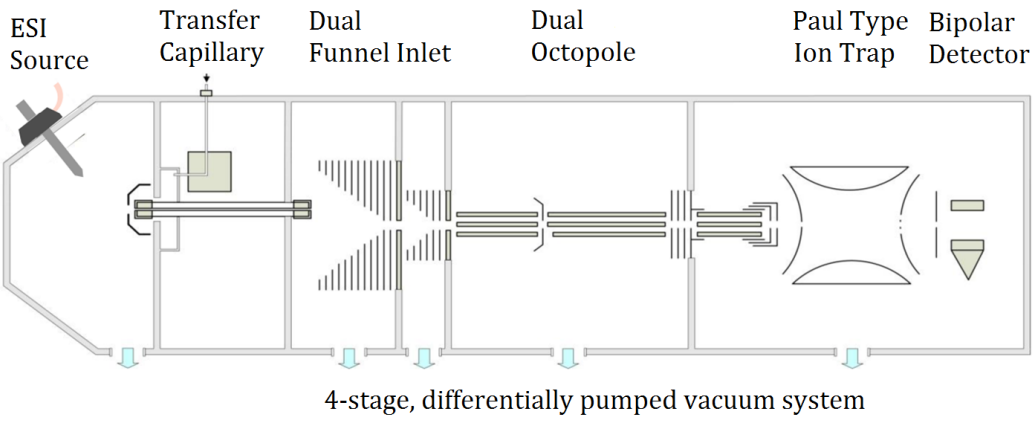

Figure 2: Schematic cross section of the Bruker amaZonSL mass spectrometer[23].

The Paul trap is a three dimensional quadrupole ion trap. It consists of a ring electrode and two end caps (cf. Fig 3) forming a nearly hyperbolic inner profile. The ions enter and exit the trap through pinholes in the end caps. A high voltage RF potential (781 kHz) is applied to the ring electrode, while the end caps are grounded. The resulting oscillating quadrupolar electric field allows for the accumulation of the ions within the three electrodes. Depending on the amplitude of the RF voltage, the field traps ions within a wide mass range. An auxiliary dipolar voltage is fed to either the exit cap or both end caps of for subsequent ion isolation and fragmentation. It is vital to slow down the arriving ions in order to trap them effectively. A proportional integral derivative (PID) gas controller maintains a partial Helium buffer gas pressure of ca. 10^{-3} mbar inside the

trap. The ions decelerate by collisions with the He atoms, which allows for their efficient trapping. It is possible to accumulate weak signals over an extended period of time. Typical accumulation times vary between 0.01 ms and 200 ms.

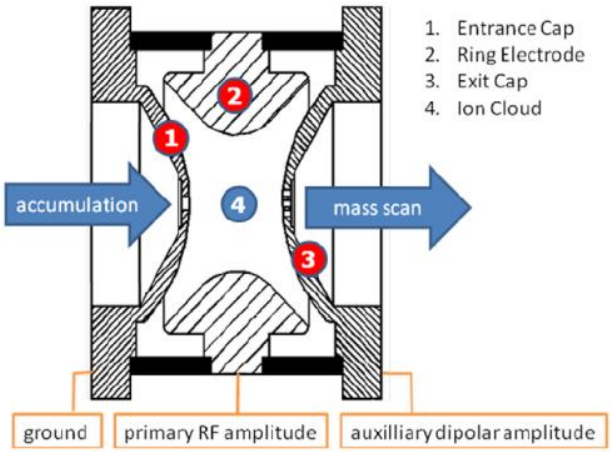

Figure 3: Schematic cross section of a Paul type ion trap[23].

The motion of ions in an electric field comprises oscillations in both the radial as well as the axial direction. The oscillations depend on the m/z ratios as well as on the field parameter (voltage, amplitude, frequency etc.). The solutions of the Mathieu equations[45] describe such motions analytically and provide a two dimensional stability diagram, which indicates stable orbits of ions within the trap (cf. Fig. 4). An orbit is stable if its oscillatory amplitudes in radial direction (described by the parameter β_r) and axial direction (described by the parameter β_z) lie between 0 and 1. Other orbits are unstable and the ions can collide with the walls of the ion trap. β_z and β_r are inversely proportional to the mass of the ions and directly proportional to the RF voltage. In a particular field the m/z ratio of an ion determines the stability of its orbit. The axial motion (β_z) is of primary importance because this is the direction of ion injection and ion ejection. In RF only mode (during accumulation of ions) the stability diagram reveals a boundary of stability along the line $\beta_z = 1$. This determines the lowest m/z ratio in the particular field, which allows for a stable orbit. All ions exhibiting lower m/z ration have unstable orbits. Therefore, the range of m/z ratios that can be stored simultaneously in the trap has a lower cut-off that is determined by the RF amplitude at the ring electrode. Theoretically, there is no upper limit to the storable mass range. However, for practical purposes and thermal reasons, there is an upper limit. This upper limit is about 20–30

times the lower cut-off m/z ratio. Ions with an m/z above this limit are not efficiently trapped by the RF field.

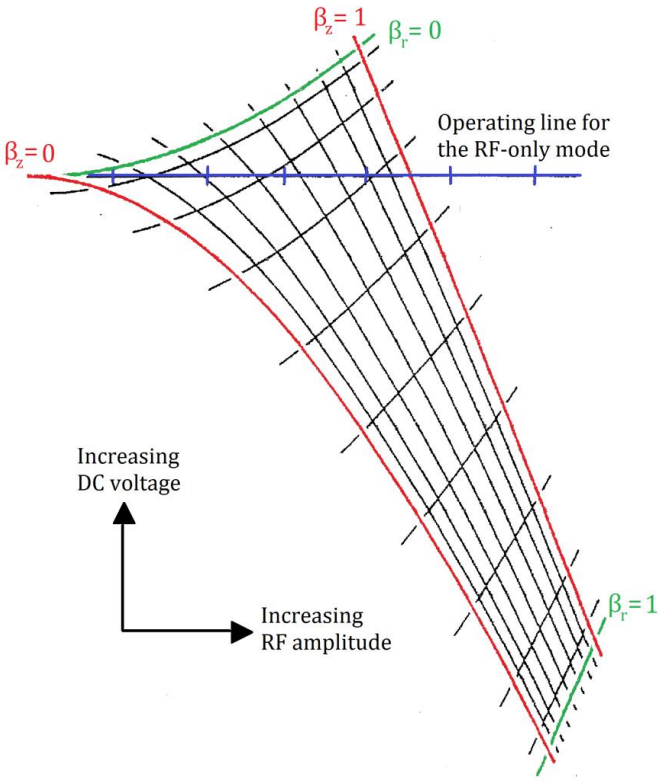

Figure 4: Stability diagram for ions in a Paul trap[36]. Oscillation in radial direction is described by the parameter β_r and the oscillation axial direction is described by the parameter β_z. Stable orbits exhibit $0 \leq \beta_r, \beta_z \leq 1$.

Variation of RF voltages in addition to applying DC voltages allows for the continuous ejection of the trapped ions under m/z control. The ejected ions are detected by a Daly detector[46]. A scan of ion ejection with various m/z rations yields a mass spectrum (MS Scan). Typical scan speeds lie around 32500 (m/z)/s (Ultrascan mode). This mode yields resolutions of ~0.3 FWHM / m/z. Isolation of ions with particular m/z ratios is possible by applying specific voltages, such that all other ions have instable orbits. A subsequent mass scan (MS^n scan; n = 2,3, ...) exhibits only the isolated species.

Several modifications of the amaZonSL mass spectrometer allow for IR-MPD experiments: Two pinholes drilled in the ring electrode of the Paul trap create an optical path through the center of the ion trap passing the ion cloud (cf. Fig. 5). The holes tamper from 6 mm on the outer side to 2 mm on the inner side to limit Helium loss of the trap. Associated windows and mirrors have been installed to guide the laser beam inside and outside the mass spectrometer. The software of the instrument has been

updated to allow for a synchronization of the duty cycle of the mass spectrometer to the 10 Hz trigger signal of the pump laser. Further details on the modifications of the amaZonSL mass spectrometer are available in the PhD thesis of Fabian S. Menges[47].

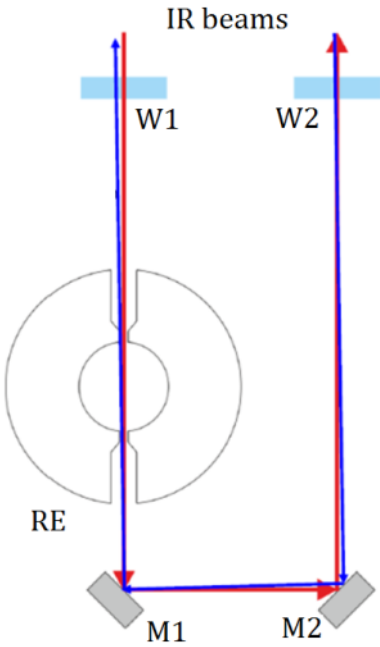

Figure 5: Scheme of the modified ring electrode (RE) of the Paul trap. IR laser beams pass the BaF_2 windows (W1, W2) and are reflected by two mirrors (M1, M2).

2.2.2 FRITZ - Tandem Mass Spectrometer

The customized Fourier Transform-Ion Cyclotron Resonance (FT-ICR)-mass spectrometer[48-50] "FRITZ" (cf. Fig. 6) serves to conduct temperature controlled IR-(M)PD studies. It is based on a Bruker Apex Ultra FT-ICR and is equipped with an Apollo 2 ESI source (cf. chapter 2.1.1). An additional Laser VAPorization Source[51, 52] (LVAP) stands by, but was not utilized in this work. The ESI generated ions are injected into a cryogenic hexapole ion trap passing different ion lenses, a 90 degrees ion beam bender and a quadrupole mass filter.

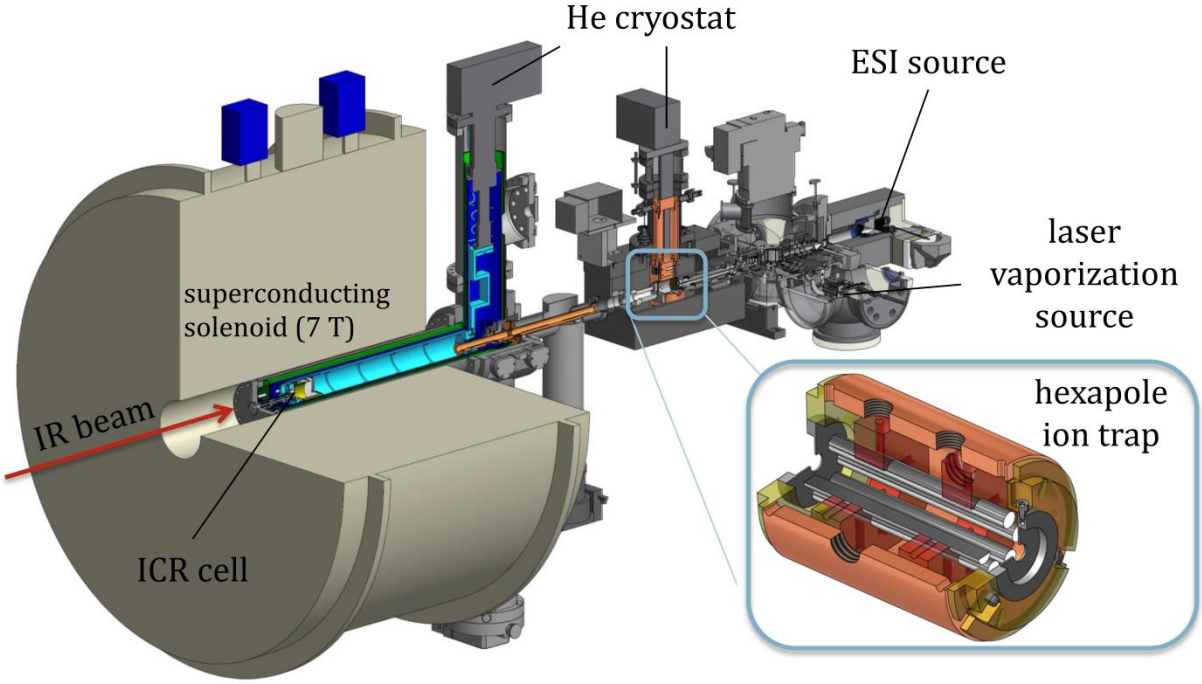

Figure 6: 3 D model of the FRITZ setup[52]. The inset shows a 3 D model of the hexapole ion trap.

The hexapole is cooled by a two stage closed cycle Helium cryostat (Sumitomo SRDK-101E). Two sensors (LakeShore, Cernox™) monitor the temperature of both cooling stages. Heating resistors (Catridge Heater, Janis Research, R = 50 Ω) in combination with a temperature controller (LakeShore, model 336) provide a constant temperature of 26 K for the measurements of this thesis. Lower temperatures up to 11 K are possible. Buffer and/or reaction gas can be introduced into the hexapole both pulsed and continuously. In this work two continuous gas inlets were used. The pressure is first increased by N_2 gas from 1.7×10^{-7} mbar up to 3.0×10^{-7} mbar and subsequently increased with He gas up to 4.0×10^{-6} mbar to accomplish N_2 attachment as well as efficient trapping and cooling of the ions. Storage of the ions for a variable time (0–10 s)

allows them to react with N_2. The product ions are guided by electrostatic lenses into the FT-ICR cell of the "infinity" type[53]. This cell is cooled at a temperature of about 10 K with a two stage closed cycle Helium cryostat (Sumitomo) to prevent heating of the ions by black body radiation. Three temperature sensors (LakeShore, CernoxTM) monitor the temperature within the ultra high vacuum region.

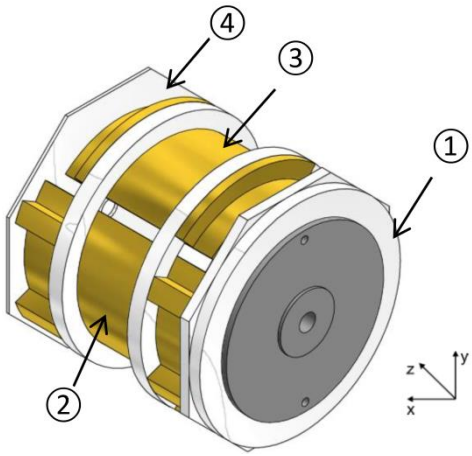

Figure 7: Infinity™ type ICR Cell: (1) front trapping plate, (2) excitation plate, (3) detection plate, (4) back trapping plate[52].

The ICR cell (cf. Fig. 7) is located in the high field region (7 T) of a superconducting solenoid and serves to trap, isolate and mass analyze the ions of interest. It consists of six plates. The ions enter the cell through the front plate. The strong magnetic field induces Lorentz forces on the ions which lead to a circular ion trajectory within the trap[54-56]. Electrostatic fields applied to the front and back plate serve to trap the ions. A RF is applied to the two excitation plates. Frequency sweeps applied to the excitation plates accelerate the ions on their trajectory. As a result, their orbits increase while they retain their specific cyclotron frequency. Ions passing the two detection plates induce an image current. Recording the time dependence of these signals yields a spectrum in the frequency domain. Fourier transformation of this data yields a mass spectrum of the trapped ions. Frequency sweeps can also be applied to eliminate ions with unwanted m/z ratios from the trap and therefore isolate ions of interest. A BaF_2 window on the backside of the high vacuum chamber and a hole in the back trapping plate of the ICR cell provide optical access to the isolated ions in order to conduct IR-(M)PD experiments. Further instrumentational details of the FRITZ tandem mass spectrometer are available in the PhD thesis of Jennifer Mohrbach[52].

2.2.3 NanoClusterTrap

The custom build NanoClusterTrap instrument[57-60] (cf. Fig. 8) serves to measure X-ray absorption (XAS) and XMCD spectra of isolated TM complexes and clusters. It has been build by the groups of Thomas Möller, Bernd von Issendorff and Tobias Lau and is located at the UE52-PGM beamline at the BESSY II (Helmhotz Zentrum Berlin) synchroton facility. In this work the NanoClusterTrap is coupled with a custom build ESI - ion source (cf. chapter 2.1.2) kindly provided by the group of Thomas Schlathölter, University of Groningen.

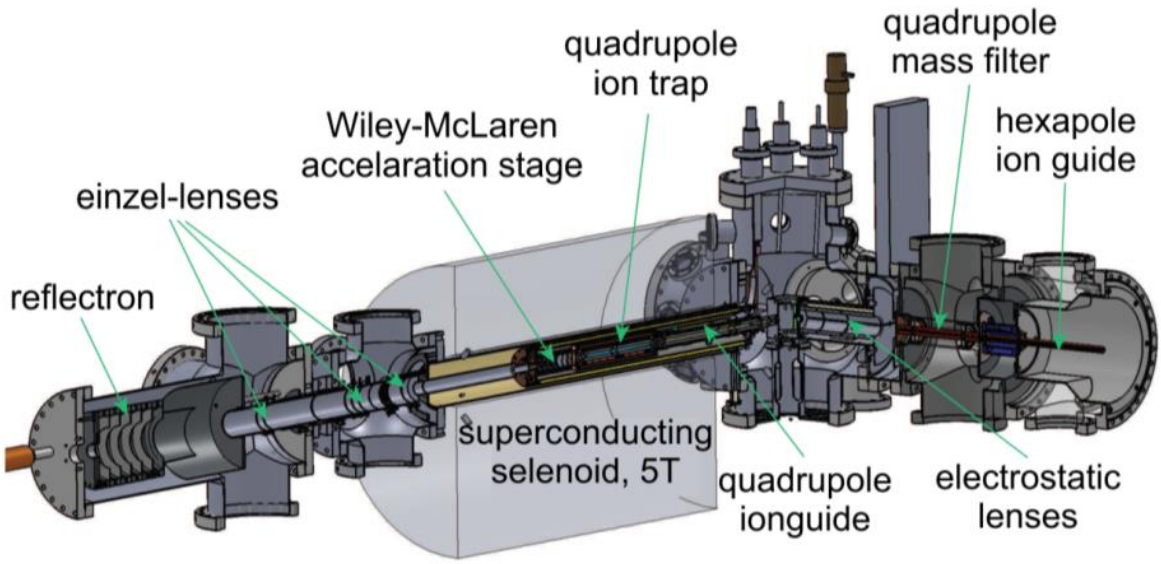

Figure 8: Schematic cross section of the NanoClusterTrap instrument[61]. The ESI ion source is omitted for clarity.

Gaseous ions of interest are mass selected in a linear quadrupole mass filter (Extrel, 40-4000 m/z) and transported through several electrostatic lenses into the quadrupole ion bender. It bends the ion beam by 90 ° onto the axis of the superconducting solenoid and the X-ray propagation direction. The electrostatic lenses compensate for deflection of the ions by the stray field of the superconducting solenoid. Passing the ion bender the ions are constantly injected into a (liquid helium cooled) linear quadrupole (cf. Fig 9), where they are stored for cooling and irradiation by the X-Ray beam. The trap is operated between 2 and 4 MHz (~500 V peak to peak voltage) depending on the mass of the investigated ions. The quadrupolar electric field of the linear quadrupole focuses the ions to the X-Ray beam axis benefitting the overlap between the light and ion cloud. Static potential on entrance and exit plate serve for axial ion trapping. Evaporation of the liquid Helium (pressure of ~8 x 10^{-7} mbar within the vacuum chamber) cools down

the ion trap to cryo temperatures around 4 K. Collisional cooling of the trapped ions leads to thermalized ions at slightely elevated temperatures of ~15 K[62] due to RF heating. The ion cooling is necessacy to reduce temperature induced orientation randomization of the magnetic moments of the investigated species. The ion trap is located inside the high field region of a superconducting solenoid (up to 5 - 4.5 T) to allign the magnetic moments of the investigated ions to the light pass of the X-Ray beam. Accordinglly, all rods and side electrodes of this linear quadrupole are made of non-magnetic molybdenum. Irradiation of the ions with circularly polarized X-Ray radiation from the UE52-PGM beamline (10 - 15 s irradiation time per set photon energy) leads to their fragmentation. After Irradiation the parent ions as well as the associated fragment ions are ejected from the ion trap into an in line reflectron time of flight mass spectrometer (~100 Hz) to record the resulting mass spectra, specifically to record the intensity of the X-Ray induced fragments. Further instrumentational details of the NanoClusterTrap is available in the PhD thesis of Andreas. Langenberg[61].

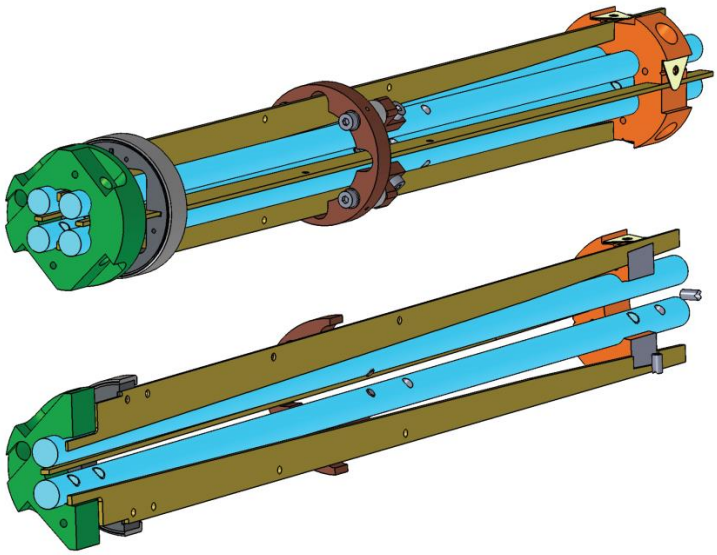

Figure 9: Schematic drawing of the cryogenically cooled quadrupole of the NanoClusterTrap[61]. It comprises four parallel rods (d = 6 mm, L = 25 cm) along with four side electrodes, which increase trapping efficiency. The rods and side electrodes are made of non-magnetic molybdenum, since the quadrupole is located in the high field region of a superconducting solenoid.

2.3 Light Sources

2.3.1 Optical Parametric Oscillator/Amplifier IR Laser Systems

The wavelength of laser radiation can be converted within non linear optical crystals by means of second order non linear optical interaction[63]. This provides an approach to tune the frequency of laser radiation[64]. Non linear optical process demand very intensive and coherent light (laser light) as pump sources, since their frequency conversion efficiency is intrinsically low[65]. An optical parametrical oscillator[66] (OPO) essentially consists of a non linear optical crystal and an optical resonator (e.g. two mirrors). It converts one entering "pump photon" into two photons with lower photon energies, called signal and idler photons. Changing the incident angle between laser beam and crystal surface allows to tune the outgoing signal and idler frequencies by phase matching[67]. An optical parametric amplifier[68] (OPA) consists of one or several non linear crystals and serves to amplify seeded (tunable) laser light. The generation of intensive and tunable laser radiation makes OPO/OPA laser systems extremely useful for laser spectroscopic investigations[69].

In this work, two commercially available "Dean Guyer LaserVision" OPO/OPA IR laser systems[70] enable (two color) IR-(M)PD investigations on isolated TM complexes. The laser systems are coupled to the amaZonSL (cf. chapter 2.2.1) as well as the FRITZ (cf. chapter 2.2.3) instruments and provide identical frequency conversion schemes (cf. Scheme 2 and Figure 10):

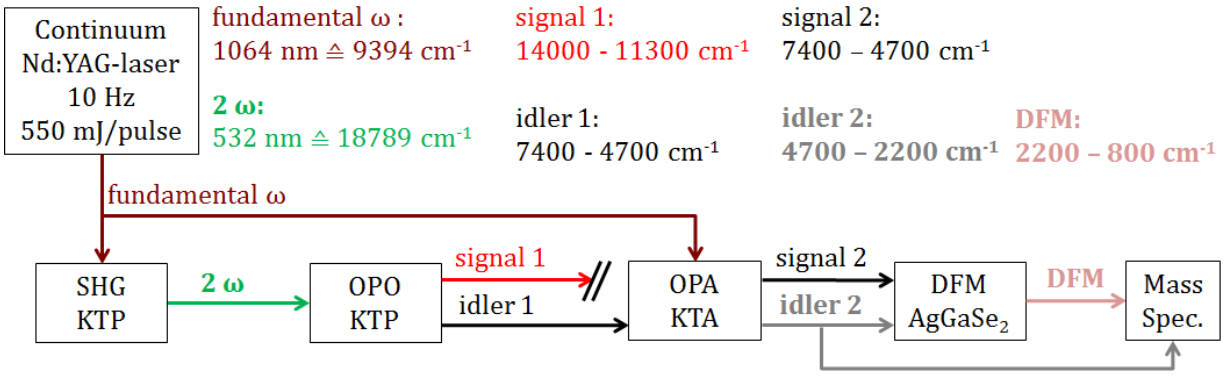

Scheme 2: Non linear optical processes and frequency conversions of the LaserVision OPO/OPA laser systems. Potassium titanyl phosphate (KTP) crystals serve for second harmonic generation (SHG) and for the optical parametric oscillator (OPO) process. Potassium titanyl arsenate (KTA) crystals serve for the optical parametrical amplification (OPA) process. $AgGaSe_2$ crystals enable difference frequency mixing (DFM).

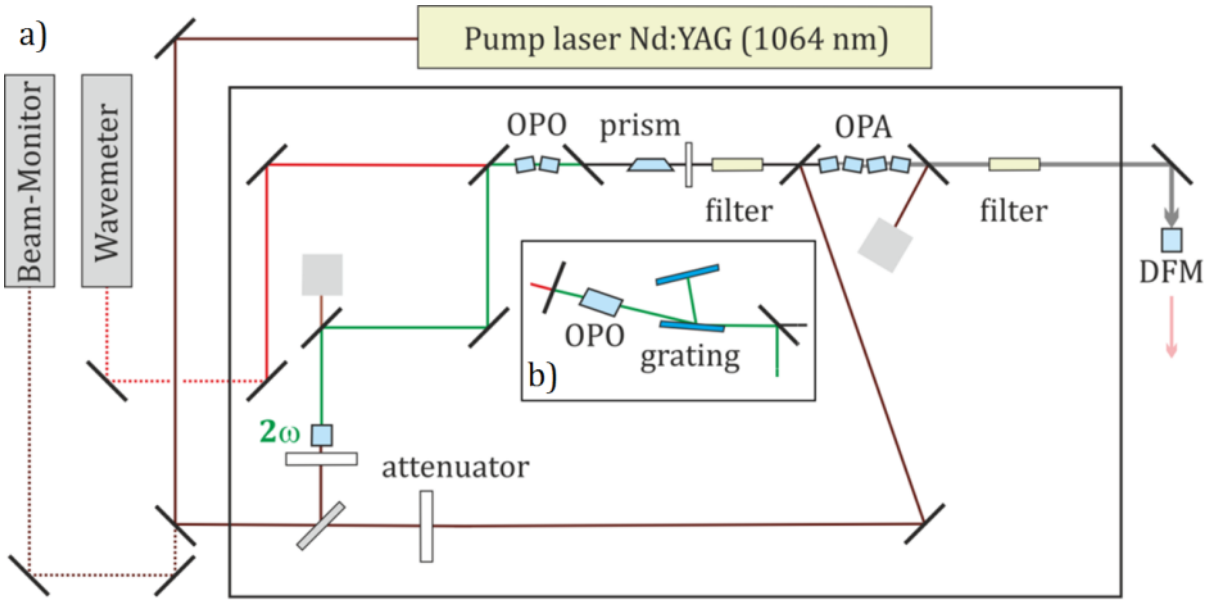

Figure 10: a) Optical setup of the LaserVision broadband OPO/OPA laser system. Lines and arrow indicate the pathway of the incoming and outcoming laser beam. **b)** The inset shows the OPO configuration for the narrowband system.

An injection seeded Nd:YAG laser (Continuum-PL8000; 10 Hz, 540 – 560 mJ/pulse) provides intensive fundamental laser radiation pulses at 1064 nm (9394 cm^{-1}) and a pulse length of ~7 ns. This fundamental beam ω pumps the OPO/OPA system. A beam splitter guides one third of the ω photons to a potassium titanyl phosphate crystal (KTP) for second harmonic generation[65](SHG). The intensity of the fundamental beam ω can be attenuated by a λ/2 wave plate. Two ω photons of the pump beam combine to one photon with the doubled frequency 2ω (532 nm, 18789 cm^{-1}). The 2ω beam enters the OPO resonator. The OPO converts one entering 2ω photon into two photons: a signal 1 and an idler 1 photon. Per definition, the frequency of the signal photon is higher than the frequency of the idler photon. The frequency (ν) of these photons can be tuned by varying the incident angle between the 2ω beam and the surface of the KTP crystal. The photon energy sum of signal 1 and an idler 1 has to be identical to the photon energy of 2ω (cf. eq. 1 and 2) due to energy conservation.

$$2\omega = 532\ nm = \nu_{Signal\ 1} + \nu_{Idler\ 1} \qquad (1)$$

$$2\omega = 18789\ cm^{-1} = \tilde{\nu}_{Signal\ 1} + \tilde{\nu}_{Idler\ 1} \qquad (2)$$

A silicon filter blocks the signal 1 beam and the idler 1 beam enters the OPA stage consisting of four potassium titanyl arsenate (KTA) crystals. Within the OPA stage the

idler 1 beam overlaps with two thirds of the fundamental beam ω. By the OPA process the ω photon splits in two photons, a signal 2 and an idler 2 photon. The idler 1 beam is amplified by this process since the generated signal 2 photon has the same frequency as the idler 1 photon (cf. eq. 3 to 5). Thus the frequency of idler 1 determines the frequency of the new photon called idler 2. The intensity of the OPA output can be attenuated by a λ/2 wave plate and a thin film polarizer.

$$v_{Idler\,1} = v_{Signal\,2} \tag{3}$$

$$1064\,nm = v_{Signal\,2} + v_{Idler\,2} \tag{4}$$

$$9394\,cm^{-1} = \tilde{v}_{Signal\,2} + \tilde{v}_{Idler\,2} \tag{5}$$

The idler 2 and signal 2 beams exhibit different linear polarizations of their electric field vectors. A silicon filter tuned to the associated Brewster angle selectively filters out either the signal 2 or the idler 2 beam. This provides IR laser light radiation in the spectral range of 7400–2200 cm^{-1} (idler 2: 2200 - 4700 cm^{-1}; signal 2: 4700 - 7400 cm^{-1}). Difference frequency mixing[71] (DFM) of the idler 2 and signal 2 beams in an $AgGaSe_2$ crystal generates an new beam, whose frequency ($\tilde{v}_{DFM}$) is the difference frequency of the idler 2 and signal 2 photons (cf. eq. 6). The DFM process extends the available spectral range to 800 - 2200 cm^{-1}. Residual idler 2 and/or signal 2 photons are filtered out by a ZnSe filter.

$$\tilde{v}_{DFM} = \tilde{v}_{Signal\,2} - \tilde{v}_{Idler\,2} \tag{6}$$

The two utilized laser systems differ by their OPO resonators (cf. Fig. 10). The “broadband” OPO consists of two potassium titanyl phosphate (KTP) crystals within the optical resonator. The “narrowband” OPO consists of one larger KTP crystal and implements a grating within its optical resonator (cf. Fig. 10b). The grating reduces the linewidth of the resulting radiation[72] enabling a resolution of < 0.3 cm^{-1} (hence the name “narrowband”). The broadband OPO provides a spectral resolution of ~0.9 cm^{-1}. Both lasers are synchronized with each other and the mass spectrometers by a delay generator (Stanford Research Systems, DG645). The wavelengths of the OPO outputs are calibrated and monitored of by wave meters (Bristol Instruments: 821B-NIR and TopticaPhotonics: HighFinesse IRII-WS7). Power detector heads (i.a. gentec-eo. UP-19K-H5D0) serve to record pulse energies during scanning. The beam profiles of the pump lasers are continuously monitored by beam profiler cameras (WinCamD, DataRay Inc) to avoid hot spots.

2.3.2 X-Ray Synchrotron Radiation @ BESSY II (UE52-PGM Beamline)

Large scale synchrotron facilities provide very intense and coherent light in a wide spectral range[73]. Brilliant synchrotron X-Ray radiation[74] is very useful for various analytical and spectroscopic applications[75, 76]. Electrons are accelerated to relativistic energies and transferred into a storage ring. Dipole magnets bend the electron beam path into a circular trajectory, due to radial acceleration of the electrons within these dipoles. Concurrently the electrons emit characteristic synchrotron radiation, which is monochromatized and used for subsequent experiments. Within the straight sections of the storage ring additional instruments called "undulators" provide an additional approach to generate synchrotron radiation. Undulators consist of several neighboring permanent magnets with alternating polarity. The magnet field accelerates the electrons and induces an oscillatory electron motion (cf. Fig. 11), which induces the emission of synchrotron radiation. The (tunable) gap between the magnets within the undulator determines the emitted photon energy[77].

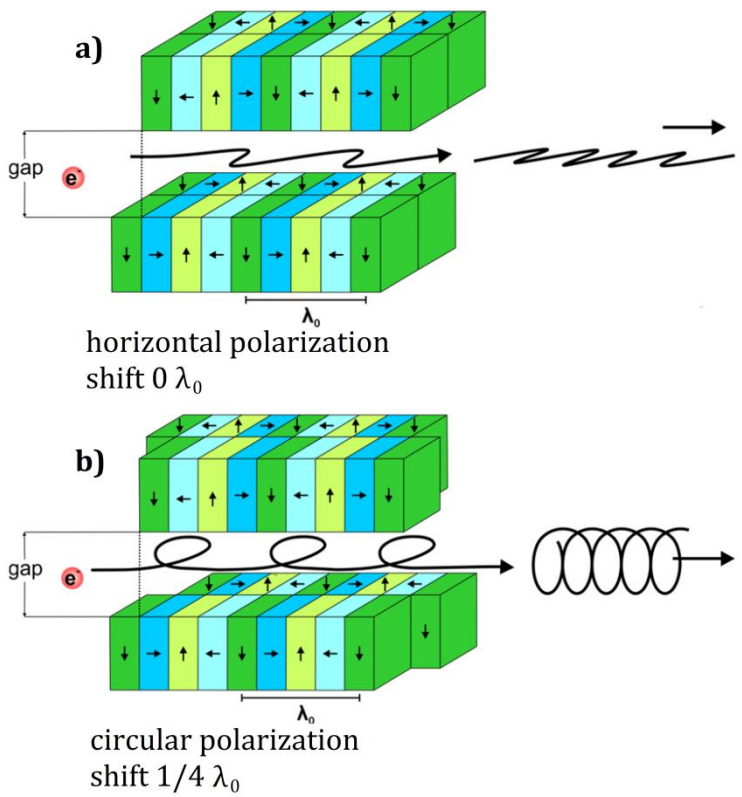

Figure 11: Arrangement of the permanent magnets within an APPLE 2[78, 79] (advanced planar polarized light emitter) undulator[77]. **a)** Horizontal photon polarization. **b)** Circular photon polarization.

The NanoClusterTrap (cf. chapter 2.2.3) is connected to the UE52-PGM undulator beamline at the BESSY II synchrotron facility of the Helmholtz Zentrum in Berlin. An APPLE2[78, 79] (advanced planar polarized light emitter) undulator (cf. Fig. 11) provides photons with variable polarization in the soft X-Ray spectral range (85 – 1600 eV). The APPLE 2 undulator consists of four rows of permanent magnets of alternating polarizations. Al rows can be shifted independently from each other. Depending on the arrangement of these magnets the APPLE 2 undulator generates horizontal or circularly (left or right handed) polarized X-Ray photons. A grating serves to provide monochromatic light with photon fluxes of 10^{12} photons/s. New electrons are constantly injected into the storage ring to compensate electron loss by collisions with the tube or residual gas. In the "top up" operation the storage ring exhibits a constant current of 300 mA.

2.4 InfraRed (Multiple) Photon Dissociation (IR-(M)PD)

The vibrational fingerprint of a molecule provides vital information to understand its structure and reactivity[80]. Electrospray Ionization Mass Spectrometry (ESI-MS) allows to transfer molecular ions into the gas phase (cf. chapter 2.1 and 2.2). Isolation of these molecular ions enables their investigation without any solvent influences. However, classical absorption spectroscopy methods reach their limits, since the ion density in the gas phase is often too low (< 10^8 cm^{-3}) to observe a light attenuation due to absorption[81].

InfraRed-(Multiple) Photon Dissociation[82] (IR-(M)PD) spectroscopy provides an "action spectroscopy" type approach to record vibrational spectra of isolated molecular ions. Absorption of a single or multiple IR photons results in a fragmentation (change of the m/z ratio) of the isolated ion, which is detected by a mass spectrometer. IR photon energies lie in a range of 10-50 kJ/mol (800 - 4000 cm^{-1}), which is sufficient to break noncovalent bonds, e.g. hydrogen bonds[83] or messenger tags[84, 85]. The cleavage of stronger (covalent) bonds requires the absorption of multiple IR photons to pump enough energy into the molecule[86, 87]. This makes the usage of coherent and intensive IR laser light sources (cf. chapter 2.3) mandatory.

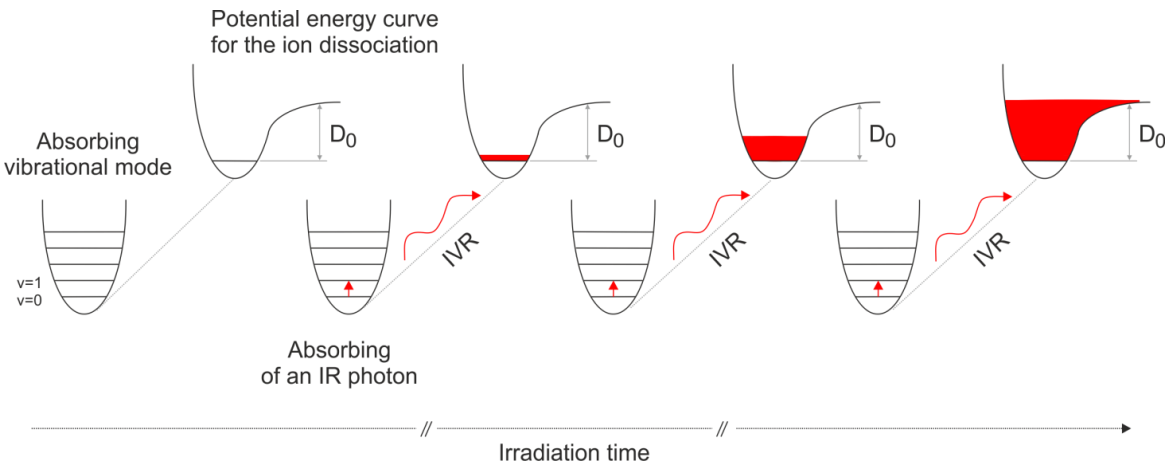

Scheme 3: Representation of the non-coherent IR-MPD processes[88]: A resonant IR photon is absorbed by the isolated ion. The additional energy is redistributed within the ion by internal vibrational redistribution[89] (IVR). This process repeats until the dissociation limit of the ion is exceeded and it fragmentizes. The irradiation time is ~ 7 ns (a single IR laser pulse).

An isolated molecular ion absorbs one IR photon if the photon frequency is in resonance with a molecular energy transition (cf. Scheme 3). In the non-coherent IR-MPD model internal vibrational redistribution[89] (IVR) rapidly results in dissipation of the additional energy into molecular vibrational degrees of freedom. This effectively heats up the isolated molecular ion. The original oscillation mode is thereby able to absorb additional IR photons. This process repeats until the molecular dissociation threshold is exceeded and it fragmentizes. The weakest bond of the ion breaks even if it has not been excited directly by the IR laser[90, 91], since the absorbed energy is stored in the entire molecular ion. The IR-(M)PD fragmentation yield ($Y(\nu)$) is defined by eq. (6).

$$Y(\nu) = \left(\frac{\sum_i I_i^{fr}(\nu)}{\sum_i I_i^{fr}(\nu) + \sum_i I_i^{p}(\nu)} \right) \qquad (6)$$

where I_i^{fr}= intensity of the fragment ions and I_i^{p}= intensity of the parent ions. An experimental IR-(M)PD spectrum arises from a plot of the fragmentation efficiency as a function of laser frequency (ν).

IR-(M)PD spectra provide a multitude of information on the isolated ions, which are to be compared with quantum chemical calculations to extract valuable structural information. In practice, the IR-(M)PD spectra combine with calculated linear absorption spectra of geometry optimized energy minimum structures. Note, that the IR-MPD band

intensities may not linearly dependent on the laser intensity and the absorption intensity of the oscillation mode due to the multi photon process. High dissociation thresholds and/or inefficient IVR processes may prevent fragmentation within one laser pulse. This may result in undetected vibrational bands[92, 93]. Utilizing two IR lasers in a resonant 2-color (2c)-IR-MPD scheme enhances fragmentation efficiency of TM complexes[94]. The wavelength of the additional laser (IR_{fix}) is set to a fixed frequency at resonant absorption, while the second laser scans the IR spectral region (IR_{scan}: 800 - 4000 cm^{-1}). This scheme allows to investigate isomer populations[95, 96] by systematically varying the temporal delay between the two laser pulses.

Within this work, 1c/2c-IR-(M)PD measurements have been performed utilizing the modified Bruker amaZonSL mass spectrometer and the FRITZ tandem mass spectrometer (cf. chapters 2.2.1 and 2.2.3).

2.5 Collision Induced Dissociation (CID)

Molecular fragmentation induced by collisional activation (CID) has been noticed in the form of diffuse peaks in the mass spectra[97, 98] since the early days of mass spectrometry. With the advancement of mass spectrometers, CID has matured to a standard tandem-MS method[99, 100] for the characterization of organic molecules[101] and TM complexes[102].

In the case of a Paul trap (cf. Fig. 12), application of DC voltages (in addition to the trapping potentials) accelerate the mass-selected precursor ions on their trajectory. This increases the kinetic energy of the ions as well as the number of collisions of the ions with the buffer gas (Helium). Inelastic collisions with the Helium atoms transfer the additional kinetic energy into intramolecular degrees of freedom[103]. The transferred energy accumulates in the inner degrees of freedom of the molecular ion until its dissociation threshold is exceeded and it fragmentizes[104]. Ionic fragments can be detected by the mass spectrometer. The mass of the fragments and the fragmentation pathways may yield information about the structure on the precursor ion.

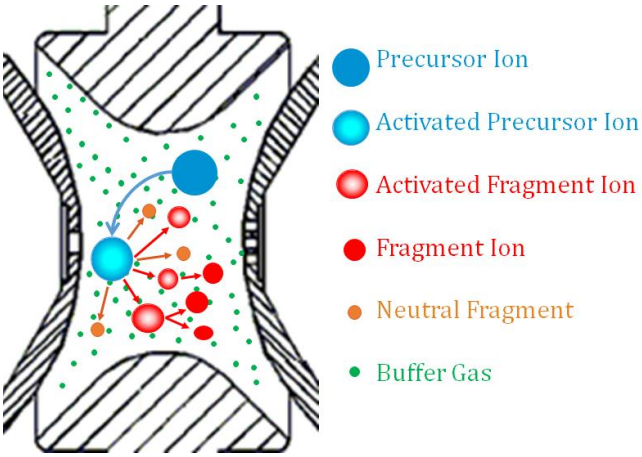

Figure 12: Schematic representation of the processes during the CID process in a Paul trap. Precursor ions are activated by an acceleration voltage and collide with the buffer gas. The precursor ion fragmentizes and forms neutral and activated ionic fragments, which decelerate by collisional cooling.

An additional method to investigate the stability and fragmentation pathways of isolated ions is to continuously increase the acceleration voltage while recording the relative frequency of the precursor ions and the resulting fragment ions. A corresponding plot of the acceleration voltage versus the relative intensity of fragment ion is referred to as a CID appearance curve. The DC excitation amplitudes within the laboratory frame (E_{LAB} in V) determine the internal energy scale of the mass spectrometer. Thus, relative fragment ion abundances are calculated by eq. (7):

$$I_{tot}^{fr}.(E_{lab}) = \left(\frac{\sum_i I_i^{fr}(E_{lab})}{\sum_i I_i^{fr}(E_{lab}) + \sum_i I_i^{p}(E_{lab})}\right) \qquad (7)$$

where I_i^{fr} = intensity of the fragment ions and I_i^{p} = intensity of the parent ions.

The amount of energy transfer by inelastic collisions depends on both the mass of the ion (m_{ion}) and the mass of the Helium atoms (m_{He}). Therefore, the excitation amplitude (E_{LAB}) is corrected by a center of mass transformation (cf. eq. (8)).

$$E_{com} = \left(\frac{m_{He}}{m_{He} + m_{ion}}\right) \cdot E_{lab} \qquad (8)$$

Note, that the current application of the CID technique by RF excitation in presence of multiple collisions results in a so called “slow multi collision heating” mode of operation[105].

The CID curves are modeled and fitted by sigmoidal functions (cf. eq. (9)) using a least-squares criterion.

$$I_{fit}^{fr}(E_{com}) = \left(\frac{1}{1 + e^{(E_{com}^{50} - E_{com})\,B}}\right) \qquad (9)$$

The E_{COM}^{50} fit parameter is the excitation amplitude at which the sigmoid function is at half maximum value, whereas B describes the rise of the sigmoid curve. Due to the correlation of excitation amplitude and relative fragment intensities, it is feasible to assume, that E_{COM}^{50} values can be associated to the relative stability of the complex. This provides an experimental access to activation energies[106-108].

2.6 X-Ray Absorption and X-Ray Magnetic Circular Dichroism (XMCD)

Synchrotron facililities provide very intensive and coherent X-Ray synchrotron radiation (cf. chapter 2.3.2) for various spectroscopic applications. The element selective X-ray Magnetic Circular Dichroism[109] (XMCD) spectroscopy allows to investigate magnetic properties of isolated TM Complexes and Clusters[110-112].

Resonant as well as non resonant X-Ray photon absorption may excite core shell electrons of a given atom[113]. In this case the atom is part of an investigated molecule. Resonant absorption (cf. Fig. 13) excites the core electrons into empty valence states ("valence holes"), while non resonant absorption leads to electron excitation into the continuum with subsequent ionization of the molecule. Both cases lead to the presence of empty core states ("core holes"). Electrons occupying higher energy states may fill up this core holes by "dropping down" into the energetically lower core states. Concurrently, these electrons release the difference energy eigher by photons (fluorescence) or auger electrons[114].

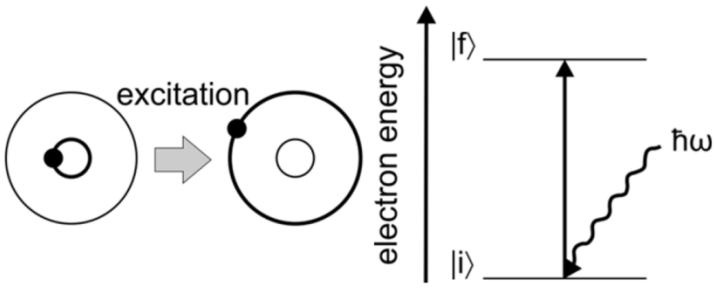

Figure 13: Resonant X-Ray absorption in an one electron picture[115]. A core electron is excited from the core state $|\boldsymbol{i}\rangle$ into empty valence shell $|\boldsymbol{f}\rangle$.

In the following discussion resonant absorption takes place exclussively by an one electron process. In such a case, the time dependent pertubation of the molecule by the X-Ray´s electromagnetic field leads to an immediate excitation from the initial $|i\rangle$ into the final state $|f\rangle$ without crossing any intermediate states. "Fermi´s Golden Rule No. 2" as derived by Dirac[116] describes the transition probability from $|i\rangle$ to $|f\rangle$ ($T_{if,}$ cf. eq. 10) as well as the X-Ray absorption resonance intensity (I_{res}, cf. Eq. 11)

$$T_{if} = \frac{2\pi}{\hbar}\left|\langle f|\hat{H}_{int}|i\rangle\right|^2 \delta(\varepsilon_i - \varepsilon_f)\, \rho\,(\varepsilon_f) \tag{10}$$

$$I_{res} = A|\langle f|\hat{\epsilon}\cdot\hat{r}|i\rangle|^2 \tag{11}$$

with $\hat{H}_{int}$ = interaction Hamiltonian[117], $\varepsilon_{i,f}$ = energy of the initial and final state, $\rho\,(\varepsilon_f)$= density of the final state per unit energy, A = probability factor[115], $\hat{\epsilon}$= unit photon polarization operator and $\hat{r}$ = lenght operator.

X-ray Magnetic Circular Dichroism (XMCD) is described by a straight forward "two step" model (cf. Fig. 14):

1.) The circular polrized X-Ray Photon is absorbed by an electron in a spin-orbit split ground state $|i\rangle$ (e.g. $2p_{3/2}$ and $2p_{1/2}$ in the case of $L_{2,3}$ edges). The angular momentum of the photon is transferred partly to the spin of the core electron leading to its spin polarization. The spin polarization is opposite for the two core levels, since their spin orbit coupling is opposite (l + s and l - s). The quantization axis of the excited electrons is identical to that of the photon angular momentum (parallel or antiparallel to the X-Ray propagation axis)
2.) The excited (spin polarized) core electrons transit into uneven populated "spin up" and "spin down" valence holes (e.g. empty 3d orbitals) with different transition probabilities. This results in different X-Ray absorption depending on the helicity of the circular polarized photons (XMCD). The empty valence holes thus act as a detector for the spin polarization of the core electrons. The maximum dichroic effect can be detected if the spins of the valence shell are alligned to the photon angular momentum (the X-Ray propagation direction). Allignment of the spin is achived by an high magnetic field of a superconducting solenoid.

The angular momentum of the photon is not completely transferred to the core electron spin. It is partly transferred into the electron´s angular momentum. This angular momentum of the excited electron is also "detected" by the valence shell, if the valence shell exhibits an angular momentum. The spin and orbital contributions to the difference in X-Ray absorptions have been derived by Thole and Carra in the form of the „sum rules"[118, 119]. The sum rules have been confirmed experimentally by Chen et al[120] for the $L_{3,2}$ edges.

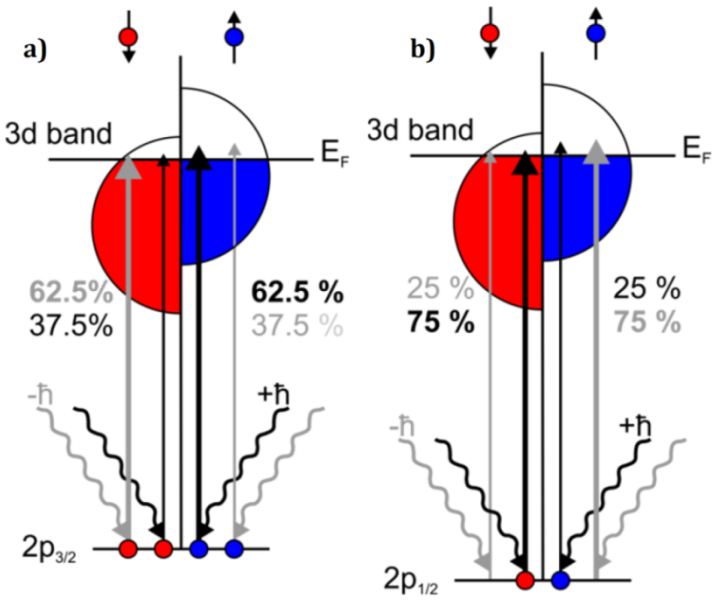

Figure 14: Relative transition probabilities for spin up (↑) and spin down (↓) electrons from the $2p_{3/2}$ **(a)** and the $2p_{1/2}$ **(b)** core states upon excitation with circularly polarized photons (helicity q = +ħ (black) and q = -ħ (grey)). The transition probability of spin up (↑) and spin down electrons (↓) switches if the photon helicity is reversed[113, 115].

In this work XMCD spectroscopy is on utilized isolated TM complexes *via* an "action spectroscopy" approach. The NanoClusterTrap located at the BESSY II synchrotron facility in Berlin (cf. chapter 2.2.3) offers an ion cloud of mass selected complexes. X-Ray absorption of the trapped ions induces their fragmentation due to the excess energy. The fragment ions can be detected by the mass spectrometric instumentation. Resonant X-Ray absorption results in drastically increased fragmentation yields as the absorption intensity increases. We gain X-ray absorption spectra by plotting the intensity of the fragment ions as a function of the X-Ray photon energy. A GaAs-diode records the X-Ray beam intensity from the undulator beamline (cf. chapter 2.3.2), which serves to normalize the recorded spectra for photon flux. The spectra were recorded on the Fe absorption edges with a spectral resolution of 500 meV at 711 eV and an increment size

of 200 meV. For a single data point exhibiting a single photon energy the "single shot mass spectra" time of flight instrument were added over 10 - 15 s with a frequency of 80 - 120 Hz. Several spectra for left and right handed circularly polarized light were recorded in an alternating manner to generate XMCD spectra. 5 - 6 raw spectra were added for both X-Ray polarizations for further analysis. Further details of the XMCD data evaluation is available in the PhD thesis of Matthias Tombers[115].

2.7 Density Functional Theory (DFT)

The interpretation of experimental data significantly benefits from comparisons with quantum chemical calculations. A widely utilized approach to calculate molecular properties is the Density Functional Theory[121-123] (DFT).

In the 1920´s Thomas and Fermi formulated the basic idea of DFT: All information required to calculate the energy E of a molecule (and other properties) is given by the electron density $\rho(\vec{r})$ of the molecule[124, 125]. Hohenberg and W. Kohn proved the correctness of this idea in the 1960´s *via* the 1st Hohenberg-Kohn-Theorem[126]. The 2nd Hohenberg-Kohn Theorem proved that the variational principle is applicable to compute electron densities providing more accurate results. A significant simplification of the energy E minimization by the variational principle was obtained by W. Kohn and L. Sham[127]. They described the energy E as a function of $\rho(\vec{r})$ as in eq. (13).

$$E(\rho) = T_0(\rho) + \int dr\, \rho(\vec{r})(V_{eff}(\vec{r}) + \frac{1}{2}\varphi(\vec{r})) + E_{XC}(\rho) \tag{13}$$

$T_0(\rho)$ is the kinetic energy of the system with the electron density $\rho(\vec{r})$. The electron density depends on the distance r of the electrons from the nucleus. $\varphi(\vec{r})$ is the Coulomb potential and $E_{XC}(\rho)$ defines the exchange-correlation energy.

The electron density corresponds to a normalized wave function of a system with N electrons. The Kohn-Sham wave function is a single Slater determinant constructed from a set of orbitals that are the lowest energy solutions to the Schrödinger equation (14). ε_i indicates orbital energies of corresponding Kohn-Sham orbitals i. The electron density of the whole N electron system is defined in eq. 15.

$$\left(-\frac{\hbar^2}{2m}\nabla^2 + V_{eff}(\vec{r})\right)\Phi_i(r) = \varepsilon_i \Phi_i(r) \tag{14}$$

$$\rho(\vec{r}) = \sum_{i}^{N} |\Phi_i(r)|^2 \tag{15}$$

$T_0(\rho)$ and $\int dr\, \rho(\vec{r})(V_{eff}(\vec{r}) + \frac{1}{2}\varphi(\vec{r}))$ in eq. (13) are relatively easy to compute, since they comprise only one electron or two-electron integrals. $E_{XC}(\rho)$ consists of all unknown factors and is not negligible. In fact, the approximation of $E_{XC}(\rho)$ plays a crucial role within DFT and is the main difference in relation to other methods.

The local spin density (LSD) approach[128] approximates $E_{XC}(\rho)$ according to eq. 16:

$$E_{XC}(\rho) = \int dr\, \rho(\vec{r})\varepsilon_{XC}\big(\rho \uparrow (\vec{r}), \rho \downarrow (\vec{r})\big) \tag{16}$$

$\varepsilon_{XC}\big(\rho \uparrow (\vec{r}), \rho \downarrow (\vec{r})\big)$ describes the exchange-correlation energy per particle in a homogeneous electron gas. A distinction is made between the spin up ($\rho \uparrow (\vec{r})$) and spin down ($\rho \downarrow (\vec{r})$) electron density. The LSD approach is applicable to systems with constant electron densities, such as ideal metals. The more the electron density varies, the less accurate is this approximation. Gradient-corrected functionals expand the spin density according to their gradient.

Hybrid functionals[129, 130] are often used to compute atomic and molecular properties. Their exchange terms (cf. eq. 17) consist of exchange terms from Hartree-Fock theory[131] (E_X^{HF}) and correlation terms originating from DFT (E_{XC}^{DFT}). c^{HF} and c^{DFT} are parametric prefactors, which are estimated empirically by adjusting the calculated results to experimental data (e.g. ionization potentials).

$$E_{XC,hybrid} = c^{HF} E_X^{HF} + c^{DFT} E_{XC}^{DFT} \tag{17}$$

The methodical advancements throughout the years established DFT as a standard tool for quantum chemical calculations. It is routinely used by scientists from various fields of research.

2.7.1 Geometry Optimization and Vibrational Frequencies

The Born-Oppenheimer approximation[132] serves to compute the electronic energy of molecules with an arbitrary arrangement of N nuclei. The energy is a function of 3N-6 coordinates (for a molecule with three translational and three rotational degrees of freedom) and thus forms a potential energy surface. So called stationary points along this energy surface occur, if its first derivative with respect to 3N-6 spatial degrees of freedom equals zero. Such stationary points indicate nuclei arrangements (geometries) in energetic minima (minima structures) as well as geometries in energy saddle points (transition state structures). The second derivatives of the potential energy surface discriminate between energetic minima structures and transition state structures: If all values of the second derivatives with respect to 3N-6 spatial degrees of freedom are positive an energetic minimum structure is reached. Transition state structures are indicated by exactly one negative second derivative among positive second derivatives with respect to 3N-6 spatial degrees of freedom. The process of finding geometries corresponding to the stationary points of the energy surface is called geometry optimization. It is usually achieved by iterative methods for energy gradient optimization.

Minima structures represent stable isomers of a molecule, which may also exist in experimental environment. Computed molecular properties (e.g. linear absorption spectra) can be compared to experimental data to confirm or exclude the existence of such isomers. Transition state structures separate adjacent energetic minima along the minimum potential energy surface path. Transition state structures are very useful to characterize reaction mechanisms (e.g. isomerization processes).

Vibrational Frequencies

Geometry optimization of the molecular geometry of a molecule provides structures located at stationary points of the potential energy surface. Such structures can be analyzed with regards to their vibrational frequencies. Their second derivatives are transformed to mass-weighted coordinates and 3N eigenvectors/eigenvalues are determined. Rotational and translational motions of the molecule are sorted out and 3N-6 vibrational modes emerge (or 3N-5 for linear molecules). Vibrational frequencies are calculated by these vibrational modes. Minima structures exhibit no negative

frequencies as their second derivatives are all positive per definition. Transition state structures exhibit exactly one negative frequency (imaginary vibration) since it exhibits exactly one negative second derivative. This imaginary vibration corresponds to a force constant associated to the motion along the reaction coordinate.

In the present work all geometry optimizations and frequency calculations have been performed using the Gaussian 09[133] program package. The usage of basis set as well as functionals is addressed individually in the corresponding chapters. The calculations were gratefully performed on the computing clusters of the department of the Theoretical Chemistry group of Prof. C. van Wüllen.

2.7.2 Magnetic Couplings: Broken Symmetry Approach

Unpaired electrons within TM complexes give rise to intrinsic magnetic phenomena[134] like a magnetization of the complexes in the presence of an external magnetic field. The magnetic interaction between multiple paramagnetic metal centers within one complex is usually referred to as magnetic coupling. This magnetic coupling is phenomenologically rationalized in terms of model spin Hamiltonians such as the isotropic Heisenberg-Dirac-van Vleck (HDvV) Hamiltonian[135] in eq. 18.

$$\hat{H}_{HDvV} = -\sum_{i<j} J_{ij} \hat{\boldsymbol{S}}_{\boldsymbol{i}} \hat{\boldsymbol{S}}_{\boldsymbol{j}} \tag{18}$$

where J_{ij} are the magnetic coupling constants of metal centers i and j. They govern the energy differences between the different spin states. $\hat{\boldsymbol{S}}_{\boldsymbol{i}}$ and $\hat{\boldsymbol{S}}_{\boldsymbol{j}}$ are the total spin operators for the metal centers i and j. Ferromagnetic coupling (spins allign parallel) is represented by a positive J value while a negative J value indicates antiferromagnetic coupling (spins allign antiparallel). The ferromagnetic case presents no problem for DFT calculations, as a single Kohn-Sham determinant is readily constructed that describes the whole oligonuclear system as good as the corresponding mononuclear species. In contrast, the representation of antiferromagnetic couplings demand several determinants which are not provided by basic DFT[136-138]. The Broken Symmetry approach[139-143] provides a solution to this problem. It permits to localize anti-parallel, unpaired spins separately on the metal centers (e.g. A and B) of the system. A Broken Symmetry state ψ_{BS} is constructed from a single determinant wavefunction that reflects the antiferromagnetic coupling, but is of the “wrong” spin symmetry (eq. 19).

$$\psi_{BS} = |\Phi_A(\alpha)\Phi_B(\beta)| \tag{19}$$

Structures with one spin up electron on atom A and one spin down electron an atom B would exhibit regions of positive (atom A) and negative (atom B) spin density. This is qualitatively wrong, since proper singlet wavefunctions have zero spin density at each point in space. The orbitals (Φ) in ψ_{BS} are optimized by applying the variational principle. While $\Phi_A(\alpha)$ and $\Phi_B(\beta)$ are orthogonal by their spin parts, they are not orthogonally restricted within their space parts.

In the case of multiple magnetic centers it is very difficult to find the eigenfunctions of the HDvV Hamiltionan. An Ising model Hamiltonian[144, 145] ($\widehat{H}_{Ising}$, eq. 20) helps to solve this problem. The total spin operators $\widehat{\boldsymbol{S}}_{\boldsymbol{i}}$ are substituted by the associated z-component $\hat{S}_{z,i}$:

$$\widehat{H}_{Ising} = -2\sum_{i<j} J_{ij}\hat{S}_{z,i}\,\hat{S}_{z,j} \tag{20}$$

The eigenvalues of the Ising Hamiltonian and the HDvV Hamiltonian are not identical. However it is possible to extract coupling constants (J_{ij}) from energy differences of appropriate broken symmetry configurations by assuming that all interactions are additive[146, 147]. A linear system of equations based on the Ising operator serves to calculate the coupling constants.

In the present work Broken Symmtery calculations have been performed using the CANOSSA[148] program as implemented in a local, customized installation of the TURBOMOLE 6.5 programm package[149-151]. The CANOSSA program was provided by the research group of Prof. C. van Wüllen. The usage of basis set as well as functionals is addressed individually in the corresponding chapter.

2.8 References

1. J. B. Fenn, Angew. Chem. Int. Ed., 2003, **42**, 3871-3894.
2. M. Wilm, Molecular & Cellular Proteomics, 2011, **10**.
3. R. Aebersold and D. R. Goodlett, Chem. Rev., 2001, **101**, 269-296.
4. R. Łobiński, D. Schaumlöffel and J. Szpunar, Mass Spectrom. Rev., 2006, **25**, 255-289.
5. V. Katta, S. K. Chowdhury and B. T. Chait, J. Am. Chem. Soc., 1990, **112**, 5348-5349.
6. K. Yamaguchi, J. Mass Spectrom., 2003, **38**, 473-490.
7. K. L. Vikse, Z. Ahmadi, J. Luo, N. van der Wal, K. Daze, N. Taylor and J. S. McIndoe, Int. J. Mass spectrom., 2012, **323–324**, 8-13.
8. G. T. T. Gibson, S. M. Mugo and R. D. Oleschuk, Mass Spectrom. Rev., 2009, **28**, 918-936.
9. B. N. Pramanik, P. L. Bartner, U. A. Mirza, Y.-H. Liu and A. K. Ganguly, J. Mass Spectrom., 1998, **33**, 911-920.
10. S. J. Shields, O. Oyeyemi, F. C. Lightstone and R. Balhorn, J. Am. Soc. Mass. Spectrom., 2003, **14**, 460-470.
11. K. L. Vikse, Z. Ahmadi and J. S. McIndoe, Coord. Chem. Rev., 2014, **279**, 96-114.
12. D. Schröder, Acc. Chem. Res., 2012, **45**, 1521-1532.
13. K. L. Vikse, M. A. Henderson, A. G. Oliver and J. S. McIndoe, Chem. Commun., 2010, **46**, 7412-7414.
14. L. Konermann, E. Ahadi, A. D. Rodriguez and S. Vahidi, Anal. Chem., 2012, **85**, 2-9.
15. G. Taylor, Proceedings of the Royal Society of London. Series A. Mathematical and Physical Sciences, 1964, **280**, 383-397.
16. M. S. Wilm and M. Mann, Int. J. Mass Spectrom. Ion Processes, 1994, **136**, 167-180.
17. L. Rayleigh, Philosophical Magazine Series 5, 1882, **14**, 184-186.
18. S. Crotti, P. Traldi and R. Seraglia, European Journal of Mass Spectrometry, 2011, **17**, 85-99.
19. M. Dole, L. L. Mack, R. L. Hines, R. C. Mobley, L. D. Ferguson and M. B. Alice, J. Chem. Phys., 1968, **49**, 2240-2249.
20. G. Schmelzeisen-Redeker, L. Bütfering and F. W. Röllgen, Int. J. Mass Spectrom. Ion Processes, 1989, **90**, 139-150.
21. J. V. Iribarne and B. A. Thomson, J. Chem. Phys., 1976, **64**, 2287-2294.
22. B. A. Thomson and J. V. Iribarne, J. Chem. Phys., 1979, **71**, 4451-4463.
23. B. Daltonics, *amaZon SL Series User Manual*.
24. S. Bari, O. Gonzalez-Magaña, G. Reitsma, J. Werner, S. Schippers, R. Hoekstra and T. Schlathölter, J. Chem. Phys., 2011, **134**, 024314.
25. O. Gonzalez-Magana, G. Reitsma, S. Bari, R. Hoekstra and T. Schlatholter, PCCP, 2012, **14**, 4351-4354.
26. R. R. Julian, S. R. Mabbett and M. F. Jarrold, J. Am. Soc. Mass. Spectrom., 2005, **16**, 1708-1712.
27. J. Gross, *Mass Spectrometry*, Springer-Verlag, Heidelberg, 2011.
28. F. W. McLafferty, Proceedings of the National Academy of Sciences, 2008, **105**, 18088-18089.
29. Edmond de Hoffmann and V. Stroobant, *Mass Spectrometry: Principles and Applications*, Wiley, 2007.

30. S. Maher, F. P. M. Jjunju and S. Taylor, Reviews of Modern Physics, 2015, **87**, 113-135.
31. R. G. Cooks, G. L. Glish, S. A. McLuckey and R. E. Kaiser, Chemical & Engineering News Archive, 1991, **69**, 26-41.
32. W. Paul and H. Steinwedel, Zeitschrift für Naturforschung A, 1953, **8**, 448-450.
33. G. Stafford Jr, J. Am. Soc. Mass. Spectrom., 2002, **13**, 589-596.
34. F. M. Harris, Rapid Communications in Mass Spectrometry, 1991, **5**, 58-58.
35. R. E. March, *Quadrupole Ion Trap Mass Spectrometer*, in *Encyclopedia of Analytical Chemistry*, John Wiley & Sons, Ltd, 2006.
36. R. E. March, Int. J. Mass spectrom., 2000, **200**, 285-312.
37. D. J. Douglas, Mass Spectrom. Rev., 2009, **28**, 937-960.
38. W. Paul, Reviews of Modern Physics, 1990, **62**, 531-540.
39. A. G. Marshall, C. L. Hendrickson and G. S. Jackson, Mass Spectrom. Rev., 1998, **17**, 1-35.
40. I. J. Amster, J. Mass Spectrom., 1996, **31**, 1325-1337.
41. A. G. Marshall, Int. J. Mass spectrom., 2000, **200**, 331-356.
42. M. B. Comisarow and A. G. Marshall, Chem. Phys. Lett., 1974, **25**, 282-283.
43. J. Lang, M. Cayir, S. P. Walg, P. Di Martino-Fumo, W. R. Thiel and G. Niedner-Schatteburg, Chem.-Eur. J., 2016, **22**, 2345-2355.
44. M. Gaffga, I. Munstein, P. Müller, J. Lang, W. R. Thiel and G. Niedner-Schatteburg, J. Phys. Chem. A, 2015, **119**, 12587-12598.
45. N. W. McLachlan, *Theory and application of Mathieu functions*, Clarendon Press, Oxford, 1947.
46. N. R. Daly, Review of Scientific Instruments, 1960, **31**, 264-267.
47. F. Menges, Dissertatin, TU Kaiserslautern, 2013.
48. S. Dillinger, J. Mohrbach, J. Hewer, M. Gaffga and G. Niedner-Schatteburg, PCCP, 2015, **17**, 10358-10362.
49. J. Lang, J. Mohrbach, S. Dillinger, J. M. Hewer and G. Niedner-Schatteburg, Chem. Commun., 2017, **53**, 420-423.
50. J. Mohrbach, S. Dillinger and G. Niedner-Schatteburg, The Journal of Physical Chemistry C, 2016.
51. J. Meyer, M. Tombers, C. v. Wüllen, G. Niedner-Schatteburg, S. Peredkov, W. Eberhardt, M. Neeb, S. Palutke, M. Martins and W. Wurth, J. Chem. Phys., 2015, **143**, 104302.
52. J. Mohrbach, *Cryo Tagging Infrared Spectroscopy and Temperatrue Controlled Kinetic Studies in a Tandem Trap Mass Spectrometer*, PhD Thesis, 2017.
53. P. Caravatti and M. Allemann, Org. Mass Spectrom., 1991, **26**, 514-518.
54. A. G. Marshal and P. B. Grosshans, Anal. Chem., 1991, **63**, 215A-229A.
55. M. P. Barrow, W. I. Burkitt and P. J. Derrick, Analyst, 2005, **130**, 18-28.
56. A. G. Marshall, AIP Conference Proceedings, 1998, **430**, 3-16.
57. K. Hirsch, V. Zamudio-Bayer, A. Langenberg, M. Niemeyer, B. Langbehn, T. Möller, A. Terasaki, B. v. Issendorff and J. T. Lau, Physical Review Letters, 2015, **114**, 087202.
58. V. Zamudio-Bayer, K. Hirsch, A. Langenberg, M. Kossick, A. Ławicki, A. Terasaki, B. v. Issendorff and J. T. Lau, J. Chem. Phys., 2015, **142**, 234301.
59. M. Niemeyer, K. Hirsch, V. Zamudio-Bayer, A. Langenberg, M. Vogel, M. Kossick, C. Ebrecht, K. Egashira, A. Terasaki, T. Möller, B. v. Issendorff and J. T. Lau, Physical Review Letters, 2012, **108**, 057201.

60. K. Hirsch, J. T. Lau, K. Ph, A. Langenberg, J. Probst, J. Rittmann, M. Vogel, V. Zamudio-Bayer, T. Möller and B. v. Issendorff, Journal of Physics B: Atomic, Molecular and Optical Physics, 2009, **42**, 154029.
61. A. Langenberg, *Magnetische Momente freier, massenselektierter Eisen,- Cobalt- und Nickelcluster*, PhD Thesis, Technische Universität Berlin, 2013.
62. A. Langenberg, K. Hirsch, A. Ławicki, V. Zamudio-Bayer, M. Niemeyer, P. Chmiela, B. Langbehn, A. Terasaki, B. v. Issendorff and J. T. Lau, PhRvB, 2014, **90**, 184420.
63. J. A. Giordmaine and R. C. Miller, Physical Review Letters, 1965, **14**, 973-976.
64. R. L. Beyer and R. L. Herbst, 1977.
65. P. A. Franken, A. E. Hill, C. W. Peters and G. Weinreich, Physical Review Letters, 1961, **7**, 118-119.
66. R. C. Eckardt, C. D. Nabors, W. J. Kozlovsky and R. L. Byer, J. Opt. Soc. Am. B, 1991, **8**, 646-667.
67. J. E. Midwinter and J. Warner, British Journal of Applied Physics, 1965, **16**, 1135.
68. D. Brida, C. Manzoni, G. Cirmi, M. Marangoni, S. De Silvestri and G. Cerullo, Opt. Express, 2007, **15**, 15035-15040.
69. G. W. Baxter, M. A. Payne, B. D. W. Austin, C. A. Halloway, J. G. Haub, Y. He, A. P. Milce, J. F. Nibler and B. J. Orr, Appl Phys B, 2000, **71**, 651-663.
70. W. R. Bosenberg and D. R. Guyer, J. Opt. Soc. Am. B, 1993, **10**, 1716-1722.
71. M. Gerhards, Optics Communications, 2004, **241**, 493-497.
72. W. R. Bosenberg and D. R. Guyer, Applied Physics Letters, 1992, **61**, 387-389.
73. K. Coding, W. Gudat, E.E. Koch, A. Kotani, C. Kunz and D. W. Lynch, *Synchrotron Radiation - Techniques and Applications*, Springer, Berlin - Heidelberg - NewYork, 1979.
74. G. Margaritondo, Journal of Synchrotron Radiation, 1995, **2**, 148-154.
75. H. B. Donald, E. Pascal and W. Edgar, Journal of Physics B: Atomic, Molecular and Optical Physics, 2005, **38**, S773.
76. J. V. Smith, Analyst, 1995, **120**, 1231-1245.
77. H. Wende, Rep. Prog. Phys., 2004, **67**, 2105.
78. S. Sasaki, K. Kakuno, T. Takada, T. Shimada, K.-i. Yanagida and Y. Miyahara, Nuclear Instruments and Methods in Physics Research Section A: Accelerators, Spectrometers, Detectors and Associated Equipment, 1993, **331**, 763-767.
79. H. Asano, N. Takenaka, T. Wakabayashi and T. Fujii, Nuclear Instruments and Methods in Physics Research Section A: Accelerators, Spectrometers, Detectors and Associated Equipment, 2005, **542**, 154-160.
80. H. M. M. Hesse, B. Zeech, 2009.
81. N. C. Polfer, Chem. Soc. Rev., 2011, **40**, 2211-2221.
82. J. Oomens, B. G. Sartakov, G. Meijer and G. von Helden, Int. J. Mass spectrom., 2006, **254**, 1-19.
83. G. Niedner-Schatteburg, Angew. Chem. Int. Ed., 2008, **47**, 1008-1011.
84. A. B. Wolk, C. M. Leavitt, E. Garand and M. A. Johnson, Acc. Chem. Res., 2013, **47**, 202-210.
85. C. J. Johnson, A. B. Wolk, J. A. Fournier, E. N. Sullivan, G. H. Weddle and M. A. Johnson, J. Chem. Phys., 2014, **140**, -.
86. E. R. Grant, P. A. Schulz, A. S. Sudbo, Y. R. Shen and Y. T. Lee, Physical Review Letters, 1978, **40**, 115-118.
87. D. W. Lupo and M. Quack, Chem. Rev., 1987, **87**, 181-216.
88. J. Roithova, Chem. Soc. Rev., 2012, **41**, 547-559.

89. Y. M. E. Fung, F. Kjeldsen, O. A. Silivra, T. W. D. Chan and R. A. Zubarev, Angew. Chem. Int. Ed., 2005, **44**, 6399-6403.
90. W. Laurier, The Encyclopedia of Mass Spectronomy, 2005, **4**, 327-337.
91. N. C. Polfer and J. Oomens, Mass Spectrom. Rev., 2009, **28**, 468-494.
92. D. Schröder, H. Schwarz, P. Milko and J. Roithová, J. Phys. Chem. A, 2006, **110**, 8346-8353.
93. A. Simon, C. Joblin, N. Polfer and J. Oomens, J. Phys. Chem. A, 2008, **112**, 8551-8560.
94. Y. Nosenko, F. Menges, C. Riehn and G. Niedner-Schatteburg, PCCP, 2013, **15**, 8171-8178.
95. J. Lang, M. Gaffga, F. Menges and G. Niedner-Schatteburg, PCCP, 2014, **16**, 17417-17421.
96. J. Jašík, D. Gerlich and J. Roithová, J. Phys. Chem. A, 2015, **119**, 2532-2542.
97. R. G. Cooks, J. Mass Spectrom., 1995, **30**, 1215-1221.
98. Aston, Proc. Cambridge Philos Soc, 1919, **19**, 317.
99. L. Sleno and D. A. Volmer, J. Mass Spectrom., 2004, **39**, 1091-1112.
100. A. K. Shukla and J. H. Futrell, J. Mass Spectrom., 2000, **35**, 1069-1090.
101. F. W. McLafferty, R. Kornfeld, W. F. Haddon, K. Levsen, I. Sakai, P. F. Bente, S.-C. Tsai and H. D. R. Schuddemage, J. Am. Chem. Soc., 1973, **95**, 3886-3892.
102. F. Menges, C. Riehn and G. Niedner-Schatteburg, Z. Phys. Chem., 2011, **225**, 595.
103. V. Gabelica and E. D. Pauw, Mass Spectrom. Rev., 2005, **24**, 566-587.
104. K. Levsen and H. Schwarz, Angew. Chem. Int. Ed., 1976, **15**, 509-519.
105. S. A. McLuckey and D. E. Goeringer, J. Mass Spectrom., 1997, **32**, 461-474.
106. E.-L. Zins, C. Pepe and D. Schröder, J. Mass Spectrom., 2010, **45**, 1253-1260.
107. E.-L. Zins, D. Rondeau, P. Karoyan, C. Fosse, S. Rochut and C. Pepe, J. Mass Spectrom., 2009, **44**, 1668-1675.
108. E.-L. Zins, C. Pepe, D. Rondeau, S. Rochut, N. Galland and J.-C. Tabet, J. Mass Spectrom., 2009, **44**, 12-17.
109. A. Scherz, H. Wende and K. Baberschke Appl. Phys. A, 2004, **78**, 843-846.
110. S. T. Akin, V. Zamudio-Bayer, K. Duanmu, G. Leistner, K. Hirsch, C. Bülow, A. Ławicki, A. Terasaki, B. v. Issendorff, D. G. Truhlar, J. T. Lau and M. A. Duncan, The Journal of Physical Chemistry Letters, 2016, **7**, 4568-4575.
111. M. Tombers, J. Meyer, A. Lawicki, V. Zamdio-Bayer, E. K. T. Lau, C. van Wüllen and G. Niedner-Schatteburg, under review in Nature - Communications.
112. V. Zamudio-Bayer, R. Lindblad, C. Bülow, G. Leistner, A. Terasaki, B. v. Issendorff and J. T. Lau, J. Chem. Phys., 2016, **145**, 194302.
113. J. Stöhr and H. Siegmann, *Magnetism, Solid-State Sciences*, Springer-Verlag, Berlin, Heidelberg, 2006.
114. O. Hardouin Duparc, International Journal of Materials Research, 2009, **100**, 1162-1166.
115. M. Tombers, *Spin and orbital magnetic moments of isolated single molecule magnets and transition metal clusters*, PhD Thesis, University of Kaiserslautern, 2015.
116. P. A. M. Dirac, Proceedings of the Royal Society of London. Series A, 1927, **114**, 243-265.
117. J. Als-Nielsen and D. McMorrow, *Elements of modern X-ray physics*, John Wiley and Sons, 2011.
118. B. T. Thole, P. Carra, F. Sette and G. van der Laan, Physical Review Letters, 1992, **68**, 1943-1946.

119. P. Carra, B. T. Thole, M. Altarelli and X. Wang, Physical Review Letters, 1993, **70**, 694-697.
120. C. T. Chen, Y. U. Idzerda, H. J. Lin, N. V. Smith, G. Meigs, E. Chaban, G. H. Ho, E. Pellegrin and F. Sette, Physical Review Letters, 1995, **75**, 152-155.
121. I. N. Levine, *Quantum Chemistry*, Upper Saddle River, N.J.: Prentice Hall, 2000.
122. R. G. Parr and R. G. Y. Weitao, Density-Functional Theory of Atoms and Molecules, http://public.eblib.com/choice/publicfullrecord.aspx?p=271295.
123. D. S. Sholl and J. A. Steckel, *{Density functional theory: a practical introduction}*, 2009.
124. L. H. Thomas, Mathematical Proceedings of the Cambridge Philosophical Society, 1927, **23**, 542-548.
125. E. Fermi, Z. Physik, 1928, **48**, 73-79.
126. P. Hohenberg and W. Kohn, Physical Review, 1964, **136**, B864-B871.
127. W. Kohn and L. J. Sham, Physical Review, 1965, **140**, A1133-A1138.
128. W. Kohn, A. D. Becke and R. G. Parr, J. Phys. Chem., 1996, **100**, 12974-12980.
129. A. D. Becke, J. Chem. Phys., 1993, **98**, 5648-5652.
130. A. D. Becke, J. Chem. Phys., 1993, **98**, 1372-1377.
131. A. Szabo and N. S. Ostlund, *Modern Quantum Chemistry: Introduction into Advanced Electronic Structure Theory*, N.Y.: Dover Publications, Mineola, 1996.
132. M. Born and R. Oppenheimer, Annalen der Physik, 1927, **389**, 457-484.
133. M. J. Frisch, et al.,, 2009.
134. R. S. D. Gatteschi, J. Villain *Molecular Nanomagnets*, Oxford University Press, Oxford 2006.
135. W. Heisenberg, Z. Physik, 1928, **49**, 619-636.
136. F. Illas, I. de P. R. Moreira, J. M. Bofill and M. Filatov, PhRvB, 2004, **70**, 132414.
137. F. Neese, Coord. Chem. Rev., 2009, **253**, 526-563.
138. C. J. Cramer and D. G. Truhlar, PCCP, 2009, **11**, 10757-10816.
139. F. Illas, I. P. R. Moreira, C. de Graaf and V. Barone, Theor Chem Acc, 2000, **104**, 265-272.
140. L. Noodleman and J. G. N. Jr., J. Chem. Phys., 1979, **70**, 4903-4906.
141. L. Noodleman, J. Chem. Phys., 1981, **74**, 5737-5743.
142. E. M. V. Kessler, S. Schmitt and C. van Wüllen, J. Chem. Phys., 2013, **139**, 184110.
143. R. Caballol, O. Castell, F. Illas, I. de P. R. Moreira and J. P. Malrieu, J. Phys. Chem. A, 1997, **101**, 7860-7866.
144. E. Ising, Z. Physik, 1925, **31**, 253-258.
145. C. N. Yang, Physical Review, 1952, **85**, 808-816.
146. J. M. Ricart, R. Dovesi, C. Roetti and V. R. Saunders, PhRvB, 1995, **52**, 2381-2389.
147. J.M. Ricart, R. Dovesi, C. Roetti and V. R. Saunders, PhRvB, 1997, **55**, 15942-15942.
148. S. Schmitt, *Berechnung der Magnetischen Anisotropie mit Hilfe von ein- und zweikomponentigen dichtefunktionaltheoretischen Rechnungen: Weiterentwicklung vorhandener Methoden und Anwendung auf mehrkernige Übergangsmetallkomplexe*, PhD Thesis, Technische Universität Kaiserslautern, 2015.
149. O. Treutler and R. Ahlrichs, J. Chem. Phys., 1995, **102**, 346-354.
150. R. Ahlrichs, M. Bär, M. Häser, H. Horn and C. Kölmel, Chem. Phys. Lett., 1989, **162**, 165-169.
151. M. Von Arnim and R. Ahlrichs, Journal of Computational Chemistry, 1998, **19**, 1746-1757.

3 Vibrational Blue Shift of Coordinated N_2 in $[Fe_3O(OAc)_6(N_2)_n]^+$:"Non Classical" Dinitrogen Complexes

Johannes Lang, Jennifer Mohrbach, Sebastian Dillinger, Joachim M. Hewer and Gereon Niedner-Schatteburg

Fachbereich Chemie and Forschungszentrum OPTIMAS,
Technische Universität Kaiserslautern,
67663 Kaiserslautern, Germany

3.1 Preamble

The following chapter is a reprint of a publication in the journal "Chemical Communications". Supplementary information is available in chapter 10.1.

A team consisting of Jennifer Mohrbach, Sebastian Dillinger, Joachim M. Hewer and myself performed the measurements. I evaluated the experimental data and conducted the presented quantum chemical calculations. I wrote and revised the manuscript with the help of Gereon Niedner-Schatteburg and Jennifer Mohrbach.

Full Reference:

Vibrational Blue Shift of coordinated N_2 in $[Fe_3O(OAc)_6(N_2)_n]^+$:"Non Classical" Dinitrogen Complexes
J. Lang, J. Mohrbach, S. Dillinger, J. M. Hewer and G. Niedner-Schatteburg, *Chemical Communications,* **2017**, 53, 420-423.
http://dx.doi.org/10.1039/C6CC07481B

3.2 Reprint

Reprint Licence

ChemComm

COMMUNICATION

View Article Online
View Journal

CrossMark click for updates

Cite this: DOI: 10.1039/c6cc07481b

Received 14th September 2016,
Accepted 2nd December 2016

DOI: 10.1039/c6cc07481b

www.rsc.org/chemcomm

Vibrational blue shift of coordinated N_2 in $[Fe_3O(OAc)_6(N_2)_n]^+$: "non-classical" dinitrogen complexes†

Johannes Lang,* Jennifer Mohrbach, Sebastian Dillinger, Joachim M. Hewer and Gereon Niedner-Schatteburg

We present "non-classical" dinitrogen Fe(III) oxo acetate complexes *in vacuo* utilizing Infrared Photodissociation (IR-PD) at cryo temperatures. The IR-PD spectra reveal a blue shift of the N_2 stretching vibration frequencies in the complexes. Density Functional Theory (DFT) calculations confirm the experiments and indicate strengthened N–N bonds due to pronounced σ bonding and a lack of π back donation.

The discovery of transition metal dinitrogen complexes in 1965[1] launched the ever growing research field of N_2 coordination chemistry.[2,3] One of the main goals is the conversion of N_2 to ammonia under mild conditions[4] by homogenous catalysis.[5,6] The basic idea is to weaken N–N bonds upon coordination to enable subsequent functionalization. Precursors to N_2 activation manifest by elongated N–N distances and by red shifting of stretching frequencies[7,8] with respect to the vibration of the free N_2 molecule. Such bond activation and vibrational red shifts have been interpreted before, *e.g.* in terms of the Dewar–Chatt–Duncanson (DCD) model,[9] and the Blyholder surface coordination (BSC)[10] model. Theoretical as well as spectroscopic investigations confirmed these interpretations.[11] However, FT-IR studies on N_2 coordinated to Lewis acid centers in zeolites[12] and alumina[13] revealed blue shifted vibrational N_2 stretching frequencies (up to 24 cm^{-1}). This indicates N–N bond strengthening rather than weakening – much beyond these established models. A similar effect has been observed in the case of isoelectronic carbon monoxide: so called "non-classical" metal carbonyl complexes[14,15] exhibit blue shifted vibrational CO stretching frequencies (up to 138 cm^{-1}).[16] Gas phase studies of isolated non-classical metal carbonyl clusters[17,18] proved the intrinsic molecular origin of this effect. The cause for the CO blue shift was a topic of debate[19] and is now understood in terms of an interplay between π back donation and electrostatic effects.[20] It is paramount to characterize the geometrical and electronic structures of such complexes in order to acquire a fundamental insight into the prevailing interactions leading to such non-classical behaviour.

The combination of Electrospray Ionization Mass Spectrometry[21] (ESI-MS) and infrared (IR) laser spectroscopy is suitable for the characterization of isolated coordination complexes with defined stoichiometry. Infrared (Multiple) Photon Dissociation (IR-(M)PD) provides direct access to structural and vibrational information, both under cryogenic conditions[22,23] and at room temperature.[24] The experimental results and dedicated *ab initio* calculations are combined in order to obtain detailed insight into the geometrical structure and intrinsic properties of the isolated molecular ions.

In this work we investigate isolated dinitrogen complexes $[Fe_3O(OAc)_6(N_2)_n]^+$ (n = 1–3, OAc = $CH_3CO_2^-$, *cf.* Scheme 1), which exhibit a significant blue shift (17 cm^{-1}) of N_2 vibrations in the complex with respect to the free N_2 molecule. We examine the N_2 coordination in detail to rationalize the blue shift and N–N bond strengthening. This is, to the best of our knowledge, the first report on the "non-classical" behaviour of isolated N_2 complexes.

We utilize a customized Fourier Transform-Ion Cyclotron Resonance (FT-ICR)-mass spectrometer (Apex Ultra, Bruker Daltonics) equipped with an ESI ion source (Apollo 2, Bruker).

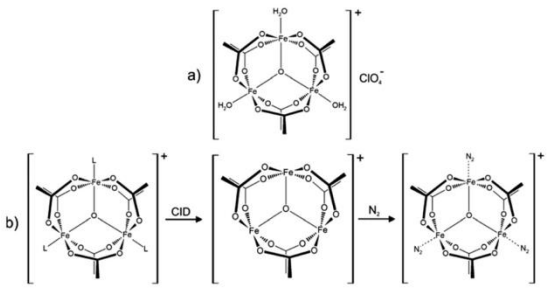

Scheme 1 (a) Molecular structure of the precursor $[Fe_3O(OAc)_6(H_2O)_3](ClO_4)$ salt. In solution the water molecules exchange with solvent molecules (L = *e.g.* acetonitrile). (b) ESI-MS reveals the formation of $[Fe_3O(OAc)_6(L)_n]^+$ (n = 0, 1, 2, 3). Collision induced dissociation (CID) of L yields the under-coordinated $[Fe_3O(OAc)_6]^+$ complex, which binds 1–3 N_2 molecules at 26 K.

Fachbereich Chemie and Forschungszentrum OPTIMAS, Technische Universität Kaiserslautern, 67663 Kaiserslautern, Germany. E-mail: jlang@chemie.uni-kl.de

† Electronic supplementary information (ESI) available. See DOI: 10.1039/c6cc07481b

We coupled the ICR cell with a KTP/KTA optical parametric oscillator/amplifier (OPO/A) IR laser system (LaserVision). Optimized minimum energy structures and linear IR absorption spectra were calculated at the B3LYP[25] level of theory using cc-pVTZ basis sets[26] and Stuttgart RSC 1997[27] effective core potential basis sets (Gaussian 09[28]). We present calculations with 15 unpaired alpha electrons yielding a spin multiplicity of 16 with other multiplicities (2–18) found to be significantly less stable (*cf.* Fig. S12, ESI†). We scale the calculated frequencies with two different scaling factors: one scaling factor (0.951) is specifically designed to elucidate N_2 stretching bands in $[Fe_3O(OAc)_6(N_2)_n]^+$. It scales the calculated N_2 stretching frequencies such that a calculated free N_2 stretching vibration frequency matches the experimental value[29] of 2330 cm^{-1}. This approach conveniently reveals any effects of Fe–N_2 coordination on N_2 stretching frequencies. A second unspecific scaling factor (0.986) is applied for all other bands below 1800 cm^{-1}. It scales the calculated asymmetric carboxylate stretching vibration frequencies of $[Fe_3O(OAc)_6(N_2)_1]^+$ to match our own experimental value of 1587 cm^{-1}. Unscaled spectra are provided in the ESI† (*cf.* Fig. S4).

Upon spraying the sample solution and recording mass spectra in the ICR-cell, we observe a series of isotopic peaks matching convincingly with simulated isotopic patterns (*cf.* Fig. S1, ESI†). We assign those peaks to $[Fe_3O(OAc)_6(L)_n]^+$ (L = H_2O, acetonitrile, acetic acid; n = 0, 1, 2, 3). Elimination of L by Collision Induced Dissociation (CID) and subsequent coordination of N_2 in the hexapole at cryo temperatures (26 K) leads to the formation of $[Fe_3O(OAc)_6(N_2)_n]^+$ (*cf.* Scheme 1b and Fig. S2, ESI†). Note that we observe n_{max} = 3, thus "titrating" the three available Fe coordination sites. The calculated Gibbs energies at various temperatures reveal N_2 binding energies of 11, 9, and 8 kJ mol^{-1} for the first, second, and third N_2 (26 K; BSSE corrected, *cf.* Fig. S3, ESI†). The N_2 binding Gibbs energies diminish with increasing temperature, vanishing above 80 K.

We recorded IR-PD spectra of cryocooled $[Fe_3O(OAc)_6(N_2)_n]^+$ (n = 1, 2, 3, Fig. 1, black traces) and conducted DFT simulations to obtain their linear IR absorption spectra (Fig. 1, green traces). The DFT calculations reveal optimized minimum structures as depicted in the insets of Fig. 1. We observe several bands between 1300 cm^{-1} and 1500 cm^{-1}, coinciding with the predicted CH_3 bending modes of the acetate ligands. While the calculated band frequencies around 1423 cm^{-1} and 1467 cm^{-1} agree well with the IR-PD spectrum, the calculated intensities differ significantly. Switching the DFT functional from B3LYP to PBE0 yields a much better match of IR intensities but significant deviations of calculated and observed vibrational frequencies (*cf.* Fig. S5, ESI†). Neither of these empirical functionals predicts both entities correctly. In the following we utilize the B3LYP results for further discussion.

The amount of N_2 coordination (n = 1, 2, 3) has no significant influence on the frequency and intensity of the CH_3 bending bands (neither in the IR-PD experiments nor in the DFT calculations). This finding likely originates from the spatial separation of the affected methyl groups from the Fe–N_2 coordination sites.

We find a strong IR-PD band at 1587, 1590, and 1591 cm^{-1} in the cases of n = 1, 2, 3. We assign this band to carboxylic CO stretching bands of the six coordinated acetate ligands. The n = 1 CO stretching band is red shifted by ≈3–4 cm^{-1} with

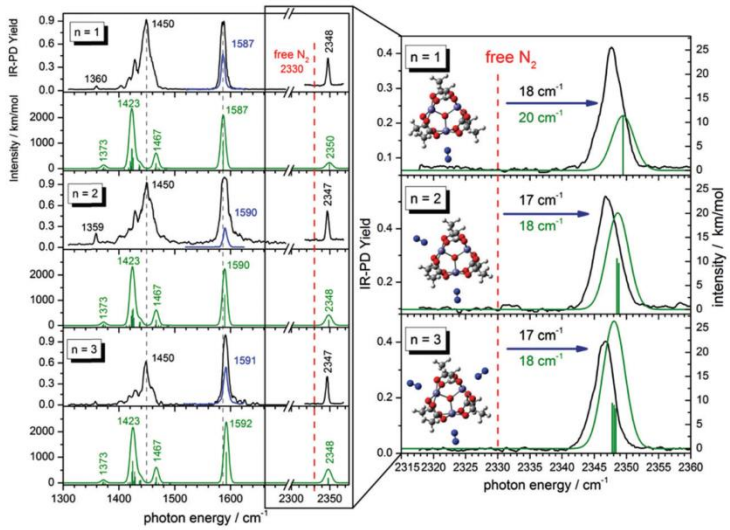

Fig. 1 Left: IR-PD spectra of $[Fe_3O(OAc)_6(N_2)_n]^+$ (n = 1, 2, 3) at 26 K (black and blue curves) and calculated IR absorption spectra of optimized $[Fe_3O(OAc)_6(N_2)_n]^+$ (n = 1–3) (green curves) in the range of 1300–2400 cm^{-1}. The blue IR-PD spectrum shows the CO stretching band (recorded with highly attenuated laser power to avoid saturation effects). The calculations were performed at the B3LYP/cc-pVTZ (H,C,N,O) and Stuttgart 1997 ECP (Fe) level of theory. The multiplicity is 16 and frequencies are scaled with 0.951 (0.986) above 2300 cm^{-1} (below 2300 cm^{-1}). Calculated stick spectra were convoluted with a Gaussian envelope of FWHM = 7 cm^{-1}. Right: A zoom into the N_2 stretching vibration region. Calculated lines were convoluted with a Gaussian envelope of FWHM = 3.5 cm^{-1}. Insets show associated geometry optimized structures.

respect to the n = 2, 3 bands, and with respect to the corresponding band of the free acetate anion[30] at 1591 cm^{-1}. The DFT calculated asymmetric carboxylate stretching frequencies – scaled to match the experiment at n = 1 – reproduce well the reduced redshift of the experiments on n = 2, 3. The coordinated carboxylate groups thus sense N_2 coordination through their common Fe centers. We provide an illustrative visualization of the calculated displacement vectors of these modes in Fig. S6 of the ESI.† Note that the n = 1 and 2 coordinations lift the sixfold degeneracy of these asymmetric stretching bands of the six coordinated acetate ligands. The recorded bands (slightly broadened to FWHM $\approx$ 7 cm^{-1}) may well contain the predicted splittings of $\approx$0.5 cm^{-1} – yet unresolved (*cf.* Fig. S7, ESI†).

We observe sharp bands (FWHM $\approx$ 3.5 cm^{-1}) above 2300 cm^{-1} revealing the IR active N_2 stretching vibrations of $[Fe_3O(OAc)_6(N_2)_n]^+$ (*cf.* the displacement vector visualization of these modes in Fig. S8, ESI†). Isotope labeling of the N_2 molecule confirms our assignment of these IR-PD bands to the N_2 stretching frequencies. We observe a red shift of the ^{15}N–^{15}N vibration band relative to the ^{14}N–^{14}N vibration band (79 cm^{-1}; *cf.* Fig. S17, ESI†) and the same blue shift with respect to the free N_2 in both isotopomers.

In all cases (n = 1, 2, 3) the solitary $^{14}N_2$ stretching bands of the experimental IR-PD spectra shift to the blue (17–18 cm^{-1}) with respect to the (IR inactive) stretching frequency of the free $^{14}N_2$ molecule (2330 cm^{-1}).[29] These blue shifts indicate N–N bond strengthening upon coordination. Our DFT calculations predict this blue shift remarkably well (18–20 cm^{-1}). Multiple coordinated N_2 molecules have almost identical stretching frequencies. There seems to be no coupling between the N_2 molecules adsorbing at distinct, equivalent Fe sites. In contrast to the carboxylate asymmetric stretching bands the N_2 stretching bands shift slightly to lower frequencies with increasing n (IR-PD spectrum: 1 cm^{-1}; DFT: 1.5 cm^{-1}). However, in all three cases (n = 1–3) the N_2 stretching band is blue shifted with respect to the free N_2.

The DFT calculations reveal subtle distortions of the triangular Fe_3O-core upon coordination of N_2 (*cf.* Scheme 2 and Table S2, ESI†). Each N_2 molecule binds end on to the respective Fe atom. In general, the coordination of N_2 enlarges Fe–Fe distances and Fe–$O_{central}$ bond lengths (by 0.03 Å resp. 0.01 Å) of those bonds which involve the N_2 coordinating Fe-center. All the other Fe–Fe distances and Fe–$O_{central}$ bond lengths shorten by approx. 0.03 Å or 0.01 Å. Natural Population Analysis (NPA) of $[Fe_3O(OAc)_6(N_2)_n]^+$ (n = 0, 1, 2, 3) reveals the dependence upon n of local charge densities within the triangular Fe_3O-core (*cf.* Scheme 2). The Fe centers gain 0.058–0.064 e electron density per coordinating N_2. The non-coordinated N atoms donate 0.121–0.134 e electron density in about equal parts to the coordinating N and Fe atoms. Free, non-polar N_2 molecules thus polarize and oxidize significantly upon Fe coordination, both magnitudes decreasing with n – as does the blue shift of the N_2 stretching bands. Note that the N–N bond length contracts slightly upon coordination (−0.002 Å). The high positive charge on the Fe centers (1.862–1.922 e) diminishes their electron donating capability and thus inhibits the π back donation. Such charge effects seem to increase the "non-classical" effect in metal carbonyl complexes.[31]

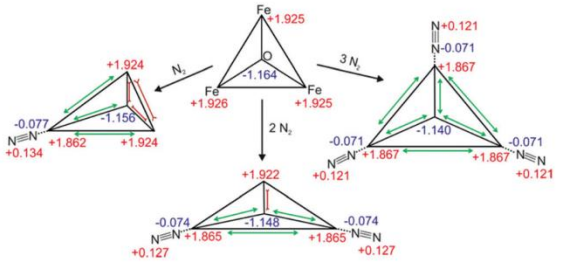

Scheme 2 Calculated geometries and natural charge distributions of the Fe_3O-core and the coordinated N_2 in $[Fe_3O(OAc)_6(N_2)_n]^+$ (n = 0, 1, 2, 3).

Non covalent interaction (*cf.* Fig. 2 for n = 1 and Fig. S11 for n = 2, 3, ESI†) analysis reveals a rather strong attractive, but non covalent interaction between the Fe atoms and the coordinated N atoms at rather long Fe–N coordination distances of 2.451–2.501 Å (n = 1–3). At such distances the π back donation is doomed to weakness due to scant π orbital overlap. Instead, it stands to reason that σ-donation of the N_2 molecule constitutes the driving force of attraction in the Fe–N_2 coordination in $[Fe_3O(OAc)_6(N_2)_n]^+$. Besides the obvious attractive Fe–N interaction, we identify repulsive interactions between the carboxylate O atoms and the coordinated N atoms.

Simple considerations as *e.g.* by the DCD and BSC models do not explain the observed blue shift of the N_2 stretching vibrations upon coordination. To rationalize this effect in a fairly perspicuous way we refer to the molecular orbital (MO) diagram of N_2 (*cf.* Scheme S1, ESI†): all bonding MOs are populated. When ruling out short range π back donation into empty anti-bonding MOs (inhibited by the net positive charge of the coordinating complex), there is a way to increase the formal N–N bond order (and thus strengthen the N–N bond and increase the stretching frequency): this is a depopulation of the antibonding 4σ* orbital into appropriate Fe centered acceptor orbitals. We have elucidated the prevailing coordination and bonding by inspection of computed molecular orbitals in $[Fe_3O(OAc)_6(N_2)_n]^+$. Indeed, we found that the 4σ* MO of the N_2 unit overlaps efficiently with MOs located at the Fe centers and at the carboxylate oxygen atoms of the $[Fe_3O(OAc)_6]^+$ subunit (*cf.* Fig. 3 for n = 1 and

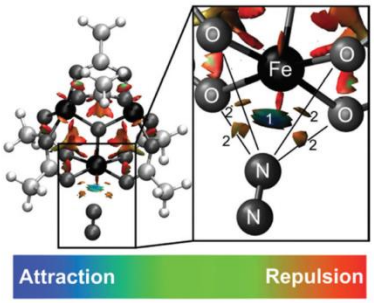

Fig. 2 NCI plot of geometry optimized $[Fe_3O(OAc)_6(N_2)_1]^+$ (*cf.* Fig. S10 for n = 2, 3, ESI†). The NCI plot reveals attractive interaction between the Fe center and the coordinated N atom (1) and repulsive interaction between of the O atoms and the N atom (2).

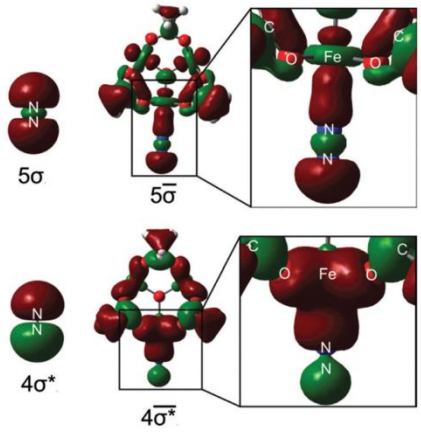

Fig. 3 Left: $4\sigma^*/5\sigma$ molecular orbitals of free N_2. Right: Selected molecular orbitals of $[Fe_3O(OAc)_6(N_2)_1]^+$ involving the former $4\sigma^*(N_2)$ and $5\sigma(N_2)$ orbitals. $4\sigma^*(N_2)$ electron density delocalizes into the whole complex, thus strengthening the N–N bond.

Fig. S13 for $n = 2, 3$, ESI†). The electrons of the anti-bonding $4\sigma^*(N_2)$ orbital delocalize into a $4\bar{\sigma}^*$ MO of the whole complex, whereby the $4\sigma^*(N_2)$ orbital polarizes towards the Fe center. Note that the node plane of $4\sigma^*(N_2)$ (between the N atoms) shifts somewhat towards the Fe center. The depletion of the anti-bonding electron density along the N–N bond increases the net bond order of N_2 and blue shifts the N_2 stretching vibration. The bonding $5\sigma(N_2)$ contributes to a $5\bar{\sigma}$ MO of the complex. This is expected to result in N–N bond weakening counteracting the effect of $4\sigma^*(N_2)$ delocalization. However, $5\sigma(N_2)$ receives a partial $4\sigma^*(N_2)$ character to form the $5\bar{\sigma}$ MO *via* hybridization. The strengthening effect of $4\sigma^*(N_2)$ electron density delocalization thus seems to be the critical factor for the "non-classical" behavior of $[Fe_3O(OAc)_6(N_2)_n]^+$. The involvement of the $4\sigma^*(N_2)$ orbital in the M–N_2 bonding scheme as well as $4\sigma^*/5\sigma$ hybridization has been suggested in the context of X-ray absorption studies of N_2 adsorbed on metal surfaces.[32] Inspection of all other delocalized MOs in the $[Fe_3O(OAc)_6(N_2)_1]^+$ complex reveals a total lack of π back donation from the $[Fe_3O(OAc)_6]^+$ unit to empty $\pi^*(N_2)$ orbitals. Considering the high charge on the Fe center and the long Fe–N_2 distance (see above) this seems reasonable. The N_2 coordination and thus the "non-classical" behavior of $[Fe_3O(OAc)_6(N_2)_n]^+$ originate from σ bonding effects.

Our fundamental insight into the class of "non-classical" N_2–Fe complexes is remarkable in view of the industrial use of bulk iron for N_2 activation and hydrogenation. It might help to advance a general understanding of dinitrogen chemistry beyond established coordination models.

This work was supported by the German Research Foundation DFG within the Transregional Collaborative Research Center SFB/TRR 88 "Cooperative effects in homo and heterometallic complexes" (3MET).

Notes and references

1 M. D. Fryzuk, *Chem. Commun.*, 2013, **49**, 4866–4868.
2 J. L. Crossland and D. R. Tyler, *Coord. Chem. Rev.*, 2010, **254**, 1883–1894.
3 N. Khoenkhoen, B. de Bruin, J. N. H. Reek and W. I. Dzik, *Eur. J. Inorg. Chem.*, 2015, 567–598.
4 S. F. McWilliams and P. L. Holland, *Acc. Chem. Res.*, 2015, **48**, 2059–2065.
5 D. V. Yandulov and R. R. Schrock, *Science*, 2003, **301**, 76–78.
6 H. Tanaka, K. Arashiba, S. Kuriyama, A. Sasada, K. Nakajima, K. Yoshizawa and Y. Nishibayashi, *Nat. Commun.*, 2014, **5**, 1–11.
7 N. Lehnert and F. Tuczek, *Inorg. Chem.*, 1999, **38**, 1659–1670.
8 N. Lehnert and F. Tuczek, *Inorg. Chem.*, 1999, **38**, 1671–1682.
9 J. Chatt and L. A. Duncanson, *J. Chem. Soc.*, 1953, 2939–2947.
10 G. Blyholder, *J. Phys. Chem.*, 1964, **68**, 2772–2777.
11 F. Studt and F. Tuczek, *J. Comput. Chem.*, 2006, **27**, 1278–1291.
12 K. Hadjiivanov and H. Knözinger, *Catal. Lett.*, 1999, **58**, 21–26.
13 R. Wischert, C. Coperet, F. Delbecq and P. Sautet, *Chem. Commun.*, 2011, **47**, 4890–4892.
14 H. Willner and F. Aubke, *Angew. Chem., Int. Ed.*, 1997, **36**, 2402–2425.
15 A. J. Lupinetti, G. Frenking and S. H. Strauss, *Angew. Chem., Int. Ed.*, 1998, **37**, 2113–2116.
16 P. K. Hurlburt, J. J. Rack, J. S. Luck, S. F. Dec, J. D. Webb, O. P. Anderson and S. H. Strauss, *J. Am. Chem. Soc.*, 1994, **116**, 10003–10014.
17 J. Velasquez, B. Njegic, M. S. Gordon and M. A. Duncan, *J. Phys. Chem. A*, 2008, **112**, 1907–1913.
18 A. Fielicke, G. von Helden, G. Meijer, B. Simard and D. M. Rayner, *J. Phys. Chem. B*, 2005, **109**, 23935–23940.
19 A. S. Goldman and K. Krogh-Jespersen, *J. Am. Chem. Soc.*, 1996, **118**, 12159–12166.
20 G. Bistoni, S. Rampino, N. Scafuri, G. Ciancaleoni, D. Zuccaccia, L. Belpassi and F. Tarantelli, *Chem. Sci.*, 2016, **7**, 1174–1184.
21 J. B. Fenn, *Angew. Chem., Int. Ed.*, 2003, **42**, 3871–3894.
22 N. Heine and K. R. Asmis, *Int. Rev. Phys. Chem.*, 2014, **34**, 1–34.
23 J. Jašík, J. Žabka, J. Roithová and D. Gerlich, *Int. J. Mass Spectrom.*, 2013, **354–355**, 204–210.
24 J. Lang, M. Gaffga, F. Menges and G. Niedner-Schatteburg, *Phys. Chem. Chem. Phys.*, 2014, **16**, 17417–17421.
25 A. D. Becke, *J. Chem. Phys.*, 1993, **98**, 5648–5652.
26 T. H. Dunning, *J. Chem. Phys.*, 1989, **90**, 1007–1023.
27 M. Dolg, H. Stoll, H. Preuss and R. M. Pitzer, *J. Phys. Chem.*, 1993, **97**, 5852–5859.
28 M. J. Frisch, G. W. Trucks, H. B. Schlegel, G. E. Scuseria, M. A. Robb, J. R. Cheeseman, G. Scalmani, V. Barone, B. Mennucci, G. A. Petersson, H. Nakatsuji, M. Caricato, X. Li, H. P. Hratchian, A. F. Izmaylov, J. Bloino, G. Zheng, J. L. Sonnenberg, M. Hada, M. Ehara, K. Toyota, R. Fukuda, J. Hasegawa, M. Ishida, T. Nakajima, Y. Honda, O. Kitao, H. Nakai, T. Vreven, J. A. Montgomery, Jr., J. E. Peralta, F. Ogliaro, M. Bearpark, J. J. Heyd, E. Brothers, K. N. Kudin, V. N. Staroverov, R. Kobayashi, J. Normand, K. Raghavachari, A. Rendell, J. C. Burant, S. S. Iyengar, J. Tomasi, M. Cossi, N. Rega, J. M. Millam, M. Klene, J. E. Knox, J. B. Cross, V. Bakken, C. Adamo, J. Jaramillo, R. Gomperts, R. E. Stratmann, O. Yazyev, A. J. Austin, R. Cammi, C. Pomelli, J. W. Ochterski, R. L. Martin, K. Morokuma, V. G. Zakrzewski, G. A. Voth, P. Salvador, J. J. Dannenberg, S. Dapprich, A. D. Daniels, Ö. Farkas, J. B. Foresman, J. V. Ortiz, J. Cioslowski and D. J. Fox, *Gaussian 09, Revision E.01*, Gaussian, Inc., Wallingford CT, 2009.
29 K. P. Huber and G. Herzberg, *Constants of Diatomic Molecules*, Van Norstrand, New York, 1979.
30 J. D. Steill and J. Oomens, *J. Phys. Chem. A*, 2009, **113**, 4941–4946.
31 A. M. Ricks, J. M. Bakker, G. E. Douberly and M. A. Duncan, *J. Phys. Chem. A*, 2009, **113**, 4701–4708.
32 A. Nilsson and L. G. M. Pettersson, *Surf. Sci. Rep.*, 2004, **55**, 49–167.

4 Intermetallic Competition in the Fragmentation of Trimetallic Au-Zn-Alkali Complexes

Johannes Lang, Merve Cayir-Kücükdisli, Simon P. Walg, Patrick Di Martino-Fumo,

Werner R. Thiel and Gereon Niedner-Schatteburg

Fachbereich Chemie and Forschungszentrum OPTIMAS,
Technische Universität Kaiserslautern,
67663 Kaiserslautern, Germany

4.1 Preamble

The following chapter is a reprint of a publication in the journal "Chemistry – A European Journal". Supplementary information is available in chapter 10.2.

I conducted the measurements, data evaluations and the quantum chemical calculations. I received experimental support by Patrick Di Martino-Fumo. Merve Cayir-Kücükdisli and Simon P. Walg synthesized the precursor complex. I wrote and revised the manuscript with the help of Gereon Niedner-Schatteburg and Werner R. Thiel.

Full Reference:

Intermetallic Competition in the Fragmentation of Trimetallic Au–Zn–Alkali Complexes
J. Lang, M. Cayir, S. P. Walg, P. Di Martino-Fumo, W. R. Thiel and G. Niedner-Schatteburg, *Chemistry – A European Journal* **2016**, 22, 2345-2355

http://dx.doi.org/10.1002/chem.201504093

4.2 Reprint

Reprint Licence

JOHN WILEY AND SONS LICENSE
TERMS AND CONDITIONS

Mar 08, 2017

This Agreement between Johannes Lang ("You") and John Wiley and Sons ("John Wiley and Sons") consists of your license details and the terms and conditions provided by John Wiley and Sons and Copyright Clearance Center.

License Number	4064231190298
License date	Mar 08, 2017
Licensed Content Publisher	John Wiley and Sons
Licensed Content Publication	Chemistry - A European Journal
Licensed Content Title	Intermetallic Competition in the Fragmentation of Trimetallic Au–Zn–Alkali Complexes
Licensed Content Author	Johannes Lang,Merve Cayir,Simon P. Walg,Patrick Di Martino-Fumo,Werner R. Thiel,Gereon Niedner-Schatteburg
Licensed Content Date	Jan 19, 2016
Licensed Content Pages	11
Type of use	Dissertation/Thesis
Requestor type	Author of this Wiley article
Format	Print and electronic
Portion	Full article
Will you be translating?	No
Title of your thesis / dissertation	Structure, reactivity and magnetism of isolated mononuclear and oligonuclear transition metal complexes elucidated by action spectroscopy and theory in concert
Expected completion date	Apr 2017
Expected size (number of pages)	200
Requestor Location	Johannes Lang Raiffeisenstraße 3 Kaiserslautern, 67655 Germany Attn: Johannes Lang
Publisher Tax ID	EU826007151
Billing Type	Invoice
Billing Address	Johannes Lang Raiffeisenstraße 3 Kaiserslautern, Germany 67655 Attn: Johannes Lang
Total	0.00 EUR

ChemPubSoc Europe
DOI: 10.1002/chem.201504093
CHEMISTRY A European Journal
Full Paper

Mass Spectrometry

Intermetallic Competition in the Fragmentation of Trimetallic Au–Zn–Alkali Complexes

Johannes Lang, Merve Cayir, Simon P. Walg, Patrick Di Martino-Fumo, Werner R. Thiel, and Gereon Niedner-Schatteburg*[a]

Dedicated to the memory of the late John Fenn

Abstract: Cationization is a valuable tool to enable mass spectrometric studies on neutral transition-metal complexes (e.g., homogenous catalysts). However, knowledge of potential impacts on the molecular structure and catalytic reactivity induced by the cationization is indispensable to extract information about the neutral complex. In this study, we cationize a bimetallic complex [$AuZnCl_3$] with alkali metal ions (M^+) and investigate the charged adducts [$AuZnCl_3M$]$^+$ by electrospray ionization mass spectrometry (ESI-MS). Infrared multiple photon dissociation (IR-MPD) in combination with density functional theory (DFT) calculations reveal a μ^3 binding motif of all alkali ions to the three chlorido ligands. The cationization induces a reorientation of the organic backbone. Collision-induced dissociation (CID) studies reveal switches of fragmentation channels by the alkali ion and by the CID amplitude. The Li^+ and Na^+ adducts prefer the sole loss of $ZnCl_2$, whereas the K^+, Rb^+, and Cs^+ adducts preferably split off MCl_2ZnCl. Calculated energetics along the fragmentation coordinate profiles allow us to interpret the experimental findings to a level of subtle details. The Zn^{2+} cation wins the competition for the nitrogen coordination sites against K^+, Rb^+, and Cs^+ , but it loses against Li^+ and Na^+ in a remarkable deviation from a naive hard and soft acids and bases (HSAB) concept. The computations indicate expulsion of MCl_2ZnCl rather than of MCl and $ZnCl_2$.

Introduction

The advent of homogenous catalysis for industrial applications has led to a great interest in organometallic and coordination chemistry.[1] Novel complexes are introduced regularly as catalysts for new reactions.[2] The elucidation of cooperative effects between two or more metal centers stands out as a very active field of research,[3] and bimetallic systems for organic synthesis have dramatically gained interest[4] throughout the past decade. It is of paramount importance to characterize the three-dimensional structure of such complexes in order to acquire a fundamental insight into their functionality. It is equally relevant to elucidate structural changes upon activation, which often precedes catalytic activity.

Soft ionization techniques such as electrospray ionization[5] (ESI) enable mass spectrometric investigations on solvent-free organometallic complexes in vacuo, and of their activation by either photons or collisions. Tandem-MS-based methods[6] such as infrared multiple photon dissociation (IR-MPD)[7] and collision-induced dissociation[8] (CID) provide direct access to structural information, both under cryogenic conditions[9] and at room temperature.[7f,10] Two color IR-MPD schemes are applied to overcome internal vibrational redistribution (IVR) bottlenecks[11] or to investigate isomer populations.[12] The experimental results and dedicated ab initio calculations combine to obtain detailed insight into the structure and intrinsic properties of likely binding motifs.[10,13] Furthermore ESI-MS studies of reaction mixtures are useful to intercept and investigate key intermediates of catalytic reaction pathways and thus gain information on the reaction mechanism.[14]

Neutral complexes can be charged by several methods. One approach is the exchange of a neutral ligand by a similar, although charged ligand (charge tag).[15] This is a widely applied and successful method, however, not without drawbacks. The presence of the charge tag may influence the functionality of the tagged complex in the course of a catalytic cycle.[16] Cationization by coordination of (alkali) metal ions is particularly useful in the cases of organic molecules such as peptides[17] or fatty acids.[18] Alkali ion cationization has also been utilized for mononuclear organometallic complexes.[19] There is a quite widespread impact of alkali coordination—sometimes labeled as the chaotropic effect[20]—on the structure and reactivity of biomolecules, macromolecules, and surfaces.[21] To the best of our knowledge, there are no reports on the effect of alkali cationization on bimetallic coordination complexes. It is of paramount importance to acquire insight into the structure and re-

[a] J. Lang, M. Cayir, Dr. S. P. Walg, P. Di Martino-Fumo, Prof. Dr. W. R. Thiel, Prof. Dr. G. Niedner-Schatteburg
Fachbereich Chemie and Forschungszentrum OPTIMAS
Technische Universität Kaiserslautern
67663 Kaiserslautern (Germany)
E-mail: gns@chemie.uni-kl.de

Supporting information and ORCID(s) from the author(s) for this article is available on the WWW under http://dx.doi.org/10.1002/chem.201504093.

activity of such alkali adducts to advance the understanding of bare complexes.

Here, we report alkali (M^+) cationized gold–zinc complexes $[AuZnCl_3M]^+$ (Scheme 1) and their fragmentation behavior

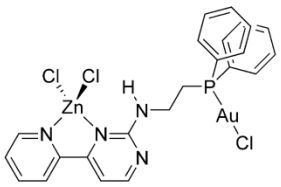

Scheme 1. Precursor complex $[AuZnCl_3]$, where the square brackets indicate a short hand notation for the otherwise lengthy PNN ligand *N*-(2-(diphenylphosphino)ethyl)-4-(pyridin-2-yl)pyrimidin-2-amine ($C_{23}H_{21}N_4P$).

(Scheme 2). The square brackets indicate a short hand notation for the otherwise lengthy PNN ligand, *N*-(2-(diphenylphosphino)ethyl)-4-(pyridin-2-yl)pyrimidin-2-amine. Such complexes are of particular interest for investigating cooperative effects between gold and zinc metal centers.[22]

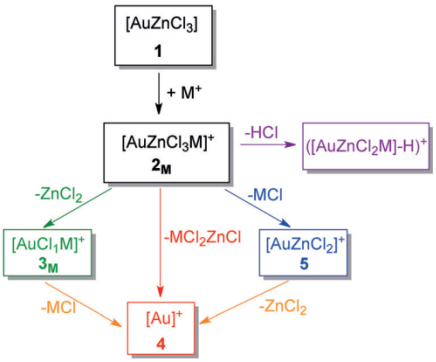

Scheme 2. Formation and subsequent CID fragmentation of $[AuZnCl_3M]^+$, $M = Li^+$, Na^+, K^+, Rb^+, Cs^+. The relative intensities of each channel depend strongly on CID amplitude and on the alkali ion. HCl elimination is weak in all observed cases (Table 1 and Figure 3) and shall not be discussed further. The indicated interpretation of the conceivable $MZnCl_3$ fragment in terms of a MCl_2ZnCl structure finds strong support from our DFT survey. Bold numerals indicate the calculated minimum structures of the respective species.

The combination of CID and IR-MPD studies with DFT calculations provides unprecedented insight into the structure and fragmentation behavior of isolated $[AuZnCl_3M]^+$. We highlight the structural changes upon alkali ion coordination as well as the changes in fragmentation behavior with variation of the alkali ions. Reaction coordinate profiles help to elucidate the dynamics of the fragmentation processes, as well as enthalpic changes by the variations of the associated alkali ion.

Experimental and computational methods

We suspended 0.5 mg of $[AuZnCl_3]$ (Scheme 1, for synthesis see the Supporting Information) in 1 mL acetonitrile (optigrade). The suspension was centrifuged and the supernatant solution was used without further purification. LiCl (99% p.a.), NaCl (99% p.a.), KCl (99% p.a.), RbCl (99.8%, Sigma-Aldrich), and CsI (99.999%, ChemPur) were dissolved in 50:50 (% volume) acetonitrile/water (optigrade) solutions at a concentration of 10^{-2} mol L^{-1}. These were added to the $[AuZnCl_3]$ solution to generate the ionic alkali adducts. The resulting alkali salt concentration in the sample solutions was 10^{-4} mol L^{-1}.

ESI-MS and CID measurements were performed by a Paul-type quadrupole ion trap instrument (Bruker Esquire 3000plus). The ion source was set to positive electrospray ionization mode. The scan speed was 13000 $m/z\,s^{-1}$ in standard resolution scan mode (0.3 FWHM/m/z) and the scan range was 15–1200 m/z. Mass spectra were accumulated for at least two minutes. MS^n spectra were accumulated for at least twenty seconds. Sample solutions were continuously infused into the ESI chamber by a syringe pump at a flow rate of 2 µL min^{-1}. Nitrogen was used as drying gas with a flow rate of 3.0 L min^{-1} at 210 °C. The solutions were sprayed at a nebulizer pressure of 280 mbar (4 psi) and the electrospray needle was held at 4.5 kV.

Collision-induced dissociation (CID) appearance curves were recorded with varying excitation amplitudes (0.0 V to 1.5 V), which determine the internal energy scale of the mass spectrometer (E_{lab} in V). Relative abundances were calculated according to Equation (1):

$$I^{fr}_{tot}.(E_{lab}) = \left(\frac{\sum_i I^{fr}_i(E_{lab})}{\sum_i I^{fr}_i(E_{lab}) + \sum_i I^{p}_i(E_{lab})}\right) \quad (1)$$

where I^{fr}_i = intensity of the fragment ions and I^{p}_i = intensity of the parent ions. Center of mass transferred fragmentation amplitudes (E_{com}) were calculated from internal amplitudes by Equation (2):

$$E_{com} = \left(\frac{m_{He}}{m_{He} + m_{ion}}\right) \cdot E_{lab} \quad (2)$$

where m_{ion} stands for the isotopically averaged mass of the molecular ion. Note that the current application of the CID technique by radio frequency (RF) excitation in the presence of multiple collisions results in a so called "slow multi collision heating" mode of operation.[23]

Fragmentation amplitude dependent CID spectra were modeled and fitted by sigmoidal functions of the type:

$$I^{fr}_{fit}(E_{com}) = \left(\frac{1}{1 + e^{(E^{50}_{com} - E_{com})B}}\right) \quad (3)$$

by using a least-squares criterion. The E^{50}_{com} fit parameter is the amplitude at which the sigmoid function is at half the maximum value, whereas B describes the rise of the sigmoid curve. Owing to the correlation of the fragmentation amplitude and appearance energy, it is feasible to assume that the appearance curves can be associated with the relative stability of the cationized alkali adducts.[17c,24] The according plots are available in the Supporting Information.

Infrared multiple photon dissociation (IR-MPD) measurements were performed by using a modified Paul-type quadrupole ion trap instrument (AmaZon SL, Bruker Daltonics). The ion source was set to positive electrospray ionization mode. The scan speed was 32500 $m/z\,s^{-1}$ (0.3 FWHM/m/z) with a scan range of 70–1200 m/z. The sample solutions were continuously infused into the ESI chamber by a syringe pump at a flow rate of 2 mL min^{-1}. Nitrogen was used as drying gas with a flow rate of 3.0 L min^{-1} at 210 °C. The solutions were sprayed at a nebulizer pressure of 280 mbar (4 psi) and the electrospray needle was held at 4.5 kV.

A KTP/KTA (KTP = potassium titanyl phosphate; KTA = potassium titanyl arsenate) optical parametric oscillator/amplifier (OPO/A, LaserVision) system pumped by a pulsed 10 Hz injection seeded Nd^{3+}:YAG laser (PL8000, Continuum) was used as a source of tunable IR radiation ($\delta n = 0.9$ cm^{-1}, $\delta t = 7$ ns) for recording vibrational spectra. The OPA idler wave (≤ 10 mJ per pulse) was used to record spectra within 2600–3900 cm^{-1}. The difference frequency (DF) between the OPA signal and idler waves generated in a $AgGaSe_2$ crystal (≤ 2 mJ per pulse) was applied in the range 1200–2100 cm^{-1}. After passing through the vacuum chamber, the IR beam was directed onto a power meter sensor. The idler beam was focused by a 50 cm CaF_2 lens. The DF radiation was focused tighter, by a 90° off-axis parabolic silver mirror with an effective focal length of 15 cm. The IR spectra were recorded as ion chromatograms while continuously scanning the IR wavelength. An experimental IR-MPD spectrum arises from the plot of the fragmentation efficiency as a function of laser frequency (ν). The IR-MPD yield $Y(\nu)$ is defined as:

$$Y(\nu) = \left(\frac{\sum_i I_i^{fr}(\nu)}{\sum_i I_i^{fr}(\nu) + \sum_i I_i^{P}(\nu)}\right) \quad (4)$$

The IR frequency was calibrated by using a wave meter (821B-NIR, Bristol instruments). Laser power curves were recorded in parallel to the IR-MPD spectra through digitizing the analog output of the laser power meter by an ample ADC input of the AmaZon SL mass spectrometer electronics. Despite the online IR power measurement, the recorded spectra were not normalized because of the intrinsically nonlinear power dependence of the IR-MPD fragmentation efficiencies.

Optimized minimum energy structures, transition state geometries, binding energies, and linear IR absorption spectra were calculated at the B3LYP[25] level of theory by using cc-pVDZ[26] basis sets (C, H, Li, N, O, Na), and Stuttgart RSC 1997[27] effective core potential (Au, Cs, K, Rb, Zn) basis sets, respectively, as implemented in the Gaussian 09 program package.[28] Standard convergence criteria were applied. Full geometry optimization of all nuclear coordinates yielded multiple locally stable minimum structures. The lowest energy structure is assumed to represent the most stable isomer. Standard Gibbs energies of structures, ΔG^0, and of fragmentation pathways, $\Delta_{frag}G^0$, also known as free enthalpies, were calculated at 300 K. Harmonic vibrational frequencies were scaled with 0.955 (0.975) above (below) 2000 cm^{-1} to match the most intense experimental bands (e.g., $\tilde{\nu}_{NH}$ at 3374 cm^{-1} for $[AuZnCl_3Li]^+$). We checked for triplet and quintet states and found those to be at least 100 kJ mol^{-1} less stable and thus of no relevance in the present context—in remarkable contrast to the CID of a Fe–Pd complex, which revealed a direct singlet to quintet crossover.[29]

Infrared absorption spectra of powder samples were measured with an attenuated total reflection (ATR) spectrometer (PerkinElmer Spectrum 100 FT-IR with a universal ATR sampling accessory). Background spectra were subtracted from the sample spectrum for background correction. The scan range was 4000–450 cm^{-1} and 10 scans were averaged for each spectrum.

Results and Discussion

Characterizing the precursor compound $[AuZnCl_3]$

We characterized the molecular structure of the neutral precursor complex $[AuZnCl_3]$ by ATR-IR spectroscopy of the synthesized powder and by DFT simulations (Figure 1). The observed

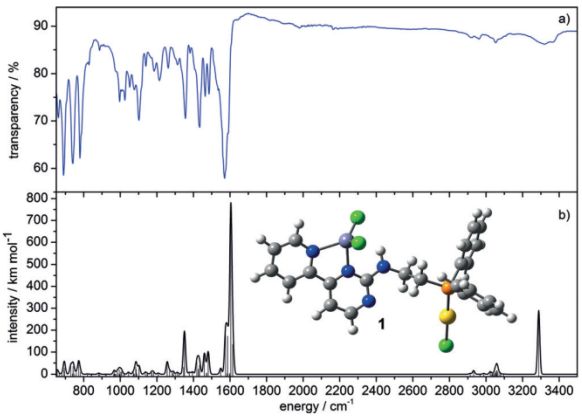

Figure 1. a) ATR-IR spectrum of $[AuZnCl_3]$ powder. b) Calculated linear absorption spectrum of **1** (inset) by DFT.

bands agree well with the linear absorption spectrum of the optimized structure **1**. However, the NH stretching vibration band around 3300 cm^{-1} is broad and weak in ATR but sharp and medium in DFT. Note that standard DFT calculations do not cover likely band broadening[30] through intra and/or inter molecular hydrogen bonding. We are confident to assign the neutral $[AuZnCl_3]$ complex the molecular structure of **1**. Note that in **1** the $ZnCl_2$ unit and the AuCl unit are in *trans* orientation. The neutral $[AuZnCl_3]$ complex thus acquires an open structure that offers a large variety of possible coordination sites for alkali ion charge tags. Further standard precursor characterization is available in the Supporting Information.

Collision-induced dissociation (CID) of alkali ion adducts

Upon spraying the above-described sample solution, we observed mass spectra of cationized alkali metal adducts of

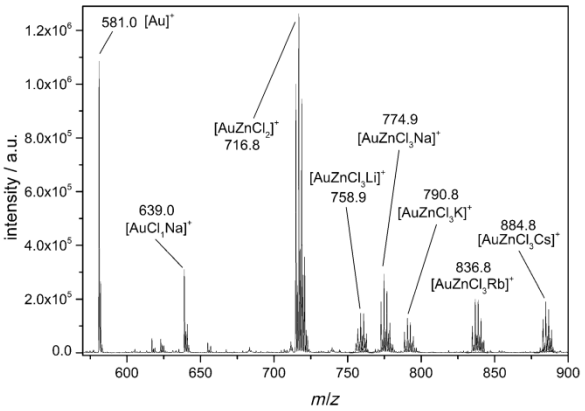

Figure 2. Overlaid stack of five cationic ESI-MS spectra of $[AuZnCl_3]$ in Li, Na, K, Rb, or Cs salt acetonitrile solutions. In each case there is a sole dominating adduct, $[AuZnCl_3M]^+$ (M = Li, Na, K, Rb, Cs). The mass labeling refers to the most abundant isotope peak.

$[AuZnCl_3]$ (Figure 2). Evidence of $[AuZnCl_3M]^+$ (M = Li^+, Na^+, K^+, Rb^+, Cs^+) emerges through series of isotopic peaks centered around m/z = 758.9, 774.9, 790.8, 836.8, and 884.8 (most abundant peaks indicated) in close agreement to simulated isotopic pattern (Figure SI-1 in the Supporting Information).

CID of isolated $[AuZnCl_3M]^+$ reveals four fragments in all the cases of the alkali adducts (Scheme 2). Note that the same fragments also appear without excitation. This indicates a decomposition of the complex in solution, possibly by hydrolysis by the small amounts of water present in the solution.

The relative fragment abundances vary depending on the coordinating alkali ion (Figure 3, Table 1, and Figure SI-2 in the Supporting Information). The variation of CID amplitudes reveals so-called breakdown curves of the $[AuZnCl_3M]^+$ complexes and appearance curves of the fragments (Figure 3). The alkali effect is most apparent at low CID amplitudes ($E_{com} \leq$ 0.004 a.u. (arbitrary units)). In the case of $[AuZnCl_3Li]^+$, loss of $ZnCl_2$ dominates (shown by $[AuClLi]^+$ detection: 84%, E_{com} = 0.004 a.u.); concomitant elimination of $ZnCl_2$ and LiCl is secondary ($[Au]^+$ detected: 4%). In the cases of $[AuZnCl_3K]^+$, $[AuZnCl_3Rb]^+$, and $[AuZnCl_3Cs]^+$, concomitant loss of $ZnCl_2$ and MCl dominates ($[Au]^+$: 74%, 87%, 87%, respectively). The sole loss of $ZnCl_2$ is hardly observable ($\leq$1%). In the case of $[AuZnCl_3Na]^+$, these competing fragments occur with comparable probability: $ZnCl_2$ + NaCl elimination ($[Au]^+$: 29%) and $ZnCl_2$ loss ($[AuClNa]^+$: 50%). It has been shown long ago that fragment pathways with low activation barriers tend to dominate in the low CID amplitude regime.[8a] We will show that our above findings are well in line with such behavior (see below).

The mere observation of a charged $[Au]^+$ fragment leaves open the question as to whether the concomitant neutral fragment consists of two entities (e.g., $ZnCl_2$ and MCl) or of a single one, a $MZnCl_3$ molecule. We will show that thermodynamic stabilities, however, clearly favor the latter case (see below) and these computations reveal a MCl_2ZnCl motif with threefold Zn coordination.

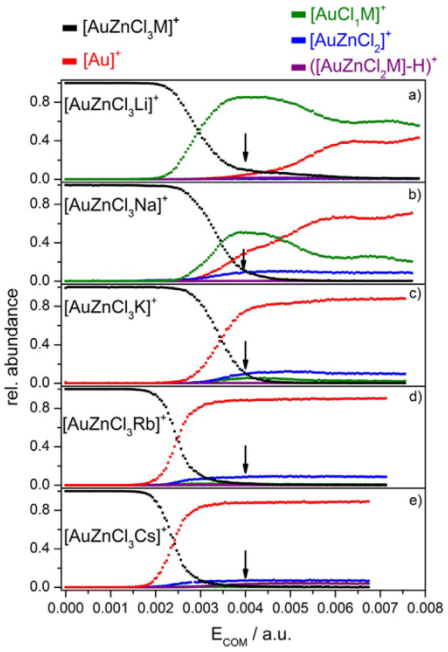

Figure 3. CID appearance curves of fragments from $[AuZnCl_3M]^+$ (M = Li^+, Na^+, K^+, Rb^+, Cs^+). They reveal a significant change in relative intensities by variation of M. Loss of $ZnCl_2$ ($[AuCl_1M]^+$, green) is the main fragmentation channel for M = Li^+, and it is significant for M = Na^+. The large alkali ions M = K^+, Rb^+, and Cs^+ exhibit a switch of the most abundant fragment towards $[Au]^+$ (red, elimination of MCl_2ZnCl). The arrow indicates the excitation amplitude that was utilized to extract numerical values of observed fragment intensities as listed in Table 1.

In the case of high CID amplitudes, we expect fragment pathways with higher activation barriers to gain abundance.[31] The pattern of fragments of $[AuZnCl_3Li]^+$ changes significantly with higher CID amplitudes. The sole loss of $ZnCl_2$ decreases and, in turn, the competing elimination of MCl_2ZnCl rises; in the case of $[AuZnCl_3Na]^+$, these two fragment channels even switch at high CID amplitudes. In both complexes, the MCl_2ZnCl loss clearly proceeds through a higher activation barrier than the $ZnCl_2$ loss. In contrast, the appearance of curved patterns of fragments from $[AuZnCl_3K]^+$, $[AuZnCl_3Rb]^+$, and $[AuZnCl_3Cs]^+$ is dominated by the MCl_2ZnCl loss channel ($[Au]^+$ detected) at all levels of excitation. All other channels are unlikely and reveal merely recordable intensities. This observation may be rationalized in principle either by an enthalpic preference or by a loose transition state that entropically favors a single fragment channel. Our enthalpic considerations are outlined below.

Infrared-induced multiple photon dissociation (IR-MPD) and DFT simulations of the alkali adducts

We have recorded IR-MPD spectra of the alkali complexes (Figure 4a), and we have conducted DFT simulations to obtain their linear IR absorption spectra (Figure 4b). The DFT calculations reveal optimized minimum structures $\mathbf{2}_M$ and $\mathbf{2}_{LiPh}$ as de-

Table 1. Compilation of ESI-MS data for $[AuZnCl_3M]^+$ (M = Li^+, Na^+, K^+, Rb^+, Cs^+) and of the corresponding fragments after collision-induced dissociation (CID). The indicated mass labels refer to the most abundant isotope peaks.

Precursor	Fragment	Loss	*m/z*	Assigned formula	Rel. abundance @ E_{com} = 0.004 a.u.
$[AuZnCl_3Li]^+$	–	–	758.9	$[C_{23}H_{21}AuCl_3N_4PZnLi]^+$	0.10
	$([AuZnCl_2Li]-H)^+$	HCl	723.0	$[C_{23}H_{20}AuCl_2N_4PZnLi]^+$	0.01
	$[AuZnCl_2]^+$	LiCl	716.8	$[C_{23}H_{21}AuCl_2N_4PZn]^+$	0.01
	$[AuClLi]^+$	$ZnCl_2$	623.0	$[C_{23}H_{21}AuCl_1N_4PLi]^+$	0.84
	$[Au]^+$	$LiCl_2ZnCl$	581.0	$[C_{23}H_{21}AuN_4P]^+$	0.04
$[AuZnCl_3Na]^+$	–	–	774.9	$[C_{23}H_{21}AuCl_3N_4PZnNa]^+$	0.11
	$([AuZnCl_2Na]-H)^+$	HCl	739.0	$[C_{23}H_{20}AuCl_2N_4PZnNa]^+$	0.00
	$[AuZnCl_2]^+$	NaCl	716.8	$[C_{23}H_{21}AuCl_2N_4PZn]^+$	0.10
	$[AuClNa]^+$	$ZnCl_2$	639.0	$[C_{23}H_{21}AuCl_1N_4PNa]^+$	0.50
	$[Au]^+$	$NaCl_2ZnCl$	581.0	$[C_{23}H_{21}AuN_4P]^+$	0.29
$[AuZnCl_3K]^+$	–	–	790.8	$[C_{23}H_{21}AuCl_3N_4PZnK]^+$	0.11
	$([AuZnCl_2K]-H)^+$	HCl	755.0	$[C_{23}H_{20}AuCl_2N_4PZnK]^+$	0.00
	$[AuZnCl_2]^+$	KCl	716.8	$[C_{23}H_{21}AuCl_2N_4PZn]^+$	0.10
	$[AuClK]^+$	$ZnCl_2$	655.0	$[C_{23}H_{21}AuCl_1N_4PK]^+$	0.05
	$[Au]^+$	KCl_2ZnCl	581.0	$[C_{23}H_{21}AuN_4P]^+$	0.74
$[AuZnCl_3Rb]^+$	–	–	836.8	$[C_{23}H_{21}AuCl_3N_4PZnRb]^+$	0.02
	$([AuZnCl_2Rb]-)H^+$	HCl	800.9	$[C_{23}H_{20}AuCl_2N_4PZnRb]^+$	0.01
	$[AuZnCl_2]^+$	RbCl	716.8	$[C_{23}H_{21}AuCl_2N_4PZn]^+$	0.09
	$[AuClRb]^+$	$ZnCl_2$	700.9	$[C_{23}H_{21}AuCl_1N_4PRb]^+$	0.01
	$[Au]^+$	$RbCl_2ZnCl$	581.0	$[C_{23}H_{21}AuN_4P]^+$	0.87
$[AuZnCl_3Cs]^+$	–	–	884.8	$[C_{23}H_{21}AuCl_3N_4PZnCs]^+$	0.01
	$([AuZnCl_2Rb]-H)^+$	HCl	848.8	$[C_{23}H_{20}AuCl_2N_4PZnCs]^+$	0.05
	$[AuZnCl_2]^+$	CsCl	716.8	$[C_{23}H_{21}AuCl_2N_4PZn]^+$	0.07
	$[AuClRb]^+$	$ZnCl_2$	748.9	$[C_{23}H_{21}AuCl_1N_4PCs]^+$	0.00
	$[Au]^+$	$CsCl_2ZnCl$	581.0	$[C_{23}H_{21}AuN_4P]^+$	0.87

picted in Figure 5 (see the Supporting Information for the less stable isomers).

In the fingerprint region (below 1700 cm^{-1}), the IR-MPD spectra of all the investigated $[AuZnCl_3M]^+$ species exhibit two strong bands around 1580 cm^{-1} and 1600 cm^{-1}, coinciding with the predicted -C=N- skeletal vibration modes of $\mathbf{2}_M$. Note that the computed absolute IR intensities of the -C=N- skeletal vibration modes do diminish (596 km mol^{-1} to 487 km mol^{-1} in Rb and Cs complexes) much like the experimental IR-MPD bands do.

In the range of C–H stretching modes (2800–3150 cm^{-1}), the experiments reveal bands that are weak and coincide with the predicted C–H stretching modes of $\mathbf{2}_M$. They are discernible experimentally only in the case of $[AuZnCl_3Li]^+$, although the computed IR intensities of all $\mathbf{2}_M$ species are comparable.

In the range of the N–H stretching modes, the IR-MPD spectrum of $[AuZnCl_3Li]^+$ reveals an intensive band at 3373 cm^{-1}. This band nicely coincides with computed NH stretching in $\mathbf{2}_{Li}$. The respective IR-MPD spectra of $[ZnAuCl_3M]^+$, where M = Na, K, Rb, Cs, also show bands around 3375 cm^{-1}. We assign these to the NH stretching modes of $\mathbf{2}_{Na,K,Rb,Cs}$ (Figure 5). However, in comparison to the Li^+ complex, all the alkali complexes reveal drastically reduced fragmentation efficiencies of the NH stretching mode around 3375 cm^{-1}, despite computed IR intensities of comparable magnitudes.

In the IR-MPD spectrum of $\mathbf{2}_{Li}$, there is a second weak feature at 3319 cm^{-1} (Figure 4a), which we assign to the NH stretching mode of the less stable isomer $\mathbf{2}_{LiPh}$ (+9 kJ mol^{-1}, Figure 5, calcd. spectrum in Figure 4b). No corresponding IR-MPD feature arises in case of the other alkali ions.

Through the convincing agreement of the IR-MPD and DFT spectra, the calculations acquire additional credibility. We, thus, feel able to survey the calculated structures in somewhat more detail. The three chlorido ligands of the Au and Zn centers in $\mathbf{2}_M$ coordinate to the alkali ion through a μ^3 intramolecular bridge (Figure 5). This is quite remarkable in view of the much more open and almost linear structure of **1**, the neutral $[AuZnCl_3]$ complex. Therefore, we assume a rearrangement of the organic backbone upon alkali ion coordination to facilitate the μ^3 binding motif. It is well known that the Hofmeister series of alkali cations affects the salting out of proteins. In the present case, the very same alkali cations are expected to cause systematic effects in the structure and function of the affected complexes.[32] Visual inspection of the displayed structures in Figure 5 reveals, at first sight, that the alkali coordination varies systematically, namely by alkali cation size. Small Li^+ coordinates in the plane of the three chlorine atoms. We define a dihedral angle, α, between Cl^1, Cl^2, Cl^3 and M, which in the case of M = Li^+ is 28° (Table 2). A weak hydrogen bond[33] between the NH group of the organic backbone and Cl^1 stabilizes $\mathbf{2}_{Li}$ (d(NH–Cl) = 2.607 Å). The formation of a μ^3-coordinated alkali ion provides the most stable structure in this and all other cases ($\mathbf{2}_{Li}$ to $\mathbf{2}_{Cs}$, Figure 5). However, the alkali ions are pushed further out of the plane spanned by the three chlorido ligands with increasing ion radius (Table 2). The dihedral angle α(Cl^1-Cl^2-Cl^3-M) increases to a value of 67° for M = Cs^+. Weak hydrogen bonds (NH···Cl) are also observed in $\mathbf{2}_{Na}$ to $\mathbf{2}_{Cs}$. The NH–Cl distances decrease slightly to 2.552 Å for M = Cs^+, (Table 2). The distance between Au and Zn enlarges with alkali ion size (Table 2). The Au–Zn distance in $\mathbf{2}_{Li}$ (5.08 Å) is shorter by 0.37 Å compared with $\mathbf{2}_{Cs}$ (5.45 Å).

In contrast to all of the above-described $\mathbf{2}_M$ structures with preformed MCl_3 motifs, the geometry of $\mathbf{2}_{LiPh}$ is comprised of a $LiCl_2$ unit that π-coordinates directly to the diphenylphosphane moiety.

DFT simulations of CID fragment species

Optimized fragment structures (Figure 6) of alkali adducts $\mathbf{2}_M$ allow us to investigate the peculiar fragmentation behavior of $[AuZnCl_3M]^+$ as observed in the CID experiments (Scheme 2 and Figure 3).

It shows that a more or less torsional reorganization by a N-CH_2-CH_2-P backbone twist enables the fragmentation of $\mathbf{2}_M$ through expulsion of either $ZnCl_2$ (yielding fragment $\mathbf{3}_M$) or of MCl_2ZnCl (yielding fragment **4**). It is instructive to examine the associated dihedral angle φ(NCCP) in the $\mathbf{2}_M$ parent and $\mathbf{3}_M$ and

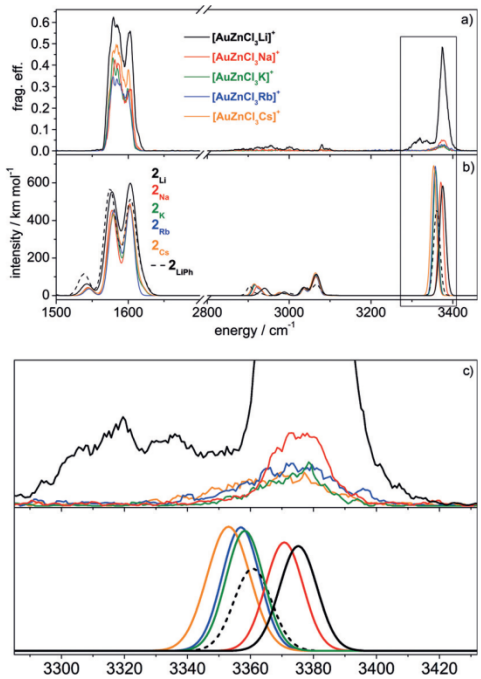

Figure 4. IR-MPD spectra of $[AuZnCl_3M]^+$ (M = Li^+, Na^+, K^+, Rb^+, Cs^+) (a) and calculated IR absorption spectra of $\mathbf{2}_M$ (solid lines) and $\mathbf{2}_{LiPh}$ (dashed line) (b). The calculations were performed at the B3LYP/cc-pVDZ (H, C, Li, N, O) and Stuttgart 1997 ECP (Au, Zn, K, Rb, Cs) levels of theory. Frequencies are scaled with 0.955 (0.975) above (below) 2000 cm^{-1}. Calculated lines were broadened with Gaussian envelope curves (FWHM = 7 cm^{-1}). The calculated intensities above 2800 cm^{-1} were multiplied by a factor of 4. c) Enlarged section of the IR absorption spectra in (a) and (b), which helps to elucidate the broad features below 3360 cm^{-1}.

Table 2. Structural data for $[AuZnCl_3M]^+$ (M = Li^+, Na^+, K^+, Rb^+, Cs^+) by DFT calculations at the B3LYP/cc-pVDZ (H, C, N, O) and Stuttgart 1997 ECP (Au, Zn) levels of theory. The dihedral angle α indicates how far the alkali ions (in local C_{3v} coordination) are pushed out of the plane spanned by the three coordinating chlorido ligands.

	d(Zn–Au) [Å]	d(NH–Cl^1) [Å]	α (Cl^1-Cl^2-Cl^3-M) [°]	Alkali ion radius [Å]
$\mathbf{2}_{Li}$	5.08	2.61	28	0.60
$\mathbf{2}_{Na}$	5.13	2.59	45	0.95
$\mathbf{2}_K$	5.33	2.56	59	1.33
$\mathbf{2}_{Rb}$	5.39	2.55	63	1.48
$\mathbf{2}_{Cs}$	5.45	2.55	67	1.69

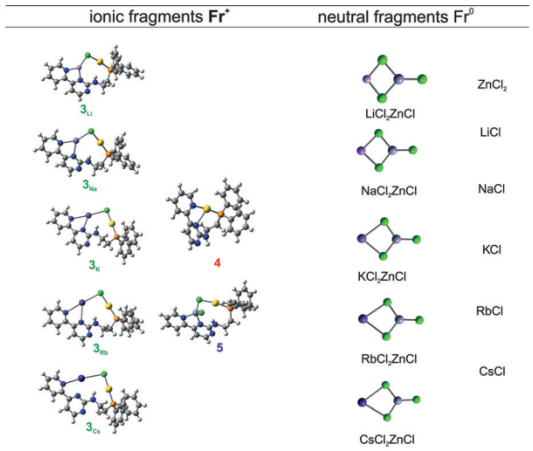

Figure 6. Optimized CID fragment structures of $\mathbf{2}_M$ (M = Li^+, Na^+, K^+, Rb^+, Cs^+) by DFT calculation at the B3LYP/cc-pVDZ (H, C, N, O) and Stuttgart 1997 ECP (Au, Cs, Zn) levels of theory.

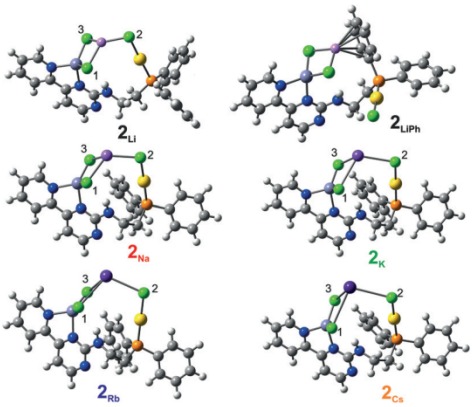

Figure 5. Optimized structures of $\mathbf{2}_M$ (M = Li^+, Na^+, K^+, Rb^+, Cs^+) and $\mathbf{2}_{LiPh}$ by DFT calculations at the B3LYP/cc-pVDZ (H, C, N, O) and Stuttgart 1997 ECP (Au, Cs, Zn) levels of theory: Light gray: H; dark gray: C; dark blue: N; orange: P; green: Cl; light blue Zn; yellow: Au; purple: Li, Na, K, Rb, or Cs.

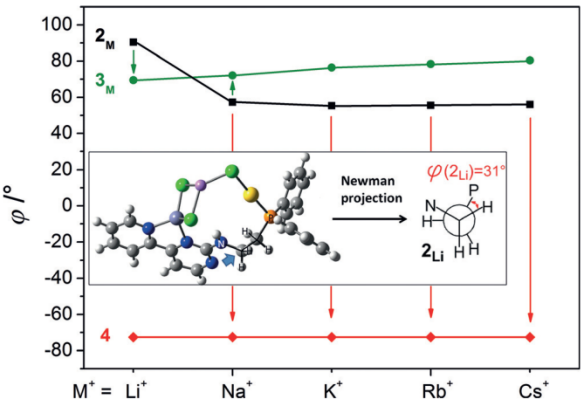

Figure 7. Calculated dihedral angles φ(NCCP) of parent and CID fragment structures. The arrows indicate experimentally observed fragmentation channels.

4 fragments (Figure 7). Fragmentation implies a large twist of $\varphi(\mathbf{2})\rightarrow\varphi(\mathbf{4})$ and a small twist of $\varphi(\mathbf{2})\rightarrow\varphi(\mathbf{3}_M)$. The large twist rotates the NH group in **4** by about 180° with respect to $\mathbf{2}_M$ and it thus enables Au–N,N coordination. Such reorganization of the backbone is not necessary for $ZnCl_2$ expulsion; a minor twist suffices.

In the cases of M = K, Rb, and Cs, we observe almost exclusive MCl_2ZnCl expulsion. In these cases, the large twist $\varphi(\mathbf{2})\rightarrow\varphi(\mathbf{4})$ is favored energetically (see below). In the cases of $\mathbf{2}_{Li}$ and

$\mathbf{2}_{Na}$, the $ZnCl_2$ expulsion presents an easy route of fragmentation without need for a large-scale backbone twist.

Enthalpic and entropic considerations

Computed thermochemical data of the optimized fragments and parent structures (Figures 5 and 6) serve to give the Gibbs energy/free enthalpy of fragmentation $\Delta_{frag}G^{300K}$ for various dissociation pathways:

$$\Delta_{frag}G^{300K}(2_M \rightarrow Fr^+) = \Delta_f G(Fr^+)^{300K} + \Delta_f G(Fr^0)^{300K} - \Delta_f G(2_M)^{300K} \quad (5a)$$

where $\Delta_f G(Fr^+)^{300K}$ are the Gibbs energies/free enthalpies of ionic fragments $Fr^+ = \mathbf{3}_M$, **4**, **5**, and $\Delta_f G(Fr^0)^{300K}$ are the Gibbs energies/free enthalpies of neutral fragments $Fr^0 = ZnCl_2$, MCl_2ZnCl, and MCl utilized in appropriate pairings as in Scheme 2. The Gibbs energy of consecutive $MnCl + ZnCl_2$ expulsion computes according to:

$$\Delta_{frag}G^{300K}(\mathbf{2_M} \rightarrow \mathbf{4})_{con.} = \Delta_f G(\mathbf{4})^{300K} + \Delta_f G(MCl)^{300K} + \Delta_f G(ZnCl_2)^{300K} - \Delta_f G(\mathbf{2_M})^{300K} \quad (5b)$$

These Gibbs energies, $\Delta_{frag}G^{300K}$, of the competing fragmentation pathways (Figure 8) serve to evaluate the influence of the alkali ions on the branching ratios (Table 1 and Scheme 2). We omit a discussion of the HCl elimination pathway in the following as it is minor in all cases.

The fragmentation of $\mathbf{2}_M$ into **4** may occur through one of three competing fragmentation pathways (Scheme 2): The overall loss may proceed through expulsion of $ZnCl_2$ and of MCl, through expulsion of MCl and of $ZnCl_2$, or through expulsion of MCl_2ZnCl.

In our computations, we took all three possibilities into account and found that the elimination of the MCl_2ZnCl unit (Figure 8, red) is energetically much more favorable than elimination of the separate $ZnCl_2$ and MCl species for all alkali adducts (Figure 8, orange). Likewise, the sole expulsion of MCl is highly endoergic (+130-150 kJ mol^{-1}, Figure 8, blue), whereas the $ZnCl_2$ expulsion is favorable in all cases (less than 120 kJ mol^{-1}, Figure 8, green). Note that three out of the four fragmentation channels (orange, blue, green) reveal the same and distinct alkali effect; $\Delta_{frag}G^{300K}$ increases with alkali ion size. Such an effect is absent in the case of MCl_2ZnCl expulsion (red). Consequently, we find a crossover of favorable $ZnCl_2$ expulsion (green) to favorable MCl_2ZnCl expulsion (red) when going from Na to K. This prediction by DFT of the most favorable fragmentation channels nicely agrees with the experimental fragmentation behavior of $\mathbf{2}_M$, $[AuZnCl_3M]^+$, as verified by CID (Figure 3 a–e) and by IR-MPD (Figure 4 a).

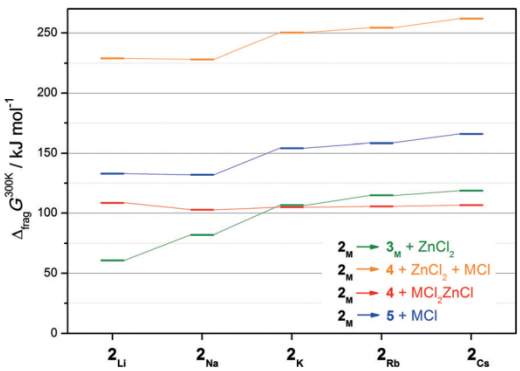

Figure 8. Calculated free binding Gibbs energies (300 K) of the main fragmentation pathways. DFT calculations were performed at the B3LYP/cc-pVDZ (H, C, N, O, Li, Na) and Stuttgart 1997 ECP (Au, K, Rb, Cs, Zn) levels of theory.

Reaction coordinates of alkali association and of $ZnCl_2$ and MCl_2ZnCl expulsion

It is worthwhile to inspect the reaction coordinates of the observed fragmentation channels in more detail. This is all the more interesting as the optimized minimum structure of MCl_2ZnCl (Figure 6) exhibits a planar geometry with two chlorine atoms bridging the alkali and zinc metal centers. The third chlorine atom binds solely to the zinc atom. However, in the case of $\mathbf{2}_M$, two chlorine atoms serve as the bridging atoms between Zn^{2+} and M^+ and the third chlorine atom binds to the alkali ion, without coordination to Zn^{2+}. Thus, it seems necessary that either one chlorido ligand migrates to Zn^{2+} during fragmentation or that the $ZnCl_2$ group migrates to the third chlorido ligand. Furthermore, we note that the NH groups of **4** and $\mathbf{2}_M$ point in opposite directions. It is conceivable that a torsion of the NNC–NHC bond enables MCl_2ZnCl elimination.

We calculated stationary points along the reaction coordinates for alkali coordination, MCl_2ZnCl elimination, and for $ZnCl_2$ elimination (Figure 9; black, green, and red, respectively). We find the same attachment mechanism for all alkali ions, M^+ (Figure 9 for energetics and Figure 10 for structures). The formation of $\mathbf{2}_M$ occurs in two steps: M^+ coordinates to the chlorido ligands of the $ZnCl_2$ group of **1**, represented by the local minimum $\mathbf{2}_M$. Subsequently, the aliphatic sidechain of the organic backbone twists (transition state $\mathbf{TS\,2}_M/\mathbf{2}_M$) to facilitate the μ^3 binding motif of the alkali ion in $\mathbf{2}_M$. This enables the third chlorido ligand to bind to the alkali ion, thereby gaining significant stabilization. The stabilization Gibbs energy decreases with alkali ion size, $\Delta G_{ass}(Li^+) = -396$ kJ mol^{-1} and $\Delta G_{ass}(Cs^+) = -189$ kJ mol^{-1}. The activated complex $\mathbf{2}_M^{\ddagger}$ decays through the various fragmentation channels described above. Here, we compare the MCl_2ZnCl elimination (yielding **4**) to the loss of $ZnCl_2$ (yielding $\mathbf{3}_M$).

The $ZnCl_2$ elimination (Figure 9 for energetics and Figure 11 for structures) is straight forward and similar for all alkali ions: M^+ displaces the $ZnCl_2$ group and coordinates to the nitrogen atoms owing to the excess of energy through excitation. Subsequent $ZnCl_2$ elimination proceeds via the transition state $\mathbf{TS\,2}_M/\mathbf{3}_M$ to form the product $\mathbf{3}_M$.

The MCl_2ZnCl elimination (Figure 9 for energetics, and Figure 12 for structures in the cases of $M = Li^+$ and Cs^+ and Figures SI-12–14 in the Supporting Information) proceeds

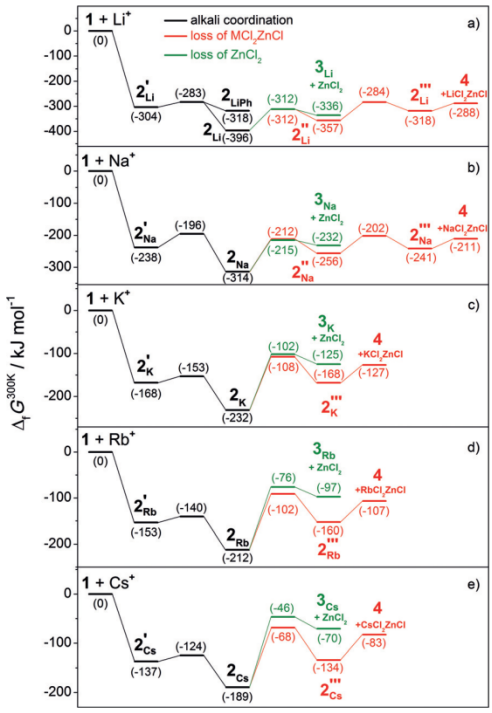

Figure 9. Calculated stationary points (minima and transition states) along the reaction coordinates of alkali association (black) and subsequent elimination of MCl_2ZnCl (red) or $ZnCl_2$ (green). Gibbs energies $\Delta_r G^{300K}$ are relative to $1+M^+$. Structures and enthalpies arise from DFT calculations at the B3LYP/cc-pVDZ (H, C, N, Li, Na) and Stuttgart 1997 ECP (Au, Zn, K, Rb, Cs) levels of theory. Note the systematic variation of Gibbs energies, in particular, at the transition states **TS 2**$_M$/**3**$_M$ and **TS 2**$_M$/**2'''**$_M$.

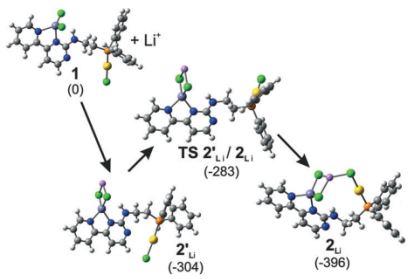

Figure 10. Optimized structures of local minima and transition state along the reaction coordinate of Li^+ association to **1**. Corresponding diagrams for $M=Na^+$, K^+, Rb^+, and Cs^+ are provided in the Supporting Information. Thermally corrected Gibbs energies $\Delta_r G^{300K}$ (in brackets in kJ mol^{-1}) are relative to $1+Li^+$. The structures originate from DFT calculations at the B3LYP/cc-pVDZ (H, C, N, Li, Na) and Stuttgart 1997 ECP (Au, Zn, K, Rb, Cs) levels of theory.

through a much more involved multistep rearrangement of the complex. Furthermore, we clearly observe an alkali size effect on the fragmentation mechanism. Complexes $\mathbf{2}_{Li}$ and $\mathbf{2}_{Na}$ isomerize prior to the actual MCl_2ZnCl (M = Li or Na) elimination. M^+ displaces the $ZnCl_2$ group and coordinates to the nitrogen atoms. The Zn^{2+} binds to the third chlorido ligand (**TS 2**$_M$/**2''**$_M$) followed by preformation of the MCl_2ZnCl group, which is represented by a local minimum on the potential energy surface (**2''**$_M$). This indicates that the formation of the MCl_2ZnCl binding motif is achieved by the migration of the $ZnCl_2$ unit in $\mathbf{2}_{Li}$ and $\mathbf{2}_{Na}$. Note that the NH groups of **2''**$_{Li}$ and **2''**$_{Na}$ still point towards the chlorido ligands. Therefore, the next step in the fragmentation mechanism is the torsion of the NNC–NHC bond of **2''**$_M$. The torsion proceeds via the transition state **TS 2''**$_M$/**2'''**$_M$ to form the local minimum **2'''**$_M$. Note that the MCl_2ZnCl unit is attached to the complex during the torsion by a NH···Cl hydrogen bond. The alkali ion size effect manifests itself at **2'''**$_M$: in the case of **2'''**$_{Li}$, the Li atom binds to the nitrogen atom of the pyrimidine ring. In the case of **2'''**$_{Na}$, the Zn atom binds to that nitrogen atom. In both cases, the next step is the dissociation of the MCl_2ZnCl unit, which yields the final product **4**.

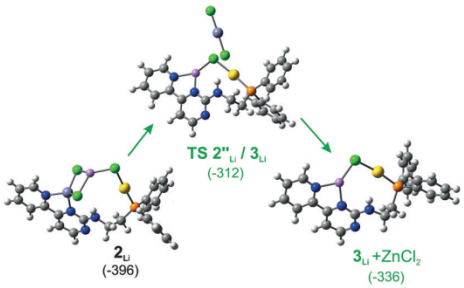

Figure 11. Optimized structures of local minima and transition state along the reaction coordinate of $ZnCl_2$ elimination from $\mathbf{2}_{Li}$. Corresponding diagrams of $M=Na^+$, K^+, Rb^+, and Cs^+ are given in the Supporting Information. Thermally corrected Gibbs energies $\Delta_r G^{300K}$ (in brackets in kJ mol^{-1}) are relative to $1+Li^+$. Structures and Gibbs energies originate from DFT calculations at the B3LYP/cc-pVDZ (H, C, N, Li, Na) and Stuttgart 1997 ECP (Au, Zn, K, Rb, Cs) levels of theory.

In the cases of the large alkali ions M = K, Rb, and Cs, the calculated fragmentation mechanism omits any **2''**$_M$ intermediates. Several concurrent torsions of $\mathbf{2}_M$ suffice to arrive at the local minimum **2'''**$_M$ (M = K, Rb, and Cs): the pyrimidine ring twists against the pyridine ring, which is enabled by the big alkali ions binding all three chlorido ligands, forming a MCl_3Zn group and breaking the Cl–Au bond. The activated Au atom binds to the vacant nitrogen coordination site of the pyridine ring through a N-CH_2-CH_2-P torsion (**TS 2**$_M$/**2'''**$_M$ (M = K, Rb, and Cs)). In parallel, the transitional complex undergoes a 180° torsion around its NNC–NHC bond. Without further activation, expulsion of a MCl_3Zn unit follows, which likely isomerizes to the more stable MCl_2ZnCl unit. The remainder of the dissociated complex is the final product **4**.

Next, we inspected the energetics of the calculated reaction coordinates of $ZnCl_2$ elimination and of Cl_2ZnCl elimination, and checked for correspondence with the observations from the CID experiments.

The large alkali ions (K, Rb, and Cs) manage to bind all three chlorido ligands, which eases the torsions that are necessary

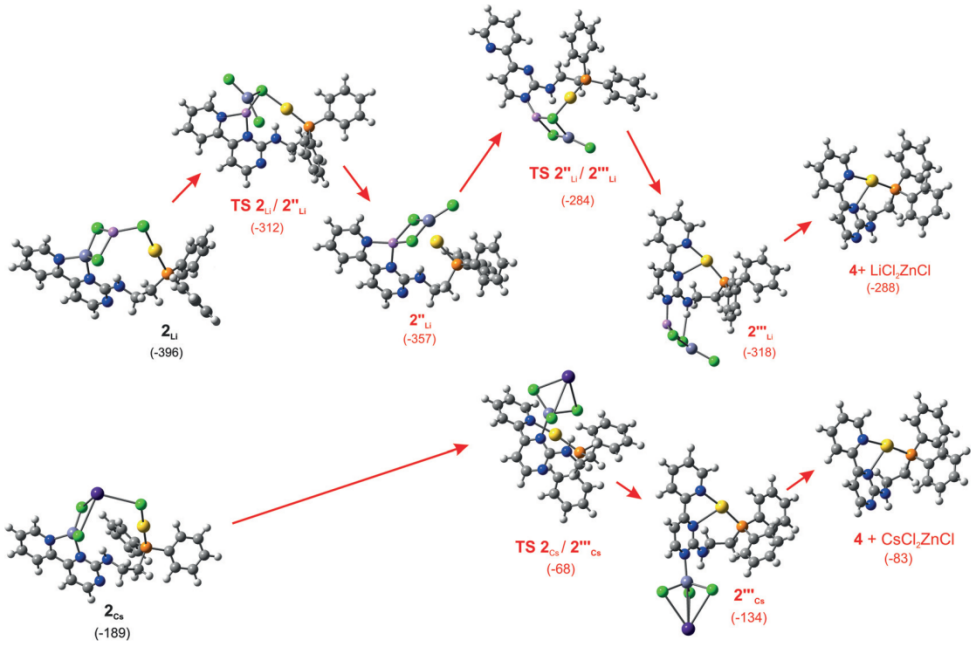

Figure 12. Optimized structures of local minima and transition state along the reaction coordinate of MCl_2ZnCl elimination from $\mathbf{2}_M$. Thermally corrected Gibbs energies $\Delta_f G^{300K}$ (in brackets in kJ mol^{-1}) are relative to $\mathbf{1}+M^+$. Structures and Gibbs energies originate from DFT calculations at the B3LYP/cc-pVDZ (H, C, N, Li, Na) and Stuttgart 1997 ECP (Au, Zn, K, Rb, Cs) levels of theory.

for the formation of product **4**. The MCl_2ZnCl elimination path is energetically lower than of the $ZnCl_2$ elimination path. Consequently, the CID experiments prove MCl_2ZnCl elimination ($[Au]^+$, **4**) as the main fragmentation channel.

The small alkali ions (Li and Na) cannot manage to bind all three chlorido ligands. This impedes the above-discussed sequence of torsions along a multistep reaction pathway to enable product **4** by MCl_2ZnCl elimination. The $ZnCl_2$ elimination proceeds through a single activation step to $\mathbf{3}_M$, and it requires as much activation energy as formation of $\mathbf{2''}_M$. The $\mathbf{3}_M+ZnCl_2$ product channel is clearly favored over the second part of the MCl_2ZnCl elimination path, from $\mathbf{2''}_M$ to $\mathbf{4}+MCl_2ZnCl$. Note that its transition states, **TS** $\mathbf{2''}_M/\mathbf{2'''}_M$, are rate determining and less stable than the product state $\mathbf{3}_M+ZnCl_2$.

The CID experiments on $[AuZnCl_3M]^+$ compare well to the calculated activation of $\mathbf{2}_M$. The experiments with small alkali cations (M = Li or Na) showed that the MCl_2ZnCl and $ZnCl_2$ elimination routes compete. At low excitation magnitudes, CID yields dominant $ZnCl_2$ elimination ($[AuMCl]^+$ product, $\mathbf{3}_M$) and only a small amount of MCl_2ZnCl elimination. The calculated reaction profiles support this finding under the condition that the CID excitation energy stays below the activation barrier of **TS** $\mathbf{2''}_M/\mathbf{2'''}_M$. Larger levels of CID excitation may overcome the calculated barrier, which in turn triggers the MCl_2ZnCl elimination, yielding product $[Au]^+$ (in calculations: **4**).

Finally, two subtle details deserve attention. The CID of $[AuZnCl_3K]^+$ shows much less $ZnCl_2$ elimination than the M = Li^+ or Na^+ complexes, and the M = Rb and Cs complexes do not exhibit any $ZnCl_2$ elimination at all. These CID findings nicely correspond to the calculated activation barriers **TS** $\mathbf{2}_M/\mathbf{3}_M$. In addition, the barrier for the competing $MZnCl_3$ elimination, **TS** $\mathbf{2}_M/\mathbf{2'''}_M$, diminishes somewhat in $\mathbf{2}_{Rb}$ and $\mathbf{2}_{Cs}$.

At very high CID excitation, $\mathbf{2}_{Li}$ and $\mathbf{2}_{Na}$ exhibit a further increase of the $[Au]^+$ yield (Figure 3a and b), corresponding to $\mathbf{4}+MCl_2ZnCl$. We interpret this as a two-step decay of initially formed, hot $[AuCl_1M]^+$ ($\mathbf{3}_M$) into $[Au]^+$ (**4**), which yields two neutral fragments, $ZnCl_2+MCl$, instead of MCl_2ZnCl. The calculated energetics (Figure 8, orange channel) are in line with this additional high energy fragmentation path (Scheme 2, $\mathbf{2}_M \rightarrow \mathbf{3}_M \rightarrow \mathbf{4}$).

Conclusion

We have cationized the neutral, bimetallic complex $[AuZnCl_3]$ by simple addition of alkali chlorides to the solution. This allowed for mass spectrometric studies of charged alkali metal adducts $[AuZnCl_3M]^+$ (M = Li^+, Na^+, K^+, Rb^+, Cs^+). By applying IR-MPD spectroscopy in combination with DFT calculations, we showed that alkali ion coordination has a profound effect on the geometry of $[AuZnCl_3]$. The aliphatic backbone of the ligand rearranges to enable a μ^3 binding motif of the alkali ion to all three chlorido ligands. Therefore, the distance between Au and Zn is reduced with respect to the neutral compound. This distance increases systematically with the alkali ion size.

Likewise, fragmentation channels of the alkali adducts vary. The Li^+ and Na^+ adducts prefer loss of $ZnCl_2$, whereas the K^+, Rb^+, and Cs^+ adducts preferably lose a MCl_2ZnCl unit. Fragment-specific CID appearance curves show a change in the favorable fragmentation pathway at high CID amplitudes.

The calculated structures at stationary points along the reaction pathways help to explain these observations. In the cases of small alkali cations $M^+ = Li^+$ and Na^+, inspection of the reaction path (Figure 12) reveals isomerization of $\mathbf{2}_M$ prior to the fragmentation: Zn and the alkali ion swap their coordination sites such that a planar MCl_2ZnCl units forms, yet is still attached. A subsequent twist of the backbone follows to release the MCl_2ZnCl fragment. Ultimately, MCl_2ZnCl elimination thus proceeds across two reaction barriers, the second, higher barrier is only overcome at high CID amplitudes of excitation. In the cases of the large alkali cations $M^+ = K^+$, Rb^+, Cs^+, the reaction path proceeds through a single barrier, which is due to the backbone twist. There is no intermetallic coordination swapping and no (in case of $M = K^+$ only a little) concomitant $ZnCl_2$ elimination. MCl_3Zn expulsion occurs exclusively with concurrent isomerization into MCl_2ZnCl.

In summary, the present study reveals that the seeming order of interaction strength with nitrogen coordination sites of the given ligand is as follows: $Li^+ > Na^+ > Zn^{2+} > K^+ > Rb^+ \approx Cs^+$. This finding is novel with respect to the relative interaction strength of the Zn^{2+} coordination. It may relate to the specific case of mixed coordination to nitrogen and chlorido ligands in parallel.

The outlook of the present study is clear: it remains to elucidate how alkali ion coordination affects the reactivity of $[AuZnCl_3]$ in conceivable applications, such as, for example, as homogenous hydroamination catalysis. In upcoming studies, such reaction mixtures will be the focus of our investigations. It is conceivable to identify cationized key intermediates of prospective catalytic cycles. If done, an enhanced modelling might become desirable. This could involve molecular dynamics simulations and subsequent autocorrelation analysis, aiming at verification of the solution-phase IR spectra.[34]

Acknowledgements

This work was supported by the German research foundation, DFG, within the transregional collaborative research center SFB/TRR 88 "Cooperative effects in homo and heterometallic complexes" (3MET.de) and by the state research center OPTIMAS.

Keywords: alkali metal ions · bimetallic complexes · collision-induced dissociation · electrospray ionization · mass spectrometry

[1] a) W. A. Herrmann, B. Cornils, *Angew. Chem. Int. Ed. Engl.* **1997**, *36*, 1048–1067; *Angew. Chem.* **1997**, *109*, 1074–1095; b) D. K. Böhme, H. Schwarz, *Angew. Chem. Int. Ed.* **2005**, *44*, 2336–2354; *Angew. Chem.* **2005**, *117*, 2388–2406; c) R. H. Grubbs, *Angew. Chem. Int. Ed.* **2006**, *45*, 3760–3765; *Angew. Chem.* **2006**, *118*, 3845–3850; d) D. J. Gorin, B. D. Sherry, F. D. Toste, *Chem. Rev.* **2008**, *108*, 3351–3378; e) P. Braunstein, F. Naud, *Angew. Chem. Int. Ed.* **2001**, *40*, 680–699; *Angew. Chem.* **2001**, *113*, 702–722.

[2] a) G. W. Parshall, S. D. Ittel, *Homogeneous Catalysis*, John Wiley & Sons, New York, **1992**; b) R. Bates, *Organic Synthesis Using Transition Metals*, John Wiley & Sons, Chichester, **2000**; c) A. S. K. Hashmi, G. J. Hutchings, *Angew. Chem. Int. Ed.* **2006**, *45*, 7896–7936; *Angew. Chem.* **2006**, *118*, 8064–8105; d) A. S. K. Hashmi, *Angew. Chem. Int. Ed.* **2010**, *49*, 5232–5241; *Angew. Chem.* **2010**, *122*, 5360–5369.

[3] a) J. Goura, V. Mereacre, G. Novitchi, A. K. Powell, V. Chandrasekhar, *Eur. J. Inorg. Chem.* **2015**, 156–165; b) J. M. Serrano-Becerra, A. F. G. Maier, S. González-Gallardo, E. Moos, C. Kaub, M. Gaffga, G. Niedner-Schatteburg, P. W. Roesky, F. Breher, J. Paradies, *Eur. J. Org. Chem.* **2014**, 4515–4522; c) Y. Schmitt, K. Chevalier, F. Rupp, M. Becherer, A. Grun, A. M. Rijs, F. Walz, F. Breher, R. Diller, M. Gerhards, W. Klopper, *Phys. Chem. Chem. Phys.* **2014**, *16*, 8332–8338; d) A. Fromm, C. van Wüllen, D. Hackenberger, L. J. Gooßen, *J. Am. Chem. Soc.* **2014**, *136*, 10007–10023; e) J. Chmela, M. E. Harding, D. Matioszek, C. E. Anson, F. Breher, W. Klopper, *ChemPhysChem* **2016**, *17*, 37–45.

[4] a) N. Tsukada, T. Mitsuboshi, H. Setoguchi, Y. Inoue, *J. Am. Chem. Soc.* **2003**, *125*, 12102–12103; b) P. Buchwalter, J. Rosé, P. Braunstein, *Chem. Rev.* **2014**, *115*, 28–126.

[5] a) R. Colton, A. D'Agostino, J. C. Traeger, *Mass Spectrom. Rev.* **1995**, *14*, 79–106; b) J. B. Fenn, *Angew. Chem. Int. Ed.* **2003**, *42*, 3871–3894; *Angew. Chem.* **2003**, *115*, 3999–4024; c) M. Yamashita, J. B. Fenn, *J. Phys. Chem.* **1984**, *88*, 4451–4459.

[6] E. de Hoffmann, *J. Mass Spectrom.* **1996**, *31*, 129–137.

[7] a) R. C. Dunbar in *Spectroscopy of Metal–Ion Complexes with Peptide-Related Ligands, Vol. 364* (Eds.: A. M. Rijs, J. Oomens), Springer, Cleveland (USA), **2015**, pp. 183–223; b) M. A. Duncan, *Int. J. Mass Spectrom.* **2008**, *272*, 99–118; c) J. R. Eyler, *Mass Spectrom. Rev.* **2009**, *28*, 448–467; d) N. Heine, K. R. Asmis, *Int. Rev. Phys. Chem.* **2015**, *34*, 1–34; e) N. C. Polfer, *Chem. Soc. Rev.* **2011**, *40*, 2211–2221; f) N. C. Polfer, J. Oomens, *Mass Spectrom. Rev.* **2009**, *28*, 468–494; g) A. M. Rijs, J. Oomens in *IR Spectroscopic Techniques to Study Isolated Biomolecules, Vol. 364* (Eds.: A. M. Rijs, J. Oomens), Springer, Nijmegen (The Netherlands), **2015**, pp. 1–42.

[8] a) K. Levsen, H. Schwarz, *Angew. Chem. Int. Ed. Engl.* **1976**, *15*, 509–519; *Angew. Chem.* **1976**, *88*, 589–599; b) R. G. Cooks, *J. Mass Spectrom.* **1995**, *30*, 1215–1221; c) A. K. Shukla, J. H. Futrell, *J. Mass Spectrom.* **2000**, *35*, 1069–1090; d) K. M. Ervin, P. B. Armentrout, *J. Chem. Phys.* **1987**, *86*, 2659–2673.

[9] a) J. Jašík, J. Žabka, J. Roithová, D. Gerlich, *Int. J. Mass Spectrom.* **2013**, *354–355*, 204–210; b) C. J. Johnson, A. B. Wolk, J. A. Fournier, E. N. Sullivan, G. H. Weddle, M. A. Johnson, *J. Chem. Phys.* **2014**, *140*, 221101; c) A. B. Wolk, C. M. Leavitt, E. Garand, M. A. Johnson, *Acc. Chem. Res.* **2014**, *47*, 202–210.

[10] J. Oomens, B. G. Sartakov, G. Meijer, G. von Helden, *Int. J. Mass Spectrom.* **2006**, *254*, 1–19.

[11] Y. Nosenko, F. Menges, C. Riehn, G. Niedner-Schatteburg, *Phys. Chem. Chem. Phys.* **2013**, *15*, 8171–8178.

[12] a) J. Lang, M. Gaffga, F. Menges, G. Niedner-Schatteburg, *Phys. Chem. Chem. Phys.* **2014**, *16*, 17417–17421; b) J. Jašík, D. Gerlich, J. Roithová, *J. Am. Chem. Soc.* **2014**, *136*, 2960–2962; c) B. M. Elliott, R. A. Relph, J. R. Roscioli, J. C. Bopp, G. H. Gardenier, T. L. Guasco, M. A. Johnson, *J. Chem. Phys.* **2008**, *129*, 094303.

[13] a) O. Kurka, J. Roithová, P. Bednář, *J. Mass Spectrom.* **2014**, *49*, 1314–1321; b) T. S. Rodrigues, V. H. C. Silva, P. M. Lalli, H. C. B. de Oliveira, W. A. da Silva, F. Coelho, M. N. Eberlin, B. A. D. Neto, *J. Org. Chem.* **2014**, *79*, 5239–5248.

[14] a) A. Fedorov, P. Chen, *Organometallics* **2010**, *29*, 2994–3000; b) A. Fedorov, E. P. A. Couzijn, N. S. Nagornova, O. V. Boyarkin, T. R. Rizzo, P. Chen, *J. Am. Chem. Soc.* **2010**, *132*, 13789–13798; c) A. Fedorov, M.-E. Moret, P. Chen, *J. Am. Chem. Soc.* **2008**, *130*, 8880–8881; d) C. M. Frech, O. Blacque, H. W. Schmalle, H. Berke, C. Adlhart, P. Chen, *Chem. Eur. J.* **2006**, *12*, 3325–3338; e) D. Serra, M.-E. Moret, P. Chen, *J. Am. Chem. Soc.* **2011**, *133*, 8914–8926; f) J. Roithová, *Chem. Soc. Rev.* **2012**, *41*, 547–559; g) K. L. Vikse, Z. Ahmadi, J. S. McIndoe, *Coord. Chem. Rev.* **2014**, *279*, 96–114; h) K. L. Vikse, M. A. Henderson, A. G. Oliver, J. S. McIndoe, *Chem. Commun.* **2010**, *46*, 7412–7414; i) A. Skriba, J. Schulz, J. Roithova, *Organometallics* **2014**, *33*, 6868–6878; j) D. Schröder, *Acc. Chem. Res.* **2012**, *45*, 1521–1532.

[15] a) D. M. Chisholm, J. S. McIndoe, *Dalton Trans.* **2008**, 3933–3945; b) C. Adlhart, C. Hinderling, H. Baumann, P. Chen, *J. Am. Chem. Soc.* **2000**, *122*, 8204–8214; c) J. Limberger, B. C. Leal, A. L. Monteiro, J. Dupont, *Chem. Sci.* **2015**, *6*, 77–94.

[16] a) S. J. P'Poo, H.-J. Schanz, *J. Am. Chem. Soc.* **2007**, *129*, 14200–14212; b) C. W. Bielawski, R. H. Grubbs, *Macromolecules* **2001**, *34*, 8838–8840.

[17] a) J. Wei, A. W. T. Bristow, P. B. O'Connor, *J. Am. Soc. Mass Spectrom.* **2015**, *26*, 166 – 173; b) L. M. Teesch, J. Adams, *Org. Mass Spectrom.* **1992**, *27*, 931 – 943; c) F. Menges, C. Riehn, G. Niedner-Schatteburg, *Z. Phys. Chem. (Muenchen Ger.)* **2011**, *225*, 595.
[18] J. Adams, M. L. Gross, *Anal. Chem.* **1987**, *59*, 1576 – 1582.
[19] a) H. Wang, J. O. Metzger, *Organometallics* **2008**, *27*, 2761 – 2766; b) H.-Y. Wang, W.-L. Yim, Y.-L. Guo, J. O. Metzger, *Organometallics* **2012**, *31*, 1627 – 1634; c) H.-Y. Wang, W.-L. Yim, T. Klüner, J. O. Metzger, *Chem. Eur. J.* **2009**, *15*, 10948 – 10959; d) G. K. Poon, P. Mistry, S. Lewis, *Biol. Mass Spectrom.* **1991**, *20*, 687 – 692.
[20] P. Ball, J. E. Hallsworth, *Phys. Chem. Chem. Phys.* **2015**, *17*, 8297 – 8305.
[21] a) R. D. Mountain, D. Thirumalai, *J. Phys. Chem. B* **2004**, *108*, 19711 – 19716; b) N. Tomaskova, R. Varhac, G. Zoldak, L. Oleksakova, D. Sedlakova, E. Sedlak, *J. Biol. Inorg. Chem.* **2007**, *12*, 257 – 266; c) Y. J. Zhang, P. S. Cremer, *Current Op. Chem. Biol.* **2006**, *10*, 658 – 663; d) Y. J. Zhang, S. Furyk, D. E. Bergbreiter, P. S. Cremer, *J. Am. Chem. Soc.* **2005**, *127*, 14505 – 14510; e) R. Zangi, M. Hagen, B. J. Berne, *J. Am. Chem. Soc.* **2007**, *129*, 4678 – 4686.
[22] a) A. S. Demir, M. Emrullahoglu, K. Buran, *Chem. Commun.* **2010**, *46*, 8032 – 8034; b) Y. Wang, L. Liu, L. Zhang, *Chem. Sci.* **2013**, *4*, 739 – 746.
[23] a) J. Laskin, J. H. Futrell, *Mass Spectrom. Rev.* **2005**, *24*, 135 – 167; b) S. A. McLuckey, D. E. Goeringer, *J. Mass Spectrom.* **1997**, *32*, 461 – 474.
[24] a) E.-L. Zins, C. Pepe, D. Schröder, *J. Mass Spectrom.* **2010**, *45*, 1253 – 1260; b) E.-L. Zins, C. Pepe, D. Rondeau, S. Rochut, N. Galland, J.-C. Tabet, *J. Mass Spectrom.* **2009**, *44*, 12 – 17; c) K. V. Barylyuk, K. Chingin, R. M. Balabin, R. Zenobi, *J. Am. Soc. Mass Spectrom.* **2010**, *21*, 172 – 177.
[25] a) B. Miehlich, A. Savin, H. Stoll, H. Preuss, *Chem. Phys. Lett.* **1989**, *157*, 200 – 206; b) A. D. Becke, *J. Chem. Phys.* **1993**, *98*, 5648 – 5652.
[26] T. H. Dunning, *J. Chem. Phys.* **1989**, *90*, 1007 – 1023.
[27] M. Dolg, H. Stoll, H. Preuss, R. M. Pitzer, *J. Phys. Chem.* **1993**, *97*, 5852 – 5859.
[28] a) Gaussian 03 (Revision C.02), M. J. Frisch, G. W. Trucks, H. B. Schlegel, G. E. Scuseria, M. A. Robb, J. R. Cheeseman, J. A. Montgomery, Jr., T. Vreven, K. N. Kudin, J. C. Burant, J. M. Millam, S. S. Iyengar, J. Tomasi, V. Barone, B. Mennucci, M. Cossi, G. Scalmani, N. Rega, G. A. Petersson, H. Nakatsuji, M. Hada, M. Ehara, K. Toyota, R. Fukuda, J. Hasegawa, M. Ishida, T. Nakajima, Y. Honda, O. Kitao, H. Nakai, M. Klene, X. Li, J. E. Knox, H. P. Hratchian, J. B. Cross, C. Adamo, J. Jaramillo, R. Gomperts, R. E. Stratmann, O. Yazyev, A. J. Austin, R. Cammi, C. Pomelli, J. W. Ochterski, P. Y. Ayala, K. Morokuma, G. A. Voth, P. Salvador, J. J. Dannenberg, V. G. Zakrzewski, S. Dapprich, A. D. Daniels, M. C. Strain, O. Farkas, D. K. Malick, A. D. Rabuck, K. Raghavachari, J. B. Foresman, J. V. Ortiz, Q. Cui, A. G. Baboul, S. Clifford, J. Cioslowski, B. B. Stefanov, G. Liu, A. Liashenko, P. Piskorz, I. Komaromi, R. L. Martin, D. J. Fox, T. Keith, M. A. Al-Laham, C. Y. Peng, A. Nanayakkara, M. Challacombe, P. M. W. Gill, B. Johnson, W. Chen, M. W. Wong, C. Gonzalez, J. A. Pople, Gaussian, Inc., Pittsburgh, PA, **2003**; b) Gaussian 09, Revision E.01, M. J. Frisch, G. W. Trucks, H. B. Schlegel, G. E. Scuseria, M. A. Robb, J. R. Cheeseman, G. Scalmani, V. Barone, B. Mennucci, G. A. Petersson, H. Nakatsuji, M. Caricato, X. Li, H. P. Hratchian, A. F. Izmaylov, J. Bloino, G. Zheng, J. L. Sonnenberg, M. Hada, M. Ehara, K. Toyota, R. Fukuda, J. Hasegawa, M. Ishida, T. Nakajima, Y. Honda, O. Kitao, H. Nakai, T. Vreven, J. A. Montgomery, Jr., J. E. Peralta, F. Ogliaro, M. Bearpark, J. J. Heyd, E. Brothers, K. N. Kudin, V. N. Staroverov, R. Kobayashi, J. Normand, K. Raghavachari, A. Rendell, J. C. Burant, S. S. Iyengar, J. Tomasi, M. Cossi, N. Rega, J. M. Millam, M. Klene, J. E. Knox, J. B. Cross, V. Bakken, C. Adamo, J. Jaramillo, R. Gomperts, R. E. Stratmann, O. Yazyev, A. J. Austin, R. Cammi, C. Pomelli, J. W. Ochterski, R. L. Martin, K. Morokuma, V. G. Zakrzewski, G. A. Voth, P. Salvador, J. J. Dannenberg, S. Dapprich, A. D. Daniels, Ö. Farkas, J. B. Foresman, J. V. Ortiz, J. Cioslowski, D. J. Fox, Gaussian, Inc. Wallingford CT, **2009**.
[29] M. Gaffga, I. Munstein, P. Müller, J. Lang, W. R. Thiel, G. Niedner-Schatteburg, *J. Phys. Chem. A* **2015**, *119*, 12587 – 12598.
[30] The current IUPAC definition of hydrogen bonds (E. Arunan, G. R. Desiraju, R. A. Klein, J. Sadlej, S. Scheiner, I. Alkorta, D. C. Clary, R. H. Crabtree, J. J. Dannenberg, P. Hobza, H. G. Kjaergaard, A. C. Legon, B. Mennucci, D. J. Nesbitt, *Pure Appl. Chem.* **2011**, *83*, 1637 – 1641, DOI: 10.1351/PAC-REC-10-01-02) does certify a likely redshift of the vibrational stretching modes upon hydrogen bond formation, and it does not comment on likely broadening of these; nevertheless, knowledge of such broadenings has become generally accepted (G. C. Pimentel, *The Hydrogen Bond*, W. H. Freeman, San Francisco, **1960**). The general occurrence of band broadening upon hydrogen bond formation finds its conceptual understanding in terms of highly anharmonic multidimensional potential hyper surfaces.
[31] J. D. Dill, C. L. Fischer, F. W. McLafferty, *J. Am. Chem. Soc.* **1979**, *101*, 6531 – 6534.
[32] R. L. Baldwin, *Biophys. J.* **1996**, *71*, 2056 – 2063.
[33] a) K. Biradha, G. R. Desiraju, D. Braga, F. Grepioni, *Organometallics* **1996**, *15*, 1284 – 1295; b) K. Okamoto, T. Yamamoto, T. Kanbara, *J. Nanosci. Nanotechnol.* **2009**, *9*, 646 – 649.
[34] S. K. Min, M. Park, N. J. Singh, H. M. Lee, E. C. Lee, K. S. Kim, A. Lagutschenkov, G. Niedner-Schatteburg, *Chem. Eur. J.* **2010**, *16*, 10373 – 10379.

Received: October 12, 2015
Published online on January 19, 2016

5 Two Color Delay Dependent IR Probing of Torsional Isomerization in a $[AgL_1L_2]^+$ Complex

Johannes Lang, Maximilian Gaffga, Fabian Menges

and Gereon Niedner-Schatteburg

Fachbereich Chemie and Forschungszentrum OPTIMAS,
Technische Universität Kaiserslautern,
67663 Kaiserslautern, Germany

5.1 Preamble

The following chapter is a reprint of a publication in the journal "Physical Chemistry Chemical Physics". Supplementary information is available in chapter 10.3.

I wrote the first draft of this publication on behalf of my diploma thesis. I revised it during my doctoral studies with the help of Fabian Menges and Gereon Niedner-Schatteburg. Chapter 5.3 comprises associated (unpublished) experimental data collected during my doctoral studies. I conducted the measurements and data evaluations with the help of M. Gaffga. Fabian Menges and I conducted the presented quantum chemical calculations.

Full Reference:

Two-color delay dependent IR probing of torsional isomerization in a $AgL_1L_2^+$ complex
J. Lang, M. Gaffga, F. Menges and G. Niedner-Schatteburg, *Physical Chemistry Chemical Physics* **2014**, *16*, 17417-17421.

http://dx.doi.org/10.1039/c4cp02045f

5.2 Reprint

Reprint Licence

PCCP

COMMUNICATION

View Article Online
View Journal | View Issue

Cite this: *Phys. Chem. Chem. Phys.*, 2014, **16**, 17417

Received 11th May 2014,
Accepted 11th July 2014

DOI: 10.1039/c4cp02045f

www.rsc.org/pccp

Two-color delay dependent IR probing of torsional isomerization in a $[AgL_1L_2]^+$ complex†

Johannes Lang, Maximilian Gaffga, Fabian Menges‡ and Gereon Niedner-Schatteburg

Two-color infrared multiple photon dissociation (2c-IR-MPD) spectroscopy with delayed pulses indicates a torsional isomerization in a "ligand–metal–chelate" complex $[AgL_1L_2]^+$. *Ab initio* calculations reveal the torsional barrier as well as the change in vibrational frequencies and IR intensities along the isomerization pathway. The current approach bears prospects for further elucidation of competing interactions within naked or microsolvated complexes in gas phase coordination chemistry.

Metal ions stabilize through reversible solvation or persistent coordination. In appropriate mixtures, ligand exchange drives equilibria towards the formation of complexes with as many strongly coordinating ligands as possible within steric and electronic constraints.

Mass produced chelating agents like ethylenediaminetetraacetic acid (EDTA)[1] serve in the extraction of heavy metal ions from waste waters and in alkaline earth metal ion scavenging for water softening on a large scale.[2,3] Environmental issues[4] call for biodegradability (as *e.g.* fulfilled by Trilon M®[5,6]) and for further optimization of the chelation processes.[7] The finely tuned interplay between ligand-to-ligand and ligand-to-solvent interactions (including hydrogen bonding) plays a crucial role in the reversible stabilization of metal ions within such chelated complexes.[8,9] It is paramount to acquire insight into their structure and vibrational dynamics in order to advance our understanding of the dominating processes and the prevailing equilibria.

The combination of mass spectrometry with infrared (IR) laser spectroscopy is suitable for the characterization of stoichiometrically defined coordination complexes, and recent two-color double resonance studies proved to be instrumental in obtaining isomer sensitivity of various gas phase complexes and clusters.[10–14] Experimental spectra recorded in such solvent-free environments correspond to *ab initio* calculations of the isolated species, thus yielding insight into the structure and dynamics of likely binding motifs. We have recently applied a two-color IR-MPD detection scheme to study an isolated di-nuclear silver complex which spontaneously forms in solution by coordination with nucleobase mimicking ligands.[15]

Here, we investigate a flexible arrangement of a single Ag(I) center with two coordinating ligands, α-cyano-4-hydroxycinnamic acid (HCCA = L_1, monodentate ligand) and 2-(5-methyl-1*H*-pyrazol-3-yl)pyridine[16] (MPP = L_2, bidentate chelate), one each. The resulting $[AgL_1L_2]^+$ complex serves as a model for a ligand-to-chelate hydrogen bonding within a "ligand–metal–chelate" complex. A possible torsional isomerization (*cf.* Scheme 1) is the subject of verification and characterization by this study.

A sample solution of $AgNO_3$, HCCA and MPP[17] in acetonitrile at a concentration of 1×10^{-5} M was used without further purification and continuously infused into an electrospray ion trap instrument (Bruker amaZon SL, *cf.* Supplement for further experimental details). We deduced the formation of the self-assembled $[AgL_1L_2]^+$ complex from the signal of a cation recorded at $m/z = 455$ and 457 (due to the ^{107}Ag and ^{109}Ag isotopes). The isotopic pattern clearly proves a complexation of a Ag(I) ion (*cf.* Fig. S1, middle inset, ESI†) by neutral L_1 and L_2 ligands leading to a singly charged ligand–metal–chelate complex. Collision induced dissociation inside the ion trap exhibits the exclusive loss of the monodentate L_1 ligand (*cf.* Fig. S1, top inset, ESI†).

We employed IR-MPD spectroscopy in the 1200–3800 cm^{-1} range on the $[AgL_1L_2]^+$ complex (*cf.* top of Fig. 1) using a tunable high power OPO/OPA IR laser (IR_{scan}, LaserVision, *cf.* SI. 2 and SI. 3 for further experimental details, ESI†). The observed bands can be assigned by comparison with DFT derived vibrational spectra: OH stretching vibration of the phenolic OH group ($\tilde{\nu}_{PhOH}$ = 3639 cm^{-1}), OH stretching vibration of the carboxyl group ($\tilde{\nu}_{COOH}$ =3581 cm^{-1}), free NH stretching vibration of the L_2 chelate ($\tilde{\nu}_{NH}$ = 3490 cm^{-1}) and hydrogen bonded NH stretching vibration of the L_2 chelate ($\tilde{\nu}_{NH}^{H\text{-bound}}$ at around 3400 cm^{-1}), aliphatic CH stretching vibrations ($\tilde{\nu}_{CH}^{aliph.}$ at around 2960 cm^{-1}),

Fachbereich Chemie and Forschungszentrum OPTIMAS, Technische Universität Kaiserslautern, 67663 Kaiserslautern, Germany

† Electronic supplementary information (ESI) available. See DOI: 10.1039/c4cp02045f

‡ Current address: Dept. of Chemistry, Yale University, New Haven, CT 06520, USA.

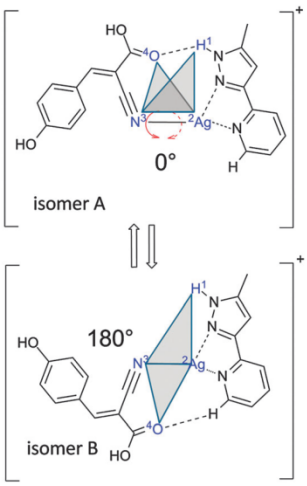

Scheme 1 Definition of the dihedral angle that describes the torsional isomerization in the $[AgL_1L_2]^+$ complex. Note, that isomer A stabilizes through a NH–O hydrogen bond and isomer B through a CH–O hydrogen bond.

C=C vibrations ($\tilde{\nu}_{C=C}$ = 1600 cm^{-1}) as well as the carboxylic CO stretching band in L_1 ($\tilde{\nu}_{COOH}$ at around 1780 cm^{-1}). A spurious dip in the $\tilde{\nu}_{PhOH}$ band at 3630 cm^{-1} is an artefact of known fluctuations in the IR_{scan} laser power. The simultaneous occurrence of a free and a hydrogen bonded NH stretching vibration cannot result from a single isomer, since there is only one NH group in the $[AgL_1L_2]^+$ complex. This indicates the coexistence of at least two isomers in the gas phase. The $\tilde{\nu}_{COOH}$ band at 3581 cm^{-1} is red shifted with respect to the calculation which is explained by a higher anharmonicity of the carboxylic $\tilde{\nu}_{COOH}$ relative to the phenolic $\tilde{\nu}_{PhOH}$.[18–20]

Minimum energy structures, relative energies and linear IR spectra were calculated at the B3LYP[21–24]/cc-pVTZ[25] level of theory as implemented in the Gaussian 09 program package.[26] The Stuttgart–Dresden effective core potential basis set was used to represent the Ag atom.[27] Harmonic vibrational frequencies were scaled by the factor 0.96 (1.0) for the stretching modes above (below) 2000 cm^{-1} to match the most intense experimental bands (*e.g.* $\tilde{\nu}_{PhOH}$ at 3639 cm^{-1}). Calculated intensities were multiplied by the photon energy (in cm^{-1}) for normalization. We found at least four energetically favored coordination motifs in $[AgL_1L_2]^+$ (*cf.* Fig. 1, structures A–D). Structure A is the energetically most favorable. Energies of structures B–D are given relative to the energy of structure A. Within the structures A and B, the silver ion is coordinated by the nitrile group of the L_1 ligand and two nitrogen atoms of the L_2 chelate. Structure A allows for the formation of a NH–O hydrogen bond (d(NH–O) = 3.011 Å, d(NH–O) = 2.035 Å) between the NH group of L_2 and the carboxyl group of L_1. Structures A and B are rotational conformers, where L_1 and L_2 twist against each other by about 180°. This rotation allows for the formation of a new CH–O hydrogen bond (d(CH–O) = 4.058 Å, d(CH–O) = 2.989 Å) between a pyridine CH in L_2 and the carboxyl group of L_1. The computed bond distances are only slightly above typical values of similar bands in the solid state.[28] Nevertheless, the CH–O hydrogen bonded structure B is less stable by 8 kJ mol^{-1} than the NH–O hydrogen bonded structure A. In isomers C and D, the silver ion is coordinated by the same two nitrogen atoms of L_2 as in A and B, whereas – from the L_1 point of view – the terminal oxygen atom of the carboxyl group serves as an electron donor in C and D, instead of the nitrile group in isomers A and B. A mere rotation by 180° transforms structure C (21 kJ mol^{-1}) into structure D (33 kJ mol^{-1}), which makes them mutual rotamers.

The experimental one-color IR-MPD spectrum can be explained by a mixture of isomers A and B. There is no evidence of isomers C and D, which would exhibit a red-shifted CO stretching vibration due to the coordination of the Ag(I) ion to the terminal carboxyl oxygen atom. The $\tilde{\nu}_{PhOH}$ and $\tilde{\nu}_{COOH}$ bands, corresponding to free OH and COOH stretching motions, result from both isomers A and B. The hydrogen bonded NH stretching vibration $\tilde{\nu}_{NH}^{H\text{-bound}}$ exclusively results from isomer A, while the NH stretching band $\tilde{\nu}_{NH}$ is indicative of isomer B. The predicted intensity of $\tilde{\nu}_{NH}^{H\text{-bound}}$ is much higher than observed, which is a known finding in hydrogen bonding that broadens and smears out the affected vibrations. Observed bands in the CO stretching region at around 1800 cm^{-1} correlate well with those of isomers A and B. The recorded spectra do not reveal the predicted strong bands (at around 1640–1650 cm^{-1}) of the high energy isomers C and D. It is a pending task to record two-color IR-MPD spectra in the fingerprint region below 2000 cm^{-1} and to perform an in-detail interpretation. However, it is already warranted at this stage that the current findings on $[AgL_1L_2]^+$ conclude in the coexistence of isomers A and B most likely in the absence of C and D.

We investigated by further DFT calculations the torsional conversion of isomer A to B through parametrical variation of an appropriate dihedral angle (between $H^1Ag^2N^3O^4$, *cf.* Scheme 1), which can be thought of as the intersection angle of the two planes spanned by $H^1Ag^2N^3$ and $Ag^2N^3O^4$ atoms. Our calculations performed full structural relaxation at fixed dihedral angles in steps of 10° with closer intervals of 4° around the minima at 0° and 180° in order to extract pointwise values of relative energies, vibrational frequencies and IR intensities (*cf.* Fig. 2, from bottom to top).

Isomers A and B are well confirmed by the energetic minima at 0° and 180° (*cf.* Fig. 2, bottom), and we find a higher (lower) torsional stiffness in the OH (CH) hydrogen bonded more (less) stable isomer A (B) with a torsional barrier of 12 kJ mol^{-1}. The majority of vibrational modes are decoupled from the torsional isomerization and their frequencies persist without a significant change in the geometries of isomers A and B and – most notably – at all dihedral angles in between. However, there are considerable red shifts of those vibrational bands that are involved in hydrogen bonding, and concomitant variations of their IR intensities. At a dihedral angle of 0°, isomer A is the favorable structure and $\tilde{\nu}_{NH}^{H\text{-bound}}$ is red shifted due to the hydrogen bond and its IR intensity is strongly enhanced. At 180°, isomer B, the pyridinic CH group is involved in a CH–O hydrogen bond. There are at least four IR active normal modes

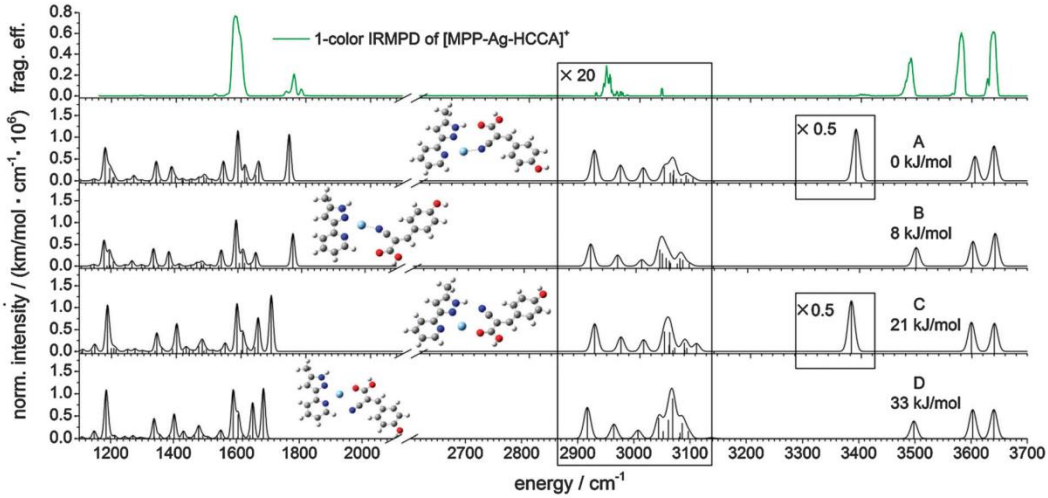

Fig. 1 IR-MPD spectrum of the $[AgL_1L_2]^+$ complex (green, L_1 loss recorded) in comparison with the DFT calculations at the B3LYP/cc-pVTZ (H, C, N, and O) and Stuttgart (1997) ECP (Ag) level of theory (black). Frequencies are scaled with the factor 0.96 (1.0) above (below) 2000 cm^{-1}. Intensities are multiplied by the photon energy (in cm^{-1}) for normalization.

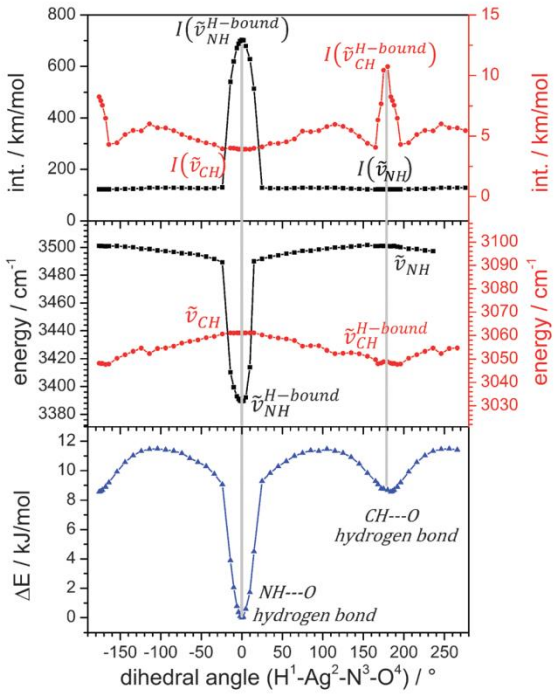

Fig. 2 Total energy of torsional twisting in the $[AgL_1L_2]^+$ complex (bottom), frequencies of hydrogen bonding vibrations (middle) and their IR intensities (top) derived by DFT calculations at the B3LYP/cc-pVTZ (H, C, N, O) and Stuttgart (1997) RSC ECP (Ag) level of theory. Formation and breaking of the hydrogen bonds by torsional isomerization leaves marks in all three diagrams. Note that the angular width of the strong NH–O bond is narrow while that of the weaker CH–O bond is wider.

of the pyridine ring that involve this CH group. We chose to plot the mode with the strongest change in IR intensities (*cf.* Fig. S2 for its definition and Fig. S3 for torsional plots of IR intensity changes in other CH stretching modes, ESI†). Its frequency shifts slightly to the red upon hydrogen bonding while its IR intensity increases considerably. All findings of the parametric torsional variation nicely confirm strong NH–O hydrogen bonding in isomer A and weak CH–O hydrogen bonding in isomer B.

In order to investigate the predicted interconversion of isomers A and B experimentally, we applied the two-color IR-MPD technique to the $[AgL_1L_2]^+$ complex. An attenuated IR laser (IR_{fix}) is set resonant to $\tilde{\nu}_{PhOH}$ at 3639 cm^{-1}, and a high power scanning IR laser (IR_{scan}) was used to measure delay dependent IR-MPD spectra (*cf.* Fig. 3a). The time delay, Δt, between the two laser pulses (6 ns each) is defined as:

$$\Delta t = t(IR_{fix}) - t(IR_{scan}) \quad (1)$$

It depends on the time delay Δt between the IR_{scan} and IR_{fix} pulses whether the hydrogen bound NH stretching band at around 3400 cm^{-1} is observable or not. Note, that the application of a second laser pulse causes some increase of the baselines in the two-color IR-MPD spectra as compared to the one-color spectrum.

When the IR_{scan} pulse excites the $[AgL_1L_2]^+$ complex ahead of the IR_{fix} pulse (Δt positive, red line spectrum in Fig. 3a) then there is some increase in the IR-MPD fragmentation yield with respect to the one-color spectrum (black curve) on all bands. In this case, the IR_{fix} pulse serves to enhance the absolute fragmentation yield. It does not, however, alter the isomer population as recorded by the one-color experiment. The two-color spectrum thus probes "cold" (here: room temperature) complexes. In particular, the hydrogen bonded NH vibration ($\tilde{\nu}_{NH}^{H\text{-bound}}$) becomes strongly enhanced and clearly observable.

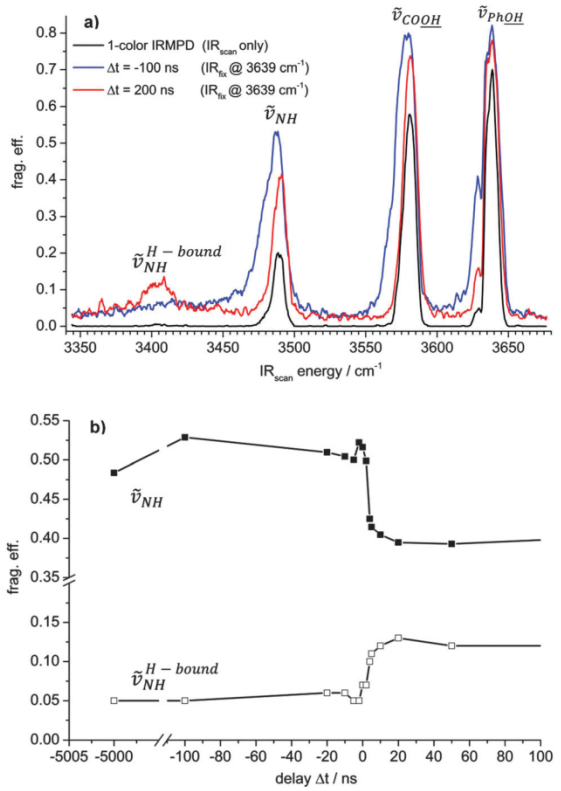

Fig. 3 (a) Details from the infrared spectra of stretching vibrations in the $[AgL_1L_2]^+$ complex. The delay dependent two-color IR-MPD spectra with selected time delay reveal heating effects and/or isomerization. (b) Fragmentation efficiency at the peak of the $\tilde{\nu}_{NH}$ band (filled squares) and the $\tilde{\nu}_{NH}^{H\text{-bound}}$ band (empty squares) in dependence of the time delay $\Delta t = t(IR_{fix}) - t(IR_{scan})$. A step-like switch amongst both vibrations around $\Delta t = 0$ ns is clearly visible.

However, when the time delay reverses (Δt negative, blue curve in Fig. 3a), such that the IR_{fix} pulse excites first, the IR-MPD yield of $\tilde{\nu}_{NH}^{H\text{-bound}}$ diminishes and the intensity of $\tilde{\nu}_{NH}$, the free NH vibration, increases with respect to the two-color IR-MPD spectrum with positive Δt. A pointwise scan of Δt reveals a fast switch amongst both vibrations (*cf.* Fig. 3b). We interpret this finding as follows: firstly, the IR_{fix} laser heats the complexes and induces an isomerization such that the population of isomer A (evidenced by the hydrogen bonded $\tilde{\nu}_{NH}^{H\text{-bound}}$ vibration) is diminished and the population of isomer B (free $\tilde{\nu}_{NH}$ vibration) is enhanced. The possibility of some isomers at skewed dihedral angles, which are void of any L_1 to L_2 bonding, is acknowledged; however, present results do not find any evidence. Subsequently, the changed isomer population is detected by the IR_{scan} laser. This interpretation matches the observation of a significant broadening and red shifting of the three recorded stretching vibrations, as known to occur from a rovibrational preheating of part of the $[AgL_1L_2]^+$ ensemble by the IR_{fix} pulse – prior to the scanning IR_{scan} pulse.

Our study revealed that strong and weak hydrogen bonds[29–31] within a given complex may break and form by torsional rearrangements that take place perpendicular to the hydrogen bond directions (here, through torsional twisting of the two ligands against each other). It confirms that the forming and breaking of hydrogen bonds is of a multidimensional character – much beyond an intuitive pulling apart of a hydrogen bond along its bond direction. It further elucidates how weak CH–O hydrogen bonds may come into play to stabilize conformers other than the global minimum structure. The importance of torsional rearrangements becomes clear once more by the gained picture, as was similarly unravelled in a previous study on intraligand torsion in a Ru complex that precedes and enables activation of the catalytic center in a somewhat surprising way.[16] Our studies benefit from two-color IR pulse probing as a valuable tool for such investigations (two-color IR-MPD). Variable time delays between the two laser pulses allow us to probe ion ensembles with variable internal energies. The preheating effect of the additional IR_{fix} pulse could be demonstrated in terms of laser induced torsional isomerization as well as a red shifting and broadening of the IR-MPD bands. The torsional isomerization path was examined by concomitant DFT calculations that served to elucidate the torsional barrier, the relative stabilities of participating isomers, and the change of vibrational frequencies and IR intensities in the course of formation and breaking of strong and weak hydrogen bonds amongst chelates and ligands in a semiflexible ligand–metal–chelate complex.

The present study presents the work in progress. Δt tuning two-color IR-MPD spectra of the $\tilde{\nu}_{CH}^{aliph.}$ range (at around 3000 cm^{-1}) and in the fingerprint region (below 2000 cm^{-1}) as well as temperature dependent measurements will help to provide more insight into the details of population dynamics in the $[AgL_1L_2]^+$ model system. Further complexes are to follow in order to learn more about the competing interactions of strong coordination and weak auxiliary bonds in multiple coordinated metal complexes.

Acknowledgements

This work was supported by the German research foundation DFG within the transregional collaborative research center SFB/TRR 88 "Cooperative effects in homo and heterometallic complexes" (3MET) and by the state research center OPTIMAS. We acknowledge valuable suggestions by the referees and conceptual discussions by Otto Dopfer.

References

1 M. S. Vohra, *Int. J. Environ. Sci. Technol.*, 2010, **7**, 687–696.
2 L. Suarez, M. A. Diez, R. Garcia and F. A. Riera, *Sep. Purif. Technol.*, 2013, **118**, 144–150.
3 D. Kołodyńska, *Desalination*, 2011, **267**, 175–183.
4 P. Römkens, L. Bouwman, J. Japenga and C. Draaisma, *Environ. Pollut.*, 2002, **116**, 109–121.
5 J. Jachuła, D. Kołodyńska and Z. Hubicki, *Chem. Eng. Res. Des.*, 2012, **90**, 1671–1679.
6 J. Jachuła, D. Kołodyńska and Z. Hubicki, *Cent. Eur. J. Chem.*, 2011, **9**, 52–65.

7 P. Muller, *Pure Appl. Chem.*, 1994, **66**, 1077.
8 B. Zhao, Z. Han and K. Ding, *Angew. Chem., Int. Ed.*, 2013, **52**, 4744–4788.
9 K. Biradha, G. R. Desiraju, D. Braga and F. Grepioni, *Organometallics*, 1996, **15**, 1284–1295.
10 C. M. Leavitt, A. B. Wolk, J. A. Fournier, M. Z. Kamrath, E. Garand, M. J. Van Stipdonk and M. A. Johnson, *J. Phys. Chem. Lett.*, 2012, **3**, 1099–1105.
11 T. R. Rizzo, J. A. Stearns and O. V. Boyarkin, *Int. Rev. Phys. Chem.*, 2009, **28**, 481–515.
12 A. Fujii and K. Mizuse, *Int. Rev. Phys. Chem.*, 2013, **32**, 266–307.
13 N. Heine, M. R. Fagiani, M. Rossi, T. Wende, G. Berden, V. Blum and K. R. Asmis, *J. Am. Chem. Soc.*, 2013, **135**, 8266–8273.
14 K. Tanabe, M. Miyazaki, M. Schmies, A. Patzer, M. Schutz, H. Sekiya, M. Sakai, O. Dopfer and M. Fujii, *Angew. Chem., Int. Ed.*, 2012, **51**, 6604–6607.
15 Y. Nosenko, F. Menges, C. Riehn and G. Niedner-Schatteburg, *Phys. Chem. Chem. Phys.*, 2013, **15**, 8171–8178.
16 L. Taghizadeh Ghoochany, C. Kerner, S. Farsadpour, F. Menges, Y. Sun, G. Niedner-Schatteburg and W. R. Thiel, *Eur. J. Inorg. Chem.*, 2013, 4305–4317.
17 K. Muller, Y. Sun, A. Heimermann, F. Menges, G. Niedner-Schatteburg, C. van Wüllen and W. R. Thiel, *Chem. – Eur. J.*, 2013, **19**, 7825–7834.
18 G. M. Florio, T. S. Zwier, E. M. Myshakin, K. D. Jordan and E. L. Sibert, *J. Chem. Phys.*, 2003, **118**, 1735–1746.
19 J. L. Leviel and Y. Marechal, *J. Chem. Phys.*, 1971, **54**, 1104–1107.
20 J. Antony, G. von Helden, G. Meijer and B. Schmidt, *J. Chem. Phys.*, 2005, **123**, 014305.
21 A. D. Becke, *Phys. Rev. A: At., Mol., Opt. Phys.*, 1988, **38**, 3098–3100.
22 C. T. Lee, W. T. Yang and R. G. Parr, *Phys. Rev. B: Condens. Matter Mater. Phys.*, 1988, **37**, 785–789.
23 B. Miehlich, A. Savin, H. Stoll and H. Preuss, *Chem. Phys. Lett.*, 1989, **157**, 200–206.
24 A. D. Becke, *J. Chem. Phys.*, 1993, **98**, 5648–5652.
25 T. H. Dunning, *J. Chem. Phys.*, 1989, **90**, 1007–1023.
26 M. J. Frisch, G. W. Trucks, H. B. Schlegel, G. E. Scuseria, M. A. Robb, J. R. Cheeseman, G. Scalmani, V. Barone, B. Mennucci, G. A. Petersson, H. Nakatsuji, M. Caricato, X. Li, H. P. Hratchian, A. F. Izmaylov, J. Bloino, G. Zheng, J. L. Sonnenberg, M. Hada, M. Ehara, K. Toyota, R. Fukuda, J. Hasegawa, M. Ishida, T. Nakajima, Y. Honda, O. Kitao, H. Nakai, T. Vreven, J. A. Montgomery, J. E. Peralta, F. Ogliaro, M. Bearpark, J. J. Heyd, E. Brothers, K. N. Kudin, V. N. Staroverov, R. Kobayashi, J. Normand, K. Raghavachari, A. Rendell, J. C. Burant, S. S. Iyengar, J. Tomasi, M. Cossi, N. Rega, J. M. Millam, M. Klene, J. E. Knox, J. B. Cross, V. Bakken, C. Adamo, J. Jaramillo, R. Gomperts, R. E. Stratmann, O. Yazyev, A. J. Austin, R. Cammi, C. Pomelli, J. W. Ochterski, R. L. Martin, K. Morokuma, V. G. Zakrzewski, G. A. Voth, P. Salvador, J. J. Dannenberg, S. Dapprich, A. D. Daniels, O. Farkas, J. B. Foresman, J. V. Ortiz, J. Cioslowski and D. J. Fox, Wallingford, CT, 2009.
27 M. Dolg, H. Stoll, H. Preuss and R. M. Pitzer, *J. Phys. Chem.*, 1993, **97**, 5852–5859.
28 G. R. Desiraju, *Acc. Chem. Res.*, 1991, **24**, 290–296.
29 I. Rozas, *Phys. Chem. Chem. Phys.*, 2007, **9**, 2782–2790.
30 E. Arunan, G. R. Desiraju, R. A. Klein, J. Sadlej, S. Scheiner, I. Alkorta, D. C. Clary, R. H. Crabtree, J. J. Dannenberg, P. Hobza, H. G. Kjaergaard, A. C. Legon, B. Mennucci and D. J. Nesbitt, *Pure Appl. Chem.*, 2011, **83**, 1619–1636.
31 E. Arunan, G. R. Desiraju, R. A. Klein, J. Sadlej, S. Scheiner, I. Alkorta, D. C. Clary, R. H. Crabtree, J. J. Dannenberg, P. Hobza, H. G. Kjaergaard, A. C. Legon, B. Mennucci and D. J. Nesbitt, *Pure Appl. Chem.*, 2011, **83**, 1637–1641.

5.3 Delay Dependent IR-MPD Spectra in the Fingerprint Spectral Region

We recorded delay dependent two color IR-MPD spectra in the fingerprint region below 2000 cm^{-1} (cf. Fig S1) and performed an in detail interpretation of the three recorded CO stretching vibration bands ($\tilde{\nu}_{CO}^{CH-bound}$, $\tilde{\nu}_{CO}^{NH-bound}$ and $\tilde{\nu}_{CO}$) and the C=C stretching band $\tilde{\nu}_{C=C}$.

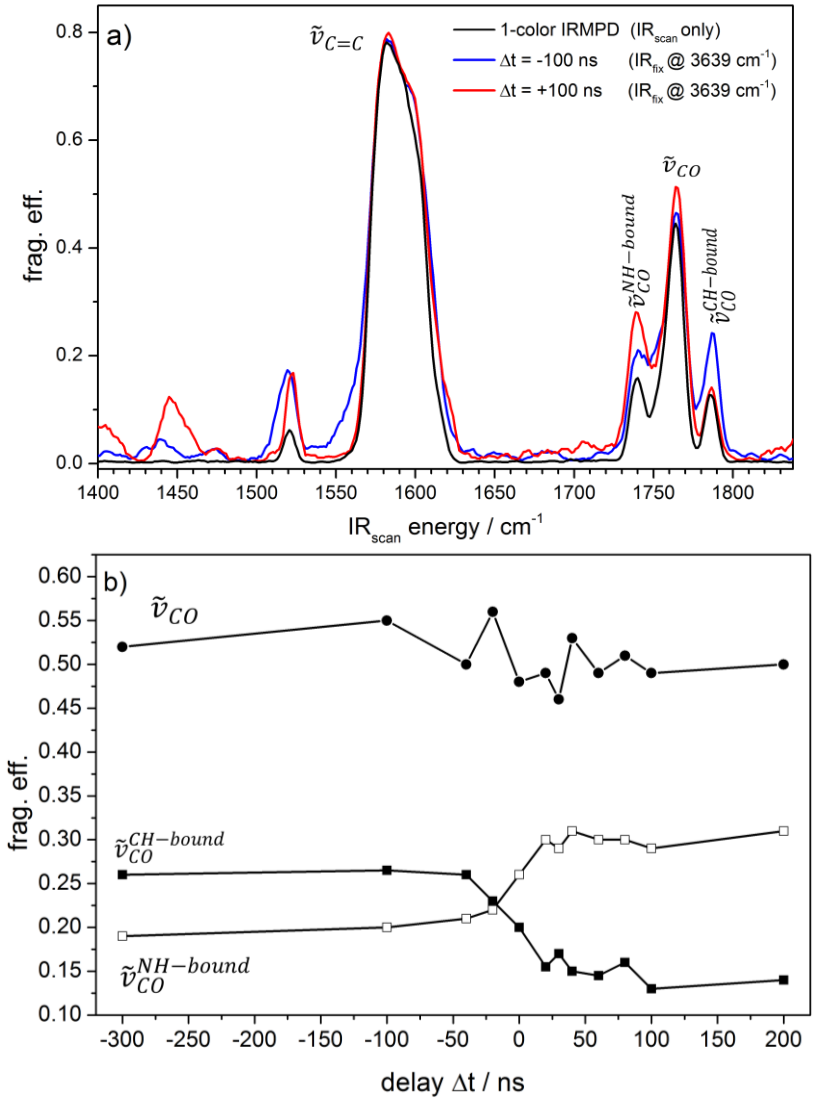

Figure S1: a): Details from the infrared spectra of the [AgL$_1$L$_2$]$^+$ complex in the fingerprint region. The delay dependent two color IR-MPD spectra with selected time delay reveal heating effects and/or isomerization. **b):** Fragmentation efficiency at the peak of the $\tilde{\nu}_{CO}^{CH-bound}$ band (filled squares), the $\tilde{\nu}_{CO}^{NH-bound}$ band (empty squares) and the $\tilde{\nu}_{CO}$ band (filled circles) in dependence of the time delay $\Delta t = t(IR_{fix}) - t(IR_{scan})$. A step like switch amongst $\tilde{\nu}_{CO}^{CH-bound}$ and $\tilde{\nu}_{CO}^{NH-bound}$ around $\Delta t = 0$ ns is clearly visible. In contrast $\tilde{\nu}_{CO}$ is approximately constant.

The C=C band is inherently strong (even in 1 color IR-MPD spectra) and exhibits almost no two color effect and no delay dependency. This confirms that the C=C band originates from both, isomer A and B, as predicted by DFT.

Two of the three observed CO bands around 1780 cm^{-1} significantly depend on the temporal delay Δt between the IR_{scan} and IR_{fix} pulses (cf. Fig. S1a). We assign the band at 1740 cm^{-1} ($\tilde{\nu}_{CO}^{NH-bound}$) to isomer A since its fragmentation efficiency is high with a positive delay (red curve) and low with negative delay Δt (blue curve). This finding is consistent with IR_{fix} laser induced isomerization of isomer A to isomer B as we discussed above. Accordingly we assign the band at 1790 cm^{-1} ($\tilde{\nu}_{CO}^{CH-bound}$) to isomer B as its intensity increases with negative delay Δt. A pointwise scan of Δt reveals a step like switch amongst $\tilde{\nu}_{CO}^{NH-bound}$ and $\tilde{\nu}_{CO}^{CH-bound}$ (cf. Fig. S1b) in analogy to the free and hydrogen bonded NH stretching vibrations.

The third CO band at 1760 cm^{-1} ($\tilde{\nu}_{CO}$) exhibits a moderate two color effect but no delay dependency (cf. Fig. S1b). This suggests that $\tilde{\nu}_{CO}$ is associated with as yet unknown isomer, which is not affected by the laser induced torsional isomerization. However, the structure of this isomer remains elusive.

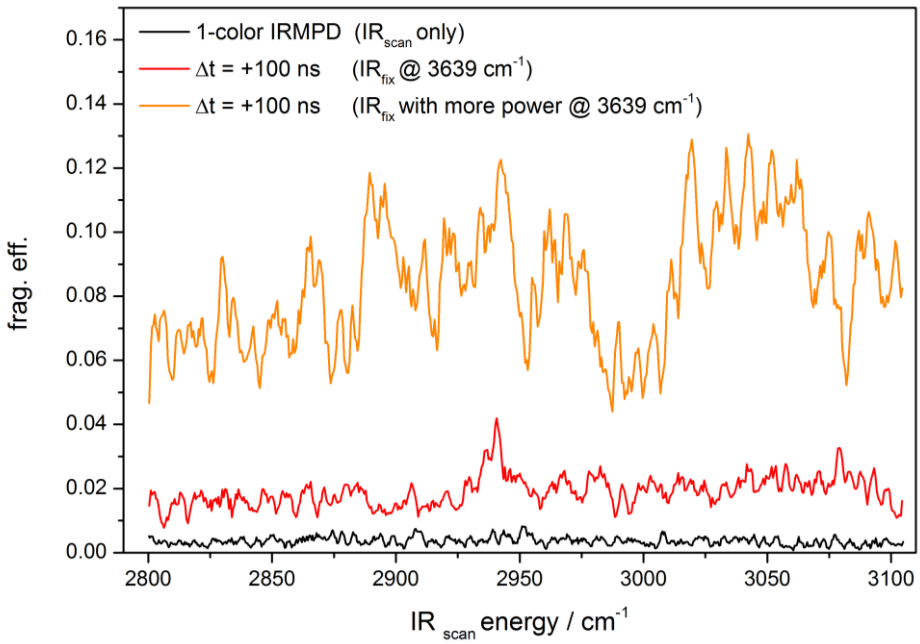

Figure S2: 1 and 2 color IR-MPD spectra of the $[AgL_1L_2]^+$ complex in the CH stretching vibration spectral range reveal no bands. An increase of the IR_{fix} laser power results in an increase of the baseline and more noise (orange curve).

We complete the delay dependent two color IR investigation of the $[AgL_1L_2]^+$ complex by probing the CH stretching vibration region (2800 – 3200 cm^{-1}; cf. Fig S2). We were not able to record more than one weak CH stretching band even with two color IR-MPD. This may originates by the very weak IR intensities of the CH stretching bands. An increase of the IR_{fix} laser power results in an increase of the baseline. Therefore, we were not able to extract any information on the isomerization of isomer A to isomer B based on CH stretching bands.

6 Magnetostructural Correlations in Isolated Trinuclear Iron(III) Oxo Acetate Complexes

Johannes Lang[a], Joachim M. Hewer[a], Matthias Klein[a], Tobias J. Lau[b], Christoph van Wüllen[a] and Gereon Niedner-Schatteburg[a]

(a) Fachbereich Chemie and Forschungszentrum OPTIMAS, Technische Universität Kaiserslautern, 67663 Kaiserslautern, Germany

(b) Helmholtz Zentrum für Materialien und Energie, BESSY II, 12489 Berlin, Germany

6.1 Preamble

The following chapter is prepared as a manuscript for publication. It is prepared for submission in the near future. Supplementary information is available in chapter 10.4.

I conducted the Collision Induced Dissociation (CID) and InfraRed - Multiple Photon Dissociation (IR-MPD) measurements, data evaluation and quantum chemical calculations. I received experimental support by Joachim Hewer. A team consisting of Joachim Hewer, Matthias Klein and myself, led by Tobias Lau at the Helmholtz Zentrum Berlin (BESSY II) performed X-Ray Magnetic Circular Dichroism measurements. I wrote and revised this manuscript with the help of Gereon Niedner-Schatteburg.

6.2 Abstract

We elucidate the intertwined variation of geometric structure and magnetic couplings in trinuclear iron(III) oxo acetate complexes $[Fe_3O(OAc)_6(Py)_n]^+$ (n = 0,1,2,3) when isolated and trapped as gaseous ions. We apply Infra Red Multiple Photon dissociation (IR-MPD) for vibrational characterization, X-ray Magnetic Circular Dichroism (XMCD) for magnetic characterization, and Density Functional Theory (DFT) via a broken symmetry approach for magnetostructural characterization. We find that the stepwise coordination of axial pyridine ligands to $[Fe_3O(OAc)_6]^+$ modulate geometric symmetries within the triangular Fe_3O core and antiferromagnetic super exchange couplings of the Fe^{III} (d^5) centers. The total spin S_T in the spin ground states of $[Fe_3O(OAc)_6(Py)_n]^+$ (n = 0,1,2) raises from spin frustrated $S_T = 1/2$ (n = 0) to 3/2 (n = 1) and 5/2 (n = 2) by symmetry lowering (from D_{3h} to C_{2v}) and lifting of degeneracy of coupling constants. Coordination of a third pyridine ligand (n = 3) re-establishes high D_{3h} symmetry and yields $S_T = 1/2$ in a spin frustrated ground state. We thus achieve a coordination controlled switching of magnetic ground states.

6.3 Introduction

Magnetic properties of polynuclear transition metal complexes relate inextricably to their geometrical structure. It is an active field of research to unravel and to describe such magnetostructural correlations[1-5]. They are crucial in the rational design of molecular nanomagnets[6] and in the context of metalloenzymes[7]. Pairwise distance-to-coupling correlations are omnipresent, e.g. through oxo bridges[8]. More complex model systems of interest are the oxo-centered trinuclear transition metal $(M^{III})_3O$ acetate complexes of the structural type $[M_3O(OAc)_6L_3]^+$ (L = axial ligands)[9-13] with M = Fe being archetypical. Three Fe ions coordinate around an O^{2-} center in a flat triangular arrangement (Fe_3O core). Each of the Fe centers achieves a pseudooctahedral geometry through equatorial coordination with four bridging acetate ligands and axial coordination with an extra monodendate ligand. It prevails an antiferromagnetic exchange coupling of the high spin Fe(III) ions[14, 15] and there is no direct Fe – Fe interaction (distances > 3 A). The electronic ground state is subject of a topological spin frustration: The triangular geometry renders a pairwise antiferromagnetic couplings of all three spins [16, 17 18] impossible. Thus the electronics of $[M_3O(OAc)_6L_3]^+$ complexes are

extremely sensitive to geometric distortions of the M_3O core[19], as e.g. crystal packing and counter ion effects in bulk samples.

We have previously investigated $[Fe_3O(OAc)_6(N_2)_n]^+$ complexes (n = 1,2,3) and we found "non classical" blue shifts of N_2 stretching vibrations[20]. In this study we investigate magnetostructural relationships in isolated $[Fe_3O(OAc)_6Py_n]^+$ (n = 0,1,2,3, cf. Scheme 1). The stepwise coordination of 1 - 3 axial pyridine ligands induces significant geometrical distortions of the Fe_3O core (a trans effect may contribute[21]). Our gas phase approach excludes bulk or crystal packing effects, and it allows for isolation of under-coordinated molecular ions (e.g. $[Fe_3O(OAc)_6]^+$), which would not be accessible in the condensed phases.

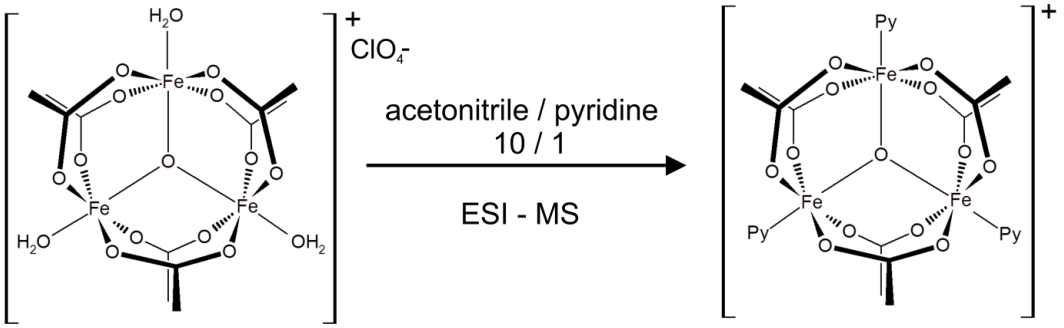

Scheme 1: The precursor $[Fe_3O(OAc)_6(H_2O)_3]^+$ (OAc = $CH_3CO_2^-$) exchanges in a acetonitrile/pyridine solution (10/1) its three axial H_2O ligands for three stronger bound pyridine ligands. Through ESI/CID we also observe under coordinated species with 0 - 2 pyridine ligands.

Electrospray ionization[22-24] (ESI) enables mass spectrometric investigations of $[Fe_3O(OAc)_6Py_n]^+$ complexes *in vacuo*, and their activation by either photons or collisions. Tandem-MS based methods like Infra Red Multiple Photon dissociation[25-27] (IR-MPD) and Collision Induced Dissociation[28-30] (CID) have helped to elucidate molecular structures and vibrations. Both techniques were instrumental under cryogenic conditions[31-36] and at room temperature[37, 38]. Two color IR-MPD schemes were applied to overcome internal vibration redistribution (IVR) bottlenecks[39] or to investigate isomer populations[40, 41]. Experimental results and dedictated *ab initio* calculations have been combined in order to obtain further insight into the structure and intrinsic properties of likely binding motifs[42-45]. The element selective X-ray Magnetic Circular Dichroism[46] (XMCD) spectroscopy allows for the investigation magnetic properties of samples such as surfaces[47, 48], thin films[49, 50], deposited nanoparticles[51] or

clusters[52]. Spin and orbital contributions to the total magnetic moment of the investigated compound can be deconstructed by sum rule analysis[53-55]. Recently the XMCD technique has been adopted for the investigation of isolated (cluster) ions in the gas phase[56-60] revealing intrinsic magnetic properties of the investigated systems, i.e. void of any alteration of a surface, and void of crystal packing effects.

We combine experimental CID, IR-MPD and XMCD investigations of isolated $[Fe_3O(OAc)_6(Py)_n]^+$.(n = 0,1,2,3) with quantum chemical calculations by broken symmetry Density Functional Theory (DFT), and we unravel the coordination induced modulation of the prevailing magnetostructural correlations.

6.4 Experimental and Computational Methods

6.4.1 Collision Induced Dissociation (CID) and InfraRed – Multiple Photon Dissociation (IR-MPD) Measurements

CID and IR-MPD measurements were performed using a modified Paul-type quadrupole ion trap instrument (AmaZon SL, Bruker Daltonics). The ESI ion source (Apollo II) was set to positive electrospray ionization mode. Scan speed was 32 500 m/z / s (0.3 FWHM / m/z) with a scan range of 70 to 1200 m/z. Sample solutions of Iron(III) oxo acetate perchlorate hydrate ($[Fe_3O(OAc)_6(H_2O)_3(ClO_4)]$; OAc = $CH_3CO_2^-$; cf. Scheme 1) in a solvent mixture of acetonitrile/pyridine = 100/1 at concentrations of 1 x 10^{-5} mol/l were continuously infused into the ESI chamber by a syringe pump at a flow rate of 2 µL min^{-1}. Nitrogen was used as drying gas with a flow rate of 3.0 L min^{-1} at 210 °C. The solutions were sprayed at a nebulizer pressure of 280 mbar (4 psi) and the electrospray needle was held at 4.5 kV.

CID-appearance and breakdown curves of $[Fe_3O(OAc)_6(Py)_n]^+$ (n = 0,1,2; OAc = $CH_3CO_2^-$; Py = pyridine) were recorded with varying excitation amplitudes (0.0 V to 1.5 V), which determine the internal energy scale of the mass spectrometer (E_{lab} in Volt). Relative abundances were calculated according to:

$$I_{tot}^{fr}.(E_{lab}) = \left(\frac{\sum_i I_i^{fr}(E_{lab})}{\sum_i I_i^{fr}(E_{lab}) + \sum_i I_i^{p}(E_{lab})}\right) \quad (1)$$

where I_i^{fr} = intensity of the fragment ions and I_i^{p} = intensity of the parent ions. Center of mass transferred fragmentation amplitudes (E_{com}) were calculated from internal amplitudes by:

$$E_{com} = \left(\frac{m_{He}}{m_{He} + m_{ion}}\right) \cdot E_{lab} \tag{2}$$

where m_{ion} stands for the isotopically averaged mass of the molecular ion. Note, that the current application of the CID technique by RF excitation in presence of multiple collisions results in a so called "slow multi collision heating" mode of operation[61, 62]. Fragmentation amplitude dependent CID spectra were modeled and fitted by sigmoid functions of the type

$$I_{fit}^{fr}(E_{com}). = \left(\frac{1}{1 + e^{(E_{com}^{50} - E_{com})\,B}}\right) \tag{3}$$

using a least-squares criterion.

The E_{com}^{50} fit parameter is the amplitude at which the sigmoid function is at half maximum value, whereas B describes the rise of the sigmoid curve. Due to the correlation of fragmentation amplitude and appearance energy, it is feasible to assume, that the appearance curves can be associated to the relative stability of the $[Fe_3O(OAc)_6(Py)_n]^+$ complexes[63-66].

A KTP/KTA optical parametric oscillator/amplifier (OPO/A, LaserVision) system pumped by a pulsed 10 Hz injection seeded Nd^{3+}:YAG laser (PL8000, Continuum) was used as a source of tunable IR radiation ($\delta n = 0.9$ cm^{-1}, $\delta t = 7$ ns) for recording vibrational spectra of $[Fe_3O(OAc)_6(Py)_n]^+$ (n = 0,1,2,3). The OPA idler wave (≤ 10 mJ per pulse) was used to record spectra within 2600–3900 cm^{-1}. The difference frequency (DF) between the OPA signal and idler waves generated in a $AgGaSe_2$ crystal (≤ 2 mJ per pulse) was applied in the range of 1200–2100 cm^{-1}. After passing through the vacuum chamber the IR beam was directed onto a power meter sensor. The idler beam was focused by a 50 cm CaF_2 lens. The DF radiation was focused tighter, by a 90° off-axis parabolic silver mirror with an effective focal length of 15 cm. The IR spectra were recorded as ion mass chromatograms while continuously scanning the IR wavelength. An experimental IR-MPD spectrum arises from a plot of the fragmentation efficiency as a function of laser frequency (ν). The IR-MPD yield $Y(\nu)$ is defined as:

$$Y(\nu) = \left(\frac{\sum_i I_i^{fr}(\nu)}{\sum_i I_i^{fr}(\nu) + \sum_i I_i^{p}(\nu)}\right) \tag{4}$$

The IR frequency was calibrated using a wave meter (821B-NIR, Bristol instruments). Laser power curves were recorded in parallel to the IR-MPD spectra through digitizing

the analog output of the laser power meter by an ample ADC input of the AmaZon SL mass spectrometer electronics. Despite the online IR power measurement (laser pulse energies are potted into the background of each IR-MPD spectrum) the recorded spectra were not normalized due to the intrinsically nonlinear power dependence of IR-MPD fragmentation efficiencies.

6.4.2 Computational Methods

Availible crystal structure data of $[Fe_3O(OAc)_6(Py)_3](FeBr_4)$[11] served as a starting point to calculate optimized minimum energy structures and linear IR absorption spectra of free $[Fe_3O(OAc)_6(Py)_n]^+$ (n = 0,1,2,3) complexes. Standard Gibbs energies of structures, ΔG^0, and of binding energies, $\Delta\Delta_{bind}G^0$ were calculated at 300 K. We utilized Density Functional Theory (DFT) using the B3LYP[67, 68] functional and cc-pVTZ basis sets[69] (C, H, N, O) in combination with the Stuttgart RSC 1997[70] effective core potential (Fe) as implemented in the Gaussian 09 program package[71]. Standard convergence criteria were applied. Full geometry optimization of all nuclear coordinates yields multiple locally stable minimum structures. We performed unrestricted DFT calculations with 1 - 17 unpaired alpha electrons yielding multiplicities of 2 (dublet) – 18 (18tet). In all cases a multiplicity of 16 was most stable (cf. Fig. S8) therby indicating three Fe high spin (d^5) centers. Harmonic vibrational frequencies of all calculated spectra are scaled with 0.98 and broadened with gaussian envelope curves (6 cm^{-1} FWHM). The Basis Set Superposition Error (BSSE) of calculated binding energies was corrected using the Counterpoise routine[72, 73] of Gaussian 09.

We investigated the antiferromagnetic couplings between the three high spin d^5 Fe centers in the optimized structures of $[Fe_3O(OAc)_6(Py)_n]^+$ (n = 0,1,2,3) with the help of a broken symmetry approach[74, 75]. This was enabled through Density Functional Theory (DFT) with the B3LYP_Gaussian[67, 68] functional and cc-pVTZ basis sets[69] (C, H, N, O) in combination with the Stuttgart RSC 1997[70] effective core potential (Fe) and a CANOSSA program[76] as implemented in a local, customized installation of the TURBOMOLE 6.5 program package[77-79]. The single point energies of the four possible broken symmetry configurations (cf. Scheme 2) served to extract three magnetic coupling constants[76] (J_{ij}) per complex.

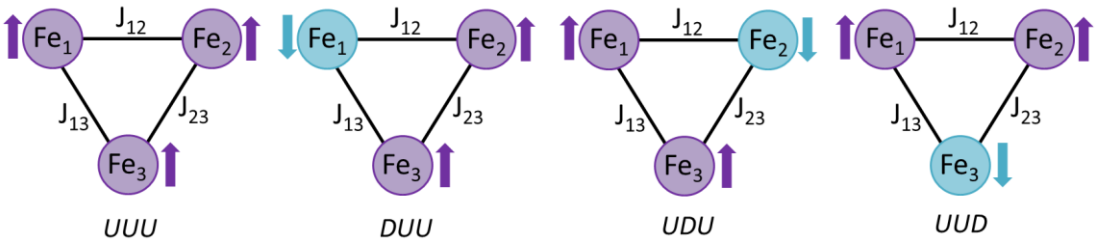

$$UUU = \left|\frac{5}{2}\ \frac{5}{2}\ \frac{5}{2}\right\rangle \quad DUU = \left|-\frac{5}{2}\ \frac{5}{2}\ \frac{5}{2}\right\rangle \quad UDU = \left|\frac{5}{2}\ -\frac{5}{2}\ \frac{5}{2}\right\rangle \quad UUD = \left|\frac{5}{2}\ \frac{5}{2}\ -\frac{5}{2}\right\rangle$$

Scheme 2: Broken symmetry configurations of the triangular Fe_3O core in $[Fe_3O(OAc)_6(Py)_n]^+$ (n = 0,1,2,3). Purple and turquoise arrows indicate alpha (U) and beta (D) spins, respectively. J_{ij} is the coupling constant between two adjacent Fe-centers. The coordinating ligands are ommitted for clarity.

The magnetic coupling between the three spin center in $[Fe_3O(OAc)_6(Py)_n]^+$ (n = 0,1,2,3) is governed by the isotropic Heisenberg-Dirac-van Vleck (HDvV) Hamiltonian[80]:

$$\hat{H}_{HDvV} = -\sum_{i<j} J_{ij}\hat{\boldsymbol{S}}_i\hat{\boldsymbol{S}}_j \tag{5}$$

where J_{ij} are the spin only coupling constants of Fe centers i and j. Ferromagnetic coupling is represented by a positive J value while a negative J value indicates antiferromagnetic coupling. In the case of high spin d^5 Fe ions in nearly octahedral coordination orbital angular momenta are small, and we are entitled to neglect them in the following. In the case of multiple magnetic centers (as in the present case) it is very difficult to find the eigenfunctions of the HDvV Hamiltionan – even when neglecting orbital momenta. To overcome this issue we make use of an Ising model Hamiltonian[81, 82] in which the total spin operators $\hat{\boldsymbol{S}}_i$ are substituted by the associated z-component $\hat{S}_{z,i}$:

$$\hat{H}_{Ising} = -2\sum_{i<j} J_{ij}\hat{S}_{z,i}\,\hat{S}_{z,j} \tag{6}$$

The eigenvalues of the Ising Hamiltonian and the HDvV Hamiltonian are not identical. However it is possible to extract coupling constants (J_{ij}) from energy differences of appropriate broken symmetry configurations by assuming that all interactions are additive[83, 84]. Using the Ising operator on the four broken symmetry configurations (cf. Scheme 2) yields the following eigenvalues:

$$\langle UUU \rangle = E_0 - 2J_{13}\frac{25}{4} - 2J_{12}\frac{25}{4} - 2J_{23}\frac{25}{4} \tag{7}$$

$$\langle DUU \rangle = E_0 + 2J_{13}\frac{25}{4} + 2J_{12}\frac{25}{4} - 2J_{23}\frac{25}{4}$$

$$\langle UDU \rangle = E_0 - 2J_{13}\frac{25}{4} + 2J_{12}\frac{25}{4} + 2J_{23}\frac{25}{4}$$

$$\langle UUD \rangle = E_0 + 2J_{13}\frac{25}{4} - 2J_{12}\frac{25}{4} + 2J_{23}\frac{25}{4}$$

By solving this linear system of equations and by the known energies of the four broken symmetry configurations we obtain the three coupling constants J_{12}, J_{13} and J_{23} for $[Fe_3O(OAc)_6(Py)_n]^+$ (n = 0,1,2,3) - together with an energy offset E_0 - as:

$$E_0 = \frac{1}{4}(UUU + DUU + UDU + UUD) \tag{8}$$

$$J_{12} = \frac{1}{50}(-UUU + DUU - UDU + UUD)$$

$$J_{13} = \frac{1}{50}(-UUU - DUU + UDU + UUD)$$

$$J_{23} = \frac{1}{50}(-UUU + DUU + UDU - UUD)$$

6.4.3 X-Ray Magnetic Circular Dichroism (XMCD) Measurements

X-ray absorption (XAS) and XMCD measurements were performed using the NanoClusterTrap operated at the UE52-PGM beamline at the BESSY II (Helmhotz Zentrum Berlin) synchroton facility. This setup is a custom build mass spectrometer to record Total Ion Yield (TIY) gas phase spectra of isolated ions[85, 86]. We combined the NanoClusterTrap with a custom build ESI - ion source[87, 88], kindly provided by the group of Thomas Schlathölter (University of Groningen, The Netherlands). Sample solutions of Iron(III) oxo acetate perchlorate hydrate ($[Fe_3O(OAc)_6(H_2O)_3(ClO_4)]$; OAc = $CH_3CO_2^-$; cf. Scheme 1) in a solvent mixture of acetonitrile/pyridine = 100/1 at concentrations of 1 x 10^{-4} mol/l were continuously infused into the ESI chamber by a syringe pump at a flow rate of 2 µL min^{-1}.

A detailed experimental description has been published previously[89]. In short, the ESI - generated ions of interest ($[Fe_3O(OAc)_6(Py)_n]^+$) are mass selected in a quadrupole mass filter (Extrel, 40-4000 m/z) and constantly injected into a (liquid helium cooled) linear quadrupole ion trap where they are stored for cooling and irradiation with the X-Ray

beam. The trap is operated between 2 and 4 MHz depending on the mass of the investigated ions (in this case: 3.3 MHz). Evaporation of the liquid Helium (preasure of ~ 8 x 10^{-7} mbar within the vacuum chamber) cools down the down the ion trap down to cryo temperatures around 4 K. Collisional cooling of the trapped ions leads to thermalized ions at slightely elevated temperatures of ~ 15 K[90] due to radio frequency heating. The ion cooling is necessacy to reduce temperature induced orientation randomization of the magnetic moments of the investigated species. The ion trap is located inside the high field region of a superconducting solenoid (up to 5 T, in our case: 4.5 T) to allign the magnetic moments of the investigated ions to the light pass of the X-Ray beam. Irradiation of the ions for with circularly polarized X-Ray radiation from the UE52-PGM beamline (10 -15 s irradiation per set photon energy) leads to fragmentation of the mass selected ions. Subsequently the ions as well as the associated fragments are ejected from the ion trap into an in line reflectron time of flight mass spectrometer (~100 Hz) to record the resulting mass spectra, specifically to record the intensity of the X-Ray induced fragments. We gain X-ray absorption spectra by plotting the intensity of the fragment ion as a function of the X-Ray photon energy. A GaAs-diode records the X-Ray beam intensity from the undulator beamline which serves to normalize the recorded spectra for photon flux. The spectra were recorded on the Fe absorption edges with a spectral resolution of 500 meV at 711 eV (exit slit size of 250 µm) and an increment size of 200 meV. We recorded several spectra for left and right handed circularly polarized light in an alternating manner, and we perform a qualitative analysis. Quantitative elucidation by rule analysis[53-55] would be hampered by the large uncertainties which are known to occur through d^5 configurations[91]. It would not provide for further insight beyond what we obtain anyway – as to discuss in the following.

6.5 Results and Discussion

6.5.1 CID of $[Fe_3O(OAc)_6(Py)_n]^+$ and Free Binding Energies of the Pyridine Ligands

Assignment of mass peaks to molecular species of interest: Upon spraying the above described sample solution and recording mass spectra using the Paul type trap, we observe a series of isotopic peaks at m/z = 538, 617, 696 and 775 matching convincingly with simulated isotopic patterns of $[Fe_3O(OAc)_6(Py)_n]^+$ (n = 0,1,2,3, cf. Fig. 1 and Table S1 in the Supplentary Information). In solution the axial H_2O ligands of the precursor ion $[Fe_3O(OAc)_6(H_2O)_3]^+$ exchange with the stronger binding pyridine ligand[11] (Py, C_5H_5N). However, the intensity of the n = 3 mass peak is significantly lower than that of n = 2. This indicates that $[Fe_3O(OAc)_6(Py)_3]^+$ loses one or more pyridine molecules during the ESI and/or trapping process. The decreased resolution of the isotope mass peaks of $[Fe_3O(OAc)_6(Py)_3]^+$ at m/z =775 (cf. inset of Fig. 1) hints at fragmentation of $[Fe_3O(OAc)_6(Py)_3]^+$ during isolation within the Paul trap or the resonance ejection during mass analysis[92]. We did not observe any attachment of H_2O or acetonitril.

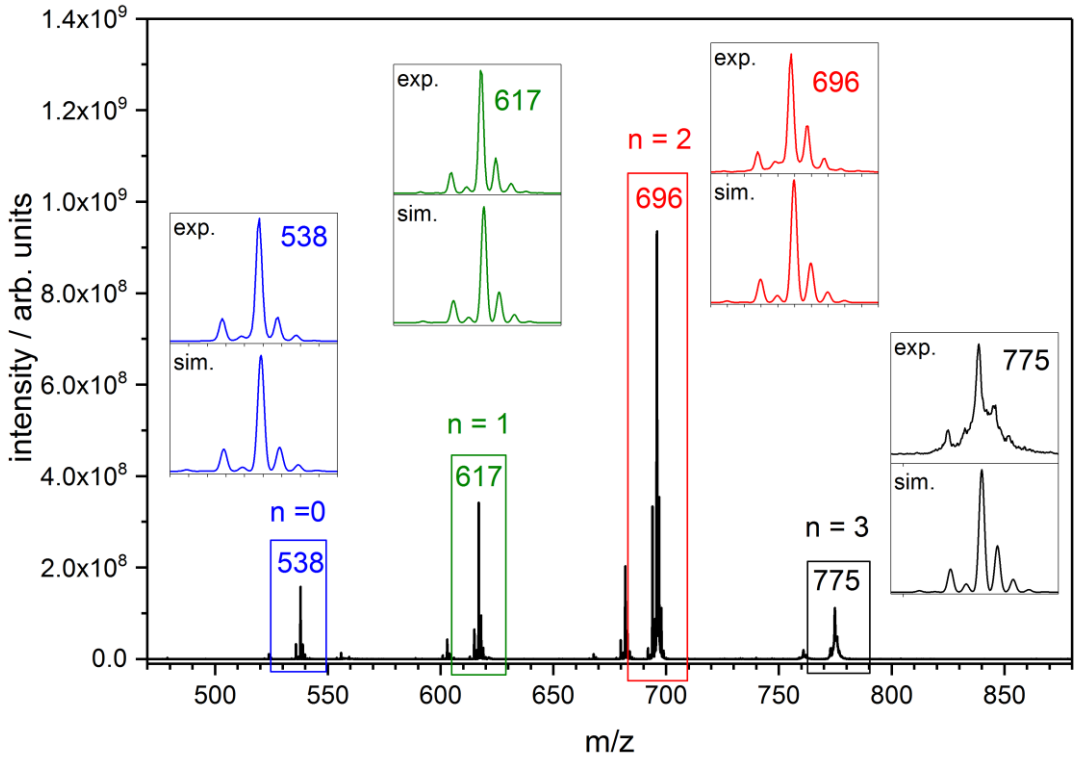

Figure 1: Cationic mass spectrum of a $[Fe_3O(OAc)_6(H_2O)_3]ClO_4$ acetonitrile/pyridine = 1/10 solution using the Paul type ion trap. Insets: Experimental and simulated isotopic pattern of $[Fe_3O(OAc)_6(Py)_n]^+$ (n = 0,1,2,3; OAc = $CH_3CO_2^-$; Py = C_5H_5N). The mass labeling refers to the most intensive peak.

Fragmentation routes and CID curves: CID of isolated $[Fe_3O(OAc)_6(Py)_n]^+$ (n = 0,1,2,3) reveal fragment mass peaks (cf. Fig. S1-S4) indicating a cleavage of neutral pyridine ligands. This is the main fragmentation route. In addition there is some cleavage of neutral acetate radicals (OAc*) – when no pyridine ligands are availible (cf. Scheme 3).

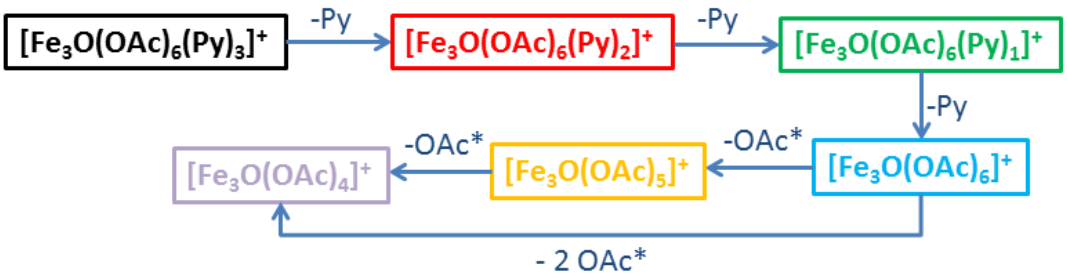

Scheme 3: CID fragmentation routes of $[Fe_3O(OAc)_6(Py)_n]^+$ (n = 0,1,2,3). The relative intensities of the fragments depend strongly on the CID amplitude. The subsequent manner of pyridine elimination finds experimental evidence by our CID appearance curves (cf. Fig. 2).

We elucidate the relative stability of $[Fe_3O(OAc)_6(Py)_n]^+$ (n = 0,1,2,3) by recording so-called CID breakdown curves of the complexes and CID appearance curves of the associated fragments (cf. Fig. 2). In the case of $[Fe_3O(OAc)_6(Py)_3]^+$ (cf. Fig. 2; n = 3; black squares) single pyridine elimination is the primary fragmentation channel as recorded by the fragment peak $[Fe_3O(OAc)_6(Py)_2]^+$ (red squares). It prevails to an CID amplitude of $E_{com} \sim 5$ a.u. Higher CID amplitudes reveal additional elimination of the second pyridine ligand ($[Fe_3O(OAc)_6(Py)_1]^+$, green squares) which we attribute to secondary fragmentation. The intensity of the double pyridine elimination increases with the CID amplitude while the intensity of single pyridine elimination decreases underlining the subsequent manner of the fragmentation process. We exclude a concurrent elimination process of the first two pyridine ligands. CID amplitudes > 6 a.u reveal the rising of the next secondary fragment: triple pyridine elimination as recorded fragment peak $[Fe_3O(OAc)_6]^+$ (blue squares). Both secondary fragments gain intensity with CID amplitudes with $[Fe_3O(OAc)_6(Py)_1]^+$ exhibiting a maximum around $E_{com} = 7.5$ a.u. We observed no (secondary) elimination of acetate (OAc*) at all applied CID amplitudes. In the case of $[Fe_3O(OAc)_6]^+$ (cf. Fig. 2; n = 0; blue squares) there is no pyridine ligand availible. Accordingly we observe single and double acetate (OAc*) eliminatation ($[Fe_3O(OAc)_5]^+$ and $[Fe_3O(OAc)_4]^+$) as primary fragments. Both fragment channels gain intensity beyond $E_{com} = 4.5$ a.u. They reach a constant level at $E_{com} = 4.5$ a.u and remain constant throughout the range of applied CID amplitudes.

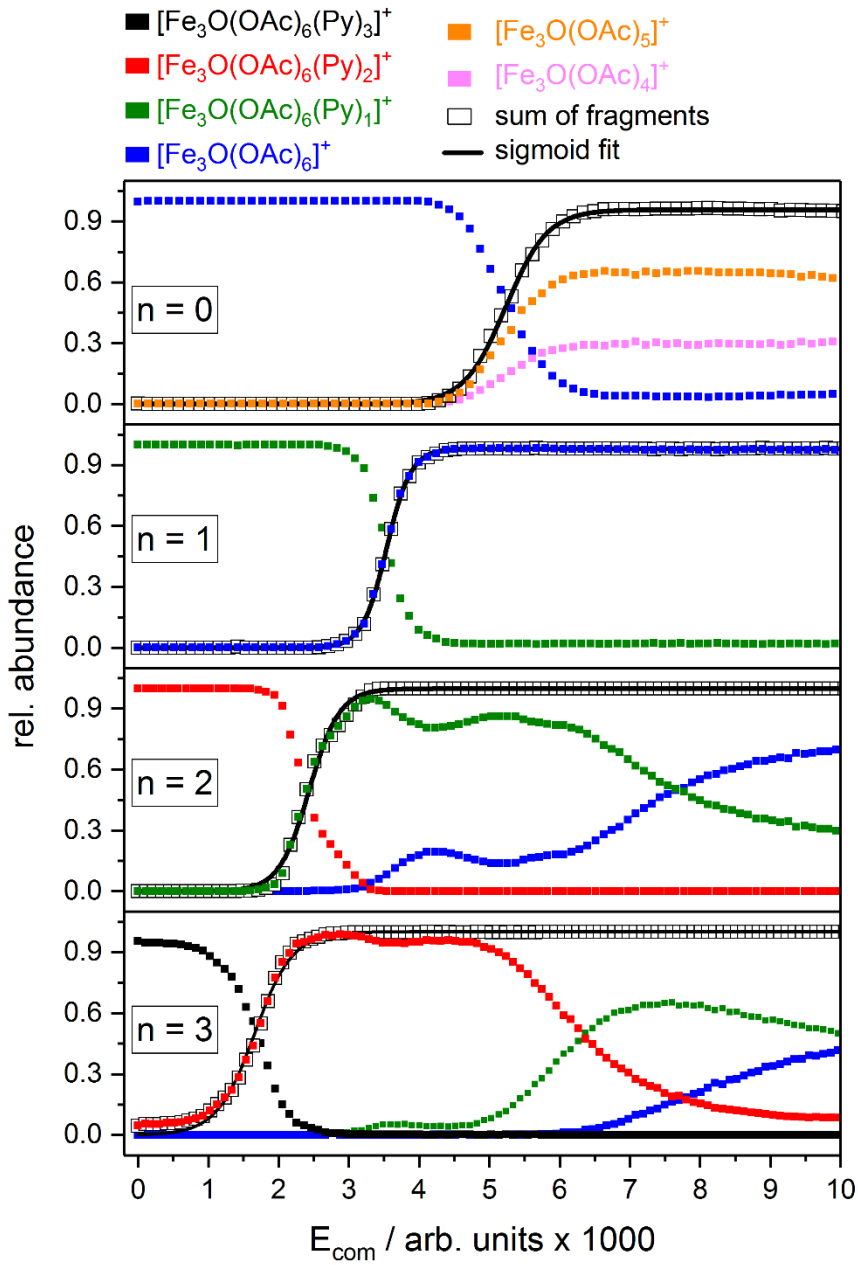

Figure 2: CID breakdown curves of $[Fe_3O(OAc)_6(Py)_n]^+$ (n = 0,1,2,3) and appearance curves of the associated fragments.

The fragmentation behavior of $[Fe_3O(OAc)_6(Py)_2]^+$ (cf. Fig. 2; n = 2; red squares) is similar to n = 3 (cf. Fig. 2; n = 3; black squares). The primary fragmention channel in n = 2 is single pyridine elimination as recorded by the fragment peak $[Fe_3O(OAc)_6(Py)_1]^+$ (green squares). It prevails to an CID amplitude of E_{com} = 3.5 a.u. Higher CID amplitudes reveal additional elimination of the second pyridine ligand (double pyridine elimination) as a secondary fragment ($[Fe_3O(OAc)_6]^+$; blue squares). The intensity of the double pyridine elimination increases with the CID amplitude while the intensity of single pyridine elimination decreases. This indicates subsequent elimination of the

pyridine ligands. We observed no additional secondary elimination of acetate (OAc*) at all applied CID amplitudes. The case of n = 1 (cf. Fig. 2; n = 1; blue squares) is straight forward: Pyridine cleavage as recorded by the fragment peak $[Fe_3O(OAc)_6]^+$, and it prevails at all CID amplitudes. We detected no secondary fragments.

Correlation between E_{com}^{50} CID values and calculated binding energies: In all cases where a pyridine ligand is available (n = 1,2,3) a single pyridine elimination dominates the sigmoid rise of the fragment appearance curves. This offers an unique opportunity to investigate the binding energies of the pyridine ligands in $[Fe_3O(OAc)_6(Py)_n]^+$ (n = 1,2,3). By fitting the experimental CID appearances curves (sum of all fragments) we extract E_{com}^{50}values, which we compare to calculated pyridine free binding energies $\Delta\Delta_{bind}G_n^0$ (cf. Fig. 3 and formula (11)). Molecular fragmentation might bear an activation barrier on top of the endothermicity of bond breaking[93, 94]. In such cases it would be more appropriate to compare the relative energies of transition state structures to E_{com}^{50} values rather than simple binding energies[44, 66, 95]. However, in the presented case we investigate a direct bond cleavage void of any involved structural reorganizations. Such cases are known to lack any activation barrier beyond plain endothermicity of the mere bond breaking[96, 97], and we are entitled to assume the same for our present case.

The first eliminated pyridine ligand from $[Fe_3O(OAc)_6(Py)_3]^+$ (cf. Fig. 3 left; n = 3) has the lowest free binding energy $\Delta\Delta_{bind}G_n^0$ of 28 kJ/mol (19 kJ/mol including BSSE correction). Accordingly we measure the lowest E_{com}^{50} value of 1.66 a.u for $[Fe_3O(OAc)_6(Py)_3]^+$ (cf. Fig. 3 right; n = 3). The binding energy of the second pyridine molecule to (cf. Fig.3 left; n = 2) increases to 55 kJ/mol (46 kJ/mol including BSSE correction) doubling the free binding energy of the first pyridine ligand. The associated E_{com}^{50} value of $[Fe_3O(OAc)_6(Py)_2]^+$ increases to 2.44 a.u (cf. Fig. 3 right; n = 2). The last pyridine ligand has the highest free binding energy of 82 kJ/mol (73 kJ/mol including BSSE correction) and we observe highest E_{com}^{50} value of 3.54 a.u. in the case of $[Fe_3O(OAc)_6(Py)_1]^+$.

$$\Delta\Delta_{bind}G_n^0 = \Delta G^0([Fe_3O(OAc)_6(Py)_{n-1}]^+) + \Delta G^0(Py) - \Delta G^0([Fe_3O(OAc)_6(Py)_n]^+) \quad (9)$$

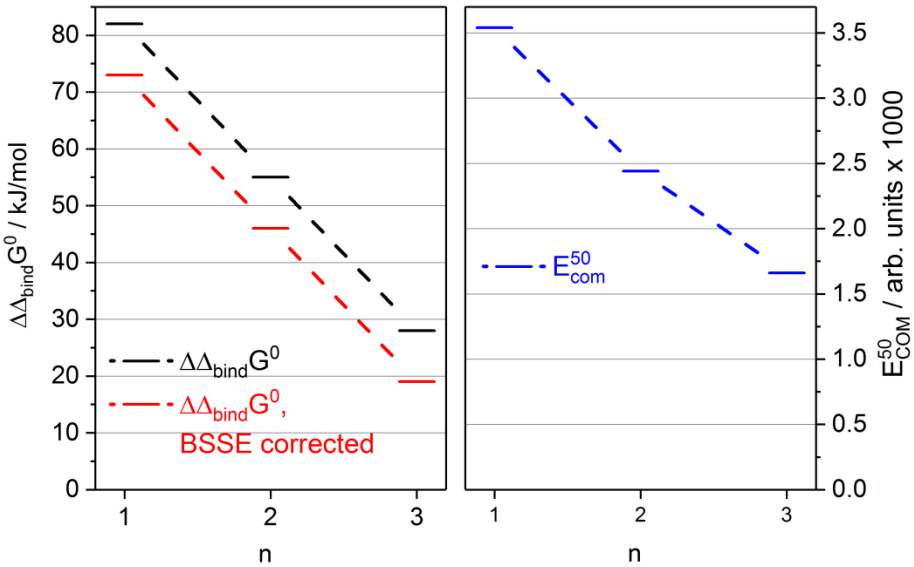

Figure 3: Left: Calculated binding energies $\Delta\Delta_{\mathbf{bind}}\mathbf{G_n^0}$ of pyridine ligands in $[Fe_3O(OAc)_6(Py)_n]^+$ (n = 1,2,3). **Right:** E_{com}^{50} values (multiplied by a factor of 1000) extracted from CID appearance curves (cf. Fig. 2).

Both, the calculations as well as the experimental E_{com}^{50} value indicate an obvious trend: The free binding energy of pyridine ligands decreases with the number of pyridine ligands coordinated to the $[Fe_3O(OAc)_6]^+$ subunit. This hints at significant influences on the structural properties of the $[Fe_3O(OAc)_6]^+$ subunit by the coordination of each axial pyridine ligand. We elucidate this influence in the following chapter, by investigating the geometry of $[Fe_3O(OAc)_6(Py)_n]^+$ (n = 0,1,2,3) *via* IR-MPD.

6.5.2 IR-MPD and DFT Simulations of $[Fe_3O(OAc)_6(Py)_n]^+$

We have recorded IR-MPD spectra of $[Fe_3O(OAc)_6(Py)_n]^+$ (n = 0,1,2,3) (cf. Fig. 4; red and blue curves) and we have conducted DFT simulations to obtain their linear IR absorption spectra (cf. Fig. 4, black curves). The DFT calculations reveal optimized minimum structures as depicted in Fig. 4 (see Fig. S5-S7 for the less stable isomers).

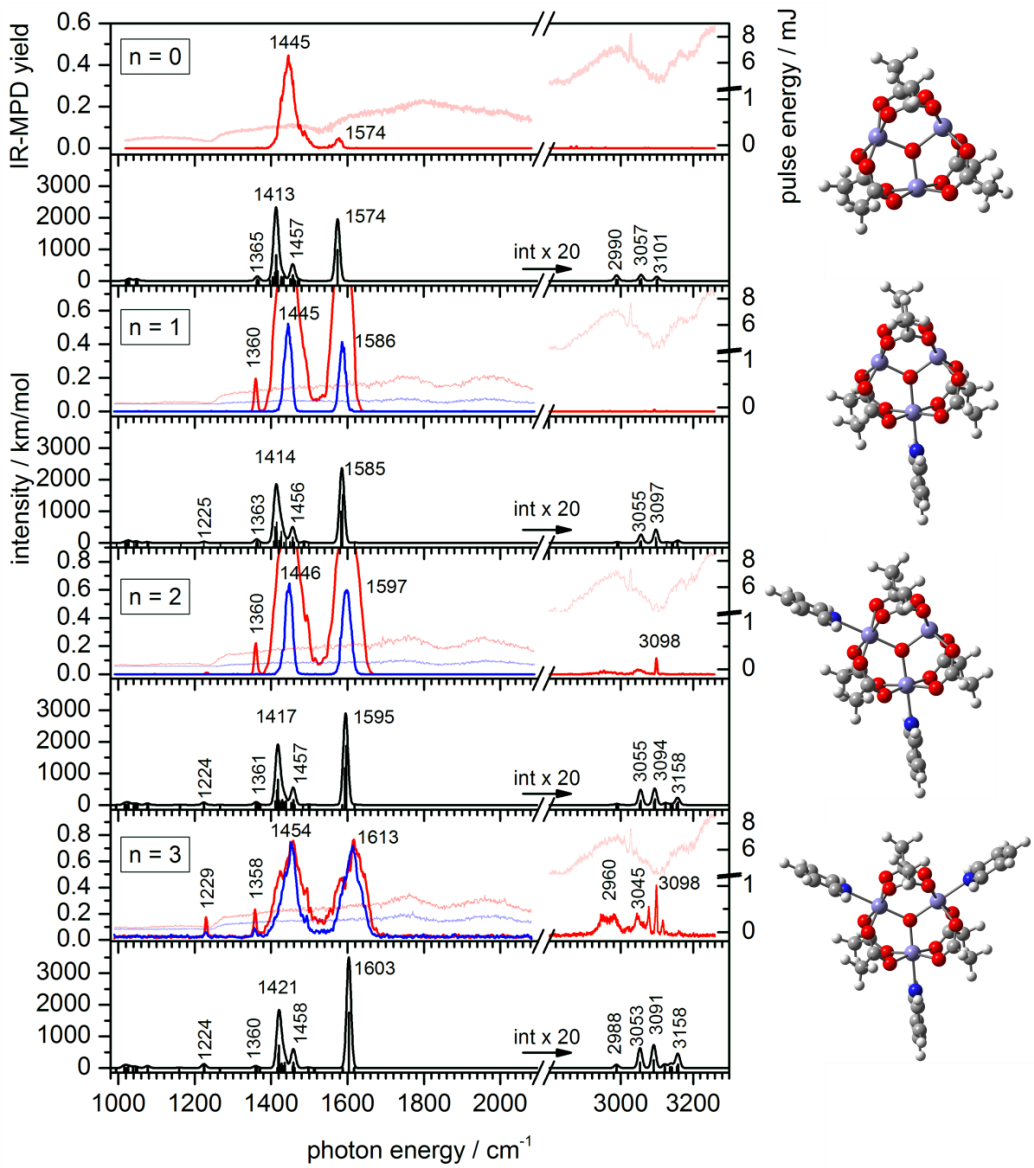

Figure 4: IR-PMD spectra of $[Fe_3O(OAc)_6(Py)_n]^+$ (n = 0,1,2,3) (colored curves) and calculated IR absorption spectra of geometry optimized $[Fe_3O(OAc)_6(Py)_n]^+$ (n = 0,1,2,3) (black curves) in the range of 1000 – 3300 cm^{-1}. Red curves indicate measurements at maximum photon flux while blue curves show spectra with attenuated pulse energies (~ 50%). The calculations were performed at the B3LYP/cc-pVTZ (H, C, N, O) and Stuttgart 1997 ECP (Fe) level of theory. The multiplicity is 16 and frequencies are scaled with 0.98. The associated geometry optimized structures are shown next to the spectra (white = hydrogen, grey = carbon, red = oxygen, blue = nitrogen and purple = iron).

Assignment of recorded bands to vibrational modes: The IR-MPD spectra of n = 2 and 3 reveal bands around 2960, 3045 and 3098 cm^{-1}, which coincide with predicted CH stretching vibration frequencies (ν(CH)) of the six coordinated acetate ligands. However, in the case of n = 0 and 1 we observe no analogue CH stretching vibration bands. Note, that the calculated IR absorption intensity of the CH stretching vibration bands is very low in all cases (< 50 km/mol) and increases somewhat with n. This is expected to increase the IR-MPD yield as observed. In the fingerprint region below 2000 cm^{-1} we observe in the case of n = 0 two bands: a broad band at 1445 cm^{-1} (FWHM = 25 cm^{-1}) coinciding with several CH_3 bending vibration frequencies ($\delta(CH_3)$) and a weak band at 1574 cm^{-1} coinciding with the nearly degenerate carboxylic CO stretching vibration frequencies (ν(CO)) of the acetate ligands. The calculated intensities of those bands are very high (> 1000 km/mol) making IR laser induced fragmention accessible.

Influence of pyridine coordination on the IR-MPD spectra: Axial pyridine ligands, coordinated to $[Fe_3O(OAc)_6]^+$, modulate the shape, frequency and intensity of the CH_3 bending vibration bands and CO stretching vibration bands: The frequencies of $\delta(CH_3)$ and ν(CO) increase with the number of coordinated pyridine ligands n, both in experiments and calculations (cf. Fig. 5). The experimental CO stretching vibration bands of n = 1,2,3 are blue shifted by 12, 23 and 39 cm^{-1}, with respect to n = 0. The associated DFT calculated asymmetric carboxylate stretching frequencies – scaled to match the experiment at n = 0 – reproduces this blueshift (11, 21 and 29 cm^{-1}). The coordinated carboxylate groups thus sense pyridine coordination through their common Fe centers. The n = 1 and 2 coordinations lift the sixfold degeneracy of carboxylic CO stretching vibration frequencies (ν(CO)) of the six coordinated acetate ligands (cf. Fig. S9). The calculations predict a splitting of ~4 cm^{-1} which may be contained within the unresolved recorded IR-MPD bands. The CH_3 bending vibrations are signifficcantly less affected by pyridine coordination. The experimental $\delta(CH_3)$ frequencies of n = 1,2,3 are blue shifted by 0, 1 and 9 cm^{-1}, with respect to n = 0. The calculated $\delta(CH_3)$ frequencies reproduce the less pronounced blue shift (1, 3 and 7 cm^{-1}).

Through the convincing agreement of the IR-MPD and DFT spectra, the calculations acquire additional credibility. We, thus, feel able to survey the geometries of the calculated structures of $[Fe_3O(OAc)_6(Py)_n]^+$ (n = 0,1,2,3).

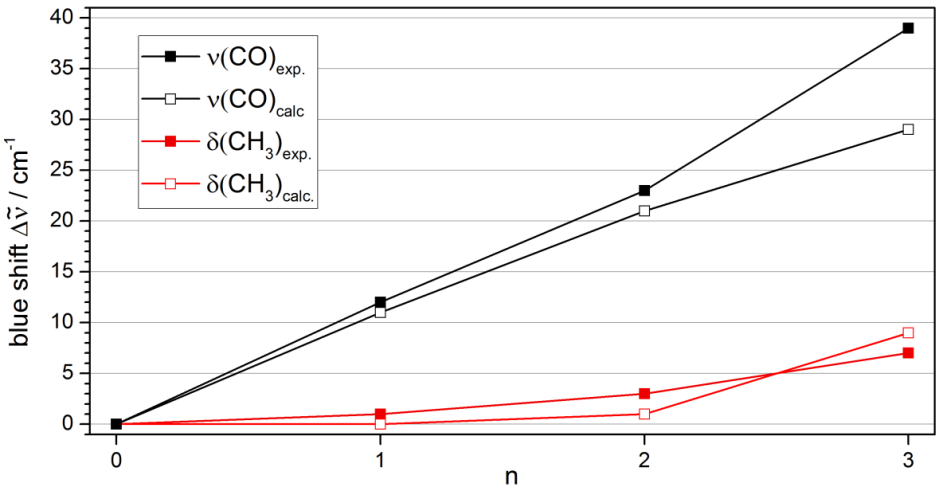

Figure 5: Vibrational shifts of the CH_3 bending vibration frequency ($\delta(CH_3)$) as well as the asymmetric carboxylic CO stretching vibration frequency (v(CO)) in $[Fe_3O(OAc)_6(Py)_n]^+$ (n = 0,1,2,3). The calculations were performed at the B3LYP/cc-pVTZ (H,C,N,O) and Stuttgart 1997 ECP (Fe) level of theory. The multiplicity is 16 and frequencies are scaled with 0.98.

Geometry of $[Fe_3O(OAc)_6(Py)_n]^+$ (n = 0,1,2,3): All three Fe atoms are coordinated in an pseudooctahedral geometry by four oxygen atoms of the bridging acetate ligands and by the central O^{2-} di-anion. The nitrogen atoms of the pyridine ligands coordinate in axial position thereby closing the octahedral coordination sphere. In the lowest energy structures the ring planes of the pyridine ligands orient perpendicular to the plane spanned by the three Fe atoms. Parallel alignment would result in less stable isomers (4 kJ/mol per pyridine torsion). The calculated linear absorption spectra of these high energy isomers are nearly identical with the spectra of the lowest energy structure (cf. Fig. S5-S7). Note, that in the crystal stucture of $[Fe_3O(OAc)_6(Py)_3](FeBr_4)$[11] the pyridine rings are found parallel to the Fe_3 plane. We do not exclude the existence of those isomers in the gas phase. However, the orientation of the pyridine is of minor interest as we focus on the distorsions of the triangular Fe_3O-core of the $[Fe_3O(OAc)_6]^+$ subunit (cf. Scheme 4 and Table S2) upon pyridine coordination.

In general the coordination of a single pyridine enlarges Fe - Fe distances (d_{FeFe}) and Fe - $O_{central}$ bond lengths (d_{FeO}) (by ~0.1 Å) of those bonds which involve the pyridine coordinating Fe-center. All the other Fe - Fe distances and Fe - $O_{central}$ bond lengths shorten by 0.1 Å and 0.02 Å respectively. This induces a symmetry lowering from a equilateral Fe-Fe-Fe ($[Fe_3O(OAc)_6]^+$) triangle nearly in D_{3h} symmetry to a isosceles triangle ($[Fe_3O(OAc)_6(Py)_1]^+$ in C_{2v} symmetry. The coordinated Fe center moves away from the two uncoordinated ones which slightly approach each other. Coordination of a

second and a third pyridine molecule distracts each affected Fe site slightly from the other Fe centers. The isosceles triangular geometries (C_{2v} symmetry in the cases of n = 1 and 2) eventually relax upon n = 3 (coordination of three pyridine molecules) to an equilateral D_{3h} geometry (as upon n = 0). However, all Fe - Fe distances and Fe - $O_{central}$ bond lengths are elongated with respect to the uncoordinated complex by 0.1 Å. The elongantion of Fe-Fe distances hampers the orbital overlap with the orbitals of the bridging acetate and leads to the experimentally observed blueshift of ν(CO). The binding distance between the Fe center and the nitrogen atom of the pyridine ligand (cf. Table S2) increases from 2.15 Å (n =1) to 2.22 Å (n = 3) indicating a lower bond strength, which we observed in the CID experiments.

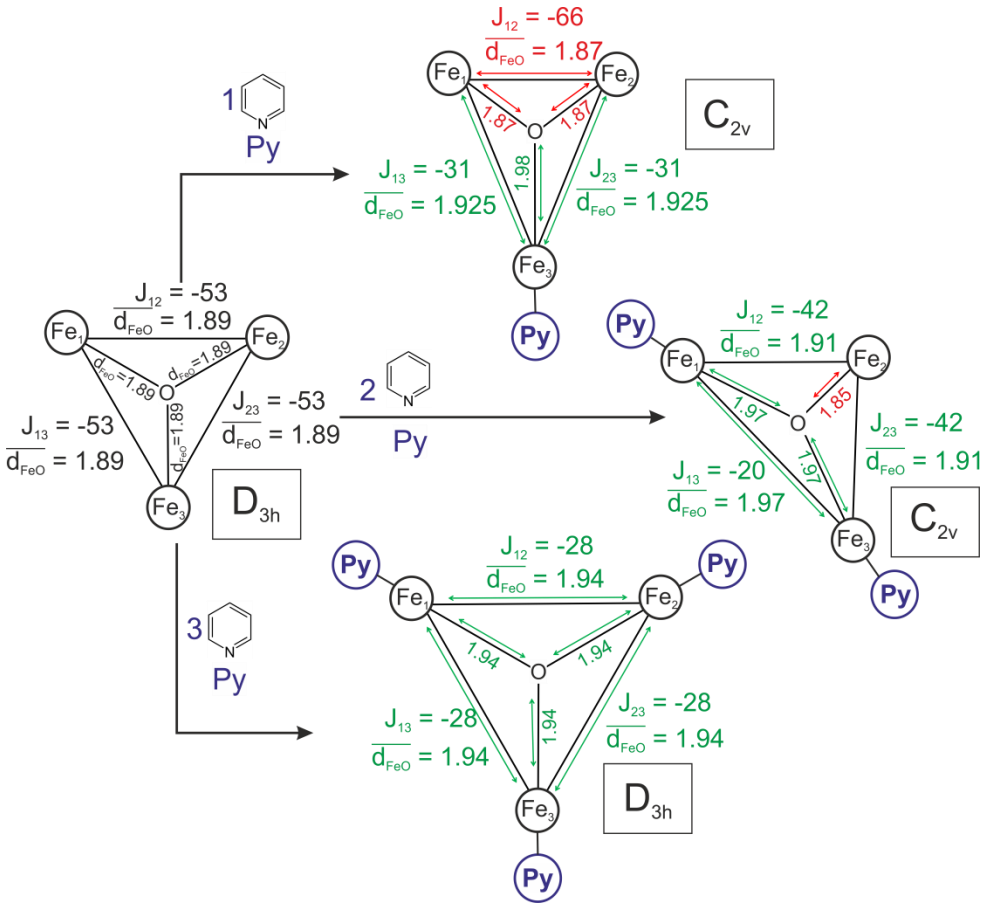

Scheme 4: Symmetries, atom distances (Fe-$O_{central}$ distances and mean Fe-O distances $\overline{d_{FeO}}$, averaged over two adjacent Fe atoms, all in Å) and magnetic coupling constants (J_{ij} in cm^{-1}) of the Fe_3O-core in $[Fe_3O(OAc)_6(Py)_n]^+$ (n = 0,1,2,3). The calculations were performed at the B3LYP/cc-pVTZ (H,C,N,O) and Stuttgart 1997 ECP (Fe) level of theory and the multiplicity is 16. The acetate ligands are omitted for clarity. Green (red) indicates a larger (smaller) magnitude with respect to the (black) values of the n = 0 case.

Simulation of antiferromagnetic couplings via the broken symmetry approach: Simulations of antiferromagnetic coupling in $[Fe_3O(OAc)_6(Py)_n]^+$ via broken symmetry calculations in all possible configurations reveal an energetic stabilization of 17 - 32 kJ/mol (cf. Fig. 7) relative to the ferromagnetic case (16-tet). This result is in line with the prevailing antiferromagnetic coupling in complexes of the structural type $[M_3O(OAc)_6(L)_3]^+$ (M = transition metal, L = ligand) as investigated in the condensed phase[9, 98, 99]. Our spin density isosurfaces reveal localized unpaired spin density on the Fe centers with minor delocalization onto the donor atoms of the ligands (oxygen atoms of acetate and nitrogen atoms of pyridine).

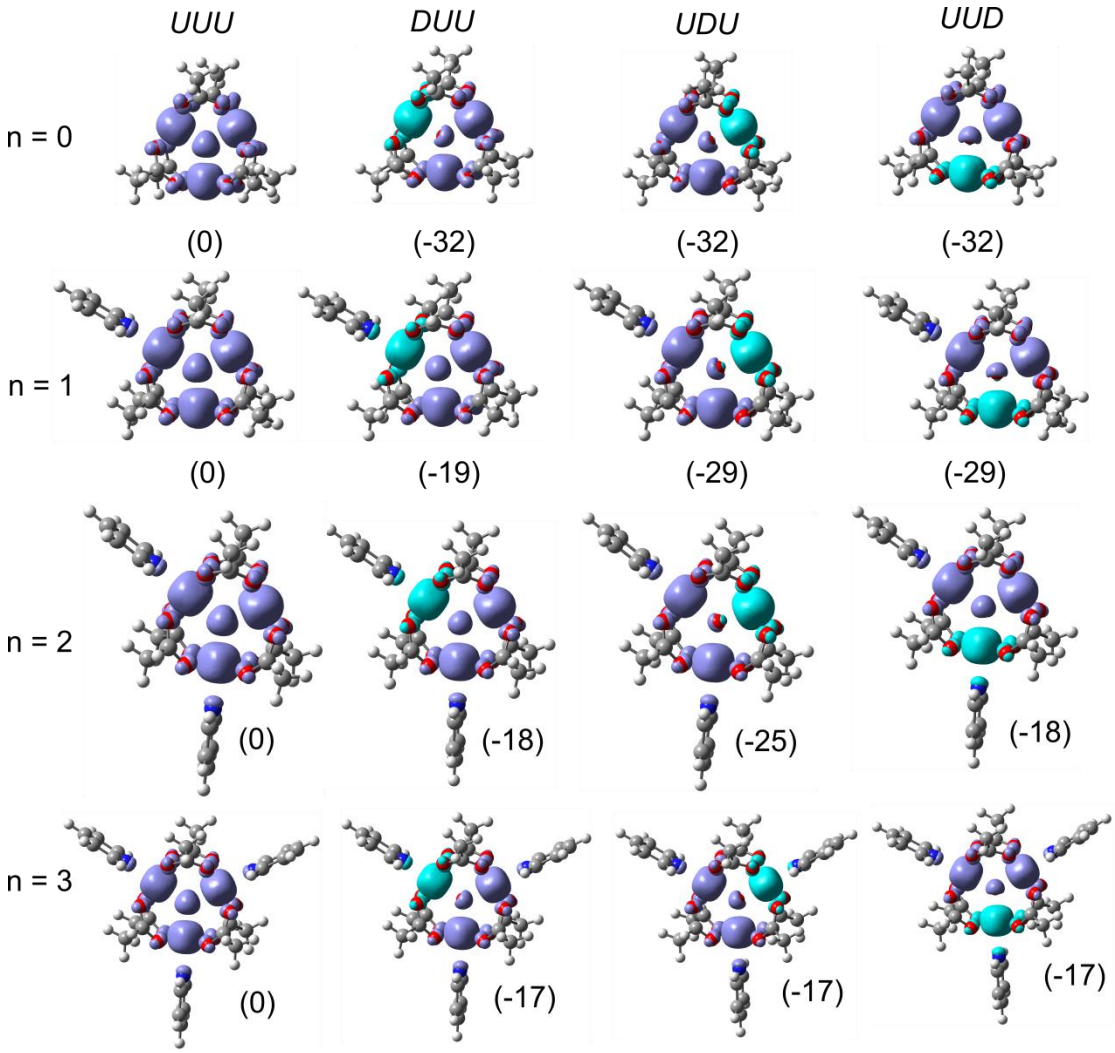

Figure 6: Spin density iso surfaces (Iso = 0.01) of $[Fe_3O(OAc)_6(Py)_n]^+$ (n = 0,1,2,3) in the one ferromagnetic and the three broken symmetry configurations. Purple and turquoise surfaces indicate alpha and beta spin, respectively. The relative energies in paratheses is given in kJ/mol. The calculations were performed at the B3LYP_Gaussian/cc-pVTZ (H,C,N,O) and Stuttgart 1997 ECP (Fe) level of theory.

The energetic gain depends on the number of coordinated pyridine ligands and on the broken symmetry configuration. In the case of n = 0 all configurations have a relative energy of -32 kJ. This stabilization decreases in the case of n = 3 to -17 kJ/mol (cf. Fig. 7). Note, that in these cases (n = 0 and 3) the triangular Fe_3O core exhibit a nearly equilateral D_{3h} geometry. The energies of the three antiferromagnetic broken symmetry configurations are therefore bound to be identical. Accordingly the three coupling constants are nearly identical for n = 0 and 3 and decrease in magitude (J_{12}=J_{13}=J_{23} = -53 cm^{-1} and -28 cm^{-1} for n = 0 and 3; cf. Scheme 4). Neutron scattering experiments on $[Fe_3O(CD_3CO_2)_6(Py)_3](NO_3)$ powder[10] determined two non identical coupling constants (J_1 = -26.8 cm^{-1} and J_2 = -32.9 cm^{-1}) which was attributed to small geometry distortions induced by spin frustration effects[100]. Our values of J_{12}=J_{13}=J_{23} = 28 cm^{-1} seem to resemble an average of the two powder values – void of any minor spin frustrations. Coordination asymmetry induces much stronger effects, as we will see in the following.

We observe a correlation of the magnetic coupling with the symmatry/geometry of the triangular Fe_3-core: In order to demonstrate this magnetostructural correlation we introduce the geometrical parameter $\overline{d_{FeO}}$, which we define as the average of two Fe-O distances along the shortest superexchange pathway (through the central O^{2-} atom) between two adjacent metal centers ($\overline{d_{FeO}}$ = [d($Fe_{(i)}$-$O_{central}$)+ ($Fe_{(j)}$-$O_{central}$)]/2), as suggested before[3]. Since the Fe-Fe distances are longer than 3 Å we expect no direct metal metal interaction[8]. Elongation of $\overline{d_{FeO}}$ within the Fe_3O core leads to a significant weakening of antiferromagnetic coupling while shortening of $\overline{d_{FeO}}$ distances strengthens the same. We observe both by stepwise coordination of pyridine ligands to the Fe_3O core: A single pyridine ligand (n = 1) lowers the symmetry of the triagular Fe_3O core to an isosceles C_{2v} geometry (cf. Scheme 4). In the case of n = 1 the $\overline{d_{FeO}}$ parameter of the coordinated Fe center elongates by ~0.035 Å with respect to n = 0 while the $\overline{d_{FeO}}$ parameter of the non coordinated Fe centers shortens by ~0.02 Å. Accordingly we identify two non identical coupling constants: J_{13}=J_{23}= -31 cm^{-1} (the Fe-$O_{central}$-Fe coupling weakened due to the enlarged $\overline{d_{FeO}}$) and J_{12}= -66 cm^{-1} (the Fe-$O_{central}$-Fe coupling strengthened due to the shortened $\overline{d_{FeO}}$). We take these changes in geometries and coupling constants as clear indications of signficant spin frustration,

the magnitude of which is much beyond the postulated effect by mere bulk phase distortions.

In the case of n = 2 both $\overline{d_{FeO}}$ parameters elongate by 0.02 Å and 0.08 Å. The Fe_3O core remains in low isoceles C_{2v} symmetry. This results in two different coupling constants: $J_{12}=J_{23}= -42\ cm^{-1}$ and $J_{13} = -20\ cm^{-1}$. In this particular case we observe the weakest antiferromagnetic coupling ($J_{13} = -20\ cm^{-1}$) due to the large $\overline{d_{FeO}}$ value. In the case of n = 3 all $\overline{d_{FeO}}$ parameters elongate evenly by 0.05 Å leading to an equilateral D_{3h} symmetry. We extract three identical coupling constants ($J_{12}=J_{13}=J_{23} = 28\ cm^{-1}$). We applied a fit function (eq. 10) that describes well the correlation between the magnetic coupling constants (J_{ij}) and the geometric parameter $\overline{d_{FeO}}$ (cf. Fig. 7). Such a fit function has been used before to correlate experimentally determined coupling constants of oxo-diiron complexes with the associated geometrical parameters as derived from crystal structures[3]. The exponential form of the analytical expression represents the variation of the overlap integral of two s type orbitals which determines the magnitude of the coupling constant.

$$-J = A \cdot exp\left(B \cdot \overline{d_{FeO}}\right) \qquad (10)$$

Our fit parameters $A = 7.8 \cdot 10^{11}\ cm^{-1}$ and $B = -12.4\ Å^{-1}$ are well in line with the previous treatment [3]. We thus feel confident that our chosen level of theory describes both the geometrical and magnetic properties of $[Fe_3O(OAc)_6(Py)_n]^+$ (n = 0,1,2,3) properly.

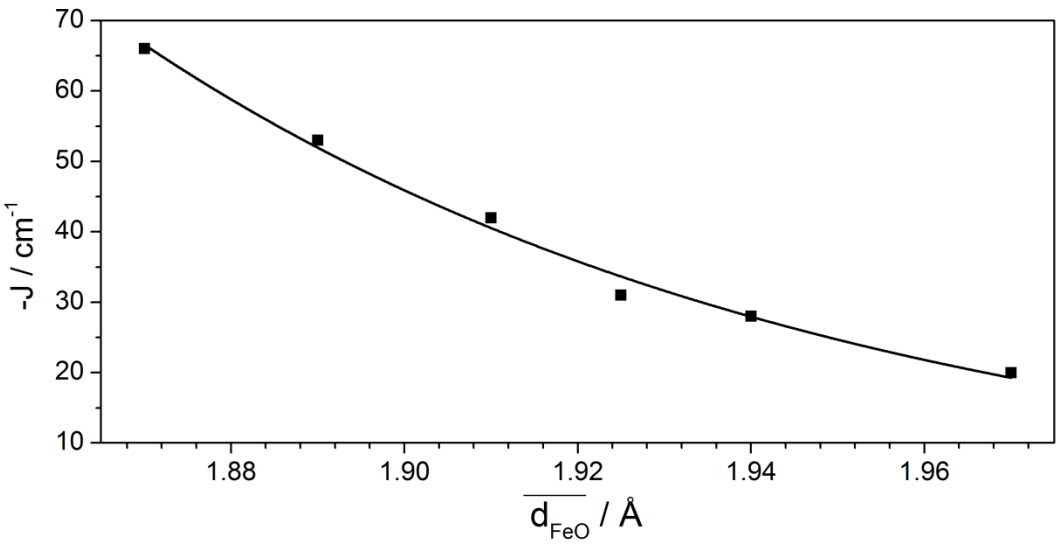

Figure 7: Correlation between the calculated magnetic coupling constant J and the geometric parameter $\overline{d_{FeO}}$ in $[Fe_3O(OAc)_6(Py)_n]^+$ (n = 0,1,2,3). The solid line ist a least squares fit with an exponential fit function (eq. 10).

Spins states of [Fe$_3$O(OAc)$_6$(Py)$_n$]$^+$: We established that [Fe$_3$O(OAc)$_6$(Py)$_n$]$^+$ (n = 0,1,2,3) exhibits either an equilateral (n = 0 and 3) Fe$_3$O core geometry with three identical coupling constants, or an isosceles (n = 1 and 2) Fe$_3$O core geometry with up to two different coupling constants (e.g. J_{12} and $J_{13} = J_{23}$). In the following we will discuss two coupling constants J and J*, which may or may not be identical, J=J* in the equilateral geometry and J ≠ J* in the isosceles case. This simplified nomenclature allows to write down a HDvV Hamiltonian as follows[19]:

$$\hat{H}_{HDvV} = -4J\left(\hat{S}_{Fe1}\hat{S}_{Fe2} + \hat{S}_{Fe1}\hat{S}_{Fe3}\right) - 2J^*\left(\hat{S}_{Fe2}\hat{S}_{Fe3}\right) \quad (11)$$

By defining a total spin operator $\hat{S}_T$ (eq. 12)) and a partial spin operator $\hat{S}_A$ (eq. 13)) we obtain a descriptive Hamiltonian (eq. 14):

$$\hat{S}_T = \hat{S}_A + \hat{S}_{Fe1} \quad (12)$$

$$\hat{S}_A = \hat{S}_{Fe2} + \hat{S}_{Fe2} \quad (13)$$

$$\hat{H}_{HDvV} = -2J\left(\widehat{S_T^2} - \widehat{S_A^2}\right) - J^*\left(\widehat{S_A^2}\right) \quad (14)$$

We have omitted three additional, constant value, single-ion $\widehat{S_{Fe}^2}$ terms as they are not relevant in the following discussion. This Hamiltonian yields 27 eigenstates. Depending on the J/J* ratio, six of these are the ground states (cf. Fig. 8). The higher the J/J* ratio, the higher the S_A value of the ground state. The total spin (S_T) of these ground states can be 1/2, 3/2 and 5/2. Note, that small changes in the J/J* ratio (e.g. induced by subsequent pyridine coordination) suffice to change the ground spin state and therefore the total spin S_T. We interpret this finding as a notably strong spin frustration in the Fe$_3$O core upon exchange interaction ratios J/J* close to unity. In summary, the ratio of the coupling constants (J and J*) in [Fe$_3$O(OAc)$_6$(Py)$_n$]$^+$ (n = 0,1,2,3) uniquely determines spin ground states and their S_T and S_A values (cf. Fig. 8 and Table 1).

Table 1: Coupling constants of [Fe$_3$O(OAc)$_6$(Py)$_n$]$^+$ (n = 0,1,2,3) and their associated spin ground states by Hamiltonian in eq. 14.

n	J / cm^{-1}	J* / cm^{-1}	J/J*	$S_T = S_A+S_1$	$S_A=S_2+S_3$
0	-53	-53	1.0	1/2	2 ; 3
1	-31	-66	0.5	3/2	1
2	-42	-20	2.1	5/2	5
3	-28	-28	1.0	1/2	2 ; 3

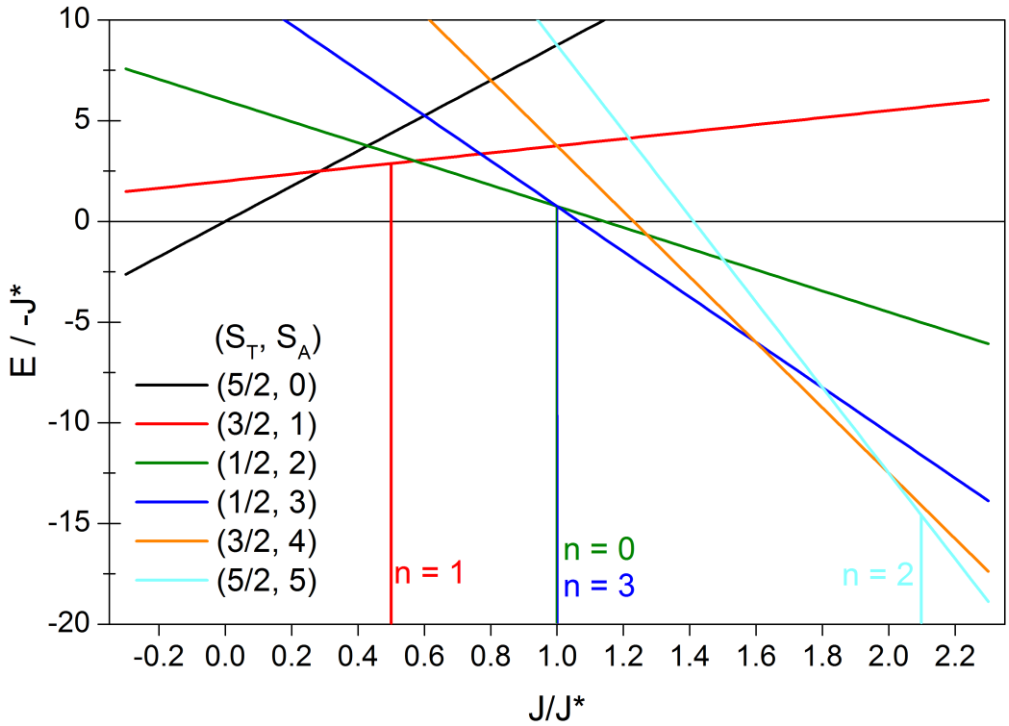

Figure 8: Eigenvalues of the HDvV Hamiltonian (14) for a triangular Fe_3-core in units of J* in dependence of J/J* (only ground states indicated). The vertical lines indicate J/J* ratios and spin states of $[Fe_3O(OAc)_6(Py)_n]^+$ (n = 0,1,2,3). The spin states are labeled as (S_T,S_A).

The occurance of two non identical coupling constants by symmetry lowering in $[Fe_3O(OAc)_6(Py)_n]^+$ (n= 0, 1, 2, 3) and the resulting change of spin state is consistent with some previous investigation of asymmetric $[Fe_3O(TIEO)_2(O_2CPh)Cl_3]$ complexes in the condensed phase by Lippard et al[101, 102]. In this case the symmetry is lowered by non equivalent bridging ligands. This results in two non identical coupling constants J = -8.0 cm^{-1} and J* = -55 cm^{-1} with a S_T = 5/2 ground state (J/J* = 0.145). Note, that in our case the symmetry of the Fe_3O core is lowered by stepwise coordination of axial pyridine ligands while all bridging ligands are equivalent.

We observe the symmetry lowering of $[Fe_3O(OAc)_6(Py)_n]^+$ (n = 0,1,2,3) experimentally by the vibrational blue shift of the asymmetric carboxylic CO stretching vibration frequency in the IR-MPD spectra (cf. Fig 5, up to 39 cm^{-1}). In the following chapter we strive to investigate the associated magnetic evolution of cryo cooled $[Fe_3O(OAc)_6(Py)_n]^+$ via XMCD experiments.

6.5.3 X-Ray absorption and XMCD Spectra of Isolated Sample Ions

Mass spectra at NanoClusterTrap: We sprayed the above described sample solution by the customized ESI source at the liquid helium cooled NanoClusterTrap, and we recorded mass spectra by its reflectron time of flight (TOF) mass spectrometer. We observe a series of isotopic peaks at m/z = 523, 538, 588, 602 and 617 (cf. Fig. 9, upper trace). We assign the mass peaks at m/z = 538 and 617 to $[Fe_3O(OAc)_6(Py)_n]^+$ (n = 0 and 1), in line with some species as observed by the Paul trap instrument (cf. Fig. 1) – the n = 2 and 3 of the Paul trap spectrum missing, however. This indicates stronger fragmentation of $[Fe_3O(OAc)_6(Py)_3]^+$ by the customized ESI source at the ClusterNanoTrap and/or in the course of trapping and detecting. Note, that the additional peaks at the ClusterNanotrap (m/z= 523, 588, 602) likely originate from CH_3 and C_2H_5 losses. When isolating the $[Fe_3O(OAc)_6(Py)_1]^+$ species there is some spontaneous, non-photonic fragmentation which yields further fragments at m/z = 538 and 558 (losses of 79 and 59 m/z) which we assign to pyridine and neutral acetate (OAc*) loss. When isolating $[Fe_3O(OAc)_6]^+$ we observe spontaneous fragments at m/z = 479 and 494 (losses of 59 and 44 m/z) which we assign to a loss of an acetate radical (OAc*) and to CO_2 elimination, respectively. When irradiating X-rays at the Fe $L_{3,2}$ absorption edges of the isolated $[Fe_3O(OAc)_6(Py)_n]^+$ (n = 0 and 1) we obtain two fragments at m/z = 47 (fragment 1, assigned to ($C_2H_7O^+$) and at m/z = 56 (fragment 2, assigned to Fe^+).

XAS spectra of $[Fe_3O(OAc)_6(Py)_n]^+$: We recorded fragment specific X-Ray absorption spectra (XAS) of isolated $[Fe_3O(OAc)_6(Py)_n]^+$ (n = 0 and 1; cf. Fig. 10) utilizing negative and positive circularly polarized photons at the Fe $L_{3,2}$ absorption edges ($2p_{1/2} \rightarrow 3d$ and $2p_{3/2} \rightarrow 3d$ transitions). Remarkably, the two fragment traces reveal significant differences in the resulting XAS spectra: The spectra of fragment 2 (m/z = 81) exhibit a douple peaks at 710.6/712.2 eV (L_3 edge) with an intensity ratio of approx. 1/2. This represents a prototypical spectrum of a Fe^{3+} ion in octahedrical symmetry with an appropriate ligand field splitting as simulated by Laan et al.[103]. This is consistent with the molecular structure of $[Fe_3O(OAc)_6(Py)_n]^+$, which contains three Fe^{3+} ions with (distorted) octahedral symmetry. The XAS spectra of fragment 1 (m/z = 73) exhibit a douple peak at 710.6/712.2 eV (L_3 edge) with an intensity ratio of approx. 1/1 with an additional shoulder on the low energy flank of the edge. Such spectra are expected to

result in cases of Fe^{2+}/Fe^{3+} mixtures as investigated in minerals by Cressey et al.[104]. Thus we assume that fragment 1 originates from contaminations containing Fe^{2+} ions. The cleavage of acetate radicals (which we observe as base fragmentation while isolating $[Fe_3O(OAc)_6(Py)_n]^+$) might lead to reduction Fe^{3+} centers which in turn might lead to the observed signals for Fe^{2+}/Fe^{3+} mixtures. In the following we only discuss the spectra of relevance, which is those of fragment 2.

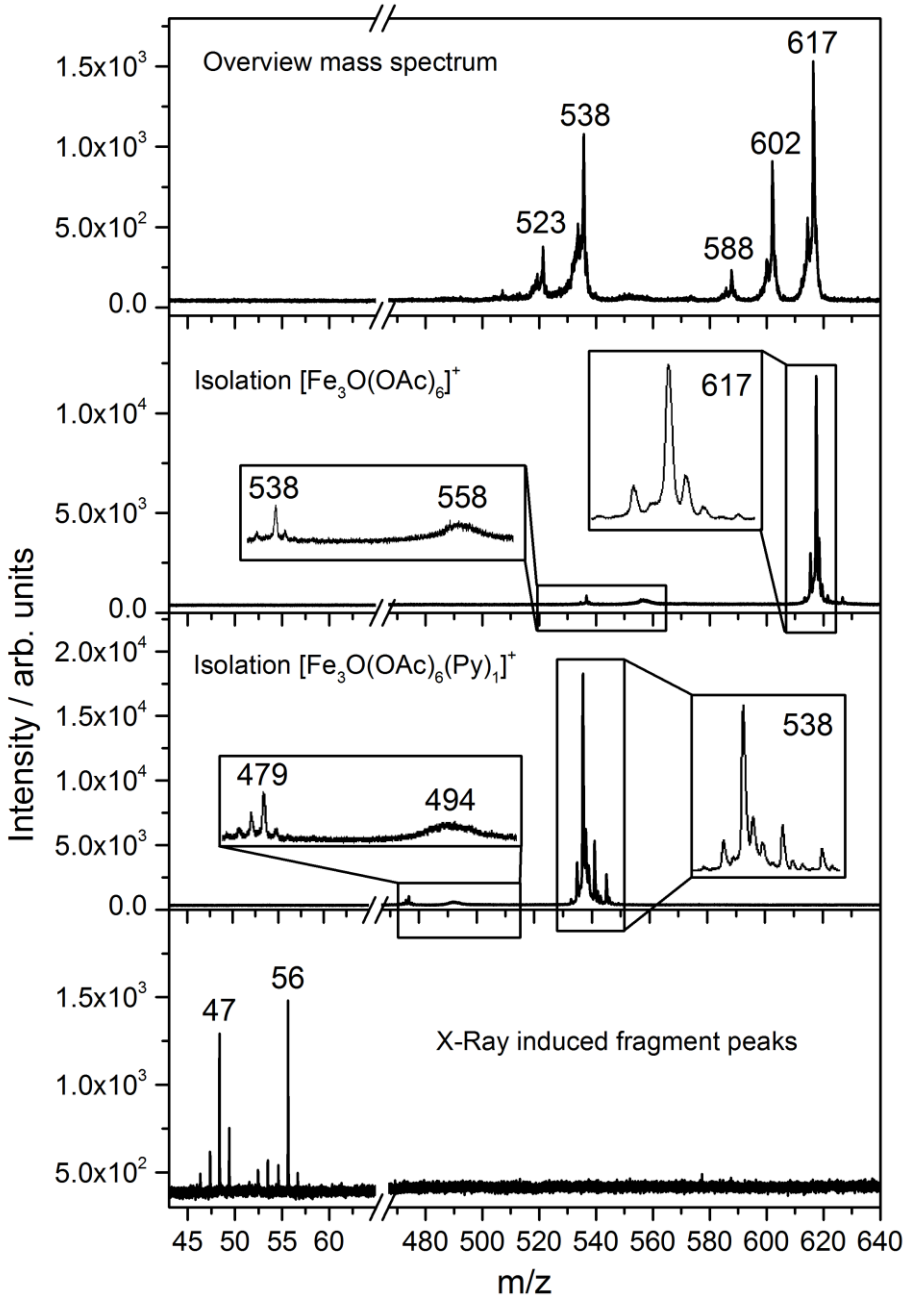

Figure 9: Upper trace: Cationic mass spectrum of a $[Fe_3O(OAc)_6(H_2O)_3]ClO_4$ acetonitrile/pyridine = 1/10 solution using the liquid helium cooled NanoClusterTrap. **Middle traces:** mass spectra with a mass filter for m/z = 617 and 538. **Lower Trace**: Mass spectra showing X-Ray induced fragments.

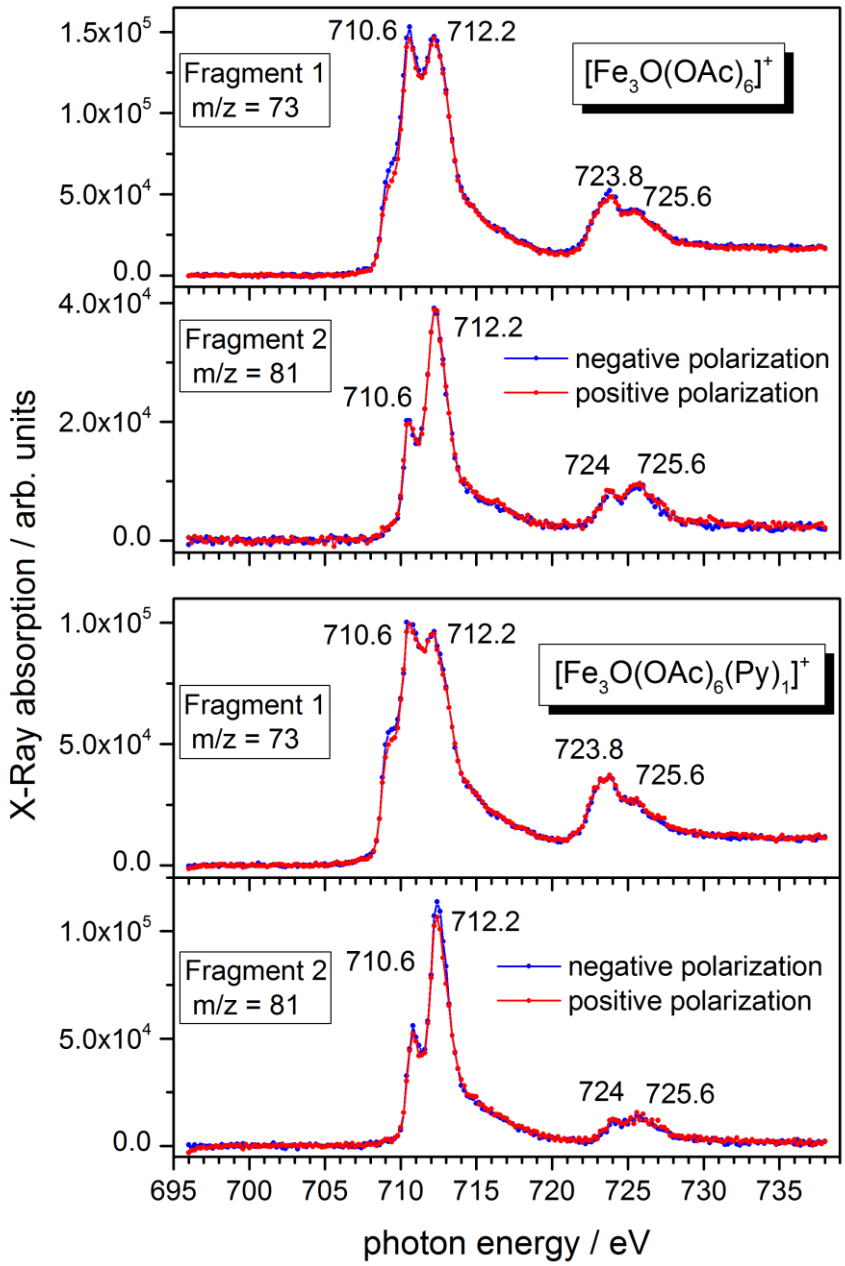

Figure 10: Polarization dependent XAS spectra of $[Fe_3O(OAc)_6(Py)_n]^+$ (n = 0, 1) on the Fe $L_{3,2}$ absorption edge monitoring the mass peak intensities of fragment 1 (m/z = 47) and fragment 2 (m/z = 56).

XMCD Spectra of $[Fe_3O(OAc)_6(Py)_n]^+$: The difference of negative and positive polarization in the XAS spectra reveals a dichroic effect that manifests in the XMCD spectra which contain information on the magnetism of the complexes (cf. Fig. 11). The high spin Fe^{3+} ions of $[Fe_3O(OAc)_6(Py)_n]^+$ (n = 0 and 1) provide for 5 unpaired electrons each. According to Hunds rules this would lead to a spin magnetic moment per atom of $m_s = 5\ \mu_B$ and an orbital magnetic moment per atom of $m_L = 0\ \mu_B$. Such a magnetizations would yield significant XMCD effects. However, the XMCD spectra reveal zero dichroiic

effect in the case of $[Fe_3O(OAc)_6]^+$ and a minor dichroic effect in the case of $[Fe_3O(OAc)_6(Py)_1]^+$). It is evident, that the overall low magnetization of the complexes increases slightly from n = 0 to n = 1. We accord the overall low dichroic effects to a prevailing antiferromagnetic coupling of the Fe atoms in $[Fe_3O(OAc)_6(Py)_n]^+$. The XMCD technique determines the average magnetic moment of all Fe atoms within the complex. Thus, antiferromagnetic coupling lowers the average magnetic moment per atom which leads to decreased dichroic effects.

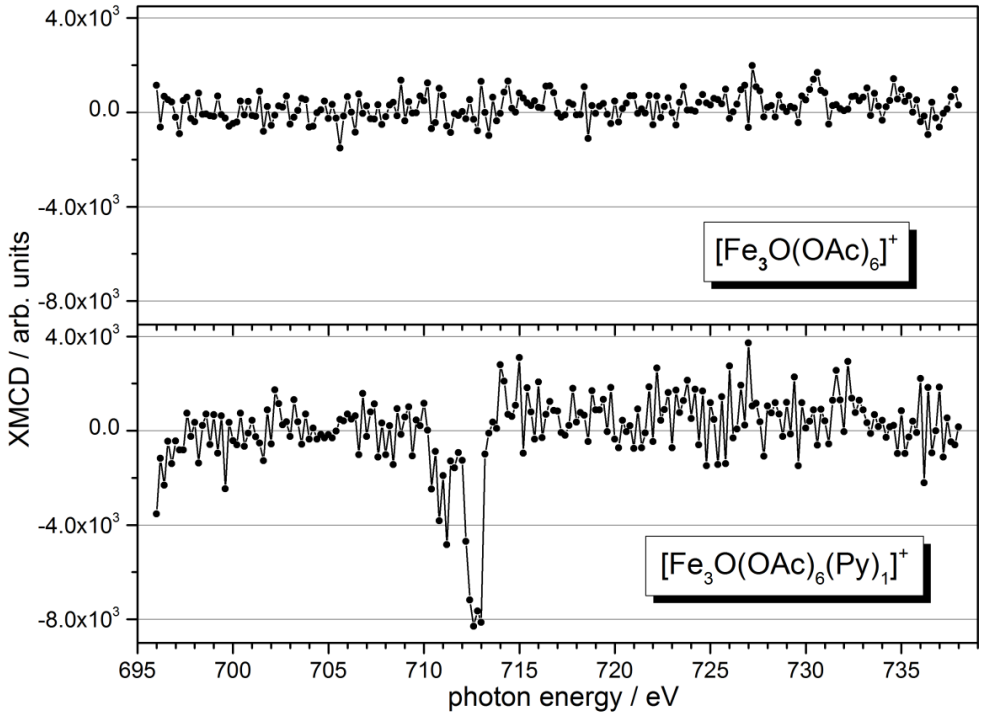

Figure 11: XMCD spectra of $[Fe_3O(OAc)_6(Py)_n]^+$ (n = 0, 1) on the Fe $L_{3,2}$ absorption edge monitoring the mass peak intensities of fragment 2 (m/z = 56).

The magnetization of the complexes is affected by the coordination of one pyridine ligand as we observe a small magnetization for n = 1 and no magnetization at all for n = 0. In the case of n = 0 ($[Fe_3O(OAc)_6]^+$) the Fe_3O core is in equilateral D_{3h} symmetry and all coupling constants are equal ($J/J^* = 1$) leading to a total spin of $S_T = 1/2$ (cf. Scheme 5 and Fig. 8) according to the model Hamiltonian (eq. 14). It is conceivable that this low total spin does not allow for efficient alignment of the spin with the magnetic field such that we observe no magnetization in the XMCD spectrum of $[Fe_3O(OAc)_6]^+$. The introduction of one pyridine ligand lowers the symmetry of the Fe_3O core to an isosceles C_{2v} triangle with two non-equal coupling constants ($J/J^* = 0.5$). This leads to a total spin of $S_T = 3/2$ in the case of $[Fe_3O(OAc)_6(Py)_1]^+$. The higher total spin

may lead to a more efficient alignment of the spin with the magnetic field and thus enabling the observation of a weak dichroic effect in the XMCD spectrum of $[Fe_3O(OAc)_6(Py)_1]^+$. We would expect to measure an even larger dichroic effect in the case of n = 2 which would lead to an even higher total spin (S_T) of 5/2 in the ground state (J/J* = 2.1). In the case of n = 3 ($[Fe_3O(OAc)_6(Py)_3]^+$) the Fe_3O core isomerizes back to equilateral D_{3h} symmetry with J/J* = 1 leading to a low total spin of $S_T = 1/2$. We would expect a very low dichroic effect via XMCD. Unfortunately, we were not able to detect $[Fe_3O(OAc)_6(Py)_n]^+$ (n = 2,3) in the current setup of the NanoClusterTrap.

6.6 Conclusions

We investigated the stability, geometry and magnetism of isolated $[Fe_3O(OAc)_6(Py)_n]^+$ (n = 0,1,2,3) in the gas phase and observed remarkable trends upon stepwise introduction of pyridine ligands. CID studies establish the elimination of a single pyridine ligand as the primary fragmentation route. The Fe-Py bond strenghts decrease with the number of coordinated pyridine ligands as indicated experimentally by CID appearance curves (E_{com}^{50}) as well as by calculated binding energies ($\Delta\Delta_{bind}G^0$).

Experimental IR-MPD spectra as well as calculated IR absorption spectra reveal significant blue shifts of the asymmetric carboxylic CO stretching vibration frequency upon coordination of pyriddine ligands (up to 39 cm^{-1}). This provides a spectroscopic evidence for distinct shortenings and elongations of Fe-Fe distances accompanied by symmetry lowering of the triangular Fe_3O core: An equilateral triangular Fe_3O core in D_{3h} symmetry (in the case of n = 0) distorts to an isosceles structure with C_{2V} symmetry (in the case of n = 1 and 2). The coordination of the third pyridin ligand (n = 3) regains the equilateral D_{3h} symmetry of the Fe_3O core.

The geometrical modulation correlates with the magnetic properties of $[Fe_3O(OAc)_6(Py)_n]^+$. Broken symmetry based calculations reveal antiferromagnetic magnetic couplings which are crucialy affected by the geometric modulation. Equilateral geometries lead to three identical coupling constants while the lower symmetry isosceles geometries lead to two non identical coupling constants (J and J*). The magnitude of the coupling constants offers a wide range (-22 cm^{-1} to -71 cm^{-1}) depending critically on the average distance $\overline{d_{FeO}}$. We utilized J/J* ratios in combination with a model spin Hamiltonian (eq. 14) to determine the ground spin states of

$[Fe_3O(OAc)_6(Py)_n]^+$: In equilateral Fe_3O cores with D_{3h} symmetries (n =0 and 3) the J/J* ratio is 1 leading to total spin (S_T) of 1/2 in the ground states. Lowering the symmetries to C_{2V} leads to J/J* = 0.5 (n=1) and J/J* = 2.1 (n=2) which results in total spins (S_T) of 3/2 (n =1) and 5/2 (n=2) in the ground states.

Our XMCD spectra reveal in general low magnetizations of $[Fe_3O(OAc)_6(Py)_n]^+$ (n = 0,1) which we attribute to a dominant antiferromagnetic coupling. While $[Fe_3O(OAc)_6]^+$ exhibits no magnetization at all, $[Fe_3O(OAc)_6(Py)_1]^+$ exhibits an observable dichroic effect. We contribute this finding to an increase of the total spin of the complex ($S_{T,n=0} = 1/2 \rightarrow S_{T,n=1} = 3/2$) induced by the symmetry lowering upon coordination of a single pyridine ligand.

6.7 Acknowledgement

This work was supported by the German research foundation DFG within the transregional collaborative research center SFB/TRR 88 “Cooperative effects in homo and heterometallic complexes” (3MET) and by the state research center OPTIMAS. We gratefully acknowledge the financial support and generous allocation of X-ray beam time at the UE52 – PGM beamline from HZB at the BESSY II synchrotron radiation facility.

6.8 References

1. S. Bi, C. Liu and H. Hu, *The Journal of Physical Chemistry B*, 2002, **106**, 10786-10792.
2. T. Cauchy, E. Ruiz and S. Alvarez, *Journal of the American Chemical Society*, 2006, **128**, 15722-15727.
3. S. M. Gorun and S. J. Lippard, *Inorganic Chemistry*, 1991, **30**, 1625-1630.
4. L. Gregoli, C. Danieli, A.-L. Barra, P. Neugebauer, G. Pellegrino, G. Poneti, R. Sessoli and A. Cornia, *Chemistry – A European Journal*, 2009, **15**, 6456-6467.
5. J. P. S. Walsh, S. Sproules, N. F. Chilton, A.-L. Barra, G. A. Timco, D. Collison, E. J. L. McInnes and R. E. P. Winpenny, *Inorganic Chemistry*, 2014, **53**, 8464-8472.
6. D. Gatteschi and R. Sessoli, *Angew. Chem., Int. Ed.*, 2003, **42**, 268.
7. Y.-W. Lin, *Coordination Chemistry Reviews*, 2017, **336**, 1-27.
8. R. Werner, S. Ostrovsky, K. Griesar and W. Haase, *Inorganica Chimica Acta*, 2001, **326**, 78-88.
9. F. E. Sowrey, C. Tilford, S. Wocadlo, C. E. Anson, A. K. Powell, S. M. Bennington, W. Montfrooij, U. A. Jayasooriya and R. D. Cannon, *Journal of the Chemical Society, Dalton Transactions*, 2001, 862-866.
10. R. D. Cannon, U. A. Jayasooriya, R. Wu, S. K. arapKoske, J. A. Stride, O. F. Nielsen, R. P. White, G. J. Kearley and D. Summerfield, *Journal of the American Chemical Society*, 1994, **116**, 11869-11874.

11. V. Amani, N. Safari and H. R. Khavasi, *Spectrochimica Acta Part A: Molecular and Biomolecular Spectroscopy*, 2012, **85**, 17-24.
12. R. Wu, M. Poyraz, F. E. Sowrey, C. E. Anson, S. Wocadlo, A. K. Powell, U. A. Jayasooriya, R. D. Cannon, T. Nakamoto, M. Katada and H. Sano, *Inorganic Chemistry*, 1998, **37**, 1913-1921.
13. M. K. Johnson, D. B. Powell and R. D. Cannon, *Spectrochimica Acta Part A: Molecular Spectroscopy*, 1981, **37**, 995-1006.
14. A. N. Georgopoulou, Y. Sanakis and A. K. Boudalis, *Dalton Transactions*, 2011, **40**, 6371-6374.
15. G. Filoti, J. Bartolome, D. P. E. Dickson, C. Rillo, I. Prisecaru, T. Jovmir, V. Kuncser and C. Turta, *Journal of Magnetism and Magnetic Materials*, 1999, **196–197**, 561-563.
16. O. Kahn, *Chemical Physics Letters*, 1997, **265**, 109-114.
17. J. Schnack, *Dalton Transactions*, 2010, **39**, 4677-4686.
18. C. T. Dziobkowski, J. T. Wrobleski and D. B. Brown, *Inorganic Chemistry*, 1981, **20**, 671-678.
19. D. N. Hendrickson, in *Research Frontiers in Magnetochemistry*, ed. C. J. O´Connor, World Scientific Co. Pte. Ltd., Singapore1993, pp. 87-108.
20. J. Lang, J. Mohrbach, S. Dillinger, J. M. Hewer and G. Niedner-Schatteburg, *Chemical Communications*, 2017, **53**, 420-423.
21. B. J. Coe and S. J. Glenwright, *Coordination Chemistry Reviews*, 2000, **203**, 5-80.
22. R. Colton, A. D'Agostino and J. C. Traeger, *Mass Spectrometry Reviews*, 1995, **14**, 79-106.
23. J. B. Fenn, *Angewandte Chemie International Edition*, 2003, **42**, 3871-3894.
24. M. Yamashita and J. B. Fenn, *The Journal of Physical Chemistry*, 1984, **88**, 4671-4675.
25. N. C. Polfer and J. Oomens, *Mass Spectrometry Reviews*, 2009, **28**, 468-494.
26. J. Roithova, *Chemical Society Reviews*, 2012, **41**, 547-559.
27. N. C. Polfer, *Chemical Society Reviews*, 2011, **40**, 2211-2221.
28. K. Levsen and H. Schwarz, *Angewandte Chemie International Edition*, 1976, **15**, 509-519.
29. K. M. Ervin and P. B. Armentrout, *The Journal of Chemical Physics*, 1987, **86**, 2659-2673.
30. A. K. Shukla and J. H. Futrell, *Journal of Mass Spectrometry*, 2000, **35**, 1069-1090.
31. S. Dillinger, J. Mohrbach, J. Hewer, M. Gaffga and G. Niedner-Schatteburg, *Physical Chemistry Chemical Physics*, 2015, **17**, 10358-10362.
32. J. Mohrbach, J. Lang, S. Dillinger, M. Prosenc, P. Braunstein and G. Niedner-Schatteburg, *Journal of Molecular Spectroscopy*.
33. A. B. Wolk, C. M. Leavitt, E. Garand and M. A. Johnson, *Accounts of Chemical Research*, 2013, **47**, 202-210.
34. C. T. Wolke, J. A. Fournier, L. C. Dzugan, M. R. Fagiani, T. T. Odbadrakh, H. Knorke, K. D. Jordan, A. B. McCoy, K. R. Asmis and M. A. Johnson, *Science*, 2016, **354**, 1131-1135.
35. J. Jašík, J. Žabka, J. Roithová and D. Gerlich, *International Journal of Mass Spectrometry*, 2013, **354–355**, 204-210.
36. J. Seo, W. Hoffmann, S. Warnke, X. Huang, S. Gewinner, W. Schöllkopf, M. T. Bowers, G. von Helden and K. Pagel, *Nat Chem*, 2017, **9**, 39-44.
37. M. Gaffga, *Diplomarbeit, TU Kaiserslautern*, 2012.

38. J. Oomens, J. D. Steill and B. Redlich, *Journal of the American Chemical Society*, 2009, **131**, 4310-4319.
39. Y. Nosenko, F. Menges, C. Riehn and G. Niedner-Schatteburg, *Physical Chemistry Chemical Physics*, 2013, **15**, 8171-8178.
40. J. Lang, M. Gaffga, F. Menges and G. Niedner-Schatteburg, *Physical Chemistry Chemical Physics*, 2014, **16**, 17417-17421.
41. J. Jašík, D. Gerlich and J. Roithová, *Journal of the American Chemical Society*, 2014, **136**, 2960-2962.
42. A. Fielicke, G. Meijer and G. von Helden, *European Physical Journal D*, 2003, **24**, 69-72.
43. A. M. Ricks, J. M. Bakker, G. E. Douberly and M. A. Duncan, *The Journal of Physical Chemistry A*, 2009, **113**, 4701-4708.
44. J. Lang, M. Cayir, S. P. Walg, P. Di Martino-Fumo, W. R. Thiel and G. Niedner-Schatteburg, *Chemistry – A European Journal*, 2016, **22**, 2345-2355.
45. N. C. Polfer, J. Oomens, D. T. Moore, G. von Helden, G. Meijer and R. C. Dunbar, *Journal of the American Chemical Society*, 2006, **128**, 517-525.
46. A. Scherz, H. Wende and K. Baberschke *Applied Physics A*, 2004, **78**, 843-846.
47. M. Tischer, O. Hjortstam, D. Arvanitis, J. Hunter Dunn, F. May, K. Baberschke, J. Trygg, J. M. Wills, B. Johansson and O. Eriksson, *Physical Review Letters*, 1995, **75**, 1602-1605.
48. K. Baberschke, *Applied Physics A*, 1996, **62**, 417-427.
49. S. S. Dhesi, E. Dudzik, H. A. Dürr, N. B. Brookes and G. van der Laan, *Surface Science*, 2000, **454–456**, 930-935.
50. S. Bornemann, O. Šipr, S. Mankovsky, S. Polesya, J. B. Staunton, W. Wurth, H. Ebert and J. Minár, *Physical Review B*, 2012, **86**, 104436.
51. J. Bansmann, A. Kleibert, M. Getzlaff, A. F. Rodríguez, F. Nolting, C. Boeglin and K.-H. Meiwes-Broer, *physica status solidi (b)*, 2010, **247**, 1152-1160.
52. J. T. Lau, A. Föhlisch, M. Martins, R. Nietubyc, M. Reif and W. Wurth, *New Journal of Physics*, 2002, **4**, 98.
53. B. T. Thole, P. Carra, F. Sette and G. van der Laan, *Physical Review Letters*, 1992, **68**, 1943-1946.
54. P. Carra, B. T. Thole, M. Altarelli and X. Wang, *Physical Review Letters*, 1993, **70**, 694-697.
55. C. T. Chen, Y. U. Idzerda, H. J. Lin, N. V. Smith, G. Meigs, E. Chaban, G. H. Ho, E. Pellegrin and F. Sette, *Physical Review Letters*, 1995, **75**, 152-155.
56. S. Peredkov, A. Savci, S. Peters, M. Neeb, W. Eberhardt, H. Kampschulte, J. Meyer, M. Tombers, B. Hofferberth, F. Menges and G. Niedner-Schatteburg, *Journal of Electron Spectroscopy and Related Phenomena*, 2011, **184**, 113-118.
57. J. Meyer, M. Tombers, C. v. Wüllen, G. Niedner-Schatteburg, S. Peredkov, W. Eberhardt, M. Neeb, S. Palutke, M. Martins and W. Wurth, *The Journal of Chemical Physics*, 2015, **143**, 104302.
58. S. T. Akin, V. Zamudio-Bayer, K. Duanmu, G. Leistner, K. Hirsch, C. Bülow, A. Ławicki, A. Terasaki, B. v. Issendorff, D. G. Truhlar, J. T. Lau and M. A. Duncan, *The Journal of Physical Chemistry Letters*, 2016, **7**, 4568-4575.
59. V. Zamudio-Bayer, K. Hirsch, A. Langenberg, M. Kossick, A. Ławicki, A. Terasaki, B. v. Issendorff and J. T. Lau, *The Journal of Chemical Physics*, 2015, **142**, 234301.
60. V. Zamudio-Bayer, R. Lindblad, C. Bülow, G. Leistner, A. Terasaki, B. v. Issendorff and J. T. Lau, *The Journal of Chemical Physics*, 2016, **145**, 194302.
61. J. Laskin and J. H. Futrell, *Mass Spectrometry Reviews*, 2005, **24**, 135-167.

62. S. A. McLuckey and D. E. Goeringer, *Journal of Mass Spectrometry*, 1997, **32**, 461-474.
63. F. Menges, C. Riehn and G. Niedner-Schatteburg, *Zeitschrift fur Physikalische Chemie*, 2011, **225**, 595.
64. E.-L. Zins, C. Pepe and D. Schröder, *Journal of Mass Spectrometry*, 2010, **45**, 1253-1260.
65. E.-L. Zins, C. Pepe, D. Rondeau, S. Rochut, N. Galland and J.-C. Tabet, *Journal of Mass Spectrometry*, 2009, **44**, 12-17.
66. K. V. Barylyuk, K. Chingin, R. M. Balabin and R. Zenobi, *Journal of the American Society for Mass Spectrometry*, 2010, **21**, 172-177.
67. B. Miehlich, A. Savin, H. Stoll and H. Preuss, *Chemical Physics Letters*, 1989, **157**, 200-206.
68. A. D. Becke, *The Journal of Chemical Physics*, 1993, **98**, 5648-5652.
69. T. H. Dunning, *The Journal of Chemical Physics*, 1989, **90**, 1007-1023.
70. M. Dolg, H. Stoll, H. Preuss and R. M. Pitzer, *The Journal of Physical Chemistry*, 1993, **97**, 5852-5859.
71. M. J. Frisch, et al.,, 2009.
72. S. Simon, M. Duran and J. J. Dannenberg, *The Journal of Chemical Physics*, 1996, **105**, 11024-11031.
73. S. F. Boys and F. Bernardi, *Molecular Physics*, 1970, **19**, 553-566.
74. E. M. V. Kessler, S. Schmitt and C. van Wüllen, *The Journal of Chemical Physics*, 2013, **139**, 184110.
75. F. Illas, I. P. R. Moreira, C. de Graaf and V. Barone, *Theoretical Chemistry Accounts*, 2000, **104**, 265-272.
76. S. Schmitt, *Dissertation, TU Kaiserslautern*, 2015.
77. O. Treutler and R. Ahlrichs, *The Journal of Chemical Physics*, 1995, **102**, 346-354.
78. R. Ahlrichs, M. Bär, M. Häser, H. Horn and C. Kölmel, *Chemical Physics Letters*, 1989, **162**, 165-169.
79. M. Von Arnim and R. Ahlrichs, *Journal of Computational Chemistry*, 1998, **19**, 1746-1757.
80. W. Heisenberg, *Zeitschrift für Physik*, 1928, **49**, 619-636.
81. E. Ising, *Zeitschrift für Physik*, 1925, **31**, 253-258.
82. C. N. Yang, *Physical Review*, 1952, **85**, 808-816.
83. J. M. Ricart, R. Dovesi, C. Roetti and V. R. Saunders, *Physical Review B*, 1995, **52**, 2381-2389.
84. J. M. Ricart, R. Dovesi, C. Roetti and V. R. Saunders, *Physical Review B*, 1997, **55**, 15942-15942.
85. K. Hirsch, V. Zamudio-Bayer, A. Langenberg, M. Niemeyer, B. Langbehn, T. Möller, A. Terasaki, B. v. Issendorff and J. T. Lau, *Physical Review Letters*, 2015, **114**, 087202.
86. M. Niemeyer, K. Hirsch, V. Zamudio-Bayer, A. Langenberg, M. Vogel, M. Kossick, C. Ebrecht, K. Egashira, A. Terasaki, T. Möller, B. v. Issendorff and J. T. Lau, *Physical Review Letters*, 2012, **108**, 057201.
87. S. Bari, O. Gonzalez-Magaña, G. Reitsma, J. Werner, S. Schippers, R. Hoekstra and T. Schlathölter, J. Chem. Phys., 2011, 134, 024314.
88. O. Gonzalez-Magana, G. Reitsma, S. Bari, R. Hoekstra and T. Schlatholter, PCCP, 2012, 14, 4351-4354.

89. K. Hirsch, J. T. Lau, K. Ph, A. Langenberg, J. Probst, J. Rittmann, M. Vogel, V. Zamudio-Bayer, T. Möller and B. v. Issendorff, Journal of Physics B: Atomic, Molecular and Optical Physics, 2009, 42, 154029.
90. A. Langenberg, K. Hirsch, A. Ławicki, V. Zamudio-Bayer, M. Niemeyer, P. Chmiela, B. Langbehn, A. Terasaki, B. v. Issendorff and J. T. Lau, Physical Review B, 2014, 90, 184420.
91. C. Piamonteze, P. Miedema and F. M. F. de Groot, PhRvB, 2009, 80, 184410.
92. J. E. McClellan, J. P. Murphy, J. J. Mulholland and R. A. Yost, Anal. Chem., 2002, 74, 402-412.
93. J. Laskin, R. P. W. Kong, T. Song and I. K. Chu, Int. J. Mass spectrom., 2012, 330–332, 295-301.
94. J. Laskin and Z. B. Yang, Int. J. Mass spectrom., 2011, 308, 275-280.
95. X.-N. Wu, H.-T. Zhao, J. Li, M. Schlangen and H. Schwarz, PCCP, 2014, 16, 26617-26623.
96. P. B. Armentrout and J. Simons, Journal of the American Chemical Society, 1992, 114, 8627-8633.
97. O. W. Wheeler, D. R. Carl, T. E. Hofstetter and P. B. Armentrout, J. Phys. Chem. A, 2015, 119, 3800-3815.
98. S. Chaudhary and J. D. Van Horn, J. Inorg. Biochem., 2007, 101, 329-335.
99. A. Figuerola, V. Tangoulis, J. Ribas, H. Hartl, I. Brüdgam, M. Maestro and C. Diaz, Inorganic Chemistry, 2007, 46, 11017-11024.
100. M. L. Baker, G. A. Timco, S. Piligkos, J. S. Mathieson, H. Mutka, F. Tuna, P. Kozłowski, M. Antkowiak, T. Guidi, T. Gupta, H. Rath, R. J. Woolfson, G. Kamieniarz, R. G. Pritchard, H. Weihe, L. Cronin, G. Rajaraman, D. Collison, E. J. L. McInnes and R. E. P. Winpenny, Proceedings of the National Academy of Sciences, 2012, 109, 19113-19118.
101. S. M. Gorun, G. C. Papaefthymiou, R. B. Frankel and S. J. Lippard, Journal of the American Chemical Society, 1987, 109, 4244-4255.
102. S. M. Gorun and S. J. Lippard, J. Am. Chem. Soc., 1985, 107, 4568-4570.
103. G. v. d. Laan and I. W. Kirkman, Journal of Physics: Condensed Matter, 1992, 4, 4189.
104. G. Cressey, C. M. B. Henderson and G. van der Laan, Phys. Chem. Miner., 1993, 20, 111-119.

7 Structural Characterization of Mononuclear and Binuclear Palladium Complexes in Isolation

Johannes Lang[a], Dagmar Hackenberger[b], Saeid Farsadpour[a], Werner R. Thiel[a], Lukas Gooßen[b] and Gereon Niedner-Schatteburg[a]

(a) Fachbereich Chemie and Forschungszentrum OPTIMAS,
Technische Universität Kaiserslautern,
67663 Kaiserslautern, Germany

(b) Lehrstuhl für Organische Chemie I
Ruhr-Universität Bochum
44801 Bochum

7.1 Preamble

The following chapter is a manuscript for publication. It is prepared for submission in the near future. Supplementary information is available in chapter 10.5.

Saeid Farsadpour of the group of Prof. Dr. W. R. Thiel synthesized the ligand (2-pyrrolidino-pyrimidine-4-yl-triphenylphosphane) which served to synthesize the mononuclear and binuclear precursor complexes of this study. Dagmar Hackenberger of the Group of Prof. Dr. L. Gooßen performed the synthesis of the precursor complexes. I conducted the measurements, data evaluations and quantum chemical calculations of this study and wrote this manuscript.

7.2 Abstract

This study elucidates the structures and fragmentation behaviors of mononuclear and binuclear palladium complexes as isolated cations in the gas phase. Both, the Pd^{II} centers in the mononuclear complexes and the two Pd^{I} centers in the binuclear complexes coordinate to a bidentate (2-pyrrolidino-pyrimidine-4-yl-triphenylphosphane) ligand. We present InfraRed Multiple-Photon Dissociation (IR-MPD) spectra in combination with quantum chemical calculations. They indicate intramolecular CH activation at the pyrimidine ring in the mononuclear case (via Pd-*P,C* binding). The binuclear Pd complexes exhibit Pd-*P,N* binding, which is modulated by a coordination of anions (Cl^- and OTf^-). The mononuclear complexes eliminate HCl and Pd^0 upon Collision Induced Dissociation (CID) indicating a metal to ligand charge transfer upon activation. In the binuclear case Pd-Pd bond breaking is the main fragmentation channel. The presented results help to gain a fundamental insight into the Pd complexes void any packing or solvent effects.

7.3 Introduction

Palladium complexes are widely employed as homogenous catalysts in C-C bond formation[1-5] reactions, which importance for organic chemistry was acknowledged by a Nobel Prize in 2010[6]. Additionally, the elucidation of cooperative effects between two or more metal (e.g. Pd) centers is an active field of research[7-10] as bimetallic systems for organic synthesis have gained interest throughout recent years[11, 12]. Optimizing the ligands complexing the palladium center(s) is crucial for an effective catalysis. In most catalytic reactions (e.g. Suzuki-Miyaura coupling[13]) the usage of chelating *P,N*-ligands seem to yield longer reaction times, harsher reaction condition and higher catalyst loading in comparison to Pd - phosphine catalysts[14-16]. On the other hand, palladium complexes with *P,N* ligands may undergo intramolecular CH activation which results in a Pd-*P,C* binding motif[17, 18]. Such catalysts exhibit very excellent catalytic properties. Subtle electronic and steric effects control the preference of Pd-*P,N* vs. Pd-*P,N* binding in such complexes.

In previous studies we investigated the synthesis and catalytic activities of mononoclear[19-23] and binuclear[7, 8, 24-26] Pd complexes. We found that steric demand and electronic effects due an amino group moiety of a [(2-aminopyrimidin-4-

yl)aryl]phosphine *P,N*-ligand enable intramolecular CH activation of the catalysts which results in better catalytic reactivity on mononuclear Pd complexes[27] as well as in Ru complexes[28, 29]. It is of paramount importance to characterize the three-dimensional structure of such complexes void of any packing or solvent effects in order to acquire a fundamental insight into their functionality. It is equally relevant to elucidate structural changes upon activation, which often precedes catalytic activity.

Electrospray Ionization[30-32] (ESI) enables mass spectrometric investigations of solvent-free charged complexes *in vacuo*. Tandem mass spectrometric (MS) based methods[33] help to acquire a fundamental insight into their intrinsic functionality by collisional and/or optical activation: Collision Induced Dissociation[34-37] (CID) provides information on the fragmentation routes while InfraRed Multiple Photon Dissociation (IR-MPD)[38-41] and yields access to structural information, both under cryogenic conditions[42-46] and at room temperature[47, 48]. Experimental results and dedicated quantum chemical calculations combine to obtain detailed insight into the structure and intrinsic properties of likely binding motifs.

In this study we investigate the binding motifs (e.g. Pd-*P,N* vs. Pd-*P,N* binding) and fragmentation behavior of mononuclear and binuclear Pd complexes as isolated cations in the gas phase. The precursor complexes $[Pd^{II}Cl_2]$ and $[Pd^{I}\text{-}Pd^{I}(CH_3CN)_2]^{2+}$ (cf. Scheme 1) are ligated by one and two (2-pyrrolidino-pyrimidine-4-yl-triphenylphosphane) ligands respectively. We generate various charged species *via* ESI, which will be in the focus of the present study.

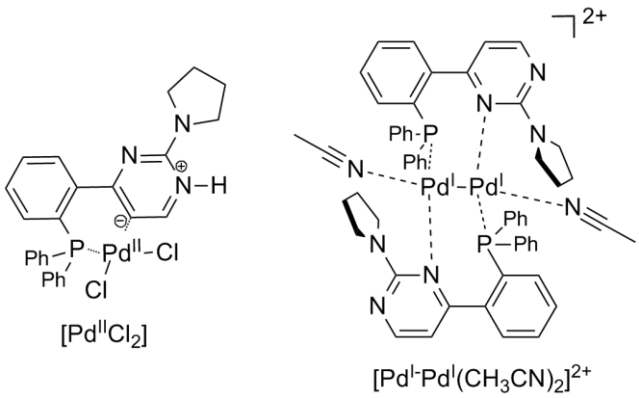

Scheme 1: Mononuclear[27] $[Pd^{II}Cl_2]$ and binuclear[49] $[Pd^{I}\text{-}Pd^{I}(CH_3CN)_2]^{2+}$ precursor palladium complexes. The square brackets indicate a short hand notation for one or two 2-pyrrolidino-pyrimidine-4-yl-triphenylphosphane ligands ($C_{26}H_{24}N_3P$).

The combination of CID and IR-MPD studies with DFT calculations provides unprecedented insight into the structure and fragmentation behavior of these homogeneous palladium catalysts. We highlight the structural changes upon cationization, fragmentation and adduct formation with Cl^- and triflat anions.

7.4 Experimental and Computational Methods

ESI-MS and CID measurements were performed by a Paul type quadrupole ion trap instrument (Bruker Esquire 3000plus). The ion source (Apollo II) was set to positive electrospray ionization mode. Scan speed was 13000 m/z / s in standard resolution scan mode (0.3 FWHM / m/z) and the scan range was 15 to 1200 m/z. Mass spectra were accumulated for at least two minutes. MS^n spectra were accumulated for at least twenty seconds. Sample solutions of $[Pd^{II}Cl_2]$ (in acetonitrile/dichloromethane = 1/1) and $[Pd^{I}Pd^{I}(CH_3CN)_2]^{2+}$ (in a acetonitrile) at concentrations of 1 x 10^{-5} mol/l were continuously infused into the ESI chamber by a syringe pump at a flow rate of 2 µL min^{-1}. The Pd precursor complexes were prepared as described in the literature[27, 49]. Nitrogen was used as drying gas with a flow rate of 3.0 L min^{-1} at 210 °C. The solutions were sprayed at a nebulizer pressure of 280 mbar (4 psi) and the electrospray needle was held at 4.5 kV. The

Collision induced dissociation (CID) appearance curves were recorded with varying excitation amplitudes (0.0 V to 1.5 V), which determine the internal energy scale of the mass spectrometer (E_{LAB} in V). Relative abundances were calculated according to:

$$I_{tot}^{fr}.(E_{lab}) = \left(\frac{\sum_i I_i^{fr}(E_{lab})}{\sum_i I_i^{fr}(E_{lab}) + \sum_i I_i^{p}(E_{lab})}\right) \quad (1)$$

where I_i^{fr} = intensity of the fragment ions and I_i^{p} = intensity of the parent ions. Center of mass transferred fragmentation amplitudes (E_{COM}) were calculated from internal amplitudes by:

$$E_{com} = \left(\frac{m_{He}}{m_{He} + m_{ion}}\right) \cdot E_{lab} \quad (2)$$

where m_{ion} stands for the isotopically averaged mass of the molecular ion. Note, that the current application of the CID technique by RF excitation in presence of multiple collisions results in a so called “slow multi collision heating” mode of operation[50, 51].

Fragmentation amplitude dependent CID spectra were modelled and fitted by sigmoidal functions of the type

$$I_{fit}^{fr}(E_{com}). = \left(\frac{1}{1 + e^{(E_{com}^{50} - E_{com})\,B}}\right) \quad (3)$$

using a least-squares criterion. The E_{COM}^{50} fit parameter is the amplitude at which the sigmoid function is at half maximum value, whereas B describes the rise of the sigmoid curve. Due to the correlation of fragmentation amplitude and appearance energy, it is feasible to assume, that the appearance curves can be associated to the relative stability of the isolated palladium complexes[52-55]. The according plots are available in the Supplementary Information (cf. Fig. S2 and S3).

InfraRed Multiple Photon Dissociation (IR-MPD) measurements were performed using a modified Paul type quadrupole ion trap instrument (AmaZon SL, Bruker Daltonics). The ion source was set to positive electrospray ionization mode. Scan speed was 32 500 m/z / s (0.3 FWHM / m/z) with a scan range of 70 to 1200 m/z. The sample solutions were continuously infused into the ESI chamber by a syringe pump at a flow rate of 2 µL min^{-1}. Nitrogen was used as drying gas with a flow rate of 3.0 L min^{-1} at 210 °C. The solutions were sprayed at a nebulizer pressure of 280 mbar (4 psi) and the electrospray needle was held at 4.5 kV.

A KTP/KTA (KTP = potassium titanyl phosphate; KTA = potassium titanyl arsenate) optical parametric oscillator/amplifier (OPO/A, LaserVision) system pumped by a pulsed 10 Hz injection seeded Nd^{3+}:YAG laser (PL8000, Continuum) was used as a source of tunable IR radiation (δn = 0.9 cm^{-1}, δt = 7 ns) for recording vibrational spectra. The OPA idler wave (≤ 10 mJ per pulse) was used to record spectra within 2600 - 3900 cm^{-1}. The difference frequency (DF) between the OPA signal and idler waves generated in a $AgGaSe_2$ crystal (≤ 2 mJ per pulse) was applied in the range of 1200 – 2100 cm^{-1}. After passing through the vacuum chamber the IR beam was directed onto a power meter sensor. The idler beam was focused by a 50 cm CaF_2 lens. The DF radiation was focused tighter, by a 90° off-axis parabolic silver mirror with an effective focal length of 15 cm. The IR spectra were recorded as ion chromatograms while continuously scanning the IR wavelength. An experimental IR-MPD spectrum arises

from a plot of the fragmentation efficiency as a function of laser frequency (ν). The IR-MPD yield $Y\ (\nu)$ is defined as:

$$Y(\nu) = \left(\frac{\sum_i I_i^{fr}(\nu)}{\sum_i I_i^{fr}(\nu) + \sum_i I_i^{p}(\nu)} \right) \tag{4}$$

The IR frequency was calibrated using a wave meter (821B-NIR, Bristol instruments). Laser power curves were recorded in parallel to the IR-MPD spectra through digitizing the analog output of the laser power meter by an ample ADC input of the AmaZon SL mass spectrometer electronics. Despite the online IR power measurement the recorded spectra were not normalized due to the intrinsically nonlinear power dependence of IR-MPD fragmentation efficiencies.

Optimized minimum energy structures and linear IR absorption spectra were calculated at the B3LYP[56, 57] level of theory using cc-pVDZ basis sets[58] (C, H, N, O, P), and Stuttgart RSC 1997[59] effective core potential (Pd) basis sets, respectively, as implemented in the Gaussian 09 program package[60]. Standard convergence criteria were applied. Full geometry optimization of all nuclear coordinates yields multiple locally stable minimum structures. The lowest energy structure is assumed to represent the most stable isomer. Harmonic vibrational frequencies were scaled with 0.965 to account for prevailing inharmonicity. We discuss triplet states structures of the binuclear complex. The triplet state structures of the mononuclear complexes are at least 200 kJ/mol less stable and thus of no relevance in the present context.

7.5 Results and Discussion

7.5.1 Electrospray Ionization Mass Spectrometry (ESI-MS) and Collision Induced Dissociation (CID)

Assignment of recorded mass peaks to molecular species of interest: Upon spraying the above described sample solutions and recording cationic mass spectra, we observe a series of isotopic peaks at m/z = 514 and 552 in the case of the $[Pd^{II}Cl_2]$ solution (cf. Fig. 1a) and m/z = 516, 1067 and 1181 in the case of the $[Pd^{I}\text{-}Pd^{I}(CH_3CN)_2]^{2+}$ solution (cf. Fig. 1b). The recorded isotopic patterns match convincingly with simulated isotopic patterns of $[Pd^{II}Cl_1]^+$, $[Pd^{II}]^+$, $[Pd^{I}\text{-}Pd^{I}]^{2+}$, $[Pd^{I}\text{-}Pd^{I}Cl]^+$ and $[Pd^{I}\text{-}Pd^{I}OTf]^+$ (cf. insets in Fig. 1 and Table 1).

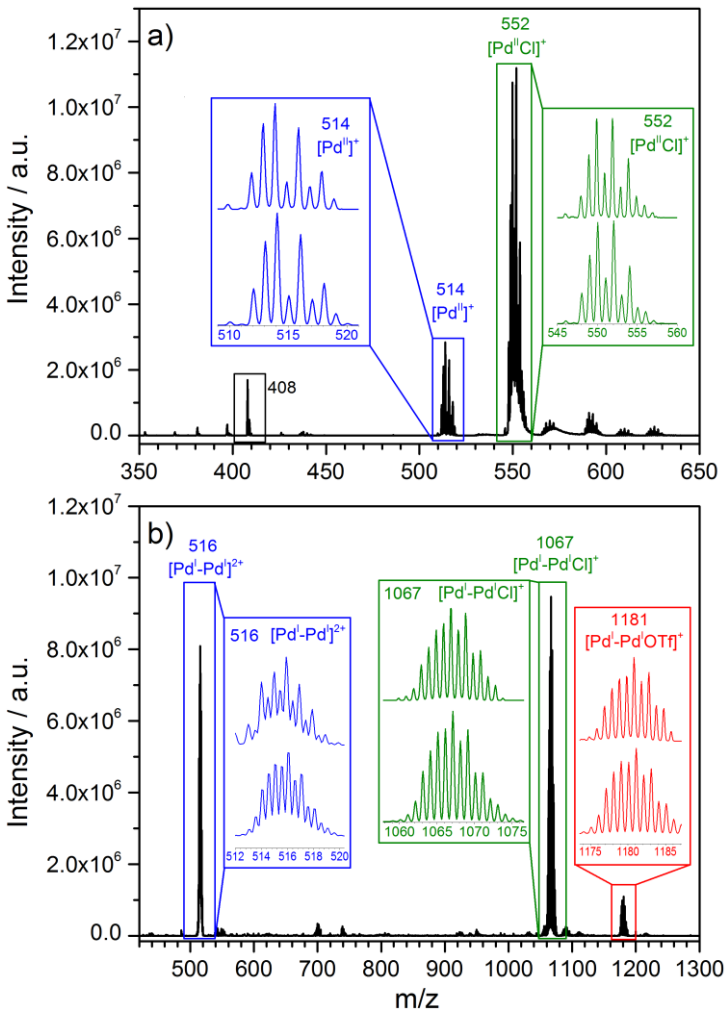

Figure 1: a) Cationic mass spectrum of a $[Pd^{II}Cl_2]$ in acetonitrile/dichloromethane = 1/1 solution. **b)** Cationic mass spectrum of a $[Pd^{I}\text{-}Pd^{I}(CH_3CN)_2]^{2+}$ in acetonitrile solution. Insets: Experimental and simulated isotopic pattern of $[Pd^{II}Cl_1]^+$, $[Pd^{II}]^+$, $[Pd^{I}\text{-}Pd^{I}]^{2+}$, $[Pd^{I}\text{-}Pd^{I}Cl]^+$ and $[Pd^{I}\text{-}Pd^{I}OTf]^+$ The mass labelling refers to the most intensive peak of the isotope distributions.

The mononuclear precursor complex $[Pd^{II}Cl_2]$ is neutral. Accordingly, we observe cationic species via elimination of a chlorido ligand (yielding $[Pd^{II}Cl_1]^+$ at m/z = 552) and Cl^-+HCl elimination (yielding $[Pd^{II}]^+$ at m/z = 514).

The binuclear precursor complex $[Pd^I\text{-}Pd^I(CH_3CN)_2]^{2+}$ is intrinsically doubly charged. However, we do not observe the species with its two axial coordinating acetonitrile ligands. Instead we detect the under-coordinated species $[Pd^I\text{-}Pd^I]^{2+}$. Additionally we detect mono cationic species $[Pd^I\text{-}Pd^ICl]^+$ and $[Pd^I\text{-}Pd^IOTf]^+$ assuming a reaction of $[Pd^I\text{-}Pd^I]^{2+}$ with Cl^- and OTf^- contaminations in solution or during the electrospray process.

Table 1: Compilation of ESI-MS data on the palladium complexes of interest and of the corresponding fragments after collision induced dissociation (CID). The indicated mass labels refer to the most abundant isotope peaks. We provide for CID mass spectra via the supplement (cf. Fig. S1).

Species	Fragment	Loss	m/z	Assigned formula
$[Pd^{II}Cl_1]^+$	-	-	552	$(C_{26}H_{24}N_3PPdCl)^+$
	$[Pd^{II}]^+$	HCl	514	$(C_{26}H_{23}N_3PPd)^+$
	$(C_{26}H_{23}N_3P)^+$	HCl + Pd	408	$(C_{26}H_{23}N_3P)^+$
$[Pd^{II}]^+$	-	-	514	$(C_{26}H_{23}N_3PPd)^+$
	$(C_{26}H_{23}N_3P)^+$	Pd	408	$(C_{26}H_{23}N_3P)^+$
$[Pd^I\text{-}Pd^I]^{2+}$	-	-	516	$(C_{52}H_{48}N_6P_2Pd_2)^{2+}$
	$(C_{38}H_{34}N_3P_2Pd)^+$	$C_{14}H_{14}N_3Pd$	700	$(C_{38}H_{34}N_3P_2Pd)^+$
	$(C_{32}H_{26}N_3P_2Pd)^+$	$C_{20}H_{22}N_3Pd$	621	$(C_{32}H_{26}N_3P_2Pd)^+$
	$(C_{20}H_{16}N_3PPd)^+$	$C_{32}H_{32}N_3PPd$	435	$(C_{20}H_{16}N_3PPd)^+$
	$(C_{26}H_{23}N_3P)^+$	$C_{26}H_{25}N_3PPd_2$	408	$(C_{26}H_{23}N_3P)^+$
	$(C_{20}H_{17}N_3P)^+$	$C_{32}H_{31}N_3PPd_2$	332	$(C_{20}H_{17}N_3P)^+$
$[Pd^I\text{-}Pd^ICl]^+$	-	-	1067	$(C_{52}H_{48}N_6P_2Pd_2Cl)^+$
	$(C_{46}H_{42}N_6P_2Pd_2Cl)^+$	C_6H_6 (Ph)	990	$(C_{46}H_{42}N_6P_2Pd_2Cl)^+$
	$(C_{38}H_{34}N_3P_2Pd)^+$	$C_{14}H_{14}N_3PdCl$	700	$(C_{38}H_{34}N_3P_2Pd)^+$
	$[Pd^{II}]^+$	$C_{26}H_{25}N_3PPdCl$	514	$(C_{26}H_{23}N_3PPd)^+$
	$(C_{20}H_{16}N_3PPd)^+$	$C_{32}H_{32}N_3PPdCl$	435	$(C_{20}H_{16}N_3PPd)^+$
$[Pd^I\text{-}Pd^IOTf]^+$	-	-	1181	$(C_{52}H_{48}N_6P_2Pd_2CF_3SO_3)^+$
	$[Pd^I\text{-}Pd^I]^+$	CF_3SO_3H	1030	$(C_{52}H_{47}N_6P_2Pd_2)^+$
	$(C_{38}H_{34}N_3P_2Pd)^+$	$C_{14}H_{14}N_3PdCF_3SO_3H$	700	$(C_{38}H_{34}N_3P_2Pd)^+$
	$[Pd^{II}]^+$	$C_{26}H_{25}N_3PPdClCF_3SO_3H$	514	$(C_{26}H_{23}N_3PPd)^+$

CID fragmentation routes and breakdown curves: Isolation of the detected palladium complexes and subsequent fragmentation with increasing CID amplitudes reveals so-called breakdown curves of the isolated complexes and appearance curves of the associated fragments (cf. Table 1 and Fig. 2).

The mononuclear complex $[Pd^{II}Cl_1]^+$ exhibits two fragmentation channels: loss of HCl and loss of HCl+Pd. Sole HCl loss (detected via the $[Pd^{II}]^+$ fragment peak at m/z = 514) is the predominant fragmentation channel emerging at a CID amplitude of 0.002 a.u. Note that the same $[Pd^{II}]^+$ peak also appears without excitation (cf. Fig. 1) in the mass spectrum. This indicates a decomposition of $[Pd^{II}Cl_1]^+$ in solution and/or the electrospray process. Amplitudes of 0.006 a.u and higher lead to secondary fragmentation of $[Pd^{II}]^+$ (Pd^0 loss detected via the $(C_{26}H_{23}N_3P)^+$ fragment peak at m/z = 408). Accordingly fragmenting isolated $[Pd^{II}]^+$ directly reveals sole Pd^0 loss emerging at a CID amplitude of 0.007 a.u. This implies a metal to ligand charge transfer.

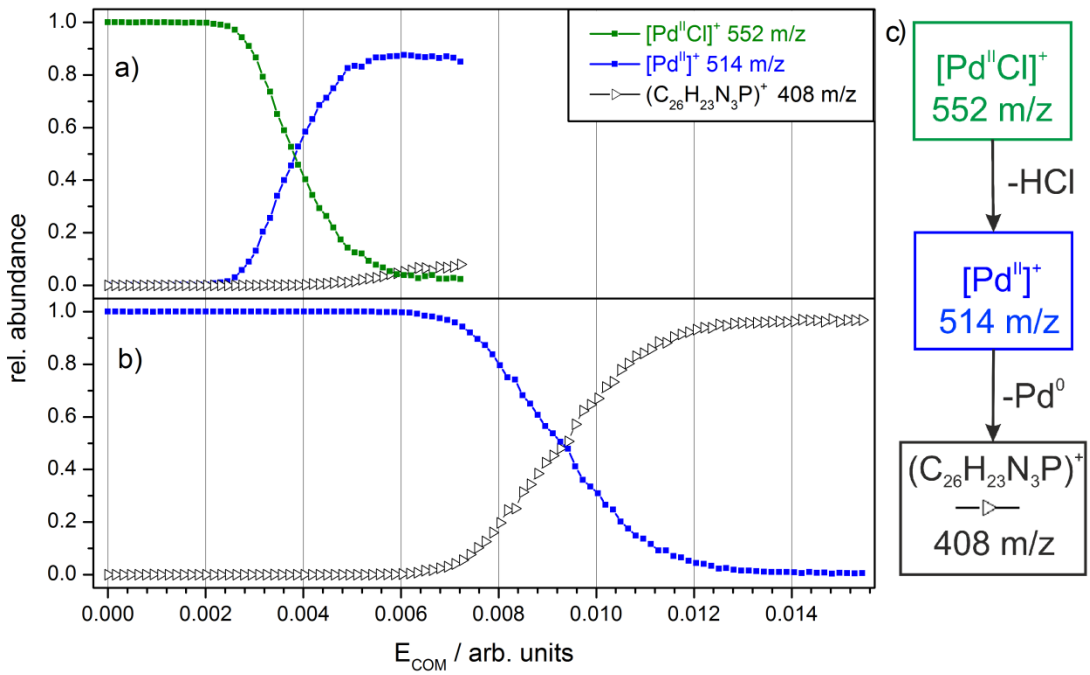

Figure 2: a,b) CID breakdown curves of $[Pd^{II}Cl_1]^+$ and $[Pd^{II}]^+$ and appearance curves of their associated fragments. **c)** Schematic fragmentation route of $[Pd^{II}Cl_1]^+$.

The binuclear palladium complexes $[Pd^{I}\text{-}Pd^{I}]^{2+}$, $[Pd^{I}\text{-}Pd^{I}Cl]^+$ and $[Pd^{I}\text{-}Pd^{I}OTf]^+$ exhibit intricate and non-obvious fragmentation routes (cf. Fig. 3 and Scheme 2). We give an assignment of all fragment peaks to molecular formulae (cf. Scheme 2) thereby gaining a

broad understanding of the fragmentation routes. However, the exact nature of the fragmentation process as well as molecular structures of the fragments remain elusive.

$[Pd^{I}\text{-}Pd^{I}OTf]^{+}$ and $[Pd^{I}\text{-}Pd^{I}Cl]^{+}$ exhibit in total four fragmentation channels (cf. Fig. 3 a/b and Scheme 2 a/b). The fragments $(C_{38}H_{34}N_3P_2Pd)^{+}$ and $[Pd^{II}]^{+}$ at m/z = 700 and 514 dominate the CID mass spectra in both cases. $(C_{38}H_{34}N_3P_2Pd)^{+}$ indicates the cleavage of Cl/OTf, Pd and a partial decomposition of one ligand. The $[Pd^{II}]^{+}$ fragment indicates a disproportion of the palladium centers (Pd^{I}-Pd^{I} to Pd^{II} and Pd^{0}) upon CID activation. We assign $[Pd^{II}]^{+}$ to the loss of one neutral ligand, Pd^{0} and HCl or HOTf respectively. A minor, but exclusive fragmentation channel of $[Pd^{I}\text{-}Pd^{I}OTf]^{+}$ is the loss of neutral HOTf as detected by the mono cationic binuclear $[Pd^{I}\text{-}Pd^{I}]^{+}$ complex at m/z = 1030 (with one ligand being deprotonated).

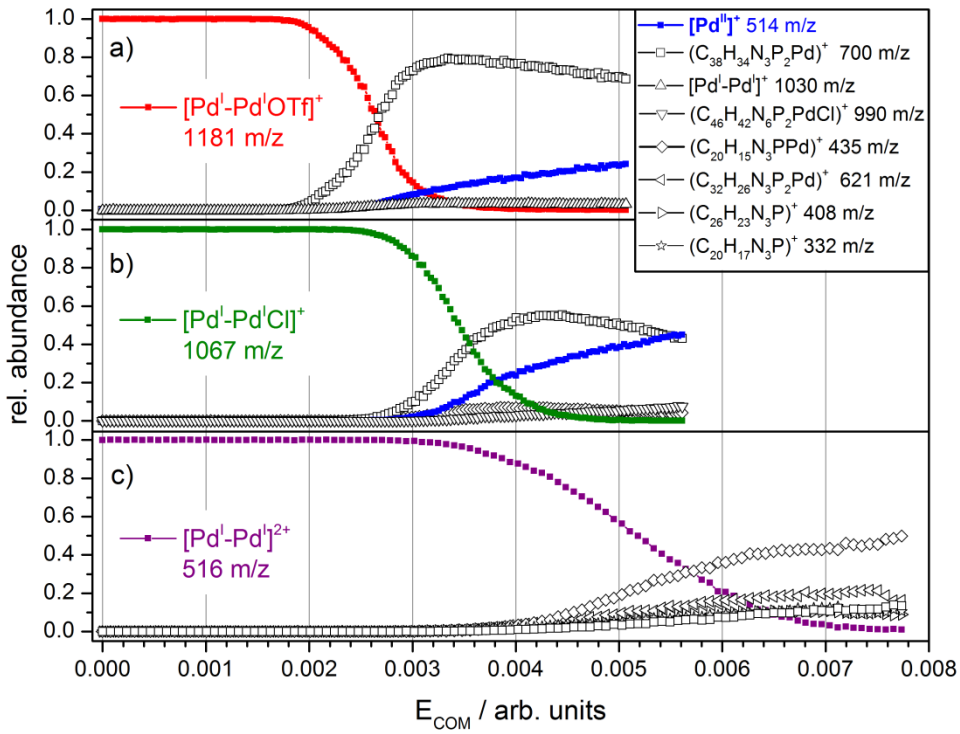

Figure 3: CID breakdown curves of $[Pd^{I}\text{-}Pd^{I}OTf]^{+}$ **(a)**, $[Pd^{I}\text{-}Pd^{I}Cl]^{+}$ **(b)** and $[Pd^{I}\text{-}Pd^{I}]^{2+}$ **(c)** as well as appearance curves of the associated fragments.

The doubly charged $[Pd^{I}\text{-}Pd^{I}]^{2+}$ reveals an intricate fragmentation behavior (cf. Fig. 3c and Scheme 2c) exhibiting only mono cationic fragment species. This indicates the breaking of the Pd-Pd bond upon CID activation. In contrast to $[Pd^{I}\text{-}Pd^{I}OTf]^{+}$ and $[Pd^{I}\text{-}Pd^{I}Cl]^{+}$ we are not able to detect $[Pd^{II}]^{+}$ (m/z = 514) as fragment species, because the isotopic pattern of $[Pd^{II}]^{+}$ overlaps with $[Pd^{I}\text{-}Pd^{I}]^{2+}$ (m/z = 516). It fragments directly after formation. Accordingly we observe a multitude fragment peaks at m/z = 332, 408

and 435. We already identified the fragment at m/z = 408 ($(C_{26}H_{23}N_3P)^+$) in the fragmentation of isolated $[Pd^{II}]^+$ (see above).

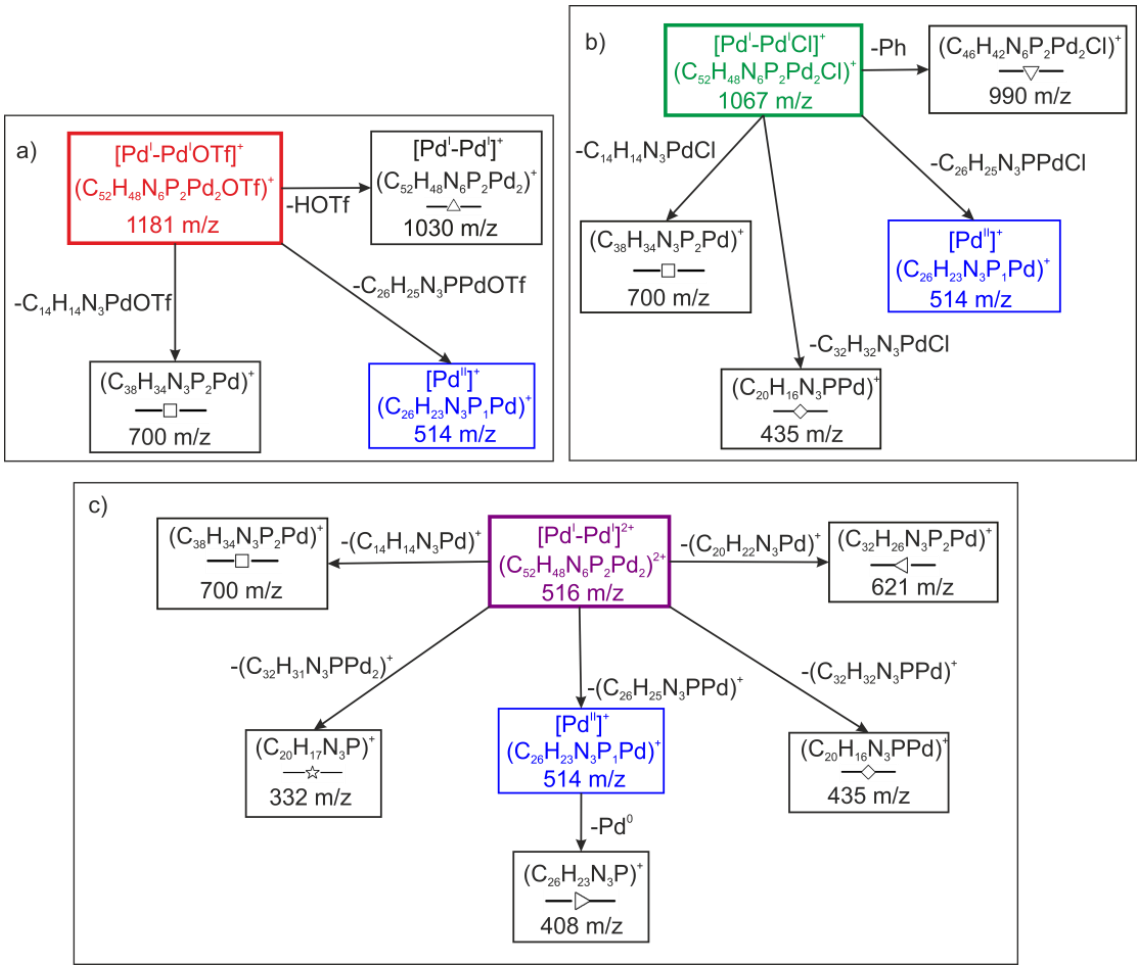

Scheme 2: Fragmentation routes of $[Pd^{I}\text{-}Pd^{I}OTf]^+$ **(a)**, $[Pd^{I}\text{-}Pd^{I}Cl]^+$ **(b)** and $[Pd^{I}\text{-}Pd^{I}]^{2+}$ **(c).**

7.5.2 InfraRed Multiple Photon Dissociation (IRMPD) and Density Functional Theory (DFT)

Spectral features and vibrational analysis of [Pd^{II}Cl]$^+$ and [Pd^{II}]$^+$: We have recorded IR-MPD spectra of the mononuclear palladium complexes and we have conducted DFT simulations to obtain their linear IR absorption spectra. The IR-MPD spectrum of [Pd^{II}Cl]$^+$ (cf. Fig 4a, green curve) exhibits a multitude of bands in the investigated spectral thus providing valuable information to compare with our DFT predictions. The DFT calculations reveal optimized minimum structures $\boldsymbol{P,N,N}_{[Pd^{II}Cl]^+}$ and $\boldsymbol{P,C}_{[Pd^{II}Cl]^+}$ as depicted in Fig. 4b and 4c. We assign the experimental band at 3437 cm^{-1} to the NH stretching vibration band ($\tilde{\nu}$(NH)) of $\boldsymbol{P,C}_{[Pd^{II}Cl]^+}$. This band provides spectroscopic evidence for a Pd-*P,C* binding motif via CH activation at the pyrimidine ring (forming a NH group). This agrees with our previous findings on the precursor complex [Pd^{II}Cl$_2$] in the condensed phase[27].

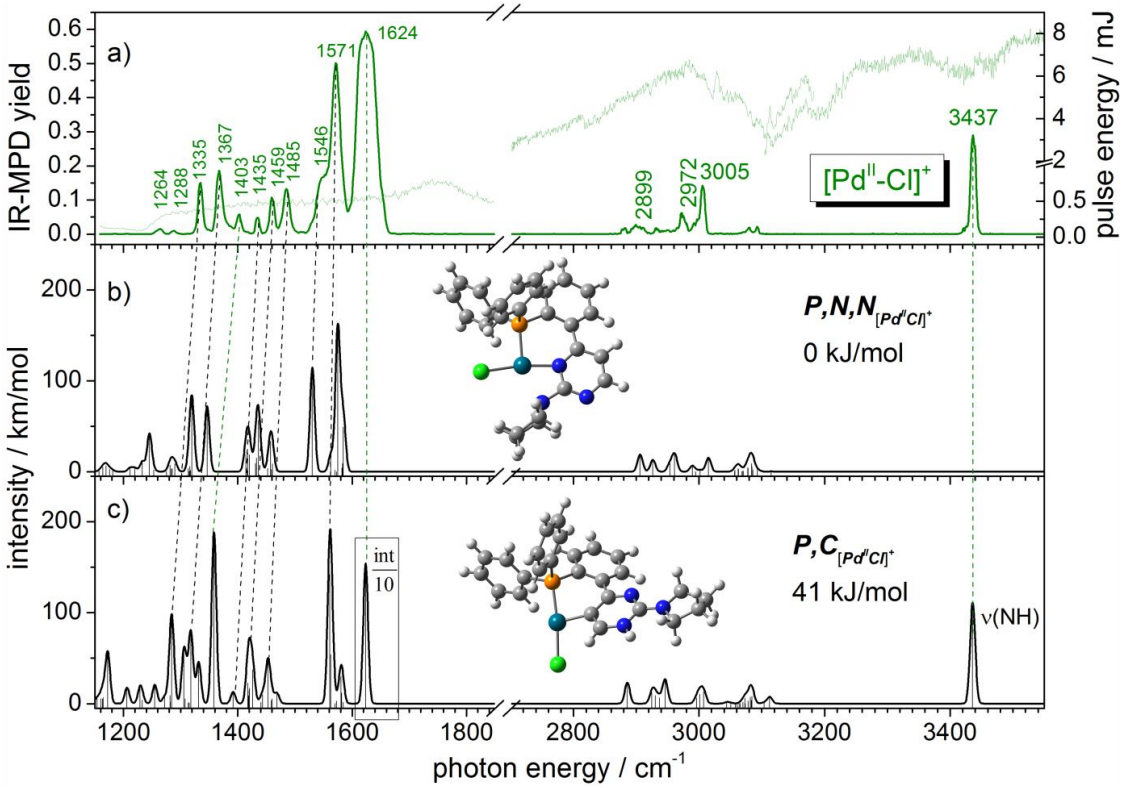

Figure 4: a) IR-MPD spectrum of [Pd^{II}Cl$_1$]$^+$ in the spectral range of 1150 - 3600 cm^{-1} including the power curve of the IR laser. **b,c)** Calculated IR absorption spectra of geometry optimized isomers of [Pd^{II}Cl$_1$]$^+$. The insets show associated geometry optimized structures. The calculations were performed at the B3LYP/cc-pVDZ (H, C, Cl, N, O) and Stuttgart 1997 ECP (Pd) level of theory with a multiplicity of 1. The harmonic frequencies are scaled with 0.965.

$\boldsymbol{P,N,N}_{[\boldsymbol{Pd^{II}Cl}]^+}$ exhibts a Pd-*P,N* binding motif and no NH stretching vibration band and is 41 kJ/mol more stable than $\boldsymbol{P,C}_{[\boldsymbol{Pd^{II}Cl}]^+}$. The Pd^{II} center interacts with the nitrogen atom of the pyrrolidino ring and thereby gains a stabilizing (distorted) square planar coordination geometry. The IR-MPD spectrum of $[Pd^{II}Cl]^+$ in the fingerprint region (below 1700 cm^{-1}) reveals in total eleven bands. We assign the broad IR-MPD band (FWHM = 38 cm^{-1}) at 1624 cm^{-1} exclusively to $\boldsymbol{P,C}_{[\boldsymbol{Pd^{II}Cl}]^+}$ since it coincides with the very strong NH bending mode. We provide an illustrative visualization of the calculated displacement vectors of this mode in Fig. S4a. Naturally $\boldsymbol{P,N,N}_{[\boldsymbol{Pd^{II}Cl}]^+}$ lacks such NH modes. Instead we find that the experimental shoulder at 1546 cm^{-1} coincides with a CH bending mode exclusive to $\boldsymbol{P,N}_{[\boldsymbol{Pd^{II}Cl}]^+}$ (cf. Fig. S4b for displacement vectors). All other IR-MPD bands can be assigned to of both isomers. Thus both isomers, $\boldsymbol{P,N,N}_{[\boldsymbol{Pd^{II}Cl}]^+}$ and $\boldsymbol{P,C}_{[\boldsymbol{Pd^{II}Cl}]^+}$ contribute to the IR-MPD spectrum of $[Pd^{II}Cl]^+$.

The IR-MPD spectrum of $[Pd^{II}]^+$ (cf. Fig 5a, blue curve) exhibits fewer bands in the investigated spectral region than $[Pd^{II}Cl]^+$. However, we can extract valuable structural information by comparing with our DFT predictions. The DFT calculations reveal optimized minimum structures $\boldsymbol{P,N,C}_{[\boldsymbol{Pd^{II}}]^+}$ and $\boldsymbol{P,C}_{[\boldsymbol{Pd^{II}}]^+}$ as depicted in Fig. 5b and 5c. The IR-MPD spectrum of $[Pd^{II}]^+$ exhibits no NH stretching vibration band indicating that the NH group of $[Pd^{II}Cl_1]^+$ deprotonates upon HCl elimination. However, isomer $\boldsymbol{P,N}_{[\boldsymbol{Pd^{II}Cl}]^+}$ of $[Pd^{II}Cl_1]^+$ exhibits no NH groups and thus demands at least one additional deprotonation site for the HCl elimination. Isomers $\boldsymbol{P,N,C}_{[\boldsymbol{Pd^{II}}]^+}$ and $\boldsymbol{P,C}_{[\boldsymbol{Pd^{II}}]^+}$differ by deprotonation site and the Pd binding motif. $\boldsymbol{P,C}_{[\boldsymbol{Pd^{II}}]^+}$ is structurally analogous to $\boldsymbol{P,C}_{[\boldsymbol{Pd^{II}Cl}]^+}$, with a deprotonated NH group (HCl elimination). $\boldsymbol{P,N,C}_{[\boldsymbol{Pd^{II}}]^+}$ is 33 kJ/mol more stable than $\boldsymbol{P,C}_{[\boldsymbol{Pd^{II}}]^+}$ and exhibits Pd-*P,N,C* coordination: Deprotonation of the closest CH_2 group of the pyrrolidino ring to the Pd center is the most favorable deprotonation site. The resulting nucleophilic carbanion coordinates to the Pd^{II} center, which stabilizes the system. Deprotonation at the pyrimidine ring results in very unstable structures (cf. Fig. S6).

The calculated absorption spectrum of $\boldsymbol{P,C}_{[\boldsymbol{Pd^{II}}]^+}$ matches the recorded IR-MPD spectrum. The broad IR-MPD band (FWHM = 50 cm^{-1}) at 1567 cm^{-1} coincides with a very strong CN stretching mode (displacement vectors cf. Fig. S5) and the weak bands at

1460 and 1484 cm^{-1} coincide with -C=N- skeletal vibration modes. We assign the bands at 2898, 2970 and 2995 cm^{-1} to CH stretching vibration modes of $\boldsymbol{P,C}_{[Pd^{II}]^+}$. In contrast, the spectrum of $\boldsymbol{P,N,C}_{[Pd^{II}]^+}$ provides less agreement with the experimental spectrum. We therefore conclude, that the energetically higher isomer $\boldsymbol{P,C}_{[Pd^{II}]^+}$ prevails. The activation barrier for deprotonation at the pyrrolidino ring might be to to high to form $\boldsymbol{P,N,C}_{[Pd^{II}]^+}$ from $\boldsymbol{P,N,N}_{[Pd^{II}Cl]^+}$. Instead $\boldsymbol{P,N,N}_{[Pd^{II}Cl]^+}$ would isomerize to form $\boldsymbol{P,C}_{[Pd^{II}Cl]^+}$ which efficiently deprotonates the NH group to form $\boldsymbol{P,C}_{[Pd^{II}]^+}$ upon activation.

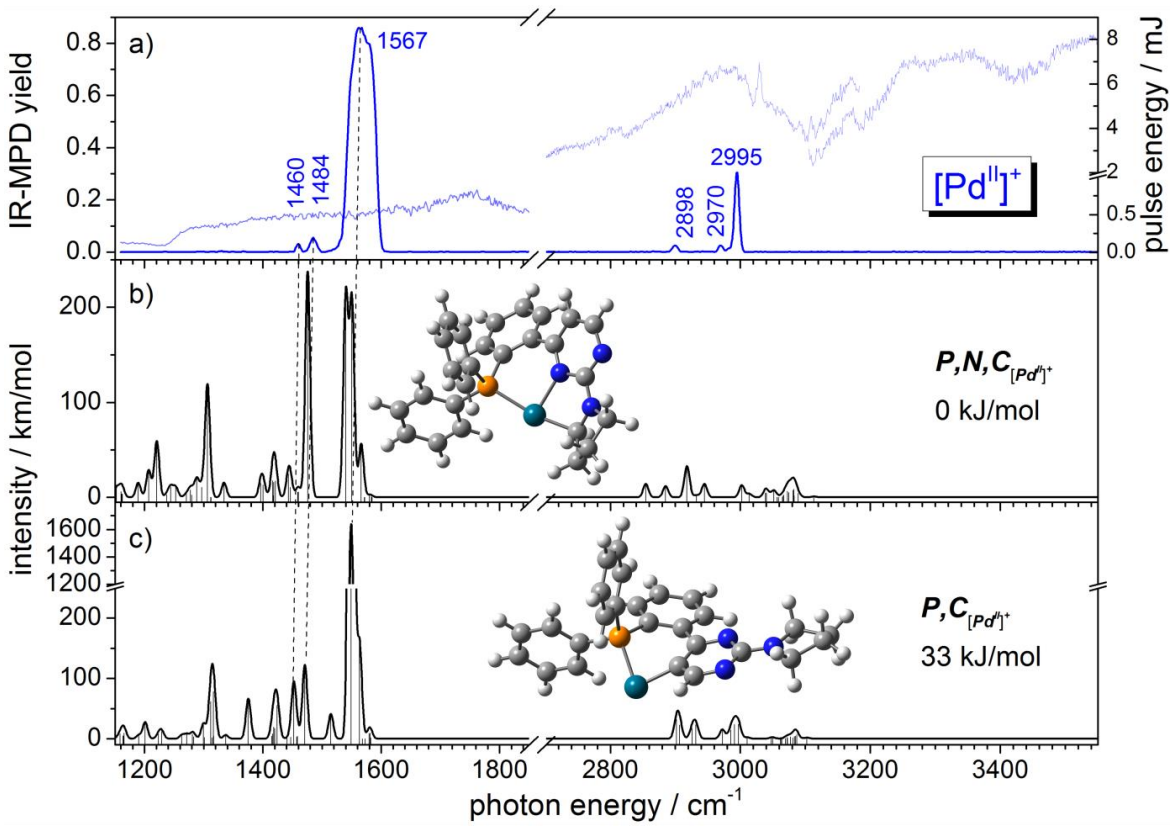

Figure 5: a) IR-MPD spectrum of $[Pd^{II}]^+$ in the spectral range of 1150 - 3600 cm^{-1} including the power curve of the IR laser. **b,c)** Calculated IR absorption spectra of geometry optimized isomers of $[Pd^{II}]^+$. The insets show associated geometry optimized structures. The calculations were performed at the B3LYP/cc-pVDZ (H, C, Cl, N, O) and Stuttgart 1997 ECP (Pd) level of theory with a multiplicity of 1. The harmonic frequencies are scaled with 0.965.

Spectral features and vibrational analysis of $[Pd^{I}\text{-}Pd^{I}]^{2+}$, $[Pd^{I}\text{-}Pd^{I}Cl]^{+}$ and $[Pd^{I}\text{-}Pd^{I}OTf]^{+}$: The IR-MPD spectra of the binuclear palladium complexes (cf. Fig. 6) exhibit remarkable sensitivity towards the coordination of Cl^- and OTf to $[Pd^{I}\text{-}Pd^{I}]^{2+}$. Bare $[Pd^{I}\text{-}Pd^{I}]^{2+}$ exhibits three peaks in the fingerprint region. The main peaks at

1560 and 1588 cm^{-1} overlap partially but are discernible. We observe and three sharp bands in the CH stretching vibration region (2861, 2891 and 2887 cm^{-1}). Coordination of Cl$^-$ results in a splitting of the fingerprint bands. [Pd^I-Pd^{I}Cl]$^+$ exhibits two bands: One band at 1552 cm^{-1} (with an shoulder on the low energy flank) and a band at 1590 cm^{-1}. In this case the bands are clearly separated in the IR-MPD spectrum. The CH stretching vibration bands of [Pd^I-Pd^{I}Cl]$^+$ are redshifted in relation to [Pd^I-Pd^I]$^{2+}$. We observe an additional band at 3065 cm^{-1}. Coordination of OTf$^-$ has the opposite effect: The bands in the fingerprint region shift together. We observe one broad band (at 1569 cm^{-1}), which exhibits shoulders on both sides of the band (1532 and 1588 cm^{-1}). The CH stretching vibration bands shift to higher frequencies in relation to [Pd^I-Pd^{I}Cl]$^+$. Note, that we do not observe any NH stretching vibration bands in all cases. This indicates prevalent Pd-*P,N;* Pd-*P,N* binding.

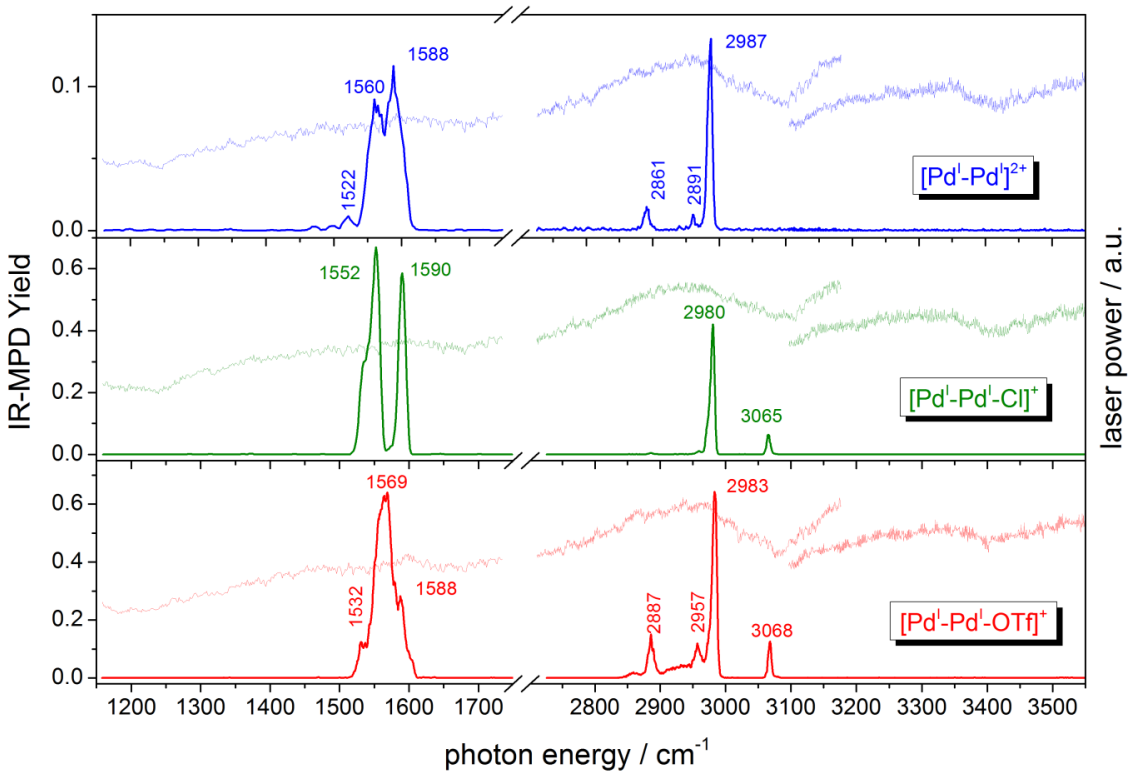

Figure 6: IR-MPD spectra of [Pd^I-Pd^I]$^{2+}$, [Pd^I-Pd^{I}Cl]$^+$ and [Pd^I-Pd^{I}OTf]$^+$ in the spectral range of 1150 - 3600 cm^{-1} including the power curve of the IR laser.

We have conducted DFT simulations of [Pd^I-Pd^I]$^{2+}$, [Pd^I-Pd^{I}Cl]$^+$ and [Pd^I-Pd^{I}OTf]$^+$ to obtain their linear IR absorption spectra and compare them with the IR-MPD spectra. The DFT calculations of [Pd^I-Pd^I]$^{2+}$ reveal optimized minimum structures as depicted in Fig. 7b-d.

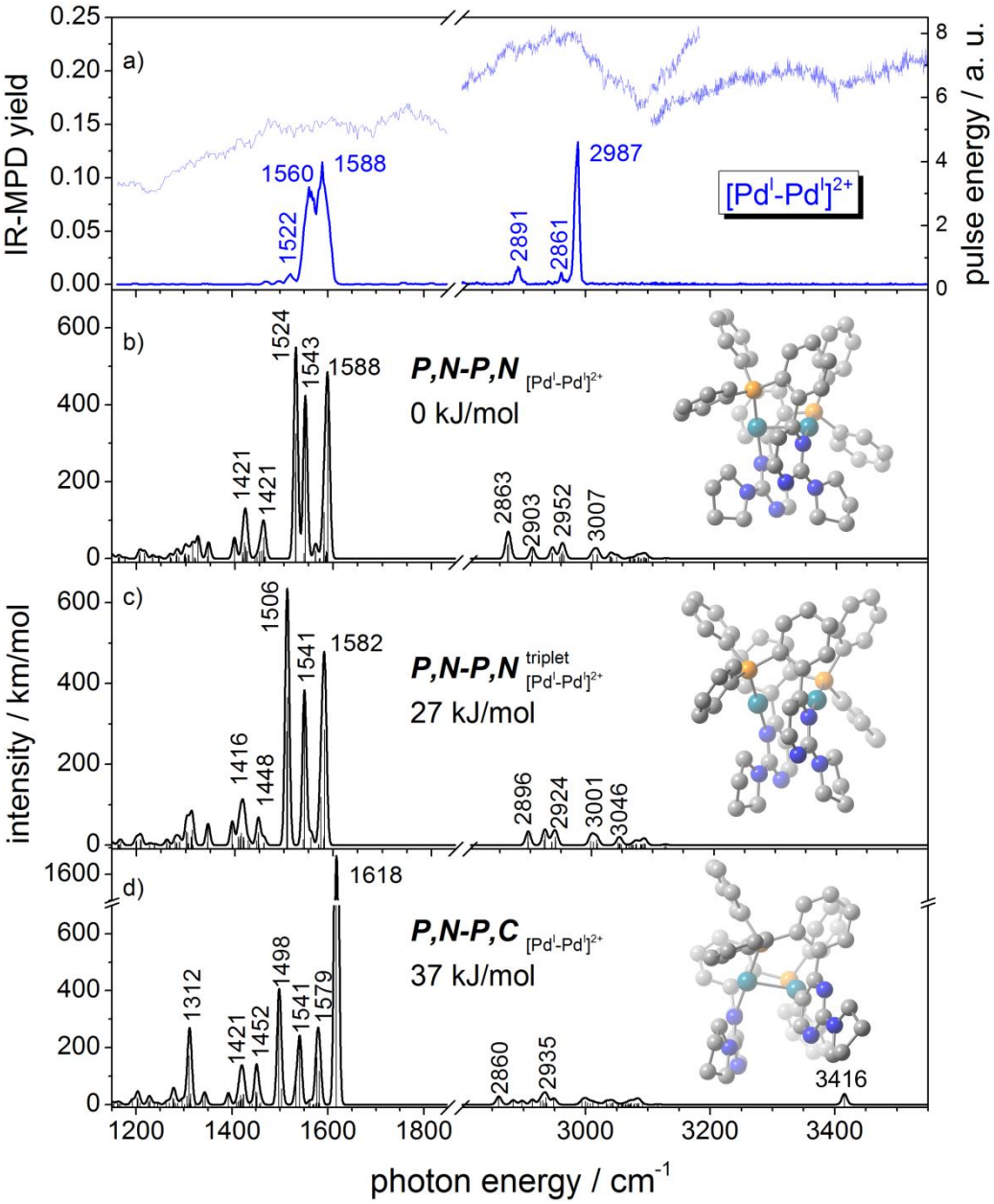

Figure 7: a) IR-MPD spectra of $[Pd^I\text{-}Pd^I]^{2+}$ in the spectral range of 1150 - 3600 cm^{-1} including the power curve of the IR laser. **b-c)** Calculated IR absorption spectra of geometry optimized isomers of $[Pd^I\text{-}Pd^I]^{2+}$. The insets show associated geometry optimized structures. The calculations were performed at the B3LYP/cc-pVDZ (H, C, N, O) and Stuttgart 1997 ECP (Pd) level of theory. The harmonic frequencies are scaled with 0.965.

We identify $\boldsymbol{P,N-P,N}_{[Pd^I-Pd^I]^{2+}}$ (cf. Fig. 7b) as the most stable isomer. It exhibits a Pd-*P,N*; Pd-*P,N* binding motif in a singlet electronic state. Its linear absorption spectrum agrees with the IR-MPD spectrum reasonably well. We assign the IR-MPD bands of $[Pd^I\text{-}Pd^I]^{2+}$ to the C=N- skeletal vibration frequencies at 1524, 1543 and 1588 cm^{-1}. A triplet state isomer with Pd-*P,N*; Pd-*P,N* binding ($\boldsymbol{P,N-P,N}^{triplet}_{[Pd^I-Pd^I]^{2+}}$, cf. Fig 7c) is

27 kJ/mol higher in energy. It provides a similar linear absorption spectrum as the singlet structure and therefore we do not rule out that a triplet structure contributes to the IR-MPD spectrum of $[Pd^{I}\text{-}Pd^{I}]^{2+}$. However we can rule out Pd-*P,C* coordination. $\boldsymbol{P,C-P,N}_{[Pd^{I}-Pd^{I}]^{2+}}$ (cf. Fig. 7d) exhibits Pd-*P,C* coordination at one palladium site. This results in a destabilization of 37 kJ/mol. The linear absorption spectrum does not match the IR-MPD spectrum. We observe no NH stretching vibration band (predicted at 3416 cm^{-1}) and no NH bending band (predicted at 1618 cm^{-1}), which would be characteristic in the fingerprint region (as we discussed for the mononuclear palladium complexes).

The DFT calculations of $[Pd^{I}\text{-}Pd^{I}Cl]^{+}$ reveal optimized minimum structures as depicted in Fig. 8b-e. The most stable isomer $\boldsymbol{P,N\text{-}P,N}_{[Pd^{I}-Pd^{I}-Cl]^{+}}$ (cf. Fig. 8b) resembles the structure of $[Pd^{I}\text{-}Pd^{I}]^{2+}$, the Cl^{-} anion coordinating to the free coordination site of one Pd center. However, the linear absorption spectrum of $\boldsymbol{P,N\text{-}P,N}_{[Pd^{I}-Pd^{I}Cl]^{+}}$ does not reproduce the splitting of the bands in the fingerprint region as observed in the IR-MPD spectrum of $[Pd^{I}\text{-}Pd^{I}Cl]^{+}$ (bands at 1552 and 1590 cm^{-1}). Instead it exhibits three clearly discernible bands at 1513, 1549 and 1581 cm^{-1}.

In contrast, the linear absorption spectrum of the higher energy isomer $\boldsymbol{P,N,\mu^{2}Cl\text{-}P}_{[Pd^{I}-Pd^{I}Cl]^{+}}$ (57 kJ/mol, cf. Fig. 8c) exhibits two main peaks at 1528 (with a shoulder at 1546 cm^{-1}) and 1584 cm^{-1} matching the experimental band splitting. $\boldsymbol{P,N,\mu^{2}Cl\text{-}P}_{[Pd^{I}-Pd^{I}Cl]^{+}}$ exhibits a μ^{2} chlorido ligand shared by the Pd centers. The pyrimidyl-triphenylphosphine ligands reorganize to accommodate the steric demand: One phenyl ring rotates away from the palladium centers thereby taking the pyrimidinyl group with it. Thus one Pd-N bond breaks destabilizing the system. We exclude the triplet state structure $\boldsymbol{P,N\text{-}P,N}^{triplet}_{[Pd^{I}-Pd^{I}Cl]^{+}}$ as well as an Pd-*P,C* binding as represented by isomer $\boldsymbol{P,C\text{-}P,N}_{[Pd^{I}-Pd^{I}Cl]^{+}}$ (cf. Fig. 8d and e). Both isomers are very unstable (93 and 73 kJ/mol) and do not match the IR-MPD spectrum of $[Pd^{I}\text{-}Pd^{I}Cl]^{+}$.

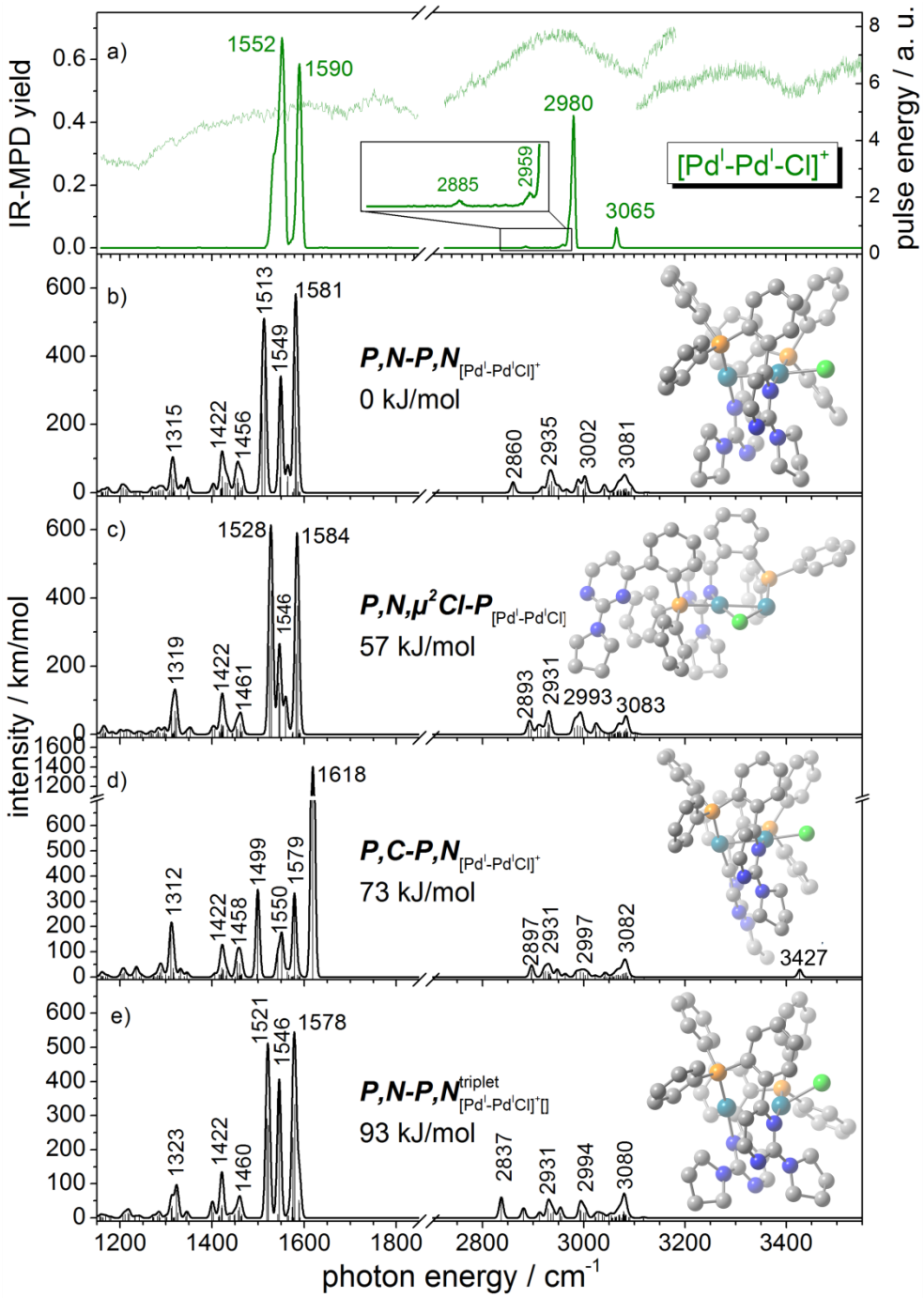

Figure 8: a) IR-MPD spectra of [Pd^{I}-Pd^{I}Cl]$^{+}$ in the spectral range of 1150 – 3600 cm^{-1} including the power curve of the IR laser. **b-e)** Calculated IR absorption spectra of geometry optimized isomers of [Pd^{I}-Pd^{I}Cl]$^{+}$. The insets show associated geometry optimized structures. The calculations were performed at the B3LYP/cc-pVDZ (H, C, N, O) and Stuttgart 1997 ECP (Pd) level of theory. The harmonic frequencies are scaled with 0.965.

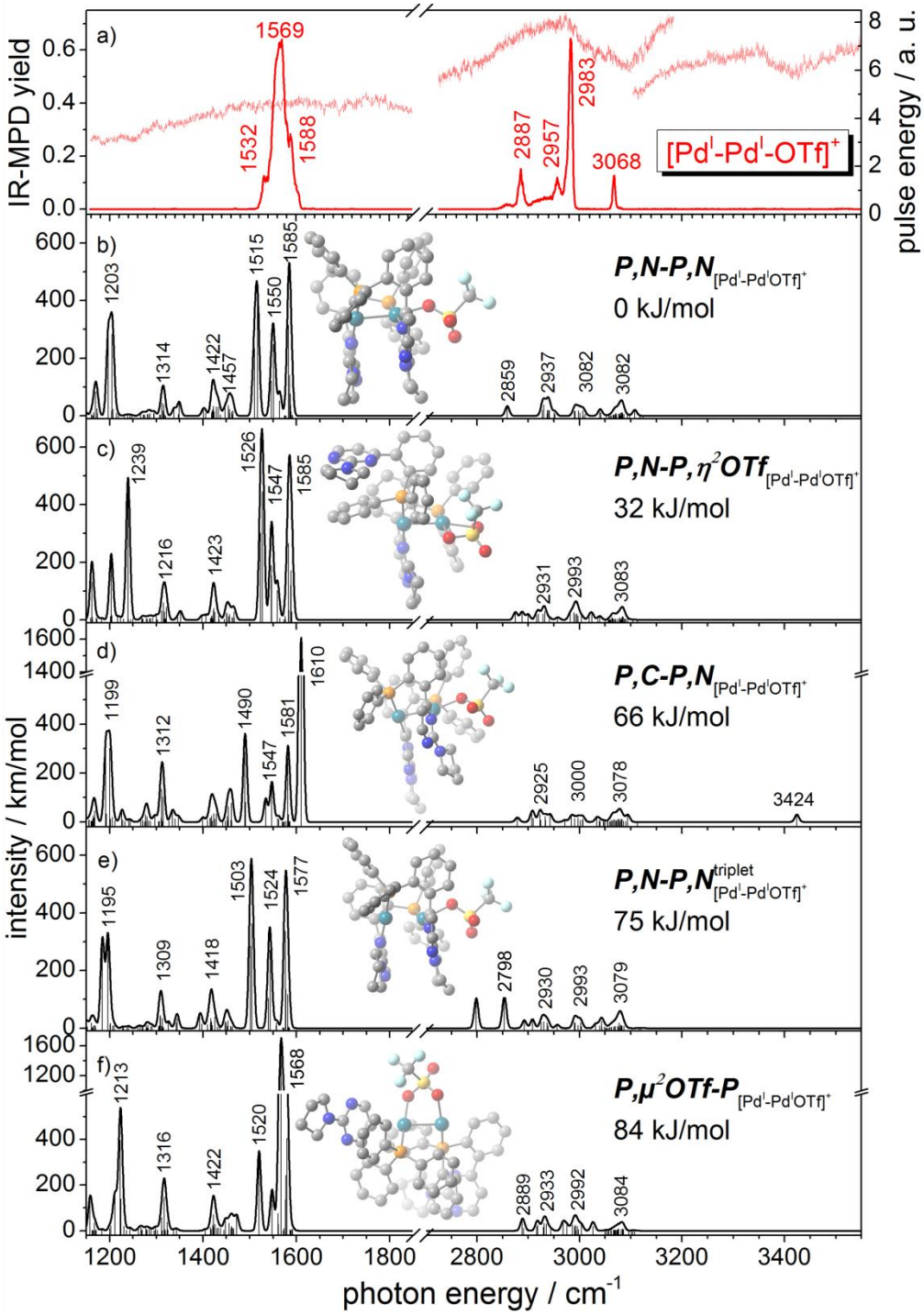

Figure 9: a) IR-MPD spectra of $[Pd^{I}\text{-}Pd^{I}OTf]^{+}$ in the spectral range of 1150 - 3600 cm^{-1} including the power curve of the IR laser. **b-e)** Calculated IR absorption spectra of geometry optimized isomers of $[Pd^{I}\text{-}Pd^{I}OTf]^{+}$. The insets show associated geometry optimized structures. The calculations were performed at the B3LYP/cc-pVDZ (H, C, N, O) and Stuttgart 1997 ECP (Pd) level of theory. The harmonic frequencies are scaled with 0.965.

The DFT calculations of $[Pd^{I}\text{-}Pd^{I}OTf]^{+}$ reveal optimized minimum structures as depicted in Fig. 9b-e. The most stable isomer $\boldsymbol{P,N\text{-}P,N}_{[Pd^{I}-Pd^{I}OTf]^{+}}$ (cf. Fig. 9b) is very similar to

$\boldsymbol{P,N\text{-}P,N}_{[Pd^{I}-Pd^{I}Cl]^{+}}$ the OTf^{-} anion coordinating to the free coordination site of one Pd center in a monodentate fashion. In the case of isomer $\boldsymbol{P,N\text{-}P,\eta^{2}OTf}_{[Pd^{I}-Pd^{I}OTf]^{+}}$ (32 kJ/mol) the OTf^{-} ligand binds bidentate to one Pd center. The linear absorption spectra of both isomers do not satisfactory reproduce the broad band at 1569 cm^{-1} in the IR-MPD spectrum of [Pd^{I}-Pd^{I}OTf]$^{+}$. The OTf^{-} is able to bridge both Pd center as in isomer $\boldsymbol{P,\mu^{2}OTf\text{-}P,}_{[Pd^{I}-Pd^{I}OTf]^{+}}$. The pyrimidyl-triphenylphosphane ligands reorganize to accommodate the steric demand of the bridging OTf: One phenylring ring rotates away from the palladium centers thereby taking the pyrimidinyl group with it. Thus both Pd-N bonds break, which destabilizes the system. However, the linear absorption spectrum of $\boldsymbol{P,\mu^{2}OTf\text{-}P,}_{[Pd^{I}-Pd^{I}OTf]^{+}}$ does nicely reproduce the IR-MPD spectrum. It exhibits a very strong C=N- vibration band at 1568 cm^{-1} and a significantly weaker band at 1520 cm^{-1}. We exclude the triplet state structure $\boldsymbol{P,N\text{-}P,N}^{triplet}_{[Pd^{I}-Pd^{I}OTf]^{+}}$ as well as an Pd-*P,C* binding as represented by isomer $\boldsymbol{P,C\text{-}P,N}_{[Pd^{I}-Pd^{I}OTf]^{+}}$ (cf. Fig. 9d and e). Both isomers are very unstable (75 and 66 kJ/mol) and do not match the IR-MPD spectrum of [Pd^{I}-Pd^{I}OTf]$^{+}$.

7.6 Conclusions

We characterized the fragmentation pathways and binding motifs of five structurally analogous mono and binuclear Pd complexes as isolated ions in the gas phase using Electrospray Ionization tandem mass spectrometry (ESI-MS).

Collision Induced Dissociation (CID) studies on [Pd^{II}Cl]$^{+}$ and [Pd^{II}]$^{+}$ indicate HCl elimination as the first fragmentation step followed by the cleavage of neutral Pd^{0} atoms. The second step implies a metal to ligand charge transfer, which is yet to be explored. The binuclear complexes [Pd^{I}-Pd^{I}]$^{2+}$, [Pd^{I}-Pd^{I}Cl]$^{+}$ and [Pd^{I}-Pd^{I}OTf]$^{+}$ exhibit a multitude of intricate and non-obvious fragmentation routes involving the breaking of the Pd-Pd bond. Additionally the palladium centers disproportionate (Pd^{I}-Pd^{I} to Pd^{II} and Pd^{0}) upon CID activation as evident by the CID fragment [Pd^{II}]$^{+}$.

InfraRed Multiple Photon Dissociation (IRMPD) spectra in combination with Density Functional Theory (DFT) based calculations suggest that both, [Pd^{II}Cl]$^{+}$ and [Pd^{II}]$^{+}$ exhibit at least one isomer with a Pd-*P,C* bonding motif. However, Pd-*P,N* bonding is predicted to be more stable in the gas phase in both cases. The under-coordinated Pd

center in $[Pd^{II}Cl]^+$ and $[Pd^{II}]^+$ stabilizes due to interaction with additional donor sites such as the nitrogen atom of the pyrrolidino ring.

In the case of the binuclear complexes $[Pd^{I}\text{-}Pd^{I}]^{2+}$, $[Pd^{I}\text{-}Pd^{I}Cl]^+$ and $[Pd^{I}\text{-}Pd^{I}OTf]^+$ we exclude a Pd-*P,C* binding motif. Additionally we observe a modulation of the IR-MPD spectra by the anions Cl^- and OTf^-. DFT calculations show, that both anions are able to act as a bridging ligand between Pd-Pd, which results in an significant reorganization of the complex.

7.7 Acknowledgement

This work was supported by the German research foundation DFG within the transregional collaborative research center SFB/TRR 88 “Cooperative effects in homo and heterometallic complexes” (3MET).

7.8 References

1. G. Brahmachari, *RSC Advances*, 2016, 6, 64676-64725.
2. V. Ritleng, C. Sirlin and M. Pfeffer, *Chem. Rev.*, 2002, 102, 1731-1770.
3. J. Tang, D. Hackenberger and L. J. Goossen, *Angew. Chem. Int. Ed.*, 2016, 55, 11296-11299.
4. E. M. Beccalli, G. Broggini, M. Martinelli and S. Sottocornola, *Chem. Rev.*, 2007, 107, 5318-5365.
5. N. T. S. Phan, M. Van Der Sluys and C. W. Jones, *Advanced Synthesis & Catalysis*, 2006, 348, 609-679.
6. X.-F. Wu, P. Anbarasan, H. Neumann and M. Beller, *Angew. Chem. Int. Ed.*, 2010, 49, 9047-9050.
7. A. Fromm, C. van Wüllen, D. Hackenberger and L. J. Gooßen, *J. Am. Chem. Soc.*, 2014, 136, 10007-10023.
8. D. Hackenberger, B. Song, M. F. Grünberg, S. Farsadpour, F. Menges, H. Kelm, C. Groß, T. Wolff, G. Niedner-Schatteburg, W. R. Thiel and L. J. Gooßen, *ChemCatChem*, 2015, 7, 3579-3588.
9. J. M. Serrano-Becerra, A. F. G. Maier, S. González-Gallardo, E. Moos, C. Kaub, M. Gaffga, G. Niedner-Schatteburg, P. W. Roesky, F. Breher and J. Paradies, *Eur. J. Org. Chem.*, 2014, 2014, 4515-4522.
10. Y. Schmitt, K. Chevalier, F. Rupp, M. Becherer, A. Grun, A. M. Rijs, F. Walz, F. Breher, R. Diller, M. Gerhards and W. Klopper, *PCCP*, 2014, 16, 8332-8338.
11. P. Buchwalter, J. Rosé and P. Braunstein, *Chem. Rev.*, 2014, DOI: 10.1021/cr500208k.
12. N. Tsukada, O. Tamura and Y. Inoue, *Organometallics*, 2002, 21, 2521-2528.
13. S. Jindabot, K. Teerachanan, P. Thongkam, S. Kiatisevi, T. Khamnaen, P. Phiriyawirut, S. Charoenchaidet, T. Sooksimuang, P. Kongsaeree and P. Sangtrirutnugul, *J. Organomet. Chem.*, 2014, 750, 35-40.

14. P. Kočovský, Š. Vyskočil, I. Císařová, J. Sejbal, I. Tišlerová, M. Smrčina, G. C. Lloyd-Jones, S. C. Stephen, C. P. Butts, M. Murray and V. Langer, *J. Am. Chem. Soc.*, 1999, 121, 7714-7715.
15. J. Yin and S. L. Buchwald, *J. Am. Chem. Soc.*, 2000, 122, 12051-12052.
16. J. W. Faller and N. Sarantopoulos, *Organometallics*, 2004, 23, 2008-2014.
17. U. Christmann, D. A. Pantazis, J. Benet-Buchholz, J. E. McGrady, F. Maseras and R. Vilar, *J. Am. Chem. Soc.*, 2006, 128, 6376-6390.
18. R. Pratap, D. Parrish, P. Gunda, D. Venkataraman and M. K. Lakshman, *J. Am. Chem. Soc.*, 2009, 131, 12240-12249.
19. S. Farsadpour, L. T. Ghoochany, S. Shylesh, G. Dörr, A. Seifert, S. Ernst and W. R. Thiel, *ChemCatChem*, 2012, 4, 401-407.
20. F. Rajabi, J. Trampert, Y. Sun, M. Busch, S. Bräse and W. R. Thiel, *J. Organomet. Chem.*, 2013, 744, 101-107.
21. M. Cayir, L. T. Ghoochany, A. Walli, M. Busch, Y. Sun, F. Meyer, S. Bräse and W. R. Thiel, *Eur. J. Inorg. Chem.*, 2014, 2014, 2618-2624.
22. C. Sarcher, S. Farsadpour, L. Taghizadeh Ghoochany, Y. Sun, W. R. Thiel and P. W. Roesky, *J. Organomet. Chem.*, 2014, 758, 29-35.
23. L. Wang, S. Shylesh, D. Dehe, T. Philippi, G. Dörr, A. Seifert, Z. Zhou, M. Hartmann, R. N. Klupp Taylor, M. Jia, S. Ernst and W. R. Thiel, *ChemCatChem*, 2012, 4, 395-400.
24. L. J. Gooßen, G. Deng and L. M. Levy, *Science*, 2006, 313, 662-664.
25. S. Baader, P. E. Podsiadly, D. J. Cole-Hamilton and L. J. Goossen, *Green Chemistry*, 2014, 16, 4885-4890.
26. D. M. Ohlmann, N. Tschauder, J.-P. Stockis, K. Gooßen, M. Dierker and L. J. Gooßen, *J. Am. Chem. Soc.*, 2012, 134, 13716-13729.
27. S. Farsadpour, L. T. Ghoochany, Y. Sun and W. R. Thiel, *Eur. J. Inorg. Chem.*, 2011, 2011, 4603-4609.
28. C. Kerner, J. Lang, M. Gaffga, Y. Sun, G. Niedner-Schatteburg and W. R. Thiel, *ChemPlusChem*, 2016, DOI: 10.1002/cplu.201600526, n/a-n/a.
29. L. Taghizadeh Ghoochany, C. Kerner, S. Farsadpour, F. Menges, Y. Sun, G. Niedner-Schatteburg and W. R. Thiel, *Eur. J. Inorg. Chem.*, 2013, 2013, 4305-4317.
30. R. Colton, A. D'Agostino and J. C. Traeger, *Mass Spectrom. Rev.*, 1995, 14, 79-106.
31. J. B. Fenn, *Angew. Chem. Int. Ed.*, 2003, 42, 3871-3894.
32. M. Yamashita and J. B. Fenn, *J. Phys. Chem.*, 1984, 88, 4451-4459.
33. E. de Hoffmann, *J. Mass Spectrom.*, 1996, 31, 129-137.
34. K. M. Ervin and P. B. Armentrout, *J. Chem. Phys.*, 1987, 86, 2659-2673.
35. R. G. Cooks, *J. Mass Spectrom.*, 1995, 30, 1215-1221.
36. K. Levsen and H. Schwarz, *Angew. Chem. Int. Ed.*, 1976, 15, 509-519.
37. A. K. Shukla and J. H. Futrell, *J. Mass Spectrom.*, 2000, 35, 1069-1090.
38. N. C. Polfer and J. Oomens, *Mass Spectrom. Rev.*, 2009, 28, 468-494.
39. J. Oomens, B. G. Sartakov, G. Meijer and G. von Helden, *Int. J. Mass spectrom.*, 2006, 254, 1-19.
40. J. R. Eyler, *Mass Spectrom. Rev.*, 2009, 28, 448-467.
41. J. Roithova, *Chem. Soc. Rev.*, 2012, 41, 547-559.
42. J. Lang, J. Mohrbach, S. Dillinger, J. M. Hewer and G. Niedner-Schatteburg, *Chem. Commun.*, 2017, 53, 420-423.
43. C. J. Johnson, A. B. Wolk, J. A. Fournier, E. N. Sullivan, G. H. Weddle and M. A. Johnson, *J. Chem. Phys.*, 2014, 140, -.

44. J. Jašík, J. Žabka, J. Roithová and D. Gerlich, *Int. J. Mass spectrom.*, 2013, 354–355, 204-210.
45. S. Dillinger, J. Mohrbach, J. Hewer, M. Gaffga and G. Niedner-Schatteburg, *PCCP*, 2015, 17, 10358-10362.
46. J. Seo, J. Jang, S. Warnke, S. Gewinner, W. Schöllkopf and G. von Helden, *J. Am. Chem. Soc.*, 2016, 138, 16315-16321.
47. J. D. Steill and J. Oomens, *J. Phys. Chem. A*, 2009, 113, 4941-4946.
48. A. Gunther, P. Nieto, G. Berden, J. Oomens and O. Dopfer, *PCCP*, 2014, 16, 14161-14171.
49. D. Hackenberger, Diploma Thesis, 2013.
50. J. Laskin and J. H. Futrell, *Mass Spectrom. Rev.*, 2005, 24, 135-167.
51. S. A. McLuckey and D. E. Goeringer, *J. Mass Spectrom.*, 1997, 32, 461-474.
52. F. Menges, C. Riehn and G. Niedner-Schatteburg, *Z. Phys. Chem.*, 2011, 225, 595.
53. E.-L. Zins, C. Pepe and D. Schröder, *J. Mass Spectrom.*, 2010, 45, 1253-1260.
54. E.-L. Zins, C. Pepe, D. Rondeau, S. Rochut, N. Galland and J.-C. Tabet, *J. Mass Spectrom.*, 2009, 44, 12-17.
55. K. V. Barylyuk, K. Chingin, R. M. Balabin and R. Zenobi, *J. Am. Soc. Mass. Spectrom.*, 2010, 21, 172-177.
56. B. Miehlich, A. Savin, H. Stoll and H. Preuss, *Chem. Phys. Lett.*, 1989, 157, 200-206.
57. A. D. Becke, *J. Chem. Phys.*, 1993, 98, 5648-5652.
58. T. H. Dunning, *J. Chem. Phys.*, 1989, 90, 1007-1023.
59. M. Dolg, H. Stoll, H. Preuss and R. M. Pitzer, *J. Phys. Chem.*, 1993, 97, 5852-5859.
60. M. J. Frisch, et al.,, 2009.

8 Summary and Outlook

This thesis reports research studies on **transition metal complexes** as trapped ions in isolation. Electrospray Ionization (ESI) serves to transfer ions from solution into the gas phase for mass spectrometric investigations. Subsequently, a variety of experimental and theoretical methods provide fundamental insights into molecular properties of the complexes.

InfraRed (Multiple) Photon Dissociation (IR-(M)PD) spectroscopy and computed linear absorption spectra of structural isomers serve to elucidate molecular **structures** at cryo temperatures as well as at room temperature. Collision Induced Dissociation (CID) of the complexes and computed transition state structures serve to elucidate molecular **fragmentation pathways** as well as relative **stabilities** of the complexes at room temperature. X-Ray Magnetic Circular Dichroism (XMCD) spectra and modelling of magnetic couplings between metal centers serve to elucidate molecular **magnetism** of the complexes at cryo temperatures.

End-on coordinated dinitrogen molecules exhibit significant (**"non-classical"**) **blue shifts** of N_2 stretching vibration frequencies in $[Fe_3O(OAc)_6(N_2)_n]^+$ (OAc = acetate; n = 1, 2, 3). The N_2 coordination to the respective Fe centers is dominated by an interplay of the N_2 σ orbitals with iron acetate orbitals. Electron density delocalizes from the **anti-bonding 4σ*(N_2) orbital** into the coordinated iron acetate core increasing the formal N_2 bond order and thereby increasing the N_2 stretching vibration frequency. This insight into the class of "non-classical" N_2 - Fe complexes is remarkable in view of the industrial use of bulk iron for N_2 activation and hydrogenation. It might help to advance a general understanding of dinitrogen chemistry beyond established coordination models. Future investigations utilizing a systematic variation of the metal centers in $[M_3O(OAc)_6(N_2)_n]^+$ (e.g. Co^{III}, Cr^{III}, Ru^{III} etc.) might provide deeper insights into the ("non-classical") behavoir of N_2. Furthermore, heterometallic $[M_2M^*O(OAc)_6(N_2)_n]^+$ (e.g. M=Fe^{III}; M*=Ru^{III}) complexes are of high interest in upcoming studies. Such complexes might reveal cooperativity between the metal centers.

Cationization of the bimetallic complex $[AuZnCl_3]$ by coordination of alkali metal ions (M^+) results in a reorientation of its organic backbone. This enables a μ^3 binding motif of the alkali ions to the three chlorido ligands. The organic backbone binds the Zn^{2+} cation

by two nitrogen donor atoms and the Au^+ cation by a phosphorus donor atom. The complexes switch their preferred CID fragmentation pathways by the alkali ion and by the CID amplitude: The Li^+ and Na^+ adducts prefer to eliminate $ZnCl_2$, whereas the K^+, Rb^+ and Cs^+ adducts most preferably split off MCl_2ZnCl. Several **intramolecular rearrangements** take place upon CID activation. Li^+ and Na^+ displace the Zn^{2+} cation and coordinate to the nitrogen coordination sites of the organic backbone. This represents a remarkable deviation from a naive hard and soft acids and bases (HSAB) concept. This particular effect may relate to the specific case of mixed coordination to nitrogen and chlorido ligands in parallel. In contrast, the Zn^{2+} cation wins the competition for the nitrogen coordination sites against K^+, Rb^+, and Cs^+. It remains to elucidate how alkali ion coordination affects the reactivity of $[AuZnCl_3]$ in conceivable applications, such as hydroamination catalysis. In future studies, reaction mixtures will be the focus of further investigations. It is conceivable to identify cationized key intermediates of prospective catalytic cycles.

Two color IR-MPD spectroscopy utilizing two delayed pulses on a “ligand-metal-chelate” complex $[AgL_1L_2]^+$ reveals **laser induced torsional isomerization.** This indicates, that variable time delays between the two laser pulses allow to probe ion ensembles with variable internal energy. A calculated torsional isomerization pathway elucidates the torsional barrier, the relative stabilities of participating isomers and the change of vibrational frequencies and IR intensities in the course of the torsion. It reveals the **formation and breaking of strong and weak hydrogen bonds** amongst chelate and ligand. This study underlines that hydrogen bonds within the given complex may break and form by torsional rearrangments that take place perpendicular to the hydrogen bond directions. The hydrogen bonding is of **multi dimensional character**– much beyond an intuitive pulling apart of a hydrogen bond along its bond direction. Upcoming temperature dependent measurements might provide more insight into the population dynamics in the $[AgL_1L_2]^+$ model system. The general concept of laser induced activation of trapped complexes might prove useful, e.g. to overcome reaction barriers and propel (catalytic) reactions in the gas phase.

Geometric structures and magnetic couplings intertwine in trinuclear iron(III) oxo acetate complexes $[Fe_3O(OAc)_6(Py)_n]^+$ (n = 0,1,2,3, Py = pyridine). Stepwise coordination of pyridine ligands to the $[Fe_3O(OAc)_6]^+$ unit induces interdependent

modulation of relative stabilities, vibrational frequencies, geometries and magnetic couplings: The Fe-Py bond strengths decrease with the number of coordinated pyridine ligands. Concurrently, the asymmetric carboxylic CO stretching vibration frequencies increase. This provides spectroscopic evidence for distinct shortenings and elongations of Fe-Fe distances accompanied by **symmetry lowering of the triangular Fe_3O core**: An equilateral triangular Fe_3O core in D_{3h} symmetry (in the case of n = 0) distorts to an isosceles structure with C_{2V} symmetry (in the case of n = 1 and 2). The coordination of the third pyridin ligand (n = 3) regains the equilateral D_{3h} symmetry. Broken symmetry based calculations reveal antiferromagnetic coupling constants, which are crucialy affected by the geometric modulation. Equilateral geometries result in three identical coupling constants in the complex. In contrast, the lower symmetry isosceles geometries lead to two different coupling constants (J and J*) in the complex. The J/J* ratios in concunction with a model spin Hamiltonian determine the **ground spin states** of $[Fe_3O(OAc)_6(Py)_n]^+$: In equilateral Fe_3O cores with D_{3h} symmetries (n = 0 and 3) the J/J* ratio is 1 leading to total spin of 1/2 in the ground states. Lowering the symmetries to C_{2V} leads to J/J* = 0.5 (n = 1) and J/J* = 2.1 (n = 2) resulting in total spins of 3/2 (n = 1) and 5/2 (n = 2) in the ground states. XMCD spectra of $[Fe_3O(OAc)_6(Py)_n]^+$ (n = 0,1) reveal low magnetizations, which we attribute to a dominant antiferromagnetic coupling. While $[Fe_3O(OAc)_6]^+$ exhibits no magnetization at all, $[Fe_3O(OAc)_6(Py)_1]^+$ exhibits an observable dichroic effect. This finding is consistent with an increase of the total spin in the complexes. This study thus reveals a **coordination controlled switching of magnetic ground states**. Dedicated calculations may deepen the fundamental understanding of molecular magnetism in $[Fe_3O(OAc)_6(Py)_n]^+$ by geometry optimizations and frequency calculations *via* broken symmetry. The IR-(MPD) investigations will most definitely benefit from temperature control by (helium) buffer gas within the ion trap. Cooling the complexes will result in sharper bands. This might reveal yet unresolved splittings to be compared with theory. Asymmetric iron(III) oxo complexes exhibiting two different sets of bridging ligands exhibit intrinsically lowered symmetries of the Fe_3O core. Systematic variation of these bridging ligands may provide stable complexes with different magnetic ground states. Such complexes will be of high interest in future IR-(M)PD and XMCD investigations.

Mononuclear Pd^{II} catalysts with a bidentate (2-pyrrolidino-pyrimidine-4-yl-triphenylphosphane) ligand exhibit intramolecular **CH activation** at the pyrimidine ring *via* a **Pd-*P,C* binding**. Upon activation these catalysts eliminate HCl in the first fragmentation step followed by the cleavage of neutral Pd^0 atoms. The second fragmentation step implies a metal to ligand charge transfer. Binuclear Pd^I-Pd^I catalysts with two coordinating bidentate (2-pyrrolidino-pyrimidine-4-yl-triphenylphosphane) ligands show **Pd-*P,N* bindings** and no CH activation**.** The binding motif is modulated by a coordination of additional Cl^- and OTf^- (triflate) anions to the Pd^I-Pd^I core. Both anions are able to act as bridging ligands between the Pd-Pd centers, which results in a significant reorganization of the ligands. Upon activation of the complexes the Pd^I-Pd^I centers disproportionate to Pd^{II} and Pd^0 . In future studies mass spectrometric studies of reaction mixtures may serve to identify key intermediates of prospective catalytic cycles. The usage of two (temperature controlled) ion traps in tandem may provide fundamental insight into elementary steps of such (catalytical) reactions.

9 Zusammenfassung und Ausblick

Diese Arbeit beinhaltet Forschungsstudien über **Übergangsmetallkomplexe** als isolierte Ionen in der Gasphase. Elektrospray-Ionisation (ESI) ermöglicht es, Ionen aus der Lösung in die Gasphase zu überführen und somit für massenspektrometrische Untersuchungen zugänglich zu machen. Eine Vielzahl von experimentellen und theoretischen Methoden gibt grundlegende Einblicke in **molekulare Eigenschaften** der Komplexe.

InfraRote (Multi) Photonen Dissoziationsspektroskopie (IR-(M)PD) und berechnete lineare Absorptionsspektren von Strukturisomeren dienen zur Aufklärung molekularer **Strukturen** bei Kryo-Temperaturen sowie bei Raumtemperatur. Stoß-Induzierte Dissoziation (CID) der Komplexe und berechnete Übergangszustandsstrukturen dienen zur Aufklärung von molekularen **Fragmentierungskanälen** sowie relativen **Stabilitäten** der Komplexe bei Raumtemperatur. Zirkularer Magnetischer Röntgendichroismus (XMCD) und die Modellierung magnetischer Kopplungen zwischen Metallzentren dienen zur Aufklärung des molekularen **Magnetismus** der Komplexe bei Kryo-Temperaturen.

End-on koordinierte Distickstoffmoleküle in $[Fe_3O(OAc)_6(N_2)_n]^+$ Komplexen (OAc = Acetat; n = 1, 2, 3) zeigen signifikante (**"nicht klassische"**) **Blauverschiebungen** der N_2-Streckschwingungsfrequenzen. Die Koordination von N_2 an die jeweiligen Fe-Zentren wird durch ein Zusammenspiel der N_2 σ Orbitale mit Eisenacetatorbitalen dominiert. Die Elektronendichte des **anti-bindenden 4σ*(N_2)-Orbitals** wird in den koordinierten Eisenacetatkern delokalisiert, wodurch die formale N_2-Bindungsordnung und die N_2-Streckschwingungsfrequenz erhöht wird. Dieser Einblick in die Klasse der "nicht-klassischen" N_2-Fe-Komplexe ist angesichts der industriellen Verwendung von Eisen für die N_2-Aktivierung und Hydrierung bemerkenswert. Er könnte dazu beitragen, das allgemeine Verständnis der Distickstoffchemie, über die etablierten Koordinationsmodelle hinaus, voranzutreiben. Eine systematische Variation der Metallzentren in $[M_3O(OAc)_6(N_2)_n]^+$ (z.B. Co^{III}, Cr^{III}, Ru^{III} etc.) in zukünftigen Untersuchungen, könnte einen tieferen Einblick in das (nicht klassische) Verhalten von N_2 liefern. Weiterhin sind heterometallische Komplexe $[M_2M^*O(OAc)_6(N_2)_n]^+$

(z.B. M=Fe^{III}; M*=Ru^{III}) in anstehenden Studien von hohem Interesse. Solche Komplexe könnten eine Kooperativität zwischen den Metallzentren zeigen.

Eine **Kationisierung** des dimetallischen Komplexes [$AuZnCl_3$] durch Koordination von Alkalimetallionen (M^+) führt zu einer Umorientierung seines organischen Grundgerüsts. Dies ermöglicht ein μ^3 Bindungsmotiv der Alkaliionen zu drei Chloridliganden. Der Ligand bindet das Zn^{2+}-Kation durch zwei Stickstoffdonoratome und das Au^+ Kation durch ein Phosphor-Donoratom. Die bevorzugten Fragmentierungskanäle von [$AuZnCl_3M$]$^+$ wechseln mit den Alkaliionen und mit der CID-Amplitude: Die Li^+- und Na^+ Addukte eliminieren bevorzugt $ZnCl_2$, während die K^+, Rb^+- und Cs^+ Addukte MCl_2ZnCl abspalten. Bei der CID-Aktivierung finden mehrere **Umlagerungen im Komplex** statt. Li^+ und Na^+ verdrängen das Zn^{2+} Kation und koordinieren und die Stickstoff Koordinationsstellen des Liganden. Dies stellt eine bemerkenswerte Abweichung vom Prinzip der harten und weichen Säuren und Basen (HSAB) dar. Dieser Effekt kann durch den spezifischen Fall der gemischten Koordination von Stickstoff- und Chloridionen herrühren. Im Gegensatz dazu gewinnt das Zn^{2+} Kation den intramolekularen Wettbewerb um die Stickstoff-Koordinationsstellen gegen K^+, Rb^+ und Cs^+. Es bleibt zu klären, wie die Koordination von Alkaliionen die Reaktivität von [$AuZnCl_3$] in denkbaren Anwendungen (beispielsweise homogene Hydroaminierungskatalyse) beeinflusst. In zukünftigen Studien werden Reaktionsmischungen im Mittelpunkt weiterer Untersuchungen stehen. Es ist denkbar, kationisierte Schlüsselintermediate in den katalytischen Zyklen zu identifizieren.

Zwei farbige IR-MPD-Spektroskopie unter Verwendung von zwei verzögerten Pulsen an einem "Ligand-Metall-Chelat"-Komplex [AgL_1L_2]$^+$ zeigt eine **laserinduzierte Torsionsisomerisierung.** Dies zeigt, dass variable Zeitverzögerungen zwischen den beiden Laserpulsen es erlauben, Ionenensembles mit variablen internen Energien zu untersuchen. Ein berechneter Torsionsisomerisierungsweg gibt Informationen über die Torsionsbarriere, die relativen Stabilitäten der teilnehmenden Isomere und die Veränderung der Schwingungsfrequenzen und IR-Intensitäten im Verlauf der Torsion. Somit wird die Bildung und Brechung von **starken und schwachen Wasserstoffbrücken** zwischen Chelat und Ligand aufgezeigt. Diese Studie unterstreicht, dass Wasserstoffbrücken innerhalb des gegebenen Komplexes durch Torsionen, die senkrecht zu den Wasserstoffbindungsrichtungen stattfinden, brechen und sich bilden

können. Dies bestätigt, dass das Bilden und Brechen von Wasserstoffbrücken einen **mehrdimensionalen Charakter** aufweist. Dies geht weit über ein intuitives Auseinanderziehen einer Wasserstoffbindung entlang seiner Bindungsrichtung hinaus. Zukünftige, temperaturabhängige Messungen könnten einen Einblick in die Populationsdynamik im $[AgL_1L_2]$+ Modellsystem liefern. Das allgemeine Konzept der laserinduzierten Aktivierung von eingefangenen Komplexen könnte sich als nützlich erweisen, z.B. um energetische Barrieren von Reaktionen in der Gasphase zu überwinden und somit katalytische Zyklen voranzutreiben.

Geometrische Strukturen und magnetische Kopplungen in dreikernigen Eisen (III)-oxoacetat-Komplexen $[Fe_3O(OAc)_6(Py)_n]^+$ (OAc = Acetat; n = 0,1,2,3) sind **untrennbar miteinander verflochten**. Eine schrittweise Koordination von Pyridinliganden an die $[Fe_3O(OAc)_6]^+$ Einheit induziert eine voneinander abhänge Modulation von relativen Stabilitäten, Schwingungsfrequenzen, Geometrien und magnetischen Kopplungen. Die Fe-Py-Bindung wird mit der Anzahl der koordinierten Pyridin-Liganden stärker. Gleichzeitig erhöhen sich die asymmetrischen Carboxyl-CO-Streckschwingungsfrequenzen. Dies ist ein spektroskopischer Hinweis auf Veränderungen von Fe-Fe-Abständen, die von einer **Symmetriereniedrigung des dreieckigen Fe_3O-Kerns** begleitet sind: Ein gleichseitiger dreieckiger Fe_3O-Kern in D_{3h}-Symmetrie (im Fall von n = 0) verzerrt sich zu einer gleichschenkligen Struktur mit C_{2V}-Symmetrie (im Fall von n = 1 und 2). Durch die Koordination des dritten Pyridinliganden (n = 3) erlangt der Fe_3O-Kerns wieder eine gleichseitige D_{3h}-Symmetrie. *Broken Symmetry* basierte Rechnungen liefern antiferromagnetische Kopplungenkonstanten, die durch die geometrische Modulation entscheidend moduliert werden. Gleichseitige Geometrien führen zu drei identischen Kopplungskonstanten. Im Gegensatz dazu ergeben erniedrigte Symmetrien der gleichschenkligen Fe_3O Kerne zwei verschiedenen Kopplungskonstanten (J und J*). Die somit ermittelten J/J*-Verhältnisse in $[Fe_3O(OAc)_6(Py)_n]^+$ (n = 0,1,2,3) bestimmen nach einem Modell-Spinhamilton-Operator deren **Grundzustandspinzustände**: In gleichseitigen Fe_3O-Kernen mit D_{3h}-Symmetrien (n = 0 und 3) ist das J/J*-Verhältnis 1, was zu einem Gesamtspin (S_T) von 1/2 in den Grundzuständen führt. Die Senkung der Symmetrie zu C_{2V} führt zu J/J*=0,5 (n = 1) und J/J*=2,1 (n = 2), was zu Gesamtspins (S_T) von 3/2 (n = 1) und 5/2 (n = 2) in den Grundzuständen führt. XMCD-Spektren $[Fe_3O(OAc)_6(Py)_n]^+$ (n = 0,1) zeigen im

Allgemeinen niedrige Magnetisierungen, die wir einer dominierenden antiferromagnetischen Kopplung zuschreiben. Während $[Fe_3O(OAc)_6]^+$ überhaupt keine Magnetisierung aufweist, zeigt **$[Fe_3O(OAc)_6(Py)_1]^+$** einen beobachtbaren **dichroitischen Effekt**. Dieser Befund ist mit einer Erhöhung des Gesamtspins in den Komplexen konsistent. Die Studie offenbart somit eine **koordinationsgesteuerte Umschaltung von magnetischen Grundzuständen**. Geometrieoptimierungen und Frequenzberechnungen mit einem *Broken Symmetry* Ansatz könnten das grundlegende Verständnis des molekularen Magnetismus in $[Fe_3O(OAc)_6(Py)_n]^+$ vertiefen. IR-(MPD) Untersuchungen werden von einer Temperaturregelung durch (Helium-) Puffergas innerhalb der Ionenfalle profitieren. Das Abkühlen der Komplexe führt zu schärferen Banden, was bislang noch unaufgelöste Bandenspaltungen zeigen könnte. Asymmetrische Eisen (III) -Oxokomplexe, die zwei verschiedene Arten von Brückenliganden aufweisen, weisen intrinsisch erniedrigte Symmetrien der Fe_3O Kerne auf. Eine systematische Variation dieser Brückenliganden kann stabile Komplexe mit unterschiedlichen magnetischen Grundzuständen liefern.

Mononukleare Pd^{II}-Katalysatoren mit einem zweizähnigen (2-Pyrrolidino-pyrimidin-4-yl-triphenylphosphan) Liganden weisen eine **intramolekulare CH-Aktivierung** am Pyrimidinring mittels einer **Pd-*P,C*-Bindung** auf. Bei Aktivierung der Komplexe eliminieren sie HCl im ersten Fragmentierungsschritt, gefolgt von der Abspaltung von neutralen Pd^0-Atomen. Der zweite Fragmentierungschritt deutet auf einen Metall-Ligand-Ladungstransfer hin. Binukleare Pd^I-Pd^I-Katalysatoren mit zwei koordinierenden zweizähnigen (2-Pyrrolidino-pyrimidin-4-yl-triphenylphosphan) Liganden zeigen keine CH-Aktivierung und weisen **Pd-*P,N*-Bindungen** auf. Das Bindungsmotif wird die durch die Koordination von Cl^- und OTf^-(Triflat) Anionen zum Pd^I-Pd^I-Kern beeinflusst. Beide Anionen können als Brückenliganden zwischen den Pd-Pd-Zentren fungieren, was zu einer signifikanten Umlagerung der Liganden führt. Bei Aktivierung der Komplexe disproportionieren die Pd^I-Pd^I-Zentren zu Pd^{II} und Pd^0. In zukünftigen Studien könnten massenspektrometrische Untersuchungen an Reaktionsgemischen zur Identifizierung von Reaktionsintermediaten beitragen . Der Einsatz von (temperaturgesteuerten) Tandem-Ionenfallen könnte grundlegende Einblicke in elementare Schritte solcher (katalytischer) Reaktionen liefern.

10 Supplementary Information

Content

10.1 Vibrational Blue Shift of Coordinated N_2 in $[Fe_3O(OAc)_6(N_2)_n]^+$:"Non Classical" Dinitrogen Complexes

Johannes Lang, Jennifer Mohrbach, Sebastian Dillinger, Joachim M. Hewer and Gereon Niedner-Schatteburg

Fachbereich Chemie and Forschungszentrum OPTIMAS,
Technische Universität Kaiserslautern,
67663 Kaiserslautern, Germany

Content

10.1.1 Mass Spectra

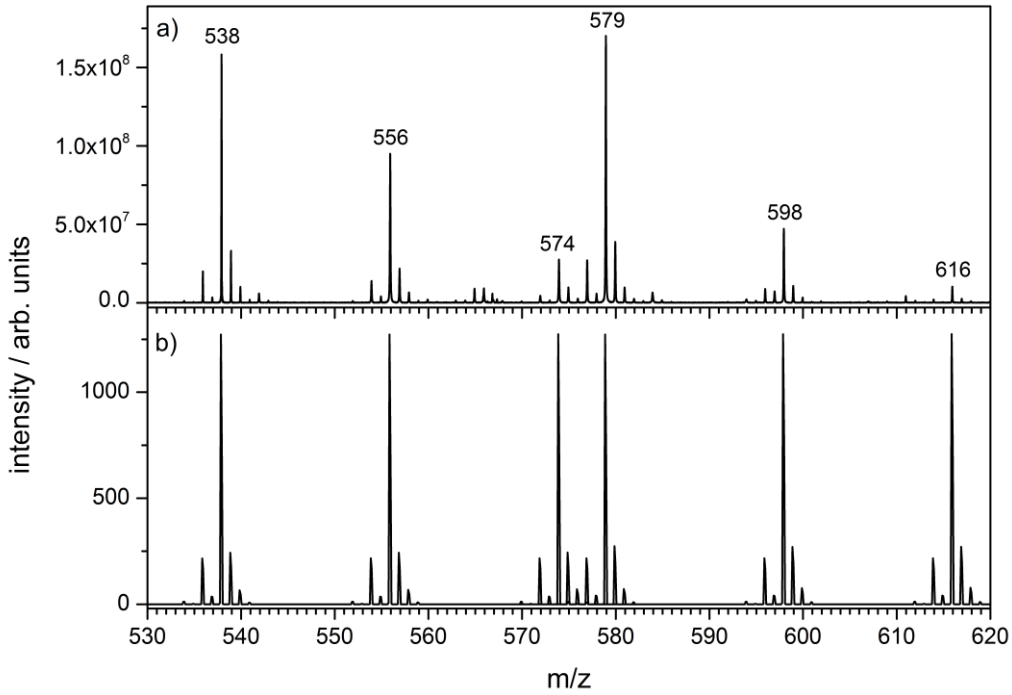

Figure S1: Cationic mass spectrum of a $[Fe_3O(OAc)_6(H_2O)_3]ClO_4$ acetonitrile solution a). Simulated isotopic pattern of $[Fe_3O(OAc)_6(L)_n]^+$ (n=0,1,2,3; L= H_2O, acetonitrile and acetic acid) b). For peak assignment refer to table S1.

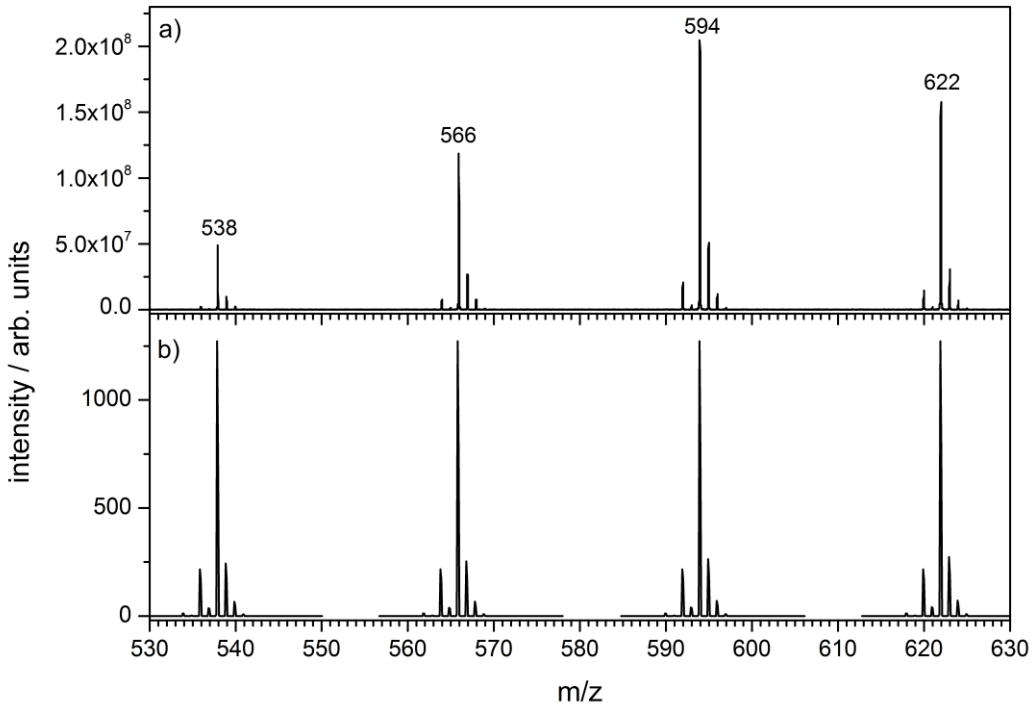

Figure S2: Cationic mass spectrum of a $[Fe_3O(OAc)_6(H_2O)_3]ClO_4$ acetonitrile solution after collision induced dissociation and subsequent N_2 coordination to $[Fe_3O(OAc)_6]^+$ a). Simulated isotopic pattern of $[Fe_3O(OAc)_6(N_2)_n]^+$ (n=0,1,2,3) b). For peak assignment refer to table S1.

Table S1: Compilation of ESI-MS data on $[Fe_3O(OAc)_6(L)_n]^+$ (n=1,2,3; OAc=CH_3CO_2). The indicated mass labels refer to the most abundant isotope peaks.

Species	m/z
$[Fe_3O(OAc)_6]^+$	538
$[Fe_3O(OAc)_6(H_2O)_1]^+$	556
$[Fe_3O(OAc)_6(N_2)_1]^+$	566
$[Fe_3O(OAc)_6(H_2O)_2]^+$	574
$[Fe_3O(OAc)_6(CH_3CN)_1]^+$	579
$[Fe_3O(OAc)_6(N_2)_2]^+$	594
$[Fe_3O(OAc)_6(HOAc)_1]^+$	598
$[Fe_3O(OAc)_6(HOAc)_1(H_2O)_1]^+$	616
$[Fe_3O(OAc)_6(N_2)_3]^+$	622

10.1.2 Calculated N_2-Free Binding Energies

$\Delta\Delta_{bind}G_n^T$ $=\Delta_f G^T(\mathbf{[Fe_3O(OAc)_6(N_2)_n]^+}) + \Delta_f G^T(N_2) - \Delta_f G^T(\mathbf{[Fe_3O(OAc)_6(N_2)_{n+1}]^+})$

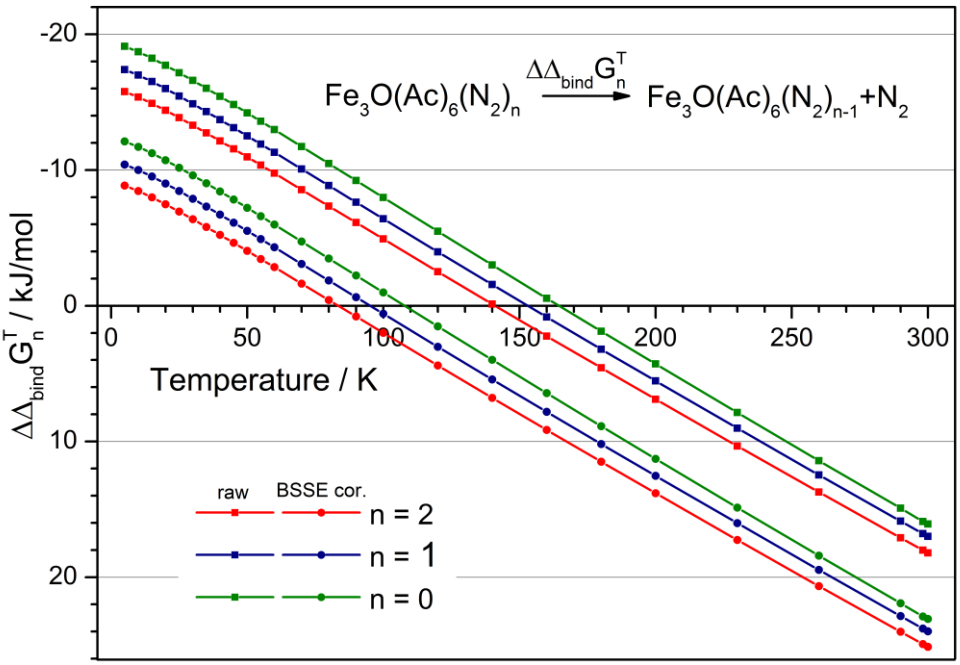

Figure S3: Temperature dependence of N_2-binding Gibbs energies ($\Delta\Delta_{bind}G_n^T$) of $[Fe_3O(OAc)_6(N_2)_n]^+$ (n = 0,1,2,3). DFT calculations were performed at the B3LYP/cc-pVTZ (H, C, N, O) and Stuttgart 1997 ECP (Fe) level of theory.

10.1.3 Details of the DFT Calculations

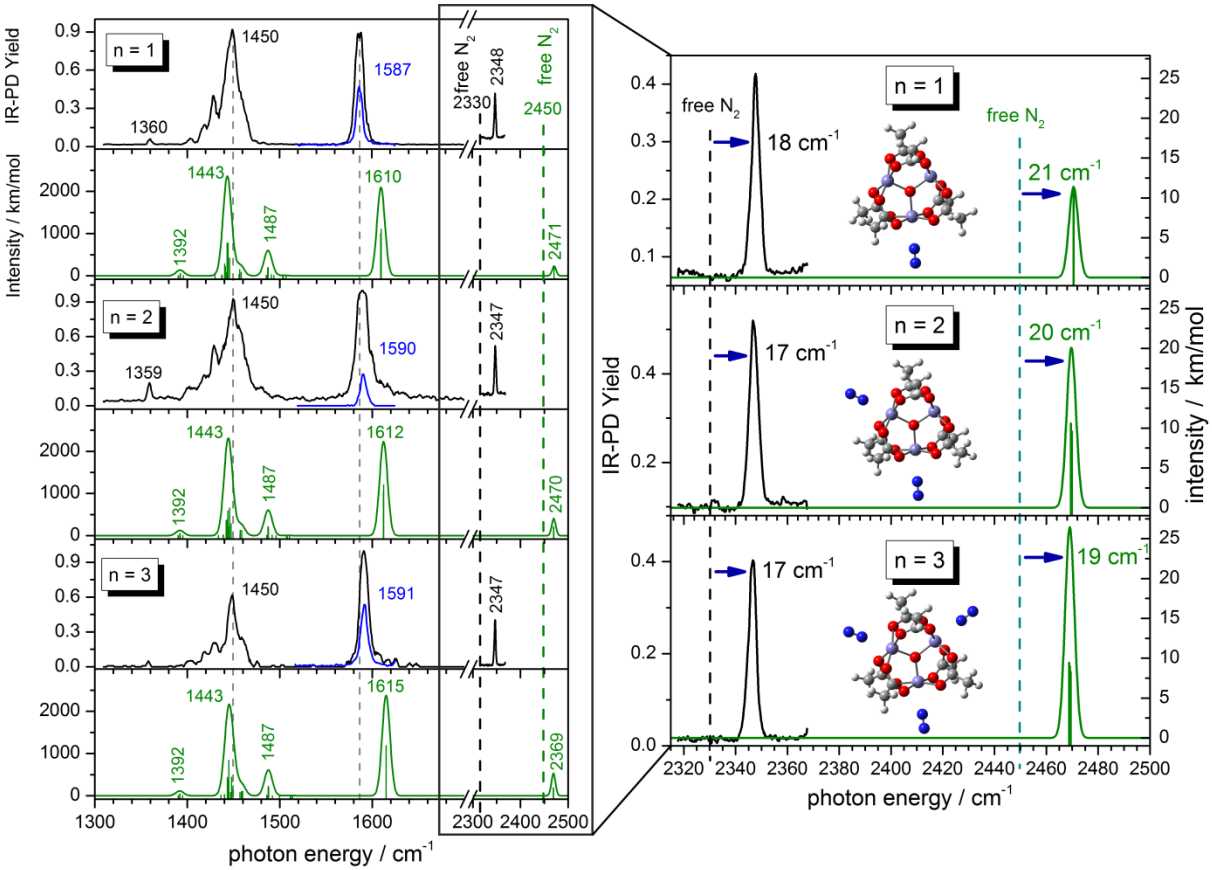

Figure S4: Left: IR-PD spectra of $[Fe_3O(OAc)_6(N_2)_n]^+$ (n=1,2,3) at 26 K (black and blue curves) and calculated IR absorption spectra of optimized $[Fe_3O(OAc)_6(N_2)_n]^+$ (n=1-3) (green curves) in the range of 1300–2500 cm^{-1}. The blue IR-PD spectrum shows the CO stretching band (recorded with highly attenuated laser power to avoid saturation effects). The calculations were performed at the B3LYP/cc pVTZ (H,C,N,O) and Stuttgart 1997 ECP (Fe) level of theory. The multiplicity is 16 and frequencies are unscaled. Calculated stick spectra were convoluted with a Gaussian envelope of FWHM = 7 cm^{-1}. Right: A zoom into the N_2 stretching vibration region. Calculated lines were convoluted with a Gaussian envelope of FWHM = 3.5 cm^{-1}. Insets show associated geometry optimized structures.

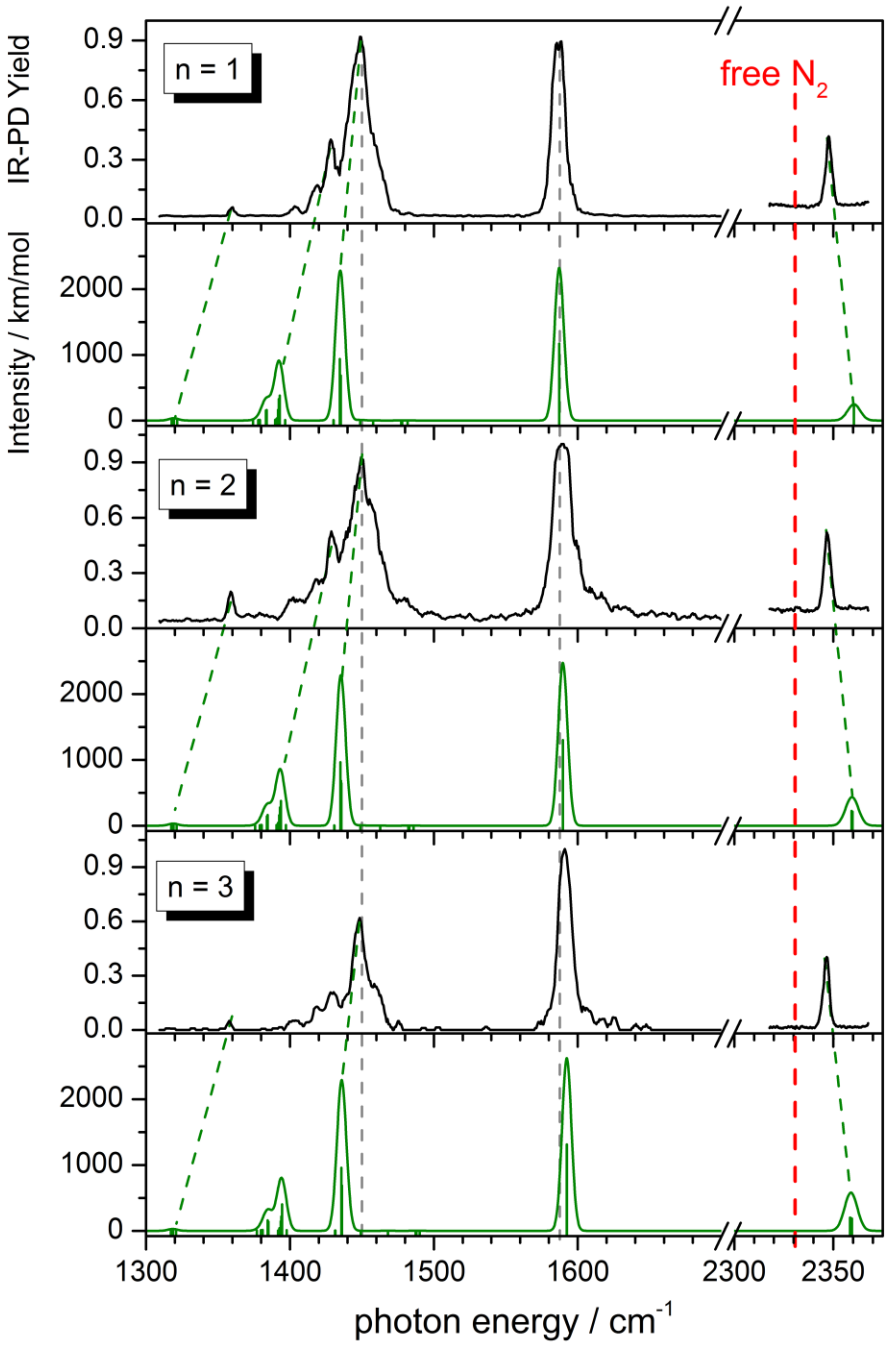

Figure S5: IR-PD spectra of $[Fe_3O(OAc)_6(N_2)_n]^+$ (n=1,2,3) at 26 K (black curves) and calculated IR absorption spectra of geometry optimized $[Fe_3O(OAc)_6(N_2)_n]^+$ (n=1,2,3) (green curves) in the range of 1300 – 2400 cm^{-1}. The calculations were performed at the PBE0 /cc-pVTZ (H, C, N, O) and Stuttgart 1997 ECP (Fe) level of theory. The multiplicity is 16 and frequencies are scaled with 0.951 (0.946) above 2300 cm^{-1} (below 2300 cm^{-1}). Calculated stick spectra were convoluted with a Gaussian envelope of FWHM = 7 cm^{-1}. The calculated intensities above 2300 cm^{-1} were multiplied by a factor of 20 for clarity

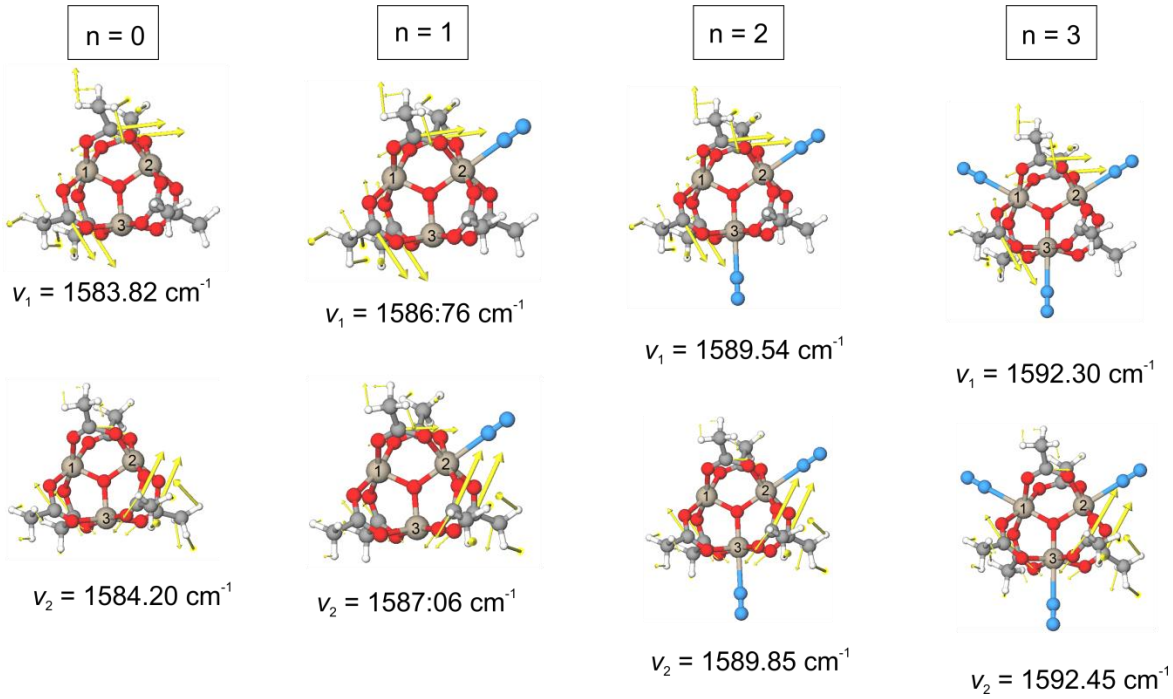

Figure S6: Displacement vectors and vibrational frequencies of IR active asymmetric carboxylate stretching vibrations in $Fe_3O(OAc)_6(N_2)_n]^+$ (n = 0 - 3) The calculations were performed at the B3LYP/cc-pVTZ (H, C, N, O) and Stuttgart 1997 ECP (Fe) level of theory. The multiplicity is 16 and frequencies are scaled with 0.986.

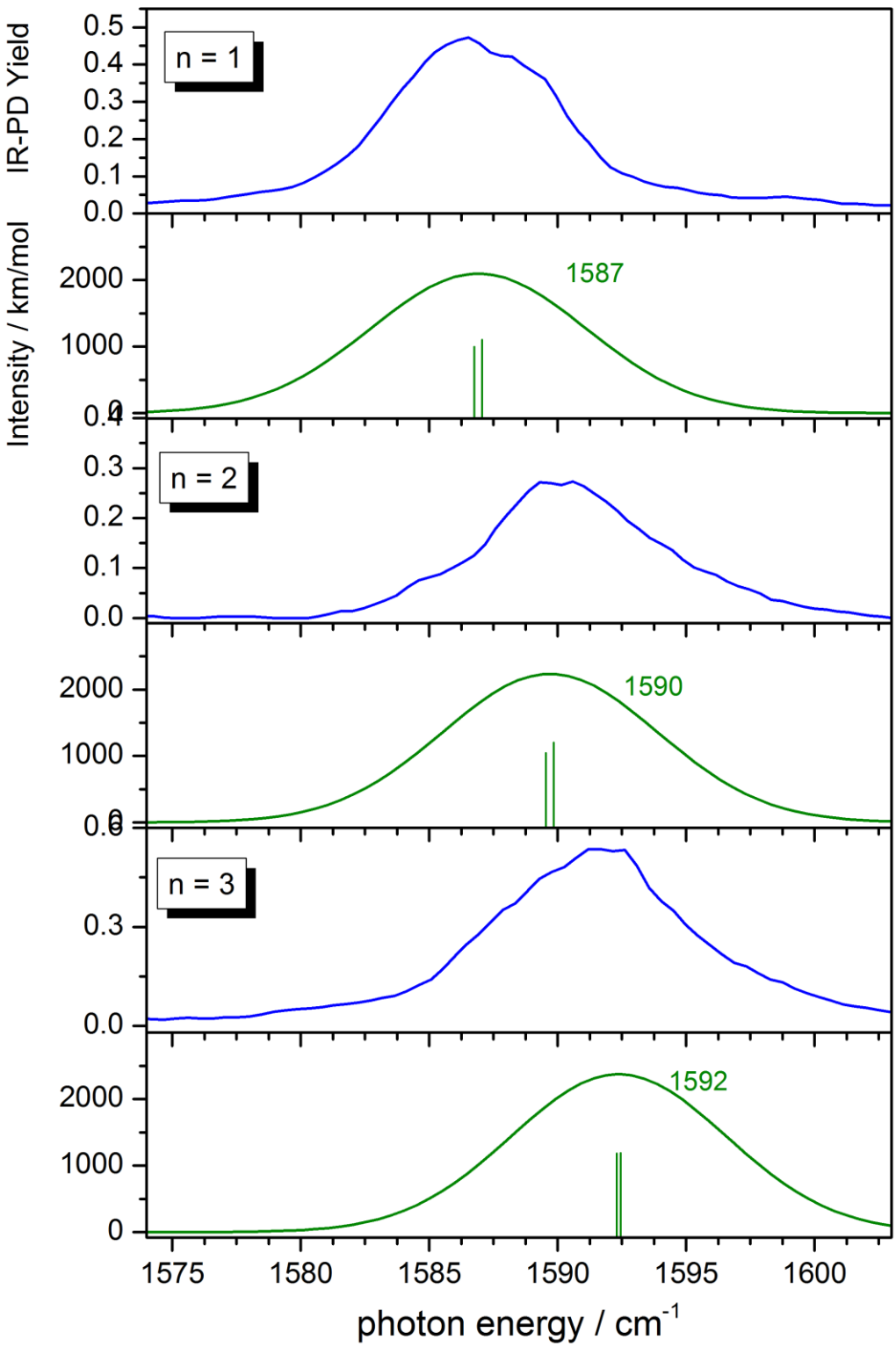

Figure S7: IR-PD spectra of $[Fe_3O(OAc)_6(N_2)_n]^+$ (n = 1,2,3) at 26 K (black curves) and calculated IR absorption spectra of geometry optimized $[Fe_3O(OAc)_6(N_2)_n]^+$ (n = 1,2,3) (green sticks and curves, FWHM = 7 cm^{-1} assumed) in the range of the asymmetric carboxylate stretching vibration. The calculations were performed at the B3LYP/cc-pVTZ (H, C, N, O) and Stuttgart 1997 ECP (Fe) level of theory. The multiplicity is 16 and frequencies are scaled with 0.986.

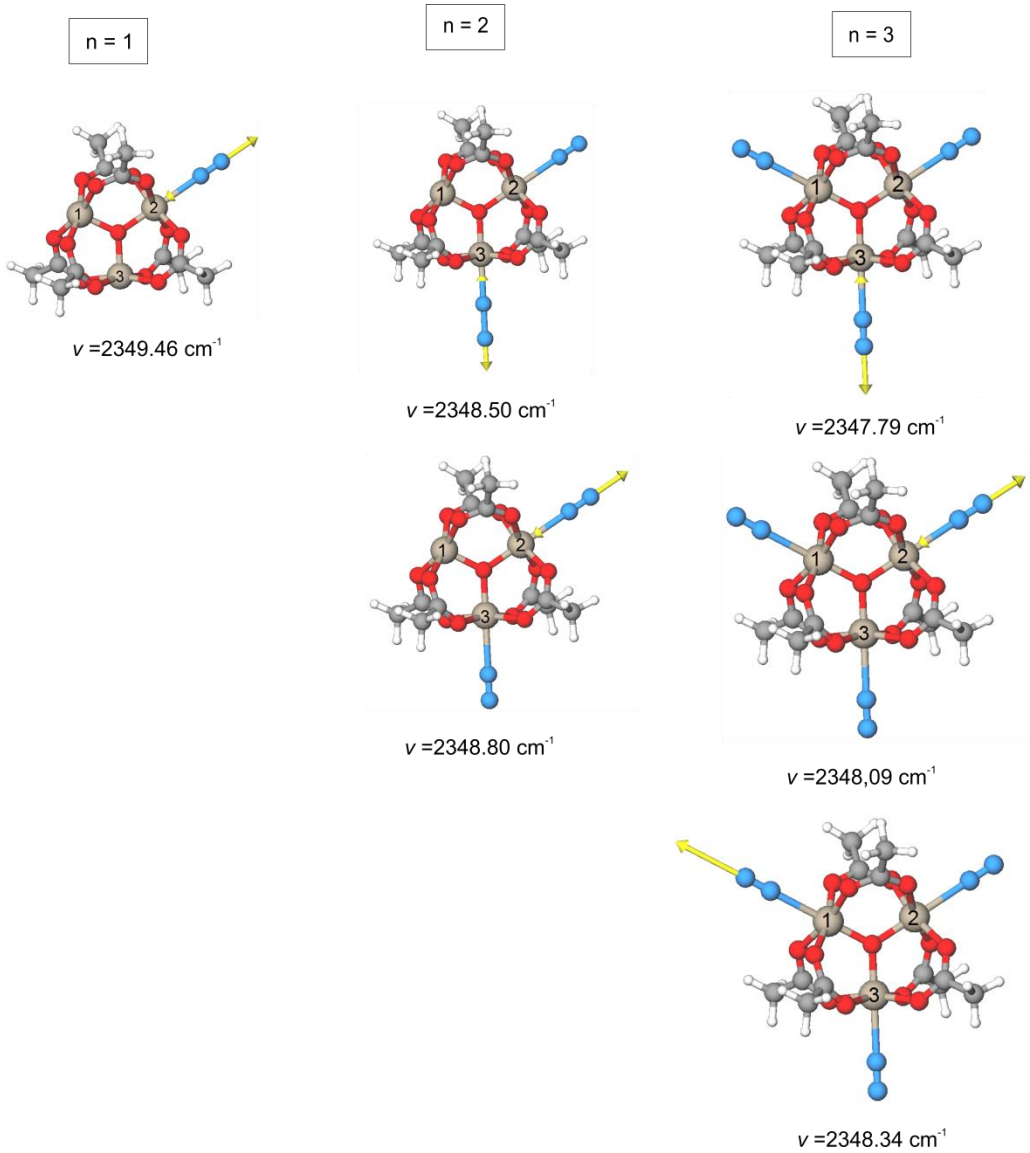

Figure S8: Displacement vectors and vibrational frequencies of IR active N-N stretching vibrations in $Fe_3O(OAc)_6(N_2)_n]^+$. The calculations were performed at the B3LYP/cc-pVTZ (H, C, N, O) and Stuttgart 1997 ECP (Fe) level of theory. The multiplicity is 16 and frequencies are scaled with 0.951.

Table S2: Structural data of $[Fe_3O(OAc)_6(N_2)_n]^+$ (n=0,1,2,3) by DFT at B3LYP/cc-pVTZ (H, C, N, O) and Stuttgart 1997 ECP (Fe) level of theory. The multiplicity is 16. Note that the calculated N-N bond length of free N_2 is 1.091 Å.

	$[Fe_3O(OAc)_6]^+$	**$[Fe_3O(OAc)_6(N_2)_1]^+$**	**$[Fe_3O(OAc)_6(N_2)_2]^+$**	**$[Fe_3O(OAc)_6(N_2)_3]^+$**
Fe-$O_{central}$ distance / Å	1.892 1.893 1.892	1.884 1.913 1.884	1.880 1.909 1.908	1.905 1.905 1.904
Fe-Fe distance / Å	3.271 3.271 3.269	3.298 3.238 3.303	3.270 3.269 3.329	3.300 3.301 3.296
Fe-N distance / Å	-	2.451	2.476 2.476	2.501 2.497 2.499
N<u>N</u>-<u>O</u> distances/ Å	-	3.046 3.046 3.049 3.046	3.041 3.042 3.043 3.044 3.041 3.043 3.046 3.046	3.041 3.038 3.042 3.042 3.041 3.040 3.042 3.043 3.039 3.039 3.042 3.039
N-N bond length/ Å	-	1.089	1.089 1.089	1.089 1.089 1.089 1.089

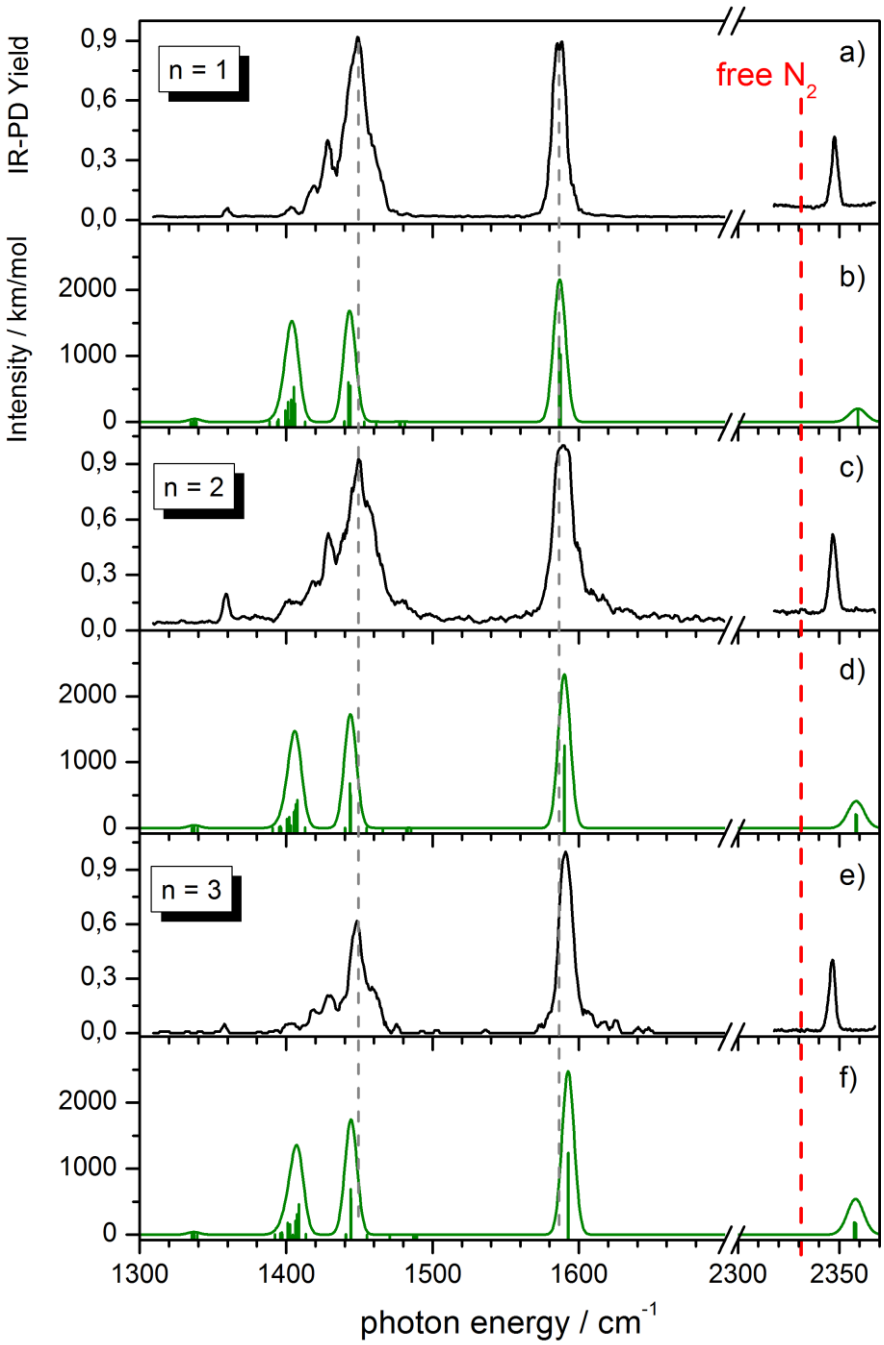

Figure S9: IR-PD spectra of $[Fe_3O(OAc)_6(N_2)_n]^+$ (n=1,2,3) at 26 K (black curves) and calculated IR absorption spectra of geometry optimized $[Fe_3O(OAc)_6(N_2)_n]^+$ (n = 1,2,3) (green curves) in the range of 1300 - 2400 cm^{-1}. The calculations were performed at the B3P86/cc-pVTZ (H, C, N, O) and Stuttgart 1997 ECP (Fe) level of theory. The multiplicity is 16 and frequencies are scaled with 0.968 (0.949) above 2300 cm^{-1} (below 2300 cm^{-1}). Calculated stick spectra were convoluted with a Gaussian envelope of FWHM = 7 cm^{-1}. The calculated intensities above 2300 cm^{-1} were multiplied by a factor of 20 for clarity.

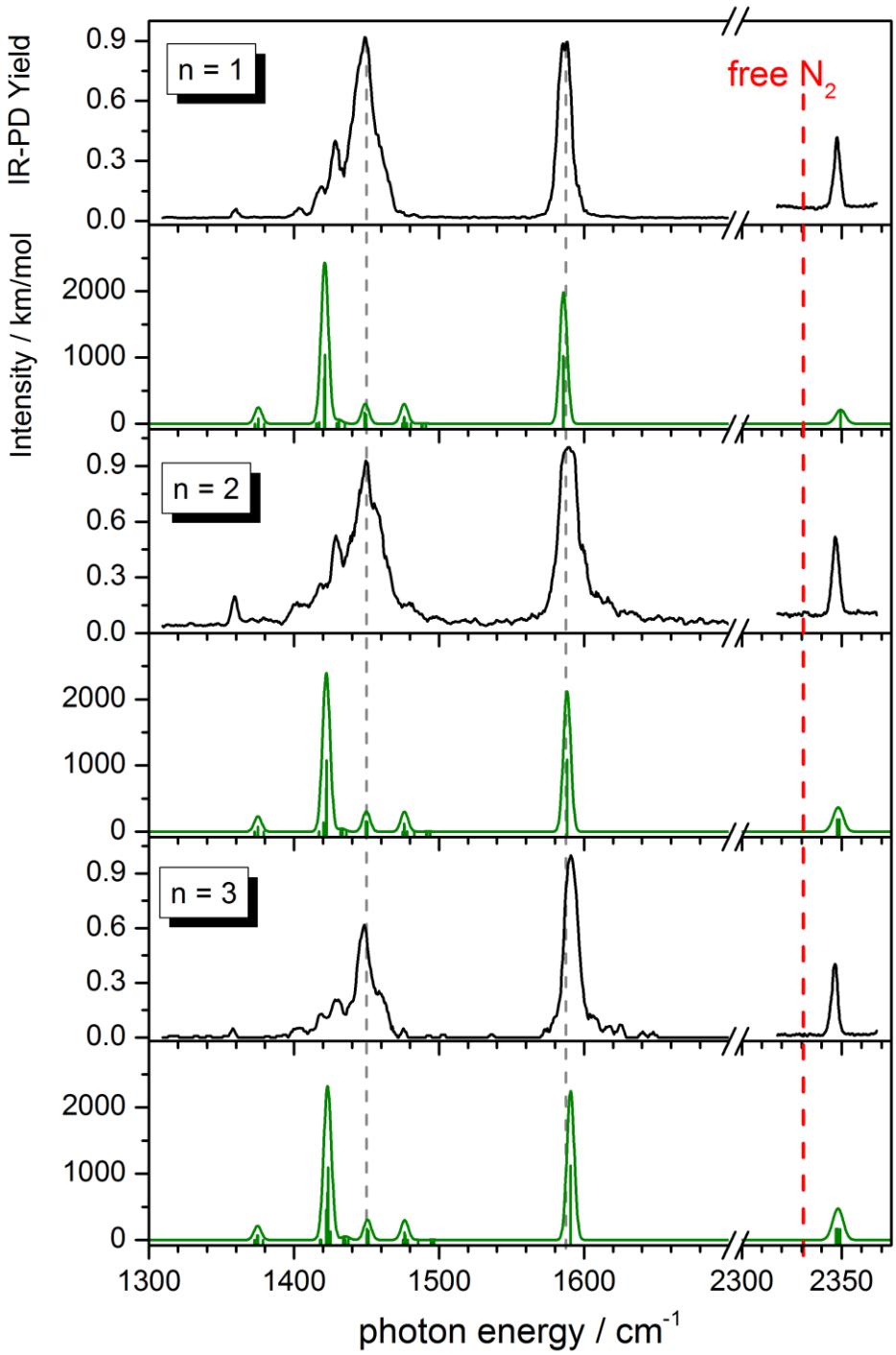

Figure S10: IR-PD spectra of $[Fe_3O(OAc)_6(N_2)_n]^+$ (n=1,2,3) at 26 K (black curves) and calculated IR absorption spectra of geometry optimized $[Fe_3O(OAc)_6(N_2)_n]^+$ (n=1,2,3) (green curves) in the range of 1300 – 2400 cm^{-1}. The calculations were performed at the TPSSh/cc-pVTZ (H, C, N, O) and Stuttgart 1997 ECP (Fe) level of theory. The multiplicity is 16 and frequencies are scaled with 0.989 (0.962) above 2300 cm^{-1} (below 2300 cm^{-1}). Calculated stick spectra were convoluted with a Gaussian envelope of FWHM = 5 cm^{-1}. The calculated intensities above 2300 cm^{-1} were multiplied by a factor of 20 for clarity.

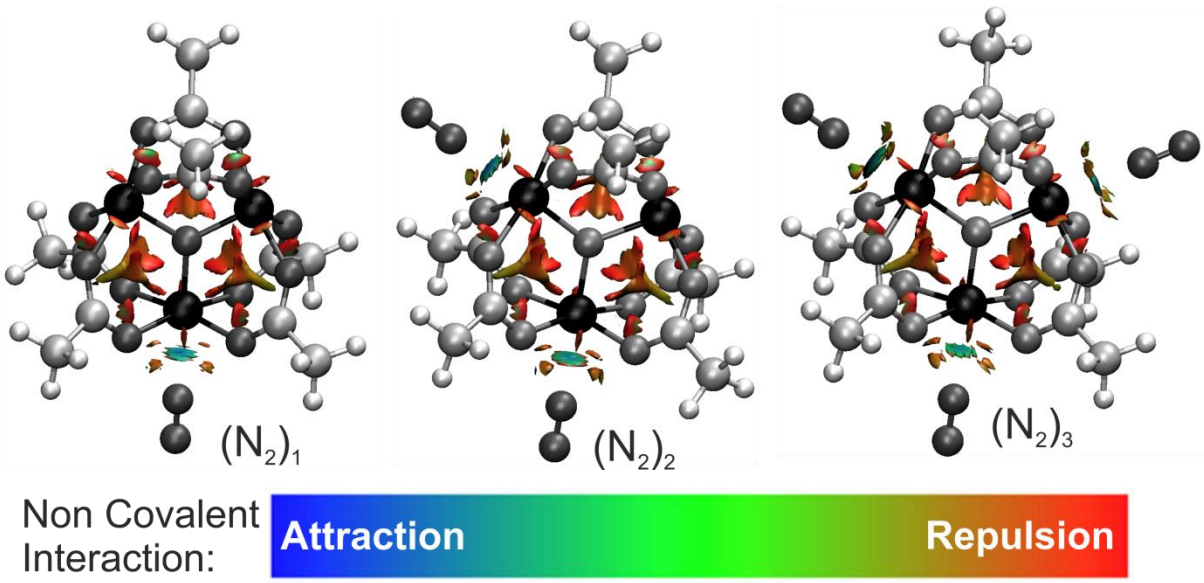

Figure S11: Geometry optimized structure and NCI plots of $[Fe_3O(OAc)_6(N_2)_{1\text{-}3}]^+$ by DFT calculations at the B3LYP/cc-pVTZ (H, C, N O) and Stuttgart 1997 ECP (Fe) level of theory. The atom colors are shown in grey scale for clarity.

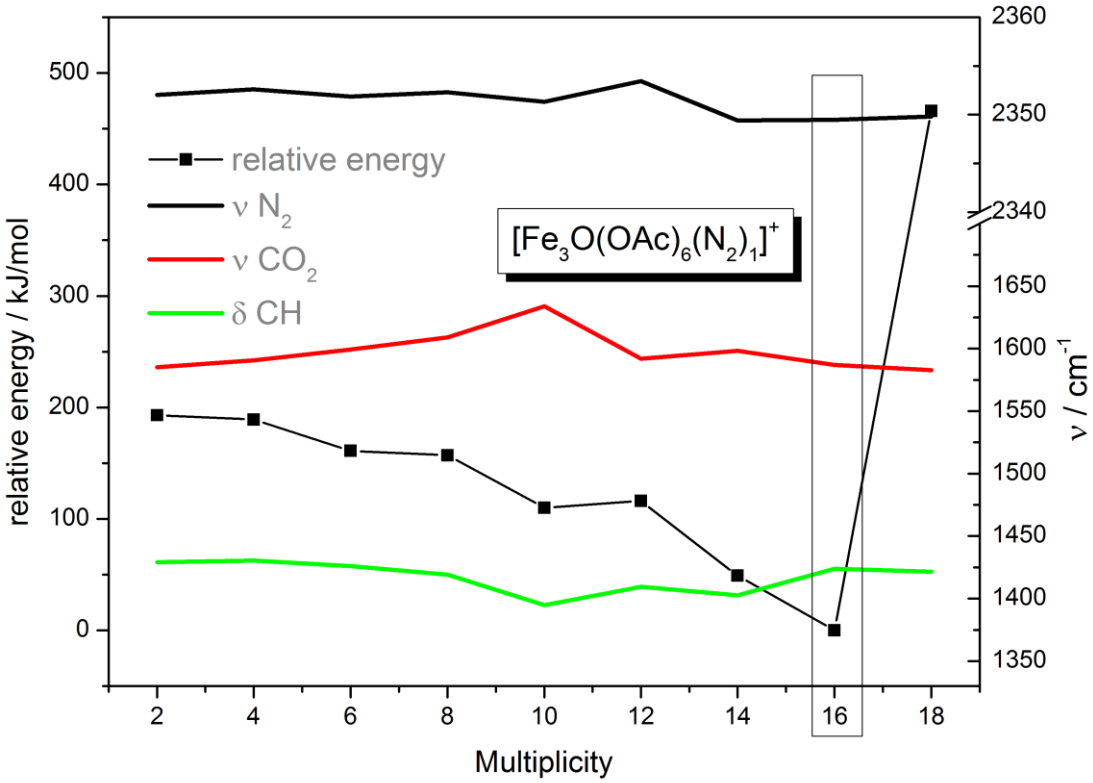

Figure S12: Relative energies and vibrational frequencies of $[Fe_3O(OAc)_6(N_2)_1]^+$ as a function of the multiplicity. The geometry was fully optimized for each multiplicity. The DFT calculations were performed at the B3LYP/cc-pVTZ (H, C, N, O) and Stuttgart 1997 ECP (Fe) level of theory.

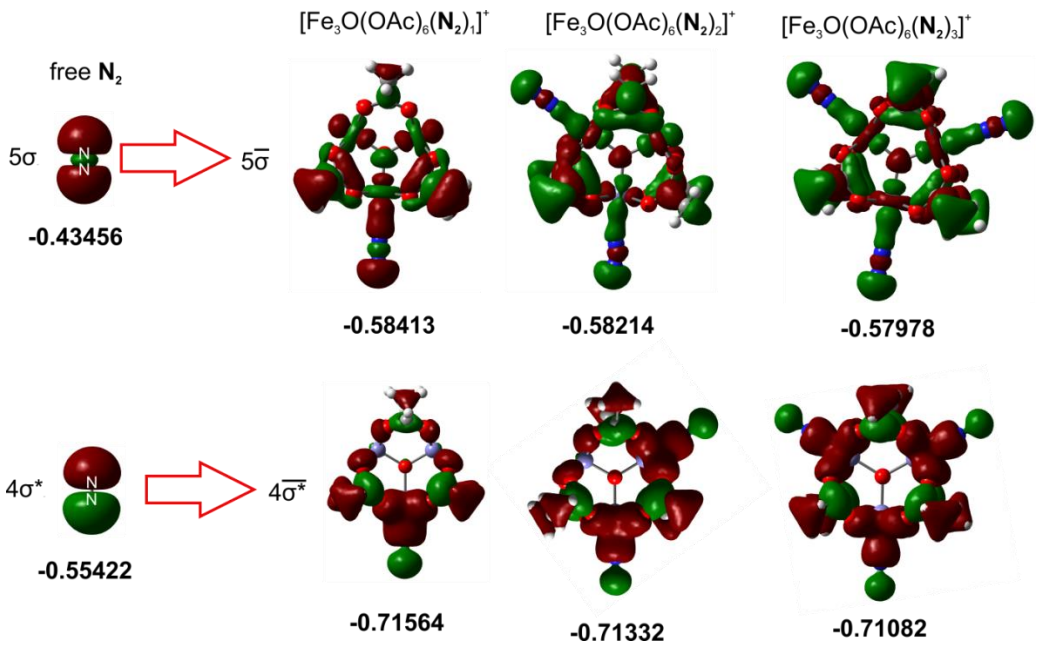

Figure S13: Left: 4σ* and 5σ molecular orbitals of isolated N_2. Right: Selected molecular orbitals of **$[Fe_3O(OAc)_6(N_2)_n]^+$** involving the former 4σ*(N_2) and 5σ(N_2) orbitals. The 4σ* and 5σ MO's of the N_2 unit overlap with orbitals of the **$[Fe_3O(OAc)_6]^+$** unit. The 4σ* electron density delocalizes into the whole complex, which leads to a slight increase of the bond order of the N_2 unit.

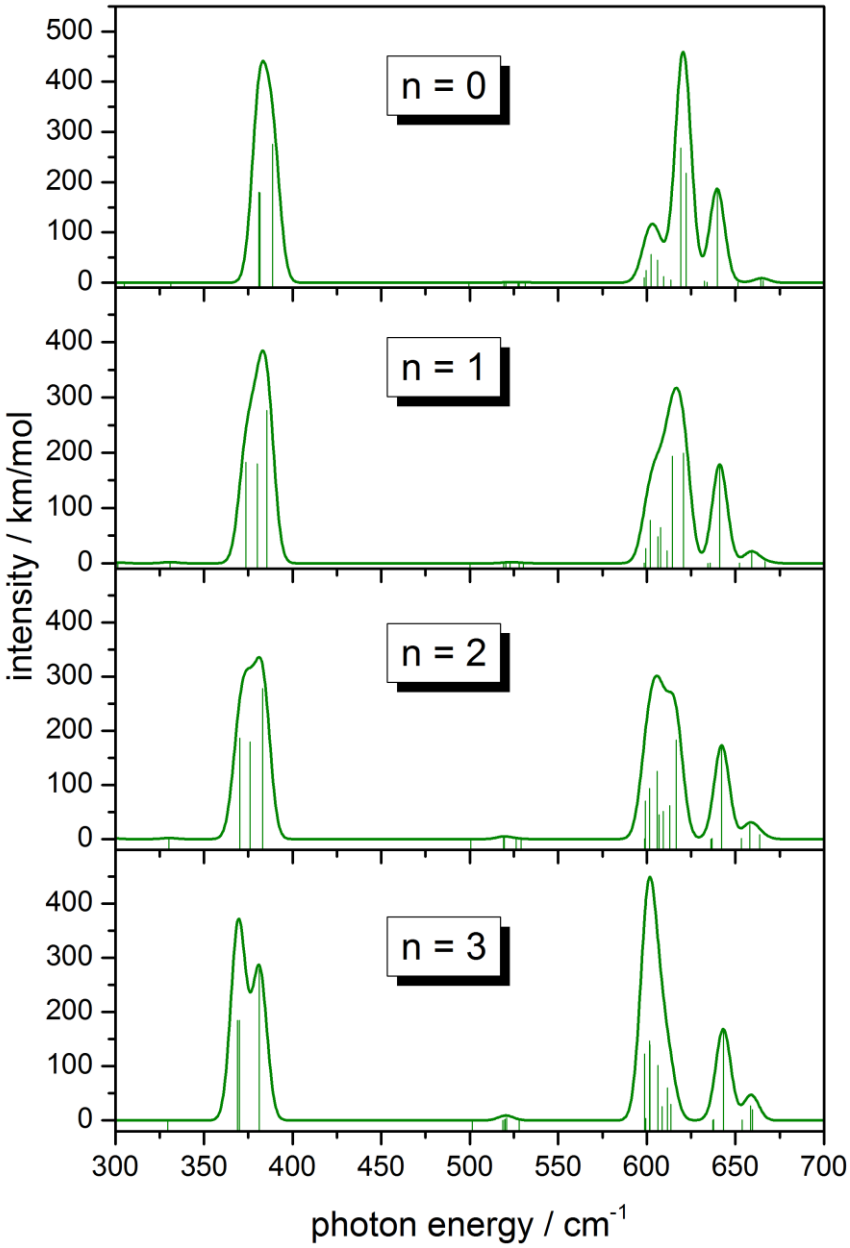

Figure S14: Calculated IR absorption spectra of geometry optimized $[Fe_3O(OAc)_6(N_2)_n]^+$ (n=1,2,3) in the range of 300 – 700 cm^{-1}. The calculations were performed at the B3LYP/cc-pVTZ (H, C, N, O) and Stuttgart 1997 ECP (Fe) level of theory. The multiplicity is 16 and frequencies are scaled with 0.986. Calculated stick spectra were convoluted with a Gaussian envelope of FWHM = 5 cm^{-1}.

10.1.4 Details of the IR-PD Spectra

Observed Masses

$[Fe_3O(OAc)_6(N_2)_1]^+$:

565.9 (Parent)

537.9 (Fragment)

$[Fe_3O(OAc)_6(N_2)_2]^+$:

593.9 (Parent)

565.9 (Fragment)

$[Fe_3O(OAc)_6(N_2)_3]^+$:

621.9 (Parent)

565.9 (Fragment)

593.9 (Fragment)

IR – Power Curve

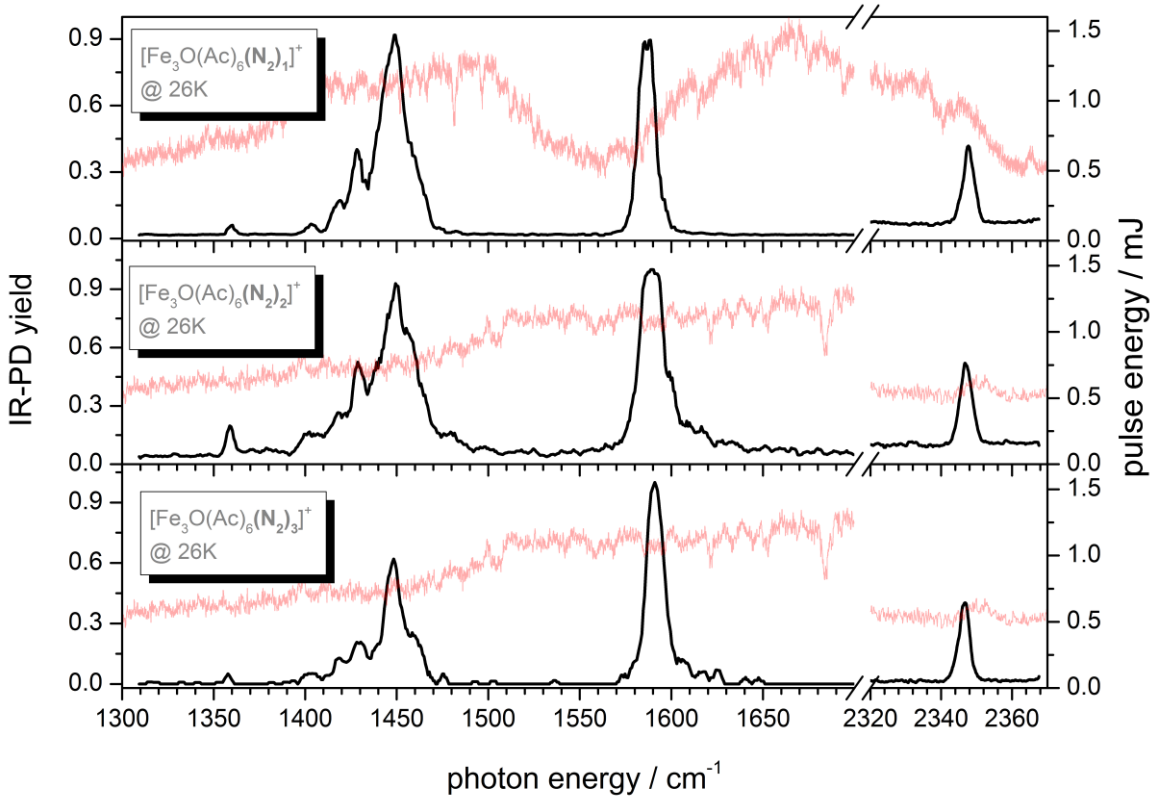

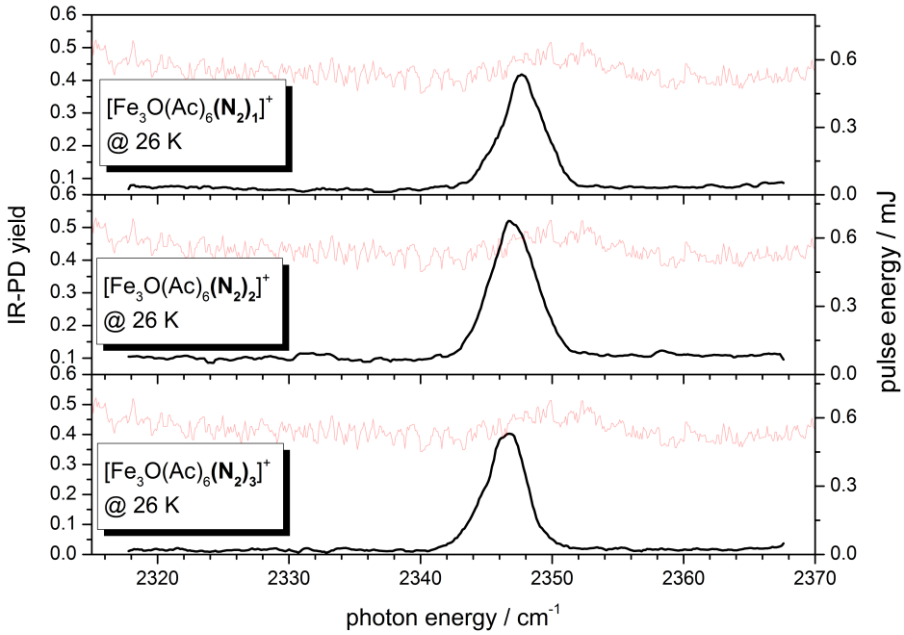

Figure S15: IR-MD spectra of $[Fe_3O(OAc)_6(N_2)_n]^+$ (n=1,2,3) at 26 K (black lines) and laser power curves (red lines).

10.1.5 XYZ Files of Geometry Optimized $[Fe_3O(OAc)_6(N_2)_n]^+$ (B3LYP, cc-pVTZ, Stuttgart Dresden ECP)

$[Fe_3O(OAc)_6]^+$

C	-7.53798	-17.72381	-2.90914
C	-8.72985	-17.80218	-2.00244
H	-8.91205	-16.84205	-1.52765
H	-8.51032	-18.52988	-1.21754
H	-9.60439	-18.14589	-2.54733
C	-4.32323	-19.42052	-3.05628
C	-3.59747	-20.47165	-2.27040
H	-2.64269	-20.66457	-2.76503
H	-4.16266	-21.39971	-2.26220
H	-3.39359	-20.12487	-1.26151
C	-5.63766	-13.94424	-4.83758
C	-6.12867	-12.53390	-4.70035
H	-5.85303	-12.12362	-3.73326
H	-7.21890	-12.54685	-4.76879
H	-5.75060	-11.91842	-5.51222
C	-2.42159	-15.63289	-4.95488
C	-0.97452	-15.24321	-4.89779
H	-0.37540	-16.14892	-5.01726
H	-0.73354	-14.80228	-3.93480
H	-0.72852	-14.56865	-5.71328
C	-7.48510	-17.24818	-7.53020
C	-8.68824	-17.09671	-8.41241
H	-9.45600	-16.56174	-7.84873
H	-9.09034	-18.07164	-8.67580
H	-8.44653	-16.51791	-9.29876
C	-4.26086	-18.92548	-7.67513
C	-3.52751	-19.77875	-8.66682
H	-2.46424	-19.75925	-8.42100
H	-3.63412	-19.35720	-9.66485
H	-3.88522	-20.80279	-8.63977
Fe	-4.86157	-16.48760	-3.43988
Fe	-6.15542	-18.80965	-5.34655
Fe	-4.81767	-16.15019	-6.69279
O	-5.27829	-17.14922	-5.15837
O	-6.61958	-16.90086	-2.61129
O	-7.50332	-18.49467	-3.91502
O	-4.15933	-18.20835	-2.72295
O	-5.04149	-19.79988	-4.03074
O	-5.46480	-14.62032	-3.77900
O	-5.44658	-14.39418	-6.00804
O	-3.00388	-15.91891	-3.86494
O	-2.97840	-15.68154	-6.09310
O	-7.47321	-18.21471	-6.70803
O	-6.55735	-16.39083	-7.63224
O	-4.99954	-19.49712	-6.81901
O	-4.08487	-17.67007	-7.73843

$[Fe_3O(OAc)_6(N_2)_1]^+$:

C	-7.54966	-17.72287	-2.90713
C	-8.74707	-17.77991	-2.00441
H	-8.92455	-16.81126	-1.54526
H	-8.53622	-18.49599	-1.20665
H	-9.62223	-18.12451	-2.54771
C	-4.30408	-19.41870	-3.05071
C	-3.55311	-20.45967	-2.27304
H	-2.59342	-20.62489	-2.76807
H	-4.09536	-21.40125	-2.27052
H	-3.35739	-20.11557	-1.26151
C	-5.64550	-13.95817	-4.83529
C	-6.13072	-12.54551	-4.69746
H	-5.84217	-12.13304	-3.73497
H	-7.22174	-12.55521	-4.75155
H	-5.76049	-11.93373	-5.51559
C	-2.43288	-15.64266	-4.96525
C	-0.98764	-15.24486	-4.90796
H	-0.38300	-16.14565	-5.03587
H	-0.74737	-14.80903	-3.94252
H	-0.74759	-14.56295	-5.71919
C	-7.49721	-17.23369	-7.53487
C	-8.70827	-17.05785	-8.40334
H	-9.44950	-16.48762	-7.83875
H	-9.14568	-18.02213	-8.64814
H	-8.45995	-16.49965	-9.30122
C	-4.25120	-18.93105	-7.68159
C	-3.48809	-19.78327	-8.65291
H	-2.47973	-19.92770	-8.25870
H	-3.39845	-19.27684	-9.61064
H	-3.95677	-20.75618	-8.76592
Fe	-4.87544	-16.50910	-3.46097
Fe	-6.18784	-18.87439	-5.35567
Fe	-4.83389	-16.17453	-6.68102
O	-5.30104	-17.19049	-5.16509
O	-6.62433	-16.90947	-2.60805
O	-7.52001	-18.50145	-3.90640
O	-4.15290	-18.20610	-2.71476
O	-5.02727	-19.80716	-4.01650
O	-5.47802	-14.63573	-3.77707
O	-5.45411	-14.40828	-6.00508
O	-3.01510	-15.92837	-3.87587
O	-2.98774	-15.69788	-6.10400
O	-7.48672	-18.20811	-6.72391
O	-6.56301	-16.38436	-7.64116
O	-4.99250	-19.51045	-6.83302
O	-4.09078	-17.67529	-7.74988
N	-7.32900	-21.03112	-5.59175
N	-7.83876	-21.98821	-5.69543

$[Fe_3O(OAc)_6(N_2)_2]^+$:

C	-7.54422	-17.71607	-2.92077
C	-8.73803	-17.77917	-2.01321
H	-8.91658	-16.81233	-1.55068
H	-8.52199	-18.49682	-1.21831
H	-9.61439	-18.12484	-2.55393
C	-4.30245	-19.40901	-3.06457
C	-3.55660	-20.45059	-2.28218
H	-2.59595	-20.62010	-2.77380
H	-4.10180	-21.39047	-2.27898
H	-3.36297	-20.10473	-1.27085
C	-5.65684	-13.95017	-4.83094
C	-6.16501	-12.54553	-4.68361
H	-5.87599	-12.13268	-3.72137
H	-7.25608	-12.57329	-4.72863
H	-5.81134	-11.92288	-5.50083
C	-2.41981	-15.64744	-4.96061
C	-0.96765	-15.27332	-4.89452
H	-0.37716	-16.18482	-5.01179
H	-0.72789	-14.83611	-3.92953
H	-0.70882	-14.59954	-5.70674
C	-7.51200	-17.23050	-7.53545
C	-8.73894	-17.04852	-8.38166
H	-9.47344	-16.48976	-7.79727
H	-9.17603	-18.01183	-8.63106
H	-8.50942	-16.47862	-9.27716
C	-4.24077	-18.94319	-7.68310
C	-3.46288	-19.80630	-8.63434
H	-2.46141	-19.94892	-8.22246
H	-3.35726	-19.31091	-9.59619
H	-3.93144	-20.77959	-8.74495
Fe	-4.87605	-16.50604	-3.49432
Fe	-6.17501	-18.84786	-5.37015
Fe	-4.81524	-16.13586	-6.74163
O	-5.28996	-17.16550	-5.20569
O	-6.62059	-16.90053	-2.62401
O	-7.51579	-18.49194	-3.92181
O	-4.14961	-18.19640	-2.73080
O	-5.02303	-19.79715	-4.03202
O	-5.47774	-14.62812	-3.77578
O	-5.45890	-14.38976	-6.00290
O	-3.01028	-15.92182	-3.87368
O	-2.96872	-15.69337	-6.10191
O	-7.49177	-18.20975	-6.73160
O	-6.57821	-16.38352	-7.65453
O	-4.99257	-19.51648	-6.84065
O	-4.08146	-17.68879	-7.76362
N	-4.20786	-14.81072	-8.74301
N	-7.32769	-21.02648	-5.59184
N	-3.94130	-14.22706	-9.62339
N	-7.83770	-21.98450	-5.68595

$[Fe_3O(OAc)_6(N_2)_3]^+$:

C	-7.55951	-17.71257	-2.92089
C	-8.76892	-17.76494	-2.03197
H	-8.94352	-16.79855	-1.56702
H	-8.57618	-18.49092	-1.23873
H	-9.64075	-18.09591	-2.58907
C	-4.29233	-19.41947	-3.06403
C	-3.53371	-20.46893	-2.30313
H	-2.58587	-20.64198	-2.81769
H	-4.08405	-21.40584	-2.29234
H	-3.31540	-20.13057	-1.29433
C	-5.66951	-13.94121	-4.83187
C	-6.20125	-12.54310	-4.69715
H	-5.95145	-12.12810	-3.72508
H	-7.28934	-12.58398	-4.78339
H	-5.82669	-11.91384	-5.50014
C	-2.40534	-15.64994	-4.96920
C	-0.94622	-15.29766	-4.91863
H	-0.37054	-16.21115	-5.08355
H	-0.67959	-14.89714	-3.94500
H	-0.69550	-14.59868	-5.71219
C	-7.50544	-17.22680	-7.52306
C	-8.72791	-17.05277	-8.37779
H	-9.47478	-16.50927	-7.79482
H	-9.15031	-18.01968	-8.63869
H	-8.49849	-16.47289	-9.26683
C	-4.23898	-18.93702	-7.66600
C	-3.46546	-19.80008	-8.62126
H	-2.46294	-19.94541	-8.21296
H	-3.36216	-19.30337	-9.58266
H	-3.93620	-20.77234	-8.73190
Fe	-4.85784	-16.48017	-3.42680
Fe	-6.16280	-18.82377	-5.35032
Fe	-4.81682	-16.13894	-6.70875
O	-5.27895	-17.14784	-5.16059
O	-6.63416	-16.90518	-2.61054
O	-7.52380	-18.49154	-3.91832
O	-4.13569	-18.21057	-2.72130
O	-5.02720	-19.80175	-4.02209
O	-5.48433	-14.60920	-3.77218
O	-5.45859	-14.38150	-6.00046
O	-2.98984	-15.91364	-3.87732
O	-2.96289	-15.68634	-6.10592
O	-7.48546	-18.20396	-6.71715
O	-6.57498	-16.37598	-7.63717
O	-4.98675	-19.51004	-6.82022
O	-4.08010	-17.68293	-7.74627
N	-4.30072	-15.60865	-1.15372
N	-4.21136	-14.81130	-8.73985
N	-7.32742	-21.02204	-5.59002
N	-4.05662	-15.22800	-0.16256
N	-3.94854	-14.23331	-9.62515
N	-7.83815	-21.97887	-5.69264

10.1.6 Molecular Orbital Diagram of N_2

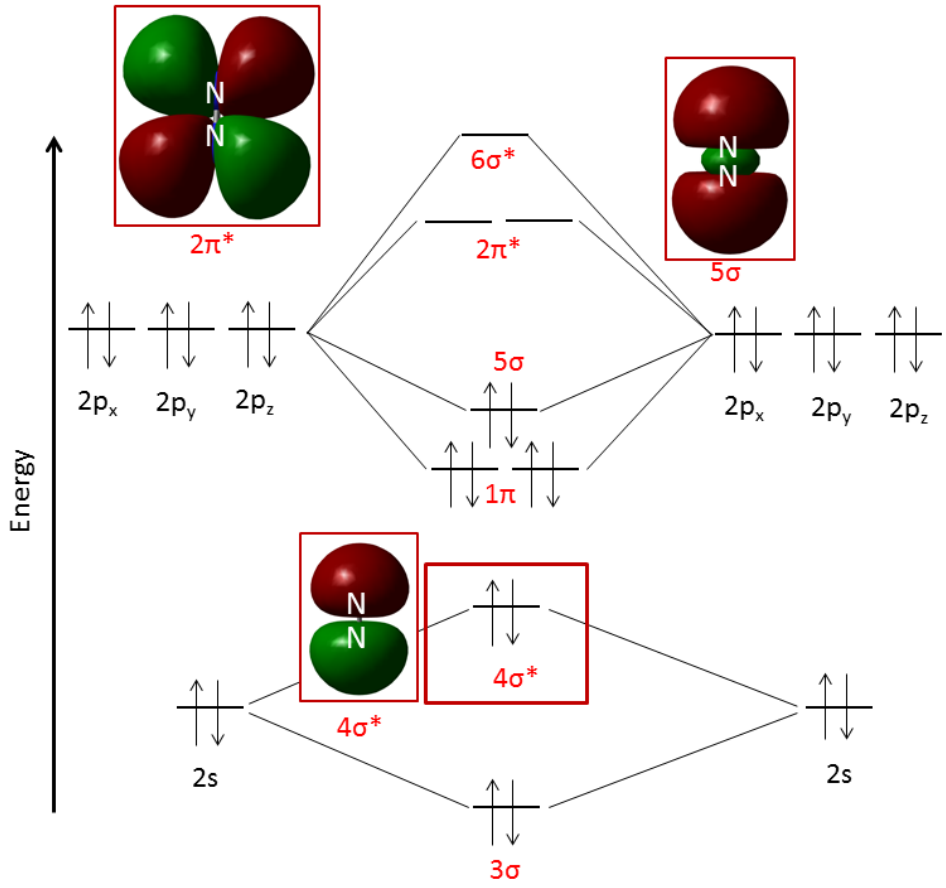

Scheme S1: Simplified molecular orbital diagram of the N_2 molecule. s-p hybridization is included, but additional connection lines are omitted for clarity.

10.1.7 Experimental and Computational Methods

We utilized a customized Fourier Transform-Ion Cyclotron Resonance (FT-ICR)-mass spectrometer (Apex Ultra, Bruker Daltonics) equipped with a Electrospray Ionization (ESI) source (Apollo 2, Bruker). Sample solutions of Iron(III) oxo acetate perchlorate hydrate ([$Fe_3O(OAc)_6(H_2O)_3(ClO_4)$]), Sigma-Aldrich, cf. Scheme 1a) in acetonitrile at concentrations of 1 x 10^{-5} mol/l were used without further purification and continuously infused into the ESI source by a syringe pump at a flow rate of 2 µL min^{-1}. The ion source was set to positive electrospray ionization mode. Nitrogen was used as drying gas with a flow rate of 6.0 L min^{-1} at 220°C. The solutions were sprayed at a nebulizer flow of 2.5 L min^{-1} and the spray shield was held at 3.6 kV.

The ESI generated ions are injected into a cryogenic hexapole ion trap passing different ion lenses, a 90 degrees ion beam bender and a quadrupole mass filter. In Source Collision Induced Dissociation (CID) of the ESI generated $[Fe_3O(OAc)_6(L)_n]^+$ ions (L = H_2O and acetonitrile, n=1,2,3) enabled us to produce the under-coordinated species $[Fe_3O(OAc)_6]^+$. The ion trap is cooled by a closed cycle Helium cryostat and held at 26 K for the measurements. Buffer or reaction gas can be introduced both pulsed and continuously. In this work we used two continuous gas inlets. The pressure is first increased by N_2 gas from 1.7 x 10^{-7} mbar up to 3.0 x 10^{-7} mbar and subsequently increased with He gas up to 4.0 x 10^{-6} mbar to accomplish N_2 attachment as well as efficient trapping and cooling of the ions. Storage of the ions for a variable time (0–10 s) allows them to react with N_2 to yield $[Fe_3O(OAc)_6(N_2)_n]^+$. The product ions are guided by electrostatic lenses into the FT-ICR cell of the so-called "infinity" type[1]. This cell is cooled at a temperature of about 10 K with a closed cycle Helium cryostat to prevent heating of the clusters by black body radiation. The cell is used for isolation and detection of the ions. It is coupled to a tunable IR laser (δn = 0.9 cm^{-1}, δt = 7 ns) to record InfraRed Photon Dissociation (IR-PD) spectra of isolated $[Fe_3O(OAc)_6(N_2)_n]^+$.

The laser is a KTP/KTA optical parametric oscillator/amplifier (OPO/A, LaserVision) system pumped by a pulsed 10 Hz injection seeded Nd^{3+}:YAG laser (Continuum, Powerlite DLS 8000). The OPA idler wave (≤ 10 mJ per pulse) can be used to record spectra within 2600–3900 cm[1]. In this work we used the difference frequency (DF) between the OPA signal and idler waves generated in a $AgGaSe_2$ crystal (0.1 – 1.2 mJ per pulse). We recorded IR-PD spectra in the range of 1200 – 2400 cm^{-1}. Each trapped and

isolated package of ions is irradiated by 10 – 15 laser pulses to yield a sufficient amount of fragment ions. The IR spectra were recorded as ion chromatograms while continuously scanning the IR frequency. An experimental IR-PD spectrum arises from a plot of the fragmentation efficiency as a function of laser frequency (ν). The IR-MPD yield $Y(\nu)$ is defined as:

$$Y(\nu) = \left(\frac{\sum_i I_i^{fr}(\nu)}{\sum_i I_i^{fr}(\nu) + \sum_i I_i^{p}(\nu)} \right) \quad (1)$$

The IR frequency was calibrated using a wave meter (821B-NIR, Bristol instruments), and we recorded laser power curves (cf. Fig. S12 in the ESI).

Optimized minimum energy structures, Gibbs energies and linear IR absorption spectra were calculated at the B3LYP[2,3] level of theory using cc-pVTZ basis sets[4] (C, H, N, O), and Stuttgart RSC 1997[5] effective core potential (Fe) basis sets, respectively, as implemented in the Gaussian 09 program package[6]. Standard convergence criteria were applied. Basis set superposition errors (BSSE) were corrected using the Counterpoise routine[7,8]. We present unrestricted DFT calculations with 15 unpaired alpha electrons yielding a spin multiplicity of 16 with other multiplicies (2 - 18) found significantly less stable (c.f. Fig. S9.). We scale calculated frequencies with two different scaling factors: One scaling factor (0.951) is specifically designed to elucidate N_2 stretching bands in $[Fe_3O(OAc)_6(N_2)_n]^+$. It scales calculated N_2 stretching frequencies such that a calculated free N_2 stretching vibration frequency matches the experimental value[9,10] of 2330cm^{-1}. This approach conveniently reveals any effects of Fe-N_2 coordination on N_2 stretching frequencies. A second unspecific scaling factor (0.986) is applied for all other bands. It scales the calculated asymmetric carboxylate stretching vibration frequencies of $[Fe_3O(OAc)_6(N_2)_1]^+$ to match our own experimental value of 1587 cm^{-1}. Unscaled spectra are provided in the supplement (cf. Fig. S4). The usage of two different scaling factors for high and low frequency vibrations is validated by many theoretical studies[11-13]. Especially frequencies calculated via DFT/B3LYP benefit from this method[14].

A Natural Population Analysis (NPA) was performed with the NB0 5.9 program[15]. We elucidate weak interactions such as hydrogen bonds or van der Waals-interactions in geometry optimized structures using the non-covalent interaction (NCI) technique[16]. This method and its application to intramolecular H-bonds has been described previously[17-19]. In short, the electron density ρ and its reduced gradient $s(\rho)$ of a

molecule are topologically analyzed in regions of small electron density and small reduced gradient. Non-covalent interactions prevail in areas where *s(ρ)* is close to zero (minima of electron density). Iso-surfaces of the reduced gradient *s(ρ)* in conjunction with a RGB-color ranking scheme visualize non-covalent interactions. The RGB-color indicates the sign of the second eigenvalue, λ_2, of the Hessian matrix. Red corresponds to positive λ_2, (repulsive areas, e.g. steric repulsion), blue to negative λ_2 (areas of favorable interactions, e.g. hydrogen bonds) and green to weak delocalized interactions (λ_2 is approximately zero). We use *Multiwfn*[20] in conjunction with *Visual Molecular Dynamics* VMD[21] software to plot these iso-surfaces.

1. P. Caravatti and M. Allemann, *Org. Mass Spectrom.*, 1991, 26, 514-518.
2. A. D. Becke, *J. Chem. Phys.*, 1993, 98, 5648-5652.
3. B. Miehlich, A. Savin, H. Stoll and H. Preuss, *Chem. Phys. Lett.*, 1989, 157, 200-206.
4. T. H. Dunning, *J. Chem. Phys.*, 1989, 90, 1007-1023.
5. M. Dolg, H. Stoll, H. Preuss and R. M. Pitzer, *J. Phys. Chem.*, 1993, 97, 5852-5859.
6. M. J. Frisch, et al.,, 2009.
7. S. Simon, M. Duran and J. J. Dannenberg, *J. Chem. Phys.*, 1996, 105, 11024-11031.
8. S. F. Boys and F. Bernardi, *Mol. Phys.*, 1970, 19, 553-566.
9. E. P. Kündig, M. Moskovits and G. A. Ozin, *Can. J. Chem.*, 1973, 51, 2710-2721.
10. K. P. Huber and G. Herzberg, *Constants of Diatomic Molecules*, Van Norstrand, New York, 1979.
11. P. Sinha, S. E. Boesch, C. Gu, R. A. Wheeler and A. K. Wilson, *J. Phys. Chem. A*, 2004, 108, 9213-9217.
12. J. P. Merrick, D. Moran and L. Radom, *J. Phys. Chem. A*, 2007, 111, 11683-11700.
13. H. Yoshida, K. Takeda, J. Okamura, A. Ehara and H. Matsuura, *J. Phys. Chem. A*, 2002, 106, 3580-3586.
14. M. D. Halls, J. Velkovski and H. B. Schlegel, *Theor Chem Acc*, 2001, 105, 413-421.
15. J. K. B. E.D. Glending, A.E. Reed, J.E Carpenter, J.A. Bohmann, C.M. Morales and F. Weinhold, Theoretical Chemistry Institute, University of Wisconsin, Madison, WI, 2009.
16. J. Contreras-García, E. R. Johnson, S. Keinan, R. Chaudret, J.-P. Piquemal, D. N. Beratan and W. Yang, *Journal of Chemical Theory and Computation*, 2011, 7, 625-632.
17. R. Chaudret, B. de Courcy, J. Contreras-Garcia, E. Gloaguen, A. Zehnacker-Rentien, M. Mons and J. P. Piquemal, *PCCP*, 2014, 16, 9876-9891.
18. E. R. Johnson, S. Keinan, P. Mori-Sánchez, J. Contreras-García, A. J. Cohen and W. Yang, *J. Am. Chem. Soc.*, 2010, 132, 6498-6506.
19. A. Bouchet, J. Klyne, G. Piani, O. Dopfer and A. Zehnacker, *PCCP*, 2015, 17, 25809-25821.
20. T. Lu and F. Chen, *Journal of Computational Chemistry*, 2012, 33, 580-592.
21. W. Humphrey, A. Dalke and K. Schulten, *J. Mol. Graphics*, 1996, 14, 33-38.

10.1.8 $^{15}N_2$ Experiments

Isotope labeling of the N_2 molecule serves to validate our assignment of the observed mass peaks to the N_2 complexes (cf. Table S3) as well as the assignment of the recorded IR-PD bands above 2200 cm^{-1} to the N_2 stretching frequencies. Exchanging the $^{14}N_2$ reaction gas with $^{15}N_2$ enriched gas (99,999 %, Sigma-Aldrich) leads to expected shifts of N_2 associated mass peaks: +2 m/z per $^{14}N_2$ to $^{15}N_2$ exchange (cf. Fig. S14 and Table S3). Residual $^{14}N_2$ gas in the hexapole leads prominent peaks of mixed $^{14}N_2/^{15}N_2$ species. Flushing the apparatus with $^{15}N_2$ enriched gas over a few hours suffices to observe exclusive $^{15}N_2$ complexes.

Table S3: Compilation of ESI-MS data on $[Fe_3O(OAc)_6(^XN_2)_n]^+$ (n=1,2,3; X = 14, 15; OAc=CH_3CO_2). The indicated mass labels refer to the most abundant isotope peaks.

Species	m/z
$[Fe_3O(OAc)_6]^+$	538
$[Fe_3O(OAc)_6(^{14}N_2)_1]^+$	566
$[Fe_3O(OAc)_6(^{15}N_2)_1]^+$	568
$[Fe_3O(OAc)_6(^{14}N_2)_2]^+$	594
$[Fe_3O(OAc)_6(^{14}N_2)_1(^{15}N_2)_1]^+$	596
$[Fe_3O(OAc)_6(^{15}N_2)_2]^+$	598
$[Fe_3O(OAc)_6(^{14}N_2)_3]^+$	622
$[Fe_3O(OAc)_6(^{14}N_2)_2(^{15}N_2)_1]^+$	624
$[Fe_3O(OAc)_6(^{14}N_2)_2(^{15}N_2)_2]^+$	626
$[Fe_3O(OAc)_6(^{15}N_2)_3]^+$	628

The IR-PD spectrum of $[Fe_3O(OAc)_6(^{14}N_2)_1(^{15}N_2)_1]^+$ (cf. Fig. S16a) reveals two bands at 2268 cm^{-1} and 2347 cm^{-1}. The $^{15}N_2$ stretching frequency decreases by 79 cm^{-1} with respect to the frequency of $^{14}N_2$. Published Raman spectroscopy data[I,II] on free $^{14}N_2$ (ν_0 = 2330 cm^{-1}) and $^{15}N_2$ (ν_0 = 2252 cm^{-1}) indicates a red shift of 78 cm^{-1}. Note, that mass scaling of the $^{14}N_2$ vibration frequency to $^{15}N_2$ yields a frequency of 2251 cm^{-1}.

Our value of 2268 cm^{-1} for the $^{15}N_2$ stretching frequency in $[Fe_3O(OAc)_6(^{14}N_2)_1(^{15}N_2)_1]^+$ represents a blue shift of 16 cm^{-1} with respect to 2252 cm^{-1} (free $^{15}N_2$ vibration frequency by Raman spectroscopy) or a blue shift of 17 cm^{-1} in respect to 2251 cm^{-1}

(free $^{15}N_2$ vibration frequency by mass scaling from $^{14}N_2$). The blue shift of $^{15}N_2$ in the complex is nearly identical with respect to the blue shift of $^{14}N_2$ frequency. Calculated linear IR spectra of $[Fe_3O(OAc)_6(^{14}N_2)_1(^{15}N_2)_1]^+$ (cf. Fig S16b) as well as $[Fe_3O(OAc)_6\,(^{15}N_2)_2]^+$ and $[Fe_3O(OAc)_6\,(^{14}N_2)_2]^+$ reveal a red shift of 79 cm^{-1} with the given scaling factor of 0.951.

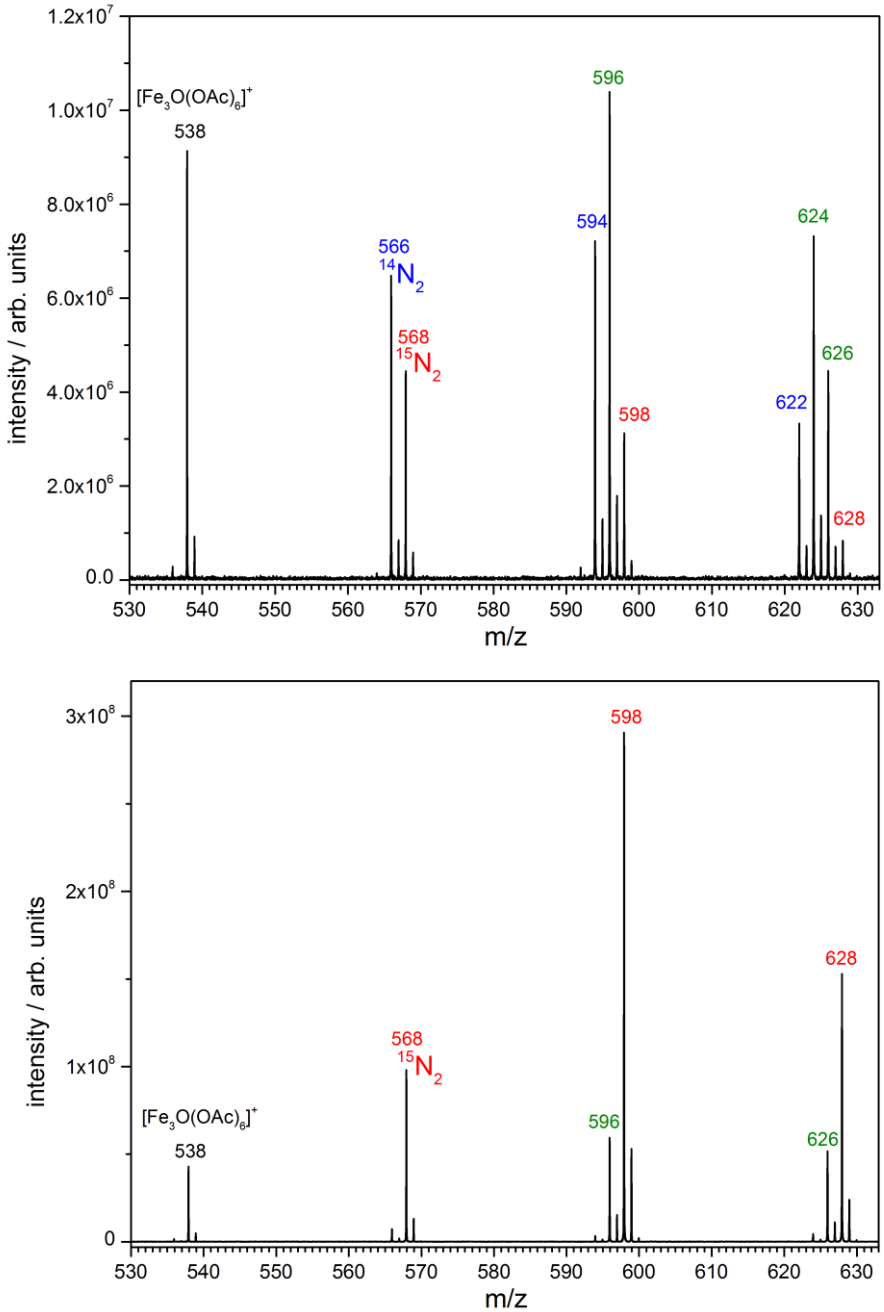

Figure S16: Cationic mass spectra of a $[Fe_3O(OAc)_6(H_2O)_3]ClO_4$ acetonitrile solution after collision induced dissociation and subsequent $^{14}N_2$ and/or $^{15}N_2$ coordination to $[Fe_3O(OAc)_6]^+$ The upper spectrum was measured directly after $^{15}N_2$ addition to the hexapole. The lower spectrum was measured after 3h of flushing with $^{15}N_2$ gas. For peak assignment refer to Table S3.

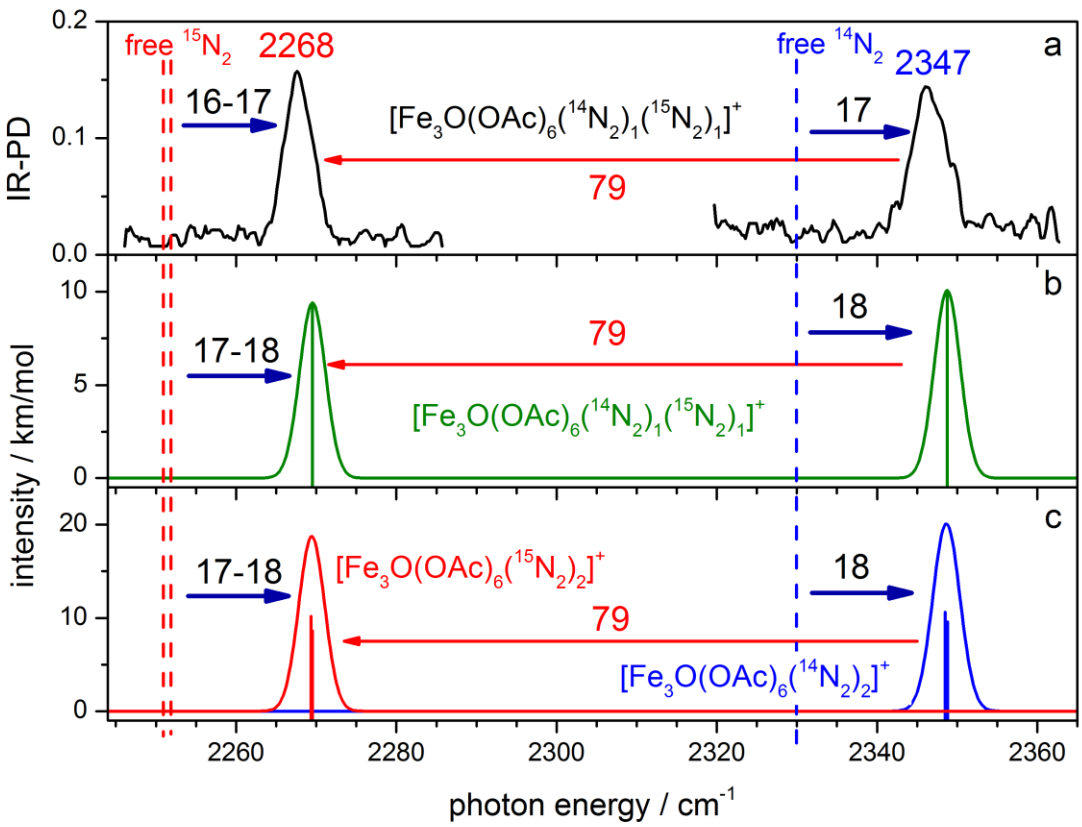

Figure S17: a) IR-PD spectrum of $[Fe_3O(OAc)_6(^{14}N_2)_1(^{15}N_2)_1]^+$ at 26 K. **b)** Calculated IR absorption spectrum of geometry optimized of $[Fe_3O(OAc)_6(^{14}N_2)_1(^{15}N_2)_1]^+$ **c)** Calculated IR absorption spectrum of geometry optimized of $[Fe_3O(OAc)_6(^{14}N_2)_2]^+$ (blue) and $[Fe_3O(OAc)_6(^{15}N_2)_2]^+$ (red). The calculations were performed at the B3LYP/cc-pVTZ (H, C, N, O) and Stuttgart 1997 ECP (Fe) level of theory. The multiplicity is 16 and frequencies are scaled with 0.951. Calculated stick spectra were convoluted with a Gaussian envelope of FWHM = 3.5 cm^{-1}. We obtain two values for the free $^{15}N_2$ vibration frequency: 2252 cm^{-1} by Raman spectroscopy[I,II] or 2251 cm^{-1} by mass scaling of the $^{14}N_2$ frequency.

References:

I R. J., Butcher, W. J. Jones, *J. Chem. Soc. Faraday Trans.* 2, 1974, 70, 560

II J. Bendtsen, *J. Raman Spectrosc.*, 1974, 2 133

10.2 Competing Fragmentation Channels in Trimetallic Au-Zn-Alkali Complexes

Johannes Lang, Merve Cayir-Kücükdisli, Simon P. Walg, Patrick Di Martino-Fumo, Werner R. Thiel and Gereon Niedner-Schatteburg

Fachbereich Chemie and Forschungszentrum OPTIMAS,
Technische Universität Kaiserslautern,
67663 Kaiserslautern, Germany

Content

10.2.1 Synthesis of [$AuZnCl_3$]

_N_-(2-(Diphenylphosphinyl)ethyl)-4-(pyridin-2-yl)pyrimidin-2-amin (L1)

To a solution of 2.40 g (3.80 mmol) of 1-(2-(diphenylphosphinyl)ethyl)guanidine sulfate in 20 ml dry EtOH were added 0.50 g (9.00 mmol) of NaOMe under nitrogen atmosphere. The reaction mixture was stirred at 78 °C. After 30 minutes, 1.00 g (6.00 mmol) of 3- (dimethylamino)-1-(pyridin-2-yl)prop-2-en-1-one were added to the solution and refluxed for 24 hours. The mixture was cooled down to room temperature and all volatiles were evaporated. The residue was extracted three times with 20 ml dichloromethane and three times with 20 ml H_2O. The combined organic phases were dried over Na_2SO_4. After evaporating the solvent, the product was obtained by washing two times with 20 ml dry MeOH.

Yield: 1.10 g (2.80 mmol, 46 %, colorless solid).

Elemental Analysis: $C_{23}H_{21}N_4P$ (384.42 g/mol) + 0.4 H_2O.

Calculated : C: 70.54% H: 5.61% N: 14.31%

Found : C: 70.45% H: 5.51% N: 14.39%

^{1}H NMR (400.1 MHz, $CDCl_3$, 20 °C): δ 8.68 (ddd, ^3JHH = 4.8 Hz, ^4JHH = 1.6 Hz and 5JHH = 0.8 Hz, 1H, H1), 8.41 (d, ^3JHH = 5.1 Hz, 1H, H8), 8.26 (d, ^3JHH = 7.9 Hz, 1H, H4), 7.79 (td, ^3JHH = 7.8 Hz and ^4JHH = 1.8 Hz, 1H, H3), 7.57 (d, ^3JHH = 5.1 Hz, 1H, H7), 7.79- 7.44 (m, 4H, HPh), 7.38-7.36 (m, 1H, H2), 7.35-7.31 (m, 6H, HPh), 5.41 (t, ^3JHH = 5.8 Hz, 1H, H10), 3.72-3.65 (m, 2H, H11), 2.49-2.46 (m, 2H, H12) ppm.

^{13}C NMR (100.6 MHz, $CDCl_3$, 20 °C): δ 163.6 (s, C8), 162.3 (s, C9), 159.5 (s, C6), 154.9 (s, C5), 149.4 (s, C1), 138.2 (d, 1JPC = 12.2 Hz, C13), 137.0 (s, C3), 133.0 (d, 2JPC = 18.8 Hz, C14), 128.8 (s, C16), 128.7 (d, 3JPC = 6.7 Hz, C15), 125.1 (s, C2), 121.6 (s, C4), 107.1 (s, C7), 38.8 (d, 2JPC = 22.7 Hz, C11), 28.9 (d, 1JPC = 13.2 Hz, C12) ppm.

^{31}P NMR (161.98 MHz, $CDCl_3$, 20 °C): δ –21.26 (s) ppm.

IR ν (cm^{-1}): 3245 (w), 3052 (w), 2148 (w), 1596 (m), 1578 (m), 1563 (s), 1535 (m), 1480 (w), 1455 (m), 1432 (m), 1415 (s), 1360 (s), 1325 (w), 1306 (w), 1291 (w), 1281 (w), 1253 (w), 1239 (w), 1204 (m), 1177 (w), 1157 (w), 1124 (m), 1092 (m), 1074 (m), 1043 (w), 1026 (w), 994 (m), 907 (w), 895 (w), 879 (w), 840 (m), 785 (s), 747 (s), 784 (s), 716 (m), 680 (s).

Chloro(*N*-(2-(diphenylphosphinyl)ethyl)-4-(pyridin-2-yl)pyrimidin-2-amine)gold(I) (L1)AuCl

156 mg (0.40 mmol) of **L1** were added to a solution of 130 mg (0.40 mmol) of Au(THT)Cl in 10 ml CH2Cl2. After stirring for 1 hour at room temperature, the solution was concentrated and product was precipitated by adding 5 ml of Et_2O. The product was collected by filtration and dried in *vacuo*.

Yield: 222 mg (0.36 mmol, 89%, colorless solid).
Elemental Analysis: $C_{23}H_{21}AuClN_4P$ (616.84 g/mol)

Calculated : C: 44.78% H: 3.43% N: 9.08%

Found : C: 44.22% H: 3.59% N: 10.70%

^{1}H NMR (400.1 MHz, $CDCl_3$, 20 °C): δ 8.68 (d, ^3JHH = 4.0 Hz, 1H, H1), 8.39 (d, ^3JHH = 5.0 Hz, 1H, H8), 8.32 (d, ^3JHH = 7.4 Hz, 1H, H4), 7.90 (t, ^3JHH = 7.5 Hz, 1H, H3), 7.71-7.66 (m, 4H, H14), 7.61 (d, ^3JHH = 5.0 Hz, 1H, H7), 7.49-7.41 (m, 6H, H15 and H16), 7.41-7.39 (m, 1H, H2), 5.48 (t, ^3JHH = 6.0 Hz, 1H, H10), 3.94-3.86 (m, 2H, H11), 2.97 -2.90 (m, 2H, H12) ppm.
^{13}C NMR (100.6 MHz, $CDCl_3$, 20 °C): δ 163.9 (s, C6), 161.7 (s, C9), 159.3 (s, C8), 154.3 (s, C5), 149.2 (s, C1), 137.4 (s, C3), 133.3 (d, 2*J*PC = 13.3 Hz, C14), 132.1 (d, 4*J*PC = 2.4 Hz, C16), 129.4 (d, 3*J*PC = 11.7 Hz, C15), 129.2 (d, 1*J*PC = 61.0 Hz, C13), 125.3 (s, C2), 121.8 (s, C4), 107.8 (s, C7), 38.7 (d, 2*J*PC = 7.8 Hz, C13), 28.5 (d, 1*J*PC = 35.5 Hz, C12) ppm.
^{31}P NMR (161.98 MHz, $CDCl_3$, 20 °C): δ 24.39 (s) ppm.

IR *v* (cm^{-1}): 3239 (w), 3051 (w), 2962 (w), 1551 (s), 1522 (m), 1479 (w), 1452 (w), 1434 (m), 1413 (m), 1354 (m), 1255 (w), 1180 (w), 1100 (m), 1074 (w), 1044 (w), 1026 (w), 995 (m), 785 (s), 641 (s), 680 (s).

Cl2Zn(L1)AuCl

To a solution 33.0 mg (0.24 mmol) of $ZnCl_2$ in 5 ml of CH_2Cl_2, a solution of 150 mg (0.24 mmol) of gold complex (L1)AuCl in 5 ml of CH_2Cl_2 were added dropwise under nitrogen atmosphere. After stirring at room temperature for 24 hours, the solvent was evaporated and the compound was washed with Et_2O.

Yield: 140 mg (0.19 mmol, 77 %, colorless solid).
Elemental Analysis: $C_{23}H_{21}AuCl_3N_4PZn$ (753.1 g/mol)

Calculated : C: 36.68% H: 2.81% N: 7.44%

Found : C: 38.20% H: 3.04% N: 7.79%

^{1}H NMR (400.1 MHz, $CDCl_3$, 20 °C): δ 8.76 (m, 1H, H1), 8.68 (br. s, 1H, H8), 8.26 (br. s, 1H, H4), 8.14 (br. s, 1H, H3), 7.73-7.68 (m, 5H, H2 and H14), 7.53-7.46 (m, 7H, H7, H15 and H16), 6.52 (s, 1H, H10), 3.90-3.85 (m, 2H, H11), 2.91 (td, 2*J*PH = 10.8 Hz and 3*J*HH = 7.8 Hz, 2H, H12) ppm.

^{13}C NMR (100.6 MHz, $CDCl_3$, 20 °C): δ 160.6 (s, C8), 149.5 (s, C1), 133.4 (d, 2*J*PC = 13.4 Hz, C14), 132.3 (d, 4*J*PC = 2.7 Hz, C16), 129.7 (s, C), 129.6 (d, 3*J*PC = 11.8 Hz, C15), 129.0 (s, C), 123.0 (s, C4), 107.0 (s, C7), 38.6 (d, 2*J*PC = 10.0 Hz, C11), 28.5 (d, 1*J*PC = 36.4 Hz, C12) ppm. Some of the carbon signals are missing due to line broadening and low solubility of the complex.

^{31}P NMR (161.98 MHz, $CDCl_3$, 20 °C): δ 23.53 (s) ppm.

IR *ν* (cm–1): 3321 (w), 3054 (w), 2924 (w), 1570 (s), 1485 (m), 1464 (m), 1432 (s), 1357 (s), 1313 (w), 1266 (w), 1215 (m), 1186 (w), 1140 (w), 1103 (m), 1077 (w), 1051 (w), 997 (m), 887 (w), 830 (w), 779 (s), 741 (s), 689 (s), 663 (m).

10.2.2 Details on the ESI-MS and CID Measurements

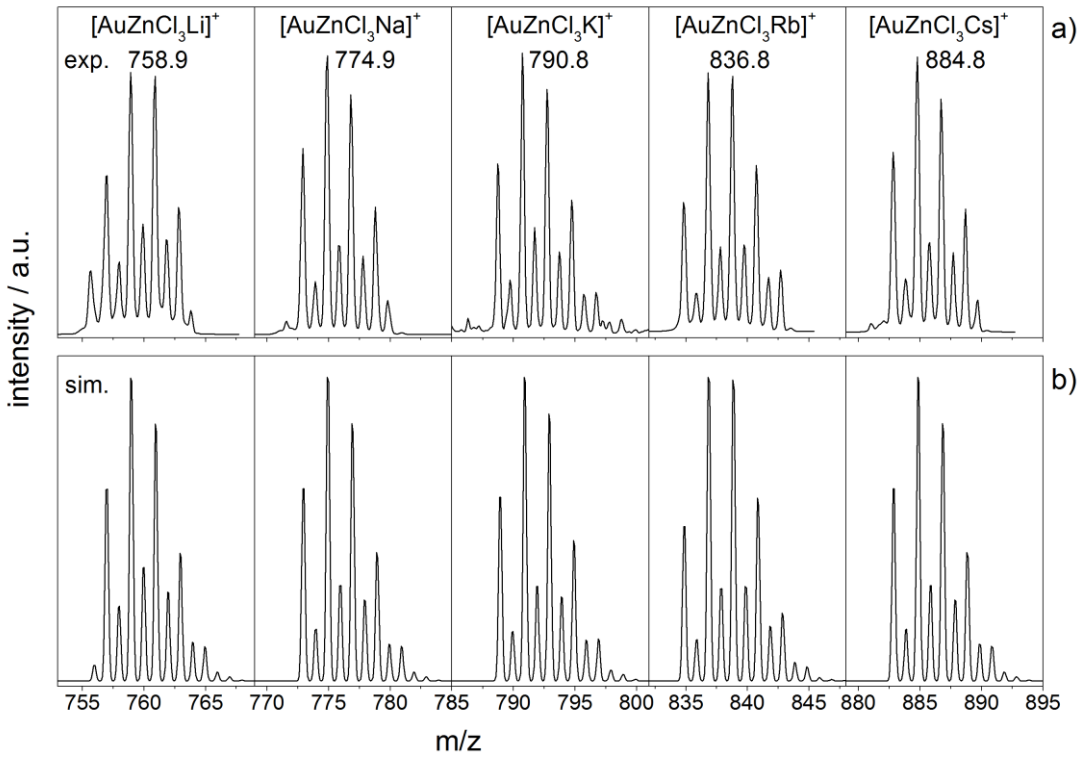

Figure S1: a) Experimental and b) simulated isotope pattern of $[AuZnCl_3M]^+$ (M = Li, Na, K, Rb, Cs). The mass labeling refers to the most abundant isotope peak.

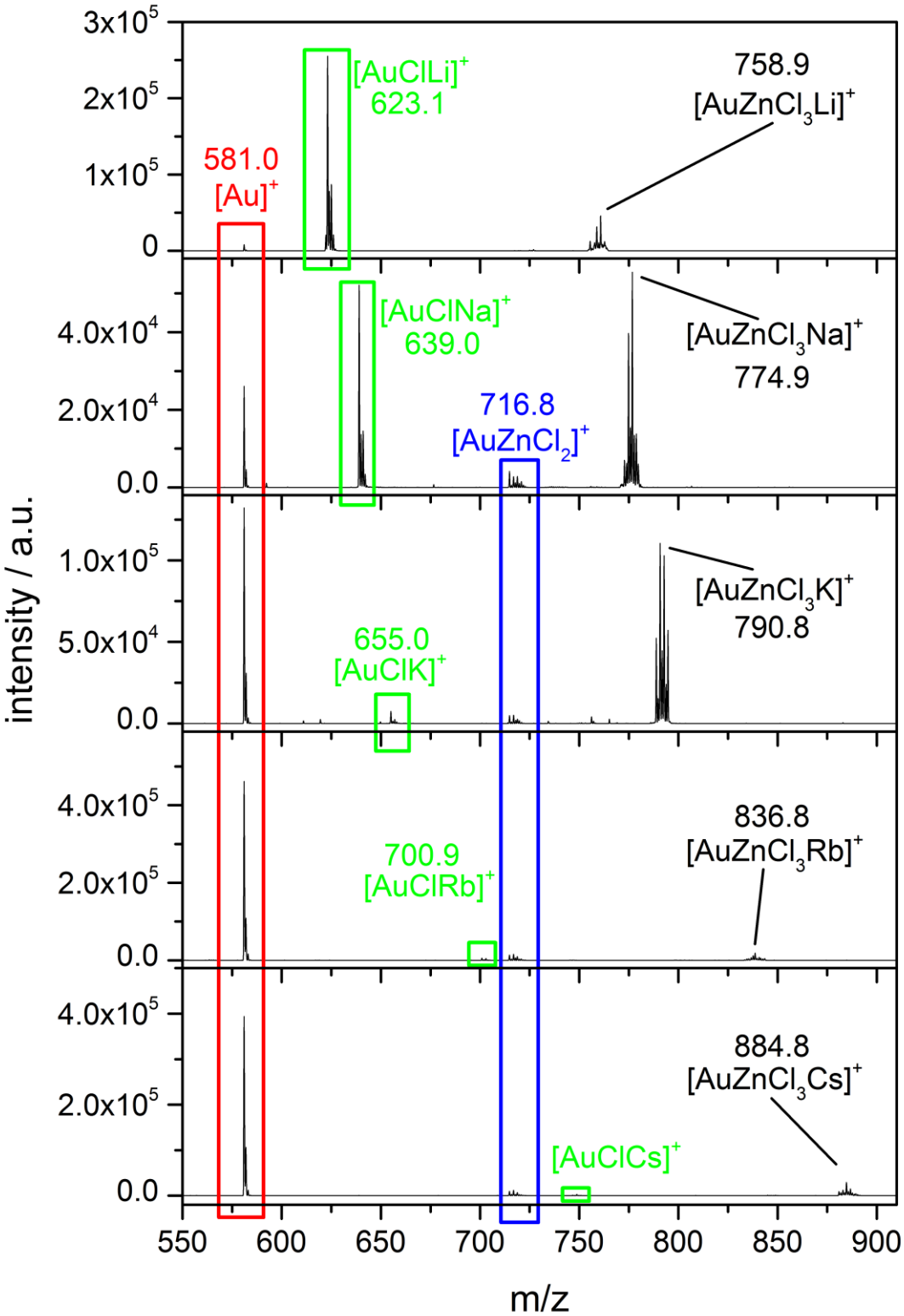

Figure S2: CID fragmentation mass spectra of isolated $[AuZnCl_3M]^+$ (M = Li, Na, K, Rb and Cs) ions, recorded at a fixed fragmentation amplitude of 0.004 a.u. corresponding to the internal energy scale of the mass spectrometer.

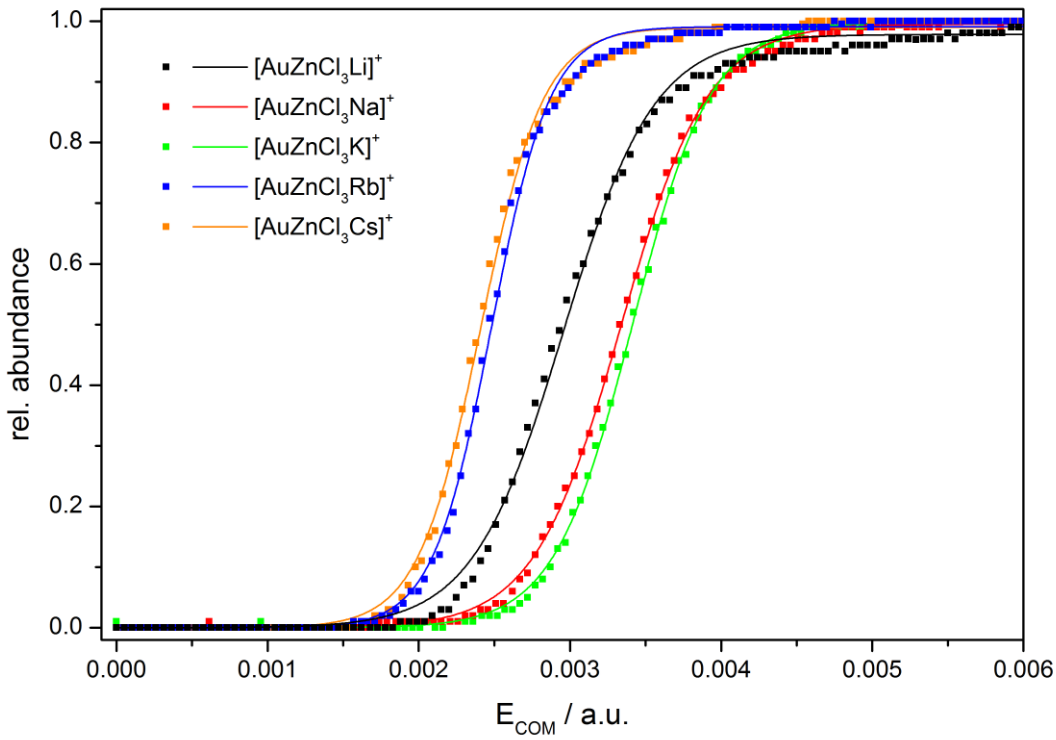

Figure S3: CID-appearance curves of **[AuZnCl$_3$M]$^+$** (sum of all fragments, colored squares,) and sigmoidal fits (colored lines)).

We obtained CID-appearance curves (all fragment signals monitored, cf Fig. S3). The fit of these curves yields respective E_{COM}^{50} values which correlate with the relative stability of [AuZnCl$_3$M]$^+$. The E_{COM}^{50} values increase from the Li$^+$ adduct (0.00296 a.u.) to the K$^+$ adduct (0.00341 a.u.). However the E_{COM}^{50} values of the Rb$^+$- and Cs$^+$ adducts are lower than the E_{COM}^{50} value of the Li$^+$ adduct.

10.2.3 Monitored m/z Values of IRMPD Spectra and CID – Appearance Curves

$[AuZnCl_3Li]^+$:

Parent signals:

MP(0)=755.7 MP(1)=756.9 MP(2)=758 MP(3)=758.9 MP(4)=759.9 MP(5)=760.9 MP(6)=761.8 MP(7)=762.8 MP(8)=763.8	$[AuZnCl_3Li]^+$

Fragment signals:

MF(0)=581.1 MF(1)=582.1 MF(2)=583.1 MF(3)=584.1	$[Au]^+$
MF(4)=622.1 MF(5)=623.1 MF(6)=624 MF(7)=625 MF(8)=626 MF(9)=627	$[AuCl_1Li]^+$
MF(10)=714.9 MF(11)=716.8 MF(12)=717.9 MF(13)=718.9	$[AuZnCl_2]^+$
MF(18)=725.9 MF(19)=726.9	$[AuZnCl_2Li]$- H^+

$[AuZnCl_3Na]^+$:

Parent signals:

MP(0)=772.9 MP(1)=773.9 MP(2)=774.9 MP(3)=775.8 MP(4)=776.8 MP(5)=777.8 MP(6)=778.8 MP(7)=779.8	$[AuZnCl_3Na]^+$

Fragment signals:

MF(0)=581.1 MF(1)=582 MF(2)=583.1	$[Au]^+$
MF(3)=639 MF(4)=640 MF(5)=641 MF(6)=642	$[AuCl_1Na]^+$
MF(7)=714.9 MF(8)=715.8 MF(9)=716.8 MF(10)=717.8 MF(11)=718.8 MF(12)=719.8 MF(13)=720.8 MF(14)=721.8 MF(15)=722.8	$[AuZnCl_2]^+$
MF(16)=736.9 MF(17)=737.9 MF(18)=738.9 MF(19)=739.9 MF(20)=740.9 MF(21)=741.9 MF(22)=742.9	$[AuZnCl_2Na]$- H^+

$[AuZnCl_3K]^+$:

Parent signals:

MP(0)=788.9 MP(1)=789.9 MP(2)=790.8 MP(3)=791.8 MP(4)=792.8 MP(5)=793.8 MP(6)=794.8 MP(7)=795.8	$[AuZnCl_3K]^+$

Fragment signals:

MF(0)=581.1 MF(1)=582 MF(2)=583.1	$[Au]^+$
MF(3)=654.9 MF(4)=655.9 MF(5)=656.9 MF(6)=657.9	$[AuCl_1K]^+$
MF(7)=714.9 MF(8)=715.9 MF(9)=716.9 MF(10)=717.9 MF(11)=718.8 MF(12)=719.8 MF(13)=720.8	$[AuZnCl_2]^+$
MP(14)=752.9 MP(15)=753.9 MP(16)=754.9 MP(17)=755.9 MP(18)=756.9 MP(19)=757.9 MP(20)=758.9 MP(21)=759.9	$[AuZnCl_2K]$- H^+

$[AuZnCl_3Rb]^+$:

Parent signals:

MP(0)=834.8	
MP(1)=835.8	
MP(2)=836.8	
MP(3)=837.8	
MP(4)=838.8	$[AuZnCl_3Rb]^+$
MP(5)=839.7	
MP(6)=840.7	
MP(7)=841.7	
MP(8)=842.7	

Fragment signals:

MF(0)=581.1	
MF(1)=582	$[Au]^+$
MF(2)=583.1	
MF(7)=700.9	
MF(8)=701.9	$[AuCl_1Rb]^+$
MF(9)=702.9	
MF(10)=703.9	
MF(7)=714.9	
MF(8)=715.9	
MF(9)=716.9	
MF(10)=717.9	$[AuZnCl_2]^+$
MF(11)=718.8	
MF(12)=719.8	
MF(13)=720.8	
MP(14)=798.9	
MP(15)=799.9	
MP(16)=800.9	
MP(17)=801.9	$[AuZnCl_2K]$-
MP(18)=802.9	H^+
MP(19)=803.9	
MP(20)=804.9	
MP(21)=805.9	

$[AuZnCl_3Cs]^+$:

Parent signals:

MP(0)=882.8 MP(1)=883.8 MP(2)=884.8 MP(3)=885.8 MP(4)=886.7 MP(5)=887.7 MP(6)=888.7 MP(7)=889.7	$[AuZnCl_3Cs]^+$

Fragment signals:

MF(0)=581.1 MF(1)=582 MF(2)=583.1	$[Au]^+$
MF(20)=748.8 MF(8)=749.9 MF(9)=750.9 MF(10)=751.9	$[AuCl_1Cs]^+$
MF(7)=714.9 MF(8)=715.9 MF(9)=716.9 MF(10)=717.9 MF(11)=718.8 MF(12)=719.8 MF(13)=720.8	$[AuZnCl_2]^+$
MF(14)=846.9 MF(15)=847.9 MF(16)=848.9 MF(17)=849.9	$[AuZnCl_2Cs]\text{-}H^+$

10.2.4 IRMPD and Calculated IR Spectra of $[AuZnCl_3M]^+$

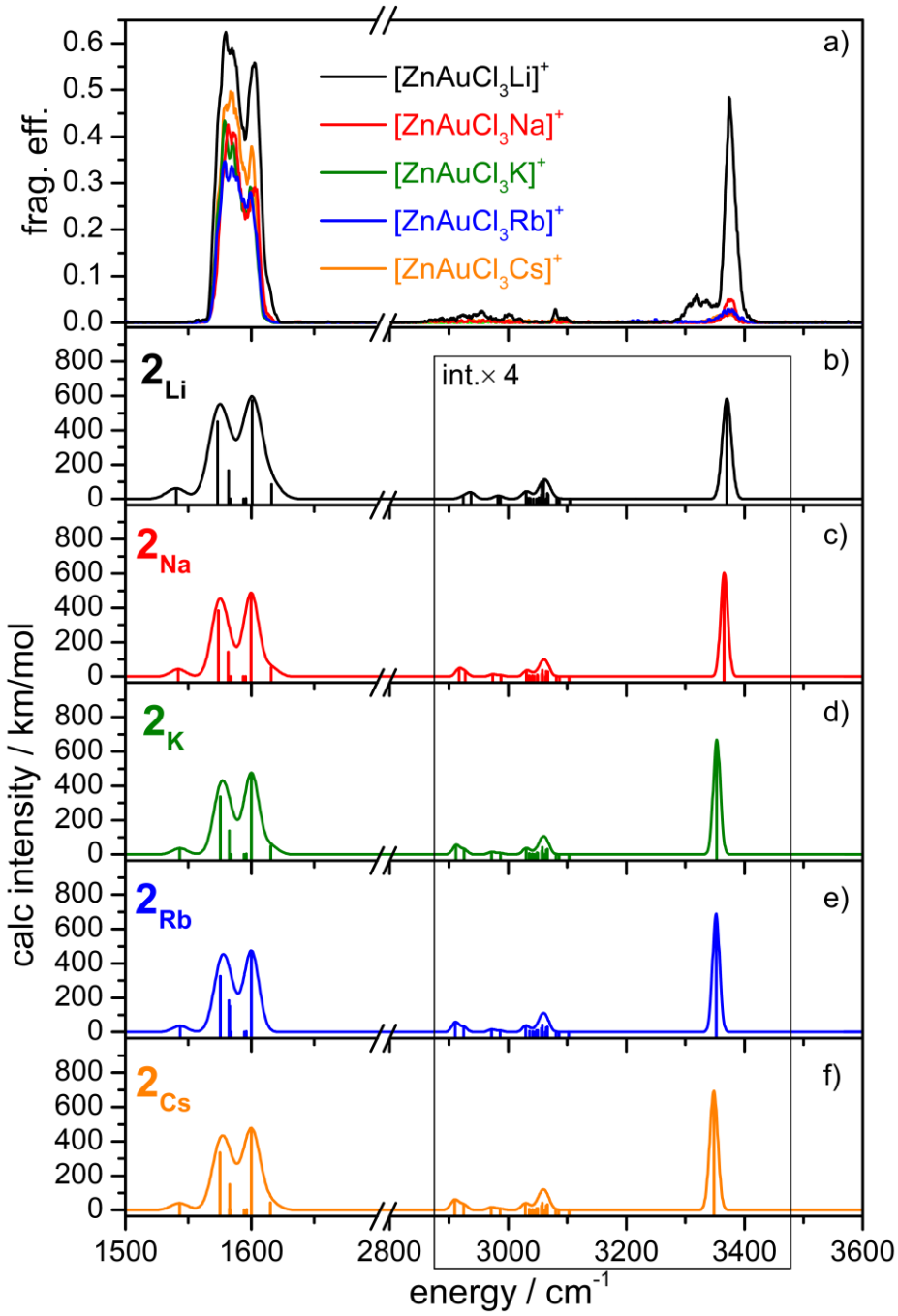

Figure S4: a) IR-MPD spectra of $[AuZnCl_3M]^+$ (M = Li, Na, K, Rb, Cs). b) - f) Calculated IR absorption spectra at the B3LYP/cc-pVDZ (H, C, Li, N, O) and Stuttgart 1997 ECP (Au, Zn, K, Rb, Cs) level of theory. Frequencies are scaled with 0.955 (0.975) above (below) 2000 cm^{-1}. The calculated intensities above 2800 cm^{-1} were multiplied by a factor of 4.

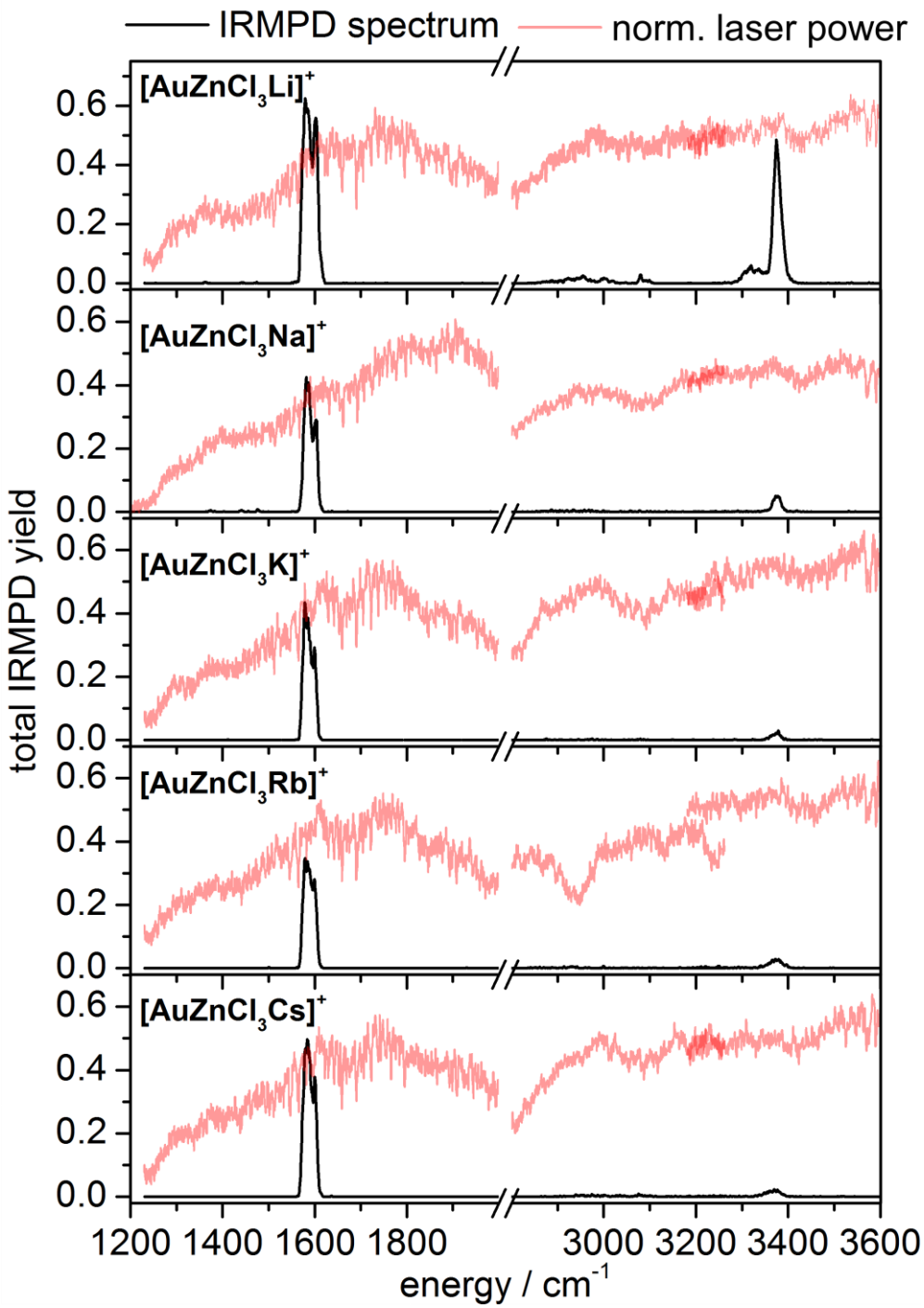

Figure S5: Black: IR-MPD spectra of $[AuZnCl_3M]^+$ (M = Li, Na, K, Rb, Cs). Red: Normalized laser power curve

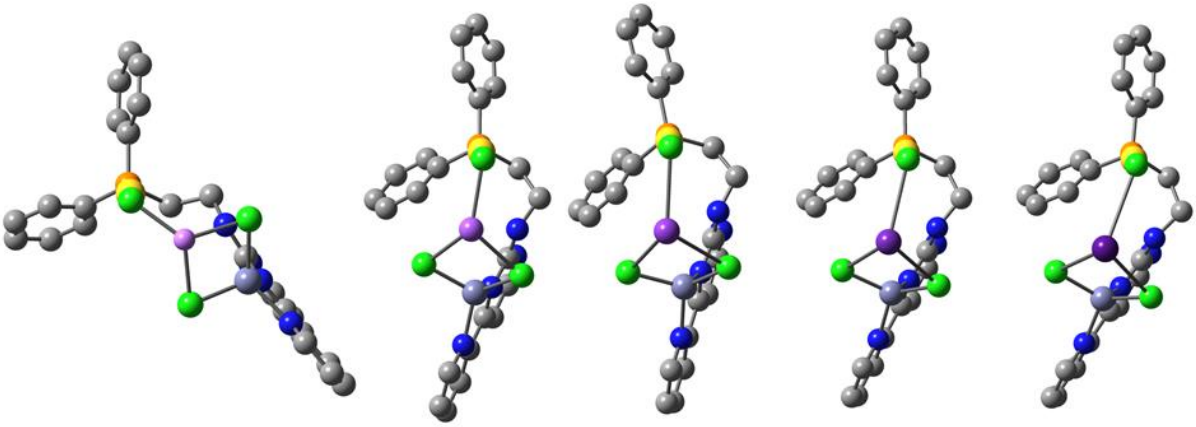

2_{Li} 2_{Na} 2_{K} 2_{Rb} 2_{Cs}

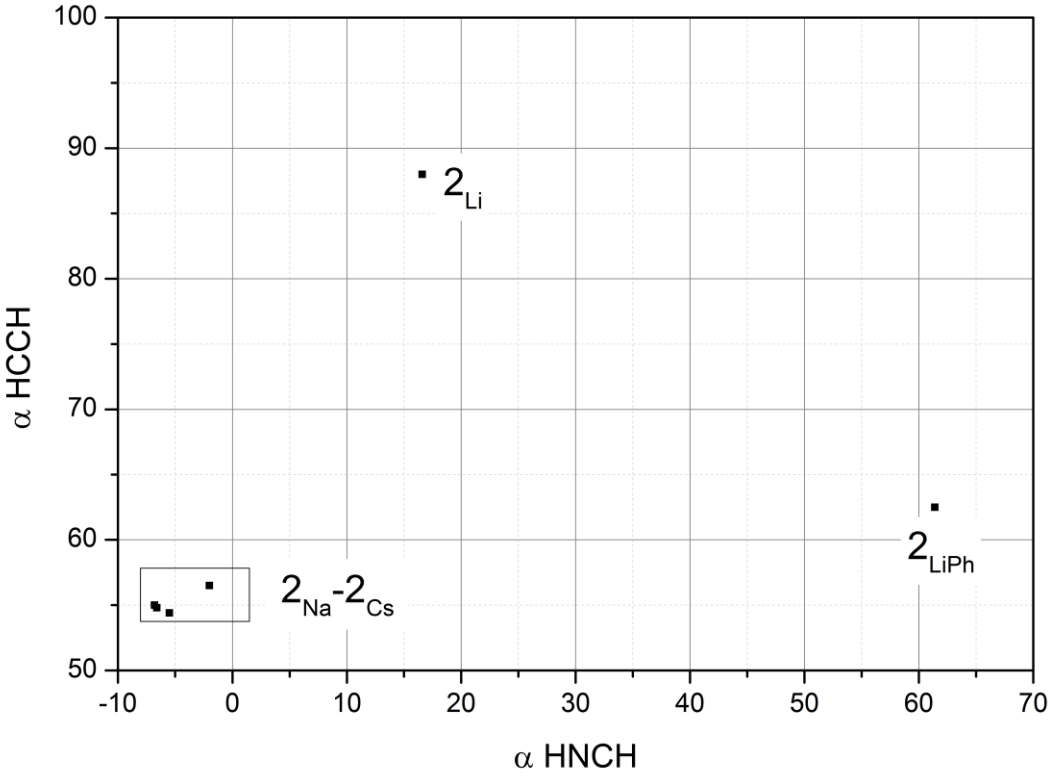

Table S1: Summary of IRMPD vibration frequencies and fragmentation efficiencies

Species	ν / cm^{-1}	Frag. eff. / %	Spectral region
[AuZnCl$_3$Li]$^+$	1579.6	62.5	fingerprint
	1602.5	55.9	
	2954.9	2.6	CH streching
	3080.4	2.9	
	3319.5	6.1	NH/OH streching
	3373.8	48.5	
[AuZnCl$_3$Na]$^+$	1583.4	49.7	fingerprint
	1599.9	37.8	
	3378.0	5.0	NH/OH streching
[AuZnCl$_3$K]$^+$	1578.8	43.4	fingerprint
	1599.2	29.2	
	3378.0	3.0	NH/OH streching
[AuZnCl$_3$Rb]$^+$	1579.1	34.7	fingerprint
	1599.5	28.0	
	3373.6	2.9	NH/OH streching
[AuZnCl$_3$Cs]$^+$	1583.4	49.7	fingerprint
	1599.9	37.8	
	3372.0	2.0	NH/OH streching

[AuZnCl$_3$Li]$^+$:

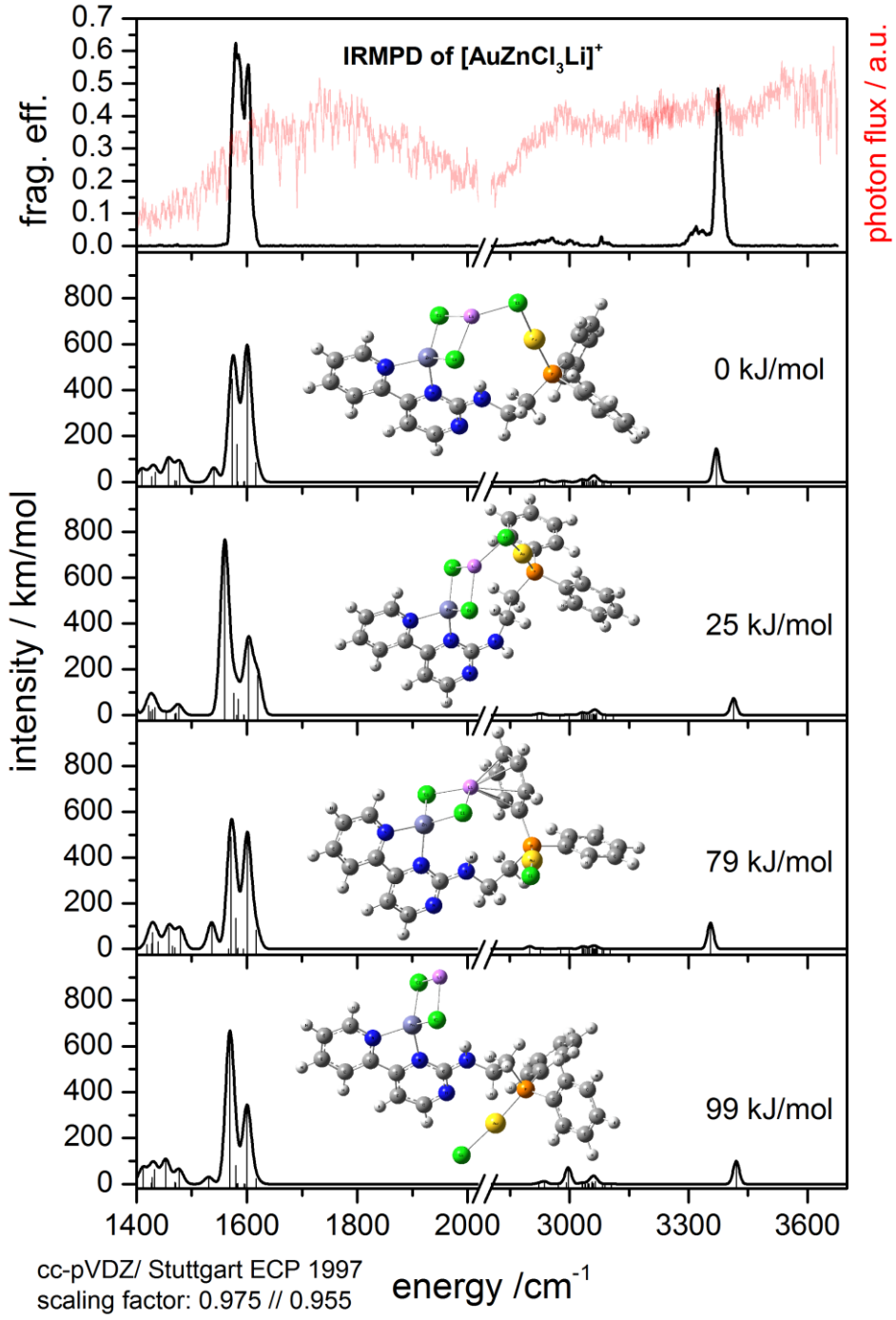

Figure S6: IRMPD spectrum of the [AuZnCl$_3$Li]$^+$ complex (top) in comparison with the DFT calculations at the B3LYP/cc-pVDZ (H, C, N, O) and Stuttgart 1997 ECP (Au,Zn) level of theory. Frequencies are scaled with 0.955 (0.975) above (below) 2000 cm^{-1}.

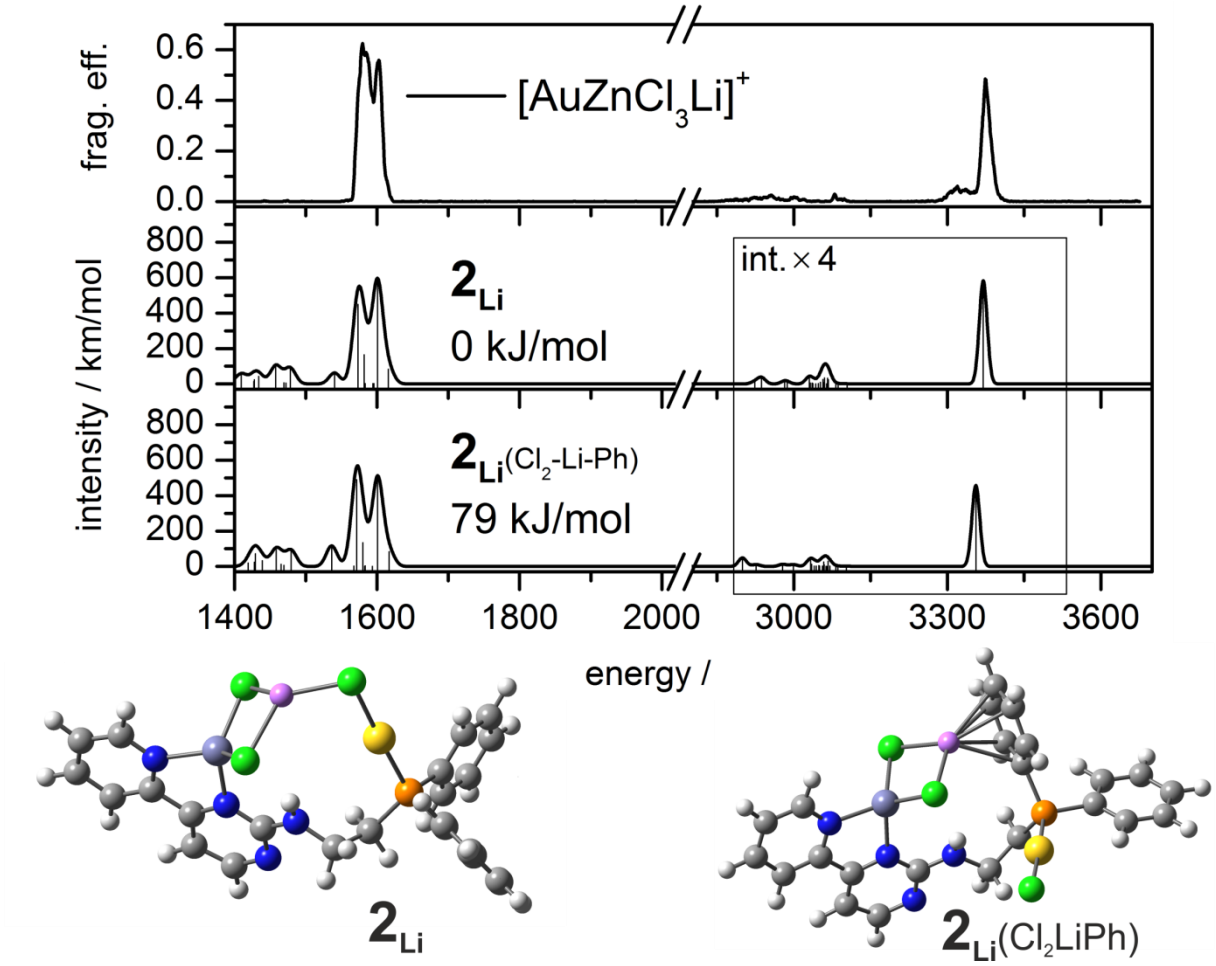
frag. eff.
0.6
0.4
0.2
0.0
[AuZnCl3Li]+
intensity / km/mol
800
600
400
200
0
2Li
0 kJ/mol
int. × 4
2Li(Cl2-Li-Ph)
79 kJ/mol
1400
1600
1800
2000
3000
3300
3600
energy /
2Li
2Li(Cl2LiPh)

[AuZnCl$_3$Na]$^+$:

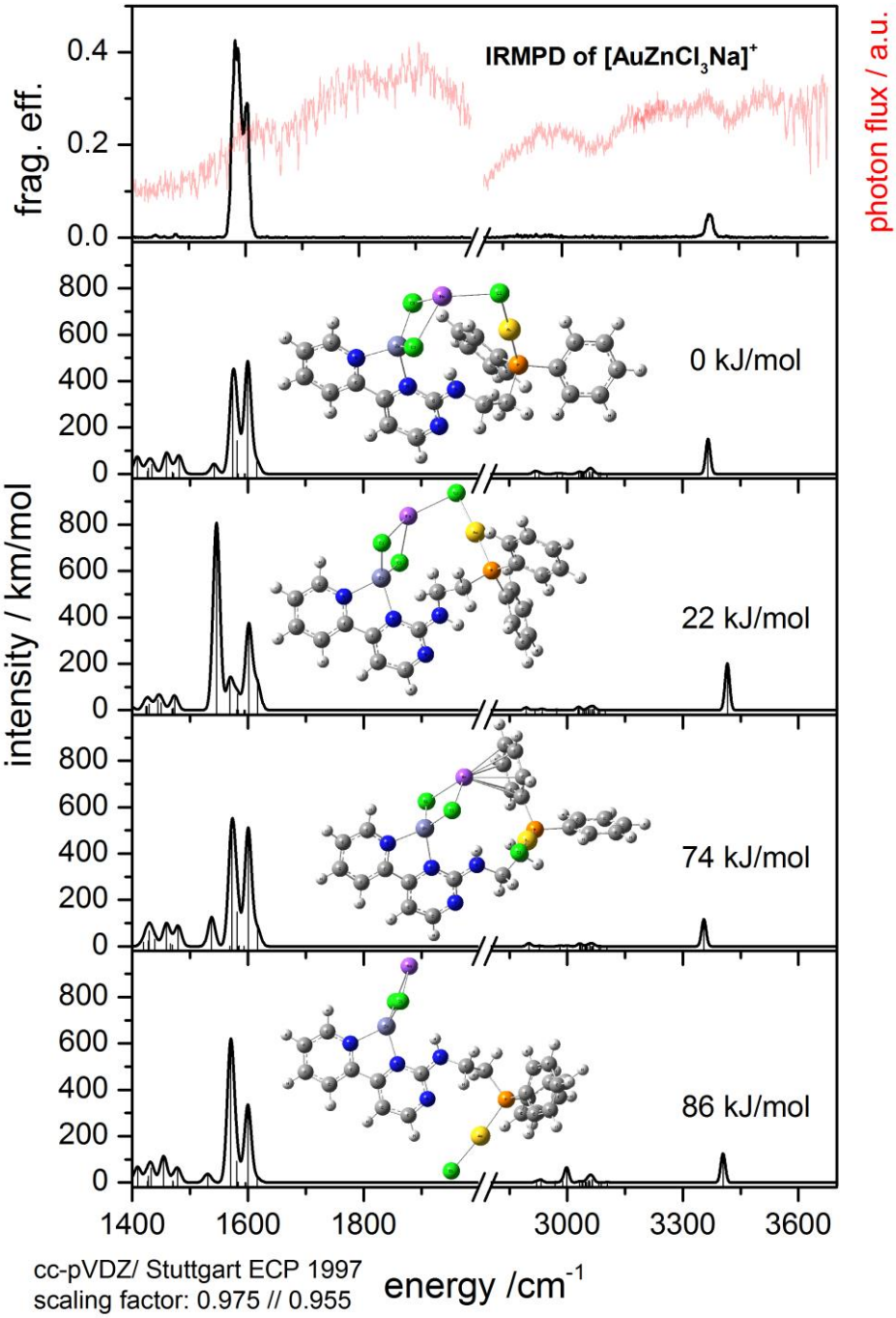

Figure S7: IRMPD spectrum of the [AuZnCl$_3$Na]$^+$ complex (top) in comparison with the DFT calculations at the B3LYP/cc-pVDZ (H, C, N, O) and Stuttgart 1997 ECP (Au,Zn) level of theory. Frequencies are scaled with 0.955 (0.975) above (below) 2000 cm^{-1}.

[AuZnCl$_3$K]$^+$:

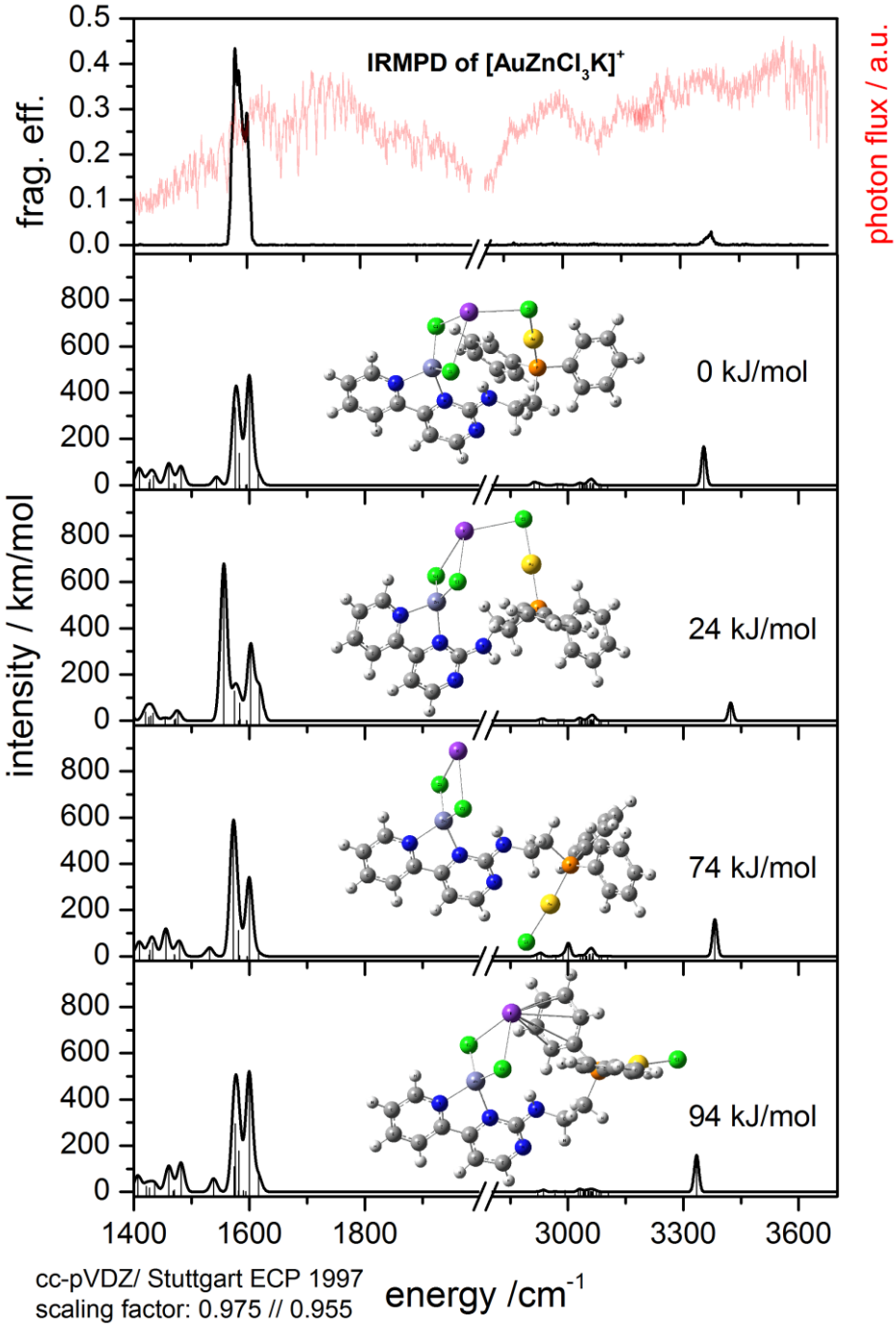

Figure S8: IRMPD spectrum of the [AuZnCl$_3$K]$^+$ complex (top) in comparison with the DFT calculations at the B3LYP/cc-pVDZ (H, C, N, O) and Stuttgart 1997 ECP (Au,Zn) level of theory. Frequencies are scaled with 0.955 (0.975) above (below) 2000 cm^{-1}.

[AuZnCl$_3$Rb]$^+$:

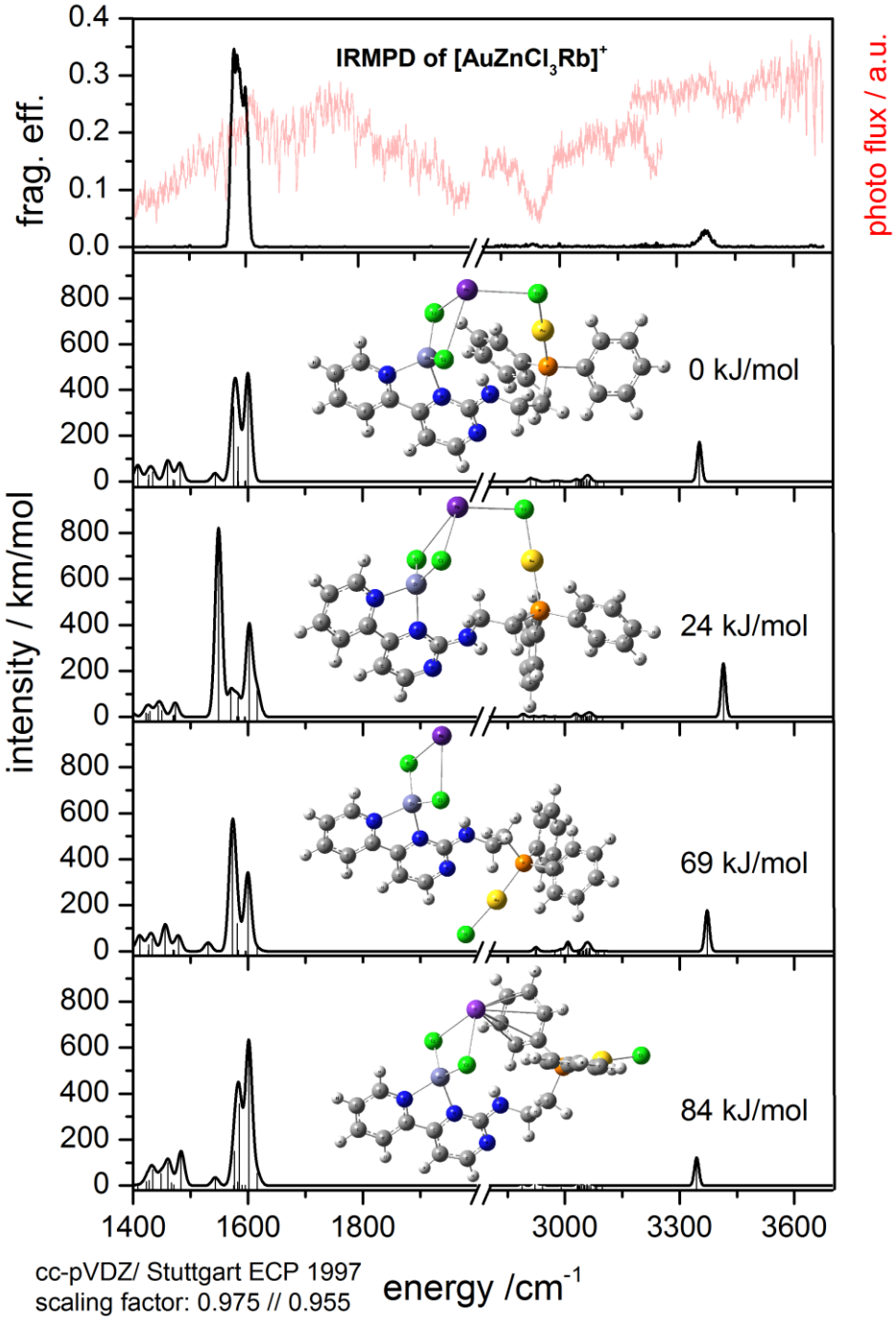

Figure S9: IRMPD spectrum of the [AuZnCl$_3$Rb]$^+$ complex (top) in comparison with the DFT calculations at the B3LYP/cc-pVDZ (H, C, N, O) and Stuttgart 1997 ECP (Au,Zn) level of theory. Frequencies are scaled with 0.955 (0.975) above (below) 2000 cm^{-1}.

[AuZnCl$_3$Cs]$^+$:

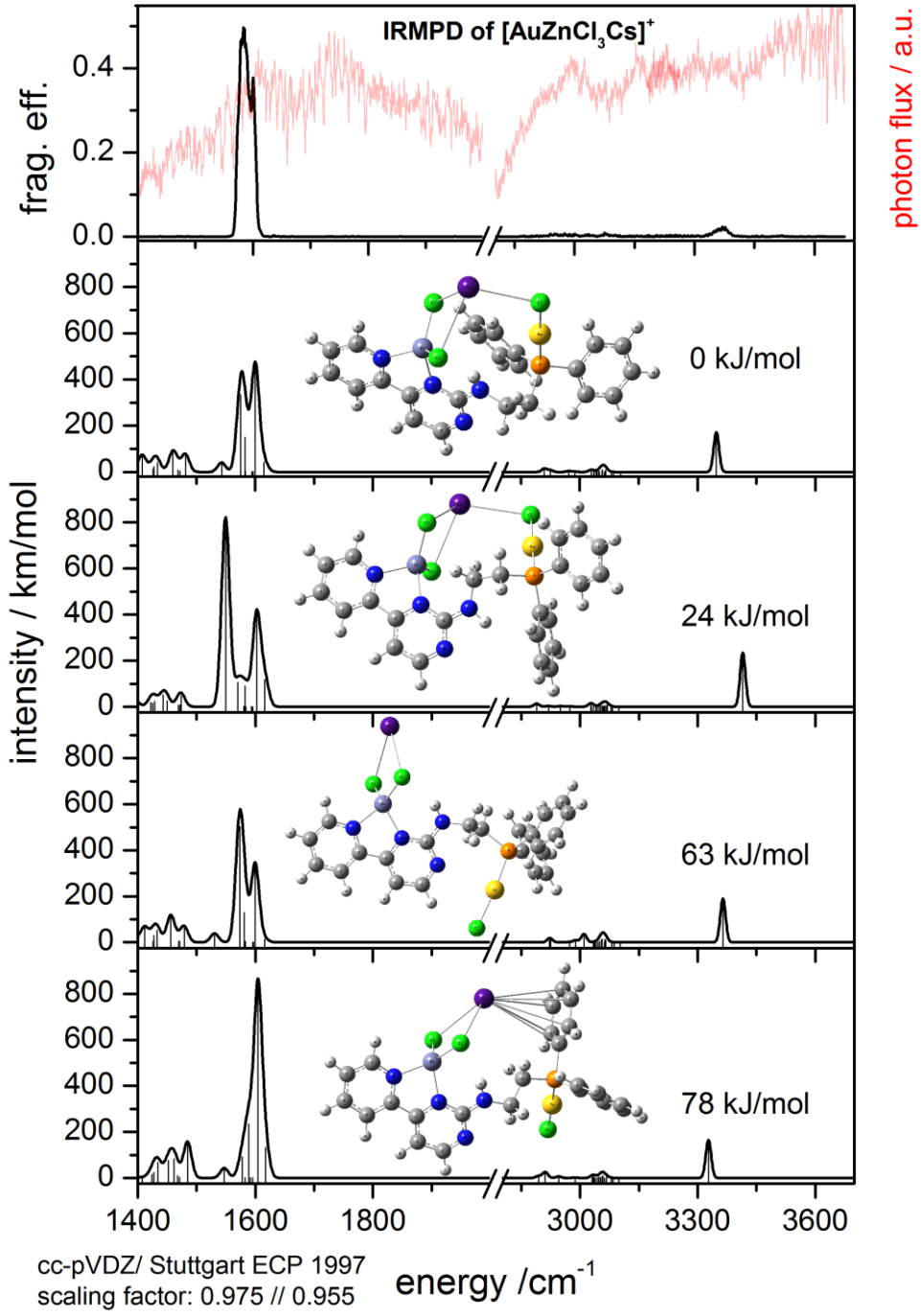

Figure S10: IRMPD spectrum of the **[AuZnCl$_3$Cs]$^+$** complex (top) in comparison with the DFT calculations at the B3LYP/cc-pVDZ (H, C, N, O) and Stuttgart 1997 ECP (Au,Zn) level of theory. Frequencies are scaled with 0.955 (0.975) above (below) 2000 cm^{-1}.

10.2.5 Reaction Coordinates of Alkali Association and of $ZnCl_2$ and MCl_2ZnCl Expulsion

M = Li^+

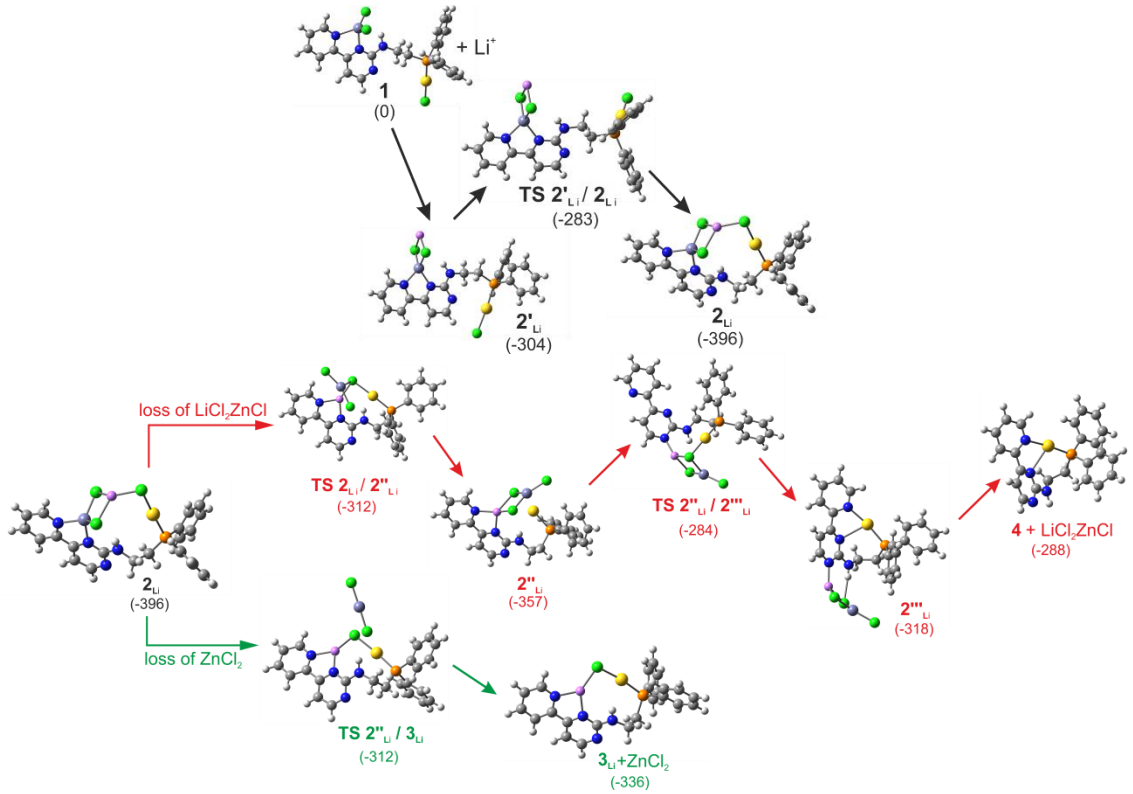

M = Na^+

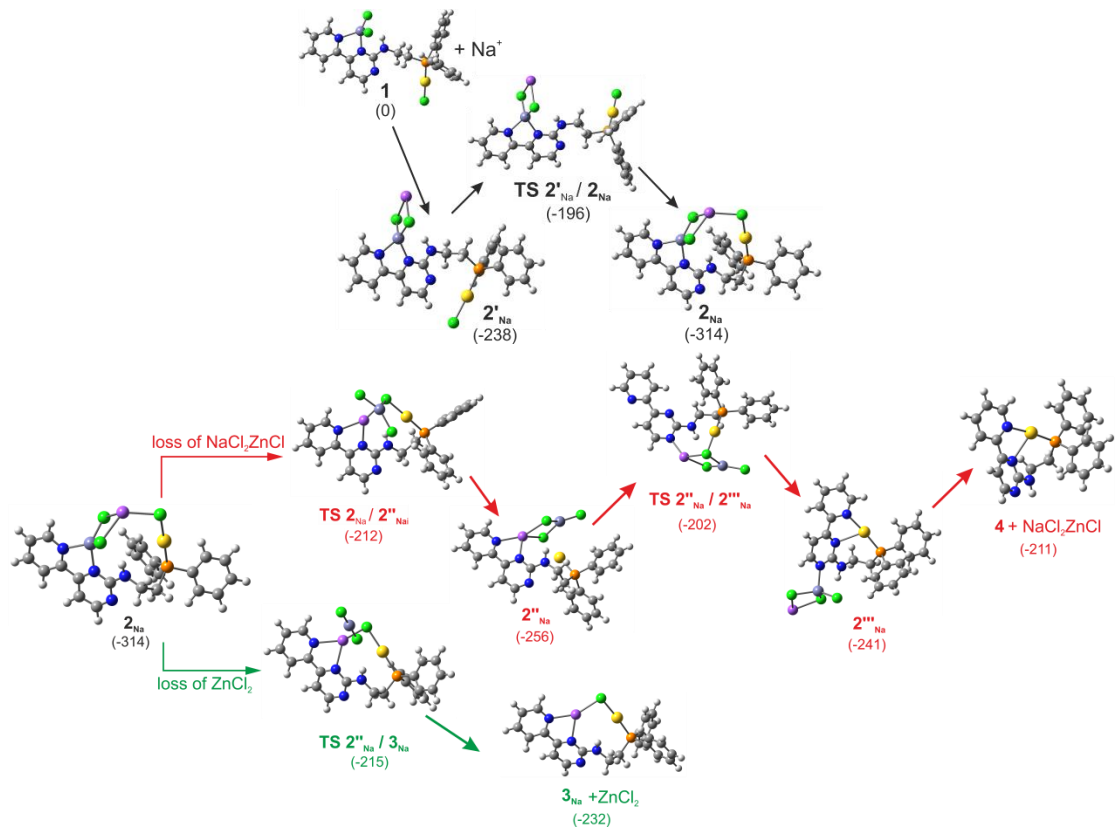

M = K⁺

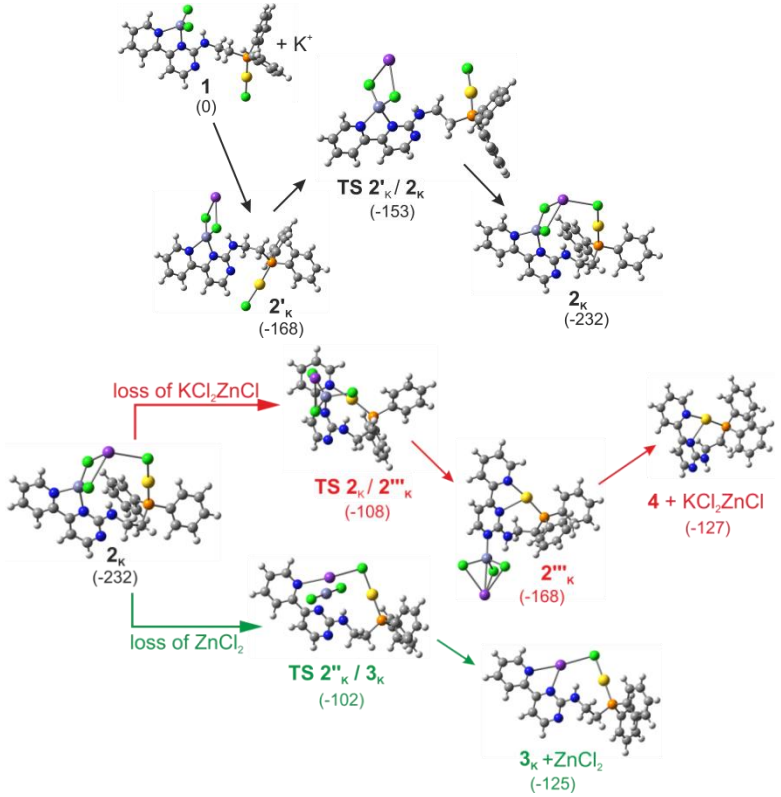
+ K⁺
1
(0)
TS 2'K / 2K
(-153)
2'K
(-168)
2K
(-232)
loss of KCl2ZnCl
TS 2K / 2'''K
(-108)
2'''K
(-168)
4 + KCl2ZnCl
(-127)
2K
(-232)
loss of ZnCl2
TS 2''K / 3K
(-102)
3K +ZnCl2
(-125)

M = Rb⁺

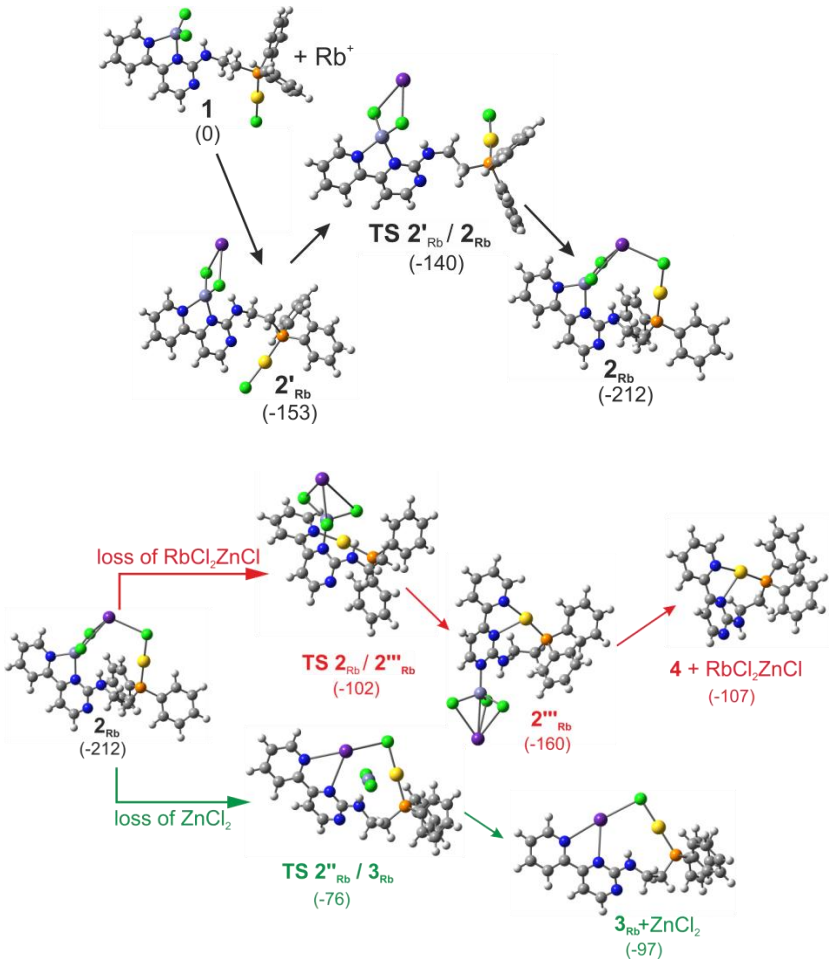
+ Rb⁺
1
(0)
TS 2'Rb / 2Rb
(-140)
2'Rb
(-153)
2Rb
(-212)
loss of RbCl2ZnCl
TS 2Rb / 2'''Rb
(-102)
2'''Rb
(-160)
4 + RbCl2ZnCl
(-107)
2Rb
(-212)
loss of ZnCl2
TS 2''Rb / 3Rb
(-76)
3Rb+ZnCl2
(-97)

M = Cs⁺

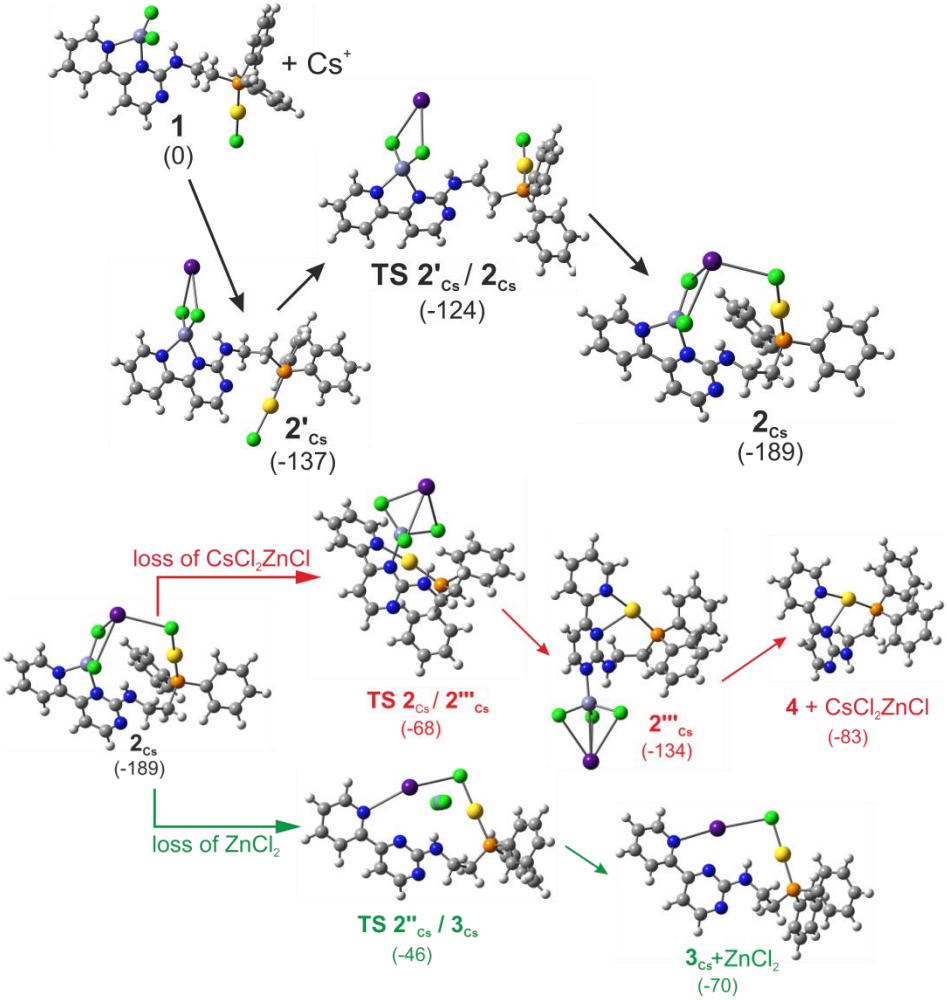
+ Cs+
1
(0)
TS 2'Cs / 2Cs
(-124)
2'Cs
(-137)
2Cs
(-189)
loss of CsCl2ZnCl
2Cs
(-189)
TS 2Cs / 2'''Cs
(-68)
2'''Cs
(-134)
4 + CsCl2ZnCl
(-83)
loss of ZnCl2
TS 2''Cs / 3Cs
(-46)
3Cs+ZnCl2
(-70)

10.2.6 Temperature Dependence of Li^+ Association and Subsequent $ZnCl_2$ Elimination

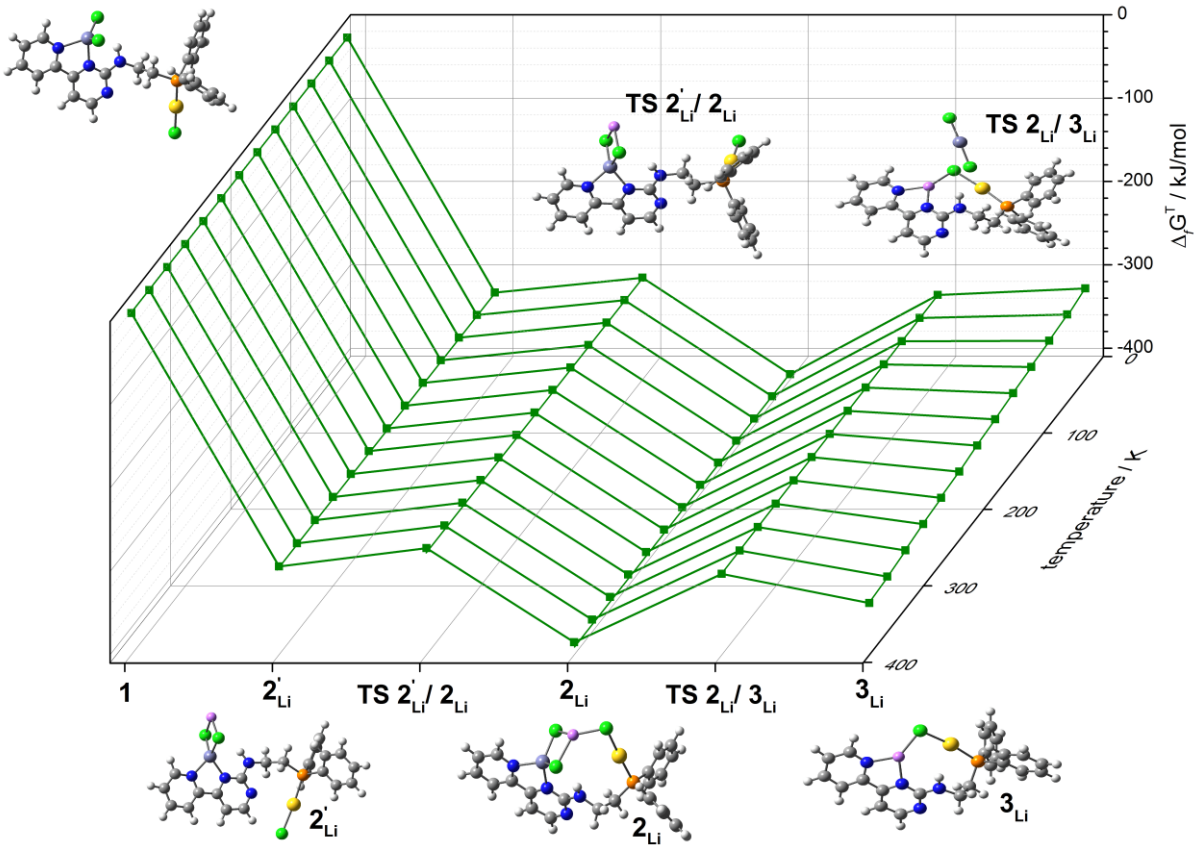

10.3 Two color Delay Dependent IR Probing of Torsional Isomerization in a $[AgL_1L_2]^+$ Complex

Johannes Lang, Maximilian Gaffga, Fabian Menges
and Gereon Niedner-Schatteburg

Fachbereich Chemie and Forschungszentrum OPTIMAS,
Technische Universität Kaiserslautern,
67663 Kaiserslautern, Germany

Content

10.3.1 Details on the Electrospray Ionization - Mass Spectra

ESI-MS was performed using a modified Paul-type quadrupole ion trap instrument (AmaZon SL, Bruker Daltonics). The ion source was used in positive electrospray ionization mode. Scan speed was 32 500 m/z per s (0.3 FWHM per m/z) with a scan range of at least 100 to 500 m/z. The sample solutions were continuously infused into the ESI chamber by a syringe pump at a flow rate of 2 mL min^{-1}. Nitrogen was used as drying gas with a flow rate of 3.0 L min^{-1} at 210 °C. The solutions were sprayed at a nebulizer pressure of 280 mbar and the electrospray needle was held at 4.5 kV. The instrument was controlled by Bruker Esquire Control 5.3 software and data analysis was performed using Bruker Data Analysis 3.4 software.

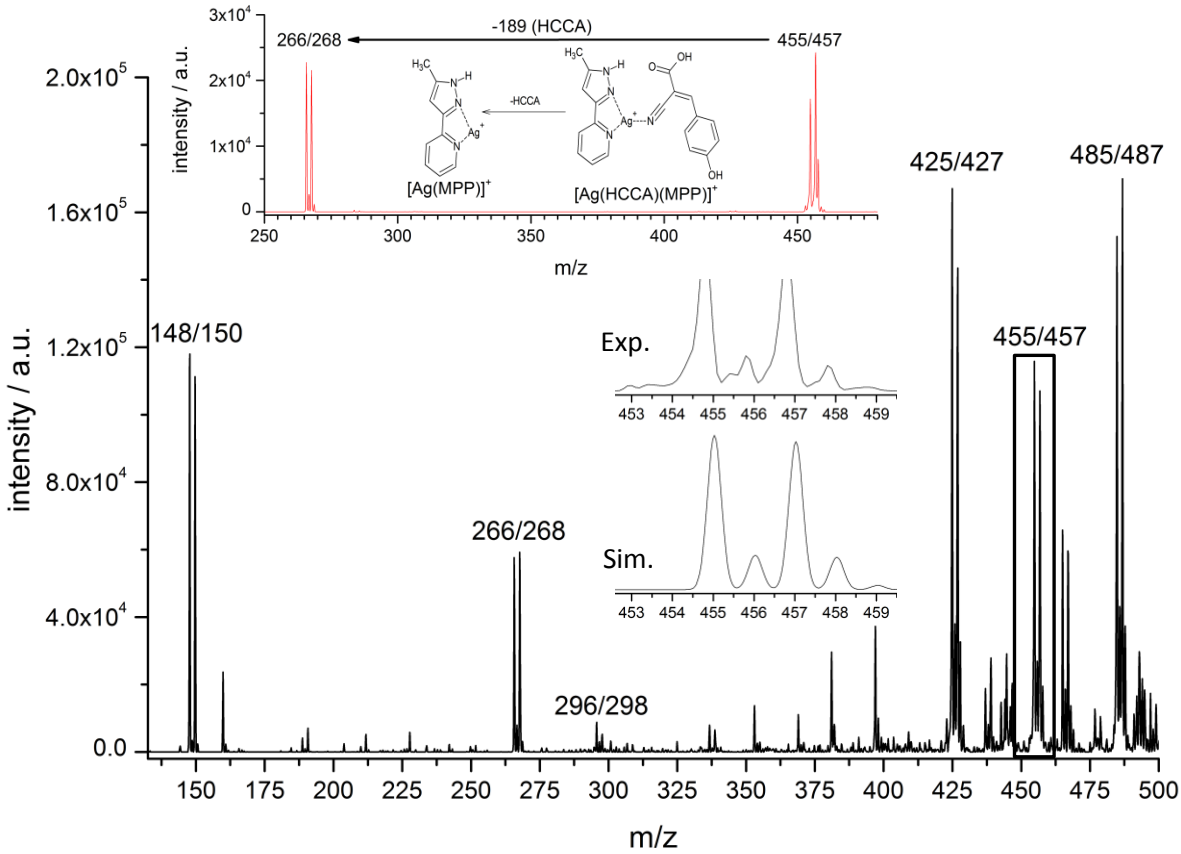

Figure S1: Cationic ESI-MS of a solution of $AgNO_3$, MPP and HCCA in acetonitrile. **Inset (middle)**: Simulated isotopic distribution of the $[Ag(HCCA)(MPP)]^+$ complex in comparison to the mass spectrum. **Inset (top)**: CID fragmentation of $[Ag(HCCA)(MPP)]^+$. Dissociation of the HCCA ligand is the exclusive fragmentation channel. The mass labeling refers to the two silver isotopes ^{107}Ag and ^{109}Ag.

Table S1: Assignment of mass peaks in the experimental spectrum. The mass labeling refers to the two silver isotopes ^{107}Ag and ^{109}Ag.

m/z	assigned formula	abbreviation
148/150	$[Ag(CH_3CN)]^+$	-
266/268	$[Ag(C_9H_9N_3)]^+$	$[Ag(MPP)]^+$
296/298	$[Ag(C_{10}H_7NO_3)]^+$	$[Ag(HCCA)]^+$
425/427	$[Ag(C_9H_9N_3)_2]^+$	$[Ag(MPP)_2]^+$
455/457	$[(C_9H_9N_3)Ag(C_{10}H_7NO_3)]^+$	$[Ag(HCCA)(MPP)]^+$
485/487	$[(C_{10}H_7NO_3)Ag(C_{10}H_7NO_3)]^+$	$[Ag(HCCA)_2]^+$

10.3.2 IR-MPD Spectra

An experimental IRMPD spectrum arises from a plot of the fragmentation efficiency as a function of laser frequency. The fragmentation efficiency (frag. eff.) is defined as:

$$frag.eff. = \left(\frac{\sum_i I_{fragment\ ion}(i)}{\sum_i I_{parent\ ion}(i) + \sum_i I_{fragment\ ion}(i)} \right)$$

With $I_{fragment\ ion}$= intensity of the fragment ion and $I_{precursor}$= intensity of the parent ion.

The monitored parent ion (MP) masses are:

MP(0)=454.9
MP(1)=455.9
MP(2)=456.9
MP(3)=457.9
MP(4)=459.1

} $[Ag(HCCA)(MPP)]^+$

The monitored fragment ion (MF) masses are:

MF(0)=265.9
MF(1)=266.9
MF(2)=267.9
MF(3)=268.9

} $[Ag(MPP)]^+$

10.3.3 Laser System

A KTP/KTA optical parametric oscillator/amplifier (OPO/A, LaserVision) system pumped with a pulsed 10 Hz injection seeded Nd^{3+}:YAG laser (PL8000, Continuum) was used as a source of tunable IR radiation ($\Delta n = 0.9\ cm^{-1}$, $\Delta t = 7$ ns) for recording the vibrational spectra (IR_{scan}). The OPA idler wave (≤ 10 mJ per pulse) was used to record spectra within 2600–3900 cm^{-1}.The difference frequency (DF) between the OPA signal and idler waves generated in a $AgGaSe_2$ crystal (≤ 2 mJ per pulse) was applied in the range of 1200–2100 cm^{-1}. After passing through the chamber the IR beam was directed onto a power meter sensor. The idler beam was focused by a 50 cm CaF_2 lens. The DF radiation was focused tighter, by a 90° off-axis parabolic silver mirror with an effective focal length of 15 cm. Optionally, the two-color IR-MPD as facilitated using a second IR OPO/A laser system (IR_{fix}) set to a selected vibrational resonance frequency. Its idler output was focused by a f = 75 cm CaF_2 lens being aligned counter-propagating with respect to the scanning laser beam. Each trapped and isolated portion of ions was irradiated by 2–4 laser pulses (or pulse pairs in two-laser experiments) to produce a sufficient amount of fragment ions. The IR spectra were recorded as ion chromatograms while continuously scanning the IR wavelength. The IR-MPD signal was evaluated as $F_k/(F_k + P_i)$, where F_k and P_i are the sums of the fragment and the parent ion signals, respectively. The IR frequency was calibrated using a wave meter. Despite the online IR power measurement the recorded spectra were not normalized. This is so because of the intrinsically nonlinear power dependence of IR-MPD yields.

10.3.4 Coordinates of $[AgL_1L_2]^+$ Isomers A-D

(B3LYP/cc-pVTZ (H, C, N, O) and Stuttgart 1997 ECP (Ag))

Isomer A:

43

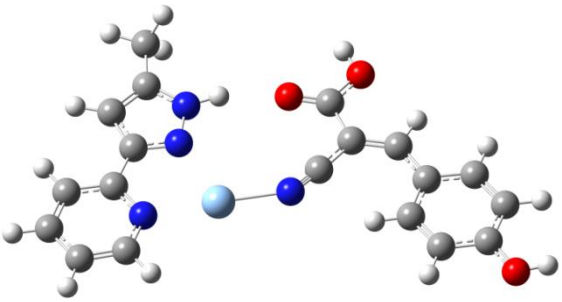

C	7.68622	3.85189	3.68348
C	6.75584	2.84091	3.85432
C	6.99262	1.58129	3.30532
C	8.84398	3.58910	2.96412
C	9.01855	2.31766	2.44562
N	8.12371	1.33489	2.60677
H	9.90539	2.07063	1.87940
H	9.59748	4.34586	2.80462
H	7.50976	4.83139	4.10578
H	5.84769	3.02039	4.40938
C	6.02669	0.48705	3.46661
N	6.28355	-0.70341	2.92734
C	4.78425	0.45638	4.13484
H	4.29094	1.24777	4.66939
C	4.30496	-0.82868	3.96630
N	5.24229	-1.48066	3.23578
H	5.24823	-2.44147	2.91328
Ag	8.38037	-0.73189	1.77718
C	11.63608	-5.58292	-1.41371
H	12.37467	-4.81622	-1.59756
C	10.47911	-5.30899	-0.72756
H	10.31989	-4.30306	-0.37239
C	9.51450	-6.31553	-0.49034
C	11.87978	-6.87950	-1.89281
C	10.94312	-7.89508	-1.67245
H	11.12907	-8.89563	-2.04143
C	9.78535	-7.61015	-0.98428
H	9.06358	-8.39861	-0.81699
O	13.03060	-7.07638	-2.55421
H	13.11355	-7.99233	-2.84526
C	8.28196	-6.13379	0.20793
H	7.67343	-7.02650	0.27664
C	7.71528	-5.04205	0.81302
C	6.39731	-5.11285	1.48361
O	5.86560	-4.17197	2.03744
O	5.83510	-6.32974	1.42300
C	8.29427	-3.75338	0.87966
N	8.70285	-2.67940	0.97581
C	3.05012	-1.48100	4.43529
H	2.43898	-0.76711	4.98194
H	2.46083	-1.85763	3.59779
H	3.26280	-2.32045	5.09921
H	4.98411	-6.28543	1.88279

Isomer B:

43

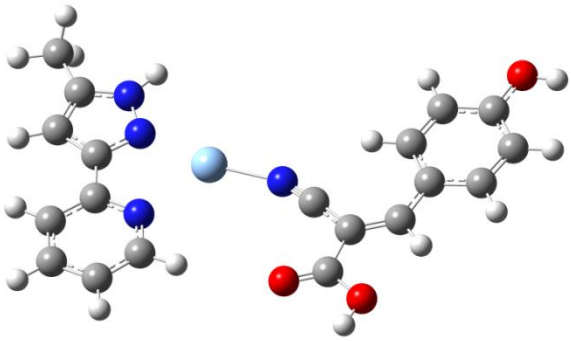

C	9.01373	1.17592	6.08202
C	7.94247	1.58731	5.30259
C	7.53793	0.78852	4.23629
C	9.65192	-0.01787	5.77865
C	9.18970	-0.75834	4.69832
N	8.16059	-0.36608	3.94703
H	9.65625	-1.69614	4.42364
H	10.48922	-0.37376	6.36070
H	9.34419	1.78121	6.91474
H	7.43063	2.51316	5.51889
C	6.40962	1.16238	3.37010
N	6.05883	0.37439	2.34938
C	5.56151	2.28473	3.42233
H	5.58327	3.09867	4.12374
C	4.67137	2.14012	2.37691
N	5.01032	0.98124	1.76482
H	4.57556	0.55948	0.96169
Ag	7.19517	-1.49657	2.00708
C	8.51130	-8.20297	-2.56885
H	8.77984	-9.11237	-3.09125
C	9.19718	-7.82222	-1.43622
H	10.00707	-8.44257	-1.07569
C	8.87179	-6.64352	-0.73311
C	7.46454	-7.40509	-3.04038
C	7.11942	-6.22793	-2.36028
H	6.30685	-5.62819	-2.74401
C	7.80908	-5.85738	-1.23151
H	7.52024	-4.94666	-0.73084
O	6.74962	-7.70753	-4.13744
H	7.05896	-8.52920	-4.53658
C	9.65204	-6.34257	0.42870
H	10.42655	-7.06756	0.64466
C	9.61268	-5.31080	1.32531
C	10.55448	-5.21285	2.47069
O	10.54378	-4.30619	3.26893
O	11.42298	-6.23954	2.52702
C	8.70482	-4.22775	1.28951
N	7.99738	-3.31902	1.32202
C	3.54278	2.99517	1.91484
H	3.70415	3.35028	0.89576
H	2.59703	2.45144	1.93609
H	3.44548	3.86344	2.56142
H	11.99200	-6.09335	3.29693

Isomer C:

43

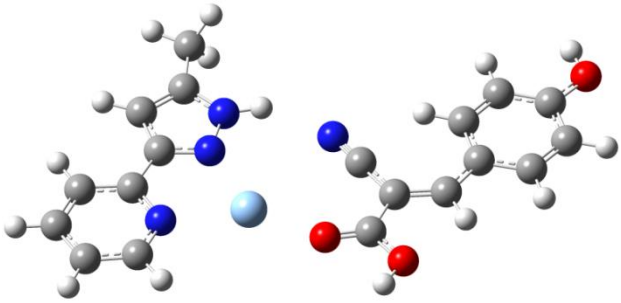

C	7.44235	2.15758	6.76086
C	6.58634	1.67650	5.78336
C	7.04152	0.70752	4.89110
C	8.73655	1.66094	6.82807
C	9.11872	0.69805	5.90683
N	8.30003	0.22942	4.96159
H	10.11830	0.28509	5.92473
H	9.43766	2.00656	7.57325
H	7.10331	2.90925	7.46015
H	5.57424	2.04517	5.70974
C	6.17453	0.16380	3.83744
N	6.65407	-0.76658	3.01344
C	4.83691	0.45432	3.50261
H	4.16901	1.15529	3.96951
C	4.53689	-0.35839	2.42456
N	5.66068	-1.06945	2.17215
H	5.84470	-1.77157	1.46440
Ag	8.81721	-1.40687	3.33083
C	7.48693	-6.29921	-2.62895
H	6.45558	-6.11934	-2.90535
C	8.06001	-5.58375	-1.60403
H	7.46045	-4.84899	-1.09144
C	9.40414	-5.80411	-1.22836
C	8.23392	-7.26482	-3.32102
C	9.56805	-7.50305	-2.97003
H	10.12796	-8.24983	-3.51364
C	10.13254	-6.78422	-1.94523
H	11.16375	-6.97107	-1.67599
O	7.72553	-7.99131	-4.32723
H	6.80466	-7.75920	-4.49601
C	10.09783	-5.12442	-0.18359
H	11.12398	-5.44456	-0.05865
C	9.71831	-4.14133	0.69893
C	10.66389	-3.62358	1.69244
O	10.42413	-2.75727	2.52959
O	11.87692	-4.17845	1.63545
C	8.42458	-3.55653	0.73063
N	7.37833	-3.07255	0.76507
C	3.28769	-0.51420	1.62756
H	2.52774	0.17592	1.98553
H	3.46171	-0.30608	0.57081
H	2.88860	-1.52658	1.70824
H	12.42430	-3.77470	2.32533

Isomer D:

43

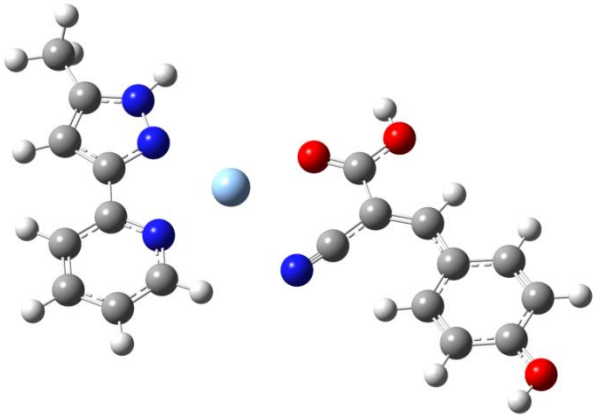

C	6.90806	2.38907	6.82609
C	6.21457	1.80635	5.77741
C	6.84524	0.84747	4.98718
C	8.21880	2.00259	7.06472
C	8.78544	1.04286	6.23980
N	8.11815	0.47858	5.22790
H	9.80338	0.70800	6.38263
H	8.79712	2.43034	7.87022
H	6.43027	3.13461	7.44650
H	5.19424	2.09140	5.57076
C	6.14709	0.20629	3.86423
N	6.77098	-0.69962	3.11030
C	4.82599	0.39754	3.40646
H	4.07267	1.05551	3.79943
C	4.67682	-0.44627	2.32600
N	5.86892	-1.07870	2.19247
H	6.12331	-1.76702	1.50428
Ag	9.03128	-1.10433	3.85389
C	16.10796	-1.71510	6.59916
H	16.11642	-1.00115	7.41320
C	14.96669	-1.89437	5.85302
H	14.09347	-1.31143	6.09919
C	14.93531	-2.82113	4.78721
C	17.26449	-2.45509	6.31025
C	17.26066	-3.38036	5.25975
H	18.16006	-3.94122	5.05183
C	16.11664	-3.55346	4.51980
H	16.11708	-4.26930	3.70839
O	18.40441	-2.32046	7.00504
H	18.31050	-1.66453	7.70594
C	13.80901	-3.08343	3.95140
H	13.98779	-3.83241	3.19080
C	12.53842	-2.56376	3.92805
C	11.55525	-3.01699	2.94199
O	10.40057	-2.60555	2.84775
O	12.00372	-3.95340	2.10260
C	12.05455	-1.56977	4.81901
N	11.61228	-0.76423	5.51736
C	3.52077	-0.70334	1.42228
H	2.67494	-0.08614	1.71445
H	3.76554	-0.46878	0.38503
H	3.20574	-1.74726	1.46527
H	11.28389	-4.18228	1.49642

10.3.5 Tables of Experimental and Calculated Vibrational Frequencies

Table S2: Experimentally observed IR-MPD bands.

	OH-stretching vibrations / cm^{-1}	**NH-stretching vibrations / cm^{-1}**	**CO-stretching vibrations / cm^{-1}**	**C=C- skeletal vibrations / cm^{-1}**
[Ag(HCCA)(MPP)]$^+$	3639 (st), 3581 (st)	3490 (m), 3400 (w)	1785 (w), 1763 (m), 1743 (w)	1583 (st), 1522(w)

Table S3: Calculated vibration frequencies of isomers A-D (theory level: B3LYP/cc-pVTZ (H, C, N, O) and Stuttgart 1997 ECP (Ag)). Frequencies above 2000 cm^{-1} are scaled with 0.96. Below 2000 cm^{-1} no scaling factor was applied.

A: ΔE(DFT) = 0 kJ/mol						
$\tilde{\nu}$/ cm^{-1}	3639	3606	3392	2948	1749	1584
assignment	ν(Ph<u>OH</u>)	ν(CO<u>OH</u>)	ν(NH)	ν(CH$_3$)	ν(<u>CO</u>OH)	C=C
B: ΔE(DFT) = 8 kJ/mol						
$\tilde{\nu}$/ cm^{-1}	3641	3603	3518	2948	1770	1586
assignment	ν(Ph<u>OH</u>)	ν(CO<u>OH</u>)	ν(NH)	ν(CH$_3$)	ν(<u>CO</u>OH)	C=C
C: ΔE(DFT) = 21 kJ/mol						
$\tilde{\nu}$/ cm^{-1}	3640	3597	3389	2947	1684	1581
assignment	ν(Ph<u>OH</u>)	ν(CO<u>OH</u>)	ν(NH)	ν(CH$_3$)	ν(<u>CO</u>OH)	C=C
D: ΔE(DFT) = 33 kJ/mol						
$\tilde{\nu}$/ cm^{-1}	3640	3602	3516	2946	1677	1589
assignment	ν(Ph<u>OH</u>)	ν(CO<u>OH</u>)	ν(NH)	ν(CH$_3$)	ν(<u>CO</u>OH)	C=C

10.3.6 CH Stretching Vibrations of the Pyridine Ring

In the range 3045-3090 cm^{-1} four vibrational modes can be assigned to the aromatic CH groups of the pyridine ring (MPP ligand L_2, cf. Fig S2). The frequency and intensity of these 4 modes depends on the torsional isomerization of the complex (cf. Fig. S3).

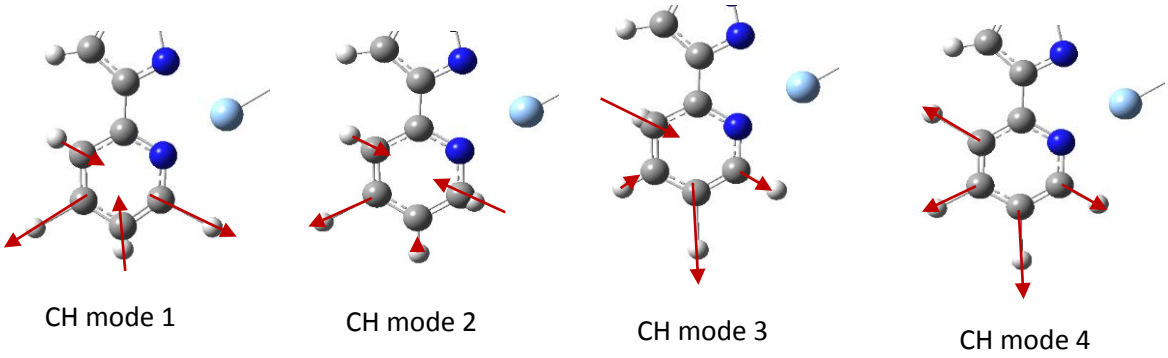

Figure S2: Definition of selected CH normal modes of the pyridine ring. Note: Arrows represent the directions of motion, the arrow lengths are not concurrent to the lengths of displacement vectors.

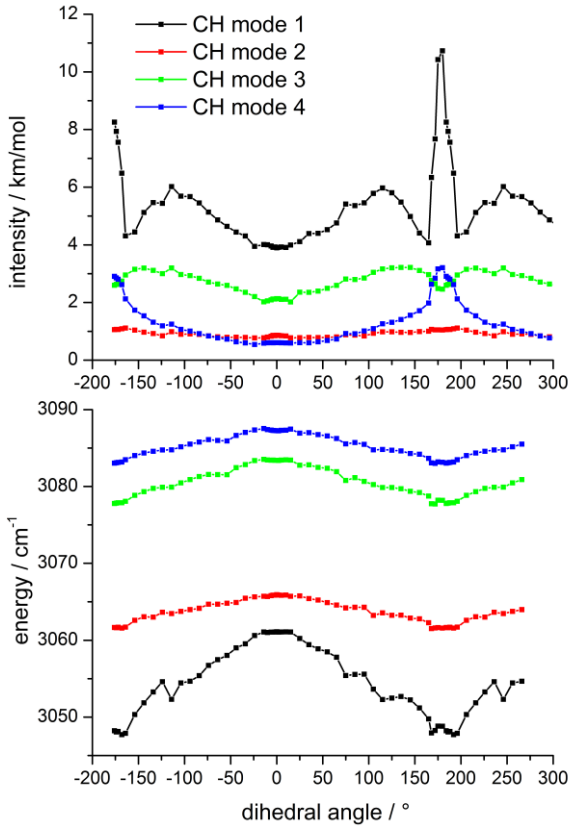

Figure S3: Intensities (top) and frequencies (bottom) of four selected CH normal modes of the pyridine ring in dependence of the dihedral angle (cf. Fig. S-2 for definition of modes). All calculations at the B3LYP/cc-pVTZ (H, C, N, O) and Stuttgart 1997 ECP (Ag) level of theory, scaling factor 0.96 .

10.4 Magnetostructural Correlations in Isolated Trinuclear Iron(III) Oxo Acetate Complexes

Johannes Lang[a], Joachim M. Hewer[a], Matthias Klein[a], Tobias J. Lau[b], Christoph van Wüllen[a] and Gereon Niedner-Schatteburg[a]

(c) Fachbereich Chemie and Forschungszentrum OPTIMAS, Technische Universität Kaiserslautern, 67663 Kaiserslautern, Germany

(d) Helmholtz Zentrum für Materialien und Energie, BESSY II, 12489 Berlin, Germany

Content

10.4.1 Details on the ESI-MS and CID Measurements (Bruker AmaZon SL)

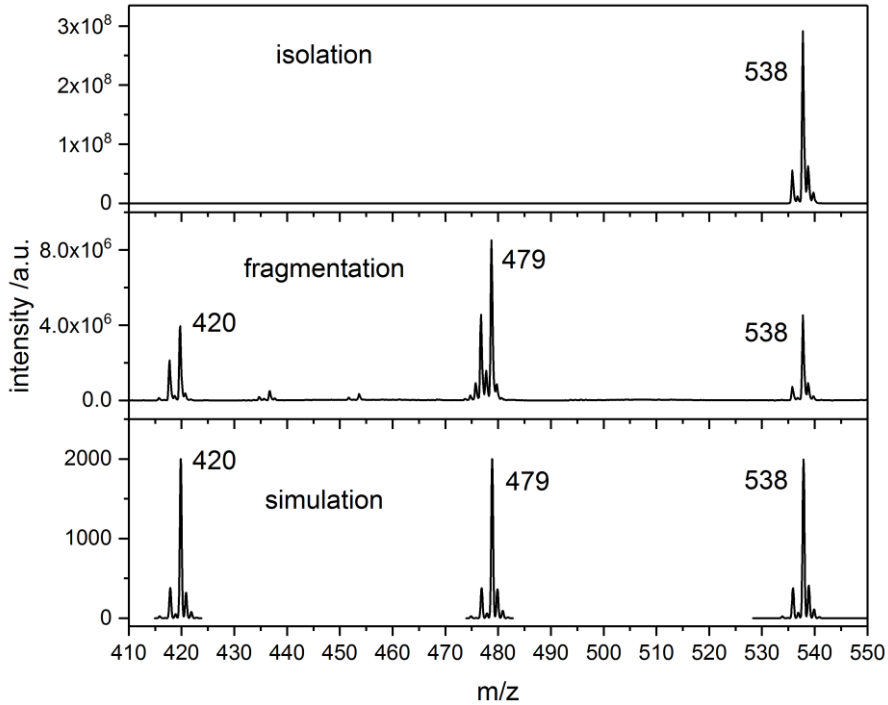

Figure S1: Mass spectra of isolated $[Fe_3O(OAc)_6]^+$ (top), its CID fragmentation mass spectra of (middle) and simulated mass peaks (FWHM = 0.4).

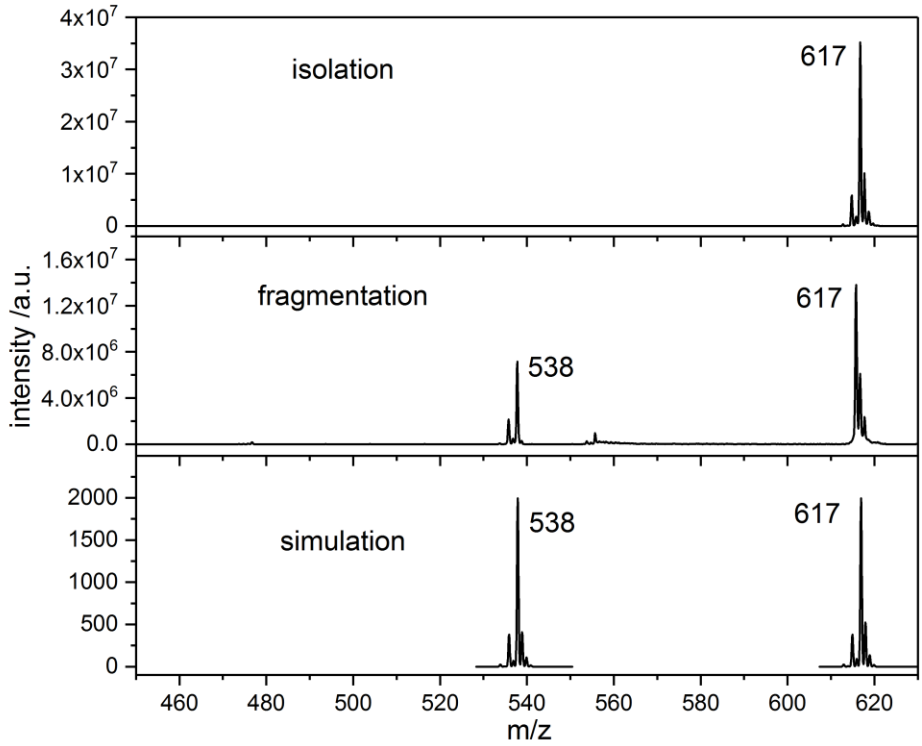

Figure S2: Mass spectra of isolated $[Fe_3O(OAc)_6(Py)_1]^+$ (top), its CID fragmentation mass spectra of (middle) and simulated mass peaks (FWHM = 0.4).

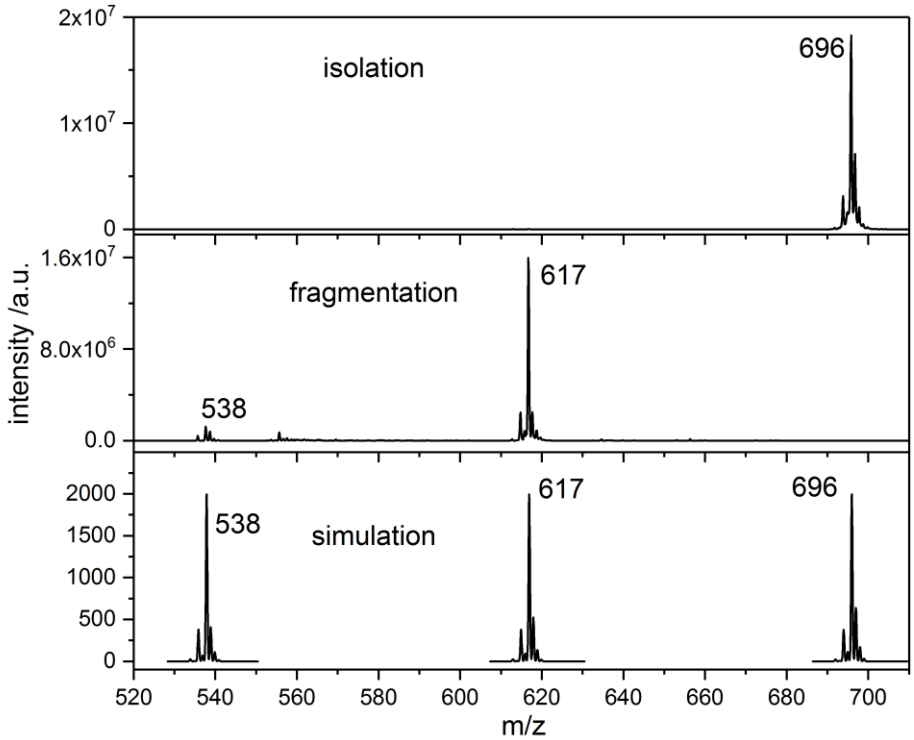

Figure S3: Mass spectra of isolated $[Fe_3O(OAc)_6(Py)_2]^+$ (top), its CID fragmentation mass spectra of (middle) and simulated mass peaks (FWHM = 0.4).

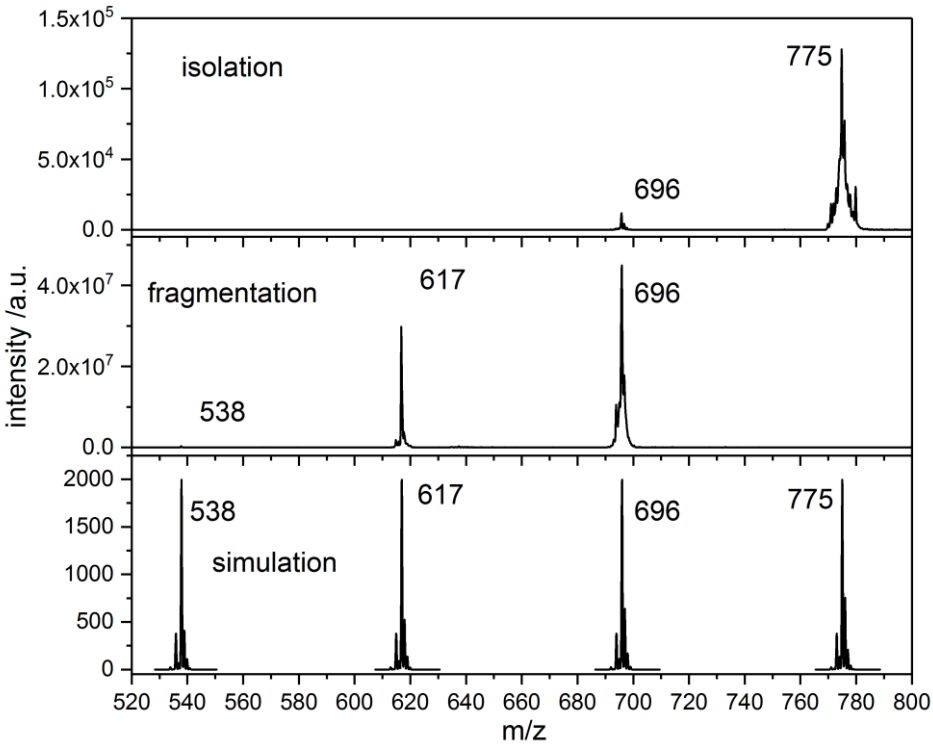

Figure S4: Mass spectra of isolated $[Fe_3O(OAc)_6(Py)_3]^+$ (top), its CID fragmentation mass spectra of (middle) and simulated mass peaks (FWHM = 0.4).

Table S1: Compilation of ESI-MS data on $[Fe_3O(OAc)_6(Py)_n]^+$ (n = 1,2,3; OAc = CH_3CO_2). The indicated mass labels refer to the most abundant isotope peaks.

Species	m/z
$[Fe_3O(OAc)_4]^+$	420
$[Fe_3O(OAc)_5]^+$	479
$[Fe_3O(OAc)_6]^+$	538
$[Fe_3O(OAc)_6(Py)_1]^+$	617
$[Fe_3O(OAc)_6(Py)_2]^+$	696
$[Fe_3O(OAc)_6(Py)_3]^+$	775

10.4.2 IR-MPD and Calculated IR Spectra of $[Fe_3O(OAc)_6(Py)_n]^+$ (n = 0,1,2,3)

Table S2: Structural data of geometry optimized minimum structures of $[Fe_3O(OAc)_6(Py)_n]^+$ (n = 0,1,2,3) by DFT at B3LYP/cc-pVTZ (H, C, N, O) and Stuttgart 1997 ECP (Fe) level of theory. The multiplicity is 16.

	$[Fe_3O(OAc)_6]^+$	$[Fe_3O(OAc)_6(Py)_1]^+$	$[Fe_3O(OAc)_6(Py)_2]^+$	$[Fe_3O(OAc)_6(Py)_3]^+$
Fe-$O_{central}$ distance / Å	1.89	1.87	1.97	1.94
	1.89	1.87	1.85	1.94
	1.89	1.98	1.97	1.94
Fe-Fe distance / Å	3.27	3.18	3.27	3.37
	3.27	3.37	3.27	3.37
	3.27	3.37	3.45	3.37
Fe-N_{Py} distance / Å	-	2.15	2.18	2.22
				2.22
			2.18	2.22

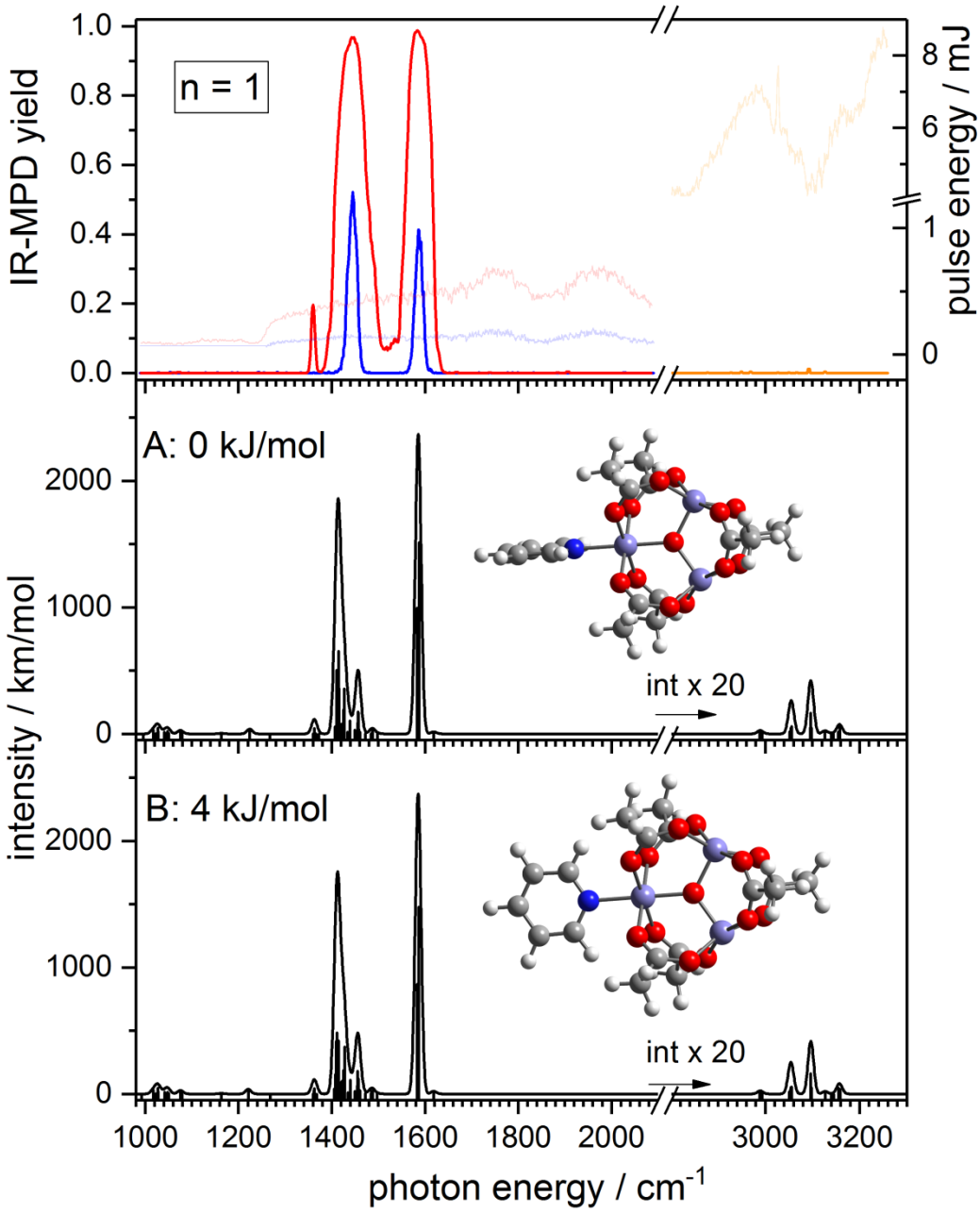

Figure S5: IR-MPD spectra of the $[Fe_3O(OAc)_6(Py)_1]^+$ complex (top) in comparison with the DFT calculations at the B3LYP/cc-pVTZ (H, C, N, O) and Stuttgart 1997 ECP (Fe) level of theory. Frequencies are scaled with 0.98 and the multiplicity is 16.

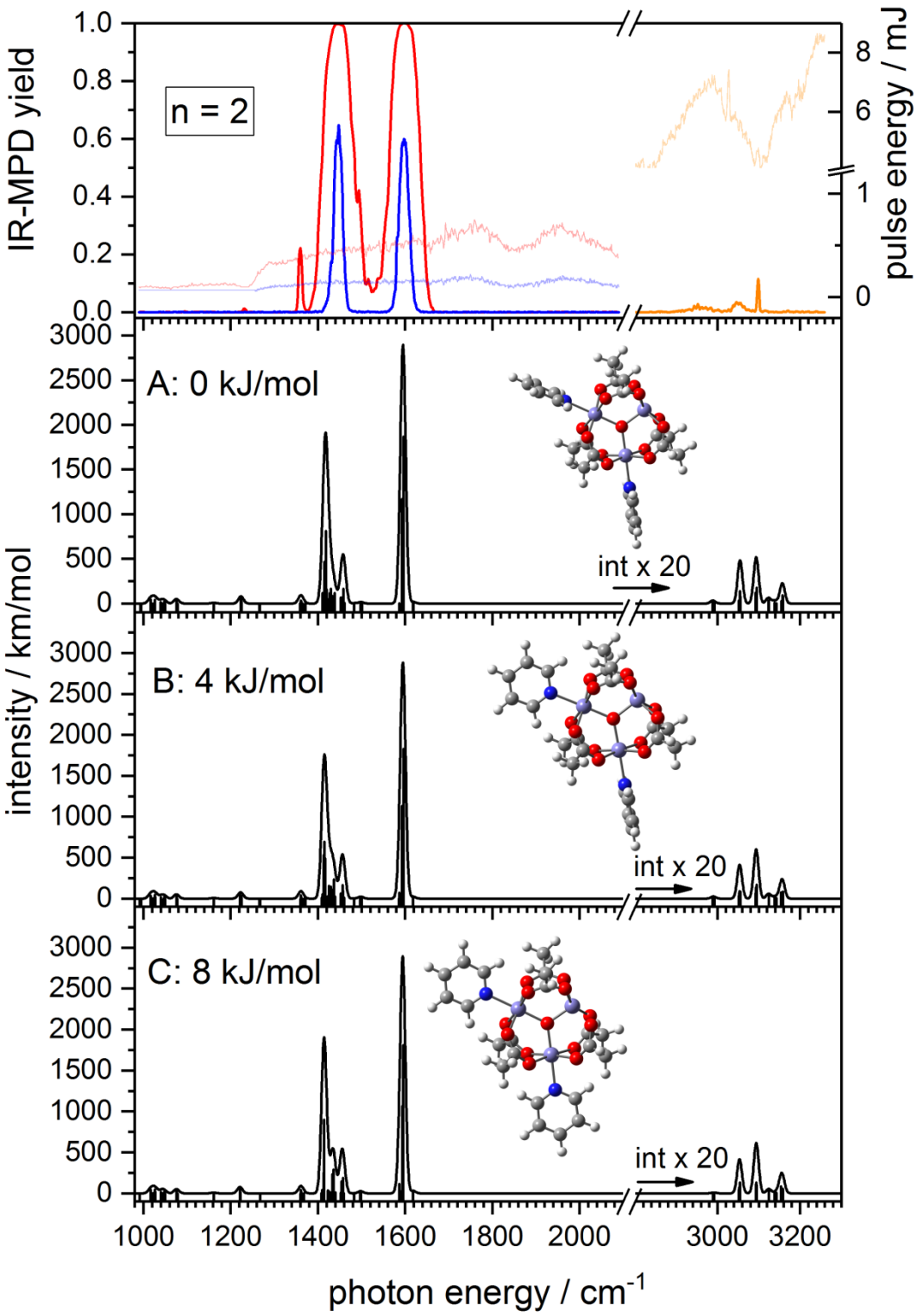

Figure S6: IR-MPD spectra of the $[Fe_3O(OAc)_6(Py)_2]^+$ complex (top) in comparison with the DFT calculations at the B3LYP/cc-pVTZ (H, C, N, O) and Stuttgart 1997 ECP (Fe) level of theory. Frequencies are scaled with 0.98 and the multiplicity is 16.

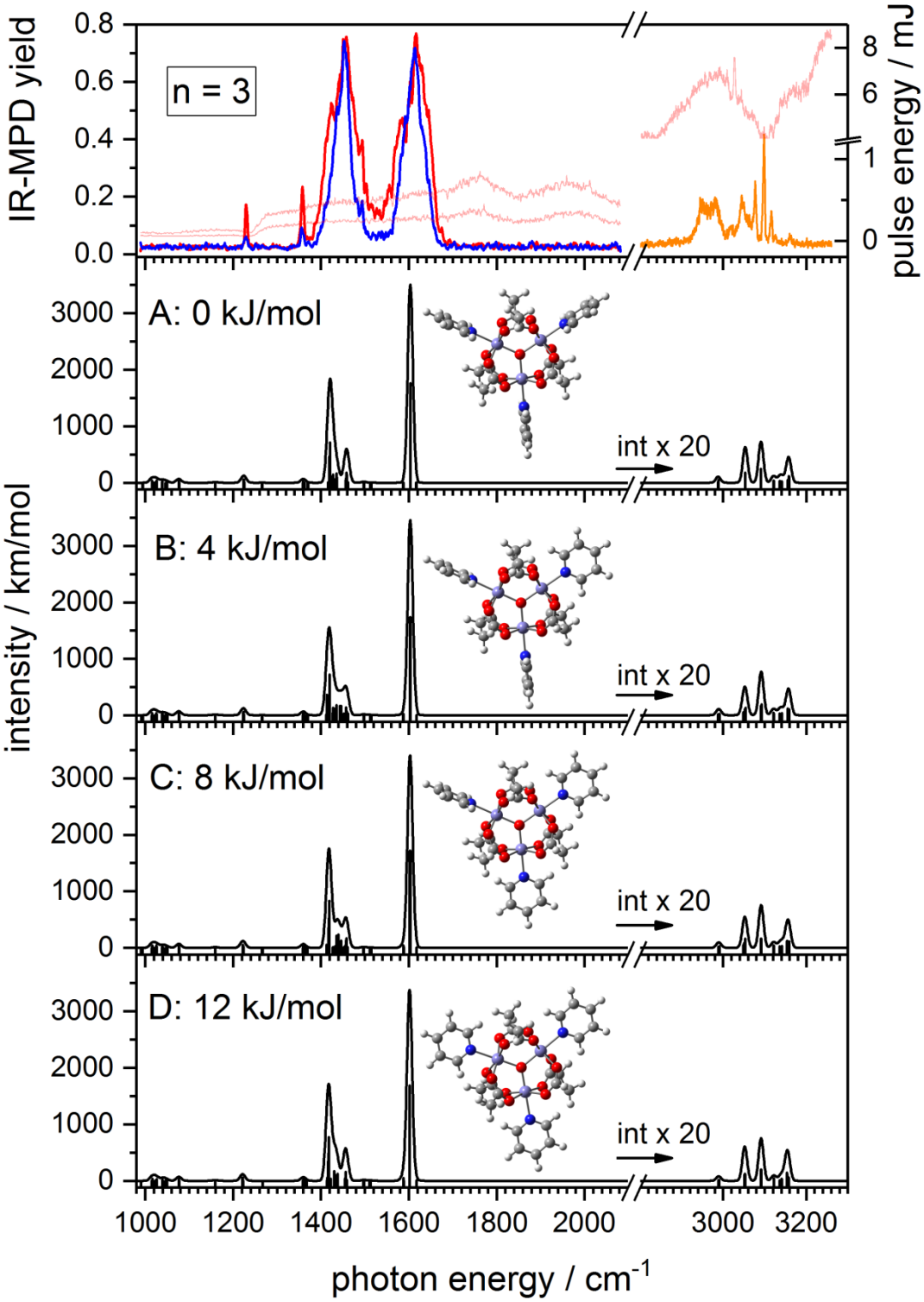

Figure S7: IR-MPD spectra of the $[Fe_3O(OAc)_6(Py)_3]^+$ complex (top) in comparison with the DFT calculations at the B3LYP/cc-pVTZ (H, C, N, O) and Stuttgart 1997 ECP (Fe) level of theory. Frequencies are scaled with 0.98 and the multiplicity is 16.

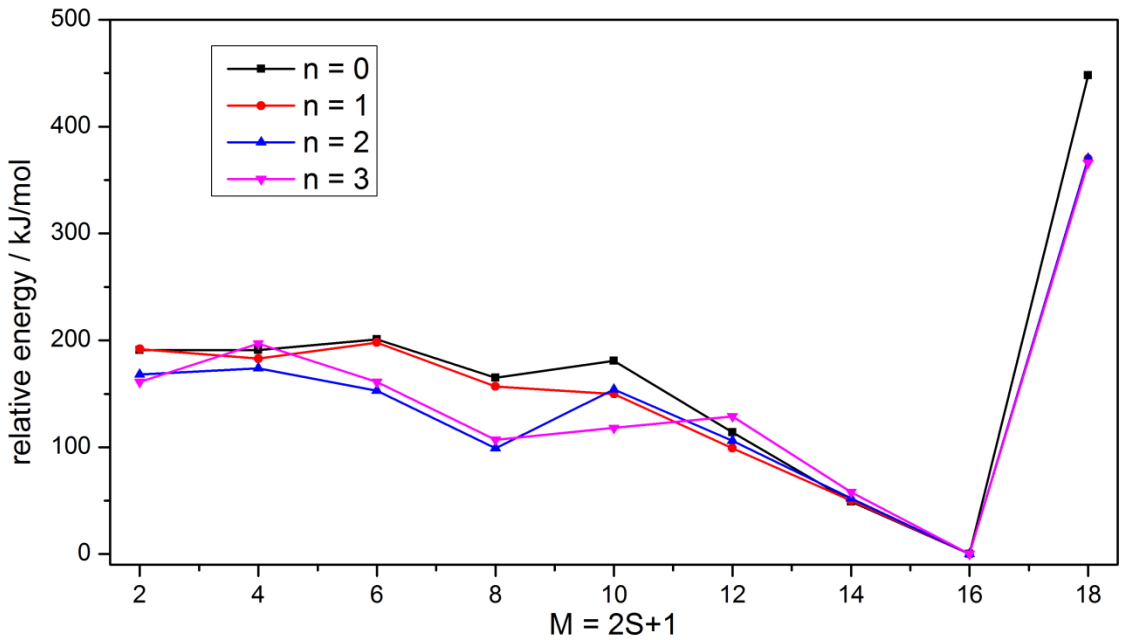

Figure S8: Relative energies of $[Fe_3O(OAc)_6(Py)_n]^+$ (n = 0,1,2,3) as a function of the multiplicity. The geometry was fully optimized for each multiplicity. The DFT calculations were performed at the B3LYP/cc-pVTZ (H, C, N, O) and Stuttgart 1997 ECP (Fe) level of theory.

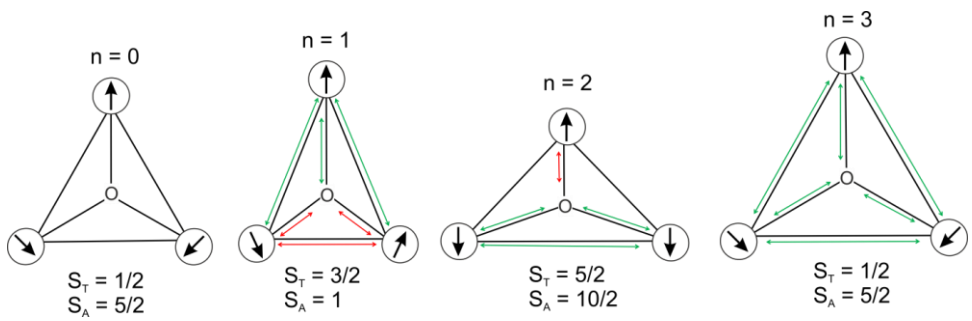

Scheme S1: Spin ground states of $[Fe_3O(OAc)_6(Py)_n]^+$ (n = 0,1,2,3). The spin orientation is visualized schematically via the direction of the arrows.

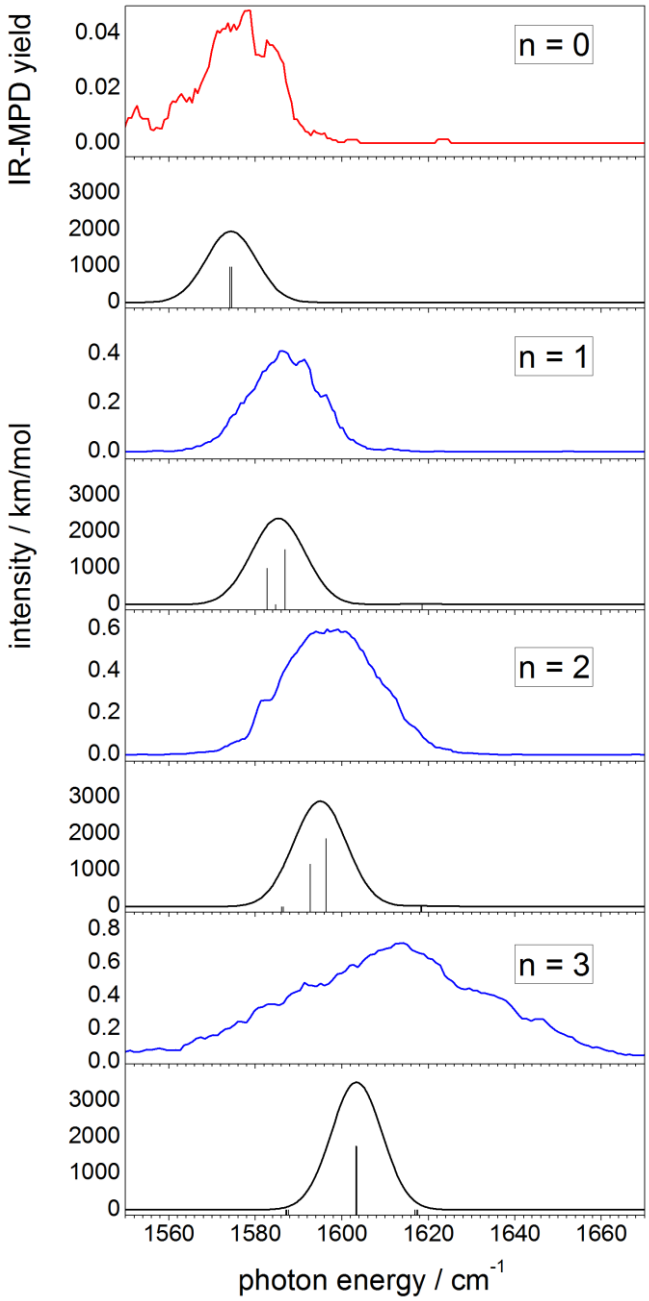

Figure S9: IR-PMD spectra of $[Fe_3O(OAc)_6(Py)_n]^+$ (n = 0,1,2,3) (colored curves) and calculated IR absorption spectra of geometry optimized $[Fe_3O(OAc)_6(Py)_n]^+$ (n = 0,1,2,3) (black curves) in the range of 1540 - 1680 cm^{-1}. Red curves indicate full power measurements while blue curves show spectra with attenuated pulse energies. The calculations were performed at the B3LYP/cc-pVTZ (H, C, N, O) and Stuttgart 1997 ECP (Fe) level of theory. The multiplicity is 16 and frequencies are scaled with 0.98.

10.4.3 Monitored m/z Values of IRMPD Spectra and CID – Appearance Curves

$[Fe_3O(OAc)_6]^+$:

Parent $[Fe_3O(OAc)_6]^+$	Fragment 1 $[Fe_3O(OAc)_5]^+$:	Fragment 2 $[Fe_3O(OAc)_4]^+$:
535.8	476.7	417.7
536.8	477.8	418.8
537.8	478.7	419.7
538.7	479.8	420.8
553.7		

$[Fe_3O(OAc)_6(Py)_1]^+$:

Parent $[Fe_3O(OAc)_6(Py)_1]^+$	Fragment $[Fe_3O(OAc)_6]^+$
614.8	535.8
615.8	536.8
616.8	537.8
617.7	538.7
618.9	553.7

$[Fe_3O(OAc)_6(Py)_2]^+$:

Parent $[Fe_3O(OAc)_6(Py)_2]^+$	Fragment 1 $[Fe_3O(OAc)_6(Py)_1]^+$	Fragment 2 $[Fe_3O(OAc)_6]^+$
693.8	614.8	535.8
694.9	615.8	536.8
695.8	616.8	537.8
696.8	617.7	538.7
698.9	618.9	553.7

$[Fe_3O(OAc)_6(Py)_3]^+$:

Parent $[Fe_3O(OAc)_6(Py)_3]^+$	Fragment 1 $[Fe_3O(OAc)_6(Py)_2]^+$	Fragment 2 $[Fe_3O(OAc)_6(Py)_1]^+$	Fragment 3 $[Fe_3O(OAc)_6]^+$
772.9	693.8	614.8	535.8
773.9	694.9	615.8	536.8
775	695.8	616.8	537.8
776	696.8	617.7	538.7
	698.9	618.9	553.7

10.4.4 Broken Symmetry Calculations with B3LYP_Gaussian and cc-pVTZ for all Atoms

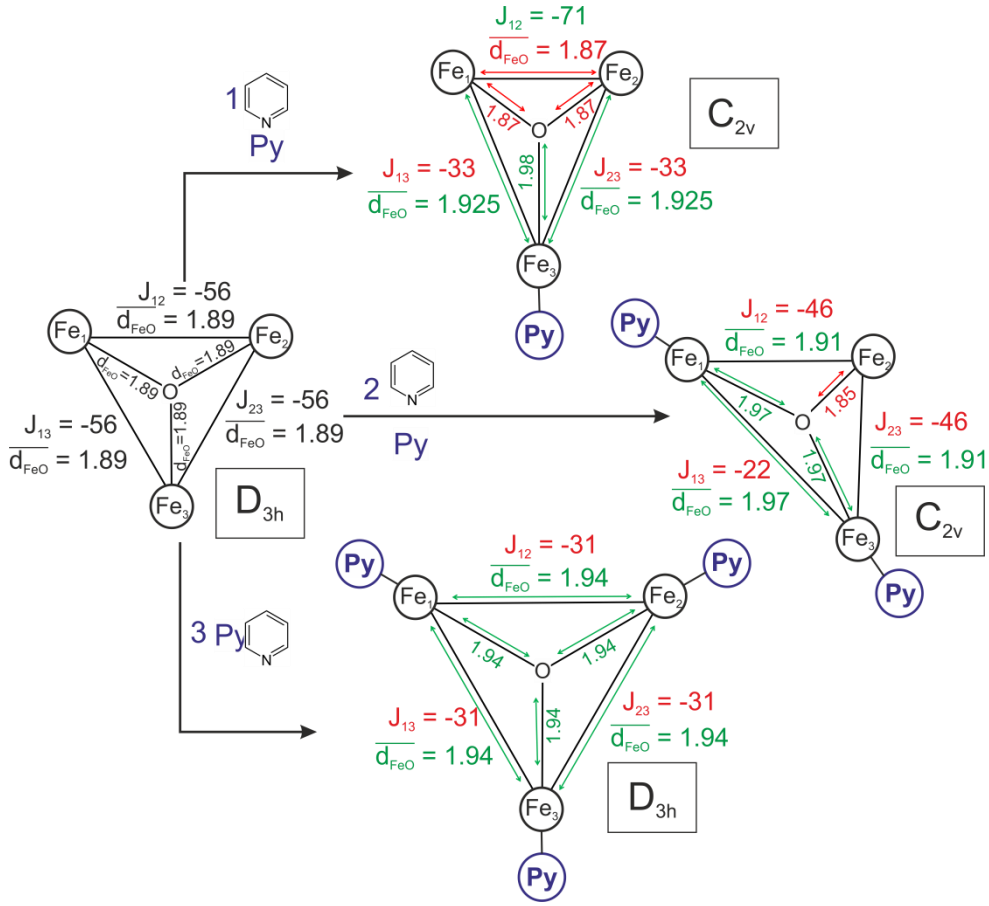

Scheme S2: Symmetries, atom distances (Fe-$O_{central}$ distances and mean Fe-O distances $\overline{d_{FeO}}$, averaged over two adjacent Fe atoms, all in Å) and magnetic coupling constants (J_{ij} in cm^{-1}) of the Fe_3O-core in $[Fe_3O(OAc)_6(Py)_n]^+$ (n = 0,1,2,3). The geometry optimizations were performed at the B3LYP/cc-pVTZ (H,C,N,O) and Stuttgart 1997 ECP (Fe)level of theory and the multiplicity is 16. The calculations of the coupling constants were performed at the B3LYP_Gaussian/cc-pVTZ (H,C,N,O, Fe) level of theory The acetate ligands are omitted for clarity. Green (red) indicates a larger (smaller) magnitude with respect to the (black) values of the n = 0 case.

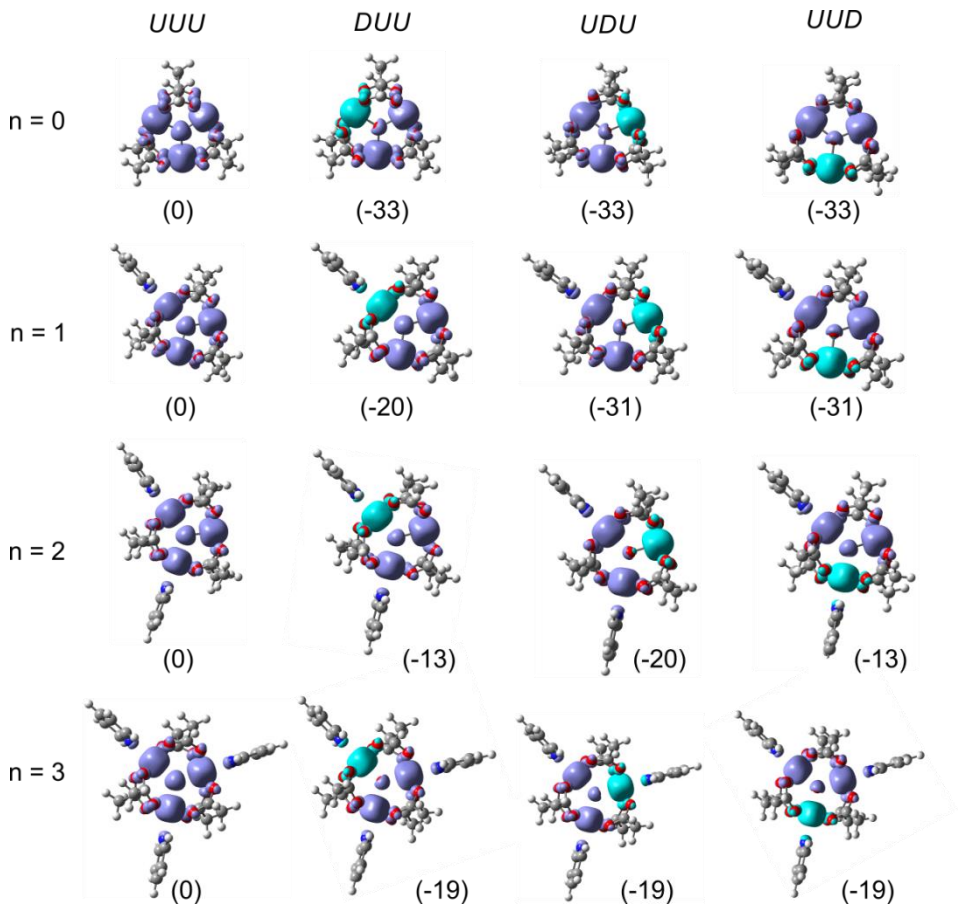

Figure S10: Spin density iso surfaces (Iso = 0.01) of $[Fe_3O(OAc)_6(Py)_n]^+$ (n = 0,1,2,3) in the one ferromagnetic and the three broken symmetry configurations. Purple and turquoise surfaces indicate alpha and beta spin, respectively. The relative energies in parentheses is given in kJ/mol. The calculations were performed at the B3LYP_Gaussian/cc-pVTZ (H,C,N,O, Fe) level of theory.

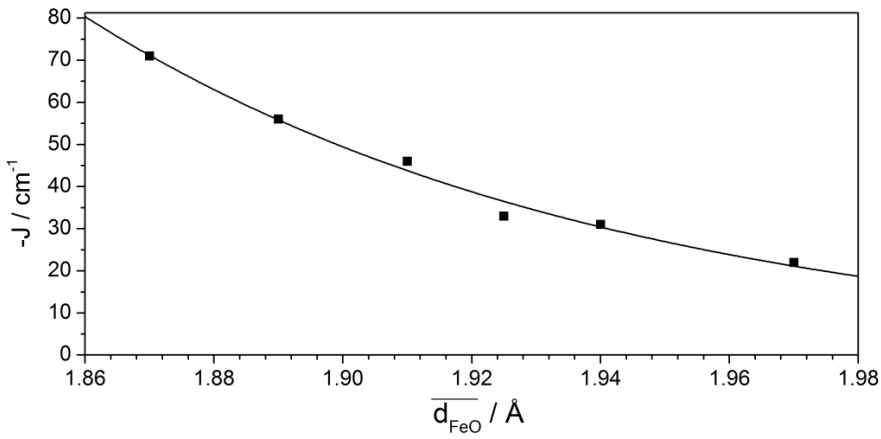

Figure S11: Correlation between the calculated magnetic coupling constant J and the geometric parameter $\overline{d_{FeO}}$ in $[Fe_3O(OAc)_6(Py)_n]^+$ (n = 0,1,2,3). The solid line ist a least squares fit with an exponential fit function (eq. 10).

10.5 Structural Characterization of Mononuclear and Binuclear Palladium Complexes in Isolation

Johannes Lang[a], Dagmar Hackenberger[b], Saeid Farsadpour[?], Werner R. Thiel[a], Lukas Gooßen[b] and Gereon Niedner-Schatteburg[a]

(a) Fachbereich Chemie and Forschungszentrum OPTIMAS,
Technische Universität Kaiserslautern,
67663 Kaiserslautern, Germany

(b) Lehrstuhl für Organische Chemie I
Ruhr-Universität Bochum
44801 Bochum

Content

10.5.1 Mass Spectra of CID Fragments and Sigmoid Fits of CID Appearance Curves

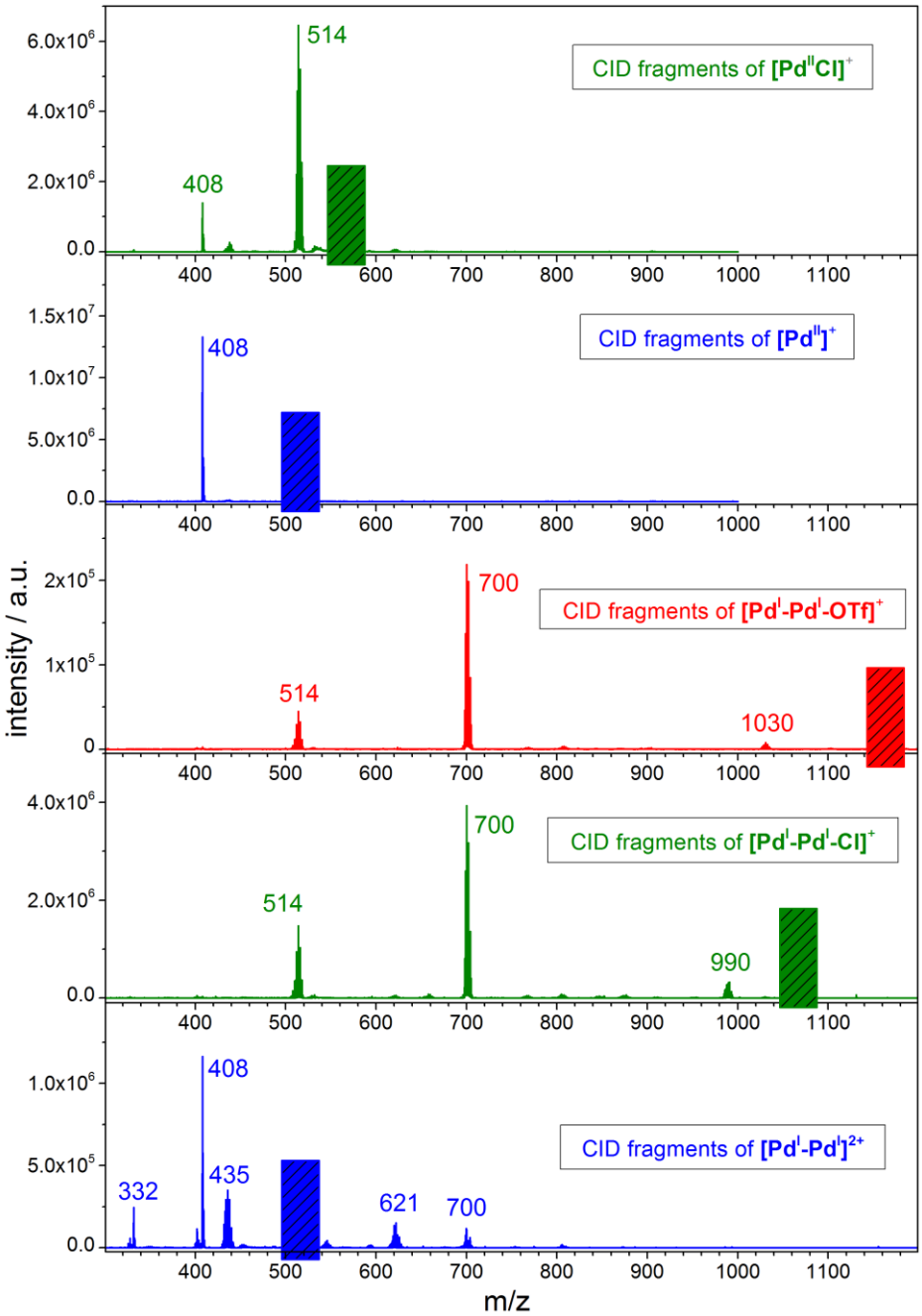

Figure S1: CID fragmentation mass spectra of $[Pd^{II}Cl]^+$, $[Pd^{II}]^+$, $[Pd^{I}\text{-}Pd^{I}OTf]^+$, $[Pd^{I}\text{-}Pd^{I}Cl]^+$, and $[Pd^{I}\text{-}Pd^{I}]^{2+}$ ions, recorded at a fixed fragmentation amplitude of 0.012 a.u. corresponding to the internal energy scale of the mass spectrometer. The vanished parent signals are indicated by rectangular markers of associated color.

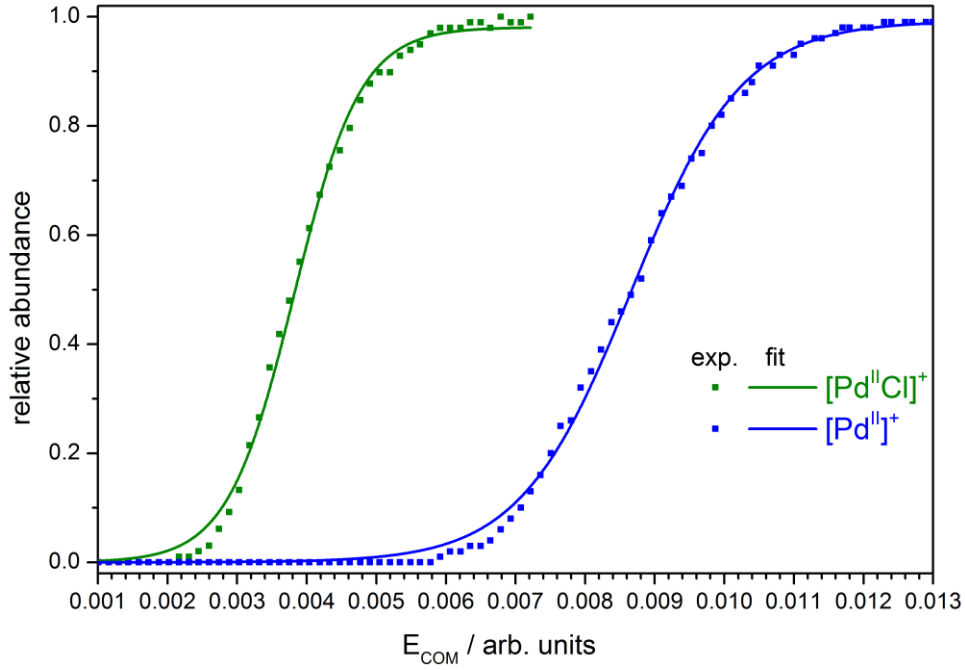

Figure S2: CID - fragment appearance curves of $[Pd^{II}Cl]^+$ (green squares) and **$[Pd^{II}]^+$** (blue squares). The colored lines indicate associated sigmoid fits according to e.g. (3).

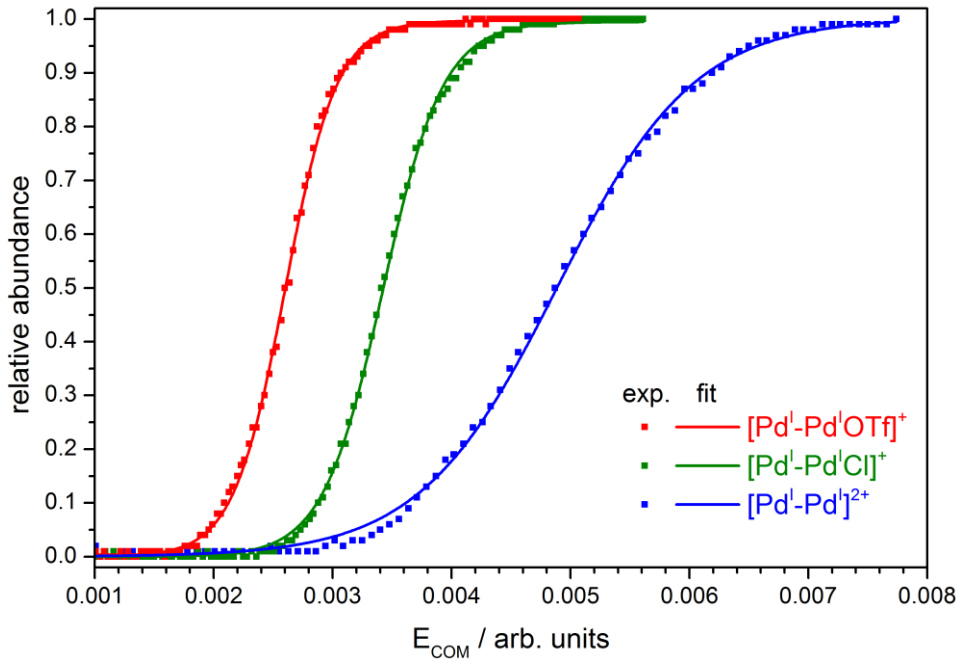

Figure S3: CID - fragment appearance curves of $[Pd^{I}\text{-}Pd^{I}OTf]^+$ (red squares), $[Pd^{I}\text{-}Pd^{I}Cl]^+$ (green squares) and $[Pd^{I}\text{-}Pd^{I}]^{2+}$ (blue squares). The colored lines indicate associated sigmoid fits according to e.g. (3).

Table S1: $\mathbf{E_{COM}^{50}}$ values extracted from the sigmoid fits of the CID appearance curves of $[Pd^{II}Cl]^+$, $[Pd^{II}]^+$, $[Pd^{I}\text{-}Pd^{I}OTf]^+$, $[Pd^{I}\text{-}Pd^{I}Cl]^+$, and $[Pd^{I}\text{-}Pd^{I}]^{2+}$ (cf. Fig. S2 and S3).

Complex	E_{COM}^{50} / a.u × 1000
$[Pd^{II}Cl]^+$	3.82
$[Pd^{II}]^+$	8.66
$[Pd^{I}\text{-}Pd^{I}OTf]^+$	2.60
$[Pd^{I}\text{-}Pd^{I}Cl]^+$	3.42
$[Pd^{I}\text{-}Pd^{I}]^{2+}$	4.89

10.5.2 Displacement vectors of Vibrational Modes of Interest

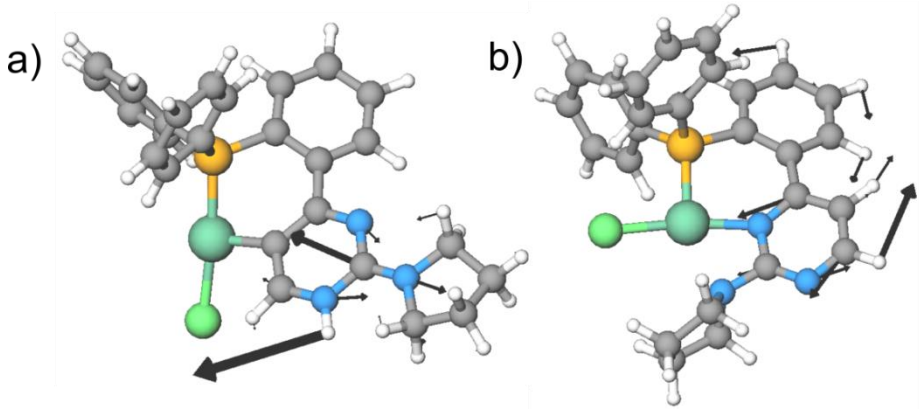

Figure S4: a) Displacement vectors of a NH bending mode at 1624 cm^{-1} in isomer $\boldsymbol{P,C_{[Pd^{II}Cl]^+}}$. **b)** Displacement vectors of CH bending mode at 1546 cm^{-1} in isomer $\boldsymbol{P,N,N_{[Pd^{II}Cl]^+}}$. The calculations were performed at the B3LYP/cc-pVDZ (H, C, N, O) and Stuttgart 1997 ECP (Pd) level of theory. Frequencies are scaled with 0.965.

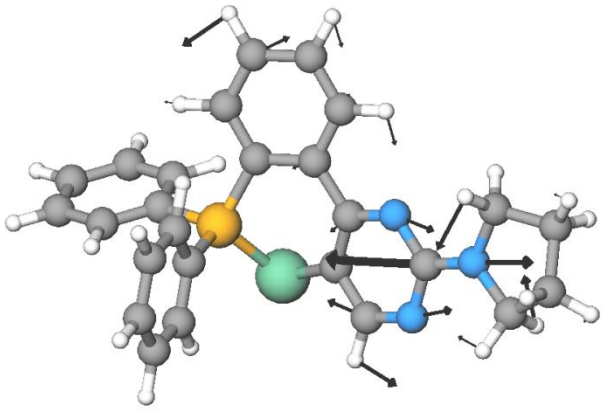

Figure S5: Displacement vectors of a CN stretching mode at 1567 cm^{-1} in isomer $\boldsymbol{P,C_{[Pd^{II}]^+}}$. The calculations were performed at the B3LYP/cc-pVDZ (H, C, N, O) and Stuttgart 1997 ECP (Pd) level of theory. Frequencies are scaled with 0.965.

10.5.3 Less Stable Isomers of $[Pd^{II}]^{+}$: Deprotonation at the Pyrimidin Ring

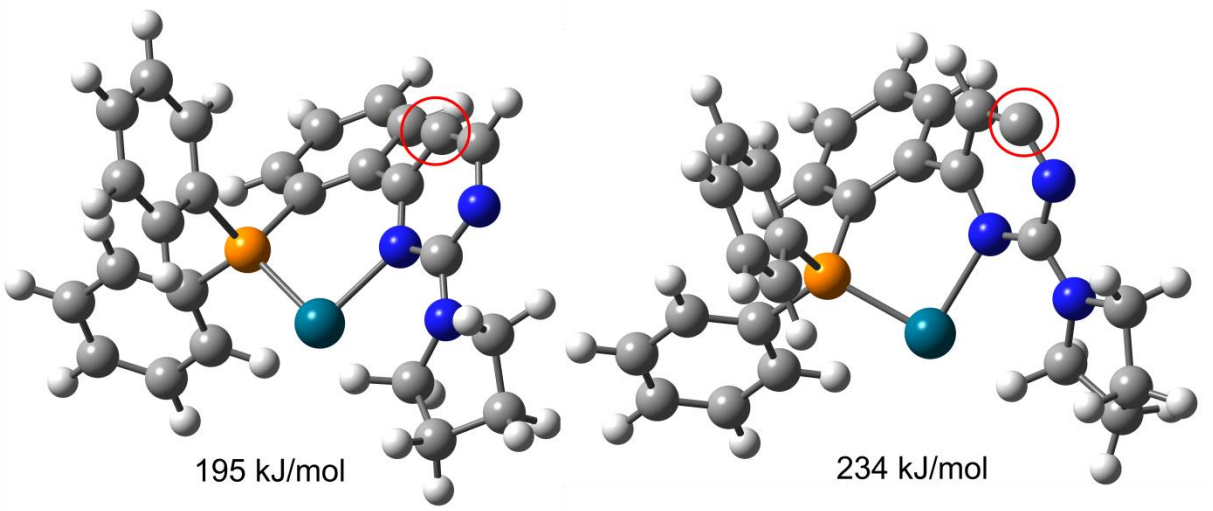

Figure S6: Isomers of $[Pd^{II}]^{+}$ exhibiting deprotonation at the pyrimidine ring. The circles indicate the deprotonated carbon atom. The calculations were performed at the B3LYP/cc-pVDZ (H, C, N, O) and Stuttgart 1997 ECP (Pd) level of theory.

11 Appendix I: Further Joint Publications

Content

11.1 Vibrational Fingerprints of a Tetranuclear Cobalt Carbonyl Cluster within an Cryo Tandem Ion Trap

Jennifer Mohrbach[a], Johannes Lang[a], Sebastian Dillinger[a], Marc H. Prosenc[a], Pierre Braunstein[b] and Gereon Niedner-Schatteburg[a]

a) Fachbereich Chemie and Forschungszentrum Optimas,
Technische Universität Kaiserslautern,
67663 Kaiserslautern, Germany

b) Laboratoire de Chimie de Coordination, Institut de Chimie,
Université de Strasbourg,
67081 Strasbourg, France

11.1.1 Preamble

The following chapter is a reprint of a publication in the "Journal of Molecular Spectroscopy".

J. Mohrbach and S. Dillinger conducted the measurements and data evaluations. The research group of P. Braunstein synthesized the precursor Co_4-complexes. I contributed with computed geometry optimized minimum structures and associated linear absorption spectra. J. Mohrbach and G. Niedner-Schatteburg prepared the manuscript and were supported by P. Braunstein and M.H. Prosenc and myself.

<u>Full Reference:</u>

Vibrational fingerprints of a tetranuclear cobalt carbonyl cluster within an cryo tandem ion trap

J. Mohrbach, **J. Lang**, S. Dillinger, M. H. Prosenc, P. Braunstein and G. Niedner-Schatteburg, *Journal of Molecular Spectroscopy*, **2017**, 332, 103-108.

http://dx.doi.org/10.1016/j.jms.2016.11.008

11.1.2 Reprint

Reprint Licence:

License Details

This Agreement between Johannes Lang ("You") and Elsevier ("Elsevier") consists of your license details and the terms and conditions provided by Elsevier and Copyright Clearance Center.

printable details

License Number	4064170249921
License date	Mar 08, 2017
Licensed Content Publisher	Elsevier
Licensed Content Publication	Journal of Molecular Spectroscopy
Licensed Content Title	Vibrational fingerprints of a tetranuclear cobalt carbonyl cluster within a cryo tandem ion trap
Licensed Content Author	Jennifer Mohrbach,Johannes Lang,Sebastian Dillinger,Marc Prosenc,Pierre Braunstein,Gereon Niedner-Schatteburg
Licensed Content Date	February 2017
Licensed Content Volume	332
Licensed Content Issue	n/a
Licensed Content Pages	6
Type of Use	reuse in a thesis/dissertation
Portion	full article
Format	both print and electronic
Are you the author of this Elsevier article?	Yes
Will you be translating?	No
Order reference number	
Title of your thesis/dissertation	Structure, reactivity and magnetism of isolated mononuclear and oligonuclear transition metal complexes elucidated by action spectroscopy and theory in concert
Expected completion date	Apr 2017
Estimated size (number of pages)	200
Elsevier VAT number	GB 494 6272 12
Requestor Location	Johannes Lang Raiffeisenstraße 3 Kaiserslautern, 67655 Germany Attn: Johannes Lang
Publisher Tax ID	GB 494 6272 12
Total	**0.00 USD**

Journal of Molecular Spectroscopy 332 (2017) 103–108

Contents lists available at ScienceDirect

Journal of Molecular Spectroscopy

journal homepage: www.elsevier.com/locate/jms

Vibrational fingerprints of a tetranuclear cobalt carbonyl cluster within a cryo tandem ion trap

Jennifer Mohrbach [a], Johannes Lang [a], Sebastian Dillinger [a], Marc Prosenc [a], Pierre Braunstein [b], Gereon Niedner-Schatteburg [a,*]

[a] Fachbereich Chemie and Forschungszentrum OPTIMAS, Technische Universität Kaiserslautern, 67663 Kaiserslautern, Germany
[b] Laboratoire de Chimie de Coordination, Institut de Chimie, UMR 7177 CNRS, Université de Strasbourg, 67081 Strasbourg, France

ARTICLE INFO

Article history:
Received 1 October 2016
In revised form 5 November 2016
Accepted 21 November 2016
Available online 22 November 2016

Keywords:
IR-MPD spectroscopy
Transition metal coordination complexes
DFT modelling
Cryo ion trapping

ABSTRACT

We present well resolved ($\Delta\tilde{\nu} = 3\ cm^{-1}$) Infrared Multiple Photon Dissociation (IR-MPD) spectra of $[Co_4(CO)_n(dppa\text{-}H^+)]^-$ (n = 3–10, dppa = $NH(PPh_2)_2$) in the carbonyl stretching range when isolating these species at low temperatures (26 K and below). We utilize IR-MPD in conjunction with DFT calculations to investigate the influence of CO ligands on structure and spin multiplicity of the Co_4 core. The recorded spectra reveal multiple bands of CO stretching vibrations which shift by reduction of CO coverage. This indicates a corresponding change of coordination motifs, and we find a conclusive interpretation of all recorded IR features in the case of the saturated n = 10 compound, likely in a singlet state as in solution. We tentatively postulate a singlet/triplet to quintet spin-flip upon removal of the first one or two CO ligands (from n = 10 to n = 9, 8) as well as a conceivable isomerization at a particular CO coverage (n = 6).

1. Introduction

High resolution mass spectrometry is currently known mostly for its favourable application in analytics, often associated with keywords like genomics, proteomics, metabolomics or petroleomics [1–3]. Other than that, high resolution MS is convenient for the spectroscopic investigation of small to medium sized species (m/z < 5000 amu/e and/or up to 200 atoms) when these form individual ions in vacuum. Direct absorption spectroscopy would fail at the number densities of typical ion experiments which do not provide for sufficient optical density. It is of help to invoke instead more elaborate schemes of indirect detection of photonic absorptions, such as so-called consequence or action spectroscopy [4–6]. IR-MPD is one of these advanced techniques [7,8]. It bears the intrinsic risk of power broadening, either by the use of free electron lasers or of table top Optical Parametric Oscillator/Amplifier (OPO/OPA) systems [9–13]. Contemporary IR-action spectroscopy achieves significant advances by so called tagging or messenger techniques where weakly bound, largely inert species (small rare gases and/or H_2) serve to provide for a preferred fragmentation channel, sometimes driven by single photon absorption [14–16]. Somewhat stronger bound messengers (Ar, Kr, Xe, CO, N_2) often preserve the structures of the hosting species, while their influence onto spectral features allows for additional insights.

Notably, most of the current IR-MPD and messenger/tagging spectroscopic studies take place through single pulse illumination of mass selected ion packages "on the fly" prior to or within Reflectron-Time-Of-Flight (ReTOF) mass spectrometer setups. Only recently, experiments started to combine the advantages of ion trapping and IR-MPD/tagging experiments.

Carbon monoxide is one of the most widely studied ligands in surface and cluster science. Transition Metal (TM) carbonyls are of major significance in organometallic and inorganic chemistry, and they provide classic examples of metal–ligand bonding [17–21]. TM cluster carbonyls act as versatile catalysts [18,22], they serve as model systems for the study of chemisorption on highly curved surfaces [23], and as precursors for the production of nanoparticles [24].

The CO stretching vibration probes the metal-ligand bonding in a sensitive way: its frequency indicates subtle details of the hosts electronic structure, and it helps to elucidate its binding site and the geometric binding arrangement [25–28]. Shifts in CO frequencies are often used for the study of binding sites on TM surfaces, and the CO molecule may be viewed as a classic probe molecule in surface science [23,29]. Vibrational CO shifts are usually discussed in terms of the Dewar-Chatt-Duncanson model, that explains coordinative complexation to single TM centers [30,31], or in terms of the Blyholder model, when interpreting surface

* Corresponding author.
E-mail address: gns@chemie.uni-kl.de (G. Niedner-Schatteburg).

http://dx.doi.org/10.1016/j.jms.2016.11.008
0022-2852/

coordination [32]. Both models describe CO coordination in terms of a donor-acceptor-synergism as follows: The carbonyls C-atom donates electron density from the doubly occupied carbon lone pair σ-orbital along the M—C—O axis into empty TM d orbitals; the coordinating TM center(s) donate(s) back electron density from its (their) occupied d-levels (or d-bands) into one of the antibonding π^* orbitals of the CO. Combined effects of σ donation and π back-bonding most often lead to a weakening of the CO bond and consequently to a lowering or red-shifting of the carbonyl stretch frequency. Most TM carbonyls follow this "classical" behaviour, although examples are known for "non-classical" metal carbonyl complexes, their main feature being a blueshift in CO stretch which is now understood in terms of an interplay between π-back donation and electrostatic effects [33–41]. The study of in situ generated TM clusters helped to elucidate the influence of net charge and oxidation state (+/0/−) onto the single molecule CO adsorption in terms of a charge dilution model [42]. Thermochemical insights – such as Co-CO binding enthalpies and more - arose from a sophisticated combination of ionization and dissociation experiments of atomic cobalt ion carbonyl complexes with *ab initio* calculations [43,44]. The IR-MPD studies of such complexes revealed an induced spin quenching (triplet to singlet) upon an increase of CO coordination (n = 4–5) [36].

The obvious progress in the elucidation of carbonyl complex structure and bonding has brought with it several nomenclatures for the description of the prevailing coordination motifs: Bonding/-coordination of a single CO molecule via its C-terminus to a single metal or TM center – irrespective of the metal coordination to its neighbours if any – has been termed as: terminal, end on, on top, atop, s1, μ_1, μ^1, and η_1 – this listing not claiming completeness. For reason of simplicity, we will exclusively utilize the term "terminal" CO and the label CO_{term} in the following. Bonding/coordination of a single CO molecule via its C-terminus to two metal or TM centers has been addressed by: bridging, s2, μ_2, μ^2, "in between". We will exclusively utilize the term μ_2-CO. The third likely coordination motif of CO involves three metal or TM centers in bonding/-coordination. This motif has been labeled as: capping, on hollow, s3, μ_3, and μ^3. We likely do not see this motif in our present study. When appropriate we will discuss it in terms of μ_3-CO.

In our current ion trapping spectroscopic study, we investigate the tetranuclear cobalt carbonyl complex $[Co_4(CO)_{10}dppa]$ [45] which is stabilized by the well-established diphosphine shortbite bridging ligand μ_2-dppa (dppa = $NH(PPh_2)_2$) [46]. IR spectra of the complex (from KBr plates and in solution) reveal seven bands in the 1930–2070 cm^{-1} range and three bands in 1770–1860 cm^{-1} range, arising from terminal and μ_2-CO ligands. This is consistent with a C_s molecular symmetry.

The complex (Scheme 1) finds application in the preparation of TM phosphides, which is generally not easy and otherwise requires

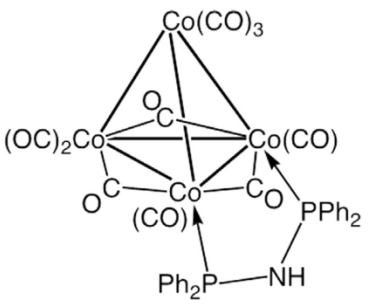

Scheme 1. Molecular structure of the neutral tetranuclear cluster $[Co_4(CO)_{10}dppa]$ (dppa = $NH(PPh_2)_2$). The complex consists of a Co_4 core, three μ_2-CO and seven terminal CO ligands. The dppa ligand bridges two basal cobalt atoms.

the direct combination of elements at high temperature, the reaction of toxic phosphide with metal or metal hydride, or metal organic chemical vapor deposition techniques. Instead, pure cobalt phosphide nanoparticles can be obtained from $[Co_4(CO)_{10}dppa]$ by anchoring and thermal treatment [47]. The $[Co_4(CO)_{10}dppa]$ complex moreover may serve as a model system for the stepwise regioselective elimination of CO ligands from a metal cluster. The dppa ligand in $[Co_4(CO)_{10}dppa]$ stabilizes the Co_4 core and orients further cluster functionalization by selective CO substitution. A second dppa ligand or a N-functionalized dppa ligand would bridge that metal–metal bond which is opposite to that spanned by the first dppa ligand [47]. The regioselective CO elimination would allow e.g. for the specific anchoring of this metal complex within a nanoporous membrane [48].

In this study, we strive for fundamental insight into the stepwise CO elimination from anionic derivatives of the $[Co_4(CO)_{10}dppa]$ complex by Collision Induced Dissociation (CID) and by IR-MPD investigations, in conjunction with Density Functional Theory (DFT) to model the anions geometries, spin couplings and force constants. The Co_4 core within these anions might be viewed as a highly curved nano-sized metal surface. Upon adoption of this analogy, it seems appropriate to view the stepwise detachment of CO ligands from the complex as a change in CO surface coverage.

2. Experimental and computational methods

We utilized a customized Fourier Transform Ion Cyclotron Resonance (FT-ICR) mass spectrometer (Apex Ultra, Bruker Daltonics) equipped with an Electrospray Ionization (ESI) source (Apollo 2, Bruker) and a home-built laser vaporization cluster ion source [49,50] (Fig. 1).

The molecular precursor complex $[Co_4(CO)_{10}dppa]$ was synthesized from $[Co_4(CO)_{12}]$ and characterized by its IR (from KBr plates and in solution) and $^1H/^{31}P$ NMR spectra [45]. Sample solutions of the $[Co_4(CO)_{10}dppa]$ complex in acetonitrile at the concentration of 1×10^{-4} mol/l were used without further purification and continuously infused into the ESI source by a syringe pump at a flow rate of 2 μL min^{-1}. The ion source was set to negative electrospray ionization mode. Nitrogen was used as drying gas with a flow rate of 3.0 L min^{-1} at 200 °C. The solutions were electro-sprayed at a nebulizer flow of 1.5 L min^{-1} and the spray shield was held at 3.6 kV. We obtained the deprotonated complex $[Co_4(CO)_{10}(dppa\text{-}H^+)]^-$, abbreviated $[Co_4(CO)_{10}L]^-$ in the following. In the ESI source, the ions may undergo Collision Induced Dissociation (CID) on demand. The successive elimination of up to seven CO ligands is achieved by stepwise increase of the skimmer voltage (at the first ion funnel) from −25 to −95 V (in source CID). Further increase of the funnel voltage did not enhance the elimination beyond seven CO ligands. We mass selected individual members from the resulting series of fragments $[Co_4(CO)_nL]^-$ (n = 3–9) and guided those into a 26 K hexapole ion trap. The ion trap is cooled by a closed cycle helium cryostat and held at 26 K for the measurements. Buffer (He) gas was introduced continuously. The pressure is increased from 1.7×10^{-7} mbar up to 3.0×10^{-6} mbar to accomplish efficient trapping and cooling of the ions. The cryo cooled ions are guided by electrostatic lenses into the FT-ICR cell of the so-called "infinity" type [51]. This cell is cooled to a temperature of about 10 K with a closed cycle helium cryostat to prevent heating of the clusters by black body radiation. The ICR cell is used for trapping, isolation and detection of the ions. It is coupled to a tuneable pulsed IR laser ($\Delta\tilde{\nu}$ = 0.9 cm^{-1}, Δt = 7 ns) to record IR-MPD spectra of isolated $[Co_4(CO)_nL]^-$ (n = 3–10) complexes. Fragmentation of the isolated species (CO elimination) indicates the absorption by a resonant vibrational frequency (Fig. 2a). The laser power was attenuated

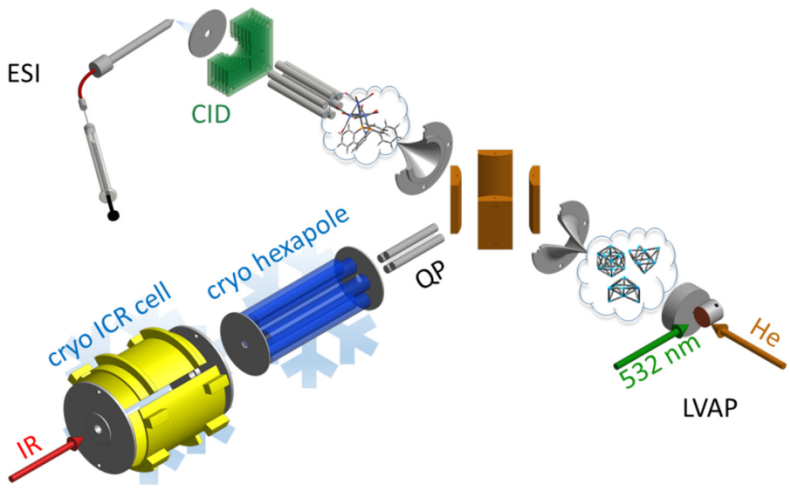

Fig. 1. Schematic drawing of our dual source tandem cryo trap FT-ICR MS setup. Ions are generated either in a Laser VAPorization (LVAP) source or in an Electro Spray Ionization (ESI) source. Either type of ions are injected into the first ion trap (cryo hexapole) via a switchable 90° ion bender and a quadrupole mass filter (QP). Buffer and reaction gases are introduced either pulsed or continuously. The cryo cooled ions and their reaction products are guided into the cryo ICR-cell, where they are isolated, irradiated by IR laser pulses and detected.

for n = 6–10 in the range from 1850 cm^{-1} to 2050 cm^{-1} to prevent excessive fragmentation. In the case of $[Co_4(CO)_nL]^-$ (n = 4–10) the only observed fragmentation channel was the loss of CO. In the case of $[Co_4(CO)_3L]^-$ the only observed fragment (395 *m/z*) may be assigned to $[Co_4(CO)_3NP_2]^-$ due to the loss of all four phenyl groups from the dppa ligand. Addition of N_2 gas in the cryo hexapole results in N_2 adsorption to coordinatively unsaturated $[Co_4(CO)_nL]^-$ (n = 6, 8) complexes. These N_2 complexes are isolated in the ICR cell and illuminated by infrared laser pulses. Here, the photo induced loss of N_2 indicates a resonant excitation of the complex (Fig. 2b). Note, that the modest mass difference between CO and N_2 of about 0.01 amu can be accurately resolved with our experimental setup.

The IR laser is a KTP/KTA optical parametric oscillator/amplifier (OPO/A, LaserVision) system pumped by a pulsed 10 Hz injection seeded Nd^{3+}:YAG laser (Continuum, Powerlite DLS 8000). In this work we used the difference frequency (DF) between the OPA signal and idler waves generated in a $AgGaSe_2$ crystal (0.1–1.2 mJ per pulse). We recorded IR-MPD spectra in the range of 1500–2300 cm^{-1}. Each trapped and isolated package of ions is irradiated by 15 laser pulses to yield a sufficient amount of fragment ions. The IR spectra were recorded as mass chromatograms while continuously scanning the IR frequency (typically <0.2 cm^{-1}/s). The IR-MPD signal was evaluated as $\Sigma_i F_i/(\Sigma_i F_i + \Sigma_i P_i)$, where F_i and P_i indicate the fragment and the parent ion signals, respectively. An experimental IR-MPD spectrum arises from a plot of the fragmentation efficiency as a function of laser frequency.

Optimized minimum energy structures and linear IR absorption spectra were calculated at the B3LYP [52,53] and PBE0 [54] level of theory using 6-31++G** basis sets (C, H, N, O, P), and Stuttgart RSC 1997 [55] effective core potential (Co) basis sets, respectively, as implemented in the Gaussian 09 program package [56]. Standard convergence criteria were applied. Full geometry optimization of all nuclear coordinates yields multiple local minimum structures. The lowest energy structure is assumed to represent the most stable isomer. We present singlet as well as quintet spin states. We scaled the calculated harmonic vibrational frequencies by a factor of 0.954 in order to match the calculated highest frequency CO vibration band in $[Co_4(CO)_{10}L]^-$ (unscaled at 2143 cm^{-1}) to our experimental value of 2044 cm^{-1}.

3. Results and discussion

3.1. IR-MPD spectra

The IR-MPD spectra of the investigated $[Co_4(CO)_nL]^-$ (n = 3–10) complexes (Fig. 3) exhibit several strong bands in the range 1880–2050 cm^{-1}, which we assign to the stretching vibrational modes of terminal CO ligands, and weaker bands around 1810 cm^{-1} which we assign to the stretching vibration modes of μ_2-CO ligands.

There are multiple bands for the terminal CO ligands for all n = 3–10 investigated. All bands are significantly redshifted by 97–247 cm^{-1} with respect to the free CO vibration at 2143 cm^{-1}. Judging by the band with highest frequency (indicated by the red line in Fig. 2), all redshifts increase by ~90 cm^{-1} upon decarbonylation (seven fold CO-elimination). The observed redshifts are indicative for a reduction of force constants and weakening of the CO bonds. The likely associated bond lengthening arises through electron density transfer from the tetranuclear cobalt core into antibonding $2\pi^*$ CO acceptor orbitals. As seen before [57] the extent of such electron density shift/charge transfer/electronic transfer does depend on CO coverage. The stepwise decrease of CO coverage reduces the total electron back donation from the Co_4 core to the antibonding CO π^* orbitals, or it enables a higher donation per CO ligand. We assume a combination of both. If so, these arguments fall in line with the observed redshifts of CO_{term} vibrations which increase by decarbonylation/CO elimination.

A conclusive interpretation of all observed CO_{term} bands is not possible at current stage of investigation. DFT modelling helps in the case of n = 10 (see subsequent section), and not beyond. Some obvious findings deserve attention: The spectra of $[Co_4(CO)_nL]^-$ (n = 10, 9, 8, 7, 5, 4, 3) reveal 4, 4, 3, 2, 2, 2 and 2 distinct CO_{term} bands. The level of distinct absorption motifs reduces in parallel to a reduction of the CO coverage. The n = 6 case is unique: We find up to 6 partially resolved CO_{term} features. This indicates either a highly specific Co-CO coordination per each CO, or it hints towards an isomeric variation that does not occur in any of the other cases. Isomeric variance may originate from Co_4 core isomers, from variation of CO coordination, or even from a coexistence of complexes in different spin multiplets (singlet/triplet/quintet/...). Naked

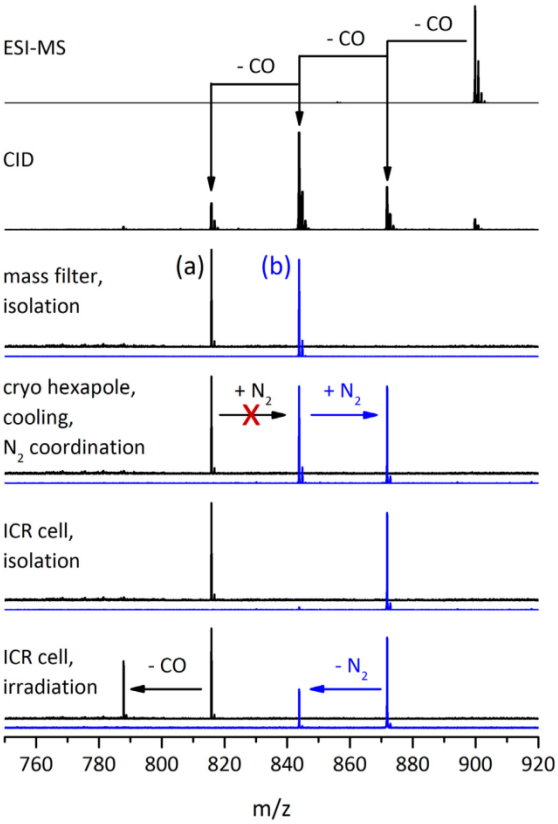

Fig. 2. Mass spectra illustrating the experimental methods. The ESI source delivers $[Co_4(CO)_{10}L]^-$ (899 *m/z*). Subsequent CID yields a series of under-coordinated $[Co_4(CO)_nL]^-$ (n = 3–9) complexes via successive decarbonylation. After isolation of one of these, the ions of choice are trapped and cryo cooled within the RF hexapole ion trap (a and b). Optional N_2 gas intake may result in the adsorption of one N_2 molecule to distinct complexes, n = 6, 8 only (blue spectra, b). Either type of ions (with or without N_2 attached) are guided into a 10 K ICR cell, isolated, irradiated by IR laser pulses, and analyzed for their fragments. (For interpretation of the references to colour in this figure legend, the reader is referred to the web version of this article.)

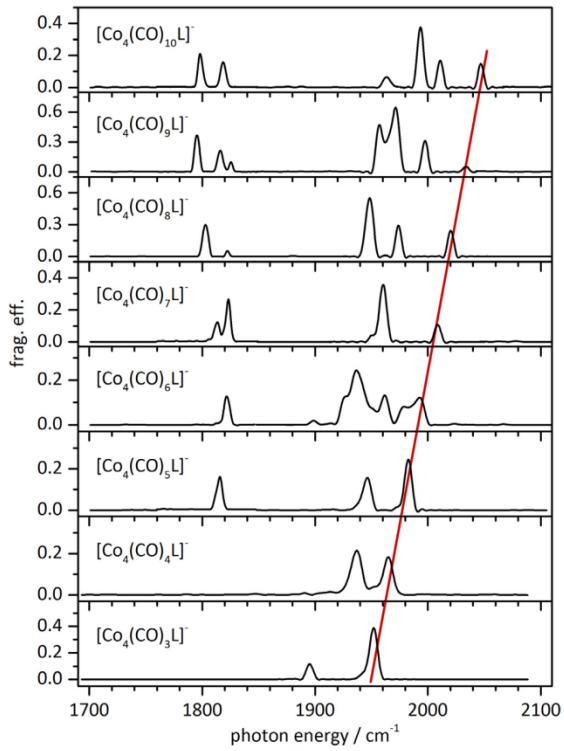

Fig. 3. IR-MPD spectra of $[Co_4(CO)_nL]^-$ (n = 3–10) complexes at 26 K. The red line serves to guide the eye, emphasizing the redshift of the terminal carbonyl stretches with decarbonylation. (For interpretation of the references to colour in this figure legend, the reader is referred to the web version of this article.)

cobalt clusters are known for their very high spin states [58,59], and an adsorbate induced partial quenching is likely [60]. Further elucidation of such effects remains to be carried out through DFT modelling in the future.

The low energy part of the spectra reveals features typical of μ_2-CO coordination. Such fingerprints prevail at n = 5–10 and vanish at n = 3, 4. Other than in the CO_{term} bands, there is no systematic redshift variation as a function of coverage for the μ_2-CO bands. The magnitude of the μ_2-CO redshift is large (~340 cm^{-1}) and in line with numerous previous observations [61,26,19]. In remarkable contrast to the up to six distinct CO_{term} bands, there are just two distinct μ_2-CO bands at 1790–1810 and 1810–1830 cm^{-1}, respectively. These two bands likely correspond to two species, μ_2^a (<1810 cm^{-1}) and μ_2^b (>1810 cm^{-1}). The μ_2^a species occurs only at highest coverages n = 8–10, and the μ_2^b species occurs only at high coverages n = 5–10. At this point the successful DFT modelling of the n = 10 case enables a convincing assignment of these two species (see below).

Our investigation did not find evidence for any IR-MPD bands in the range of 1500–1700 cm^{-1} (n = 6–10), which allow us to rule out μ_3-CO coordination in $[Co_4(CO)_nL]^-$.

An interpretation solely in terms of electrostatics and electron density shifts falls short of all prevailing effects. Surely there are coverage dependent steric effects which reflect surface "crowding" by CO adsorbates, and which likely cause concomitant terminal - μ_2 - μ_3 - rearrangements. In parallel, there will be a change in the order of individual $\Delta_{surface}H(\mu_x\text{-CO})$ values. Small coverages may go with $\Delta_{surface}H(CO_{term}) > \Delta_{surface}H(\mu_2\text{-CO}) \sim \Delta_{surface}H(\mu_3\text{-CO})$ in preference of terminal CO; high coverages may go with $\Delta_{surface}H(\mu_2\text{-CO}) \sim \Delta_{surface}H(\mu_3\text{-CO}) > \Delta_{surface}H(CO_{term})$ in preference of $\mu_{2,3}$-CO. Indeed, our spectra show that CO_{term} prevails at all levels of "coverage" while μ_2-CO fingerprints diminish upon reduction of CO coverage.

3.2. DFT modelling

We have conducted DFT modelling of the $[Co_4(CO)_{10}L]^-$ complex, and we obtained its linear IR absorption spectra in singlet and quintet (+6 kJ/mol) spin states. The calculation of force constants in triplet state did not converge, irrespective of the chosen exchange-correlation functional (B3LYP and PBE0). Geometry optimized calculations of the singlet and triplet state at the somewhat more approximate BP86 level have identified a singlet ground state and a high energy (+46 kJ/mol) triplet state. While we take this finding with a grain of caution, it shall suffice to rule out triplet contributions at the current stage of investigation.

In the following we compare two computed IR spectra (in singlet and quintet state by PBE0) to the experimental IR-MPD spectrum in the CO stretching frequency range (Fig. 4). A B3LYP singlet spectrum is virtually identical to that one by PBE0

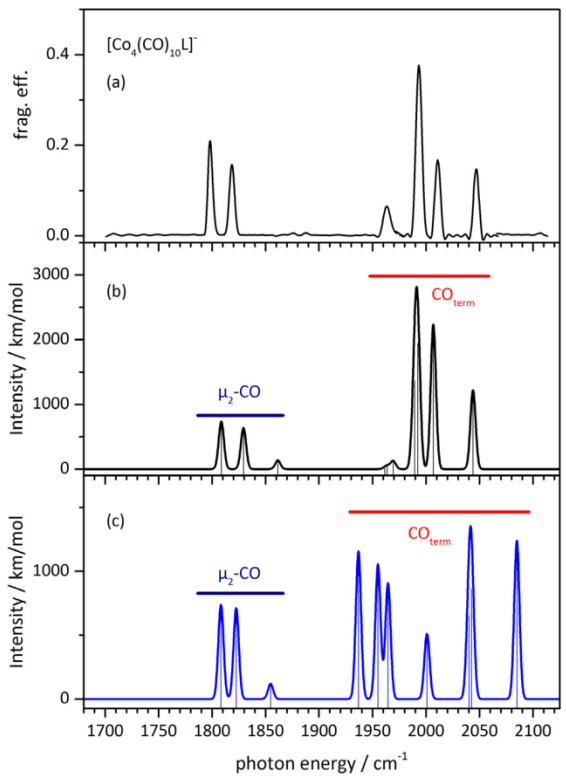

Fig. 4. IR-MPD spectrum of $[Co_4(CO)_{10}L]^-$ at 26 K (a) and calculated IR absorption spectra of geometry optimized singlet (b) and quintet (+6 kJ/mol) (c) spin state. The calculations were performed at the Stuttgart 1997 ECP (Co) and PBE0/6-31++G** (H, C, N, O, P) level of theory. The frequencies are scaled with 0.954, and calculated lines were broadened with Gaussians (FWHM = 3 cm^{-1}). The lowest triplet state (+46 kJ/mol) is discussed in the text. For the vector characters of all 10 singlet vibrations refer to Fig. S2 in the supplement.

(cf. Supplement Fig. S1). The DFT computations reveal seven CO_{term} bands and three μ_2-CO bands, some of which are almost degenerate. Upon folding in the experimental resolution of 3 cm^{-1}, the DFT modelling predicts four observable CO_{term} bands and three observable μ_2-CO bands in the case of a singlet spin state – in agreement with the experimental IR-MPD findings. We provide an illustrative visualization of the calculated displacement vectors of these modes in Fig. S2 of the supplement. We assign the two μ_2-CO species mentioned above to the one CO ligand that bridges the same cobalt atoms as the dppa ligand (μ_2^a), and to the two CO ligands that bridge one dppa bound Cobalt atom and the third basal Cobalt atom (μ_2^b). We clearly rule out contributions from the calculated quintet state, which would predict six CO_{term} bands across a wider range of frequencies in undisputable disagreement with the experiment.

Unfortunately, our current attempts of further DFT modelling (n < 10) have not yet led to converging data and to verifiable conclusions. We are tentatively assuming, that decarbonylation will allow for higher spin states, partially co-existing.

4. Conclusions and outlook

It became possible to record well resolved IR spectra of $[Co_4(CO)_{10}L]^-$ (n = 3–10) in the range of CO_{term} and μ_2-CO vibrations when isolating these species at low temperatures (26 K and below). We find several bands which shift upon reduction of CO coverage, indicating a variation of coordination motifs. In conjunction with DFT modelling, we find a conclusive interpretation of all recorded IR features in the case of the saturated n = 10 compound, likely in a singlet state similar to solution. We currently fail to achieve such conclusive interpretation in all other cases. We currently speculate about spin switching into higher multiplet states (from singlet into triplet/quintet or even higher) upon stepwise decarbonylation, and about a conceivable isomerization at a particular CO coverage (n = 6). The CO coverage dependent redshift of the highest CO_{term} is indicative of the charge dependent $2\pi^*$(CO) back donation and of its concomitant bond weakening. In contrast, the μ_2-CO bands modulate in appearance and intensity upon change of the CO coverage – without shifting significantly.

We are in the process of recording further spectra of Co_4 species with a mixed N_2–CO coverage, and we are enforcing further DFT analysis by all means. Once achieved, the then calculated $\Delta_{surface}$-H(CO) and $\Delta_{surface}H(N_2)$ values will allow for an elucidation of additional steric effects ("crowding"). We anticipate these effects to modulate the electronics in the known acceptor-donor type Co-CO and Co-N_2 bindings. Such steric effects most likely cause CO_{term} to μ_2-CO to μ_3-CO rearrangements, and it will be fascinating to compare such findings to the data of CO and N_2 adsorption on flat surfaces.

Acknowledgement

This work was supported by the German research foundation DFG within the transregional collaborative research center SFB/TRR 88 "Cooperative effects in homo- and hetero-metallic complexes" (3MET.de) and by the state research center OPTIMAS.

Appendix A. Supplementary material

Supplementary data associated with this article can be found, in the online version, at http://dx.doi.org/10.1016/j.jms.2016.11.008.

References

[1] G.J. Patti, O. Yanes, G. Siuzdak, Innovation: metabolomics: the apogee of the omics trilogy, Nat. Rev. Mol. Cell Biol. 13 (4) (2012) 263–269.
[2] M. Tyers, M. Mann, From genomics to proteomics, Nature 422 (6928) (2003) 193–197.
[3] A.G. Marshall, R.P. Rodgers, Petroleomics: chemistry of the underworld, Proc. Natl. Acad. Sci. 105 (47) (2008) 18090–18095.
[4] M. Okumura, L.I. Yeh, Y.T. Lee, The vibrational predissociation spectroscopy of hydrogen cluster ions, J. Chem. Phys. 83 (7) (1985) 3705–3706.
[5] R.L. Woodin, D.S. Bomse, J.L. Beauchamp, Multiphoton dissociation of molecules with low power continuous wave infrared laser radiation, J. Am. Chem. Soc. 100 (10) (1978) 3248–3250.
[6] D.S. Bomse, R.L. Woodin, J.L. Beauchamp, Molecular activation with low-intensity CW infrared laser radiation. Multiphoton dissociation of ions derived from diethyl ether, J. Am. Chem. Soc. 101 (19) (1979) 5503–5512.
[7] N.C. Polfer, Infrared multiple photon dissociation spectroscopy of trapped ions, Chem. Soc. Rev. 40 (5) (2011) 2211–2221.
[8] L. MacAleese, P. Maître, Infrared spectroscopy of organometallic ions in the gas phase: from model to real world complexes, Mass Spectrom. Rev. 26 (4) (2007) 583–605.
[9] J. Oomens, B.G. Sartakov, G. Meijer, G. von Helden, Gas-phase infrared multiple photon dissociation spectroscopy of mass-selected molecular ions, Int. J. Mass Spectrom. 254 (1–2) (2006) 1–19.
[10] J.J. Valle, J.R. Eyler, J. Oomens, D.T. Moore, A.F.G. van der Meer, G. von Helden, G. Meijer, C.L. Hendrickson, A.G. Marshall, G.T. Blakney, Free electron laser-Fourier transform ion cyclotron resonance mass spectrometry facility for obtaining infrared multiphoton dissociation spectra of gaseous ions, Rev. Sci. Instrum. 76 (2) (2005) 023103.
[11] N.R. Walker, R.S. Walters, M.A. Duncan, Frontiers in the infrared spectroscopy of gas phase metal ion complexes, New J. Chem. 29 (12) (2005) 1495–1503.
[12] J. Lang, M. Gaffga, F. Menges, G. Niedner-Schatteburg, Two-color delay dependent IR probing of torsional isomerization in a $[AgL_1L_2]^+$ complex, Phys. Chem. Chem. Phys. 16 (33) (2014) 17417–17421.
[13] M. Gaffga, I. Munstein, P. Müller, J. Lang, W.R. Thiel, G. Niedner-Schatteburg, Multistate-mediated rearrangements and $FeCl_2$ elimination in dinuclear FePd complexes, J. Phys. Chem. A 119 (51) (2015) 12587–12598.

[14] A.B. Wolk, C.M. Leavitt, E. Garand, M.A. Johnson, Cryogenic ion chemistry and spectroscopy, Acc. Chem. Res. 47 (1) (2014) 202–210.
[15] J.M. Headrick, J.C. Bopp, M.A. Johnson, Predissociation spectroscopy of the argon-solvated $H_5O_2^+$ "zundel" cation in the 1000–1900 cm^{-1} region, J. Chem. Phys. 121 (23) (2004) 11523–11526.
[16] O. Asvany, S. Brünken, L. Kluge, S. Schlemmer, COLTRAP: a 22-pole ion trapping machine for spectroscopy at 4 K, Appl. Phys. B 114 (1–2) (2014) 203–211.
[17] P. Braunstein, P.R. Raithby, L.A. Oro, Metal Clusters in Chemistry, vols. 1-3, Wiley-VCH, Weinheim, Germany, 1999. p. 1798.
[18] A.F. Cotton, G. Wilkinson, M. Bochmann, C.A. Murillo, Advanced Inorganic Chemistry, Wiley, 1999.
[19] J.E. Huheey, E.A. Keiter, R.L. Keiter, O.K. Medhi, Inorganic Chemistry: Principles of Structure and Reactivity, Pearson Education India, 2006.
[20] F. Aubke, C. Wang, Carbon monoxide as a σ-donor ligand in coordination chemistry, Coord. Chem. Rev. 137 (1994) 483–524.
[21] J.F. Hartwig, Organotransition Metal Chemistry: From Bonding to Catalysis, Univ Science Books, 2010.
[22] R. Heck, Organotransition Metal Chemistry A Mechanistic Approach, Academic Press, 1974.
[23] G. Somorjai, Introduction to Surface Science and Catalysis, Wiley, New York, 1994.
[24] P. Buchwalter, J. Rosé, P. Braunstein, Multimetallic Catalysis based on Heterometallic Complexes and Clusters, Chem. Rev. 115 (1) (2015) 28–126.
[25] J.E. Huheey, E. Keitler, R. Keitler, Inorganic Chemistry, Principles of Structure and Bonding, Harper Collins College Publishers, New York, 1993.
[26] M. Wrighton, Photochemistry of metal carbonyls, Chem. Rev. 74 (4) (1974) 401–430.
[27] G. Frenking, N. Fröhlich, The nature of the bonding in transition-metal compounds, Chem. Rev. 100 (2) (2000) 717–774.
[28] K. Nakamoto, Infrared and Raman Spectra of Inorganic and Coordination Compounds, Wiley Online Library, 1986.
[29] G. Ertl, Reactions at Solid Surfaces, vol. 14, John Wiley & Sons, 2010.
[30] J. Chatt, L. Duncanson, Olefin co-ordination compounds. Part III. Infra-red spectra and structure: attempted preparation of acetylene complexes, J. Chem. Soc. (Resumed) 586 (1953) 2939–2947.
[31] J. Dewar, A review of the pi-complex theory, Bull. Soc. Chim. Fr. 18 (3–4) (1951) C71–C79.
[32] G. Blyholder, Molecular orbital view of chemisorbed carbon monoxide, J. Phys. Chem. 68 (10) (1964) 2772–2777.
[33] A. Fielicke, G. von Helden, G. Meijer, B. Simard, D.M. Rayner, Gold cluster carbonyls: vibrational spectroscopy of the anions and the effects of cluster size, charge, and coverage on the CO stretching frequency, J. Phys. Chem. B 109 (50) (2005) 23935–23940.
[34] D.T. Moore, J. Oomens, J.R. Eyler, G. Meijer, G. von Helden, D.P. Ridge, Gas-phase IR spectroscopy of anionic iron carbonyl clusters, J. Am. Chem. Soc. 126 (45) (2004) 14726–14727.
[35] Z.D. Reed, M.A. Duncan, Infrared spectroscopy and structures of manganese carbonyl cations, Mn(CO)n+ (n = 1–9), J. Am. Soc. Mass Spectrom. 21 (5) (2010) 739–749.
[36] A.M. Ricks, Z.E. Reed, M.A. Duncan, Infrared spectroscopy of mass-selected metal carbonyl cations, J. Mol. Spectrosc. 266 (2) (2011) 63–74.
[37] J. Velasquez, B. Njegic, M.S. Gordon, M.A. Duncan, IR photodissociation spectroscopy and theory of Au + $(CO)_n$ complexes: nonclassical carbonyls in the gas phase, J. Phys. Chem. A 112 (9) (2008) 1907–1913.
[38] A.S. Goldman, K. Krogh-Jespersen, Why do cationic carbon monoxide complexes have high Co stretching force constants and short CO bonds? Electrostatic effects, not σ-bonding, J. Am. Chem. Soc. 118 (48) (1996) 12159–12166.
[39] A.J. Lupinetti, S. Fau, G. Frenking, S.H. Strauss, Theoretical analysis of the bonding between CO and positively charged atoms, J. Phys. Chem. A 101 (49) (1997) 9551–9559.
[40] G. Frenking, U. Pidun, Ab initio studies of transition-metal compounds: the nature of the chemical bond to a transition metal, J. Chem. Soc. Dalton Trans. 10 (1997) 1653–1662.
[41] G. Bistoni, S. Rampino, N. Scafuri, G. Ciancaleoni, D. Zuccaccia, L. Belpassi, F. Tarantelli, How π back-donation quantitatively controls the CO stretching response in classical and non-classical metal carbonyl complexes, Chem. Sci. 7 (2) (2016) 1174–1184.
[42] A. Fielicke, G. von Helden, G. Meijer, D.B. Pedersen, B. Simard, D.M. Rayner, Size and charge effects on the binding of CO to late transition metal clusters, J.
[43] Z. Gengeliczki, B. Sztáray, T. Baer, C. Iceman, P.B. Armentrout, Heats of formation of Co (CO)2NOPR$_3$, R = CH_3 and C_2H_5, and its ionic fragments, J. Am. Chem. Soc. 127 (26) (2005) 9393–9402.
[44] S. Goebel, C.L. Haynes, F.A. Khan, P.B. Armentrout, Collision-induced dissociation studies of Co (CO)x+, x = 1–5: sequential bond energies and the heat of formation of Co $(CO)_4$, J. Am. Chem. Soc. 117 (26) (1995) 6994–7002.
[45] C. Moreno, M.J. Macazaga, M.L. Marcos, J. González-Velasco, S. Delgado, $[CO_4(CO)_{12}]$ derivatives with bis(diphenylphosphino) amine, an electrochemical study, J. Organomet. Chem. 452 (1) (1993) 185–192.
[46] C. Fliedel, A. Ghisolfi, P. Braunstein, Functional short-bite ligands: synthesis, coordination chemistry, and applications of N-functionalized bis (diaryl/dialkylphosphino) amine-type ligands, Chem. Rev. 116 (16) (2016) 9237–9304.
[47] (a) P. Buchwalter, J. Rosé, B. Lebeau, O. Ersen, M. Girleanu, P. Rabu, P. Braunstein, J.-L. Paillaud, Characterization of cobalt phosphide nanoparticles derived from molecular clusters in mesoporous silica, J. Nanopart. Res. 15 (12) (2013) 1–21;
(b) P. Buchwalter, J. Rosé, B. Lebeau, P. Rabu, P. Braunstein, J.-L. Paillaud, Stoichiometric molecular single source precursors to cobalt phosphides, Inorg. Chim. Acta 409 (2014) 330–341;
(c) F. Schweyer-Tihay, P. Braunstein, C. Estournes, J. Guille, B. Lebeau, J.-L. Paillaud, M. Richard-Plouet, J. Rosé, Synthesis and characterization of supported Co_2P nanoparticles by grafting of molecular clusters into mesoporous silica matrixes, Chem. Mater. 15 (1) (2003) 57–62.
[48] P. Braunstein, H.-P. Kormann, W. Meyer-Zaika, R. Pugin, G. Schmid, Strategies for the anchoring of metal complexes, clusters, and colloids inside nanoporous alumina membranes, Chemistry 6 (24) (2000) 4637–4646.
[49] S. Maruyama, L.R. Anderson, R.E. Smalley, Direct injection supersonic cluster beam source for FT-ICR studies of clusters, Rev. Sci. Instrum. 61 (12) (1990) 3686–3693.
[50] C. Berg, T. Schindler, G. Niedner-Schatteburg, V.E. Bondybey, Reactions of simple hydrocarbons with Nb+ n: chemisorption and physisorption on ionized niobium clusters, J. Chem. Phys. 102 (12) (1995) 4870–4884.
[51] P. Caravatti, M. Allemann, The 'infinity cell': a new trapped-ion cell with radiofrequency covered trapping electrodes for Fourier transform ion cyclotron resonance mass spectrometry, Org. Mass Spectrom. 26 (5) (1991) 514–518.
[52] T.H. Dunning Jr., Gaussian basis sets for use in correlated molecular calculations. I. The atoms boron through neon and hydrogen, J. Chem. Phys. 90 (2) (1989) 1007–1023.
[53] D.E. Woon, T.H. Dunning Jr., Gaussian basis sets for use in correlated molecular calculations. III. The atoms aluminum through argon, J. Chem. Phys. 98 (2) (1993) 1358–1371.
[54] C. Adamo, V. Barone, Toward reliable density functional methods without adjustable parameters: the PBE0 model, J. Chem. Phys. 110 (13) (1999) 6158–6170.
[55] M. Dolg, H. Stoll, H. Preuss, R.M. Pitzer, Relativistic and correlation effects for element 105 (hahnium, Ha): a comparative study of M and MO (M = Nb, Ta, Ha) using energy-adjusted ab initio pseudopotentials, J. Phys. Chem. 97 (22) (1993) 5852–5859.
[56] M.J. Frisch, G. Trucks, H. Schlegel, G. Scuseria, M. Robb, J. Cheeseman, G. Scalmani, V. Barone, B. Mennucci, G. Petersson, Gaussian 09, Revision A. 1, Gaussian Inc., Wallingford, CT, 2009.
[57] F.A. Reboredo, G. Galli, Size and structure dependence of carbon monoxide chemisorption on cobalt clusters, J. Phys. Chem. B 110 (15) (2006) 7979–7984.
[58] S. Dillinger, J. Mohrbach, J. Hewer, M. Gaffga, G. Niedner-Schatteburg, Infrared spectroscopy of N_2 adsorption on size selected cobalt cluster cations in isolation, Phys. Chem. Chem. Phys. 17 (16) (2015) 10358–10362.
[59] J. Meyer, M. Tombers, C. van Wüllen, G. Niedner-Schatteburg, S. Peredkov, W. Eberhardt, M. Neeb, S. Palutke, M. Martins, W. Wurth, The spin and orbital contributions to the total magnetic moments of free Fe Co, and Ni clusters, J. Chem. Phys. 143 (10) (2015) 104302.
[60] S.T. Akin, V. Zamudio-Bayer, K. Duanmu, G. Leistner, K. Hirsch, C. Bülow, A. Ławicki, A. Terasaki, B.V. Issendorff, D.G. Truhlar, J.T. Lau, M.A. Duncan, Size-dependent ligand quenching of ferromagnetism in $Co_3(benzene)_n^+$ clusters studied with XMCD spectroscopy, 2016 (in press).
[61] C. Janiak, H.-J. Meyer, D. Gudat, R. Alsfasser, Moderne Anorganische Chemie, Walter de Gruyter, 2012.

11.2 Mechanistic Studies on the Ruthenium(II) Catalyzed Base-Free Transfer Hydrogenation Triggered by a Roll-Over Cyclometallation

Christian. Kerner[a], Johannes Lang[a,b], Maximillian Gaffga[a,b], Fabian. S. Menges[c], Yu Sun[a], Gereon Niedner-Schatteburg[a,b] and Werner R. Thiel[a]

a) Fachbereich Chemie,
Technische Universität Kaiserslautern,
67663 Kaiserslautern, Germany

b) Forschungszentrum Optimas
Technische Universität Kaiserslautern,
67663 Kaiserslautern, Germany

c) Department of Chemistry,
Yale University,
New Haven, CT 06525, USA

11.2.1 Preamble

The following chapter is a reprint of a publication in the journal "ChemPlusChem".

C. Kerner from the research group of W. R. Thiel synthesized the ruthenium complexes and investigated their catalytic reactivity. M. Gaffga, F. S. Menges and I conducted mass spectrometry and Collision Induced Dissociation (CID) experiments. I evaluated the acquired data. Yu Sun provided crystallographic data. C. Kerner and W. R Thiel prepared the manuscript and were supported by G. Niedner Schatteburg and myself.

Full Reference:

Mechanistic Studies on the Ruthenium(II) Catalyzed Base-Free Transfer Hydrogenation Triggered by a Roll-Over Cyclometallation
C. Kerner, **J. Lang**, M. Gaffga, F. S. Menges, Yu Sun, G. Niedner-Schatteburg and W. R. Thiel, *ChemPlusChem*, **2017**, 82, 212-224.
http://dx.doi.org/10.1002/cplu.201600526

11.2.2 Reprint

Reprint Licence:

JOHN WILEY AND SONS LICENSE
TERMS AND CONDITIONS

This Agreement between Johannes Lang ("You") and John Wiley and Sons ("John Wiley and Sons") consists of your license details and the terms and conditions provided by John Wiley and Sons and Copyright Clearance Center.

License Number	4064171179323
License date	Mar 08, 2017
Licensed Content Publisher	John Wiley and Sons
Licensed Content Publication	CHEMPLUSCHEM
Licensed Content Title	Mechanistic Studies on Ruthenium(II)-Catalyzed Base-Free Transfer Hydrogenation Triggered by Roll-Over Cyclometalation
Licensed Content Author	Christian Kerner,Johannes Lang,Maximilian Gaffga,Fabian S. Menges,Yu Sun,Gereon Niedner-Schatteburg,Werner R. Thiel
Licensed Content Date	Nov 22, 2016
Licensed Content Pages	13
Type of Use	Dissertation/Thesis
Requestor type	Author of this Wiley article
Format	Print and electronic
Portion	Full article
Will you be translating?	No
Title of your thesis / dissertation	Structure, reactivity and magnetism of isolated mononuclear and oligonuclear transition metal complexes elucidated by action spectroscopy and theory in concert
Expected completion date	Apr 2017
Expected size (number of pages)	200
Requestor Location	Johannes Lang Raiffeisenstraße 3 Kaiserslautern, 67655 Germany Attn: Johannes Lang
Publisher Tax ID	EU826007151
Billing Type	Invoice
Billing Address	Johannes Lang Raiffeisenstraße 3 Kaiserslautern, Germany 67655 Attn: Johannes Lang
Total	**0.00 USD**
Terms and Conditions	

ChemPubSoc Europe
DOI: 10.1002/cplu.201600526
CHEMPLUSCHEM Full Papers

Mechanistic Studies on Ruthenium(II)-Catalyzed Base-Free Transfer Hydrogenation Triggered by Roll-Over Cyclometalation

Christian Kerner,[a] Johannes Lang,[a, b] Maximilian Gaffga,[a, b] Fabian S. Menges,[c] Yu Sun,[a] Gereon Niedner-Schatteburg,*[a, b] and Werner R. Thiel*[a]

The synthesis of 2-substituted pyridine–pyrimidine ligands and their complexation with arene ruthenium(II) chloride moieties is reported. Depending on the electronic and steric influences of the ligand, the catalysts undergo CH activation by roll-over cyclometalation. This process opens up the route to the catalytic transfer hydrogenation of ketones with isopropanol as the hydrogen source under base-free and mild conditions. Barriers related to the roll-over cyclometalation process can be determined experimentally by collision-induced dissociation ESI mass spectrometry. They are supported by DFT calculations and allow the classification of the ligands according to their electronic and steric properties, which is also in accordance with critical bond parameters derived from X-ray structure data. DFT calculations furthermore reveal that the formation of a ruthenium(II) hydrido species is plausible through β-hydride elimination from isopropanol.

Introduction

In 1925, Meerwein and Schmidt, Pondorf, Verley, and Oppenhauer independently from each other discovered the transfer hydrogenation of ketones.[1] Later, catalytic versions of this transformation could be established with late-transition-metal complexes containing ruthenium, iridium, or rhodium as the catalytically active sites.[2] Noyori et al. developed the first asymmetric transfer hydrogenations with high stereoselectivities. They also discussed the potentials of a base-free hydrogenation process.[3]

Despite these efforts, only a few base-free transfer hydrogenation reactions, catalyzed by iridium, iron, osmium, or ruthenium complexes, have been described to date.[4–7] Some of them require additives, such as silver salts, to activate the catalyst, some are limited regarding the substrate scope, have long reaction times, low reaction rates, or are highly sensitive towards air and moisture.[4c, 5a, b, 7d] Nevertheless, there are clear benefits from working in the absence of a base: chiral compounds may be prevented from undergoing racemization and corrosion can be avoided.

In 2013, we reported that ruthenium(II) complexes with *N*,*N*′-chelating 2-(2-aminopyrimidin-4-yl)pyridine ligands could undergo a self-activation process: cleavage of the *ortho*-CH bond at the pyrimidine ring through a roll-over cyclometalation mechanism[8] resulted in the in situ formation of a ruthenium-coordinated carbanion. This was the key step to develop novel moisture- and air-stable catalysts that allowed the transfer hydrogenation of ketones,[9] and quite recently the reductive amination of aromatic aldehydes, to be performed under base-free conditions.[10] However, this special feature has, to date, been restricted to 2-(2-aminopyrimidin-4-yl)pyridine ligands with tertiary amino groups attached to the pyrimidine ring. The positive effect of cyclometalation occurring at the (2-dialkylamino)-pyrimidin-4-yl site on the performance of transition-metal catalysts has also been observed for chelating ligands wherein phosphines are combined with the (2-dialkylamino)pyrimidin-4-yl moiety.[11] We could synthesize highly active catalysts for the palladium-catalyzed Suzuki–Miyaura coupling reaction by applying such ligands.

Herein, we present a detailed mechanistic study on catalysts of the type $[(\eta^6\text{-arene})Ru(X)(pympyr)]^+$ (pympyr = 2-(pyrimidin-4-yl)pyridine-type ligand) for the transfer hydrogenation of aryl ketones with isopropanol as the hydrogen source (Scheme 1).

To gain a deeper insight into structure/reactivity relationships, variations of the electronic and steric impact of a series of differently substituted 2-pyrimidin-4-yl-pyridine ligands, as

Scheme 1. Transfer hydrogenation of aryl ketones with isopropanol as the hydrogen source.

[a] Dr. C. Kerner, J. Lang, Dr. M. Gaffga, Dr. Y. Sun, Prof. Dr. G. Niedner-Schatteburg, Prof. Dr. W. R. Thiel
Fachbereich Chemie, Technische Universität Kaiserslautern
Erwin-Schrödinger-Strasse 54, 67663 Kaiserslautern (Germany)
E-mail: gns@chemie.uni-kl.de
thiel@chemie.uni-kl.de

[b] J. Lang, Dr. M. Gaffga, Prof. Dr. G. Niedner-Schatteburg
Landesforschungszentrum OPTIMAS Technische Universität Kaiserslautern
Erwin-Schrödinger-Strasse 54, 67663 Kaiserslautern (Germany)

[c] Dr. F. S. Menges
Department of Chemistry,Yale University 225 Prospect St.,New Haven, CT06511 (USA)

Supporting information for this article can be found under http://dx.doi.org/10.1002/cplu.201600526.

well as of the anionic coordinating ligand X and arene ligand, were performed. The study is supported by mass spectrometry and theoretical calculations.

Results and Discussion

Synthesis of ligands and ruthenium complexes

N,N′-Chelating 2-(pyrimidin-4-yl)pyridine ligands were synthesized in a few steps starting with the condensation of 2-acetylpyridine and *N,N*-dimethylformamide dimethyl acetal (Scheme 2), leading to 3-dimethylamino-1-pyridinylprop-2-en-1-one (**1**),[12] the central intermediate for all 2-(pyrimidin-4)yl-pyridines (**2**) presented herein. The functionalized pyrimidine moieties are subsequently generated by condensation of **1** with formamidinium acetate, which results in the formation of 2-(pyrimidin-4-yl)pyridine (**2a**).[13] Alternatively, an appropriate guanidinium salt leads to 2-(2-aminopyrimidin-4-yl)pyridines **2b–d**.[9] Condensation with urea gives 2-(2-hydroxypyrimidin-4-yl)pyridine (**2e**), which can then be converted into the corresponding chloro derivative **2f**.

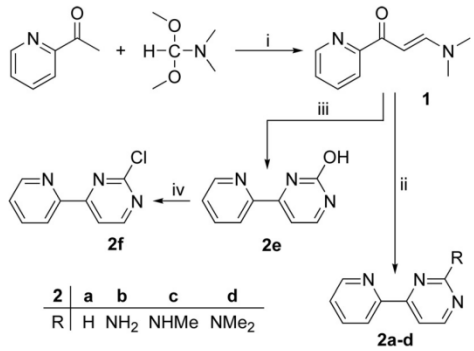

2	a	b	c	d
R	H	NH_2	NHMe	NMe_2

Scheme 2. Synthesis of the pyrimidinyl-functionalized chelating ligands: i) 80 °C, 6 h, 67 %; ii) formamidine acetate or guanidinium salt, Na, EtOH, 75 °C, 16 h, up to 66 %; iii) urea, H_2O/EtOH (18:3), 95 °C, concentrated HCl, 48 h, 85 %; iv) $POCl_3$, 105 °C, 1 h, 90 %.

Although the cyclization of **1** with formamidinium and guanidinium salts, which leads to ligands **2a–d**, requires basic conditions,[9] the condensation of **1** with urea, giving compound **2e**, has to be performed in the presence of an acid. The yield for this transformation is high, as it is for the subsequent introduction of a chloro substituent by treating **2e** with $POCl_3$.

To complete the series of ligands, 2,2′-bipyridine (**2g**) and [D_8]2,2′-bipyridine (**2h**)[14] were also applied for coordination to ruthenium(II), in addition to the *N,N′*-donors **2a–f** described above. By simply mixing [{(η^6-cymene)$RuCl_2$}$_2$], one of the ligands **2a–h**, and a salt of a weakly coordinating anion X^- in dichloromethane, the desired ionic ruthenium(II) complexes of the type [(η^6-cymene)(*N,N′*-ligand)RuCl]X **3a–hX** are formed (Scheme 3). The counteranions X^- (BF_4^-, PF_6^-, BPh_4^-, $BArF_4^-$) significantly influence the solubility of the cationic catalysts in *i*PrOH, which is used as the solvent and hydrogen source for

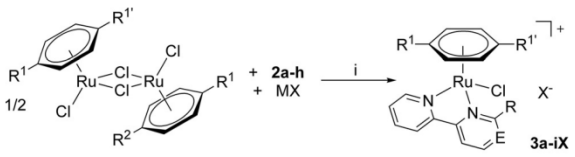

cymene complexes (R^1 = Me, $R^{1'}$ = ^{i}Pr)

3	aPF$_6$	bPF$_6$	cBF$_4$	dBF$_4$	dPF$_6$	dBPh$_4$	dBArF$_4$	eBF$_4$	fBF$_4$	gPF$_6$
R	H	NH_2	NHMe	NMe_2	NMe_2	NMe_2	NMe_2	OH	Cl	H
E	N	N	N	N	N	N	N	N	N	CH
X^-	PF_6^-	PF_6^-	BF_4^-	BF_4^-	PF_6^-	BPh_4^-	$BArF_4^-$	BF_4^-	BF_4^-	PF_6^-

3hPF$_6$: d^8-bipy, X^- = PF_6^-

benzene complex (R^1 = $R^{1'}$ = H)
3iBF$_4$: R = NMe_2, E = N, X^- = BF_4^-

Scheme 3. Synthesis of the ruthenium complexes **3a–iX**: i) CH_2Cl_2, RT, 24 h.

the transfer hydrogenation. This effect is described in more detail below. Apart from ligands **2a–f**, commercially available **2g** was coordinated to the ruthenium(II) center to give **3gX**. To study isotope effects occurring during the roll-over mechanism, compound **2h** was synthesized and coordinated to ruthenium to form **3hX**. To investigate the steric impact of the η^6-coordinating arene ring on the transfer hydrogenation, one example of a ruthenium complex with a benzene ligand (**3iX**) was included.

Molecular structures

All ruthenium(II) complexes were characterized by means of NMR spectroscopy and elemental analysis. Because the ruthenium(II) site is a center of chirality in the case of complexes **3a–fX**, the resonances of the diastereotopic hydrogen and carbon atoms of the η^6-coordinating cymene ring appear dou-

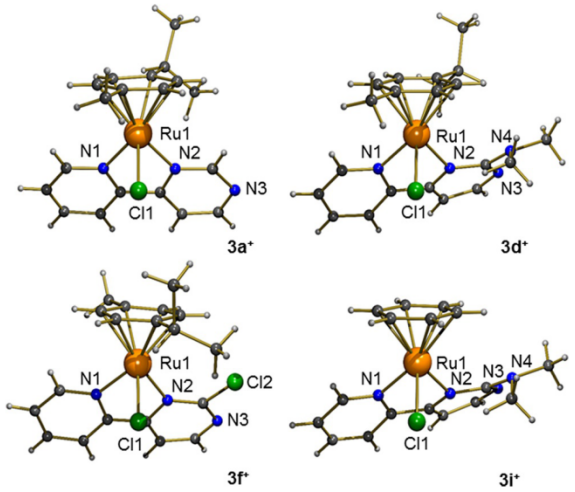

Figure 1. Molecular structures of the cations of **3a**$^+$, **3d**$^+$, **3f**$^+$, and **3i**$^+$ in the solid state. The anions and cocrystallized solvent molecules are omitted for clarity.

Table 1. Characteristic bond lengths [Å], angles [°], and dihedral angles [°] of **3aPF$_6$**,[a] **3bBF$_4$**,[b] **3dBF$_4$**, **3fBF$_4$**, and **3iBF$_4$**.

	3aPF$_6$	**3bPF$_6$**	**3dBF$_4$**	**3fBF$_4$**	**3iBF$_4$**
Ru1–N1	2.090(3)	2.082(2)	2.081(2)	2.102(4)	2.073(12)
Ru1–N2	2.080(3)	2.120(2)	2.154(2)	2.152(3)	2.159(12)
Ru1–Ar[c]	1.689(2)	1.689(1)	1.690(1)	1.694(2)	1.672(7)
Ru1–Cl1	2.398(1)	2.395(1)	2.405(1)	2.391(1)	2.418(4)
N1-Ru-N2	76.70(12)	76.55(7)	77.35(9)	76.73(14)	76.8(5)
N1-Ru1-Cl1	86.91(9)	87.61(5)	82.13(7)	84.87(11)	83.5(3)
N2-Ru1-Cl1	83.90(9)	85.50(5)	89.57(6)	85.73(10)	92.6(3)
N1-C5-C6-N2[d]	0.6(6)	0.7(3)	12.9(4)	5.6(6)	12.2(19)

[a] **3aPF$_6$** also crystallized with the inclusion of one equivalent of KCl, see the Supporting Information. [b] Data for comparison from Ref. [9]. [c] Distance between Ru1 and the centroid of the η^6-coordinated arene ligand. [d] C5, C6: carbon atoms bridging the two heterocycles of the ligands.

bled. Some of the new ruthenium complexes could be obtained as single crystals suitable for an X-ray structure analysis. Figure 1 shows the molecular structures of the cations of **3aPF$_6$**, **3dBF$_4$**, **3fBF$_4$**, and **3iBF$_4$** in the solid state. The data for **3bPF$_6$**,[9] which has already been published, is added to Table 1 for comparison with a compound containing a primary amino group at the pyrimidine ring.

For a derivative containing a secondary amino group (ArNH(*n*Pr)) that is comparable to **3bBF$_4$**, a Ru1–N2 distance of 2.108 Å and a N1-C5-C6-N2 dihedral angle of 3.4° were found.[9] The Ru–N distances for compound **3gPF$_6$**, which crystallizes with two crystallographically independent molecules in the unit cell, were reported to be in the range of 2.087–2.101 Å;[15] this is in agreement with the Ru1–N1 distances found in our study. The dihedral angle N1-C5-C6-N2 of **3gPF$_6$** is close to 0°. Together with previously published solid-state structures,[9] the structural data of the new ruthenium(II) complexes clearly prove the pronounced influence of the substituent attached in the 2-position of the 2-(pyrimidin-4-yl)pyridine-type ligand on the Ru1–N2 distance and, in particular, on the dihedral angle N1-C5-C6-N2. While the distances between the ruthenium(II) site Ru1 and the pyridine nitrogen atom N1 differ only slightly in all ruthenium complexes, there is clearly a broad variation in the Ru1–N2 distances. Here steric and electronic influences have to be considered. All heteroatomic substituents weaken the Ru–N2 bond by withdrawing electron density (–*I* effect) from the σ framework of the ligand. This electronic effect is superimposed by the steric interaction between these substituents and the π-coordinating aromatic ligand, and thus, leads to a gradation of the N1-C5-C6-N2 dihedral angles in the sequence **3aPF$_6$** ≈ **3bPF$_6$** < **3fBF$_4$** < **3iBF$_4$** ≈ **3dBF$_4$**. Even complex **3iBF$_4$**, which contains a less sterically demanding η^6-benzene ligand, still adopts a dihedral angle of 12.21°, which is similar to that in **3dBF$_4$**. Here the distance between the metal and the centroid of the arene ligand is approximately 1.672 Å, and thus, slightly shorter than those of the η^6-cymene complexes (1.689–1.694 Å). The Ru1–Cl1 bond (2.418 Å) in **3iBF$_4$** is a bit longer than in the four other complexes (2.391–2.405 Å). At this point, it can be summarized that the bond parameters, and thus, strengths of the Ru1–ligand bonds are directly influenced by the substitution motif at the *N,N'*-coordinating ligand.

CID EIS-MS measurements

Further verification arose by means of collision-induced dissociation (CID) EIS-MS measurements of isolated complexes. In 2013, we reported a first but limited study on the two [(η^6-cymene)(*N,N'*-ligand)RuCl]$^+$ cations **3a**$^+$ (tertiary amino group) and **3d**$^+$ (primary amino group), as well as on an analogous system containing a tertiary (2-pyrrolidinylpyrimidinyl) moiety.[9] It could clearly be shown that all three complexes underwent fragmentation of HCl under CID EIS-MS conditions and the proton originated from the *ortho*-CH moiety of the pyrimidine ring. The latter fact was proved by selective deuteration of this site.

However, the energies required for the fragmentation differed largely: it was much easier to detach HCl from the cations as long as a tertiary amino group was attached to the pyrimidine ring. Quantum chemical calculations performed on the three cations mentioned above and on **3a**$^+$ and **3g**$^+$ confirmed these findings and demonstrated that the process followed a roll-over cyclometalation process (Scheme 4).[16]

The whole series of cations **3a–i**$^+$ was investigated in the gas phase to evaluate in detail the steric and electronic impacts of different substituents on fragmentation. Figure 2 shows the recorded CID curves. The E_{LAB} value at 50% reflects the energy required to release HCl. In the following, it can be expressed in terms of an activation energy by calibration with

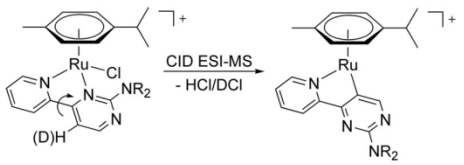

Scheme 4. Roll-over cyclometalation under CID ESI-MS conditions.

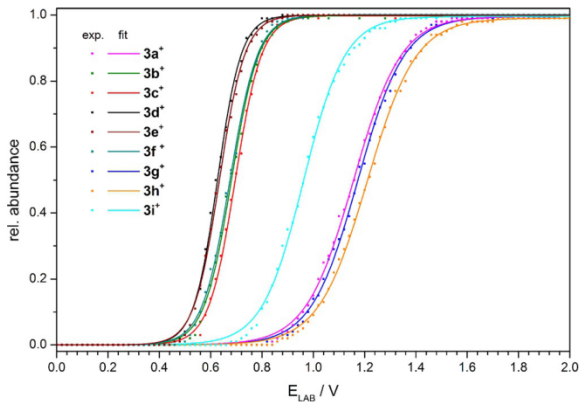

Figure 2. Measured data (dots) and sigmoidal fit (lines) of the CID ESI-MS curves for the cations **3a**$^+$–**3i**$^+$.

Table 2. Fitted E_{LAB} values and relative reaction enthalpies for the splitting of HCl or DCl for cations **3a**$^+$–**3i**$^+$.

Cation	E_{LAB} [V]	$\Delta\Delta H_{fit}$ [kJ mol^{-1}]	$\Delta\Delta H_{fit}$ [kcal mol^{-1}]
3a$^+$	1.16	264	63
3b$^+$	0.68	157	37
3c$^+$	0.70	160	38
3d$^+$	0.63	144	35
3e$^+$	0.63	149	36
3f$^+$	0.68	159	38
3g$^+$	1.17	268	64
3h$^+$	1.21	276	66
3i$^+$	0.96	220	53

so-called thermometer ions (see the Supporting Information).[17] Table 2 summarizes the resulting energies.

According to the CID ESI-MS data, the cationic ruthenium(II) species can be divided into three groups: First, there are cations **3a**$^+$, **3g**$^+$ and **3h**$^+$, which do not have any substituents in the 2-position of each six-membered heterocyclic ring. They show by far higher barriers for the roll-over cyclometalation than complexes **3b–3f**$^+$ and **3i**$^+$. Among the three high-barrier complexes, derivative **3a**$^+$ undergoes the roll-over cyclometalation somewhat easier than **3g**$^+$ and **3h**$^+$. This can be explained by the presence of a second electronegative nitrogen atom in the pyrimidine ring of **3a**$^+$, which weakens the Ru1–N2 bond. For species **3g**$^+$ and **3h**$^+$, the expected primary isotope effect is observed. This speaks, according to Olah,[18] for the fact that the highest transition state is of a σ-complex nature, which is in agreement with the results of quantum chemical calculations on compounds **3a**$^+$, **3b**$^+$, **3d**$^+$, and **3h**$^+$, as recently published by us.[9]

A second group of compounds (**3b–3f**$^+$) consists of ruthenium(II) complexes with pyrimidinylpyridine ligands containing a substituent with a heteroatom in the 2-position of the pyrimidine ring. They undergo the roll-over cyclometalation much easier than the group of compounds discussed above. Electronic and steric reasons may help to rationalize this observation: the electronegative heteroatom will withdraw electron density from the σ skeleton of the ligand. It furthermore will, together with its substituents, sterically interfere with the η^6-cymene ligand. Both effects weaken the strength of the Ru1–N2 bond, as documented by the solid-state structures discussed above, and thus, facilitate roll-over cyclometalation. Within this group of compounds, further differences can be determined: among the amino-functionalized derivatives, compounds **3b**$^+$ (NH_2) and **3c**$^+$ (NHMe) require higher activation energies than **3d**$^+$ (NMe_2). The variations in the bond lengths Ru1–N2 and torsion angles N1-C5-C6-N2 in the solid-state structures of **3b**$^+$ and **3d**$^+$ are in accordance with this observation. The activation energy of hydroxyl derivative **3e**$^+$ is almost identical to the value of **3d**$^+$. The stronger electron-withdrawing effect of the OH group seems to compensate for the bulkiness of the NMe_2 substituent. The electronically less accepting chloro substituent in **3f**$^+$ then increases the barrier up to the value found for **3b**$^+$.

Finally, there is cation **3i**$^+$, which is the only compound containing a η^6-coordinating ligand other than the bulky cymene. In comparison to **3d**$^+$, a pronounced increase in the activation barrier was measured. This does, at a first glance, not attest to the almost identical steric interference between the 2-(2-dimethylaminopyrimidin-4-yl)pyridine and arene ligands, as documented by the almost identical values of Ru1–N2 and N1-C5-C6-N2 found for **3i**$^+$ and **3d**$^+$. However, it has to be kept in mind that solid-state structures deliver a static picture of a molecule, with generally minimized intramolecular steric interactions. In solution and in the gas phase, the cymene ligand will rotate on top of the ruthenium(II) site bringing its bulky isopropyl and methyl substituents closer to the NMe_2 group of the pyrimidine ring.

In our recent study, we showed that only [(η^6-arene)(**2a**)-RuCl]$^+$ cations containing a tertiary amino group, such as **3b**$^+$, were able to catalyze the base-free transfer hydrogenation of ketones.[9] Even in the presence of a base (KOH), there are large differences in the activities between compounds of the type **3d**$^+$ and **3b**$^+$. Similar results were found for the reductive amination of benzaldehyde with anilines: compound **3d**$^+$ catalyzes this reaction with high activity without requiring a base or any other additive.[10]

Catalytic transfer hydrogenation

With a whole series of essentially new ruthenium(II) compounds in our hands, we began a general survey on the structure/reactivity relationships in base-free transfer hydrogenation. It should be noted at this point that a linear transfer of the CID ESI-MS data (gas phase) into a quantitative reactivity profile of the investigated class of compounds in solution is not possible. However, the elucidation of trends concerning the influence of the substitution pattern on the catalytic activity seems feasible. A series of parameters such as reaction temperature, nature of the solvent and counteranion, and even variations of the concentration may cause variations of the reactivity.

We therefore first investigated the influence of the counteranion on the reactivity of our most reactive catalyst **3d**$^+$ at a quite high catalyst loading of 5 mol%. The conversion was determined after a reaction time of 4 h at 82 °C. Table 3 summarizes the results obtained with acetophenone (AC) as the model substrate. Entries 1–4 show the effects of the four counteranions: complexes **3dBArF$_4$** and **3dBF$_4$** give the best results. However, there is no really dominant effect of the counteranion on the catalytic activity, as that found for the nature of the *N,N'*-donor ligand (see below). At these relatively high catalyst concentrations, the observed variations in the activities might be assigned to the solubility of the catalyst in *i*PrOH.

Attempts to form the catalyst in situ in the reaction mixture of isopropanol and AC by simply adding [(η^6-cymene)$RuCl_2]_2$, ligand **2d**, and $NaBPh_4$ in the correct molecular ratio lead to no catalytic conversion at all (Table 3, entry 5). The strongly coordinating solvent prevents the formation of the catalyst. From this finding, the conclusion can be drawn that the preformed ruthenium catalyst will not completely lose its *N,N'*-donor

Table 3. Screening of the base-free transfer hydrogenation of AC.[a]

Entry	AC [mmol]	Cat. [mol%]	Cat.	*V*(*i*PrOH) [mL]	Yield [%] (*t* [h])
1	0.5	5.0	**3dBArF$_4$**	25.0	88 (4)
2	0.5	5.0	**3dBPh$_4$**	25.0	71 (4)
3	0.5	5.0	**3dPF$_6$**	25.0	44 (4)
4	0.5	5.0	**3dBF$_4$**	25.0	89 (4)
5[b]	0.5	5.0	**3dBPh$_4$**	25.0	0 (4)
6[c]	0.5	5.0	**3dBPh$_4$**	25.0	56 (24)
7	1.0	0.5	**3dBPh$_4$**	5.0	97 (24)
8	1.0	0.5	**3iBF$_4$**	5.0	53 (24)
9	1.0	0.5	**3eBF$_4$**	5.0	0 (24)
10	1.0	0.5	**3fBF$_4$**	5.0	10 (24)
11	1.0	0.5	**3gPF$_6$**	5.0	0 (24)
12	1.0	0.5	**3aPF$_6$**	5.0	0 (24)
13	1.0	0.5	**3cPF$_6$**	5.0	0 (24)
14	1.0	0.5	**3bPF$_6$**	5.0	0 (24)
15	0.5	0.5	**3dBF$_4$**	5.0	76 (24)
16	1.5	0.5	**3dBF$_4$**	5.0	90 (24)
17	1.4	0.5	**3dBF$_4$**	5.3	100 (24)

[a] $T=82\,^{\circ}$C, catalyst, AC, *i*PrOH, yields were determined by GC analysis and are uncorrected. [b] 0.25 mol% of [(η^6-cymene)RuCl$_2$]$_2$, 0.5 mol% of ligand **2d**, and 0.5 mol% NaBPh$_4$. [c] $T=60\,^{\circ}$C.

ligand during catalysis. Otherwise, no or only little product formation should be observed.

According to CID ESI-MS measurements, the activation energy for cation **3d**$^+$ is the lowest of all compounds investigated. It therefore seemed to be feasible to lower the reaction temperature and try to get some conversion. Indeed, this is the case: even at 60 °C, compound **3dBPh$_4$** provides a reasonable yield of product (56%) after 24 h (Table 3, entry 6). To compare the catalytic activities of ruthenium(II) complexes **3a–iX**, the catalyst loading was reduced to 0.5 mol%. Concurrently, the solvent volume was decreased to 5 mL and the reaction time was extended to 24 h (Table 3, entries 7–14). From the whole series of **3a–iX**, only compounds **3dBPh$_4$** and **3iBF$_4$** showed reasonable activities. Poor activity was observed for **3fBF$_4$**; no activity at all for the other ruthenium(II) complexes. There still might be a slight influence of the counteranion (see discussion above), but the 2-(2-dimethylaminopyrimidin-4-yl)-pyridine ligand with a tertiary amino group clearly boosts the activity of the catalytically active metal site. It has to be mentioned that the compounds that are inactive under the base-free conditions discussed herein become catalytically active as soon as a base (KOH) is added to the reaction mixture. However, they are still less active than derivatives with a tertiary amino substituent.[9]

Solid-state structural data is not available for all ruthenium complexes, but for the seven derivatives discussed in the solid-state structure section above there is a clear trend that relates structural data with catalytic activities: A longer Ru–N2 bond and larger N1-C5-C6-N2 dihedral angle result in higher catalytic activity. It seems that a dihedral angle of approximately 5–6°, as found for the chloro-substituted derivative **3fBF$_4$**, marks a border between active and inactive compounds. Regarding the results of the CID ESI-MS study, a more differentiated view seems to be necessary. Cation **3d**$^+$, which shows the lowest activation barrier, gives the best results in catalytic transfer hydrogenation. However, derivative **3i**$^+$, with a η^6-coordinated benzene instead of a cymene ligand, still gives reasonable yields, although the measured barrier is much higher than that for **3d**$^+$; this finding must relate to the CID process itself. Chloro compound **3f**$^+$ is still slightly active, although its activation barrier is comparable to those of inactive **3b**$^+$ and **3c**$^+$, and hydroxyl derivative **3e**$^+$ is inactive, although its activation barrier is as low as that found for **3d**$^+$. The fact that derivatives **3b**$^+$, **3c**$^+$, and **3e**$^+$ possessing polar NH or OH units are catalytically inactive speaks for an additional influence of the solvent. From the solid-state structures of compounds with primary (NH$_2$) or secondary (NHR) amino groups on the pyrimidine ring, it is known that there is no direct N–H···Cl hydrogen bond. However, one molecule of isopropanol might bridge the gap and provide an additional contribution to keep the ligand in the *N,N′*-coordination mode (Scheme 5) by locking the N-C-

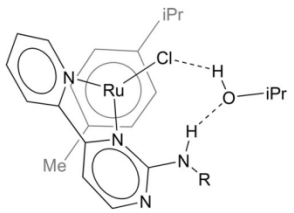

Scheme 5. Illustration of the interaction of one solvent molecule with the amino moiety and chlorido ligand.

C-N dihedral angle against further twisting. This would nicely explain the catalytic inactivity of those compounds with protic R groups (**3b**$^+$, **3c**$^+$, **3e**$^+$).

To complete the investigations into transfer hydrogenations with AC, the amount of substrate and the solvent volume were optimized (Table 3, entries 15–17). The finally found optimized conditions are described in Table 3, entry 17. They were applied to the following elucidation of the substrate scope (Table 4) with **3dBF$_4$** as the catalyst.

Generally, all substrates are converted into the corresponding ketones under base-free conditions with good yields. There are slight variations, mainly resulting from the steric impact of the substitution pattern. The *para*-functionalized arylketones with electron-withdrawing or -donating groups give high yields after a reaction time of only 4 h, while the introduction of a substituent in the *ortho* position results in lower conversions. Alkylketones give even lower yields after 4 h. However, regarding the performance after 24 h, there is not much difference between the substrates: yields of more than 80% are found, which means that the catalyst stays intact for a long time. For 2-hexanone, the yield of 91% after 24 h is close to equilibrium.

Quantum chemical calculations

From a mechanistic point of view, roll-over cyclometalation is the only possible entrance into a base-free transfer hydrogena-

Table 4. Substrate scope for the base-free transfer hydrogenation with **3dBF$_4$** as the catalyst.[a]

Entry	Substrate	Time [h]	Yield [%][a]
1		4 24	56 81
2	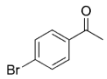	4 24	84 96
3		4 24	86 quant.
4	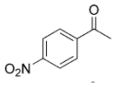	4 24	89 quant.
5	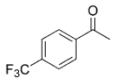	4 24	84 98
6		4 24	82 quant.
7		4 24	74 95
8	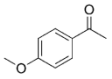	4 24	74 95
9	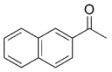	4 24	56 75
10		4 24	47 84
11		4 24	55 91

[a] 1.42 mmol of ketone, 5.3 mL (69.2 mmol) of *i*PrOH, 0.5 mol% of **3dBF$_4$**, 82 °C. [b] Yields determined by GC analysis and are corrected.

tion with this type of ruthenium(II) complex. According to CID ESI-MS data (see above) and DFT calculations,[9] it is especially favorable for 2-(pyrimidin-4-yl)pyridine ligands with a tertiary amino group in the 2-position of the pyrimidine ring because it weakens the Ru1–N2 bond by steric and electronic factors. The breaking of this bond is the first step in the roll-over cyclometalation process, which finally leads to a 16 valence electron (VE) cation in the gas phase. In solution, it is assumed that isopropanol will attack at the vacant coordination site and will subsequently undergo the transfer of a hydride anion to form a ruthenium hydrido species; the central intermediate in the transfer hydrogenation cycle. To date, there have been no theoretical calculations available for a more detailed understanding of this second part, the formation of the hydrido intermediate. This is discussed in the following section.

Because compound **3iBF$_4$**, with a η^6-coordinated benzene instead of a cymene ligand, shows similar catalytic activities to those of **3dBF$_4$**, it seemed feasible to perform DFT calculations on cation **3i$^+$**. This allows us to avoid problems in locating minima and transition states caused by the rotational flexibility of the methyl, and especially isopropyl, group of the cymene ligand. Figure 3 summarizes the calculations concerning roll-over cyclometalation occurring at cation **3i$^+$**.

The calculated $\Delta\Delta G$ values are close to the data obtained for cation **3d$^+$**.[9] Additionally, critical structural parameters obtained for the calculated molecular structure of **3i$^+$** (denoted in Figure 3 as **A**; for calculation details, see the Supporting Information) are in very good agreement with respect to the solid-state structure of **3iBF$_4$** (calcd: Ru1–N1 2.099, Ru1–N2 2.177, Ru1–Cl1 2.402 Å; N1-Ru1-N2 77.2, N1-Ru1-Cl1 81.3, N2-Ru2-Cl1 90.9, N1-C5-C6-N2 16.4°). Solely the distance Ru1–Ar (1.714 Å) is slightly overestimated compared with the structure of **3iBF$_4$**. For the last transition state, the $\Delta\Delta G$ value is slightly lower than the $\Delta\Delta G$ value of the preceding intermediate. This is because optimization is performed on the ΔE hypersurface, at which the last transition state is, as expected, higher in energy than the preceding intermediate. On the ΔG hypersurface, an increase in entropy becomes noticeable, as caused by the weekly bound HCl molecule.

Starting from the 16 VE intermediate **D**, the interaction with isopropanol can occur in two different ways: either the OH group attacks the ruthenium center or the hydrogen atom of the central carbon atom of the isopropanol molecule coordinates to ruthenium. This leads to two different reaction sequences that both finally give the same hydrido ruthenium species.

Attack of **D** by the isopropanol hydrogen atom (Figure 4) can be considered as part of an outer-sphere mechanism, wherein the isopropanol molecule does not coordinate to the ruthenium(II) site through the oxygen atom. The resulting intermediate **E** is endergonic by approximately 10.6 kcal mol^{-1}, but exothermic by approximately 1.3 kcal mol^{-1} with respect to 16 VE intermediate **D** and free isopropanol. This indicates that the stabilization of the 16 VE system by the Ru···H contact is only weak.

The transition state connecting the 16 VE system **D** with this first intermediate **E** could not be located. Subsequently, the formation of the Ru–H unit is accompanied by the transfer of a proton from the isopropanol OH group to the most basic site (carbanion) of the ligand, which allows the energetically unfavorable generation of charged species to be avoided. However, transition state **EF** of the concerted hydride/proton transfer is quite high in energy, which makes this route unfavorable. The reason for this high barrier can be elucidated from the structure of **EF**: the formation of the Ru–H bond is nearly accomplished, but the O–H bond is still far from being broken. This means that the structure of the substrate resembles a protonated molecule of acetone with a high accumulation of positive charge on the carbonyl carbon atom. Roll-over cyclodemetalation then takes place via transition state **FG**, leading to cationic ruthenium(II) hydrido complex **G** with a strongly bent backbone of the *N,N'*-donor, similar to the structure found for **3i$^+$** (**A**). This ruthenium(II) hydrido complex **G** is only slightly endergonic (3.9 kcal mol^{-1}), but rather endothermic (16.7 kcal

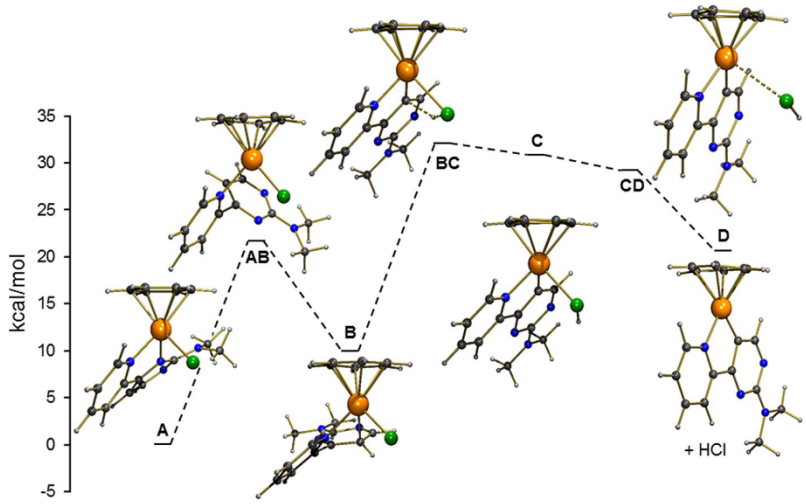

Figure 3. Calculated pathway for the roll-over cyclometalation of **3 i**$^+$ ($\Delta\Delta G$ given).

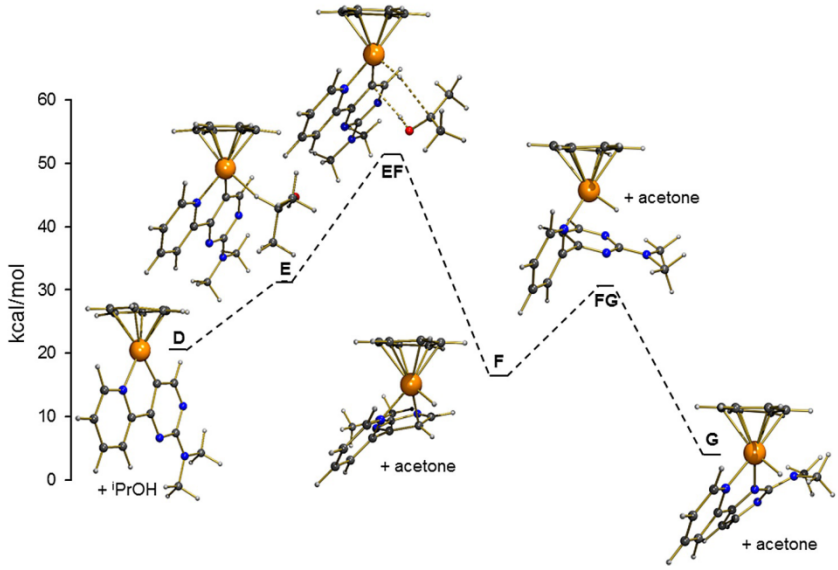

Figure 4. Calculated pathway for a concerted hydride/proton transfer leading to a ruthenium(II) hydrido species ($\Delta\Delta$G given).

mol^{-1}) with respect to **3 i**$^+$ (**A**), which explains why it cannot be observed in isopropanol.

By another conceivable route to the ruthenium(II) hydrido complex (**G**), the substrate isopropanol would attack the ruthenium(II) site by the oxygen atom. This sequence can be divided into two sections: first, the formation of the ruthenium(II) isopropanolato complex **J** (Figure 5); second, the formation of the hydrido complex **G** (Figure 6). The formation of the isopropanolato complex follows a roll-over cyclodemetalation mechanism, and thus, resembles in its intermediates and transition states the splitting of HCl from **3 i**$^+$ (**A**) in the reverse direction. The first (**DH**) and last (**IJ**) transition states could not be located. It is quite remarkable that there is only a slight stabilization of approximately 2.5 kcal mol^{-1} between final product **J** and the preceding σ-complex **I**. Because the central barrier **HI** (38.7 kcal mol^{-1}), which corresponds to the protonation of the carbanion coordinated to ruthenium, is approximately 6.7 kcal mol^{-1} higher than that for the HCl splitting process (32.0 kcal mol^{-1}), isopropanolato complex **J** should not be detectable in the reaction mixture, as long as the barrier for subsequent hydride transfer is low enough.

This hydride transfer (Figure 6) is in accordance with a β-H elimination from the isopropanolato ligand, and therefore, requires partial de-coordination of the N,N′-donor. Otherwise, β-

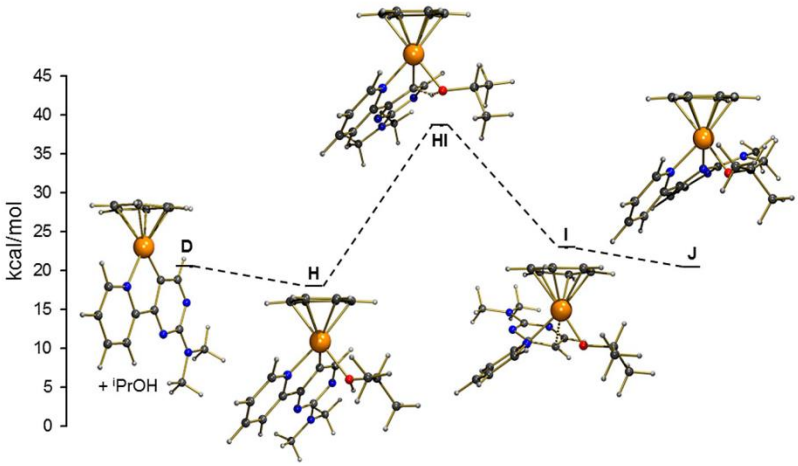

Figure 5. Calculated pathway for the formation of a ruthenium(II) isopropanolato complex ($\Delta\Delta G$ given).

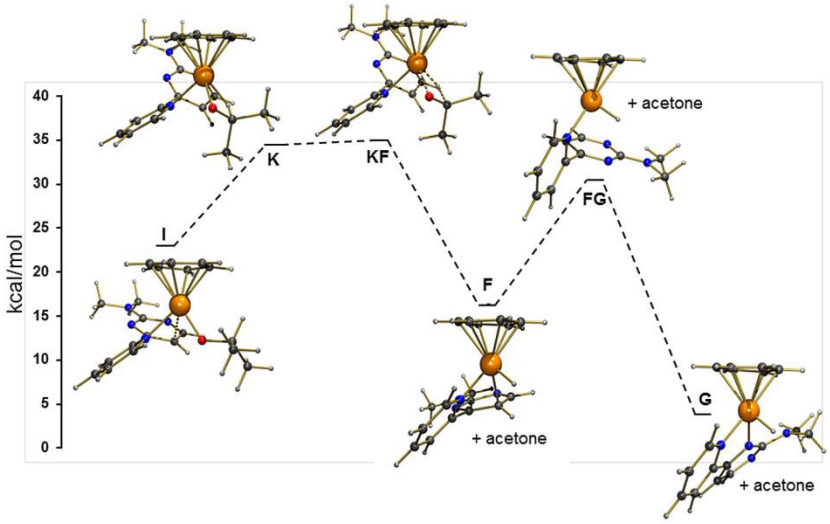

Figure 6. Calculated pathway for the formation of a ruthenium(II) hydrido from an isopropanolato complex ($\Delta\Delta G$ given).

H elimination would proceed via an energetically disfavored 20 VE species. Alternatively, the arene ligand could undergo a $\eta^6 \rightarrow \eta^4$ shift, but the calculations do not give any indication of such a process.

Starting from the second to last structure, **I**, shown in Figure 5, an agostic β-H interaction in intermediate **K** is enabled through the de-coordination of the weakly σ-bound carbon atom of the pyrimidine ring. A seemingly isoenergetic transition state (**IK**) could not be located. We assume that this barrier is slightly above the β-H bound intermediate **K**. Only a tiny barrier of 0.4 kcal mol^{-1} (**KF**) is required to release acetone from this structure and to form ruthenium(II) hydrido species **G** via intermediate **F** and transition state **FG**, which is lower in energy than that of **KF**. The overall barrier for this process is at approximately 35.0 kcal mol^{-1}. It therefore is indeed lower than the barrier for the formation of the ruthenium(II) isopropanolato complex discussed above.

From the results of the calculations, a series of conclusion can be drawn. The crucial hydrido (**G**) and isopropanolato (**J**) intermediates are higher in energy than the chlorido derivative **3 i**$^+$ (**A**), which is in agreement with the fact that these intermediates cannot be observed in isopropanol. The formation of hydrido intermediate **G** most likely does not follow an outer-sphere mechanism, but instead a classical β-H elimination takes place. The barrier (**KF**) for β-H elimination, which requires partial de-coordination of the *N,N'*-ligand, is at approximately

35.0 kcal mol^{-1}, and therefore, much lower than the barrier found for the outer-sphere hydrogen transfer (**EF**). However, it is in the same range as that of barrier **BC**, which is required for roll-over cyclometalation starting from **3i**$^+$. This is not surprising because the reverse β-H elimination is simply a roll-over cyclometalation starting from the *N,N'*-coordinated hydrido complex **G**. This fact strongly supports the idea that the activation of **3i**$^+$ proceeds through a roll-over cyclometalation process. The hydrido intermediate **G** is the starting point for the transfer of hydrogen to the ketone, which returns to compound **H** (**G**→**F**→**K**→**I**→**H**) as shown in Figures 6 and 5.

Conclusion

Weakening a critical ligand-to-metal bond by a combination of electronic and steric factors results in roll-over cyclometalation at some of the ionic ruthenium(II) complexes of the type [(η^6-arene)(*N,N'*-ligand)RuCl]X (*N,N'* = *N,N'*-chelating 2-(pyrimidin-4-yl)pyridine ligand). This crucial step allows the base-free transfer hydrogenation of ketones under mild and base-free conditions, as long as a tertiary amino group is attached to the 2-position of the pyrimidinyl ring. Because we could determine this effect for combinations of pyrimidines with two other donor sites (pyridines and phosphanes), it more and more becomes clear that it is of general importance for this type of donor site. It furthermore becomes clear that roll-over cyclometalation could provide an electronic situation at a catalytically active site that is as beneficial for catalytic reactions as it is for the photophysical properties of certain late-transition-metal complexes. We are presently working out protocols for other catalytic reactions under inclusion of the roll-over cyclometalation process.

Experimental Section

General

Organic precursors were purchased form Sigma–Aldrich, Acros, and TCI Chemicals and used without further purification. Compounds **1**,[12] **2a**,[13] **2b**,[9a] **2d**,[9a] **2h**,[14] **3gPF$_6$**,[19] and bis[(η^6-benzene)ruthenium(II)dichloride][20] were synthesized according to published procedures. The ruthenium(II) precursor [{(η^6-cymene)RuCl$_2$}$_2$] was commercially available from Strem Chemicals. The solvents CH_2Cl_2 and Et_2O were purchased from Sigma Aldrich and dried over molecular sieves in a Braun MB SPS solvent dryer. Alcohols were dried by distillation over magnesium. Isopropanol was purchased from Bernd Kraft GmbH. The starting materials for catalysis were purified by standard purification methods. All reactions were performed under an atmosphere of nitrogen by using standard Schlenk techniques. The NMR spectra were obtained on Bruker Avance 400 and 600 systems with $CDCl_3$, CD_3CN, or [D$_6$]DMSO as the solvents. For the assignment of the signals, see the structures presented in the Supporting Information. Preparative chromatographic purifications were performed with a Teledyne Isco Combi Flash Rf200 system by using prepacked silica columns from RediSep. The IR spectra were recorded with a PerkinElmer FTIR Spectrum 100 device equipped with an ATR sample assembly. For data refining, the PerkinElmer software Spectrum 6.3.5 was used. Elemental analysis measurements were performed with a Hanau Elemental Analyzer Vario Microcube.

Synthesis

Compound 2c: Methylguanidinium chloride (1.97 g, 18.0 mmol) and sodium (3.0 g) were dissolved in anhydrous ethanol (34 mL). Compound **1** (3.17 g, 18.0 mmol) was added to the resulting suspension, which was then heated to reflux for 16 h. After cooling to RT, the solvent was removed under reduced pressure and the residue was washed with cold water. The product was dried under vacuum and the resulting brown oil was purified by column chromatography (CH_2Cl_2/MeOH) to give the product as a pale yellow solid (13%). M.p. 108.0 °C; IR (ATR,): $\tilde{\nu}$ = 3359 (w), 3062 (w), 2900 (w), 1579 (s), 1545 (s), 1393 (s), 778 cm^{-1} (vs); ^{1}H NMR (400.1 MHz, $CDCl_3$, 20 °C): δ = 8.65 (dd, ^3J(H,H) = 0.68, 4.71 Hz, 1H; H1), 8.41 (d, ^3J(H,H) = 5.11 Hz, 1H; H8), 8.35 (d, ^3J(H,H) = 7.96 Hz, 1H; H4), 7.76 (td, ^3J(H,H) = 1.75, 7.76 Hz, 1H; H3), 7.53 (d, ^3J(H,H) = 5.10 Hz, 1H; H7), 7.31 (ddd, ^3J(H,H) = 1.09, 4.79, 7.49 Hz, 1H; H2), 5.61 (brs, 1H; H10), 3.02 ppm (d, ^3J(H,H) = 5.04 Hz, 3H; H11); ^{13}C{^{1}H} NMR (100.6 MHz, $CDCl_3$, 20 °C): δ = 163.7 (C6), 163.3 (C9), 159.3 (C8), 154.9 (C5), 149.5 (C1), 137.0 (C3), 125.1 (C2), 121.5 (C4), 106.9 (C7), 28.6 ppm (C11); elemental analysis calcd (%) for $C_{10}H_{10}N_4$ (186.22): C 64.50, N 30.09, H 5.41; found: C 64.54, N 29.99, H 5.44.

Compound 2e: Urea (5.11 g, 85.1 mmol) and **1** (6.00 g, 34.0 mmol) were dissolved in a mixture of H_2O/EtOH (18:3 mL). After the mixture was heated to 95 °C, concentrated HCl (18.2 mL) was added. The reaction mixture was kept at 95 °C for 48 h. After cooling to RT, the solution was neutralized by the addition of a 2 M solution of Na_2CO_3. The precipitate was filtered off, washed with Et_2O, and dried under vacuum. The product was isolated as a gray solid (85%). M.p. 250.7 °C; IR (ATR): $\tilde{\nu}$ = 3017 (w), 2696 (m), 1638 (vs), 1611 (vs), 1432 (s), 1423 (s), 781 cm^{-1} (s); ^{1}H NMR (400.1 MHz, [D$_6$]DMSO, 20 °C): δ = 12.03 (brs, 1H; H10), 8.74 (ddd, ^3J(H,H) = 0.83, 1.62, 4.70 Hz, 1H; H1), 8.32 (d, ^3J(H,H) = 6.42 Hz, 1H; H8), 8.10 (d, ^3J(H,H) = 6.42 Hz, 1H; H4), 8.01 (td, ^3J(H,H) = 1.76, 7.75 Hz, 1H; H3), 7.59 (ddd, ^3J(H,H) = 1.16, 4.75, 7.54 Hz, 1H; H7), 7.31 ppm (d, ^3J(H,H) = 6.43 Hz, 1H; H2); ^{13}C{^{1}H} NMR (100.6 MHz, [D$_6$]DMSO, 20 °C): δ = 159.7 (C6), 156.8 (C9), 152.8 (C8), 149.6 (C5), 148.4 (C1), 137.6 (C3), 126.4 (C2), 121.8 (C4), 100.0 ppm (C7); elemental analysis calcd (%) for $C_9H_7N_3O$ (173.17): C 62.42, N 24.26, H 4.07; found: C 62.43, N 23.81, H 4.11.

Compound 2f: Compound **2** (4.00 g, 23.1 mmol) were added to $POCl_3$ (40 mL). The mixture was heated to reflux for 1 h. Unreacted $POCl_3$ was removed trap-by-trap and the residue was poured onto ice (10.0 g). After neutralization by the addition of a saturated solution of Na_2CO_3, the precipitated solid was filtered off and dried under vacuum. The product was isolated as a gray solid (90%). M.p. 107.7 °C; IR (ATR): $\tilde{\nu}$ = 3067 (w), 1565 (m), 1535 (s), 1423 (m), 1345 (s), 1181 (s), 763 cm^{-1} (vs); ^{1}H NMR (400.1 MHz, [D$_6$]DMSO, 20 °C): δ = 8.92 (d, ^3J(H,H) = 5.13 Hz, 1H; H1), 8.79 (dd, ^3J(H,H) = 0.75, 4.70 Hz, 1H; H8), 8.38 (t, ^3J(H,H) = 6.90 Hz, 2H; H3, H4), 8.05 (td, ^3J(H,H) = 1.75, 7.77 Hz, 1H; H7), 7.64 ppm (ddd, ^3J(H,H) = 1.10, 4.74, 7.56 Hz, 1H; H2); ^{13}C{^{1}H} NMR (100.6 MHz, [D$_6$]DMSO, 20 °C): δ = 165.4 (C6), 161.9 (C9), 160.4 (C8), 151.6 (C5), 150.0 (C1), 138.0 (C3), 126.8 (C2), 121.8 (C5), 116.2 ppm (C7). elemental analysis calcd (%) for $C_9H_6ClN_3$ (191.62): C 56.41, H 3.16, N 21.93; found: C 56.49, H 3.22, N 21.58.

General procedure for the synthesis of the ruthenium complexes[9]: [(η^6-Cymene)RuCl$_2$]$_2$, the *N,N'*-chelating ligand, and a salt providing the desired anion were added to a Schlenk tube. CH_2Cl_2 was added and the resulting suspension was stirred for 24 h at RT. Then the reaction mixture was filtered, the amount of solvent was

reduced, and the desired complex was crystallized by the diffusion of Et_2O.

Compound 3 aPF$_6$: The reaction of **2 a** (138 mg, 0.88 mmol), KPF_6 (177 mg, 0.96 mmol), and [{(η^6-cymene)RuCl$_2$}$_2$] (245 mg, 0.40 mmol) in CH_2Cl_2 (70 mL) gave the product as an orange powder (30 %). M.p. 188 °C; IR (ATP): $\tilde{\nu}$ = 3069 (w), 2974 (w), 1597 (m), 1466 (m), 1155 (m), 827 (vs), 798 cm^{-1} (s); ^{1}H NMR (600.1 MHz, CD_3CN, 20 °C): δ = 9.92 (s, 1 H; H9), 9.40 (d, ^3J(H,H) = 5.41 Hz, 1 H; H1), 9.10 (d, ^3J(H,H) = 5.27 Hz, 1 H; H8), 8.46 (d, ^3J(H,H) = 7.98 Hz, 1 H; H4), 8.27 (dd, ^3J(H,H) = 0.92, 5.28 Hz, 1 H; H7), 8.25 (td, ^3J(H,H) = 1.32, 7.91 Hz, 1 H; H3), 7.82 (m, 1 H; H2), 6.00 (2×d, 2×^3J(H,H) = 6.58, 6.58 Hz, 2×1 H; H$_{cym}$), 5.82 (2×d, 2×^3J(H,H) = 6.79, 6.79 Hz, 2×1 H; H$_{cym}$), 2.69 (sept, 1 H; C*H*(CH$_3$)$_2$), 2.20 (s, 3 H; CH$_3$), 1.06, 1.04 ppm (2×d, 2×^3J(H,H) = 7.14, 6.96 Hz, 2×3 H; CH(C*H*$_3$)$_2$); ^{13}C{^{1}H} NMR (150.9 MHz, CD_3CN, 20 °C) δ = 163.4 (C9), 162.2 (C6), 161.1 (C8), 157.0 (C1), 153.9 (C5), 141.2 (C3), 130.6 (C2), 126.7 (C4), 120.0 (C7), 107.3, 104.6, 87.3, 86.7, 85.7, 85.4 (6×C$_{cym}$), 31.9 (CH(CH$_3$)$_2$), 22.2, 22.2 (2×CH(CH$_3$)$_2$), 18.9 ppm (CH$_3$); ^{19}F NMR (376.5 MHz, CD_3CN, 20 °C): δ = −72.9 ppm (d, ^1J(P,F) = 706 Hz); ^{31}P{^{1}H} NMR (150.9 MHz, CD_3CN, 20 °C): δ = 12.9 ppm (hept); elemental analysis calcd (%) for $C_{19}H_{23}ClF_6N_3PRu$ (574.9): C 39.83, H 3.69, N 7.33; found: C 39.71, H 3.72, N 7.29.

Compound 3 bPF$_6$: The reaction of **2 b** (74.3 mg, 0.43 mmol), KPF_6 (95.3 mg, 0.52 mmol), and [{(η^6-cymene)RuCl$_2$}$_2$] (132 mg, 0.22 mmol) in CH_2Cl_2 (10 mL) gave the product as an orange powder (63 %). M.p. 222 °C; IR (ATP): $\tilde{\nu}$ = 3438 (w), 3294 (w), 3095 (w), 1713 (w), 1557 (m), 823 (vs), 772 cm^{-1} (s); ^{1}H NMR (400.1 MHz, CD_3CN, 20 °C): δ = 9.28 (d, ^3J(H,H) = 5.61 Hz, 1 H; H1), 8.61 (d, ^3J(H,H) = 4.82 Hz, 1 H; H8), 8.28 (d, ^3J(H,H) = 7.69 Hz, 1 H; H4), 8.18 (t, ^3J(H,H) = 7.67 Hz, 1 H; H3), 7.75 (t, ^3J(H,H) = 6.12 Hz, 1 H; H2), 7.53 (d, ^3J(H,H) = 4.89 Hz, 1 H; H7), 6.51 (br s, 2 H; H10), 6.05, 5.87 (2×d, 2×^3J(H,H) = 6.04, 6.08 Hz, 1 H; H$_{cym}$), 5.67 (m, 2 H; H$_{cym}$), 2.52 (sept, 1 H; C*H*(CH$_3$)$_2$), 2.23 (s, 3 H; CH$_3$), 1.01, 0.93 ppm (2×d, 2×^3J(H,H) = 6.89, 6.85 Hz, 2×3 H; CH(C*H*$_3$)$_2$); ^{13}C{^{1}H} NMR (100.6 MHz, CD_3CN, 20 °C) δ = 165.9 (C9), 162.5 (C8), 162.3 (C6), 156.8 (C1), 155.0 (C5), 141.1 (C3), 130.0 (C2), 126.1 (C4), 110.0 (C7), 106.6, 106.2, 87.8, 86.6, 84.8, 84.5 (6×C$_{cym}$), 31.7 (*C*H(CH$_3$)$_2$), 22.2, 22.0 (2×CH(CH$_3$)$_2$), 18.9 ppm (CH$_3$); ^{19}F NMR (376.5 MHz, CD_3CN, 20 °C): δ = −73.0 ppm (d, ^1J(P,F) = 706 Hz); ^{31}P{^{1}H} NMR (162.0 MHz, CD_3CN, 20 °C): δ = −146.7 ppm (sept); elemental analysis calcd (%) for $C_{19}H_{22}ClF_6N_4PRu$ (587.9): C 38.82, H 3.77, N 9.53; found: C 38.77, H 3.93, N 9.23.

Compound 3 cBF$_4$: The reaction of **2 c** (70.0 mg, 0.38 mmol), $NaBF_4$ (69.0 mg, 0.63 mmol), and [{(η^6-cymene)RuCl$_2$}$_2$] (96.3 mg, 0.16 mmol) in CH_2Cl_2 (30 mL) gave the product as an orange powder (69 %). M.p. 199 °C (decomp); IR (ATP): $\tilde{\nu}$ = 3394 (w), 3095 (w), 2974 (w), 1596 (m), 1574 (d), 1057 (vs), 1033 cm^{-1} (vs); ^{1}H NMR (600.1 MHz, CD_3CN, 20 °C): δ = 9.46 (d, ^3J(H,H) = 5.29 Hz, 1 H; H1), 8.64 (d, ^3J(H,H) = 4.77 Hz, 1 H; H8), 8.41 (d, ^3J(H,H) = 7.96 Hz, 1 H; H4), 8.16 (d, ^3J(H,H) = 7.70 Hz, 1 H; H3), 7.75 (m, 1 H; H7), 7.60 (d, ^3J(H,H) = 4.83 Hz, 1 H; H2), 6.50 (d, ^3J(H,H) = 4.55 Hz, 1 H; H10), 6.06, 5.94, 5.89, 5.87 (4×d, 4×^3J(H,H) = 6.05, 6.02, 6.02, 6.08 Hz, 4×1 H; H$_{cym}$), 3.17 (d, ^3J(H,H) = 4.85 Hz, 3 H; H11), 2.48 (sept, 1 H; C*H*(CH$_3$)$_2$), 2.22 (s, 3 H; CH$_3$), 0.97, 0.89 ppm (2×d, 2×^3J(H,H) = 6.90, 6.94 Hz, 2×3 H; CH(C*H*$_3$)$_2$); ^{13}C NMR (50.3 MHz, CD_3CN, 20 °C) δ = 164.5 (C9), 162.6 (C8), 161.9 (C6), 157.3 (C1), 155.1 (C5), 141.0 (C3), 130.0 (C2), 126.3 (C4), 109.0 (C7), 106.2, 106.0, 87.8, 86.9, 85.0, 84.6 (6×C$_{cym}$), 31.7 (C11), 30.1 (*C*H(CH$_3$)$_2$), 22.4, 22.2 (2×CH(CH$_3$)$_2$), 18.9 ppm (CH$_3$); ^{19}F NMR (376.5 MHz, CD_3CN, 20 °C): δ = −151.8 ppm; ^{11}B NMR (128.4 MHz, CD_3CN, 20 °C): δ = −1.18 ppm; elemental analysis calcd (%) for $C_{20}H_{24}BClF_4N_4Ru$ (543.76): C 44.18, H 4.45, N 10.30; found: C 43.82, H 4.58, N 10.03.

Compound 3 dBArF$_4$: The reaction of **3 d** (64.1 mg, 0.32 mmol), $NaBArF_4$ (399 mg, 0.45 mmol), and [{(η^6-*p*-cymene)RuCl$_2$}$_2$] (91.9 mg, 0.15 mmol) in CH_2Cl_2 (25 mL) gave the product as red crystals (93 %). M.p. 130 °C; IR (ATR): $\tilde{\nu}$ = 2962 (w), 1596 (m), 1555 (m), 1353 (s), 1272 (vs), 1111 (vs), 886 cm^{-1} (s); ^{1}H NMR (400.1 MHz, $CDCl_3$, 20 °C): δ = 8.93 (d, ^3J(H,H) = 5.23 Hz, 1 H; H1), 8.46 (d, ^3J(H,H) = 4.56 Hz, 1 H; H8), 7.90 (td, ^3J(H,H) = 7.88 Hz, ^4J(H,H) = 1.37 Hz, 1 H; H4), 7.82 (d, ^3J(H,H) = 7.59 Hz, 1 H; H3), 7.70 (br s, 8 H; H$_{BArF}$), 7.55 (ddd, ^3J(H,H) = 5.68, 7.32 Hz, ^4J(H,H) = 1.36, 1 H; H2), 7.51 (br s, 4 H; H$_{BArF}$), 7.13 (d, ^3J(H,H) = 4.60 Hz, 1 H; H7), 5.47 5.35 5.31 5.28 (4×d, 4×^3J(H,H) = 6.14, 6.16, 6.40, 6.27 Hz, 1 H; H$_{cym}$), 3.41 (br s, 6 H; H10), 2.43 (hept, ^3J(H,H) = 6.93 Hz, 1 H; C*H*(CH$_3$)$_2$), 2.08 (s, 3 H; CH$_3$), 1.04, 0.89 ppm (2×d, 2×^3J(H,H) = 6.90, 6.96 Hz, 3 H; CH(C*H*$_3$)$_2$); ^{13}C{^{1}H} NMR (100.6 MHz, [D$_6$]DMSO, 20 °C) δ = 168.3 (C9), 163.7 (C8), 161.1 (m, C$_{meta}$), 158.5 (C6), 156.1 (C1), 154.0 (C5), 140.1 (C3), 134.1 (s, C$_{ipso}$), 128.5 (m, C$_{ortho}$), 128.4 (C2), 125.4 (C4), 124.0 (q, $^1J_{FC}$ = 272.4 Hz, CF$_3$), 117.4 (m, C$_{para}$), 109.9 (C7), 103.7, 102.1, 85.4, 85.2, 84.2, 83.3 (6×C$_{Cym}$), 31.7 (C10), 25.0 (*C*H(CH$_3$)$_2$), 21.9 21.0 (2×CH(CH$_3$)$_2$), 17.7 ppm (CH$_3$); ^{19}F NMR (376.5 MHz, CD_3CN, 20 °C): δ = −62.3 ppm; ^{11}B NMR (128.4 MHz, CD_3CN, 20 °C): δ = −6.63 ppm; elemental analysis calcd (%) for $C_{53}H_{38}BClF_{24}N_4Ru$ (1334.21): C 47.71, H 2.87, N 4.20; found: C 47.74, H 3.17, N 4.00.

Compound 3 eBF$_4$: The reaction of **3 e** (218 mg, 1.26 mmol), $NaBF_4$ (145 mg, 1.32 mmol), and [{(η^6-*p*-cymene)RuCl$_2$}$_2$] (367 mg, 0.6 mmol) in CH_2Cl_2 (30 mL) gave the product as an orange powder (87 %) from CH_3CN and Et_2O. M.p. 197 °C; IR (ATR): $\tilde{\nu}$ = 3061 (m), 1671 (vs), 1612 (vs), 1600 (vs), 1225 (vs), 840 (vs), 776 cm^{-1} (vs); ^{1}H NMR (400.1 MHz, CD_3CN, 20 °C): δ = 10.92 (br s, 1 H; H10), 9.43 (d, ^3J(H,H) = 5.42 Hz, 1 H; H1), 8.36 (d, ^3J(H,H) = 8.13 Hz, 1 H; H4), 8.21 (t, ^3J(H,H) = 7.81 Hz, 1 H; H3), 8.13 (d, ^3J(H,H) = 6.56 Hz, 1 H; H8), 7.81 (m, 1 H; H2), 7.18 (d, ^3J(H,H) = 6.72 Hz, 1 H; H7), 6.14, 5.98 (2×d d, 2×^3J(H,H) = 5.98, 6.01 Hz, 1 H; H$_{cym}$), 5.79 (m, ^3J(H,H) = 6.27 Hz, 2 H; H$_{cym}$), 2.64 (hept, ^3J(H,H) = 6.76 Hz, 1 H; C*H*(CH$_3$)$_2$), 2.20 (s, 3 H; CH$_3$), 1.01 ppm (2×d, ^3J(H,H) = 6.76 Hz, 6 H; CH(C*H*$_3$)$_2$); ^{13}C{^{1}H} NMR (100.6 MHz, CD_3CN, 20 °C) δ = 171.6 (C9), 157.2 (C1), 154.7 (C6), 154.1 (C5), 150.7 (C3), 140.9 (C4), 130.9 (C2), 128.7 (C8), 106.5, 105.6, 101.9, 88.5, 86.5, 85.3, 84.1 (6×C$_{cym}$), 31.9 (*C*H(CH$_3$)$_2$), 22.4, 22.3 (2×CH(CH$_3$)$_2$), 19.3 ppm (CH$_3$); ^{19}F NMR (376.5 MHz, CD_3CN, 20 °C): δ = −151.8 ppm; ^{11}B NMR (138.4 MHz, CD_3CN, 20 °C): δ = −1.18 ppm; elemental analysis calcd (%) for $C_{19}H_{21}BClF_4N_3ORu$ (530.72): C 43.00, H 3.99, N 7.92; found: C 42.76, H 4.09, N 7.87.

Compound 3 fBF$_4$: The reaction of **2 f** (241 mg, 1.26 mmol), $NaBF_4$ (145 mg, 1.32 mmol), and [{(η^6-*p*-cymene)RuCl$_2$}$_2$] (367 mg, 0.60 mmol) in CH_2Cl_2 (30 mL) gave the product as a brown–orange solid (45 %). M.p. 200 °C; IR (ATR): $\tilde{\nu}$ = 3049 (w), 2970 (w), 1587 (m), 1050 (vs), 1039 (vs), 795 (s), 760 cm^{-1} (s); ^{1}H NMR (400.1 MHz, CD_3CN, 20 °C): δ = 9.33 (dd, ^3J(H,H) = 5.56 Hz, ^4J(H,H) = 0.65 Hz, 1 H; H1), 8.95 (d, ^3J(H,H) = 5.16 Hz, 1 H; H8), 8.45 (d, ^3J(H,H) = 8.07 Hz, 1 H; H4), 8.26 (m, 2 H; H3, H7), 7.85 (m, 1 H; H2), 6.16, 5.91, 5.81, 5.76 (4×d, 4×^3J(H,H) = 6.14, 5.47, 6.25, 6.16 Hz, 1 H; H$_{cym}$), 2.61 (hept, ^3J(H,H) = 6.96 Hz, 1 H; C*H*(CH$_3$)$_2$), 2.26 (s, 3 H; CH$_3$), 1.01, 0.94 ppm (2×d, 2×^3J(H,H) = 6.93, 6.93 Hz, 3 H; CH(C*H*$_3$)$_2$); ^{13}C{^{1}H} NMR (100.6 MHz, CD_3CN, 20 °C): δ = 165.5 (C9), 165.3 (C6), 162.6 (C8), 157.1 (C1), 153.5 (C5), 141.4 (C3), 131.2 (C2), 127.6 (C4), 118.5 (C7), 108.0, 107.5, 88.9, 87.0, 86.1, 83.0 (6×C$_{cym}$), 31.9 (*C*H(CH$_3$)$_2$), 22.5, 22.2 (2×CH(CH$_3$)$_2$), 19.2 ppm (CH$_3$); ^{19}F NMR (376.5 MHz, CD_3CN, 20 °C): δ = −151.8 ppm; ^{11}B NMR (138.4 MHz, CD_3CN, 20 °C): δ = −1.19 ppm; elemental analysis calcd (%) for

$C_{19}H_{20}BCl_2F_4N_3Ru$ (549.17): N 7.65, C 41.56, H 3.67,; found: N 7.54, C 41.35, H 3.74.

Compound 3 hPF$_6$: The reaction of **2 h** (74.2 mg, 0.45 mmol), KPF_6 (82.8 mg, 0.45 mmol), and [{(η^6-*p*-cymene)$RuCl_2$}$_2$] (122 mg, 0.20 mmol) in CH_2Cl_2 (20 mL) gave the product as a yellow powder (13%). M.p. 219 °C (decomp); IR (ATR): $\tilde{\nu}$ = 2971 (w), 2933 (w), 1581 (w), 1338 (m), 1236 (m), 878 (m), 827 cm^{-1} (vs); ^{1}H NMR (400.1 MHz, CD_3CN, 20 °C): δ = 5.91, 5.71 (2×d, 2×^3J(H,H) = 6.43, 6.42 Hz, 2 H; H_{cym}), 2.64 (hept, ^3J(H,H) = 6.92 Hz, 1 H; C*H*(CH_3)$_2$), 2.19 (s, 3 H; CH_3), 1.02 ppm (d, ^3J(H,H) = 6.94 Hz, 6 H; CH(C*H*$_3$)$_2$); ^{13}C{^{1}H} NMR (100.6 MHz, CD_3CN, 20 °C) δ = 156.1 (m, C1), 155.6 (C5), 140.4 (m, C4), 128.1 (m, C3), 124.4 (m, C2), 106.0, 104.5, 87.4, 85.4 (C_{cym}), 31.8 (CH(CH_3)$_2$), 22.1 (CH(*C*H$_3$)$_2$), 18.9 ppm (CH_3); ^{19}F NMR (376.5 MHz, CD_3CN, 20 °C): δ = −72.8 ppm (d, ^1J(P,F) = 706.8 Hz); ^{31}P{^{1}H} NMR (162.0 MHz, CD_3CN, 20 °C): δ = −144.6 ppm (hept); elemental analysis calcd (%) for $C_{20}H_{14}ClD_8F_6N_2PRu$ (579.83): C 41.42, H 3.88, N 4.83; found: C 41.37, H 4.08, N 4.68%.

Compound 3 iBF$_4$: The reaction of $NaBF_4$ (64.7 mg, 0.32 mmol), **3 d** (37.2 mg, 0.34 mmol), and [{(η^6-benzene)$RuCl_2$}$_2$] (77.0 mg, 0.15 mmol) in CH_2Cl_2 (20 mL) gave the product as an orange powder (32%). M.p. 242 °C (decomp); IR (ATR): $\tilde{\nu}$ = 3093 (w), 3071 (w), 1593 (s), 1553 (s), 1048 (vs), 1034 (vs), 781 cm^{-1} (s); ^{1}H NMR (400.1 MHz, CD_3CN, 20 °C): δ = 9.24 (d, ^3J(H,H) = 5.56 Hz, 1 H; H1), 8.62 (d, ^3J(H,H) = 4.66 Hz, 1 H; H8), 8.15 (m, 2 H; H3, H4), 7.72 (td, ^3J(H,H) = 7.98 Hz, ^3J(H,H) = 2.72, 1 H; H2), 7.46 (d, ^3J(H,H) = 4.67 Hz, 1 H; H7), 5.84 (s, 6 H; H_{benz}), 3.55, 3.26 ppm (2×br s, 6 H; H10); ^{13}C{^{1}H} NMR (100.6 MHz, CD_3CN, 20 °C) δ = 170.0 (C6), 165.0 (C9), 159.4 (C8), 156.8 (C1), 155.8 (C5), 141.2 (C3), 129.2 (C2), 125.3 (C4), 110.8 (C7), 87.5 ppm (C_{benz}), C10 resonances are too broad at RT; ^{19}F NMR (376.5 MHz, CD_3CN, 20 °C): δ = −151.8 ppm; ^{11}B NMR (128.4 MHz, CD_3CN, 20 °C): δ = −1.18 ppm; elemental analysis calcd (%) for $C_{17}H_{18B}ClF_4N_4Ru$ (501.68): C 40.70, H 3.62, N 11.17,; found: C 40.40, H 3.64, N 11.02.

Catalysis experiments

The catalysis experiments were conducted in headspace vials containing a Teflon®-coated magnetic stirring bar, which were predried in an oven at 60 °C and then dried under high vacuum (10^{-3} mbar) at 82 °C for 1 h. After cooling to RT under vacuum, the vial was charged with all solid compounds, sealed with a Teflon®-coated septum cap (VWR), and the atmosphere in the vial was evacuated and reflushed with nitrogen three times within 30 min by means of a syringe. Then isopropanol and other freshly distilled liquids were added by means of a syringe. Tetradecane or hexadecane (50 µL) were used as internal standards for GC analysis. The vials were placed in an aluminum block kept at 82 °C by means of a heating plate equipped with a temperature sensor. At the end of the reaction, samples were taken by means of a syringe and filtered over a short column containing $MgSO_4$ and silica to remove the catalyst. The column was finally washed with a small amount of ethyl acetate. For GC analysis, a Perkin–Elmer Clarus 580 gas chromatograph equipped with a flame-ionization detector (FID) and a FS-OV-1701-CB-0.25 column (l = 30 m, d_i = 0.25 mm; CS Chromatographie Service GmbH) was used (carrier gas: He, 60 psi; injector T = 250 °C; split ratio: 7.1:1; T program: 80→250 °C, T ramp: 5.67 °C min^{-1}).

ESI-MS experiments

ESI-MS and CID measurements were performed by using a Paul-type quadrupole ion trap instrument (Bruker Esquire 3000plus). The ion source was set to positive and negative ESI modes. The scan speed was 13 000 m/z s^{-1} in standard resolution scan mode (0.3 full-width at half-maximum (FWHM)/m/z) and the scan range was m/z 15–1200. Mass spectra were accumulated for at least 2 min. MS^n spectra were accumulated for at least 20 s. Sample solutions were continuously infused into the ESI chamber by a syringe pump at a flow rate of 2 µL min^{-1}. Nitrogen was used as the drying gas at a flow rate of 3.0 L min^{-1} at 220 °C. The solutions were sprayed at a nebulizer pressure of 280 mbar (4 psi) and the electrospray needle was held at 4.5 kV.

CID appearance curves were recorded with varying excitation amplitudes (0.0–1.0 V), which determined the internal energy scale of the mass spectrometer (E_{LAB} in V). Relative abundances were calculated according to Equation (1):

$$I^{fr}_{tot}.(E_{lab}) = \left(\frac{\sum_i I^{fr}_i(E_{lab})}{\sum_i I^{fr}_i(E_{lab}) + \sum_i I^{p}_i(E_{lab})}\right) \quad (1)$$

in which I^{fr}_i = intensity of the fragment ions and I^{p}_i = intensity of the parent ions.

Fragmentation amplitude dependent CID spectra were modeled and fitted by sigmoidal functions of the type shown in Equation (2)] by using a least-squares criterion.

$$I^{fr}_{fit}(E_{lab}) = \left(\frac{1}{1 + e^{(E^{50}_{lab} - E_{lab})\,B}}\right) \quad (2)$$

The E^{50}_{lab} fit parameter is the amplitude at which the sigmoid function was at the half-maximum value, whereas B described the rise of the sigmoidal curve.

Quantum chemical calculations

Quantum chemical calculations on the activation of **3 i**$^+$ and the subsequent formation of the ruthenium(II) hydrido intermediate were performed with the Gaussian 03[21] program by using the B3LYP gradient-corrected exchange-correlation functional in combination with the 6-31G* basis set for C, H, N, and Cl and the Stuttgart/Dresden ECP basis set for Ru.[22] Full geometry optimizations were performed in C_1 symmetry by using analytical gradient techniques and the resulting structures were confirmed to be true minima by diagonalization of the analytical hessian matrix. The starting geometries for the calculations of **3 i**$^+$ were taken from the solid-state structure of compound **3 iBF4**.

X-ray structural analyses

Crystal data and refinement parameters for compounds **3 aPF$_6$**, **3 dBF$_4$**, **3 fBF$_4$**, and **3 iBF$_4$** are collected in Table 5. The structures were solved by using direct methods (SHELXS[23] for **3 aPF$_6$**, SIR92[24] for **3 dBF$_4$**, **3 fBF$_4$**, and **3 iBF$_4$**), completed by subsequent difference Fourier syntheses, and refined by full-matrix least-squares procedures.[23] Semiempirical absorption corrections from equivalents (Multiscan) were performed for **3 aPF$_6$**, **3 dBF$_4$**, and **3 fBF$_4$**; for **3 iBF$_4$** an analytical numerical absorption correction was applied.[25] All non-hydrogen atoms were refined with anisotropic displacement

Table 5. Details of crystallographic data, data collection, and refinement.

	3 aPF$_6$	**3 dBF$_4$**	**3 fBF$_4$**	**3 iBF$_4$**
formula	$C_{19}H_{21}Cl_2F_6KN_3PRu$	$C_{21}H_{26}BClF_4N_4Ru$	$C_{19}H_{20}BCl_2F_4N_3Ru$	$C_{17}H_{18}BClF_4N_4Ru$
M_r	647.43	557.79	549.16	501.68
crystal size [mm]	0.45×0.18×0.14	0.22×0.14×0.10	0.303×0.277×0.058	0.516×0.234×0.036
T [K]	150(2)	150(2)	150(2)	150(2)
λ [Å]	1.54184	1.54184	0.71073	1.54184
crystal system	orthorhombic	monoclinic	monoclinic	monoclinic
space group	$P2_12_12_1$	$P2_1/n$	$P2_1/c$	$P2_1/n$
a [Å]	15.1884(3)	9.4578(1)	14.6441(6)	6.6729(3)
b [Å]	15.4509(3)	10.5033(1)	8.1867(3)	15.3566(7)
c [Å]	10.5274(1)	23.2740(3)	17.8669(7)	18.1079(10)
α [°]	90	90	90	90
β [°]	90	98.255(1)	106.223(4)	99.724(5)
γ [°]	90	90	90	90
V [Å^3]	2470.51(7)	2288.04(4)	2056.71(14)	1828.91(16)
Z	4	4	4	4
ρ_{calcd} [g cm^{-3}]	1.741	1.619	1.774	1.822
μ [mm^{-1}]	9.794	7.058	1.069	8.750
θ range [°]	4.08–62.73	3.84–62.65	2.879–32.494	3.797–62.837
reflns collected	17 300	16 033	25 570	19 585
independent reflns	3945 (R_{int} = 0.0394)	3649 (R_{int} = 0.0229)	6919 (R_{int} = 0.0808)	2937 (R_{int} = 0.0828)
no. data/restraints/parameters	3945/0/301	3649/0/294	6919/0/274	2937/0/255
final R indices [$I > 2\sigma(I)$][a]	0.0482, 0.1320	0.0270, 0.0691	0.0779, 0.1972	0.0994, 0.2741
R indices (all data)	0.0482, 0.1320	0.0280, 0.0696	0.0888, 0.2059	0.1006, 0.2746
GooF[b]	1.134	1.154	1.215	1.262
Flack parameter	0.02(2)	–	–	–
$\Delta\rho_{max}/_{min}$ [e Å^{-3}]	2.431/−0.897	0.965/−0.575	3.350/−2.369	2.540/−1.927

[a] $R1 = \Sigma||F_o| - |F_c||/\Sigma|F_o|$, $\omega R2 = [\Sigma\omega(F_o^2 - F_c^2)^2/\Sigma\omega F_o^2]^{1/2}$. [b] $GooF = [\Sigma\omega(F_o^2 - F_c^2)^2/(n-p)]^{1/2}$.

parameters. All hydrogen atoms were placed in calculated positions and refined by using a riding model.

CCDC 1498206 (**3 aPF$_6$**), 1498207 (**3 dBF$_4$**) 1498209 (**3 fBF$_4$**), and 1498208 (**3 iBF$_4$**) contain the supplementary crystallographic data for this paper. These data are provided free of charge by The Cambridge Crystallographic Data Centre.

Acknowledgements

This study was supported by the German research foundation DFG within the transregional collaborative research center SFB/TRR 88 "Cooperative effects in homo and heterometallic complexes" (3MET) and by the state research center OPTIMAS. We furthermore gratefully acknowledge the research college MAGNENZ and the state research unit NanoKat for financial support.

Keywords: density functional calculations · hydrogenation · metalation · reaction mechanisms · ruthenium

[1] a) H. Meerwein, R. Schmidt, *Liebigs Ann. Chem.* **1925**, *444*, 221–233; b) A. Verley, *Bull. Soc. Fr.* **1925**, *37*, 537; c) W. Ponndorf, *Angew. Chem.* **1926**, *39*, 138–143; d) R. V. Oppenauer, *Recl. Trav. Chim. Pays-Bas* **1937**, *56*, 137.

[2] a) R. L. Chowdhury, J.-E. Bäckvall, *J. Chem. Soc. Chem. Commun.* **1991**, 1063–1064; b) N. Menashe, Y. Shvo, *Organometallics* **1991**, *10*, 3885–3891; c) G.-Z. Wang, J.-E. Bäckvall, *J. Chem. Soc. Chem. Commun.* **1992**, 337–338; d) M. L. S. Almeida, M. Beller, G.-Z. Wang, J.-E. Bäckvall, *Chem. Eur. J.* **1996**, *2*, 1533–1536; e) M. L. S. Almeida, P. Kocovsky, J.-E. Bäckvall, *J. Org. Chem.* **1996**, *61*, 6587–6590; f) A. Aranyos, G. Csjernyik, K. J. Szabo, J.-E. Bäckvall, *Chem. Commun.* **1999**, 351–352; g) Y. R. S. Laxmi, J.-E. Bäckvall, *Chem. Commun.* **2000**, 611–612; h) O. Pàmies, J.-E. Bäckvall, *Chem. Eur. J.* **2001**, *7*, 5052–5058; i) J.-E- Bäckvall, *J. Organomet. Chem.* **2002**, *652*, 105–111; j) J. Takehara, S. Hashiguchi, A. Fujii, S.-I. Inoue, T. Ikariya, R. Noyori, *Chem. Commun.* **1996**, 223–224; k) J.-X. Gao, T. Ikariya, R. Noyori, *Organometallics* **1996**, *15*, 1087–1089; l) K.-J. Haack, S. Hashiguchi, A. Fujii, T. Ikariya, R. Noyori, *Angew. Chem. Int. Ed. Engl.* **1997**, *36*, 285–288; m) S. Hashiguchi, A. Fujii, K.-J. Haack, K. Matsumura, T. Ikariya, R. Noyori, *Angew. Chem. Int. Ed. Engl.* **1997**, *36*, 288–290; *Angew. Chem.* **1997**, *109*, 300–303; n) K. Matsumura, S. Hashiguchi, T. Ikariya, R. Noyori, *J. Am. Chem. Soc.* **1997**, *119*, 8738–8739; o) S.-I. Inoue, K. Nomura, H. Shohei, R. Noyori, Y. Izawa, *Chem. Lett.* **1997**, *26*, 957–958; p) R. Noyori, S. Hashiguchi, *Acc. Chem. Res.* **1997**, *30*, 97–102; q) K. Murata, T. Ikariya, R. Noyori, *J. Org. Chem.* **1999**, *64*, 2186–2187; r) K. Murata, K. Okano, M. Miyagi, H. Iwane, R. Noyori, T. Ikariya, *Org. Lett.* **1999**, *1*, 1119–1121; s) M. Yamakawa, H. Ito, R. Noyori, *J. Am. Chem. Soc.* **2000**, *122*, 1466–1487; t) R. Noyori, M. Yamakawa, S. Hashiguchi, *J. Org. Chem.* **2001**, *66*, 7931–7944; u) M. Yamakawa, I. Yamada, R. Noyori, *Angew. Chem. Int. Ed.* **2001**, *40*, 2818–2821; *Angew. Chem.* **2001**, *113*, 2900–2903; v) I. Yamada, R. Noyori, *Org. Lett.* **2000**, *2*, 3425–3427; w) A. Matsuoka, C. A. Sandoval, M. Uchiyama, R. Noyori, H. Naka, *Chem. Asian J.* **2015**, *10*, 112–115.

[3] T. Ohkuma, M. Koizumi, K. Muniz, G. Hilt, C. Kabuto, R. Noyori, *J. Am. Chem. Soc.* **2002**, *124*, 6508–6509.

[4] a) Z.-R. Dong, Y.-Y. Li, J.-S. Chen, B.-Z. Li, Y. Xing, J.-X. Gao, *Org. Lett.* **2005**, *7*, 1043–1045; b) Z. E. Clarke, P. T. Maragh, T. P. Dasgupta, D. G. Gusev, A. J. Lough, K. Abdur-Rashid, *Organometallics* **2006**, *25*, 4113–4117; c) R. Corberán, E. Peris, *Organometallics* **2008**, *27*, 1954–1958; d) M. Watanabe, Y. Kashiwame, S. Kuwata, T. Ikariya, *Eur. J. Inorg. Chem.* **2012**, 504–511.

[5] a) P. O. Lagaditis, A. J. Lough, R. H. Morris, *J. Am. Chem. Soc.* **2011**, *133*, 9662–9665; b) G. Wienhöfer, I. Sorribes, A. Boddien, F. Westerhaus, K. Junge, H. Junge, R. Llusar, M. Beller, *J. Am. Chem. Soc.* **2011**, *133*, 12875–12879.

[6] R. Castarlenas, M. A. Esteruelas, E. Onate, *Organometallics* **2008**, *27*, 3240–3247.

[7] a) M. C. Carrion, F. Sepulveda, F. A. Jalon, B. R. Manzano, *Organometallics* **2009**, *28*, 3822–3833; b) A. G. Elliott, A. G. Green, P. L. Diaconescu,

Dalton Trans. **2012**, *41*, 7852 – 7854; c) L.-P. Hea, T. Chena, D.-X. Xuea, M. Eddaoudia, K.-W. Huang, *J. Organomet. Chem.* **2012**, *700*, 202 – 206; d) J. DePasquale, M. Kumar, M. Zeller, E. T. Papish, *Organometallics* **2013**, *32*, 966 – 979; e) M. Kumar, J. DePasquale, N. J. White, M. Zeller, E. T. Papish, *Organometallics* **2012**, *32*, 2135 – 2144.

[8] a) E. C. Tyo, A. W. Castleman, Jr., D. Schröder, P. Milko, J. Roithova, J. M. Ortega, M. A. Cinellu, F. Cocco, G. Minghetti, *J. Am. Chem. Soc.* **2009**, *131*, 13009; b) G. Minghetti, S. Stoccoro, M. A. Cinellu, G. L. Petretto, A. Zucca, *Organometallics* **2008**, *27*, 3415.

[9] L. Taghizadeh Ghoochany, C. Kerner, S. Farsadpour, F. Menges, Y. Sun, G. Niedner-Schatteburg, W. R. Thiel, *Eur. J. Inorg. Chem.* **2013**, 4305 – 4317.

[10] C. Kerner, S.-D. Straub, Y. Sun, W. R. Thiel, *Eur. J. Org. Chem.* **2016**, 3060 – 3064.

[11] a) S. Farsadpour, L. Taghizadeh Ghoochany, Y. Sun, W. R. Thiel, *Eur. J. Inorg. Chem.* **2011**, 4603; b) S. Farsadpour, L. Taghizadeh Ghoochany, S. Shylesh, G. Dörr, A. Seifert, S. Ernst, W. R. Thiel, *ChemCatChem* **2012**, *4*, 401.

[12] a) W. R. Thiel, M. Angstl, T. Priermeier, *Chem. Ber.* **1994**, *127*, 2373 – 2377; b) A.-K. Pleier, H. Glas, M. Grosche, P. Sirsch, W. R. Thiel, *Synthesis* **2001**, 55 – 62; c) D. Zabel, A. Schubert, G. Wolmershäuser, R. L. Jones, Jr., W. R. Thiel, *Eur. J. Inorg. Chem.* **2008**, 3648 – 3654; d) H. Brunner, T. Scheck, *Chem. Ber.* **1992**, *125*, 701 – 709.

[13] a) D. A. Beauchamp, S. J. Loeb, *Chem. Commun.* **2002**, 2484 – 2485; b) E. Bejan, H. A. Haddou, J. C. Daran, G. G. A. Balavoine, *Synthesis* **1996**, 1012 – 1018; c) E. Ioachim, E. A. Medlycott, M. I. J. Polson, G. S. Hanan, *Eur. J. Org. Chem.* **2005**, 3775 – 3780.

[14] W. R. Browne, C. M. O'Connor, J. S. Killeen, A. L. Guckian, M. Burke, P. James, M. Burke, J. G. Vos, *Inorg. Chem.* **2002**, *41*, 4245 – 4251.

[15] L. Colina-Vegas, W. Villarreal, M. Navarro, C. Rodrigues de Oliveira, A. E. Graminha, P. I. da S. Maia, V. M. Deflon, A. G. Ferreira, M. R. Cominett, A. A. Batista, *J. Inorg. Biochem.* **2015**, *153*, 150 – 161.

[16] G. Minghetti, S. Stoccoro, M. A. Cinellu, G. L. Petretto, A. Zucca, *Organometallics* **2008**, *27*, 3415.

[17] a) V. Gabelica, E. De Pauw, *Mass Spectrom. Rev.* **2005**, *24*, 566; b) E.-L. Zins, C. Pepe, D. Rondeau, S. Rochut, N. Galland, J.-C. Tabet, *J. Mass Spectrom.* **2009**, *44*, 12; c) E.-L. Zins, D. Rondeau, P. Karoyan, C. Fosse, S. Rochut, C. Pepe, *J. Mass Spectrom.* **2009**, *44*, 1668; d) E.-L. Zins, C. Pepe, D. Schröder, *J. Mass Spectrom.* **2010**, *45*, 1253; e) K. V. Barylyuk, K. Chingin, R. M. Balabin, R. Zenobi, *J. Am. Soc. Mass Spectrom.* **2010**, *21*, 172; f) C. Collette, E. De Pauw, *Rapid Commun. Mass Spectrom.* **1998**, *12*, 165 – 170; g) L. Drahos, R. M. Heeren, C. Collette, E. De Pauw, K. Ve 'key, *J. Mass Spectrom.* **1999**, *34*, 1673 – 1678.

[18] G. A. Olah, *Acc. Chem. Res.* **1971**, *4*, 240 – 248.

[19] S. Hohloch, L. Suntrup, B. Sarkar, *Organometallics* **2013**, *32*, 7376 – 7385.

[20] M. A. Bennett, A. K. Smith, *J. Chem. Soc. Dalton Trans.* **1974**, 233 – 241.

[21] Gaussian 03, Revision E.01, M. J. Frisch, G. W. Trucks, H. B. Schlegel, G. E. Scuseria, M. A. Robb, J. R. Cheeseman, J. A. Montgomery, Jr., T. Vreven, K. N. Kudin, J. C. Burant, J. M. Millam, S. S. Iyengar, J. Tomasi, V. Barone, B. Mennucci, M. Cossi, G. Scalmani, N. Rega, G. A. Petersson, H. Nakatsuji, M. Hada, M. Ehara, K. Toyota, R. Fukuda, J. Hasegawa, M. Ishida, T. Nakajima, Y. Honda, O. Kitao, H. Nakai, M. Klene, X. Li, J. E. Knox, H. P. Hratchian, J. B. Cross, V. Bakken, C. Adamo, J. Jaramillo, R. Gomperts, R. E. Stratmann, O. Yazyev, A. J. Austin, R. Cammi, C. Pomelli, J. W. Ochterski, P. Y. Ayala, K. Morokuma, G. A. Voth, P. Salvador, J. J. Dannenberg, V. G. Zakrzewski, S. Dapprich, A. D. Daniels, M. C. Strain, O. Farkas, D. K. Malick, A. D. Rabuck, K. Raghavachari, J. B. Foresman, J. V. Ortiz, Q. Cui, A. G. Baboul, S. Clifford, J. Cioslowski, B. B. Stefanov, G. Liu, A. Liashenko, P. Piskorz, I. Komaromi, R. L. Martin, D. J. Fox, T. Keith, M. A. Al-Laham, C. Y. Peng, A. Nanayakkara, M. Challacombe, P. M. W. Gill, B. Johnson, W. Chen, M. W. Wong, C. Gonzalez, J. A. Pople, Gaussian, Inc., Wallingford CT, **2004**.

[22] a) C. Lee, W. Yang, R. G. Parr, *Phys. Rev. B* **1988**, *37*, 785; b) A. D. Becke, *Phys. Rev. A* **1988**, *38*, 3098; c) B. Miehlich, A. Savin, H. Stoll, H. Preuss, *Chem. Phys. Lett.* **1989**, *157*, 200; d) P. C. Hariharan, J. A. Pople, *Theor. Chim. Acta* **1973**, *28*, 213; e) D. Andrae, U. Haeussermann, M. Dolg, H. Stoll, H. Preuss, *Theor. Chem. Acc.* **1990**, *77*, 123.

[23] G. M. Sheldrick, *Acta Crystallogr. Sect. A* **2008**, *64*, 112.

[24] A. Altomare, G. Cascarano, C. Giacovazzo, A. Guagliardi, M. C. Burla, G. Polidori, M. Camalli, *J. Appl. Crystallogr.* **1994**, *27*, 435.

[25] CrysAlisPro, Agilent Technologies, Version 1.171.33.66, **2010**, Version 1.171.36.32, **2013** and Version 1.171.37.35, **2014**.

Manuscript received: October 25, 2016
Final Article published: November 22, 2016

11.3 Multistate-Mediated Rearrangements and $FeCl_2$ Elimination in Dinuclear FePd Complexes

Maximillian Gaffga, Isabel Munstein, Patrick Müller, Johannes Lang,
Werner R. Thiel and Gereon Niedner-Schatteburg

Fachbereich Chemie and Forschungszentrum OPTIMAS,
Technische Universität Kaiserslautern
67663 Kaiserslautern, Germany

11.3.1 Preamble

The following chapter is a reprint of a publication in the "Journal of Physical Chemistry A".

I. Munstein from the research group of W. R. Thiel synthesized the FePd complexes. M. Gaffga and I conducted and evaluated mass spectrometry and Collision Induced Dissociation (CID) experiments. M. Gaffga measured and evaluated InfraRed Multiple Photon Dissociation Spectra (IR-MPD) as well as calculated linear absorption spectra. He was supported by P. Müller. M. Gaffga and G. Niedner-Schatteburg prepared the manuscripts and with the help of W. R. Thiel and myself.

<u>Full Reference:</u>

Multistate-Mediated Rearrangements and $FeCl_2$ Elimination in Dinuclear FePd Complexes
M. Gaffga, I. Munstein, P. Müller, **J. Lang**, W. R. Thiel and G. Niedner-Schatteburg, The Journal of Physical Chemistry A 2015, 119, 12587-12598.
http://dx.doi.org/10.1021/acs.jpca.5b06952

11.3.2 Reprint

Reprint Licence:

Copyright Clearance Center RightsLink®

Home | Account Info | Help

ACS Publications
Most Trusted. Most Cited. Most Read.

Title: Multistate-Mediated Rearrangements and FeCl2 Elimination in Dinuclear FePd Complexes

Author: Maximilian Gaffga, Isabel Munstein, Patrick Müller, et al

Publication: The Journal of Physical Chemistry A

Publisher: American Chemical Society

Date: Dec 1, 2015

Logged in as:
Johannes Lang
Account #:
3001122418
LOGOUT

PERMISSION/LICENSE IS GRANTED FOR YOUR ORDER AT NO CHARGE

This type of permission/license, instead of the standard Terms & Conditions, is sent to you because no fee is being charged for your order. Please note the following:

- Permission is granted for your request in both print and electronic formats, and translations.
- If figures and/or tables were requested, they may be adapted or used in part.
- Please print this page for your records and send a copy of it to your publisher/graduate school.
- Appropriate credit for the requested material should be given as follows: "Reprinted (adapted) with permission from (COMPLETE REFERENCE CITATION). Copyright (YEAR) American Chemical Society." Insert appropriate information in place of the capitalized words.
- One-time permission is granted only for the use specified in your request. No additional uses are granted (such as derivative works or other editions). For any other uses, please submit a new request.

THE JOURNAL OF PHYSICAL CHEMISTRY A

Article

pubs.acs.org/JPCA

Multistate-Mediated Rearrangements and $FeCl_2$ Elimination in Dinuclear FePd Complexes

Maximilian Gaffga, Isabel Munstein, Patrick Müller, Johannes Lang, Werner R. Thiel, and Gereon Niedner-Schatteburg*

Fachbereich Chemie und Forschungszentrum OPTIMAS, Technische Universität Kaiserslautern, 67663 Kaiserslautern, Germany

Supporting Information

ABSTRACT: Mass spectrometric, spectroscopic, and computational characterization of a novel bifunctional iron−palladium complex proves a change of coordination upon solvation. Collisional excitation reveals $FeCl_2$ and HCl elimination in a solvent-modulated competition. Hereby, *syn* and *anti* isomers, identified by theoretical calculations, favor and disfavor $FeCl_2$ elimination, respectively. The $FeCl_2$ elimination likely proceeds by chlorido and Cp ligand exchange among the metallic centers in a concerted, ballet-like manner. A multitude of stationary points were identified along the computed multistep reaction coordinates of the three conceivable spin states. The quintet state shows a static Jahn−Teller type relaxation by a tilt away of the Cp ligand at the iron center. The direct singlet−quintet spin crossover is an unprecedented assumption, leaving behind the triplet state as a spectator without involvement. The $FeCl_2$ elimination would decrease catalytic activity. It is kinetically hindered within a range of applicable temperatures in conceivable technical applications.

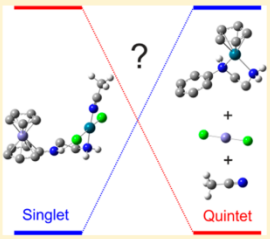

1. INTRODUCTION

The ability of transition metal complexes to catalytically activate different bonds (e.g., C−H or C−C) has made them indispensable tools in modern synthesis.[1−3] Due to a profound mechanistic basis that had been established for homogeneous transformations during the last decades, the selection of the right element for a certain catalytic reaction became obvious. In contrast, the selection of the right ligand system is a much less knowledge-based process, because the details of the electronic and steric cooperation of the ligand and the metal site are still not completely understood. Therefore, it is an important issue to develop novel ligand structures and to investigate their interactions with catalytically active metal sites.

The nature of the donor site (electronic impact), the substituents at the donor site (steric impact), and the structure of the ligand backbone (chelating ligands, stereochemistry) are the essential issues for ligand design. In this context, organometallic complexes being part of the ligand system itself have turned out to be versatile structural motifs to achieve ligand properties that cannot be realized by purely organic structures at all. Generally, 18 stable valence electron complexes are used for this purpose because they are able to survive the conditions of catalytic reactions. The most frequently found organometallic structures in such systems are based on ferrocene.[4,5] Ferrocene is a stable, quite inexpensive compound for which a multitude of transformations have been established since its discovery in 1951.[6−8] This allows the introduction of multiple donor sites on each of the cyclopentadienide (Cp) rings. On the other hand, ferrocenes allows switching the activity of the catalytic site by oxidation of the iron(II) center to iron(III) (ferrocinium).[9−14] Substitution in the 1- and 1′-position leads to chelating ligands with the ferrocene motif in the rear of the metal site, which on one hand results in special bite angles due to the fixed Cp−Cp distance. 1,1′-Bisdiphenylphosphinoferrocene, which is often used for C−C-coupling reactions, is the paradigm for such a type of ligand.[4,15,16] In contrast, functionalization of the same Cp ring in the 1- and 2-position with two different substituents results in ferrocenes possessing planar chirality, which have many applications in stereoselective catalysis.[17−25]

Formal substitution of one of the ferrocene Cp anions by a neutral six-membered arene ring results in $[\eta^5\text{-CpFe}(\eta^6\text{-arene})]^+$ complexes being isoelectronic to ferrocene but carrying a positive charge. The first member of this family had been discovered shortly after the invention of ferrocene.[26,27] Although the Cp rings of ferrocene are electron-rich, the arene motif in $[\eta^5\text{-CpFe}(\eta^6\text{-arene})]^+$ becomes electron poor. This allows a further functionalization of the arene ring by simple nucleophilic aromatic substitution reactions as long as a chloro arene ring is coordinated to iron. $[\eta^5\text{-CpFe}(\eta^6\text{-}C_6H_5Cl)]^+$ and *ortho*-, *meta*-, *para*-substituted $[\eta^5\text{-CpFe}(\eta^6\text{-}C_6H_4Cl_2)]^+$ are accessible from ferrocene by $AlCl_3$-promoted reactions with the corresponding chloro benzene derivative in reasonable yields.[28] Although many compounds have been generated from these precursors by S_NAr reactions,[29−33] to the best of our knowledge, no ligand with a $[\eta^5\text{-CpFe}(\eta^6\text{-arene})]^+$ motif linked to a donor site has been described up to now.

We considered it necessary to strive for the synthesis of such a compound, and we concluded to characterize it by classical tools of molecular chemistry and by advanced techniques of

Received: July 17, 2015
Revised: November 23, 2015
Published: November 23, 2015

DOI: 10.1021/acs.jpca.5b06952
J. Phys. Chem. A 2015, 119, 12587−12598

physical chemistry alike. Such a combined approach allows for elucidation of otherwise inaccessible molecular phenomena: Spin state changes of the transition metal centers likely modulates the product formation along reaction pathways (e.g., of dissociation). Such effects are know as a multistate reactivity scenario, which has been illustrated by numerous studies of various compounds before.[34]

Here, we report the synthesis of the chelating ligand $[\eta^5\text{-CpFe}(\eta^6\text{-C}_6\text{H}_5\text{NH}(\text{CH}_2)_2\text{NH}_2)]^+$ (**1**), its coordination to $PdCl_2$ and a series of dynamic, spectroscopic and computational studies on the activation of the CpFe bond of this compound. An important issue of this structure is the poorly-donating, arene-bound nitrogen donor, making this compound a novel type of a so-called hemilabile ligand, which easily opens up a coordination site at a (catalytically active) metal center. This special property is due to the delocalization of the free electron pair at the nitrogen atom into the arene ring being described by a second mesomeric structure including a pentadienide ligand and an exocyclic iminium cation (Scheme 1). The charge distribution of this second mesomeric form makes the generation of an imine donor by splitting of a proton feasible.

Scheme 1. Charge Distribution in the Cation 1^+

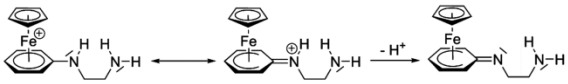

Our dynamic and spectroscopic characterization arose through infrared multiphoton dissociation (IR-MPD) spectroscopy[35,36] or collision-induced dissociation (CID) experiments[37,38] of the mass-selected ions in order to elucidate the interaction between ligand and metal center, both in conjunction with high level density functional theory (DFT) structure computations. The coupling of these methods provides powerful tools to investigate chemical structures in the gas phase and indirectly allows obtaining infrared spectra of selected ions by fragmentation. In combination with theoretical DFT calculations, it is perfectly suitable to characterize the chemical structure of transition metal−ligand complexes in the gas phase.[39−42]

2. EXPERIMENTAL AND THEORETICAL METHODS

2.1. Synthesis of Compounds 1 and 2. We performed the synthesis of (η^6-*N*-(2-aminoethyl)aniline)(η^5-cyclopentadienide)iron(II) hexafluorophosphate (**1**) as follows: 0.30 g (0.34 mL, 5.0 mmol) of freshly distilled ethylenediamine were added dropwise to a solution of 378 mg (1.0 mmol) (η^6-chlorobenzene)(η^5-cyclopentadienide)iron(II) hexafluorophosphate[28] dissolved in 20 mL of dichloromethane. The reaction mixture was stirred for 30 min at room temp. Two milliliters of a saturated aqueous solution of ammonium hexafluorophosphate was added, and the mixture was stirred for 5 min. The organic phase was washed first with 5 mL of an aqueous solution of K_2CO_3 and then twice with 5 mL of water and subsequently dried over $MgSO_4$. Removing the solvent under vacuum resulted in 360 mg (90%) of **1** as an orange-red solid. For the further characterization of **1** see the Supporting Information (Texts T1 and T2, and Scheme S1).

We performed the synthesis of [(η^6-*N*-2-(aminoethyl)-aniline)(η^5-cyclopentadienide) iron(II)]dichloridopalladium(II)hexafluorophosphate (**2**) as follows: A solution of 201 mg (0.5 mmol) of **1** in 20 mL of dichloromethane was added dropwise to a solution of 194 mg of di(benzonitrile)palladium(II) chloride (0.50 mmol) in 10 mL of dichloromethane. The reaction mixture was stirred for 16 h at room temperature. The precipitated solid was filtered off, washed with 2 mL of dichloromethane, and dried under vacuum to yield 254 mg (88%) of **2** as an ochre solid. For the further characterization of **2**, see the Supporting Information (Text T2).

2.2. Experimental Methods. Electrospray ionization mass spectra (ESI-MS) were recorded with two ion trap instruments (Bruker Esquire 6000 for CID and Bruker amaZonSL for IR-MPD measurements). The scan speed was 13 000 m/z/s in normal resolution scan mode (0.3 fwhm/m/z); the scan range was at least 70 to 1500 m/z. The sample solutions of complex **2** in CH_3CN (a), CH_3CN:DMF 9:1 (b), and CH_3CN:DMSO 9:1 (c) at concentrations of approximately 1×10^{-4} M were continuously infused into the ESI chamber at a flow rate of 2 μL/min by a syringe pump. We use nitrogen as a drying gas at a flow rate of 3.0 to 4.0 L/min at 220 °C up to 300 °C and sprayed the solutions at a nebulizer pressure of 3 to 4 psi with the electrospray needle held at 4.5 kV. We held constant the transfer parameters to the Paul trap of the mass spectrometer, and we used helium as the buffer gas with a partial pressure of about 3×10^{-3} mbar inside the ion trap. BrukerEsquireControl 5.3 (Esquire) and BrukerTrapControl 7.0 (amaZonSL) software controlled the instrument, and we carried out the data analysis using the Data Analysis 4.0 software.

Collision-induced dissociation (CID) appearance curves were recorded with varying excitation magnitude from 0.0 to 1.5. Note that the well-defined excitation amplitudes lead to *a priori* unknown exitation energies of the stored ions. The corresponding scaling factor varies by the very nature of the stored ions, and it is subject of ongoing investigations.[37] In the present case, we utilize a relative energy scale in the lab frame ($E_{\text{lab}}^{\text{rel}}$) in arbitrary units. These excitation energies were increased in a stepwise fashion until complete dissociation of the ion of interest was observed. Normalized relative and total fragmentation yields were calculated according to the following equations:

$$I_{\text{i,norm}}^{\text{fr}}(E_{\text{lab}}^{\text{rel}}) = \frac{I_{\text{i}}^{\text{fr}}(E_{\text{lab}}^{\text{rel}})}{\sum_{\text{i}} I_{\text{i}}^{\text{fr}}(E_{\text{lab}}^{\text{rel}}) + \sum_{\text{i}} I_{\text{i}}^{\text{p}}(E_{\text{lab}}^{\text{rel}})} \tag{1a}$$

$$I_{\text{tot}}^{\text{fr}}(E_{\text{lab}}^{\text{rel}}) = \sum_{\text{i}} I_{\text{i,norm}}^{\text{fr}}(E_{\text{lab}}^{\text{rel}}) \tag{1b}$$

We calculated center of mass transformed relative excitation energies ($E_{\text{COM}}^{\text{rel}}$) by

$$E_{\text{COM}}^{\text{rel}} = \frac{m_{\text{He}}}{m_{\text{He}} + m_{\text{ion}}} \cdot E_{\text{LAB}}^{\text{rel}} \tag{2}$$

where m_{ion} indicates the isotopically averaged mass of the molecular cation under investigation.

A KTP/KTA optical parametric oscillator/amplifier (OPO/OPA, LaserVision) system pumped with a pulsed 10 Hz injection seeded Nd^{3+}:YAG laser (PL8000, Continuum) was used as a source of tunable IR radiation ($\delta\bar{\nu}$ = 0.9 cm^{-1}, δt = 7 ns) for recording the vibrational spectra. Spectra within the frequency range of 2600−3700 cm^{-1} were recorded by application of the OPA idler wave (≤10 mJ per pulse). Spectra within the range of 1200−2100 cm^{-1} were recorded by difference frequency mixing (DFM) in a $AgGaSe_2$ crystal of the OPA signal and idler waves (≤2 mJ per pulse). The idler beam

DOI: 10.1021/acs.jpca.5b06952
J. Phys. Chem. A 2015, 119, 12587−12598

Scheme 2. Synthesis of Compounds 1 and 2

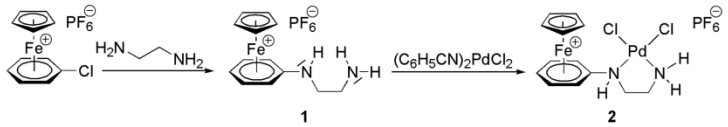

was focused by a 50 cm CaF_2 lens. The DF radiation was focused tighter, by a 90° off-axis parabolic silver mirror with an effective focal length of 15 cm. The IR pulse energy was recorded by a power meter sensor that obtained the applied photon beam after exiting the ions inside the mass spectrometer through a second window. From the recorded fragment and parent ion intensities, we determine an IR-MPD yield (Y) as

$$Y = \frac{\sum_i I_i^{fr}}{\sum_i I_i^{fr} + \sum_i I_i^{p}} \quad (3)$$

The applied IR frequencies were calibrated by a wave meter (Bristol Instruments: 821 Pulsed Laser Wavelength Meter) to a theoretical accuracy of ±0.02 cm^{-1}, which is beyond the spectral bandwidth of the utilized IR photon beams by more than an order of magnitude. Note that IR-MPD yields scale in an intrinsically nonlinear way with the applied IR photon flux.[35,43−46] Therefore, we refrained from any normalization.

2.3. Theoretical Methods. We conducted electronic structure calculations at the B3LYP[47−50] /cc-pVDZ[51−53] level of theory with the Stuttgart RSC 1997[54,55] effective core potential representing the iron and palladium atoms as implemented in the Gaussian 09 program package.[56] We searched for fully optimized molecular structures of the most stable isomers as a function of multiplicities, for linear IR absorption spectra, and for stable points and transition states along the reaction path for the $FeCl_2$ elimination in the case of **3a**. Standard convergence criteria were applied. Harmonic vibrational frequencies were scaled by a linear lump sum scaling factor of 0.97 as suggested elsewhere.[57]

3. RESULTS AND DISCUSSION

3.1. Characterization of Compounds 1, 2, and 3. Reacting $[(\eta^5\text{-Cp})Fe(\eta^6\text{-}C_6H_5Cl)]PF_6$, which was synthesized according to a published procedure, with an excess of ethylene diamine resulted in the formation of the cationic N,N'-ligand **1** in 90% yield (Scheme 2). The NMR spectra of compound **1** clearly prove the expected structure: besides the resonances of the Cp ligand (^{1}H NMR: 4.85; ^{13}C NMR: 76.7 ppm), there are three resonances in the ^{1}H NMR (6.12, 5.99, 5.80 ppm) as well as four in the ^{13}C NMR (127.7, 87.1, 81.8, 69.2 ppm) spectrum, all of them shifted to higher field compared to the precursor $[(\eta^5\text{-Cp})Fe(\eta^6\text{-}C_6H_5Cl)]PF_6$ that can be assigned to the η^6-coordinating aniline derivative. More important, there are the resonances of the ethylene linker (^{1}H NMR: 3.19, 2.90; ^{13}C NMR: 47.0, 41.7 ppm) and the ^{1}H NMR signals of the two amine units, one at low field (NH: 5.29), the other in the high field region (NH_2: 1.92 ppm), according to the different hybridization of the two amines.

In the FT-IR-ATR spectrum of the solid compound **1**, there are three well-separated absorptions at 3392 (NH), 3222 (asym. NH_2), and 3120 cm^{-1} (sym. NH_2), respectively, that can be assigned to the amino functions of the molecule. The strongest peak in the ESI mass spectrum confirms the mass of the cation $[C_{13}H_{17}FeN_2]^+$ (m/z = 256.8).

Compound **1** is well soluble in polar organic solvents, allowing to apply it as an N,N'-chelating ligand to coordinate to transition metal sites. As a model type substrate we used dibenzonitrile palladium(II) dichloride that delivers a $PdCl_2$ fragment by cleavage of the labile benzonitrile ligands (Scheme 2). The heterobimetallic compound **2** is thus formed in almost 90% yields. Although the $[CpFe(arene)]^+$ moiety is not very much influenced by the N,N'-donation, there are pronounced changes in the NMR spectra of the ligand backbone: the ^{1}H NMR resonances assigned to this part of the molecule are generally shifted to lower field. This effect is most pronounced for the $NHCH_2$ protons and the NH_2 function. The multitiplicity of the NH_2CH_2 pattern (**2**: virtual quintet) increases with respect to the precursor **1** (triplet) indicating a decrease of fluxonality at that site of the molecule. The ^{13}C NMR resonances of the ethylene chain are both observed at approximately 44.5 ppm. These data clearly prove a stable coordination of both nitrogen atoms of the ethylenediamine chain to the palladium(II) center in acetonitrile solution.

This situation changes under the conditions of ESI mass spectrometry: here the solvated cations $[(\eta^5\text{-Cp})Fe(\eta^6\text{-}C_6H_5NHCH_2CH_2NH_2\text{–}PdCl_2\text{-L})]^+$ (**3a–3c**; **3a**: L = MeCN, **3b**: L = $HC(O)NMe_2$, **3c**: Me_2SO) are observed to a small extent. We then assign structures as shown in Scheme 3 with the terminal NH_2 group staying coordinated to the palladium(II) site.

Scheme 3. Molecular Structure of the Iron Palladium Complex 2 and of Observed Microsolvation Species 3a–3c Together with Solvent Species X=CH_3CN (a), DMF (b), and DMSO (c)[a]

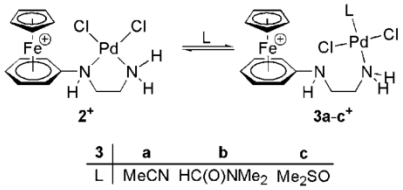

[a]Note the change of palladium coordination sphere upon solvation: The diamine Pd coordination changes from η^2 to η^1.

3.2. Collision-Induced Dissociation (CID) Studies. We have recorded fragmentation yields of mass-selected parent ions **2** and **3a–3c** by gradually increasing the activation magnitude up to complete depletion of the parent ions (Figure 1).

The thus-obtained energy-dependent fragmentation yields (formerly known as breakdown curves) reveal varying intensities of up to six fragment ions. The solvent-free complex **2** surprisingly expels $FeCl_2$ with large preference at any level of excitation (green diamonds). Note that an elimination of the cyclopentadienyl anion (Cp) moiety from Pd or the elimination of CpH was not observed at all. It is well-known, and we have

DOI: 10.1021/acs.jpca.5b06952
J. Phys. Chem. A 2015, 119, 12587−12598

The Journal of Physical Chemistry A Article

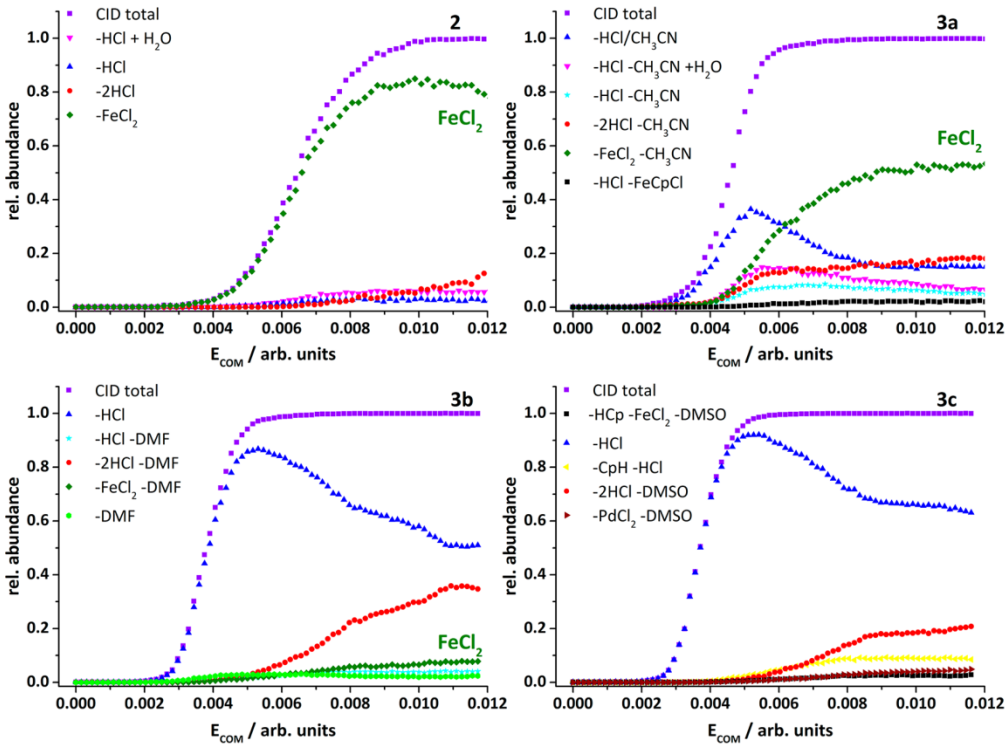

Figure 1. Normalized CID fragment yields of the complex **2** and of observed microsolvation species **3a**–**3c** as a function of relative excitation energy E_{com}. Note the solvent-dependent change in intensity of the $FeCl_2$ elimination channel. A semilog plot of the same data is available as Figure S1 in the Supporting Information.

Table 1. Observed Fragmentation Channels of Complexes 2 and 3a–3c[a]

complex	neutral loss					
2	**-$FeCl_2$**	-2HCl	-HCl + H_2O	-HCl		
3a	**-$FeCl_2$ -CH_3CN**	-2HCl -CH_3CN	-HCl/CH_3CN	-HCl -CH_3CN + H_2O	-HCl -CH_3CN	-HCl -FeCpCl
3b	**-HCl**	-2HCl -DMF	-$FeCl_2$ -DMF	-HCl -DMF	-DMF	
3c	**-HCl**	-2HCl -DMSO	-CpH -HCl	-$PdCl_2$ -DMSO	-HCp -$FeCl_2$ -DMSO	

[a]They are listed in their relative order of appearance. Dominating channels are highlighted in bold.

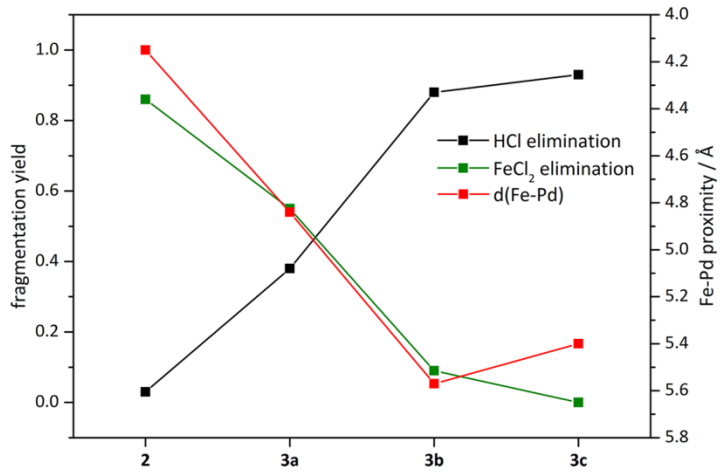

Figure 2. Maximum observed yields of the $FeCl_2$ (green) and of the HCl (black) fragmentation channels for the complex **2** and for the observed microsolvation species **3a**–**3c**. Note that the binding energy of the solvents CH_3CN, DMF, DMSO to **2** in **3a**, **3b**, **3c** increases from left to right.

DOI: 10.1021/acs.jpca.5b06952
J. Phys. Chem. A 2015, 119, 12587–12598

confirmed by swift DFT calculations, that the $FeCl_2$ formation exceeds that of $PdCl_2$ by 319 kJ/mol. Therefore, an exoergic $FeCl_2$ formation thus provides for a strong thermodynamic driving force for this fragmentation (Table S1).

The situation changes as soon as strongly coordinating solvents came into play. The CH_3CN-coordinated complex **3a** behaves differently at low excitation energies (Figure 1). The dominant fragmentation channel at low excitation energies is the elimination of either HCl and/or CH_3CN (blue triangles), which gives rise to overlapping isotopic patterns that cannot be separated unambiguously. Upon increasing the excitation energy, another fragmentation channel becomes dominant, which is the concerted elimination of $FeCl_2$ and CH_3CN (green diamonds). Note that once more the elimination of CpH is not observed. The dominant fragmentation channel of the DMF- and DMSO-coordinated complexes **3b** and **3c** is the elimination of HCl. It rises at the expense of $FeCl_2$ elimination, which diminishes in the case of **3b** and vanishes in the case of **3c**. Note that HCl elimination from **3b** and **3c** occurs without loss of solvent (DMF and DMSO, respectively). HCl elimination is weak in the cases of the complex **2** or of the CH_3CN-coordinated complex **3a**. Some further fragmentation channels are minor (Table 1).

Nevertheless it is highly unexpected to observe a likely loss of $FeCl_2$ from complexes that comprise joint units of an 18 VE FeCp(arene) fragment and a 16 VE $(N)_2PdCl_2$ moiety instead of simply expelling HCl, CpH, or $PdCl_2$. This is more so as the Cp anion remains in the complexes upon $FeCl_2$ elimination. Such an observation indicates the occurrence of an activated concerted rearrangement prior to dissociation, which may be followed conveniently these days through appropriate calculations (cf. section 3.4 in the following text).

HCl elimination and $FeCl_2$ elimination seem to compete. The competition is confirmed by the visualization of the maximum fragmentation yields in **2** and **3a**−**3c** (Figure 2). Coordination of a solvent molecule inhibits the $FeCl_2$ elimination and favors HCl elimination. Obviously the donor strength of the solvent allows tuning the fragmentation channels: the better donating the solvent, the less pronounced is the splitting of $FeCl_2$ and the more dominant becomes splitting of HCl. The latter effect can easily be explained by the transfer of electron density from the solvent molecule to the Pd site, making the Pd−Cl bond to become weaker and thus the chlorido ligand more basic, which allows the deprotonation of one of the amine sites leaving an amido ligand coordinated to Pd. The concomitant structural relaxation will be elucidated in conjunction with the discussion of IR-MPD spectra (cf. section 3.3 in the following text). Here we inspect the obtained Fe−Pd proximities and find close correlation with $FeCl_2$ yields (cf. Figure 2). An increase in solvation energy seems to hinder $FeCl_2$ elimination in favor of HCl elimination (cf. Table 2). Note that the competing fragmentation channel (HCl elimination) operates without the necessity of prior solvent detachment. In effect, the very nature of the attached solvent modulates the branching ratio of the competing $FeCl_2$ and HCl eliminations.

Table 2. Calculated Binding Energies of Attached Solvent Molecules in Complexes 3a, 3b, and 3c

complex	solvent molecule	binding energy/kJ/mol
3a	CH_3CN	143
3b	DMF	165
3c	DMSO	198

In IR-MPD experiments (discussed in the following chapter), the applied IR photonic excitation leads to fragment patterns that are similar to those of CID experiments, as e.g. in prior studies of other compounds by our group.[58] In the present case of **3a**, **3b**, **3c**, an IR photonic excitation preferentially yield fragment patterns that are similar to CIR patterns at about E^{rel}_{COM} = 0.01a.u. If we would apply previous scaling factors as obtained by prior work on so-called thermometer ions,[59] we would correlate this relative excitation energy E^{rel}_{COM} to an absolute value of $E_{COM} \approx 80$ kJ/mol. Cross check with the known solvent binding energies (Table 2) reveals that such value of fragmentation threshold would be to small by about a factor of 2. Recent work rationalized system-size-dependent correction factors for the ion number of degrees of freedom.[60] It is thus likely that similar correction would apply in our present case as well. We refrain, however, from dwelling on this issue further at the present stage.

3.3. IR-MPD Studies and Concomitant DFT Calculations. The IR-MPD spectrum of the complex **2** (Figure 3)

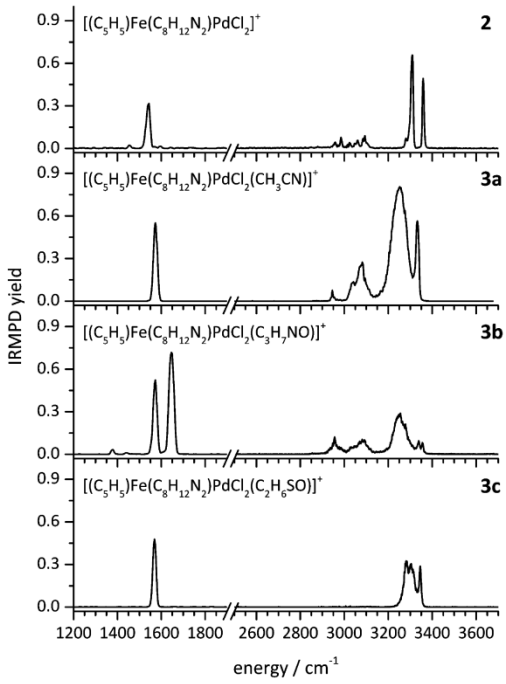

Figure 3. IR-MPD spectra of the complex **2** and of the observed microsolvation species **3a**−**3c**. Note the solvent specific broadening and enhancement of NH_2 vibrations due to NH−Cl hydrogen bonding (see text).

exhibits three bands in the region of 3380 to 3260 cm^{-1} and several weak bands between 3230 and 2920 cm^{-1}. In the fingerprint range, there is a single strong absorption at 1540 cm^{-1}. One would expect to see IR active C=C ring modes in the fingerprint range around 1500 cm^{-1}, weak aliphatic and aromatic CH stretching modes around 2920 and 3230 cm^{-1}, and NH and NH_2 strecthing vibrations around 3350 cm^{-1}. These expectations are nicely matched by the recorded observations.

DOI: 10.1021/acs.jpca.5b06952
J. Phys. Chem. A 2015, 119, 12587−12598

The IR-MPD spectrum of the CH_3CN-coordinated complex **3a** reveals a major spectral change from the complex **2**. There is a significant shift, enhancement, and broadening of NH stretching bands around 3250 cm^{-1}. There is also some enhancement and broadening in the CH stretching region. There is a sharp band at 1570 cm^{-1} in **3a**, which is blue-shifted from **2** by 30 cm^{-1}.

The IR-MPD spectrum of the DMF-coordinated complex **3b** looks much like **3a**; somewhat weaker intense in the stretching region. There is an additional band at 1650 cm^{-1}, and weak bands at 1440 and 1375 cm^{-1} originate from the CO chromophore in DMF.

The DMSO-coordinated complex **3c** exhibits no recordable signal from CH stretching modes. The NH streching modes are weaker than for **3b**. There is one broad centered at 3295 cm^{-1} and one sharp band at 3350 cm^{-1}. The single band in the fingerprint region coincident with the blueshifted bands of **3a** and **3b**. Thus, all three solvent-coordinated complexes **3a**−**3c** share some kind of electronic rearrangement that leads to a strong IR active band around 1565 cm^{-1}. It locates 30 cm^{-1} to the blue of a somewhat less strong band at 1540 cm^{-1} in the complex **2** which seems to resemble an arylic C═C stretching mode. It remains open, whether the **3a**−**3c** bands and the **2** band originate from the same type of vibration.

For further elucidation we computed energetics and geometries of likely structures of complexes **2**, **3a**−**3c** by DFT at given level of theory (cf. Theoretical Methods). Alternate structures that would involve a direct Fe−Cl coordination are less stable (by more than 120 kJ/mol) and of no relevance. We apply a Newman projection for classification and visualization of computed rotamers (see insets to Figure 4).Other than e.g. in alkane stereochemistry,

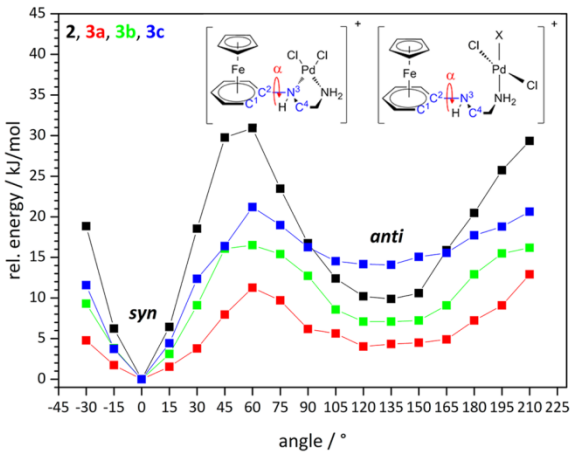

Figure 4. Computed relative energies of rotational conformers of the complexes **2**, **3a**−**3c** by variation of the dihedral angle $\alpha(C^1C^2N^3C^4)$.

the present complexes consist of two subunits of C_2 and C_3 symmetry each. We adopt a *syn* and *anti* nomenclature for the 0° and 120° rotamers of the dihedral angle α (between $C^1C^2N^3C^4$) in the cases of all complexes **2**, **3a**−**3c**. For further characterization, we varied this dihedral angle, and we performed full structural relaxation at fixed dihedral angles in steps of 15° in order to obtain optimized geometries and their relative energies (Figure 4). All complexes reveal a total and a local minimum at 0° (*syn*) and 120° (*anti*). Complex **2** shows the highest rotational barrier, which might be due to the close proximity of the Fe and Pd bearing sub units within the complex. The solvent-molecule-attached complexes **3a**−**3c** exhibit smaller barriers, which might be due to the increased distance between the subunits. The rotational barrier in complex **3a** is low (10 kJ/mol), while the barriers of the complexes **3b** and **3c** are higher, 15 and 20 kJ/mol. We will show in the following that the $FeCl_2$ elimination likely takes place from the *syn* isomer (see section 3.4).

It seems conceivable that NH−Cl- or NH_2−Cl-coordinated PdCl structures of **3a**, **3b**, **3c**, might prevail, in principle. We undertook a systematic survey for those (documented in Figures S19−S31 of the Supporting Information). It turned out that none of these optimized geometries is more stable than the previously assumed ground state structures $PdCl_2$ $^1\mathbf{3a}_{syn}$, $^1\mathbf{3b}_{syn}$, and $^1\mathbf{3c}_{syn}$, their assignment being confirmed.

We did find some NH−Cl−HN-coordinated singlet structures only in *anti* conformation. These $^1\mathbf{3a}_{anti}^{(NH\text{-}Cl)}$, $^1\mathbf{3b}_{anti}^{(NH\text{-}Cl)}$, and $^1\mathbf{3c}_{anti}^{(NH\text{-}Cl)}$ (Figures S19, S20, and S21) are as low as only 14, 10, and 14 kJ/mol above $^1\mathbf{3a}_{syn}$, $^1\mathbf{3b}_{syn}$, and $^1\mathbf{3c}_{syn}$. This makes them likely precursors for HCl elimination and maybe even for the double elimination. In any case, they are well-separated from the *syn* $PdCl_2$ structures by rotational barriers (cf. Figure 4) and by considerable activation barriers from the *anti* $PdCl_2$ species, as verified by some preliminary calculations (roughly 40−80 kJ/mol in case of **3a**). Note, moreover, that the assumed NH−Cl−HN-coordinated PdCl $^1\mathbf{3a}_{syn}^{(NH\text{-}Cl)}$, $^1\mathbf{3b}_{syn}^{(NH\text{-}Cl)}$, and $^1\mathbf{3c}_{syn}^{(NH\text{-}Cl)}$ structures do relax barrierless toward $PdCl_2$ $^1\mathbf{3a}_{syn}$, $^1\mathbf{3b}_{syn}$, and $^1\mathbf{3c}_{syn}$ (cf. Figures S22 and S23, verified for the cases of DMSO and DMF solvents). The relative population of *syn* to *anti* isomers thus determines the relative $FeCl_2$ yield as compared to the alternative HCl expulsion, which might occur from either rotational conformer and most likely from the NH−Cl−HN *anti* conformer.

In **2**, the high barrier slows down rotational isomerization. Nevertheless, it is fast (ms) compared to the experimental time scale (s). Equilibrium populations favor *syn* and diminish *anti* to less than 2%. Thus, $FeCl_2$ elimination should diminish in favor of HCl expulsion, as observed (cf. Figure 2).

Solvent attachment stabilizes *anti* in **3a** and **3b**, and it destabilizes *anti* in **3c**; the rotational barrier is reduced in all of these cases. *Anti* population increases, and $FeCl_2$ elimination diminishes (cf. Figure 2), because it is only possible after solvent abstraction and rearrangement of the molecule (see chapter 3.3). Therefore, $FeCl_2$ elimination for **3a**−**3c** is antiproportional to the solvent's binding energies (cf. Table 2), and it correlates with the Fe−Pd proximity (see Figure 2).

The electronic structure calculations provide for structures and linear IR absorption spectra of the likely, most stable isomers of complex **2** and of the solvent-coordinated complexes **3a**−**3c**. Comparison with IR-MPD spectra leads to further insights.

In the case of the complex **2**, the two rotational isomers $\mathbf{2}_{syn}$ and $\mathbf{2}_{anti}$ differ by 10 kJ/mol in favor of confomer $\mathbf{2}_{syn}$ (cf. insets in Figure 4). In both isomers, the Pd cation coordinates square planar to the NH and NH_2 functional groups and to the two chlorido ligands. Both isomers reveal linear IR absorption spectra that are well in line with the experimental IR-MPD spectrum (Figure 5). All recorded features are well-reproduced, and the above presumed assignements are confirmed. Note that there must not be a close corresponence in intensities. It is

DOI: 10.1021/acs.jpca.5b06952
J. Phys. Chem. A 2015, 119, 12587−12598

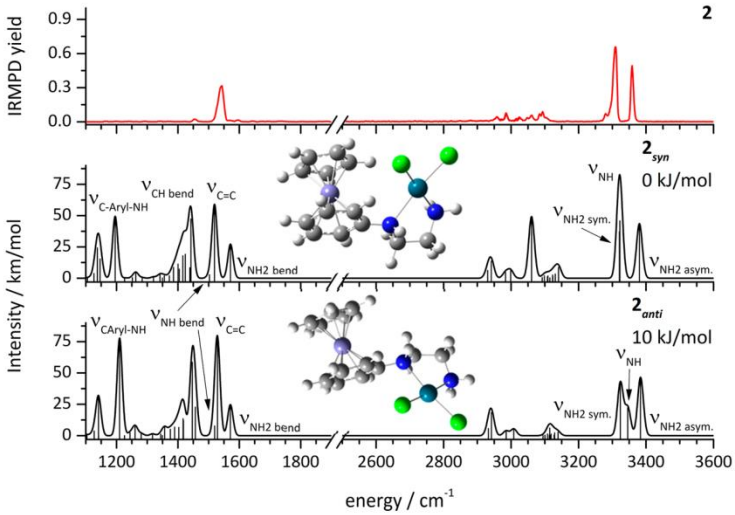

Figure 5. IR-MPD spectrum of the complex **2** in comparison to the DFT predicted IR absorption spectra of the two most stable isomers $\mathbf{2}_{syn}$ and $\mathbf{2}_{anti}$. Both isomers provide for a conceivable interpretation of the experimental spectrum.

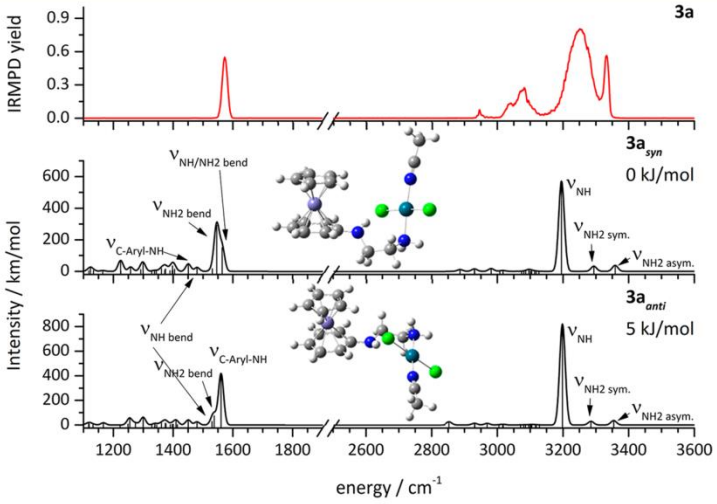

Figure 6. IR-MPD spectrum of the complex **3a** in comparison to the DFT predicted IR absorption spectra of the two most stable isomers $\mathbf{3a}_{syn}$ and $\mathbf{3a}_{anti}$. The scaled harmonic eigen modes of NH and NH_2 stretching vibrations fail to explain the experimental pattern.

well-known that IR-MPD intensities vary from those of absorption spectra.[35,43−46]

In the CH_3CN-coordinated complex **3a**, the two rotational isomers $\mathbf{3a}_{syn}$ and $\mathbf{3a}_{anti}$ differ by 5 kJ/mol (cf. insets in Figure 6) in favor of the conformer $\mathbf{3a}_{syn}$, which is much in line with the findings on the complex **2**. In both isomers, the Pd cation has lost NH coordination in favor of CH_3CN attachment. As opposed to dichlorido *syn* arrangement in **2**, the solvent changes the ligand arrangement in **3a** to *trans* configuration. In both isomers, the Pd cation coordinates square planar to the NH_2 functional group, the CH_3CN solvent and to the two chlorido ligands.

The linear IR absorption spectra of both isomers $\mathbf{3a}_{syn}$ and $\mathbf{3a}_{anti}$ reveal sharp features throughout. We assign the sharp IR-MPD band at 3330 cm^{-1} to the asymmetric NH_2 stretching mode as predicted by the calculations of isomers $\mathbf{3a}_{syn}$ and $\mathbf{3a}_{anti}$. The computed spectra fail to predict the observed broadening of the recorded bands between 3000 and 3300 cm^{-1}. This effect seems to originate from effects beyond the predictions of linear IR absorptions in harmonic approximation.

Upon close inspection, it becomes obvious that the solvent attachment to **2** causes subsequent structural changes beyond the coordinative rearrangement of the Pd center in **3a**, **3b**, and **3c**. An additional hydrogen bond forms between the secondary amine NH and the proximate chlorido ligand (d(N<u>H</u>−<u>Cl</u>): 2.26 Å in isomer $\mathbf{3a}_{syn}$ and 2.28 Å in isomer $\mathbf{3a}_{anti}$, cf. Table 3). Due to this NH−Cl hydrogen bond, the calculated value of the NH stretching mode red shifts to 3195 cm^{-1} (in $\mathbf{3a}_{syn}$), this value suffering from well-known anharmonic uncertainty inasmuch as any according hydrogen bond. Moreover this band is expected to broaden significantly as indeed observed at 3250 cm^{-1}. Adjacent CH stretching modes may couple and broaden thereby explaining the observed humps around 3075 cm^{-1}. It is gratifying to see that the predicted increase from **2** to **3a** in IR

DOI: 10.1021/acs.jpca.5b06952
J. Phys. Chem. A 2015, 119, 12587−12598

Table 3. NH−Cl Hydrogen Bond Lengths and Corresponding NH Stretching Frequencies

complex	isomer	d(NH−Cl)/Å	$\nu_{NH\ calc}$/cm^{-1}	$\nu_{NH\ exp.}$/cm^{-1}
2	$\mathbf{2}_{syn}$	-	3320	3308
	$\mathbf{2}_{anti}$	-	3347	
3a	$\mathbf{3a}_{syn}$	2.26	3195	3351
	$\mathbf{3a}_{anti}$	2.28	3195	
3b	$\mathbf{3b}_{syn}$	2.25	3218	3350
	$\mathbf{3b}_{anti}$	2.23	3220	
3c	$\mathbf{3c}_{syn}$	2.32	3275	3290
	$\mathbf{3c}_{anti}$	2.21	3205	

line strength of ν_{NH} (80 to 600 km/mol) at 3195 cm^{-1} seems to reflect in the enhancement of integrated area of the 3250 cm^{-1} hump in the IR-MPD spectrum. There is no forcing evidence that a conceivable NH stretch bend-overtone Fermi resonance contributes. Anharmonic calculations (by VPT2, cf. Supporting Information) point to a frequency mismatch. In passing, we note that the CID activation induced NH-Cl-HN *anti* conformers $^1\mathbf{3a}_{anti}^{(NH\text{-}Cl)}$, $^1\mathbf{3b}_{anti}^{(NH\text{-}Cl)}$, and $^1\mathbf{3c}_{anti}^{(NH\text{-}Cl)}$ do not contribute to the recorded IR-MPD spectra (cf. Figures S32−S37).

The calculations reveal the very nature of the 1575 cm^{-1} IR-MPD band. It is of NH/NH_2 bending character with a possible contribution of CN stretching by isomer $\mathbf{3a}_{anti}$. For sure, it does not contain contributions of arylic C═C ring breathing modes which red shift to 1390 cm^{-1} through coordination. The remaining weak IR-MPD bands between 2900 and 3050 cm^{-1} are well-predicted by various aliphatic and arylic C−H stretching modes in both isomers $\mathbf{3a}_{syn}$ and $\mathbf{3a}_{anti}$.

In the DMF-coordinated complex **3b**, the two rotational isomers $\mathbf{3b}_{syn}$ and $\mathbf{3b}_{anti}$ differ by 7 kJ/mol (cf. insets in Figure 7) in favor of the *syn* conformer $\mathbf{3b}_{syn}$, which is much in line with the findings on the complex **2** and the CH_3CN coordinating complex **3a**. All structural motifs in **3b** correspond to those of **3a** as discussed above.

The calculated IR spectra of both isomers of **3b** show the typical NH and NH_2 stretching vibrations in close resemblance to **3a**. The experimental evidence for a NH−Cl hydrogen bond in **3b** holds through observation of the broad hump around 3250 cm^{-1} as before in **3a**. However, the total IR-MPD intensities diminish in **3b** by a factor of 2 with respect to **3a**. In contrast the calculated IR intensities of the secondary amine NH stretching mode vary little (about 600 km/mol in both cases). We thus attribute the drop in IR-MPD intensity of the NH stretching band in **3b** to a suspected change in fragmentation efficiency. Due to the carbonyl group of DMF, there is a C═O stretching vibration around 1625 cm^{-1} for both isomers $\mathbf{3b}_{syn}$ and $\mathbf{3b}_{anti}$. The coordination of the carbonyl group at the Pd cation leads to a red shift of about 120 cm^{-1} with respect to free CO in similar structures. Other spectral features in **3b** resemble those of **3a**.

In the DMSO-coordinated complex **3c** the two rotational isomers $\mathbf{3c}_{syn}$ and $\mathbf{3c}_{anti}$ differ by 13 kJ/mol (cf. insets in Figure 8) in favor of the *syn* conformer $\mathbf{3c}_{syn}$, which agrees with the findings on the complex **2** and the other complexes **3a** and **3b**. All structural motifs in **3c** correspond to those of **3a** and **3b** as discussed above.

The calculations reveal a hydrogen bond between the NH functional group and a chlorido ligand that is significantly longer (+0.06 Å, cf. Table 3) in case of the *syn* isomer $\mathbf{3c}_{syn}$, and thereby weaker, than the corresponding hydrogen bonds in the *syn* isomers $\mathbf{3a}_{syn}$ and $\mathbf{3b}_{syn}$. In accord with this finding, both the calculated IR absorption spectrum of isomer $\mathbf{3c}_{syn}$ and the measured IR-MPD spectrum reveal a NH stretching band that is by about 50 cm^{-1} less red-shifted than the corresponding bands of complexes **3a** and **3b**. It seems as if the less stable isomer $\mathbf{3c}_{ant}$, which would reveal itself through a short NH−Cl hydrogen bond and a concomitant vibrational band more to the red, is not manifest by the experimental IR-MPD spectrum. In summary, we assign the recorded band at 3345 cm^{-1} in **3c** to the asymmetric NH_2 stretching vibration, and the split band with the two maxima at 3305 and 3280 cm^{-1} to the symmetric NH_2 and the NH stretching vibrations.

3.4. Multistate Profiles along the Reaction Coordinate of $FeCl_2$ Elimination in the CH_3CN Complex 3a. The $FeCl_2$ elimination deserves further attention. It is far from obvious

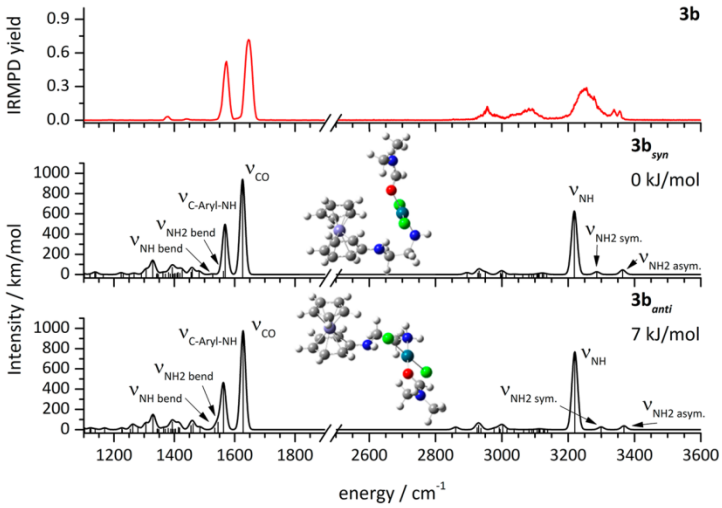

Figure 7. IR-MPD spectrum of the complex **3b** in comparison to the DFT predicted IR absorption spectra of the two most stable isomers $\mathbf{3b}_{syn}$ and $\mathbf{3b}_{anti}$. The scaled harmonic eigen modes of NH and NH_2 stretching vibrations fail to explain the experimental pattern.

DOI: 10.1021/acs.jpca.5b06952
J. Phys. Chem. A 2015, 119, 12587−12598

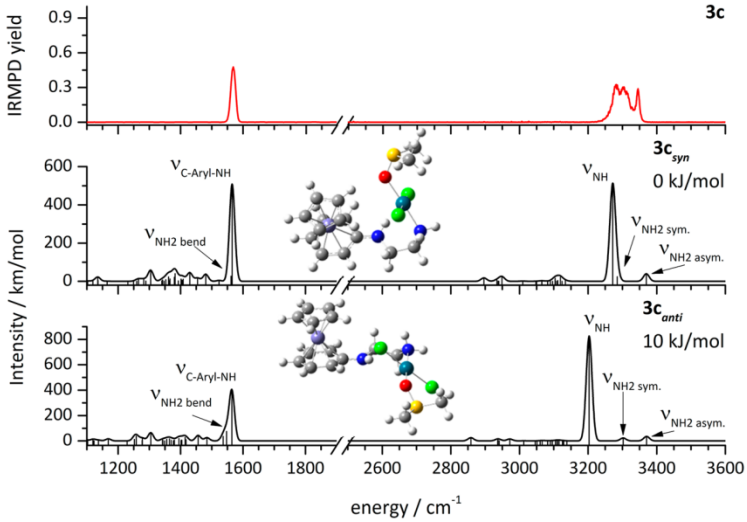

Figure 8. IR-MPD spectrum of the complex **3c** in comparison to the DFT-predicted IR absorption spectra of the two most stable isomers $\mathbf{3c}_{syn}$ and $\mathbf{3c}_{anti}$. The scaled harmonic eigen modes of NH and NH_2 stretching vibrations fail to explain the experimental pattern.

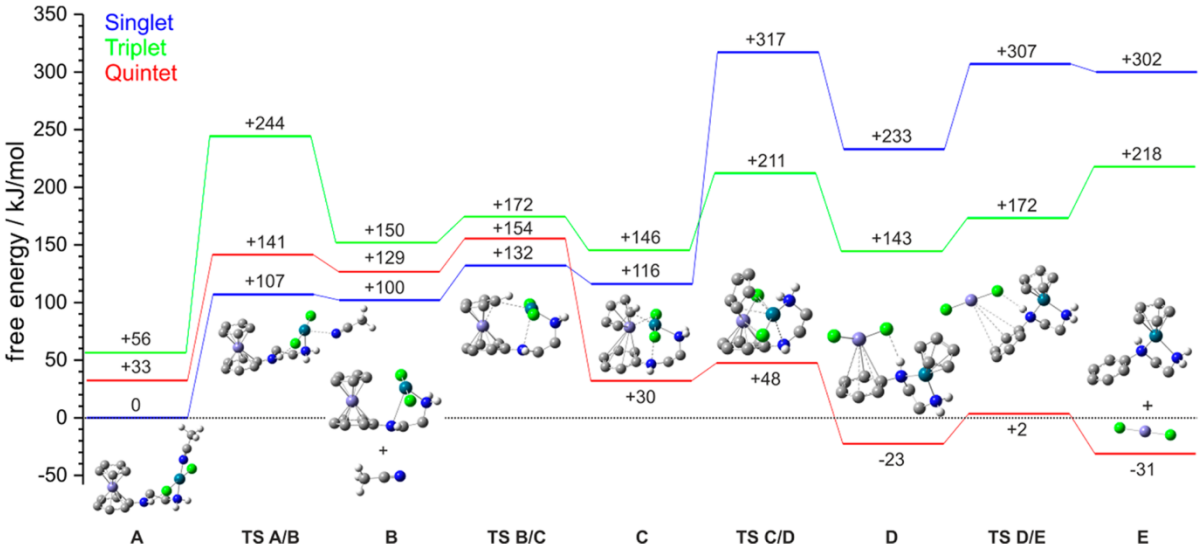

Figure 9. Normalized energetics of stationary points along the reaction coordinate of the $FeCl_2$ elimination within singlet (blue), triplet (green), and quintet (red) spin states, indicated values in kJ/mol. Depicted structures of stationary points refer to those of the lowest spin state which change along the reaction coordinate from singlet to quintet. For purpose of clarity, aliphatic and aromatic H atoms were omitted, except in CH_3CN. Note that the structures of the calculated stationary points vary in some dihedral angles by multiplicity (cf. Figures S3−S5 in Supporting Information), whereas in any case, the primary and secondary structural motifs persist.

how the Cp anion detaches from its coordination site, setting free the Fe center for release by (or after) acceptance of two chlorido ligands off their prior Pd host.

We chose to exemplify this complex multistep dissociation/fragmentation dynamic of the counterintuitive $FeCl_2$ elimination process by calculating the energy profiles of the $\mathbf{3a}_{syn}$ complex along the reaction coordinate(s), taking conceivably contributing spin state multiplicities explicitly into account (Figure 9).

We found it necessary to take into account the high and low spin states of the open shell Fe(II) cation. This leads to quintet (high spin) and singlet (low spin) multiplicities, and to a conceivable intermediate triplet state. We neglect unlikely high spin states of the Pd(II) cation where a $4d^8$ configuration in square planar coordination stabilizes a singlet state by ligand field splitting. We scale the obtained total energies to the *syn* isomer $^1\mathbf{3a}_{syn}$ where the index "1" indicates its singlet ground state. We found the eventual $FeCl_2$ elimination to proceed through a chain of four consecutive rearrangements, and we identified stationary points (minima and transitions states) along this reaction coordinate (cf. Figure 9). We chose a designation of the found minima by "**A**", "**B**", "**C**", "**D**", and "**E**" in order to achieve an unambiguous designation and for reasons of simplicity. By "**TS A/B**" we denote the transition states in

DOI: 10.1021/acs.jpca.5b06952
J. Phys. Chem. A 2015, 119, 12587−12598

between of minima **A** and **B** etc. Note that **A** in singlet (blue), triplet (red) or quintet (green) spin states equals ^{1}**3a**$_{syn}$, ^{3}**3a**$_{syn}$, or ^{5}**3a**$_{syn}$, and accordingly for the other minima (cf. blue, red, or green curves in Figure 9). We provide graphs of the minimum and transition state structures of the lowest spin state along the $FeCl_2$ elimination path (singlet in the beginning and quintet to the end).

Note that structures of any stationary point vary by the spin state. Namely, in ^{1}**A** and ^{3}**A**, the Cp and aryl ligands at the Fe center are opposite to each in an almost perfect sandwich arrangement (Cp-Fe-aryl angle of 178° and 177° for ^{1}**A** and ^{3}**A**, respectively). The computed quintet state ^{5}**A** exhibits a tilted-sandwich structure (Cp−Fe−aryl angle of 171°, cf. Figure S5 in Supporting Information).

We rationalize this significant change in geometry via inspection of the orbital energies in a ferrocene like Cp−Fe−aryl structure **4**, which is void of the diamine−Pd−Cl_2 group (cd calculated MO energies in Figure S6 in Supporting Information). The Fe d orbitals split via the distorted octaedric ligand field of the Cp and aryl ligands. We find in ascending order two (almost) degenerate e_2' orbitals, a sole a_1', and two almost degenerate e_1'' orbitals. This equates to nondegenerate singlet and triplet ground states, $(e_2')^4(a_1')^2$ and $(e_2')^4(a_1')^1(a_1'')^1$ in similar geometries ^{1}**4** and ^{3}**4**, respectively. A quintet state in a linear Cp−Fe−aryl geometry would imply an orbital occupations $(e_2')^3(a_1')^1(a_1'')^1(b_1')^1$ that enforce, however, a symmetry reduction through Jahn−Teller distortion, and effectively lifts the orbital degeneracy into a $(a_2')^2(b_2')^1(a_1')^1(a_1'')^1(b_1')^1$ configuration. Indeed ^{5}**4** is tilted to 172° − much as observed in the tilted-sandwich structure of ^{5}**A**. Thereby, we have found a rationalization of seemingly unusual ordering in computed stabilities: $E_{tot}^{0K}(^1\mathbf{A}) < E_{tot}^{0K}(^5\mathbf{A}) < E_{tot}^{0K}(^3\mathbf{A})$, explained through the sandwich relaxation/tilt in the quintet state.

With this insight, we are ready to progress further along the reaction coordinate, as depicted in Figure 9. The triplet state remains high along all of this reaction coordinate, and it does not couple to the singlet or quintet states. We thus need not to discuss it further. Endothermic elimination of the acetonitrile ligand from ^{1}**A** to ^{1}**B** and from ^{5}**A** to ^{5}**B** proceed almost barrierless via transition states ^{1}**TS A/B** and ^{5}**TS A/B**. There is some relaxation in dihedral angles with little energy gain, and the Pd center acquires a vacant coordination site. This vacancy receives electron density from the adjacent electron-rich Cp ligand in ^{1}**B** (Figure 9), while the Cp ligand tilts away from Pd in ^{5}**B** (Figure S5). The latter quintet case leaves space for a favorable approach to Fe of the two chorido ligands from Pd, while the former singlet case runs into a Pd−C bond in ^{1}**C** that needs to reopen before chlorido migration enables through ^{1}**TS C/D** at high enthalpic expenses (+ 116 to +317 kJ/mol). The ^{5}**B** may run via a low barrier ^{5}**TS B/C** transition state into a ^{5}**C** structure that reveals close Fe−Pd proximity (^{5}**C**: d(Fe−Pd) = 2.86 Å, d(Pd−C) = 2.38 Å; ^{5}**TS B/C**: d(Fe−Pd) = 3.26 Å, d(Pd−C) = 2.47 Å), other than ^{1}**C** (^{1}**C**: d(Fe−Pd) = 3.30 Å, d(Pd−C) = 2.40 Å; ^{1}**TS B/C**: d(Fe−Pd) = 3.35 Å, d(Pd−C) = 2.49 Å). Thereby, ^{5}**C** becomes most favorable since the ligand field splitting in the high spin Fe, as induced by the chloride ligands, is smaller than the splitting of the cyclopentadienyl anion.[61] Thereby, the singlet and quintet diabatic potential surfaces cross on the way from **TS B/C** to **C**. The assumption of an adiabatic progression along the reaction path would thus imply a direct singlet−quintet spin crossover—seemingly without a direct involvement of the higher triplet state. The concomitant spin flips of two electrons (likely d electrons at Fe) need to occur in concert—an unprecedented assumption, to the best of our knowledge.

Assuming further progression of reaction on the low lying singlet surface the remainder of the multistep $FeCl_2$ is obvious. The close Fe−Pd proximity in the presence of a tilt away Cp ligand allows for easy exchange/switch of the two chlorido ligands from Pd to Fe (^{5}**C** via ^{5}**TS C/D** to ^{5}**D**) in concert with opposite Cp exchange from Fe to Pd—conveniently migrating above the Fe(Cl_2)Pd plane without steric hindrance. Moderate reorganization via ^{5}**TS D/E** allows for exothermic $FeCl_2$ expulsion toward ^{5}**E** which comprises $^5FeCl_2$ and a singlet Pd fragment cation—in accord with the IR-MPD MS detection.

4. SUMMARY AND CONCLUSION

We have presented a novel bifunctional iron−palladium catalyst. Mass spectrometric characterization revealed ready solvent attachment. Computed structures show a coordination change of the Pd atom in favor of solvent attachment. Upon collisional excitation these solvent-attached complexes (**3a**, **3b**, **3c**) may lose the attached solvent, may lose HCl, may lose both in concert, or may lose—most notably—FeCl2 and solvent in concert. A solvent-modulated Fe−Pd proximity coincides, and seems to favor, $FeCl_2$ elimination. Our IR-MPD studies reveal competing HCl/$FeCl_2$ elimination with branching ratios much alike the CID ones. The solvent-modulated formation of NH−Cl hydrogen bonds help to verify computed structures and isomers. The identified *syn* and *anti* isomers favor and disfavor $FeCl_2$ elimination, respectively.

The DFT calculations reveal a multitude of stationary points along the multistep reaction coordinates of the three conceivable spin states. The quintet state shows a static Jahn−Teller type relaxation by a tilt away of the Cp ligand at the iron center. Thereby, the quintet stabilizes below the triplet state, and amidst the rearrangements toward $FeCl_2$ elimination, this quintet state steeply drops below the initially most stable singlet state—namely, by further enhancing the Cp ligand tilt at the iron center. The remainder of rearrangements likely proceed by the quintet state, allowing for chlorido and Cp ligand exchange among the metallic centers in opposite directions in a concerted, ballet-like manner. The assumption of an adiabatic progression along the reaction path would thus imply a direct singlet−quintet spin crossover—seemingly without a direct involvement of the higher triplet state. The concomitant spin flips of two electrons (likely d electrons at Fe) would need to occur in concert. Unless alternate—yet currently unkown—structures prevail, such an unprecedented assumption would ask for further elucidation and verification by sound high level quantum chemical modeling of structrues and dynamics, taking into account a likely multi reference character of transition state structures. Such treatment is much beyond the scope of the current study.

The elucidated coordination change upon solvent attachment at the Pd center nicely reveals a likely structure with conceivable catalytic activity. Electron rich hydrocarbon molecules may easily swap for the solvent and proceed toward further steps of activation.

The exoergic elimination of $FeCl_2$ would result in a deactivation of the catalytic activity of the complex. It is kinetically hindered by a barrier of 132 kJ/mol which limits the range of applicable temperatures in conceivable technical applications.

DOI: 10.1021/acs.jpca.5b06952
J. Phys. Chem. A 2015, 119, 12587−12598

■ ASSOCIATED CONTENT

Supporting Information

The Supporting Information is available free of charge on the ACS Publications website at DOI: 10.1021/acs.jpca.5b06952.

Sythetic procedures, compound characterization, and supplemental data (PDF)

■ AUTHOR INFORMATION

Corresponding Author

*E-mail: gns@chemie.uni-kl.de. Tel.: +49 631 205 4697.

Notes

The authors declare no competing financial interest.

■ ACKNOWLEDGMENTS

This work was supported by the German research foundation DFG within the transregional collaborative research center SFB/TRR 88 "Cooperative effects in homo and hetero metallic complexes" (3MET.de) and by the state research center OPTIMAS. We thank the reviewers for valuable comments.

■ REFERENCES

(1) Daugulis, O. Palladium and Copper Catalysis in Regioselective, Intermolecular Coupling of C-H and C-Hal Bonds. *Top. Curr. Chem.* **2009**, *292*, 57−84.

(2) Rana, S.; Modak, A.; Maity, S.; Patra, T.; Maiti, D. In *Iron Catalysis in Synthetic Chemistry In Progress in Inorganic Chemistry*, Karlin, K. D., Ed.; John Wiley & Sons Inc: Hoboken, NJ, 2014; Vol. *59*.

(3) Cornils, B. Metal-Catalyzed Reactions in Water. *Angew. Chem., Int. Ed.* **2013**, *52*, 9079−9080.

(4) *Ferrocenes: Ligands, Materials and Biomolecules*; Stepnicka, P., Ed.; John Wiley & Sons Inc: Hoboken, NJ, 2008.

(5) Togni, H. *Ferrocenes: Homogeneous Catalysis. Organic Synthesis. Materials Science*; John Wiley & Sons Inc: Hoboken, NJ, 1995.

(6) Kealy, T. J.; Pauson, P. L. A New Type of Organo-Iron Compound. *Nature* **1951**, *168*, 1039−1040.

(7) Fischer, E. O.; Pfab, W. Cyclopentadien-Metallkomplexe, Ein Neuer Typ Metallorganischer Verbindungen. *Z. Naturforsch., B: J. Chem. Sci.* **1952**, *7*, 377−379.

(8) Miller, S. A.; Tebboth, J. A.; Tremaine, J. F. Dicyclopentadienyliron. *J. Chem. Soc.* **1952**, 632−635.

(9) Neumann, P.; Dib, H.; Caminade, A. M.; Hey-Hawkins, E. Redox Control of a Dendritic Ferrocenyl-Based Homogeneous Catalyst. *Angew. Chem., Int. Ed.* **2015**, *54*, 311−314.

(10) Savka, R.; Foro, S.; Gallei, M.; Rehahn, M.; Plenio, H. Oxidation-Triggered Ring-Opening Metathesis Polimerization. *Chem. - Eur. J.* **2013**, *19*, 10655−10662.

(11) Arumugam, K.; Varnado, C. D.; Sproules, S.; Lynch, V. M.; Bielawski, C. W. Redox-Switchable Ring-Closing Metathesis: Catalyst Design, Synthesis, and Study. *Chem. - Eur. J.* **2013**, *19*, 10866−10875.

(12) Liu, G. Y.; He, H. Y.; Wang, J. H. Ferrocene Redox Controlled Reversible Immobilization of Ruthenium Carbene in Ionic Liquid: A Versatile Catalyst for Ring-Closing Metathesis. *Adv. Synth. Catal.* **2009**, *351*, 1610−1620.

(13) Gregson, C. K. A.; Gibson, V. C.; Long, N. J.; Marshall, E. L.; Oxford, P. J.; White, A. J. P. Redox Control Within Single-Site Polymerization Catalysts. *J. Am. Chem. Soc.* **2006**, *128*, 7410−7411.

(14) Slone, C. S.; Mirkin, C. A.; Yap, G. P. A.; Guzei, I. A.; Rheingold, A. L. Oxidation-State-Dependent Reactivity and Catalytic Properties of a Rh(I) Complex Formed From a Redox-Switchable Hemilabile Ligand. *J. Am. Chem. Soc.* **1997**, *119*, 10743−10753.

(15) Young, D. J.; Chien, S. W.; Hor, T. S. A. 1,1′-Bis(Diphenylphosphino)Ferrocene in Functional Molecular Materials. *Dalton Trans.* **2012**, *41*, 12655−12665.

(16) Bandoli, G.; Dolmella, A. Ligating Ability of 1,1′-Bis-(Diphenylphosphino)Ferrocene: a Structural Survey (1994−1998). *Coord. Chem. Rev.* **2000**, *209*, 161−196.

(17) Toma, S.; Csizmadiova, J.; Meciarova, M.; Sebesta, R. Ferrocene Phosphane-Heteroatom/Carbon Bidentate Ligands in Asymmetric Catalysis. *Dalton Trans.* **2014**, *43*, 16557−16559.

(18) Butt, N. A.; Liu, D. L.; Zhang, W. B. The Design and Synthesis of Planar Chiral Ligands and Their Application to Asymmetric Catalysis. *Synlett* **2014**, *25*, 615−630.

(19) Schaarschmidt, D.; Lang, H. Selective Synthesis of Planar-Chiral Ferrocenes. *Organometallics* **2013**, *32*, 5668−5704.

(20) Dai, H. *Chiral Ferrocenes in Asymmetric Catalysis*; John Wiley & Sons Inc: Hoboken, NJ, 2010.

(21) Gomez Arrayas, R.; Adrio, J.; Carretero, J. C. Recent Applications of Chiral Ferrocene Ligands in Asymmetric Catalysis. *Angew. Chem., Int. Ed.* **2006**, *45*, 7674−7715.

(22) Blaser, H. U.; Pugin, B.; Spindler, F.; Thommen, M. From a Chiral Switch to a Ligand Portfolio for Asymmetric Catalysis. *Acc. Chem. Res.* **2007**, *40*, 1240−1250.

(23) Eitel, S. H.; Bauer, M.; Schweinfurth, D.; Deibel, N.; Sarkar, B.; Kelm, H.; Kruger, H. J.; Frey, W.; Peters, R. Paramagnetic Palladacycles with Pd-III Centers are Highly Active Catalysts for Asymmetric Aza-Claisen Rearrangements. *J. Am. Chem. Soc.* **2012**, *134*, 4683−4693.

(24) Fischer, D. E.; Xin, Z. Q.; Peters, R. Asymmetric Formation of Allylic Amines with N-Substituted Quaternary Stereocenters by Pd-II-Catalyzed Aza-Claisen Rearrangements. *Angew. Chem., Int. Ed.* **2007**, *46*, 7704−7707.

(25) Jautze, S.; Seiler, P.; Peters, R. Macrocyclic Ferrocenyl-Bisimidazoline Paladcycle Dimers as Highly Active and Enantioselective Catalysts for the Aza-Claisen Rearrangement of Z-Configured N-Para-Methoxyphenyl Trifluoroactimidates. *Angew. Chem., Int. Ed.* **2007**, *46*, 1260−1264.

(26) Green, M. L. H.; Pratt, L.; Wilkinson, G. Spectroscopic Studies of Some Organoiron Complexes. *J. Chem. Soc.* **1960**, *206*, 989−997.

(27) Nesmeyanov, A. N.; Vol'kenau, N. A.; Bolesova, I. N. The Interaction of Ferrocene and its Derivatives with Aromatic Compounds. *Tetrahedron Lett.* **1963**, *4*, 1725−1729.

(28) Khand, I. U.; Pauson, P. L.; Watts, W. E. Dienyl Complexes of Transition Metals 2. Addition of Hydride to Halogen-Substituted Arenecyclopentadienyliron Cations. *J. Chem. Soc. C* **1968**, *17*, 2261−2262.

(29) Abdelaziz, A. S.; Lei, Y.; Dedenus, C. R. Aliphatic Diols in the Synthesis of Bis(Cyclopentadienyliron) Arene Complexes. *Polyhedron* **1995**, *14*, 1585−1591.

(30) Raouafi, N.; Belhadj, N.; Boujlel, K.; Ourari, A.; Amatore, C.; Maisonhaute, E.; Schollhorn, B. Ultrasound-Promoted Aromatic Nucleophilic Substitution of Dichlorobenzene Iron(II) Complexes. *Tetrahedron Lett.* **2009**, *50*, 1720−1722.

(31) Abd-El-Aziz, A. S.; Todd, E. K.; Afifi, T. H. Star-Shaped Polyaromatic Ethers Coordinated to Redox-Active Cyclopentadienyliron Moieties. *Macromol. Rapid Commun.* **2002**, *23*, 113−117.

(32) Abdelaziz, A. S.; de Denus, C. R.; Hutton, H. M. Iron-cyclopentadienyl Mediated 2-Alkyl-2-Arylphenylsulphonylacetonitrile Synthesis. *Can. J. Chem.* **1995**, *73*, 289−295.

(33) Sutherland, R. G.; Chowdhury, R. L.; Piorko, A.; Lee, C. C. Functionalization of Aromatic and Heterocyclic-Systems − Regioselective Introduction of 2-Oxoalkyl Chain or Cyano Functions via Organoiron Complexes. *J. Org. Chem.* **1987**, *52*, 4618−4620.

(34) Schroder, D.; Shaik, S.; Schwarz, H. Two-State Reactivity as a New Concept in Organometallic Chemistry. *Acc. Chem. Res.* **2000**, *33*, 139−145.

(35) Polfer, N. C. Infrared Multiple Photon Dissociation Spectroscopy of Trapped Ions. *Chem. Soc. Rev.* **2011**, *40*, 2211−2221.

(36) MacAleese, L.; Maitre, P. Infrared Spectrocopy of Organometallic Ions in the Gas Phase: From Model to Real World Complexes. *Mass Spectrom. Rev.* **2007**, *26*, 583−605.

DOI: 10.1021/acs.jpca.5b06952
J. Phys. Chem. A 2015, 119, 12587−12598

(37) Menges, F.; Riehn, C.; Niedner-Schatteburg, G. The Interaction of the Dipeptide Carnosine with Alkali Metal Ions Studied by Ion Trap Mass Spectrometry. *Z. Phys. Chem.* **2011**, *225*, 595−609.
(38) Schultz, R. H.; Crellin, K. C.; Armentrout, P. B. Sequential Bond-Energies of Fe(CO)X+ (X = 1−5) − Systematic Effects on Collision-Induced Dissociation Measurements. *J. Am. Chem. Soc.* **1991**, *113*, 8590−8601.
(39) Polfer, N. C.; Oomens, J.; Dunbar, R. C. IRMPD Spectroscopy of Metal-Ion/Tryptophan Complexes. *Phys. Chem. Chem. Phys.* **2006**, *8*, 2744−2751.
(40) Lang, J.; Gaffga, M.; Menges, F.; Niedner-Schatteburg, G. Two-Color Delay Dependent IR Probing of Torsinal Isomerization in a AgL1L2(+) Complex. *Phys. Chem. Chem. Phys.* **2014**, *16*, 17417−17421.
(41) Fedorov, A.; Couzijn, E. P. A.; Nagornova, N. S.; Boyarkin, O. V.; Rizzo, T. R.; Chen, P. Structure and Bonding of Isoleptic Coinage Metal (Cu, Ag, Au) Dimethylaminotrenes in the Gas Phase. *J. Am. Chem. Soc.* **2010**, *132*, 13789−13798.
(42) Chakraborty, S.; Dopfer, O. Infrared Spectrum of the Ag +-(Pyridine)(2) Ionic Complex: Probing Interactions in Artificial Metal-Mediated Base Pairing. *ChemPhysChem* **2011**, *12*, 1999−2008.
(43) Skriba, A.; Schulz, J.; Roithova, J. Monitoring of Reaction Intermediates in the Gas Phase: Ruthenium-Catalyzed C-C Coupling. *Organometallics* **2014**, *33*, 6868−6878.
(44) Oomens, J.; Sartakov, B. G.; Meijer, G.; von Helden, G. Gas-Phase Infrared Multiple Photon Dissociation Spectroscopy of Mass.Selected Molecular Ions. *Int. J. Mass Spectrom.* **2006**, *254*, 1−19.
(45) Roithova, J. Characterization of Reaction Intermediates by Ion Spectroscopy. *Chem. Soc. Rev.* **2012**, *41*, 547−559.
(46) Fridgen, T. D. Infrared Consequence Spectroscopy of Gaseous Protoneted and Metal Ion Cationized Complexes. *Mass Spectrom. Rev.* **2009**, *28*, 586−607.
(47) Becke, A. D. Density-Functional Exchange-Energy Approximation with Correct Asymptotic-Behavior. *Phys. Rev. A: At., Mol., Opt. Phys.* **1988**, *38*, 3098−3100.
(48) Becke, A. D. Density-Functional Thermochemistry, 3. The Role of Exact Exchange. *J. Chem. Phys.* **1993**, *98*, 5648−5652.
(49) Miehlich, B.; Savin, A.; Stoll, H.; Preuss, H. Results Obtained with the Correlation-Energy Density Functionals of Becke and Lee, Yang and Parr. *Chem. Phys. Lett.* **1989**, *157*, 200−206.
(50) Lee, C. T.; Yang, W. T.; Parr, R. G. Development of the Colle-Salvetti Correlation-Energy Formula into a Functional of the Electron-Density. *Phys. Rev. B: Condens. Matter Mater. Phys.* **1988**, *37*, 785−789.
(51) Dunning, T. H. Gaussian-Basis sets for Use in Correlated Molecular Calculations: 1. The Atoms Boron Through Neon and Hydrogen. *J. Chem. Phys.* **1989**, *90*, 1007−1023.
(52) Woon, D. E.; Dunning, T. H. Gaussian-Basis setsfor Use in Correlated Molecular Calculations 3: the Atoms Aluminium Through Argon. *J. Chem. Phys.* **1993**, *98*, 1358−1371.
(53) Woon, D. E.; Dunning, T. H. Calculations of the Electron-Affinities of the 2nd-Row Atoms − Al-Cl. *J. Chem. Phys.* **1993**, *99*, 3730−3737.
(54) Andrae, D.; Haussermann, U.; Dolg, M.; Stoll, H.; Preuss, H. Energy-Adjusted Abinitio Pseudopotentials for the 2nd-Row and 3rd-Row Transtion-Elements − Molecular Test for Ag2, Au2 and Ru, Os. *Theoretica Chimica Acta* **1991**, *78*, 247−266.
(55) Dolg, M.; Wedig, U.; Stoll, H.; Preuss, H. Energy-Adjusted Abinitio Pseudopotentials for the 1st-Row Transition-Elements. *J. Chem. Phys.* **1987**, *86*, 866−872.
(56) Frisch, M. J.; Trucks, G. W.; Schlegel, H. B.; Scuseria, G. E.; Robb, M. A.; Cheeseman, J. R.; Scalmani, G.; Barone, V.; Mennucci, B.; Petersson, G. A.; Nakatsuji, H., et al. *Gaussian 09*, revision D.01; Gaussian, Inc.: Wallingford, CT, 2009.
(57) NIST Standard Reference Database 101, 2013.
(58) Nosenko, Y.; Menges, F.; Riehn, C.; Niedner-Schatteburg, G. Investigation by Two-Color IR Dissociation Spectroscopy of Hoogsteen-Type Binding in a Metalated Nucleobase Pair Mimic. *Phys. Chem. Chem. Phys.* **2013**, *15*, 8171−8178.
(59) Menges, F. *Structure and Reactivity of Isolated Mononuclear and Oligonuclear Metal Complexes*. Ph.D. Thesis, TU Kaiserslautern, Kaiserslautern, Germany, 2013.
(60) Vinokur, N.; Ryzhov, V. Using Collision-Induced Dissociation with Corrections for the Ion Number of Degrees of Freedom for Quick Comparisons of Relative Bonding Strength. *J. Mass Spectrom.* **2004**, *39*, 1268−1274.
(61) Holleman, v. A. F.; Wiberg, E. *Lehrbuch der anorganischen Chemie*; de Gruyter Verlag: Berlin, 1995; Vol. *101*.

DOI: 10.1021/acs.jpca.5b06952
J. Phys. Chem. A 2015, 119, 12587−12598

11.4 P,C-Bond Cleavage in the Ligand Sphere of a Nickel(II) Complex

Simon. P. Walg[a], Alexandra. D. Schmidt[a], Marcus Schmitz[a],
Saeid Farsadpour[a], Johannes. Lang[a], Mark Niebergall[a], Yu. Sun[a],
Peter W. Roesky[b], Gereon Niedner-Schatteburg[a] and Werner R. Thiel[a]

a) Fachbereich Chemie,
Technische Universität Kaiserslautern,
67663 Kaiserslautern, Germany

b) Institut für Anorganische Chemie,
Karlsruher Institut für Technologie (KIT),
76131 Karlsruhe, Germany

11.4.1 Preamble

The following chapter is a reprint of a publication in the journal "Dalton Transactions".

S. P. Walg, A. D. Schmidt, S. Farsadpour, M. Niebergall from the research group of Prof. Dr. W. R. Thiel synthesized the nickel complex. Yu. Sun and Marcus Schmitz provided the crystallographic data. I contributed with Electrospray Ionization Mass Spectrometry (ESI-MS) measurements and Collision Induced Dissociation (CID) experiments. W. R Thiel and P. W. Roesky prepared the paper with the help of G. Niedner-Schatteburg.

<u>Full Reference:</u>

P,C-bond cleavage in the ligand sphere of a nickel(II) complex
S. P. Walg, A. D. Schmidt, M. Schmitz, S. Farsadpour, **J. Lang**, M. Niebergall, Y. Sun, P. W. Roesky, G. Niedner-Schatteburg and W. R. Thiel, *Dalton Transactions* **2015**, *44*, 1317-1322.
http://dx.doi.org/10.1039/C4DT02158D

11.4.2 Reprint

Reprint Licence

P,C-bond cleavage in the ligand sphere of a nickel(II) complex

S. P. Walg, A. D. Schmidt, M. Schmitz, S. Farsadpour, J. Lang, M. Niebergall, Y. Sun, P. W. Roesky, G. Niedner-Schatteburg and W. R. Thiel, *Dalton Trans.*, 2015, **44**, 1317
DOI: 10.1039/C4DT02158D

Dalton Transactions

PAPER

View Article Online
View Journal | View Issue

Cite this: *Dalton Trans.*, 2015, **44**, 1317

P,C-bond cleavage in the ligand sphere of a nickel(II) complex†

Simon P. Walg,[a] Alexandra D. Schmidt,[a] Marcus Schmitz,[a] Saeid Farsadpour,[a] Johannes Lang,[a] Mark Niebergall,[a] Yu Sun,[a] Peter W. Roesky,[b] Gereon Niedner-Schatteburg[a] and Werner R. Thiel*[a]

Received 18th July 2014,
Accepted 13th October 2014

DOI: 10.1039/c4dt02158d

www.rsc.org/dalton

Reacting nickel(II)perchlorate with a bidentate P,N-ligand in methanol leads to P,C-bond cleavage and gives a five-coordinate nickel complex wherein the nickel(II) site is coordinated by a tridentate P,N,P-ligand and a bidentate N,C-ligand. The carbanion of the latter is the result of the P,C-bond cleaving process. The diamagnetic nickel(II) complex was characterized by means of elemental analysis, NMR spectroscopy, cyclic voltammetry and X-ray structure analysis.

Introduction

Nickel(II) complexes have been established for a long time as catalysts for a series of catalytic transformations such as Kumada-[1] and Negishi-type[2] cross-coupling or olefin polymerization reactions.[3] The broad catalytic applications in combination with the rich variety of catalytically active nickel(II) systems led us to focus on the coordination chemistry of [(2-aminopyrimidin-4-yl)aryl]phosphanes with this metal. In the last few years we have investigated chelating ligands containing 2-aminopyrimidin-4-yl fragments bound to either a second N-donor or a phosphine moiety. In the case of tertiary amino groups being located at the 2-position of the pyrimidine ring, such ligands easily undergo a so-called roll-over metallation[4] leading to C–H activation in the 5-position of the pyrimidine ring.[5] The resulting metal complexes which are coordinated by a carbanion show good activities in transfer hydrogenation (Ru) and Suzuki–Miyaura coupling reactions (Pd). This inspired us to extend the investigation of this class of ligand to other late transition metals.

Herein we report on an unusual P–C bond cleavage performed in the ligand backbone of a nickel(II) complex leading to a stable, diamagnetic, five-coordinate nickel(II) complex. Interestingly this P,C-cleavage occurs at the P,N-ligand [(2-aminopyrimidin-4-yl)aryl]phosphane (**1**) containing a primary amine (Scheme 1), which is the most unreactive member in the series of primary, secondary and tertiary [(2-aminopyrimidin-4-yl)aryl]phosphanes we had investigated so far.

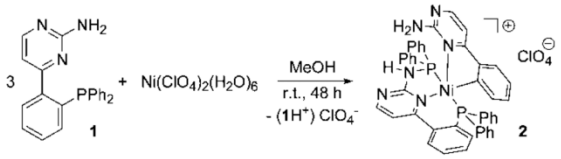

Scheme 1 Synthesis of the nickel(II) complex **2**.

P,C-cleaving reactions have frequently been described in the literature. There are even some bacteria being able to perform this reaction in the case of alkyl phosphorous species.[6] The cleavage of aryl and alkyl phosphorous bonds can be performed at clusters[7] or mono- to trinuclear metal complexes[8] leading to bridging phosphido ligands. These conversions are mainly following oxidative addition processes at the metal site. According to these findings Hartwig, Bergman and Andersen suggested that the P,C-cleavage occurring at a ruthenium(II) complex also includes an oxidative addition step.[9] The most prominent example for a reductive P,C-cleavage is the reaction of PPh_3 with lithium to provide Ph_2PLi and PhLi,[10] which is also reported for other phosphines with different reducing reagents.[11] To the best of our knowledge, there is one example, wherein an electrophile (H^+) attacks a non-coordinating phosphorous atom in the periphery of a transition metal complex (here: Zr), resulting in a P,C-bond cleavage.[12] On the other hand, the attack of a nucleophile to a metal-coordinated phosphorous atom or a phosphorous site possessing good leaving group properties can also lead to P,C-bond cleavage and generate a carbanion, which is further stabilized by coordination to the metal site or by protonation.[13]

[a]*Technische Universität Kaiserslautern, Fachbereich Chemie, Erwin-Schrödinger-Straße 54, D-67663 Kaiserslautern, Germany. E-mail: thiel@chemie.uni-kl.de*
[b]*Karlsruher Institut für Technologie (KIT), Institut für Anorganische Chemie, Engesserstraße 15, D-76131 Karlsruhe, Germany*

†Electronic supplementary information (ESI) available: Spectroscopic data, additional structure plots. CCDC-1014112. For ESI and crystallographic data in CIF or other electronic format see DOI: 10.1039/c4dt02158d

Results and discussion

Ligand **1** is accessible in a few steps starting from diphenyl(trimethylsilyl)phosphane and 1-(2-fluorophenyl)-3-*N*,*N*-dimethylaminoprop-2-en-1-one.[14] Reacting $Ni(ClO_4)_2(H_2O)_6$ with **1** in a 1 : 3 ratio in methanol gives the red-colored, five-coordinate nickel(II) complex **2** in high yields (Scheme 1).

Single crystals of **2** suitable for an X-ray structure determination were grown from a concentrated solution in methanol. The nickel(II) complex **2** crystallizes in the triclinic space group $P\bar{1}$ with two molecules of methanol in the asymmetric unit. One methanol molecule is distorted over two positions, the perchlorate counter anion is distorted as well. Fig. 1 shows the molecular structure of the cation. Characteristic bond parameters are listed in the caption.

The determination of the molecular structure of the nickel(II) complex **2** proves that a PPh_2 moiety has been split from one of the [(2-aminopyrimidin-4-yl)aryl]phosphanes and has been attached to the NH_2 group of the second ligand. The nickel(II) ion is now coordinated in a distorted square-pyramidal manner by two phosphorous atoms, two nitrogen atoms and one carbon atom. Pentacoordinate nickel complexes are not uncommon. However, they are mainly observed in a trigonal-bipyramidal geometry with nitrogen and sulphur donors.[15] Since the angle P1–Ni1–P2 is close to 140° and the angles P1–Ni1–N4 and P2–Ni1–N4 are larger than 100°, the compound adopts a geometry, which is in between a square-pyramidal and a trigonal-bipyramidal coordination mode. This coordination mode is caused by the bending in the six-membered ring (N1–C–C–C–P1–Ni1) which prevents the donor atoms of the tridentate P,N,P-ligand from being located in one plane with the nickel(II) site. The Ni–P bond lengths differ only slightly. In contrast, there is a big difference in the Ni–N bond lengths: Ni–N1 (1.978 Å) is about 15 pm shorter than Ni1–N4 (2.135 Å), although the nitrogen atom N1 is located in the *trans*-position to the carbanion site C44, exhibiting a strong *trans*-influence. This observation is frequently made for rigid tridentate ligands: due to steric restrictions, the M–L distance to the inner donor site is generally found to be considerably shortened compared to the outer ones.[16] The reason why C44 is found in the *trans*-position to N1 is probably an intramolecular hydrogen bond that exists between H6A and N1 (2.51 Å). As expected, the Ni–C44 (1.903 Å) bond is the shortest of all M–L bonds, thus approx. 23 pm shorter than the Ni–N4 bond, reflecting the anionic nature of this carbon atom and the resulting very strong Ni–C bond. The ligand backbone of compound **2** contains several sites that can act as proton donors or acceptors in intermolecular hydrogen bonds, resulting in the formation of a zig-zag chain (see the ESI†) generated by linkages between H3N and N2 as well as H6B and N5. The perchlorate anion interacts *via* a hydrogen bond with H6A. The Ni–C-bond is neither hydrolysed by the protic amino group of the molecule nor by the protic solvent methanol as a result of the almost perfect shielding by the two diphenylphosphino moieties. These are located in the *trans*-positions of the distorted square pyramidal coordination environment (see the ESI†).

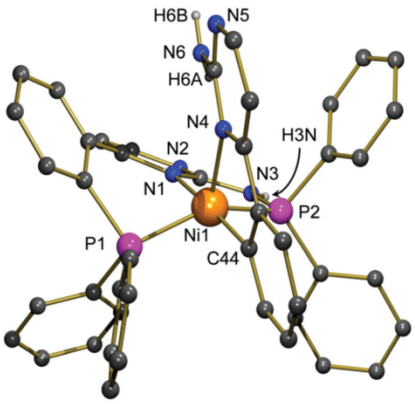

Fig. 1 Molecular structure of the cation of compound **2** in the solid state; carbon bound hydrogen atoms, the perchlorate anion and both co-crystallizing methanol molecules are omitted for clarity. Characteristic bond lengths [Å], bond angles [°], and hydrogen bond parameters: Ni1–P1 2.1968(9), Ni1–P2 2.1367(9), Ni1–N1 1.978(3), Ni1–N4 2.135(3), Ni1–C44 1.903(3), P1–Ni1–P2 149.25(4), P1–Ni1–N1 89.12(8), P1–Ni1–N4 106.20(7), P1–Ni1–C44 90.58(9), P2–Ni1–N1 86.71(8), P2–Ni1–N4 104.42(7), P2–Ni1–C44 90.53(10), N1–Ni1–N4 102.94(10), N1–Ni1–C44 174.06(12), N4–Ni1–C44 82.84(12); hydrogen bonds (O1 from perchlorate): N3–H3N 0.86(3), H3N···N2 2.07(3), N3···N2 2.929(5), N3–H3N···N2 179(4), N6–H6A 0.87(3), H6A···O1 2.58(4), N6···O1 3.129(5), N6–H6A···O1 122(3), N6–H6A 0.87(3), H6A···N1 2.51(3), N6···N1 3.150(4), N6–H6A···N1 131(3), N6–H6B 0.87(3), H6B···N5 2.14(3), N6···N5 3.013(4), N6–H6B···N5 179(5).

The $^{31}P\{^1H\}$ NMR spectrum of **2** shows two sharp resonances for the phosphorous atoms P1 (13.9 ppm) and P2 (47.2 ppm) with a $^2J_{PP}$ coupling of 231.6 Hz. The large coupling is consistent with two different phosphorous sites being located in the *trans*-position to each other. Since there is no structurally related nickel(II) complex in the literature, we took diamagnetic, four-coordinate complexes as makeshifts to assign the ^{31}P resonance of compound **2**. The ^{31}P resonance of *trans*-$(PPh_3)_2Ni(Ph)Cl$ is reported to appear at approx. 21 ppm.[17] Kirchner *et al.* investigated a square-planar nickel(II) pincer complex with two *trans*-orientated arylamino(diphenyl)-phosphine units and found a ^{31}P resonance at 77.8 ppm.[18] These values allow to assign the resonance at 13.9 ppm to the triaryl-substituted phosphorous atom and the resonance at 47.2 to the diphenylphosphine site carrying one amino group. The general shift of the ^{31}P resonances of **2** (18 VE system) to lower field compared to the model systems (16 VE systems) is due to the increased electron density. Hey-Hawkins *et al.* found the homoleptic nickel(0) complex $Ni(Ph_2P\text{-}NHPh)_2$ with a ^{31}P signal at 16.6 ppm.[19] Due to the completely asymmetric structure of **2**, resulting in four different phenyl groups, and the multiple P,H-couplings, the complete interpretation of the ^1H NMR spectrum is difficult. Nevertheless by means of a H,H-COSY experiment, the two sets of AB spin systems (8.54/7.12 ppm, $^2J_{HH}$ = 5.05 Hz; 8.19/7.33 ppm, $^2J_{HH}$ = 5.38 Hz) being affiliated to the two pyrimidine rings can easily be identified.

Since the resonance at 8.54 ppm shows a second coupling of 1.20 Hz (either to the NH-group or the N–P phosphorous atom), it can be assigned to the pyrimidine proton next to the ring nitrogen atom in the tridentate P,N,P-ligand. Furthermore there are the signals of two ABCD spin systems (7.84/7.65/7.58/7.50 and 7.62/6.75/6.35/6.26 ppm) standing for the two *ortho*-substituted phenylene rings. The latter one is considerably deshielded and can therefore be assigned to the bidentate ligand with the Ni–C bond. Examination of the course of the generation of **2** by ^{31}P NMR spectroscopy failed due to the formation of insoluble ($HL^{+}ClO_4^{-}$). However, no intermediate could be detected even at the beginning of the reaction either due to a very rapid transformation of this intermediate into **2** or due to a paramagnetic nature of the intermediate.

ESI-MS measurements further confirm the molecular composition of the cation of **2** (m/z = 767 amu with respect to ^{58}Ni, see the ESI†). In the infrared spectrum of **2**, one would expect to generally find the bands of three N–H stretching vibrations, one for the NH–PPh_2 unit and the symmetric and the asymmetric vibration of the NH_2 group. In fact, there are two bands, one at 3437 and a slightly stronger band at 3354 cm^{-1}. We assign the latter one to the overlapped bands of the N–H stretching vibration[10] and the symmetric NH_2 stretching vibration.[20]

Cyclic voltammetry was carried out to get an insight into the redox behaviour of compound **2**. The nickel(II) complex is irreversibly oxidized at a peak potential of 0.77 V in acetonitrile solution with respect to the SCE (for a graphic see the ESI†). No reduction could be observed up to a potential of −1.50 V. Electron rich square planar PCP-type pincer complexes of nickel(II) show similar oxidation potentials depending on the nature of the C-donor site,[21] while *e.g.* for less electron rich complexes such as $(PPh_3)_2Ni(NCS)_2$ no oxidation was found, but irreversible reduction processes.[22] This shows the electron-rich nature of the five-coordinate nickel(II) complex **2**.

We suggest an intramolecular mechanism for the P,C-bond cleavage and the P,N-bond formation. The nucleophilic character of the amino group of aminopyrimidines is not very strong. In the nucleophilic solvent methanol the formation of methoxy(diphenyl)phosphine as the main product should occur in an intermolecular reaction. We propose, that in the first step, the formation of the dicationic nickel(II) complex **A** takes place (Scheme 2, top). In **A** the two P,N-donors are coordinated in a square planar mode. This compound might undergo loose interaction with the perchlorate anions (not drawn). Provided that the P,N bond formation takes place in an intramolecular way, the two nitrogen resp. and the two phosphorous sites have to be oriented *trans* to each other, a situation which would also prevent steric hindrance of the two diphenylphosphino units.

We know from a X-ray structure analysis of the palladium(II) complex (**1**)$PdCl_2$,[5] wherein the palladium centre is *cis*-coordinated by the phosphorous and the nitrogen atom, that the six-membered ring including P, Pd, and N is severely bent. Due to the bending of the P,N units, compound **A** might exist in two isomeric forms (Scheme 2, top), wherein the bridging

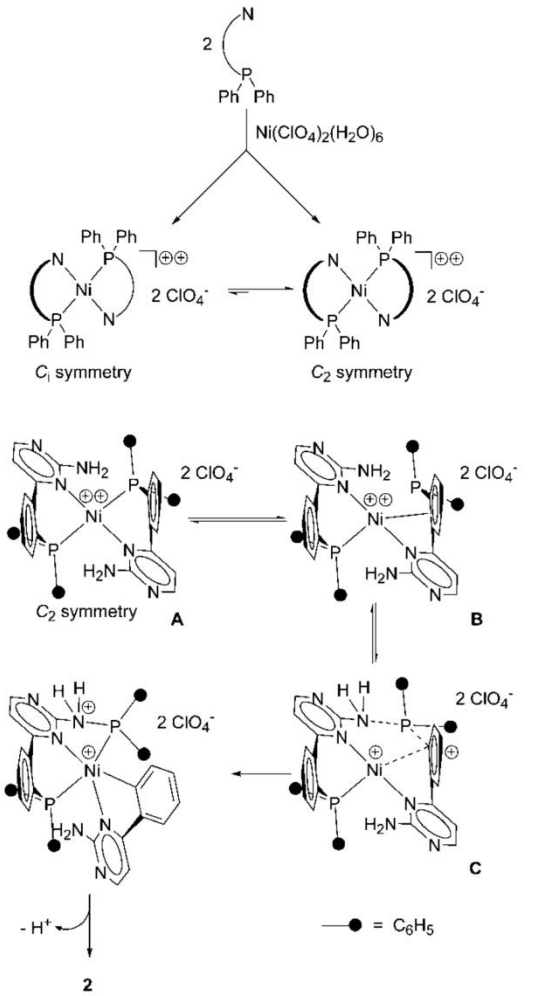

Scheme 2 Generation of the nickel(II) complex **2** by P,C-bond cleavage and subsequent P,N-bond formation.

phenylene units either point in opposite directions (C_i symmetry) or in the same direction (C_2 symmetry). According to preliminary quantum chemical calculations on the mechanism, the C_2 symmetric isomer is about 9 kcal mol^{-1} lower in energy than the C_i symmetric one. After Ni–P cleavage has occurred in the first step of the mechanism, the detached phosphorous atom has to move towards the NH_2 group of the second ligand. This is, in our opinion, strongly favoured for the C_2 symmetric isomer (Scheme 2, bottom), since the nickel site can only in this case undergo an interaction with the bridging phenylene unit, that will lead to an electrophilic attack at the phosphorous substituted carbon atom (**B**). This allows a neighboring amino group to perform a nucleophilic attack at the phosphorous atom which cleaves the P,C-bond and forms the P,N-bond (**C**). Finally a third equivalent of ligand **1**, which is necessary to obtain high yields of the product, takes over the

proton from the nitrogen atom and the aminophosphine coordinates to the nickel centre resulting in the formation of compound (**2**).

This kind of P,C-bond cleavage reaction is up to now limited to nickel(II) and ligand **1**. We have carried out the same reaction with manganese(II), iron(II), cobalt(II), copper(II) and zinc(II) perchlorates which do not show any reaction with the ligand. The same was observed for other triphenylphosphine functionalized tertiary aminopyrimidines and pyrazoles, which we frequently use in our group. In none of these cases, P,C-bond cleavage could be found. Instead, expected coordination compounds with intact ligand structures have been observed. The behaviour of these ligands might be explained by steric and electronic considerations: pyrazoles are poor nucleophiles since the N-σ orbital is occupied for the N–H bond, while the N-π orbital is conjugated in the 6-electron ring structure. For [(2-aminopyrimidin-4-yl)aryl]phosphanes carrying a tertiary amino group $-NR_2$, steric hindrance of the groups R will prevent the attack of the phosphorous atom at the amino group.

Experimental

General remarks

All reaction steps were carried out under an argon atmosphere using Schlenk techniques. Nickel(II) perchlorate hexahydrate was purchased from Sigma Aldrich and used without further purification. Ligand **1** was synthesized according to a published procedure.[5] All solvents were degassed according to standard techniques before use. ^{1}H, ^{13}C and ^{31}P NMR spectra were recorded on a Bruker Spectrospin Avance 400 device, ESI mass spectra were recorded on a Bruker Esquire 6000 equipment.

Synthesis of the nickel(II) complex 2

Nickel(II) perchlorate hexahydrate (373 mg, 1.02 mmol) was dissolved in methanol (20 ml) and **1** (1.11 g; 3.11 mmol) was added to the green solution. The resulting green suspension was stirred for 48 h at room temperature whereby its colour changed to red. The solvent was removed in vacuum and dichloromethane (20 ml) was added, leading to a red solution and a white precipitate, which was filtered off. After evaporation of the solvent from the filtrate, the remaining reddish-brown solid was stirred with toluene (15 ml) at room temperature for 16 h to dissolve residues of the free ligand **1**, then filtered off and dried under vacuum. To obtain crystals suitable for an X-ray structure analysis, the compound was recrystallized from a minimum amount of methanol. Yield: 778 mg (896 μmol; 88%) of a reddish-brown solid. Elemental analysis for $C_{44}H_{35}ClN_6NiO_4P_2$ (867.91): calcd C 60.89%, H 4.06%, N 9.68%; found C 61.19%, H 4.24%, N 9.48%.

Cyclic voltammetry

Electrochemical experiments were performed at room temperature in 0.2 M solution of NBu_4ClO_4 in acetonitrile using a potentiostat/galvanostat 273 A of Princeton Applied Research, a platinum foil as the working electrode, a platinum net as the counter electrode and a saturated calomel electrode as the reference electrode. The scan rate was 100 mV s^{-1}. The ferrocene/ferrocenium redox couple served as the internal reference (+0.42 V *vs.* SCE).

Table 1 Crystallographic data, data collection and refinement

	2
Empirical formula	$C_{46}H_{43}ClN_6NiO_6P_2$
Formula weight	931.96
Crystal size [mm]	0.16 × 0.10 × 0.06
T [K]	150(2)
λ [Å]	1.54184
Crystal system	Triclinic
Space group	$P\bar{1}$
a [Å]	11.6115(7)
b [Å]	13.4918(9)
c [Å]	14.9171(10)
α [°]	87.203(5)
β [°]	75.689(6)
γ [°]	70.567(6)
V [Å^3]	2134.0(2)
Z	2
$\rho_{calcd.}$ [g cm^{-3}]	1.450
μ [mm^{-1}]	2.417
θ-range [°]	3.48–62.85
Refl. coll.	14 868
Indep. refl.	6800 [R_{int} = 0.0275]
Data/restr./param.	6800/122/612
Final R indices [$I > 2\sigma(I)$]^a	0.0525, 0.1340
R indices (all data)	0.0610, 0.1419
GooF^b	1.027
$\Delta\rho_{max/min}$ (e Å^{-3})	1.307/−1.224

^{a} $R_1 = \sum||F_o| - |F_c||/\sum|F_o|$, $\omega R_2 = [\sum\omega(F_o^2 - F_c^2)^2/\sum\omega F_o^2]^{1/2}$. ^{b} GooF = $[\sum\omega(F_o^2 - F_c^2)^2/(n-p)]^{1/2}$.

X-ray structure analysis of 2

Crystal data and refinement parameters for compound **2** are collected in Table 1. The structure was solved using a direct method (SIR92[23]), completed by subsequent difference Fourier syntheses, and refined by full-matrix least-squares procedures.[24] A semi-empirical absorption correction from equivalents (Multiscan) was carried out.[25] The molecule was found co-crystallized with two equivalents of methanol, one of which being disordered. The hydrogen atoms bound to the nitrogen atoms N3 and N6 were located in the difference Fourier synthesis and were refined semi-freely with the help of a distance restraint, while constraining their U-values to 1.2 times the $U_{(eq)}$ values of the corresponding nitrogen atoms. All the other hydrogen atoms were placed in calculated positions and refined using a riding model. CCDC-1014112 contains the supplementary crystallographic data for this paper.

Conclusions

The reaction of [(2-aminopyrimidin-4-yl)aryl]phosphane with nickel(II)perchlorate hexahydrate leads to a novel five-coordinate nickel(II) complex in high yield wherein the nickel(II) site

is coordinated by a tridentate P,N,P′-ligand and a bidentate, carbanionic N,C-ligand. Both ligand systems are formed from the bidentate[(2-aminopyrimidin-4-yl)aryl]phosphane which undergoes a P,C-bond cleavage. The pyridinyl amino group acts as a nucleophile and takes over a PPh_2 unit in an intramolecular process from the neighbouring ligand moiety.

Acknowledgements

Financial support from the DFG-funded transregional collaborative research centre SFB/TRR 88 "Cooperative effects in homo- and heterometallic complexes (3MET)" is gratefully acknowledged.

Notes and references

1 K. Tamao, K. Sumitani and M. Kumada, *J. Am. Chem. Soc.*, 1972, **94**, 4374; R. J. P. Corriu and J. P. Masse, *J. Chem. Soc., Chem. Commun.*, 1972, 144; J. Terao, H. Watanabe, A. Ikumi, H. Kuniyasu and N. Kambe, *J. Am. Chem. Soc.*, 2002, **124**, 4222; J. Terao, A. Ikumi, H. Kuniyasu and N. Kambe, *J. Am. Chem. Soc.*, 2003, **125**, 5646; L.-C. Liang, P.-S. Chien, J.-M. Lin, M.-H. Huang, Y.-L. Huang and J.-H. Liao, *Organometallics*, 2006, **25**, 1399; O. Vechorkin and X. Hu, *Angew. Chem., Int. Ed.*, 2009, **48**, 2937; O. Vechorkin, Z. Csok, R. Scopelliti and X. Hu, *Chem. – Eur. J.*, 2009, **15**, 3889; S. Gu and W. Chen, *Organometallics*, 2009, **28**, 909.

2 A. Devasagayaraj, T. Stüdemann and P. Knochel, *Angew. Chem., Int. Ed. Engl.*, 1995, **34**, 2723; R. Giovannini and P. Knochel, *J. Am. Chem. Soc.*, 1998, **120**, 11186; A. E. Jensen, W. Dohle and P. Knochel, *Tetrahedron*, 2000, **56**, 4197; C. E. Tucker and J. G. de Vries, *Top. Catal.*, 2002, **19**, 111; J. Zhou and G. C. Fu, *J. Am. Chem. Soc.*, 2003, **125**, 12527; J. Zhou and G. C. Fu, *J. Am. Chem. Soc.*, 2003, **125**, 14726; A. Gavryushin, C. Kofink, G. Manolikakes and P. Knochel, *Org. Lett.*, 2005, **7**, 4871; A. Gavryushin, C. Kofink, G. Manolikakes and P. Knochel, *Tetrahedron*, 2006, **62**, 7521; E. Negishi, *Angew. Chem., Int. Ed.*, 2011, **50**, 6738.

3 W. Keim, B. Hoffmann, R. Lodewick, M. Peuckert and G. Schmitt, *J. Mol. Catal.*, 1979, **6**, 79; M. Peuckert and W. Keim, *Organometallics*, 1983, **2**, 594; A. Behr, V. Falbe, U. Freudenberg and W. Keim, *Isr. J. Chem.*, 1986, **27**, 277; G. Wilke, *Angew. Chem., Int. Ed. Engl.*, 1988, **27**, 185; N. A. Kolhatkar, A. M. Monfette, S. Lin and M. J. Miri, *J. Polym. Sci.*, 2002, **50**, 986; J. N. L. Dennett, A. L. Gillon, K. Heslop, D. J. Hyett, J. S. Fleming, C. E. Lloyd-Jones, A. G. Orpen, P. G. Pringle, D. F. Wass, J. N. Scutt and R. H. Weatherhead, *Organometallics*, 2004, **23**, 6077; G. Noël, J. C. Röder, S. Dechert, H. Pritzkow, L. Bolk, S. Mecking and F. Meyer, *Adv. Synth. Catal.*, 2006, **348**, 887; F.-S. Liu, H.-B. Hu, Y. Xu, L.-H. Guo, S.-B. Zai, K.-M. Song, H.-Y. Gao, L. Zhang, F.-M. Zhu and Q. Wu, *Macromolecules*, 2009, **42**, 7789.

4 G. Nord, A. C. Hazell, R. G. Hazell and O. Farver, *Inorg. Chem.*, 1983, **22**, 3429; P. J. Spellane, R. J. Watts and C. J. Curtis, *Inorg. Chem.*, 1983, **22**, 4060; P. S. Braterman, G. H. Heat, A. J. Mackenzie, B. C. Noble, R. D. Peacock and L. J. Yellowlees, *Inorg. Chem.*, 1984, **23**, 3425; E. C. Tyo, A. W. Castleman Jr., D. Schröder, P. Milko, J. Roithova, J. M. Ortega, M. A. Cinellu, F. Cocco and G. Minghetti, *J. Am. Chem. Soc.*, 2009, **131**, 13009; G. Minghetti, S. Stoccoro, M. A. Cinellu, G. L. Petretto and A. Zucca, *Organometallics*, 2008, **27**, 3415.

5 S. Farsadpour, L. Taghizadeh Ghoochany, Y. Sun and W. R. Thiel, *Eur. J. Inorg. Chem.*, 2011, 4603; S. Farsadpour, L. Taghizadeh Ghoochany, S. Shylesh, G. Dörr, A. Seifert, S. Ernst and W. R. Thiel, *ChemCatChem*, 2012, **4**, 395; L. Taghizadeh Ghoochany, C. Kerner, S. Farsadpour, Y. Sun, F. Menges, G. Niedner-Schatteburg and W. R. Thiel, *Eur. J. Inorg. Chem.*, 2013, 4305.

6 C. M. Chen, Q. Z. Ye, Z. M. Zhu, B. L. Wanner and C. T. Walsh, *J. Biol. Chem.*, 1990, **265**, 4461; J. W. McGrath, G. B. Wisdom, G. McMullan, M. J. Larkin and J. P. Quinn, *Eur. J. Biochem.*, 1995, **234**, 225; A. Inoue, H. Shinokubo and K. Oshima, *J. Am. Chem. Soc.*, 2003, **125**, 1484.

7 M. Randles, A. C. Willis, M. P. Cifuentes and M. G. Humphrey, *J. Organomet. Chem.*, 2007, **692**, 4467; W. H. Watson, G. Wu and M. G. Richmond, *Organometallics*, 2006, **25**, 930; S. M. Waterman, V.-A. Tolhurst, M. G. Humphrey, B. W. Skelton and A. H. White, *J. Organomet. Chem.*, 1996, **515**, 89; A. J. Deeming, M. K. Shinhmar, A. J. Arce and Y. De Sanctis, *J. Chem. Soc., Dalton Trans.*, 1999, 1153.

8 N. M. Doherty, G. Hogarth, S. A. R. Knox, K. A. Macpherson, F. Melchior, D. A. V. Morton and A. G. Orpen, *Inorg. Chim. Acta*, 1992, **198–200**, 257; W.-D. Wang and R. Eisenberg, *J. Am. Chem. Soc.*, 1990, **112**, 1833; H. Wachtler, W. Schuh, K.-H. Ongania, K. Wurst and P. Peringer, *Organometallics*, 1998, **17**, 5640; P. E. Garrou, *Chem. Rev.*, 1985, **85**, 171.

9 J. F. Hartwig, R. G. Bergman and R. A. Andersen, *J. Organomet. Chem.*, 1990, **394**, 417.

10 P. H. M. Budzelaar, J. A. van Doorn and N. Meijboom, *Recl. Trav. Chim. Pays-Bas*, 1991, **110**, 420–432.

11 M. F. Cain, S. C. Reynolds, B. J. Anderson, D. S. Glueck, J. A. Golen, C. E. Moore and A. L. Rheingold, *Inorg. Chim. Acta*, 2011, **369**, 55; S. A. Reiter, S. D. Nogai and H. Schmidbaur, *Z. Anorg. Allg. Chem.*, 2005, **631**, 2595.

12 Y. El Harouch, V. Cadierno, A. Igau, B. Donnadieu and J.-P. Majoral, *J. Organomet. Chem.*, 2004, **689**, 953.

13 A. Caballero, F. A. Jalón, B. R. Manzano, G. Espino, M. Pérez-Manrique, A. Mucientes, F. J. Poblete and M. Maestro, *Organometallics*, 2004, **23**, 5694; A. Inoue, H. Shinokubo and K. Oshima, *J. Am. Chem. Soc.*, 2003, **125**, 1484; T. J. Geldbach and P. S. Pregosin, *Eur. J. Inorg. Chem.*, 2002, 1907; S.-C. Tsai, Y.-S. Fu, J.-H. Liao and S. J. Yu, *Helv. Chim. Acta*, 2006, **89**, 3007.

14 A. Reis, D. Dehe, S. Farsadpour, I. Munstein, Y. Sun and W. R. Thiel, *New J. Chem.*, 2011, **35**, 2488; D. Dehe, I. Munstein, A. Reis and W. R. Thiel, *J. Org. Chem.*, 2011, **76**, 1151.
15 J. K. Stalick and J. A. Ibers, *Inorg. Chem.*, 1969, **8**, 1084; J. K. Stalick and J. A. Ibers, *Inorg. Chem.*, 1969, **8**, 1090; P. S. Shetty and Q. Fernando, *J. Am. Chem. Soc.*, 1970, **92**, 3964; T. E. Kokina, L. A. Glinskaya, R. F. Klevtsova and S. V. Larionov, *J. Struct. Chem.*, 2002, **43**, 312; S. V. Larionov, T. E. Kokina, L. A. Glinskaya and R. F. Klevtsova, *Russ. J. Coord. Chem.*, 2002, **28**, 560.
16 (*a*) F. Bachechi, *Struct. Chem.*, 2003, **14**, 263.H. Glas, K. Köhler, P. Maas, E. Herdtweck, M. Spiegler and W. R. Thiel, *Eur. J. Inorg. Chem.*, 2001, **4**, 2075.
17 A. Zeller, E. Herdtweck and T. Strassner, *Eur. J. Inorg. Chem.*, 2003, 1802; H. A. Bronstein and C. K. Luscombe, *J. Am. Chem. Soc.*, 2009, **131**, 12894.
18 D. Benito-Garagorri, V. Bocokić, K. Mereiter and K. Kirchner, *Organometallics*, 2006, **25**, 3817.
19 O. Kühl, P. C. Junk and E. Hey-Hawkins, *Z. Anorg. Allg. Chem.*, 2000, **626**, 1591.
20 (*a*) L. Varga, T. Nagy, I. Kövesdi, J. Benet-Buchholz, G. Dormán, L. Ürge and F. Darvas, *Tetrahedron*, 2003, **59**, 655.A. Alberola, C. Andrés, A. González Ortega, R. Pedrosa and M. Vicente, *Synth. Commun.*, 1987, **17**, 1309; X.-Y. Yu, P.-G. Yi, D.-H. Ji, B.-R. Zeng, X.-F. Li and X. Xu, *Dalton Trans.*, 2012, **41**, 3684.
21 A. Castonguay, A. L. Beauchamp and D. Zargarian, *Organometallics*, 2008, **27**, 5723.
22 K. Ramalingam, R. Thiruneelakandan, G. Bocelli and L. Righi, *Transition Met. Chem.*, 2012, **37**, 265.
23 A. Altomare, G. Cascarano, C. Giacovazzo, A. Guagliardi, M. C. Burla, G. Polidori and M. Camalli, *J. Appl. Crystallogr.*, 1994, **27**, 435.
24 G. M. Sheldrick, *Acta Crystallogr., Sect. A: Fundam. Crystallogr.*, 2008, **64**, 112.
25 *CrysAlisPro*, Agilent Technologies, Version 1.171.36.24, 2012.

11.5 Pump-Probe Fragmentation Action Spectroscopy: A Powerful Tool to Unravel Light-Induced Processes in Molecular Photocatalysts

Dimitri Imanbaew[a], Johannes Lang[a], Maxim F. Gelin[c], Simon Kaufhold[b], Maximilian G. Pfeffer[b], Sven Rau[b], and Christoph Riehn[a]

a) Fachbereich Chemie and Forschungszentrum OPTIMAS
Technische Universität Kaiserslautern,
67663 Kaiserslautern, Germany

b) Institut für Anorganische Chemie I
Universität Ulm
89081 Ulm, Germany

c) Fakultät für Chemie
Technische Universität München
85747 Garching, Germany

11.5.1 Preamble

The following chapter is a reprint of a publication in the journal "Angewandte Chemie – International Edition".

D. Imanbaew performed time resolved measurements and data evaluations. M. F. Gelin provided simulated transient anisotropc data and theoretical considerations thereof. S. Kaufhold and M. G. Pfeffer from the research group of Prof. S. Rau synthesized the complexes and characterized them in the condensed phase. D. Imanbaew wrote the manuscript and was supported by C. Riehn and the research group of Prof. S. Rau. I contributed with Collision Induced Dissociation (CID) experiments and discussions.

Full Reference:

Pump-probe fragmentation action spectroscopy: a powerful tool to unravel light-inducedprocesses in molecular photocatalysts
D. Imanbaew, **J. Lang**, M. F. Gelin, S. Kaufhold, M. G. Pfeffer, S. Rau and C. Riehn,
Angewandte Chemie International Edition, **2017**, 56, 5471-5474.
http://dx.doi.org/10.1002/anie.201612302

11.5.2 Reprint

Reprint Licence

Copyright Clearance Center RightsLink®

My Orders My Library My Profile Welcome jlang@chemie.uni-kl.de Log out | Help

My Orders > Orders > All Orders

License Details

This Agreement between Johannes Lang ("You") and John Wiley and Sons ("John Wiley and Sons") consists of your license details and the terms and conditions provided by John Wiley and Sons and Copyright Clearance Center.

printable details

License Number	4073750530221
License date	Mar 21, 2017
Licensed Content Publisher	John Wiley and Sons
Licensed Content Publication	Angewandte Chemie International Edition
Licensed Content Title	Pump-Probe Fragmentation Action Spectroscopy: A Powerful Tool to Unravel Light-Induced Processes in Molecular Photocatalysts
Licensed Content Author	Dimitri Imanbaew,Johannes Lang,Maxim F. Gelin,Simon Kaufhold,Michael G. Pfeffer,Sven Rau,Christoph Riehn
Licensed Content Date	Mar 1, 2017
Licensed Content Pages	1
Type of Use	Dissertation/Thesis
Requestor type	Author of this Wiley article
Format	Print and electronic
Portion	Full article
Will you be translating?	No
Title of your thesis / dissertation	Structure, reactivity and magnetism of isolated mononuclear and oligonuclear transition metal complexes elucidated by action spectroscopy and theory in concert
Expected completion date	Apr 2017
Expected size (number of pages)	200
Requestor Location	Johannes Lang Raiffeisenstraße 3 Kaiserslautern, 67655 Germany Attn: Johannes Lang
Publisher Tax ID	EU826007151
Billing Type	Invoice
Billing address	Johannes Lang Raiffeisenstraße 3 Kaiserslautern, Germany 67655 Attn: Johannes Lang
Total	**0.00 EUR**

GDCh Communications Angewandte International Edition Chemie

Supramolecular Chemistry Hot Paper

International Edition: DOI: 10.1002/anie.201612302
German Edition: DOI: 10.1002/ange.201612302

Pump-Probe Fragmentation Action Spectroscopy: A Powerful Tool to Unravel Light-Induced Processes in Molecular Photocatalysts

Dimitri Imanbaew, Johannes Lang, Maxim F. Gelin, Simon Kaufhold, Michael G. Pfeffer, Sven Rau, and Christoph Riehn**

Abstract: *We present a proof of concept that ultrafast dynamics combined with photochemical stability information of molecular photocatalysts can be acquired by electrospray ionization mass spectrometry combined with time-resolved femtosecond laser spectroscopy in an ion trap. This pump-probe "fragmentation action spectroscopy" gives straightforward access to information that usually requires high purity compounds and great experimental efforts. Results of gas-phase studies on the electronic dynamics of two supramolecular photocatalysts compare well to previous findings in solution and give further evidence for a directed electron transfer, a key process for photocatalytic hydrogen generation.*

To develop more efficient molecular photocatalysts, insight into their intrinsic photophysical properties is of utmost importance. Gathering information on the lifetimes and localization of the excited states involved in electron transfer processes usually requires high purity compounds for studies in solution such as in resonance Raman and transient absorption (TA) spectroscopy. Since the chemical stability of the photocatalyst is crucial for overall performance, corresponding studies with methods like dynamic light scattering (DLS), transmission electron microscopy (TEM), and X-ray absorption spectroscopy need to be performed.[1,2] These investigations are vital; however, they are also time-consuming and require larger amounts of samples and therefore encumber the urgently needed fast and efficient research for sustainable energy sources.[3] Herein, we show by comparing new gas-phase studies on **Ru-Pt** $[(^t\text{bbpy})_2\text{Ru}(\text{tpphz})\text{Pt}(\text{Cl})_2]^{2+}$, (^{t}bbpy = 4,4′-di-tert-butyl-2,2′-bipyridin, tpphz = tetrapyrido[3,2-a:2′3′-c:3″,2′-h:2‴,3‴-j]phenazine) and **Ru-Pd** $[(^t\text{bbpy})_2\text{Ru}(\text{tpphz})\text{Pd}(\text{Cl})_2]^{2+}$ (Figure 1) to solution-phase results that pump-probe fragmentation action spectroscopy is a powerful tool for unraveling a multitude of relevant properties in one step.

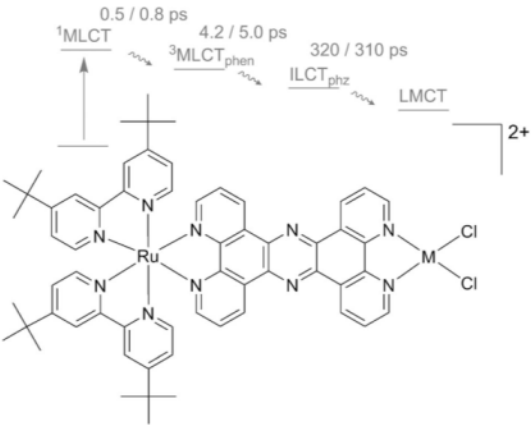

Figure 1. Schematic structure of Ru-M (M = Pt, Pd) and time constants of excited-state dynamics from previous solution experiments of **Ru-Pt**/**Ru-Pd**.[9,10].

Zewail et al. were the first to apply time-resolved photofragmentation (PF) spectroscopy to small, jet-cooled molecules for the study of bond-breaking on a picosecond (ps)[4] and femtosecond (fs)[5] time-scale. Recently, Zavras et al., further emphasized the combination of mass spectrometry (MS) with gas-phase photochemistry for the elucidation of reaction processes.[6] Inspired by this, we were eager to broaden this approach and used electrospray ionization (ESI) ion trap MS combined with UV laser photo-induced dissociation, which allows the study of ultrafast electronic dynamics by pump-probe PF.[7,8] Herein, we show that pump-probe fragmentation action spectroscopy is an extremely powerful tool for unraveling a multitude of relevant properties in one step, by comparing the gas-phase studies with solution-phase results that have been gathered over the last decade.[9–12]

Spectroscopic investigations of the excitation and charge-transfer processes in solution were performed by fs TA spectroscopy.[9,10] Photoactivation proceeds in three steps: 1) Charge localization on the phenanthroline (phen) sphere, 2) ILCT (intra-ligand charge transfer) to form a phenazine-centered (phz) state, and 3) electron transfer to the catalytic

[*] D. Imanbaew, J. Lang, Dr. C. Riehn
Fachbereich Chemie, TU Kaiserslautern
Erwin-Schrödinger-Str. 52–54, 67663 Kaiserslautern (Germany)
E-mail: imanbaew@chemie.uni-kl.de
riehn@chemie.uni-kl.de

Dr. M. F. Gelin
Fakultät für Chemie, TU München
Lichtenbergstraße 4, 85747 Garching (Germany)

S. Kaufhold, Dr. M. G. Pfeffer, Prof. Dr. S. Rau
Institut für Anorganische Chemie I, Universität Ulm
Albert-Einstein-Allee, 89081 Ulm (Germany)

Dr. C. Riehn
Landesforschungszentrum OPTIMAS
Erwin-Schrödinger-Str. 46, 67663 Kaiserslautern (Germany)

Supporting information, including experimental procedures, mass spectrometry and PF data, fitted decay parameters, DFT data, and theoretical considerations, and the ORCID identification number(s) for the author(s) of this article can be found under: http://dx.doi.org/10.1002/anie.201612302.

center (LMCT; ligand-to-metal charge transfer). Time constants for these processes are nearly identical for **Ru-Pd** and **Ru-Pt** (Figure 1).[9,10] However, the photocatalytic performance of **Ru-Pd** [turnover number (TON) ≈ 234] is much higher than that of **Ru-Pt** (TON ≈ 10).[10,11] Moreover, it became apparent that the low photostability of **Ru-Pd** leads to formation of Pd colloids, which may act as catalytically active species in solution, whereas **Ru-Pt** did not decompose.[10,11]

In the ESI-MS experiments, the main mass peaks are *m*/*z* 600.0 for **Ru-Pd** and *m*/*z* 644.0 for **Ru-Pt,** which correspond to the doubly charged complexes, verified by spacing and isotopic intensity distribution (Supporting Information, Figure S1). Upon collision-induced dissociation (CID), the formal loss of MCl_2 was found to be the major fragmentation channel (80 % for **Ru-Pd** and 60 % for **Ru-Pt**, Supporting Information, Figure S2 and Table S1). PF experiments (range 240–480 nm) were carried out to study the intrinsic response of the complex ions under irradiation. Their PF behavior is similar to results obtained by CID (Table S1), however, **Ru-Pd** exhibits a higher PF yield compared to **Ru-Pt** (under identical ESI conditions; Supporting Information, Figure S3), which is in line with the lower photostability of **Ru-Pd** under catalytic conditions.[10,11] This is also supported by DFT calculations yielding a Gibbs free energy (at RT) of 181 kJ mol^{-1} for **Ru-Pd** and 250 kJ mol^{-1} for **Ru-Pt** for the respective $RuMCl_2 \rightarrow Ru + MCl_2$ fragmentation channel, assuming singlet configuration of the parent compounds and fragments. The gas-phase PF spectra compare relatively well with the absorption spectra recorded in solution (Figure 2).

However, three differences are obvious: First, at approximately 310 nm a strong absorption band is visible in the PF spectra for both compounds, while only a weak shoulder is present in the solution spectra at 320–330 nm. The band at approximately 310 nm can be assigned to a phen/tpphz-centered π–π* transition,[13] as recent TD-DFT calculations resulted in an assignment of the 328 nm shoulder in acetonitrile to an overlap of three transitions of $\pi^*_{tpphz} \leftarrow \pi_{tpphz}, d_{Pd}, n_{Cl}$, $\pi^*_{tpphz} \leftarrow d_{Pd/Pt}, n_{Cl}$, and $\pi^*_{tpphz} \leftarrow d_{Pd/Pt}, n_{Cl}, \pi_{tpphz}$ character.[10] Excitation of the bridging tpphz ligand may lead to a high PF yield in the gas phase, as it is positioned closer and is thus probably better coupled to the $PdCl_2/PtCl_2$ formal leaving group. Second, we notice a weak and structureless charge transfer (CT) band region (> 400 nm) for both complexes in the gas phase. Weak CT bands were also observed for other Ru^{II} complexes and explained in terms of collisional quenching of long-lived photoexcited or highly vibrationally excited ions by helium buffer gas in the ion trap.[7] Furthermore, the photon energy at 440 nm corresponds to circa 272 kJ mol^{-1}, which complies with the calculated dissociation thresholds ($RuMCl_2 \rightarrow Ru + MCl_2$). Thus, at longer wavelength either only ions from the high-energy tail of the Boltzmann distribution contain enough energy for dissociation or two photons have to be absorbed prior to dissociation. This is supported by the laser power dependence of the PF signal (Supporting Information, Figure S4). Lastly, we do not observe the narrow additional features in the PF spectrum of **Ru-Pd**, which are present in the liquid-phase spectrum (350–400 nm). Based on TD-DFT calculations, this absorption band in the **Ru-Pd** spectrum was attributed to a transition of mixed $\pi^*_{tpphz} \leftarrow \pi_{tpphz}/\pi^*_{tpphz} \leftarrow d_{Pd}/\pi^*_{tpphz} \leftarrow n_{Cl}$ character.[10] A similar transition was calculated for **Ru-Pt**, however, with a bathochromic shift to 407 nm (from **Ru-Pd** to **Ru-Pt**) and a parallel decrease in intensity, explaining the less structured solution absorption spectrum for **Ru-Pt**.[10] Due to the relatively low intensity of this band in solution, the broad spectral bandwidth of our fs pulses (ca. 8–10 nm FWHM in a range of 350–400 nm) and the non-linear nature of the performed action spectroscopy, we do not consider the slight differences in the gas-phase CT bands of **Ru-Pd** and **Ru-Pt** significant for a further interpretation.

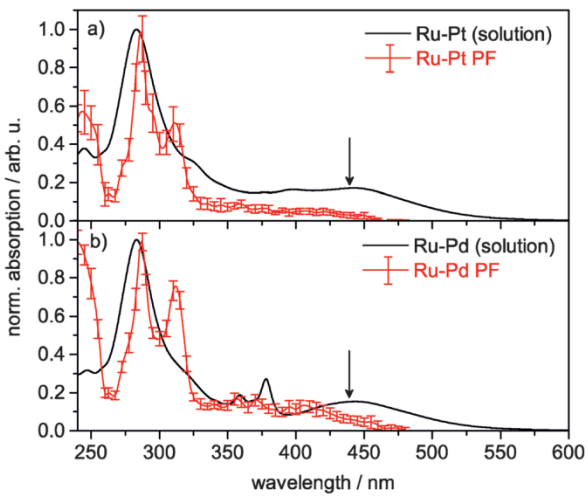

Figure 2. Gas-phase UV/Vis photofragmentation spectra (red) and normalized absorption spectra in acetonitrile solution ($c = 1 \times 10^{-5}$ M) (black) of a) **Ru-Pt** and b) **Ru-Pd**. Pump wavelength (440 nm) for time-resolved experiments marked by arrows.

Excited-state dynamics and pump-probe anisotropy were measured for both complexes by recording time-resolved PF transients generated by two-color photoexcitation (details given in Supporting Information).

The transient signal of **Ru-Pt** (Figure 3) decays within approximately 15 ps to a near constant level that is maintained for more than 800 ps (max. delay). The signal was fitted to a triexponential decay of $\tau_1 = 0.6 \pm 0.1$ ps, $\tau_2 = 6.5 \pm 1.3$ ps, and $\tau_3 \gg 800$ ps. The time constants τ_1 and τ_2 compare well to the values obtained by TA in acetonitrile (0.5 ps, 4.2 ps, and 320 ps).[10] The value for τ_3, attributable to a LMCT from the tpphz bridge to the Pt center, is much higher than the one reported in solution. For **Ru-Pd,** TA measurements showed a strong dependence of the LMCT time constant on solvent polarity,[9] which increases from 320 ps (MeCN) to 740 ps (CH_2Cl_2). Hence, we assume that the driving force for generating a strongly charge-separated state will be even smaller in the gas phase, resulting in a longer lifetime.

Transient anisotropy (theoretical considerations in the Supporting Information, p. 20 ff.) was determined by recording the transients of **Ru-Pt** at parallel ($I_{\parallel}(t)$) and perpendicular ($I_{\perp}(t)$) relative polarization of pump and probe laser pulses (Figure 4 a).

$I_{\parallel}(t)$ exhibits a strong increase and subsequently decays within circa 15 ps, while for $I_{\perp}(t)$ the increase is smaller and

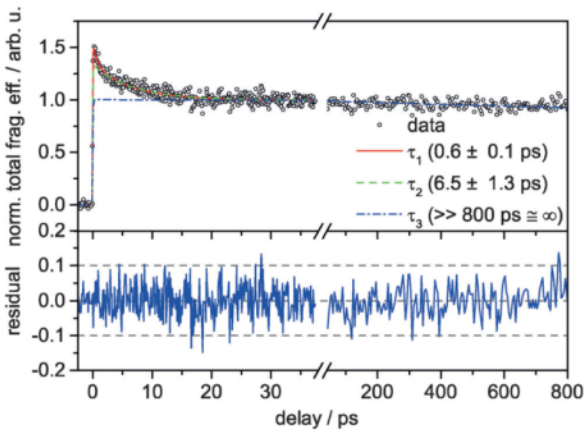

Figure 3. Normalized transient total fragment ion intensity of **Ru-Pt** recorded at the magic angle; $\lambda_{pump} = 440$ nm (1 μJ) and $\lambda_{probe} = 1200$ nm (60 μJ). Decomposition of fit plotted.

after a short (1–2 ps) decay the transient rises to coincide with $I_{\parallel}(t)$ after circa 15 ps (Figure 4a). This polarization dependence points towards molecular alignment by photoexcitation followed by rotational dephasing.[14,15] From the experimental transients the anisotropy function $r(t)$ was calculated [Figure 4b, Eq. (S1)]. The initial anisotropy $r(t=0) = r_0 = 0.31 \pm 0.04$ has a value smaller than expected for a parallel orientation of the transition dipole moment (TM) for the pump ($S_1 \leftarrow S_0$, μ_{pump}) and probe ($S_n \leftarrow S_1$, μ_{probe}) electronic transitions [0.4 for $(1+1')$ and 0.57 for $(1+2')$ excitation]. From the experimental value of r_0 we obtain an angle of 22.8° and 33.5° between the pump and probe TMs for a $(1+1')$ and $(1+2')$ photon process, respectively. If the latter process would apply to our results, its value of 33.5° could be

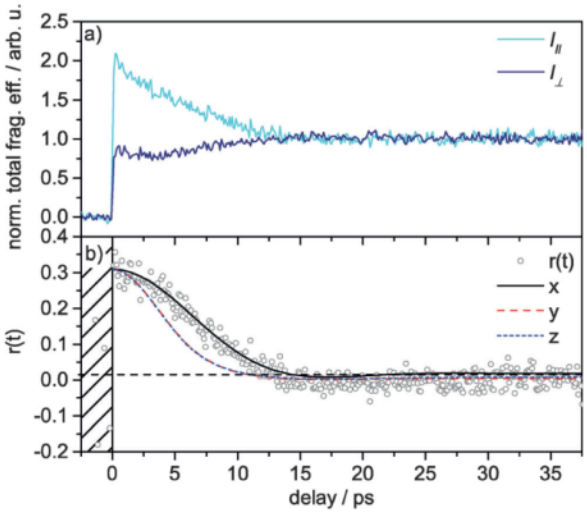

Figure 4. a) Normalized transient total fragment ion intensity of **Ru-Pt** at parallel (cyan) and perpendicular (dark blue) relative polarization of pump and probe pulses; $\lambda_{pump} = 440$ nm (1 μJ) and $\lambda_{probe} = 1200$ nm (60 μJ). b) Anisotropy function $r(t)$ calculated from data of Figure 4a. Simulations: $T = 310$ K, transition dipole moments parallel to *x*-, *y*-, or *z*-axis; rotational constants from DFT calculation (Table S3).

interpreted as the angle between the TM for the primary ^{1}MLCT excitation (Ru^{II} to ^{t}bbpy ligand) and the TM for the excited state absorption of the quickly formed $^3MLCT_{tpphz}$ state. Based on this analysis of our data on **Ru-Pt**, we infer that, even if we assume an initial excitation and charge distribution over both ^{t}bbpy ligands, the charge ends up eventually on the tpphz bridging ligand.

Moreover, from $r(t)$ (Figure 4b) we obtain an anisotropy decay time (dephasing time of the rotational coherence) of circa 15 ps. The time for reaching the minimum anisotropy value (τ_{dephas}) can be estimated from the molecular moments of inertia and the temperature T of the ensemble [Eq. (S22), Supporting Information]. It was found to be $\tau_{dephas} = 15.1$ ps (rotation around *y*-axis; Supporting Information, Figure S11), $\tau_{dephas} = 15.4$ ps (*z*-axis), and $\tau_{dephas} = 7.3$ ps (*x*-axis), which agrees with the experimental data upon assumption of an *x*-axis alignment. We calculated time-resolved orientational correlation functions of the TMs (see Supporting Information, p. 19 ff) assuming that the TMs are oriented along one of the molecular axes.[16] The simulation based on an orientation of the TM along the *x*-axis is in good agreement with our data (Figure 4b). Since **Ru-Pt** (and **Ru-Pd**) represents a near prolate top ($I_x < I_y \approx I_z$; Supporting Information, Table S3), the rotational dynamics of the *x*-axis aligned TM is determined by rotational motion along the perpendicular *y*- and *z*-axes. Thus, the assigned *x*-axis (tpphz-axis) orientation of the TM supports the estimation of τ_{dephas} above and confirms the pump-induced ultrafast charge localization on the tpphz bridge.

For **Ru-Pd** quite similar ultrafast electronic and rotational dynamics were found (a thorough discussion of the transient PF and anisotropy data is given in the Supporting Information, p. 9 ff.). The obtained time constants are $\tau_1 = 0.9 \pm 0.4$ ps, $\tau_2 = 6.9 \pm 2.1$ ps, and $\tau_3 \gg 800$ ps with τ_1 and τ_2 closely matching reported solution results but τ_3 having a much higher value. Analysis of the respective anisotropy function also suggests the fast formation of a tpphz-centered excited state.

In analogy to results published by Wächtler et al.,[12] we started transient photofragmentation measurements on both systems (**Ru-Pt** and **Ru-Pd**) at a longer pump wavelength (480 nm). This should involve an additional transition onto the phen unit of the tpphz bridge.[12] Our preliminary results confirm the previously reported acceleration of the sub-ps dynamics, when exciting at longer wavelengths.[12] Furthermore, the initial anisotropy determined from polarization-dependent measurements amounts to $r(t=0) = r_0 = 0.40 \pm 0.04$, giving a more parallel orientation of the pump and probe TMs and thus a more directed CT onto the bridging ligand. This is in accord with previous studies on the excitation-wavelength-dependent catalytic activity of **Ru-Pd**, which exhibited higher photon-to-hydrogen conversion efficiency for photons of longer wavelength, correlated with relative resonant Raman band intensities of the tpphz bridging ligand.[17] These preliminary results are presented in the Supporting Information (cf. p. 7 f. and p. 11 f.).

We studied the photo-induced fragmentation of two hydrogen-generating supramolecular photocatalysts (**Ru-Pt** and **Ru-Pd**) in an ion trap, leading to the first gas-phase UV/Vis spectra that serve as references for future ab initio

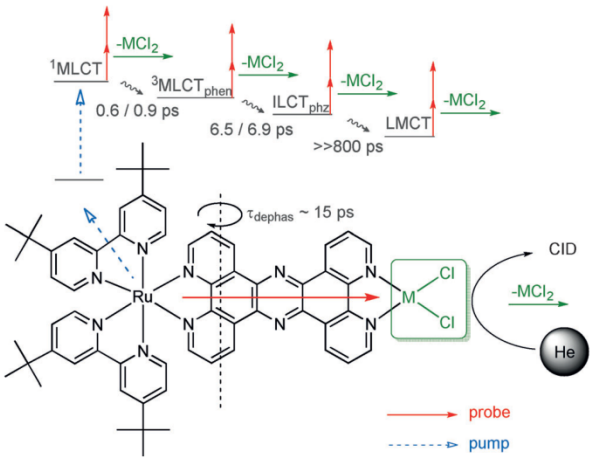

Figure 5. Summary of ultrafast electronic dynamics and rotational motion of **Ru-M** (M = Pt, Pd) by transient photofragmentation in the gas phase. Orientation of the transition dipole moments for the pump (blue, dashed) and probe (red, solid) absorption process marked by arrows. Only the most abundant neutral loss (MCl_2) after photofragmentation and collision-induced dissociation (CID) is given.

calculations. We observed an intrinsically lower photostability of **Ru-Pd**, which is in agreement with previous studies.[10,11] Furthermore, we recorded the intrinsic photodynamics of the two compounds, as summarized in Figure 5.

In analogy to the processes taking place in solution, the probe pulse leads to a ^{1}MLCT excitation based on the ^{t}bbpy ligands, followed by ultrafast intersystem crossing on a sub-100 fs timescale to form a ^{3}MLCT state delocalized over the Ru^{II} ligand sphere.[12] The latter process is not observed in this study owing to the limited time resolution (of ca. 100 fs). This triplet state converts to a phen-based $^3MLCT_{phen}$ within 1 ps followed by an ILCT process leading in less than 7 ps to a phz-based state ($ILCT_{phz}$) that, by a slow LMCT ($\gg$ 800 ps), populates a state located on the catalytic metal center M. Time constants are similar to those obtained in solution, apart from τ_3, which is shorter in solution probably owing to a better stabilization of the charge-separated state. Gas-phase transient anisotropy and the PF behavior of the compounds strongly support energy transfer to the catalytic metal center initiated by a fast and directed electron transfer on the tpphz bridge.

We conclude that ion trap PF experiments allow for valuable insights into the intrinsic spectroscopic and dynamic properties and stability of Ru^{II}-based photocatalysts. The method provides information on a molecular level with unparalleled detail and efficiency that can be a stepping stone to facilitate the fast optimization of supramolecular photocatalysts by theory-derived rational design.

Acknowledgements

D.I. and C.R. thank the DFG (SFB/TRR 88 "3MET"; project C4), the Stiftung Rheinland-Pfalz für Innovation (Project 965) and the Landesgraduiertenförderung Rheinland-Pfalz for funding. M.F.G. thanks the DFG-Cluster of Excellence "Munich-Centre for Advanced Photonics" for support. Dr. Y. Nosenko is acknowledged for technical support.

Conflict of interest

The authors declare no conflict of interest.

Keywords: electronic dynamics · femtochemistry · gas-phase laser spectroscopy · supramolecular chemistry · transient anisotropy

[1] P. Lei, M. Hedlund, R. Lomoth, H. Rensmo, O. Johansson, L. Hammarström, *J. Am. Chem. Soc.* **2008**, *130*, 26–27.
[2] P. Du, J. Schneider, F. Li, W. Zhao, U. Patel, F. N. Castellano, R. Eisenberg, *J. Am. Chem. Soc.* **2008**, *130*, 5056–5058.
[3] N. Armaroli, V. Balzani, *Angew. Chem. Int. Ed.* **2007**, *46*, 52–66; *Angew. Chem.* **2007**, *119*, 52–67.
[4] J. L. Knee, L. R. Khundkar, A. H. Zewail, *J. Chem. Phys.* **1985**, *83*, 1996–1998.
[5] N. F. Scherer, J. L. Knee, D. D. Smith, A. H. Zewail, *J. Phys. Chem.* **1985**, *89*, 5141–5143.
[6] A. Zavras, G. N. Khairallah, M. Krstić, M. Girod, S. Daly, R. Antoine, P. Maitre, R. J. Mulder, S.-A. Alexander, V. Bonačić-Koutecký, P. Dugourd, R. A. J. O'Hair, *Nat. Commun.* **2016**, *7*, 11746.
[7] D. Imanbaew, Y. Nosenko, C. Kerner, K. Chevalier, F. Rupp, C. Riehn, W. R. Thiel, R. Diller, *Chem. Phys.* **2014**, *442*, 53–61.
[8] D. Nolting, T. Schultz, I. V. Hertel, R. Weinkauf, *Phys. Chem. Chem. Phys.* **2006**, *8*, 5247–5254.
[9] S. Tschierlei, M. Presselt, C. Kuhnt, A. Yartsev, T. Pascher, V. Sundström, M. Karnahl, M. Schwalbe, B. Schäfer, S. Rau, M. Schmitt, B. Dietzek, J. Popp, *Chem. Eur. J.* **2009**, *15*, 7678–7688.
[10] M. G. Pfeffer, B. Schäfer, G. Smolentsev, J. Uhlig, E. Nazarenko, J. Guthmuller, C. Kuhnt, M. Wächtler, B. Dietzek, V. Sundström, S. Rau, *Angew. Chem. Int. Ed.* **2015**, *54*, 5044–5048; *Angew. Chem.* **2015**, *127*, 5132–5136.
[11] S. Rau, B. Schäfer, D. Gleich, E. Anders, M. Rudolph, M. Friedrich, H. Görls, W. Henry, J. G. Vos, *Angew. Chem. Int. Ed.* **2006**, *45*, 6215–6218; *Angew. Chem.* **2006**, *118*, 6361–6364.
[12] M. Wächtler, J. Guthmuller, S. Kupfer, M. Maiuri, D. Brida, J. Popp, S. Rau, G. Cerullo, B. Dietzek, *Chem. Eur. J.* **2015**, *21*, 7668–7674.
[13] M. Karnahl, S. Tschierlei, C. Kuhnt, B. Dietzek, M. Schmitt, J. Popp, M. Schwalbe, S. Krieck, H. Gorls, F. W. Heinemann, S. Rau, *Dalton Trans.* **2010**, *39*, 2359–2370.
[14] D. Imanbaew, M. F. Gelin, C. Riehn, *Struct. Dyn.* **2016**, *3*, 043211.
[15] D. A. Horke, A. S. Chatterley, J. N. Bull, J. R. R. Verlet, *J. Phys. Chem. Lett.* **2015**, *6*, 189–194.
[16] A. P. Blokhin, M. F. Gelin, E. V. Khoroshilov, I. V. Kryukov, A. V. Sharkov, *Opt. Spectrosc.* **2003**, *95*, 346–352.
[17] S. Tschierlei, M. Karnahl, M. Presselt, B. Dietzek, J. Guthmuller, L. González, M. Schmitt, S. Rau, J. Popp, *Angew. Chem. Int. Ed.* **2010**, *49*, 3981–3984; *Angew. Chem.* **2010**, *122*, 4073–4076.

Manuscript received: December 19, 2016
Revised: January 23, 2017
Final Article published: ■■ ■■, ■■■■

11.6 Exploring the Gas Phase Activation and Reactivity of a Ru Transfer Hydrogenation Catalyst by Experiment and Theory in Concert

Fabian S. Menges[a], Johannes Lang[b], Yevgeniy. Nosenko[b], Christian Kerner[b], Maximillian Gaffga[b], Leila Taghizadeh Ghoochany[b], Werner R. Thiel[b], Christoph Riehn[b], and Gereon Niedner-Schatteburg[b]

a) Department of Chemistry,
Yale University,
New Haven, CT 06525, USA

b) Fachbereich Chemie and Forschungszentrum OPTIMAS,
Technische Universität Kaiserslautern,
67663 Kaiserslautern, Germany

11.6.1 Preamble

The following chapter is a manuscript, which is accepted for publication in the Journal of Physical Chemistry A.

F. S. Menges conducted the main part of measurements, calculations and data evaluations. He was supported by Y. Nosenko (IR-MPD measurements), M. Gaffga and myself (CID measurements). C. Kerner and L. Taghizadeh Ghoochany from the research group of Prof. Dr. W. R. Thiel synthesized the investigated ruthenium complexes. F. S. Menges prepared a first draft of this manuscript, which was presented in his PhD thesis. I revised this manuscript. Herein, we were supported by G. Niedner-Schatteburg and C. Riehn.

Full Reference:

Exploring the gas phase activation and reactivity of a Ru transfer hydrogenation catalyst by experiment and theory in concert

F. S. Menges, **J. Lang**, Y. Nosenko, C. Kerner, M. Gaffga, L. Taghizadeh Ghoochany, W. R. Thiel, C. Riehn, and G. Niedner-Schatteburg, *Journal of Physical Chemistry A*, **2017**, published online.

http://dx.doi.org/10.1021/acs.jpca.7b02459

11.6.2 Manuscript

Exploring the gas phase activation and reactivity of a Ru transfer hydrogenation catalyst by experiment and theory in concert

Fabian S. Menges[a]*, Johannes Lang[b], Yevgeniy Nosenko[b], Christian Kerner[b], Maximilian Gaffga[b], Leila Taghizadeh Ghoochany[b], Werner R. Thiel[b], Christoph Riehn[b], and Gereon Niedner-Schatteburg[b]

[a] Department of Chemistry, Yale University, New Haven, CT 06525, USA

[b] Fachbereich Chemie and Forschungszentrum OPTIMAS,

Technische Universität Kaiserslautern, 67663 Kaiserslautern, Germany

*F. S. Menges, Tel: +1 203 432 2150, Email: fabian.menges@yale.edu

Keywords: Transfer Hydrogenation, Ruthenium Catalysis, Base-free Activation, Mass Spectrometry, InfraRed Multiple-Photon Dissociation, Density Functional Theory, Gas Phase Reactions, Isotope Labeling, Collision Induced Dissociation

Abstract

This study elucidates structures, activation barriers and the gas phase reactivity of cationic ruthenium transfer hydrogenation catalysts of the structural type $[(\eta^6\text{-cym})RuX(pympyr)]^+$. In these complexes, the central ruthenium(+II) ion is coordinated to a η^6-bound *p*-cymene (η^6-cym), a bidentate 2-R-4-(2-pyridinyl)pyrimidine ligand (pympyr) with R = NH_2 or $N(CH_3)_2$, and an anion X = I^-, Br^-, Cl^-, or $CF_3SO_3^-$. We present InfraRed Multiple-Photon Dissociation (IR-MPD) spectra of precursors (before HCl loss) and of activated complexes (after HCl loss) which elucidates a C-H activation as the key step in the activation mechanism. A resonant 2-color IR-MPD scheme serves to record several otherwise 'dark' bands and enhances the validity of spectral assignments. We show that Collision Induced Dissociation (CID) derived activation energies of the $[(\eta^6\text{-cym})RuX(pympyr)]^+$ (R = $N(CH_3)_2$) complexes depend crucially on the anion X. The obtained activation energies for the HX loss correlate well with quantum chemical activation barriers and are in line with the HSAB concept. We further elucidate the reaction of the activated complexes with D_2 under single collision conditions. Quantum mechanical simulations substantiate that the resulting species represent analogues for hydrido intermediates formed after abstraction of H^+ and H^- from isopropanol as postulated for the catalytic cycle of transfer hydrogenation by us before.

Introduction

Ruthenium based catalysts are widely used for transfer hydrogenation reactions[1], wherein isopropanol or formiates serve as the hydrogen source. In case of isopropanol being used as the substrate, acetone is formed as the only by-product. In a series of review articles all different aspects of transition metal catalyzed transfer hydrogenation have been illuminated.[2] For one group of catalysts, the coordination of the alcohol and the ketone to the metal center is suggested (so-called 'inner-sphere' mechanism).[3] Alternatively, there are systems, where a coordination of the substrates is not necessary at all (so-called "outer-sphere mechanism").[4]

However, for both mechanisms the presence of a base is generally requested for the activation of the catalyst.[5] There are only a few examples to be found in the literature in which catalytic activity for the transfer hydrogenation was observed even in the absence of a base.[6] In these cases, the formation of an internal basic site is the key step in the catalyst activation process. We recently reported that cationic ruthenium complexes of the type $[(\eta^6\text{-cym})RuCl(pympyr)]^+$ (cym = *p*-cymene) bearing a 2-amino-4-(2-pyridinyl)pyrimidine ligand (pympyr) are active catalysts for the transfer hydrogenation without an external base as well.[7] Interestingly, the catalytic activity of these complexes strongly depends on the amino substituent in the 2-position of the pyrimidine ring: compounds with a primary ($-NH_2$) or secondary (-NHR) amino group acquire activity by addition of a base, while systems with a tertiary amino group ($-NR_2$) are active on their own.

These findings encouraged us to strive for a deeper insight into the catalyst activation process. By means of electrospray ionization (ESI) – Collision Induced Dissociation (CID) mass spectrometry (MS) and Density Functional Theory (DFT) calculations in combination with deuterium labelling experiments, we were able to determine that such complexes undergo a so-called roll-over cyclometallation by splitting of the $Ru\text{-}N_{pyrimidine}$ bond paired with a subsequent loss of HX, leading to a carbanion bound ruthenium intermediate (Scheme 1). The activation process starts with a C-H activation step[8], which can be understood in terms of an electrophilic aromatic substitution wherein the ruthenium(II) center acts as the electrophile[9], and the resulting carbanion can subsequently act as an internal base to deprotonate an alcohol such as e.g. isopropanol. The activation barrier for $Ru\text{-}N_{pyrimidine}$ bond cleavage and subsequent loss of HX in case of a $-NH_2$ substituent is approx. 45 kJ mol^{-1} higher than the barrier in the case of a $-NR_2$ substituent, which explains the differences in catalytic activities mentioned above.[7] Recent studies on catalytically active transition metal complexes bearing aminopyrimidine ligands in combinations with donor sites other than pyridine showed that the cyclometallation of such ligands seems to be a general approach to enhance the catalysts activity. [10]

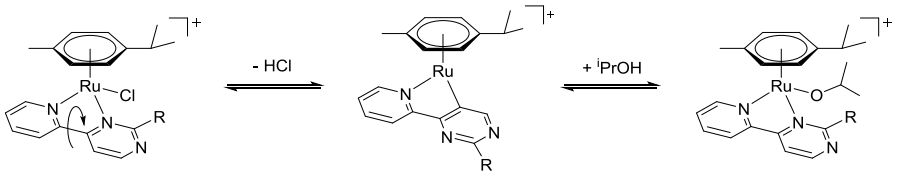

Scheme 1: Activation of the $[(\eta^6\text{-cym})RuCl(pympyr)]^+$ catalyst by HCl cleavage and addition of isopropanol as hydrogen donor.

In the present manuscript we combine multiple gas phase related methods in order to characterize the structure of these complexes, their activation barriers and reaction behavior. We utilize InfraRed Multiple Photon Dissociation (IR-MPD) spectroscopy for the structural characterization of two main representative catalysts (primary $-NH_2$ vs. tertiary $-N(CH_3)_2$ amine substituent) in their non-activated and activated form. We study the influence of the ruthenium bound anion onto the activation barrier for HX loss using ESI-CID MS measurements on a set of anion exchanged $[(\eta^6\text{-cym})RuX(dma\text{-}pympyr)]^+$ complexes (η^6-cym = *p*-cymene, dma-pympyr = 2-dimethylamino-4-(2-pyridinyl)pyrimidine and X = I^-, Br^-, Cl^-, or $CF_3SO_3^-$). Furthermore, we test two activated complexes for their reactivity towards isopropanol and deuterium under single collision conditions. DFT calculations allow for the assignment of vibrational bands, the estimation of activation barriers and the comprehension of the observed uptake of D_2.

It was shown in the literature that IR-MPD is capable to elucidate the gas phase structure of metal complexes and their reaction products [11] and a comparison of activation by CID and IR-MPD has been conducted before.[12] Recently, we could show that the photo-activation of such complexes by 450 nm excitation in an ion trap is possible as well, but not operable in acetonitrile solution.[13] We have achieved increased IR-MPD fragmentation efficiency by the use of a resonant 2-color IR-MPD scheme[14] which allows for the recording of otherwise (in 1-color IR-MPD) 'dark' vibrational bands, originating from high activation barriers for fragment loss (splitting of covalent bonds) and / or insufficient internal vibrational redistribution (IVR) of excitation energy.[15]

Prior DFT studies managed to elucidate the activation processes of alcohols and other dihydrogen sources at metal-centered hydrogenation catalysts.[16] Such DFT derived relative stabilities and activation barriers have certain inaccuracies notwithstanding their value in reconstructing reaction mechanisms. We have conducted CID studies on a series of $[(\eta^6\text{-cym})RuCl(L)]^+$ complexes (η^6-cym = *p*-cymene, L = bipyridine or 2-R-4-(2-pyridinyl)pyrimidine with R = H, NH_2, NHMe or $N(CH_3)_2$) before.[17] It is general knowledge that apparent CID thresholds and actual activation enthalpies are subject of kinetic shifts[18], which are often negligible, but sometimes reach considerable values.[18a] In the present case, we evaluate relative CID energies within one class of compounds that vary by substituents of similar size, assuming a by and large constant kinetic shift. We applied a center-of-mass correction (COM) to the derived E_{LAB} values in order to compare the activation energies of ions of different masses[19] and the phenomenological E_{com} values are then correlated to DFT derived activation barriers.

Finally, we carried out gas phase reactions of two activated ruthenium(II) complexes with D_2. We suppose that the addition of D_2 leads to the same deuterido ruthenium complex that would form by D^+ and D^- transfer from $DOCD(CH_3)_2$ to the activated complex in solution[17], which is hindered in the gas phase at room temperature.

Methods

Sample preparation

Ruthenium complexes of the type $[(\eta^6\text{-cym})RuCl(pympyr)]X_C]$ (X_C = BPh_4, BF_4, Cl or PF_6) were prepared as described in the literature.[7, 17] For the exchange of the chlorido ligand against bromide and iodide, stock solutions of these complexes in acetonitrile were stirred for 72 h at room temperature with a ten-fold excess of the corresponding sodium salt. To exchange the chlorido ligand against the trifluoromethane sulfonate anion (triflate), equimolar amounts of silver triflate were used under the same conditions.

While the binding motifs of the pympyr ligands in **1**$^+$ and **2**$^+$ (for the numbering see Scheme 2) are known from crystal structures (cf. Scheme S1 and Table S1), the binding motifs and structures in their activated forms were only inferred from results of CID experiments of isotopic labeled species and concomitant DFT calculations and ^{1}H-NMR spectroscopy.[7] The activated forms of the catalysts were prepared by CID (see below) and subsequently isolated in the ion trap of the mass spectrometer.

ESI-MS and CID

Electrospray ionization mass spectrometry (ESI-MS) in positive ion mode was performed with two different ion trap instruments (Bruker Esquire 6000 for CID and amaZonSL for IR-MPD). The scan speed was 13000 m/z / s in the normal resolution scan mode (0.3 FWHM / m/z). The scan range was set to at least 70 to 400 m/z. Sample solutions in acetonitrile at concentrations of approximately 1 x 10^{-4} M were continuously infused into the ESI chamber at a flow rate of 2 µL/min using a syringe pump. We used nitrogen as drying gas at a flow rate of 3.0 to 4.0 L/min at temperatures of 220 °C up to 300 °C and sprayed the solutions at a nebulizer pressure of 3 to 4 psi with the electrospray needle held at 4.5 kV. We held the transfer parameters to the Paul trap of the mass spectrometer constant and used Helium as a buffer gas with an estimated partial pressure of about ~10^{-3} mbar inside the ion trap. BrukerEsquireControl 5.3 (Esquire) and BrukerTrapControl 7.0 (amaZonSL) software controlled the instrument and we performed data analysis using Bruker Data Analysis 4.0 software.

We measured CID appearance curves of the activation by a stepwise variation of the fragmentation amplitude in the Paul trap of the mass spectrometer while keeping all other parameters constant. The helium pressure in the Paul trap plays a crucial role for the reproducibility of the results. Even slight changes between measurements can lead to significant shifts. Therefore, all measurements were repeated multiple times and we selected the ones with the most comparable pressure conditions instead of averaging over multiple measurements. The internal energy scale of the instrument (E_{lab}) was then

transferred to a center of mass related collisional energy scale (E_{com}) in order to account for different efficiencies of collisional energy transfer between helium and ions of different mass to charge ratios.[19]

IR-MPD

IR-MPD measurements of catalyst precursors **1**$^+$ and **2**$^+$ and their activated forms **[1(-HCl)]**$^+$ and **[2(-HCl)]**$^+$ (for numbering see Scheme 2) were performed with a modified ion trap mass spectrometer (amazon SL, Bruker Daltonics). Two KTP/KTA optical parametric oscillator/amplifier (OPO/A, LaserVision) systems, each pumped with a Q-switched (10 Hz) injection-seeded Nd^{3+}:YAG laser (PL8000, Continuum), provided for tunable IR radiation ($\delta\nu$ = 0.9 cm^{-1} and $\delta\nu$ = 0.3 cm^{-1}, δt = 7 ns) in order to record vibrational spectra via a multi-photon dissociation scheme. We used the OPA idler wave (≤10 mJ/pulse) of one system in order to record spectra (pump laser) within 2800 - 3600 cm^{-1} or the signal/idler difference frequency wave (≤2 mJ/pulse) for the 1200 – 1900 cm^{-1} spectral range. On choice, the idler wave of the second IR OPO/A served as probe laser, set to a selected and fixed vibrational resonance frequency. The probe laser beam was aligned counter-propagating with respect to the pump laser beam. Probe pulses were typically delayed by 40 ns with respect to the scanning pump pulses (delay generator DG645, SRS). Each trapped and mass isolated ion package was irradiated by 2-4 laser pulses (or pulse pairs in case of two-laser experiments) in order to produce sufficient fragment ions. IR spectra were recorded using Bruker chromatogram software for extracting the intensity of parent and fragment ions (three point averaging directly by BrukerTrapControl software). The resulting IR-MPD signal was evaluated corresponding to formula *1* (cf. Supporting Information). Origin© Plot Software served to apply a five point adjacent averaging for smoothing. The IR frequency was calibrated by a wave meter (821B-NIR, Bristol instruments) and the laser power curve was recorded in parallel to the IR-MPD spectra.

We utilized our recently developed 2-color IR-MPD technique in order to enhance the fragmentation efficiency, especially in the spectral region below 1900 cm^{-1} in which the OPO/As provide only low energy laser pulses.[14]

Theoretical methods

All DFT calculations were performed at the B3LYP [20] level of theory using the 6-311G* (C, H, N, O, F, S, Cl, Br, I) and Stuttgart RSC 1997 ECP (Ru) [21] basis sets and the Gaussian09 package.[22]

Dependent on the desired local minimum or transition state structure *tight* or *vtight* grids were used for convergence of the geometry optimization, in the latter case combined with an ultrafine integration as described in the Gaussian09 manual. In order to find the transition states, the *calcfc* keyword was used, partially combined with *modredundant* coordinates to freeze dihedral angles of dangling methyl groups to prevent the localization of non HX loss related transition states. Harmonic frequency calculations were carried out for each optimized geometry in a local minimum or transition state. Local minimum geometries were checked for no imaginary frequencies, transition states for one or two of them that correlate to the HX loss. Thermal energies, enthalpies and free enthalpies were calculated at 298.15 K (RT conditions).

We applied two different scaling factors (> 2500 cm^{-1}: 0.949 and < 2500 cm^{-1}: 0.976) to the DFT predicted IR absorption spectra. These scaling factors were derived by a comparison of experimental to DFT predicted IR spectra (position of the NH_2 stretches in **1**$^+$ for bands above 2500 cm^{-1} and the six strongest bands of **1**$^+$ and **2**$^+$ below 2500 cm^{-1}) since the published scaling factor of 0.966 for the B3LYP/6-311G* level of theory is insufficient for general application.[23]

Gas phase reactions

Gas phase reactions of the activated cationic ruthenium complexes with isopropanol and deuterium, respectively, were performed under single collision conditions at a pressure of 5 x 10^{-9} mbar in a FT-ICR-MS instrument (Bruker Apex III) equipped with a 7.0-T magnet and an electrospray ion source (APOLLO I). The collision cell integrated in the ion transfer path to the FT-ICR MS was used in order to generate the activated species **[1(-HCl)]**$^+$ and **[2(-HCl)]**$^+$ from precursor molecules **1**$^+$ and **2**$^+$. The partial pressure of

the reaction gas was set to a constant value and instruments surfaces (in the high vacuum part) were passivated for one hour ahead of data recording. Sample solutions in acetonitrile at concentrations of approximately 1 x 10^{-4} M were continuously infused into the ESI chamber at a flow rate of 3 µL/min using a syringe pump. Nitrogen was used as drying gas with flow rate of 10.0 L/min at approximately 300 °C. The solutions were sprayed at a nebulizer pressure of 25 psi and the electrospray needle was typically held at 4.0 kV. Transfer parameters to the Penning trap of the mass spectrometer were held constant. D_2 was chosen instead of H_2 in order to be able to separate the reaction products more clearly from the isotopic distribution of the educts.

Results and Discussion

We investigated in detail structure/activity relationships of a series of cationic ruthenium catalysts of the type $[(\eta^6\text{-cym})RuX(pympyr)]^+$ (η^6-cym = η^6-bound *p*-cymene, pympyr = 2-R-4-(2-pyridinyl)pyrimidine with R = NH_2, or $N(CH_3)_2$ and X = I, Br, Cl, or CF_3SO_3) by variation of both, X and R. Scheme 2 shows the molecular structures of compounds **1⁺-5⁺** and Table 1 summarizes all relevant formula and masses of the precursor (parent) species and of the fragments after HX elimination.

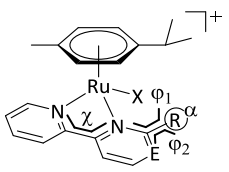

	1^+	$2(Cl)^+$	$2(OTf)^+$	$2(Br)^+$	$2(I)^+$	3^+	4^+	5^+
E	N	N	N	N	N	CH	N	N
R	NH_2	$N(CH_3)_2$	$N(CH_3)_2$	$N(CH_3)_2$	$N(CH_3)_2$	H	H	$NHCH_3$
X	Cl	Cl	CF_3SO_3	Br	I	Cl	Cl	Cl

Scheme 2: Molecular structures of compounds **1⁺-5⁺** and **2(X)⁺**. Angles are defined as follows: α is the sum of angles around the tertiary nitrogen atom of substituent R, χ is the dihedral angle between *cis* aligned atoms N_{pym}-C-C-N_{pyr}, ϕ_1 and ϕ_2 are dihedral angles between *cis* aligned atoms N_{pyr}-C-N_R-H (**1⁺**), N_{pyr}-C-N_R-C_R (**2⁺**) respectively, of the pyrimidine ring and substituent R.

Table 1: Composition and masses of the precursors **1⁺-5⁺** and **2(X)⁺** and CID ionic fragment masses. Only fragment masses of the most abundant losses are listed. Masses are due to the most abundant isotopomers (for experimental and simulated mass spectra cf. Fig. S1).

catalyst	ligand[a]	sum formula	m/z parent mass	m/z fragment mass
1⁺	R = NH_2	$[Ru(C_{10}H_{14})(C_9H_6N_3(NH_2))Cl]^+$	443.06	407.08
2⁺ = 2(Cl)⁺	R = $N(CH_3)_2$	$[Ru(C_{10}H_{14})(C_9H_6N_3(N(CH_3)_2))Cl]^+$	471.09	435.11
2(CF₃SO₃)⁺	R = $N(CH_3)_2$	$[Ru(C_{10}H_{14})(C_9H_6N_3(N(CH_3)_2))(SO_3CF_3)]^+$	557.04	435.11
2(Br)⁺	R = $N(CH_3)_2$	$[Ru(C_{10}H_{14})(C_9H_6N_3(N(CH_3)_2))Br]^+$	489.01	435.11
2(I)⁺	R = $N(CH_3)_2$	$[Ru(C_{10}H_{14})(C_9H_6N_3(N(CH_3)_2))I]^+$	534.99	435.11
3⁺	bipyridine	$[Ru(C_{10}H_{14})(C_{10}H_8N_2)Cl]^+$	427.05	389.06[b]
4⁺	pyridinylpyrimidine	$[Ru(C_{10}H_{14})(C_9H_7N_3)Cl]^+$	428.05	390.05[b]
5⁺	R = $NHCH_3$	$[Ru(C_{10}H_{14})(C_9H_6N_3(NH(CH_3))Cl]^+$	457.07	421.10[b]

[a] only the R substituent is indicated for the *pympyr* ligands

[b] according to [17]

Both, the ligands and the anion bound to the ruthenium center have a crucial effect on the activation barrier. The latter effect is studied based on complex **2**$^+$ by exchanging the chloride anion with triflate ($CF_3SO_3^-$), bromide and iodide.

IR-MPD spectra and DFT predictions

We measured 1-color IR-MPD spectra of the cationic complexes **1**$^+$ and **2**$^+$ (Fig. 1a, 3a, resp.) and of their activated forms **[1(-HCl)]**$^+$ and **[2(-HCl)]**$^+$ (Fig. 1c, 3c, resp.) as two representative catalysts of this study and in order to elucidate their gas phase structures. The main IR induced fragment channels are the neutral loss of HCl for **1**$^+$ and **2**$^+$ and the neutral loss of H_2 for **[1(-HCl)]**$^+$ and **[2(-HCl)]**$^+$. The activated complexes were prepared by CID, yielding pure **[2(-HCl)]**$^+$ as deduced from its isotopic pattern. However, CID of **1**$^+$ yields up to 40% contribution of the dehydrogenated product **[1-(HCl-H$_2$)]**$^+$ in addition to **[1(-HCl)]**$^+$ (Fig. S1). These two species are inseparable (by MS) in the ion trap due to the broad isotopic pattern of Ru. Thus the IR-MPD spectra of **[1(-HCl)]**$^+$ are slightly superimposed with spectra of the species **[1(-HCl-H$_2$)]**$^+$.

Spectral features and vibrational assignment of 1+ and [1(-HCl)]+: The 1-color and 2-color IR-MPD spectra of complex **1**$^+$ (Fig. 1a, black and red curves, resp.) exhibit clearly distinguishable peaks in the stretching vibration region above 1700 cm^{-1}. We observe a CH stretching vibration band at 2977 cm^{-1} as well as a symmetric (3345 cm^{-1}) and an antisymmetric (3484 cm^{-1}) NH_2 stretching vibration band. The NH2 stretching vibrations of **[1(-HCl)]**$^+$ (Fig. 1c) shift to higher frequencies with respect to those of **1**$^+$. Moreover, the NH_2 bands of **[1(-HCl)]**$^+$ split up into doublets at 3430/3445 cm^{-1} and 3540/3570 cm^{-1} (further details see Fig. S3). The origin of the splitting could be due to contributions of (a) multiple isomeric structures of **[1(-HCl)]**$^+$, from (b) additional contributions to the IR-MPD spectra by secondary fragment species (as e.g. **[1(-HCl-H$_2$)]**$^+$), or from (c) amino group inversion tunneling. In order to decide which of these factors causes the splitting, we have to address all of these possible contributions in more detail first.

The 1-color IR-MPD spectra in the fingerprint region below 1700 cm^{-1} reveal merely one band in the case of **1**$^+$ and two bands in the case of **[1(HCl)]**$^+$, while our DFT calculations indicate a multitude of bands in this spectral region in both cases. We took this discrepancy as a motivation to utilize our signal enhancing 2-color IR-MPD approach. Indeed, we obtained several additional bands for **1**$^+$ and **[1(-HCl)]**$^+$, and we thereby get ready to compare to our DFT predictions.

The case of **1**$^+$ is straightforward: We utilized available X-ray crystallographic data[7] to optimize the associated isolated cation and to obtain a predicted IR absorption spectrum by DFT (cf. Fig. 1b). This does indeed match closely the recorded 2-color IR-MPD spectrum thereby providing for a structural confirmation. Note the band at 1601 cm^{-1}, which corresponds to a pyrimidine ring deformation coupled to C5H bending. The IR-MPD spectra of **[1(-HCl)]**$^+$ lack this 'marker band'. As no crystal structure of activated complex **[1(-HCl)]**$^+$ is available we investigate by DFT three distinct binding motifs represented by the three isomers Iso$_1$, Iso$_2$, and Iso$_3$. They differ by deprotonation site and by pympyr ring torsion or by its coordination to the Ru center after HCl elimination of **1**$^+$ (cf. insets to Fig. 1 (d) through (f)). Iso$_1$ displays a torsion of the pyrimidine ring together with a deprotonation of the C5H proton to form a Ru-C bond. In the case of Iso$_2$ the deprotonation takes place at the pyridine ring, which also performs the torsion to form a Ru-C bond. In the case of Iso$_3$ the cymene ligand is deprotonated and no torsion of the pympyr unit takes place.

Isomer assignment of [1(-HCl)]$^+$: We assign the recorded IR-MPD spectrum of **[1(-HCl)]**$^+$ to the DFT predicted torsional isomers Iso$_1$ and sort out Iso$_2$ and Iso$_3$ – the 'marker band' at 1601 cm^{-1} serving to decide. This 'marker band' would correspond to a pyrimidine ring deformation coupled to C5H bending (labeled as C5H + pm-ring in Fig. 1b) – which is located at the site that has deprotonated to yield Iso$_1$. Thus we have identified a spectroscopic finger print that identifies the very deprotonation site of HCl elimination, and we have confirmed the roll over isomerization explicitly by spectroscopic means. Note, that the torsion of the aminopyrimidine unit (Scheme 1) was suggested previously[7], leading to a structure where the relevant hydrogen atom is missing. In contrast, a rotation of the pyridine ring (Fig. 1e, Iso$_2$)

would make this mode significantly IR active – but is not observed, however. Additionally, considering the high relative energy of Iso_2 (+33 kJ/mol) in relation to Iso_1, it is reasonable to rule out contributions of Iso_2.

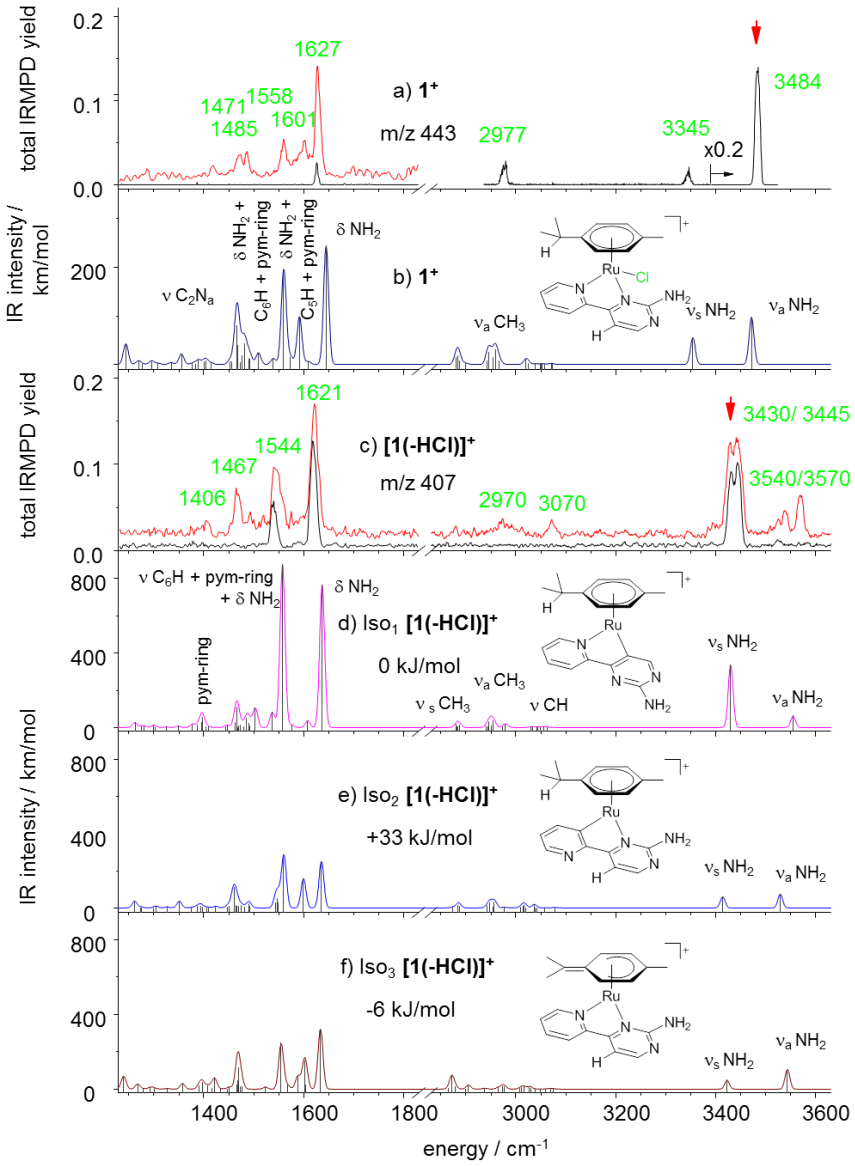

Figure 1: 1-(black) and 2-color (red) IR-MPD spectra of **1**+ (a) and **[1(-HCl)]**+ (c). DFT predicted IR absorption spectra of **1**+ (b) and of three possible isomers of **[1(-HCl)]**+ (d-f) at the B3LYP/6-311G*/ECP level of theory, frequency scaled by 0.949 (> 2500 cm^{-1}) and 0.976 (< 2500 cm^{-1}), respectively. See Table S2 for numerical values of band peak positions and assignment of bands. The arrows indicate spectral positions of the probe laser in the 2-color experiments.

Discussion of Iso_3 of [1(-HCl)]+: An extended theoretical search for alternative activation pathways led to the discovery of a third isomer (Iso_3, Fig. 1 f). The activation pathway for this last isomer would incorporate the loss of the methane proton of the isopropyl-group together with the chloride anion. This would lead to a **[1(-HCl)]**+ isomer containing a deprotonated *p*-cymene, that can be considered as a 6-electron pentadienide ligand bearing an exocyclic methylene site, and a non-rotated pympyr ligand for which we obtained a surprisingly low energy by DFT calculations (- 6 kJ/mol in relation to Iso_1). Much as in Iso_2, we would expect a strong 'marker band' at ca. 1600 cm^{-1} – other than observed. Moreover, both Iso_2 and Iso_3 would provide for an intensity ratio of NH stretching modes $I(\nu_s^{NH_2})/I(\nu_a^{NH_2}) < 1$ whereas

the experimental IR-MPD spectrum and the DFT predictions of Iso_1 reveal $I(\nu_s^{NH_2})/I(\nu_a^{NH_2}) > 1$. Based on these two independent pieces of spectral evidence we rule out contributions of structures Iso_2 and Iso_3 and confirm instead the presence of Iso_1 of **[1(-HCl)]⁺**. This clear cut spectral assignment of Iso_1 is the more of relevance as Iso_3 is predicted to be more stable than Iso_1 as calculated by DFT, at least within the uncertainty of the method. The nature of the transition state for formation of Iso_3 is yet unclear and HCl loss from the isopropyl group could be hindered due to multiple rotamers of the p-cymole ligand.

Structural changes upon activation of 1⁺: From the DFT calculations we find a pyramidal amino group in complex **1⁺** with the sum of angles between the atoms connected to the amino nitrogen atom being α = 346°, which is significantly smaller than 360° assigned to a planar structure (see Scheme 2 for definition of angles). The corresponding dihedral angles of the *cis* oriented N_{pyr}-C-N_R-H atoms are ϕ_1 = -11° and ϕ_2 = 32 – they orient out of the pympyr plane. We conclude in a partial conjugation of the residue's nitrogen lone pair with the pympyr ring's π-system, and a significant sp^3-hybrid character. In remarkable contrast, the activated complex **[1(-HCl)]⁺** (Iso1, Fig. 1d), provides for α = 360° and $\phi_1 = \phi_2$ = 0°, which indicates a planar structure with strong π-conjugation of a pure nitrogen p orbital perpendicular to three sp^2 hybrids in plane. These orbital rearrangements are accompanied by a shortening of the C-N_{amino} bond, from 135.6 to 134.1 pm. This strong conjugation of the lone pair of the nitrogen to the aromatic pyrimidine ring induces the observed blue shift of the NH_2 stretching modes in activated complex **[1(-HCl)]⁺**. Other than naively expected, there is little interaction of the amine residue with the proximate chloride in **1⁺**. More importantly, the anticipated roll-over torsional intra ligand isomerization upon activation of **1⁺** to **[1(-HCl)]⁺** is indeed a full 180° torsion within the pympyr ligand: the dihedral angle χ changes from χ = 2.84° to 178.91°. We conclude in a full conjugation of the pympyr π-system in both, ***1⁺ and [1(-HCl)]⁺***.

Origin of NH_2 band broadening and splitting in the IR-MPD spectra of [1(-HCl)]⁺ : We note an increase of the band width (~16 cm⁻¹) of the two $\delta(NH_2)$ bands at 1544 and 1621 cm⁻¹ of the activated complex **[1(-HCl)]⁺** (Fig. 1c) with respect to the bandwidth (~ 7 cm⁻¹) of those at 1158 and 1627 cm⁻¹ of the complex **1⁺** (Fig. 1a). The third $\delta(NH_2)$ band at 1467/1471 cm⁻¹ is blended by other peaks and inconclusive. Even more prominent is an undisputable splitting of the $\nu_a(NH_2)$ of $\Delta\nu \sim 30$ cm⁻¹ and of the $\nu_s(NH_2)$ of $\Delta\nu \sim 15$ cm⁻¹ in **[1(-HCl)]⁺** which does neither show in any DFT simulation nor in the spectra of **1⁺**. This activation induced broadening of the amino group bending vibrations together with the splitting of the amino group stretching vibrations originates from, in principle, any of these three causes: (a) multiple isomeric structures of **[1(-HCl)]⁺**, from (b) additional contributions to the IR-MPD spectra by secondary fragment species (as e.g. **[1(-HCl-H₂)]⁺**), or from (c) amino group inversion tunneling:

(a) Multiple isomeric structures of **[1(-HCl)]⁺**: The four vibrational bands of **[1(-HCl)]⁺** below 1700 cm⁻¹ are assigned to the modes localized on the pympyr ligand Iso_1 (Fig. 1d) which excludes Iso_2 and Iso_3 as discussed before. The orientation of the *p*-cymene ring could also not be responsible for the broadening since only those isomers were computationally found as energetic minima which have the isopropyl-methyl axis of the *p*-cymene ring aligned approximately perpendicular to the plane of the pympyr ligand. Finally, for this *p*-cymene orientation only a few isoenergetic isopropyl rotamers of **[1(-HCl)]⁺** were converged with practically identical calculated vibrational spectra as given in Fig. 1d.

(b) Additional contributions by secondary fragment species: One could tentatively assume that the observed splittings are artefacts of spectral contamination by secondary fragment species as e.g. **[1(-HCl-H₂)]⁺**. However, the IR-MPD signal recorded for the isotopomeric channels related to **[1(-HCl-H₄)]⁺** (main fragment of **[1(-HCl-H₂)]⁺**) and **[1(-HCl-H₂)]⁺** (main fragment of **[1(-HCl)]⁺**) shows no change of the intensity ratio of the doublets' components within the experimental accuracy (Fig. 2a). The stepwise dehydrogenation of **[1(-HCl)]⁺** also barely affects the corresponding IR-MPD spectra and peaks do not shift, the main features stemming from the pympyr ligand. In order to assign the origin of H_2 loss, we calculated various isomers of **[1(-HCl-H₂)]⁺** (Fig. 2c-f). The origin of H_2 loss barely effects the positions of the peaks in the linear absorption spectra but changes the relative intensities of bands. Even though the intensity distribution in Iso_2 and Iso_3 match the experimental spectra better than in Iso_1, the comparison of IR-MPD spectra to linear absorption spectra can be misleading due to the non-linear nature of the IR-

MPD process. Additionally, these two isomers can be ruled out due to their high relative energy. The same is true for Iso_4 which additionally shows the experimentally not observed marker band at 1601 cm^{-1}.

(c) Finally, we consider the inversion tunneling as the origin of the observed band splittings and their broadening. While the amino group inversion is sterically hindered in **1**$^+$ by the *p*-cymene and Cl ligands, it is free from hindrance in the activated complex. For aniline there have been reported state specific tunneling splitting values on a similar order of magnitude (20-40 cm^{-1}).[24] However, this conclusion seems to contradict the theoretically found planar amino group structure of Iso_1 of **[1(-HCl)]**$^+$ at the energy minimum as calculated at the B3LYP/6-311G* level of theory. We note, nonetheless, that the applied method could describe the inversion potential incorrectly. Finally, given the low barriers to inversion tunneling the vibrational wave function likely averages pyramidal geometries to a seemingly planar one. A multi-dimensional inharmonic analysis of such effects would be beyond the scope of this study.

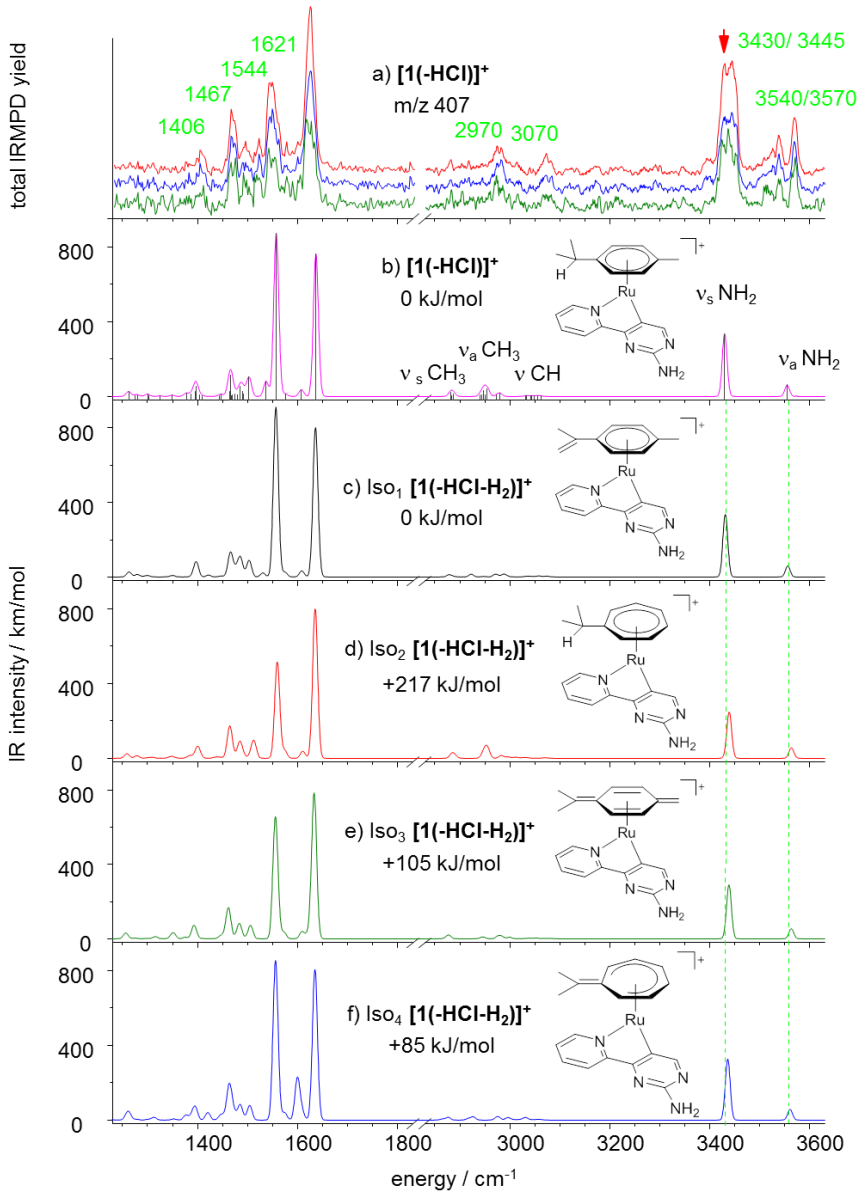

Figure 2: Analysis of fragmentation channels in the 2-color IR-MPD spectrum of **[1(-HCl)]**$^+$ (a): 2·H_2 loss (green), 1·H_2 loss (blue) and combined loss (red). DFT predicted IR absorption spectra of **[1(-HCl)]**$^+$ (b) and of four possible isomers of **[1(-HCl-H$_2$)]**$^+$ (c-f) at the B3LYP/6-311G*/ECP level of theory, frequency scaled by 0.949 (> 2500 cm^{-1}) and 0.976 (< 2500 cm^{-1}), respectively. The arrow indicates the spectral position of the probe laser in the 2-color experiments.

Spectral features and vibrational assignment of 2⁺ and [2(-HCl)]⁺: The 1- and 2-color IR-MPD spectra of **2⁺** complexes (Fig. 3a) lack any stretching bands beyond 3100 cm^{-1} due to the lack of OH and NH chromophores (R = NMe_2). The highest observed band frequency at 2981 cm^{-1} originates from several overlapping asymmetric CH stretching modes of the methyl groups of the *p*-cymene ring and some asymmetric CH stretching modes of the methyl groups of the dimethylamino group (cf. Fig. 3b). The new band at 2946 cm^{-1} – absent in the spectrum of **1⁺** – originates from an asymmetric CH stretching mode of the dimethylamino residue in **2⁺**. The fingerprint region of complex **2⁺** exhibits two very strong bands (1554 cm^{-1} and 1599 cm^{-1}), two weak bands (1420 and 1484 cm^{-1}) and one very weak band (1363 cm^{-1}). In **[2(-HCl)]⁺** only two of the fingerprint bands of **2⁺** remain active, those at 1422 cm^{-1} and 1555 cm^{-1}. Our DFT calculations of **2⁺** and **[2(-HCl)]⁺** nicely reproduce all the gross features of these bands, and we provide for individual assignments of all of these bands in the displayed spectra (Fig. 3a-e), and we refrain from re-iterating these details.

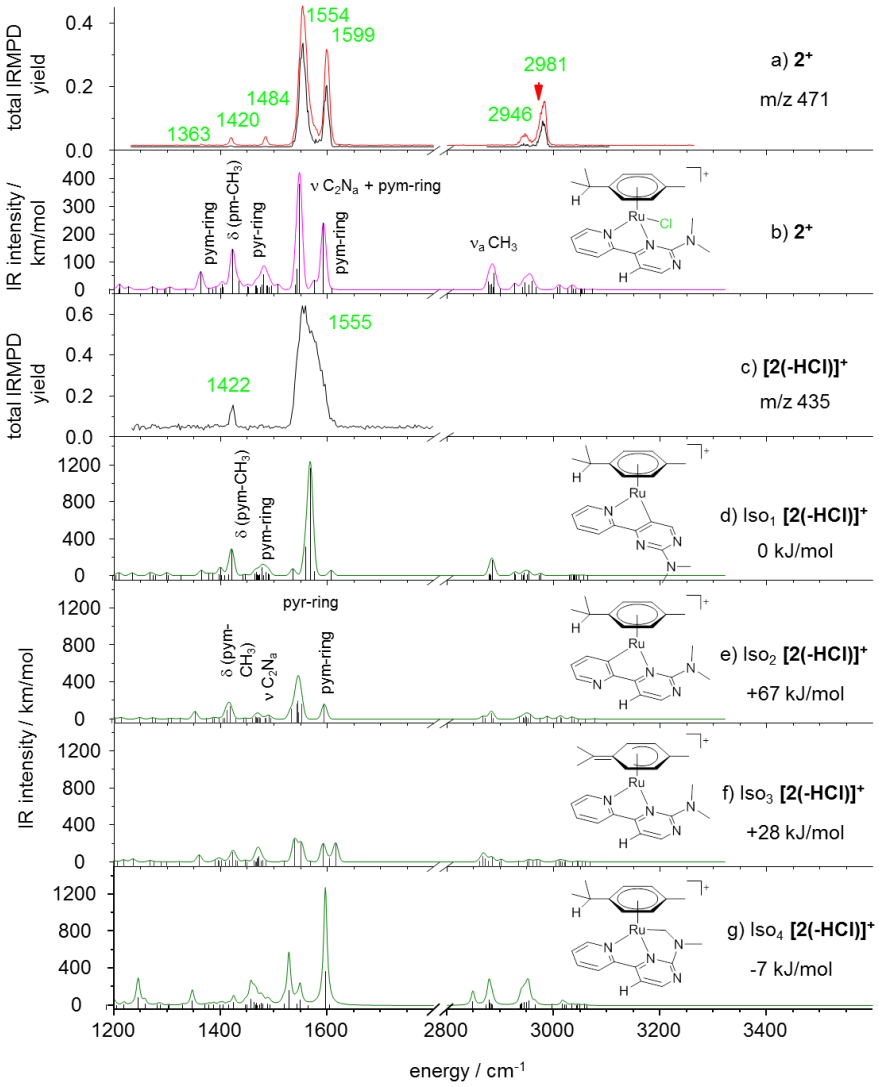

Figure 3: 1- (black) and 2-color (red) IR-MPD spectra of **2⁺** (a) and **[2(-HCl)]⁺** (c). The red line arises from the pump laser while the probe laser is fixed at 2970 cm^{-1} (red arrow). DFT predicted IR absorption spectra of **2⁺** (b) and of three possible isomers of **[2(-HCl)]⁺** (d-f) at the B3LYP/6-311G*/ECP level of theory, frequency scaled by 0.949 (> 2500 cm^{-1}) and 0.976 (< 2500 cm^{-1}), respectively.

It is most noteworthy to point out that the 1555 cm^{-1} band in **[2(-HCl)]⁺** is significantly broader than the corresponding, partially resolved bands in **2⁺**. This observation might be explained by a coupling of the

two pyrimidine ring deformations ν_a(N-C-N) and ν_d(pym-ring) with the low frequency hindered methyl rotation $\nu_{hr}(CH_3)$. The IR-MPD spectrum of **[2(-HCl)]**$^+$ revealed a smaller IR-MPD yield than that of **2**$^+$. In particular, no CH stretching motions were observed. When applying our 2-color IR-MPD probe scheme by providing a second IR pulse at 2970 cm^{-1}, we obtained a some small enhancement of IR-MPD yield with respect to the pure 1-color IR-MPD spectra (cf. e.g. in the case of **2**$^+$ in Fig. 3a), and we did not obtain any extra bands. We thus conclude that the recorded spectra of **2**$^+$ (Fig. 3a) and of **[2(-HCl)]**$^+$ (Fig. 3c) reveal all IR active features.

The agreement of the recorded IR-MPD spectrum of **[2(-HCl)]**$^+$ with the calculated spectrum of isomer Iso_1 (Fig. 3d) allows for an assignment of **[2(-HCl)]**$^+$ to this isomer. The alternative structures of the activated complex (Fig. 3e,f) are less stable and would provide for additional vibrational bands beyond those observed. Contributions of Iso_2 and Iso_3 are unlikely. Moreover, the exclusive loss of DCl upon activation of deuterated compound (at the C5 position of the pyrimidine ring)[7] had ruled out Iso_2 and Iso_3 as well (cf. isotopic patterns Fig. S3). This receives independent confirmation by the present IR spectra.

HX elimination from 2(X)$^+$ (X = SO_3CF_3, Cl, Br or I) by CID experiments and DFT calculations

Collision Induced Dissociation (CID) studies and the free enthalpies of activation: In our former publications on differently substituted Ru catalyst, we explored the influence of the substituent R on the activation barriers for HCl loss.[7, 17] In the present study, we recorded CID curves for HX loss (X = SO_3CF_3, Cl, Br, and I) from **2(X)**$^+$ (Fig. 4), and we conducted DFT calculations on activation barriers for molecules **1**$^+$ **- 5**$^+$ as well as for the variation of the anionic ligands in **2(X)**$^+$ (Fig. 5) in a uniform matter. With this approach, we aim to check for correlation of the CID barriers for activation (HX loss) to DFT derived relative energies of transition states structures. The experimental CID appearance curves of **2(X)**$^+$ (X = SO_3CF_3, Cl, Br or I) fall close to each other (Fig. 4). All of them are well fitted by a sigmoidal function[18c]. Three out of four reveal CID curves with identical slopes and slight shifts in appearance energies. One out of four, the CID curve of **2(Cl)**$^+$, possesses a steeper slope than the other three curves. We attribute this to a loose interaction of Cl^- with the C(5)H proton within the critical transition state as will be discussed later.

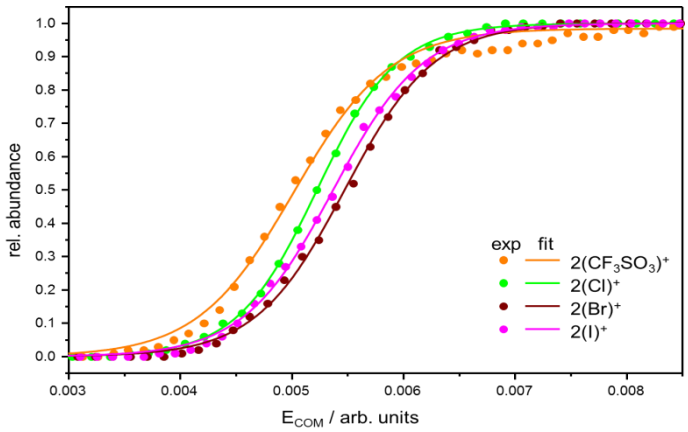

Figure 4: CID appearance curves for the loss of HX (X = SO_3CF_3, Cl, Br or I) from **2(X)**$^+$. Sigmoidal fits of the data are indicated by solid lines.

DFT modeling of the HX elimination: We calculated four local minima (***A***, ***B***, ***C*** and ***D***) and three transitions states (***TS A/B***, ***B/C*** and ***C/D***) for each complex **1**$^+$ **- 5**$^+$ (cf. upper inset in Fig. 5) in line with our previous study of **2**$^+$.[7] We extract the 300 K free enthalpies $\Delta G^{\ddagger}$ of the third transition states (***TS C/D***) which are rate determining with the HX leaving group yet formed and weakly bound to the activated molecule (lower scheme in Fig. 5). Finally, we compare these $\Delta G^{\ddagger}$ values to the CID appearance energies E_{com} (cf. Fig. 5).

CID appearance energies E_{com} and calculated barrier heights $\Delta G^{\ddagger}$: The experimental E_{com} values for the activation of **1⁺-5⁺**, and **2(X)⁺** correlate quite well to the DFT derived free enthalpies of ***TS C/D*** for the exclusive loss of HX (cf. Fig. 5).[25] **4⁺, 2(Br)⁺** and **2(CF₃SO₃)⁺** show some deviations from the otherwise linear correlation. This deviation mostly originates from the indeterminacy of ***TS C/D*** on a flat potential energy surface for the HCl loss. Otherwise, the activation energies correlate well with the size of the substituent R: The larger the substituent, the lower is the activation energy. This originates from changes in charge density of the aromatic system by variation of R, as well as from torsional strain within the π-conjugated pyridine-pyrimidine system, which increases with the size of R. The latter effect is explicitly strong within the complexes **2(X)⁺** (as indicated by the dihedral angle $\chi(N_{pym}\text{-C-C-}N_{pyr}) > 15°$) while this is less pronounced for ions **1⁺** and **4⁺** ($\chi(N_{pym}\text{-C-C-}N_{pyr})$ between 0 and 4°). The following order of activation energies was found for the **2(X)⁺** species from experiment and theory, respectively:

$$E_{com}\ \mathbf{2(CF_3SO_3)^+} < E_{com}\ \mathbf{2(Cl)^+} < E_{com}\ \mathbf{2(I)^+} < E_{com}\ \mathbf{2(Br)^+}$$

$$\Delta G^{\ddagger}\ \mathbf{2(CF_3SO_3)^+} < \Delta G^{\ddagger}\ \mathbf{2(Cl)^+} < \Delta G^{\ddagger}\ \mathbf{2(I)^+} \approx \Delta G^{\ddagger}\ \mathbf{2(Br)^+}$$

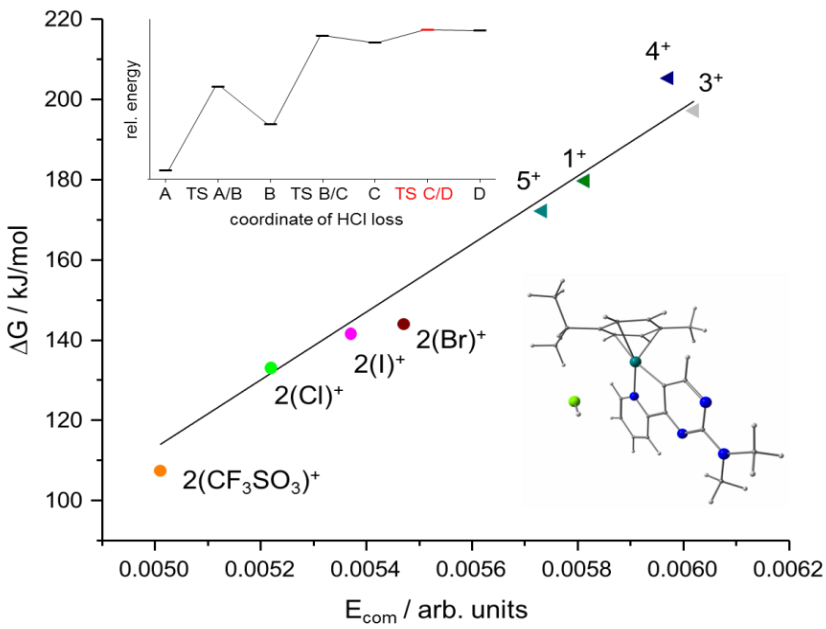

Figure 5: Experimental E_{com} values for the activation of **1⁺-5⁺** and **2(X)⁺** (X = SO_3CF_3, Br or I) and DFT derived free reaction enthalpies $\Delta G^{\ddagger}$ of the third transition state (***TS C/D***) for the loss of HX (for assignments confirm Scheme 2 and Table 1). A linear fit of the data is shown by a solid line, note that this fit does not cross the origin of axis (not shown). The inset shows a generic coordinate for the loss of HCl in the roll-over mechanism. The structure indicates the conformation in ***TS C/D***. Values for **3⁺-5⁺** taken from [17].

HSAB principle and beyond: One might be tempted to interpret the CID findings in terms of the concept of hard and soft acids and bases (HSAB) which classifies iodide as "soft base", followed by bromide, while chloride and $CF_3SO_3^-$ are "hard bases".[80] The ruthenium(II) cation has been seen as a "borderline acid" somewhere in between of "soft" and "hard".[81] The experimental center of mass transferred E_{com} values for the loss of HCl is less than those of HBr and HI, while the relative order of HBr loss and HI loss is reversed in experiments, and the free enthalpies of activation are about equal. Both findings suggesting further causes beyond the mere HASB principle, such as e.g. steric and/or entropic factors.

In this context, we additionally refer to the gas phase acidities (GA) of the acid molecules HX for the reaction $HX \rightleftharpoons H^+ + X^-$ (Δ_{acid} G(XH) in kcal/mol: HCl: 328.1±0.1, HBr: 318.3±0.1, HI: 309.3±0.1, CF_3SO_3H: 292.7±0.5).[82] The larger the value for Δ_{acid} G(XH), the more the equilibrium is shifted to the left side of the equation and proton transfer is less favorable. The relative order of these gas phase acidities is also not in line with our experimental findings and we therefore take a more detailed look at the nature of the

transition states for HX loss.[35, 66] The second transition state, TS B/C, is the crucial step for the anion-proton interaction (cf. Fig. S4b). In the case of **2(CF$_3$SO$_3$)$^+$**, an energetically favorable six-membered TS B/C can be found while the **2(X)$^+$** ions (X = Cl, Br or I) exhibit four-membered, sterically hindered ones (cf. Fig. S4b). In the TS B/C structure of **2(Cl)$^+$**, the chloride is weakly interacting with the C(5)H proton, whereas **2(Br)$^+$** shows a strong anion-proton interaction due to the larger size of the bromide. **2(I)$^+$** exhibits the strongest changes in its transition state structure with respect to the other two halides since its size allows for the most favorable interaction with the C(5)H proton. In conclusion, the bidentate interaction of $CF_3SO_3^-$ with **2$^+$** overcompensates its lower proton uptake affinity and crucially reduces the dissociation energy of CF_3SO_3H with respect to the halide ions. Differences in the anion size in combination with their gas phase acidities lead to partially different transition state structures which might explain the change in the trend of HX loss form **2(Br)$^+$** and **2(I)$^+$**.

Gas phase reactions of activated catalysts

Check for gas phase reactions of the catalysts with isopropanol: The key step in transfer hydrogenation reactions of the [(η^6-cym)Ru(L)]$^+$ complexes is the abstraction of H_2 from isopropanol and the pathway for this reaction was recently calculated by Kerner et al.[17] We have tested for isopropanol adducts of **[1(-HCl)]$^+$** and **[2(-HCl)]$^+$**, and of their conceivable products, e.g. by acetone loss. Therefore, we activated a fraction of the precursor molecules **1$^+$** and **2$^+$** in the linear ion trap of the FT-ICR-MS and stored the molecules for up to 90 s within the FT-ICR cell while undergoing collisions with isopropanol ($p = 5 \times 10^{-9}$ mbar, T = 298 K). The species (**[1(-HCl)]$^+$** and **[2(-HCl)]$^+$**) showed no reaction with isopropanol under the given, single collision reaction conditions. Such vanishingly small rate constants are in line with the calculated activation barrier for the isopropanol addition (□□G ~ 80 kJ/mol) which would involve a reverse roll-over isomerization. Additionally, the probability for reactive uptake might be low due to steric hindrance of the channel for reactive uptake within isopropanol/cation collisions.

Check for gas phase reactions of the catalysts with deuterium: We tested the gas phase reaction of **[1(-HCl)]$^+$** and **[2(-HCl)]$^+$** with deuterium, D_2, in order to characterize the product of the hydrogen transfer reaction. We recorded parent and product intensities throughout reaction delays of up to 240 s (cf. Fig. 6 and S5). The mass spectra reveal a verifiable shift (+4m/z) in the isotopic distribution of the activated complexes **[1(-HCl)]$^+$** and **[2(-HCl)]$^+$** by D_2 addition. Note that the non-activated complexes **1$^+$** and **2$^+$** do not undergo any observable reaction within the chosen reaction window that corresponds to several hundred single collisions with the prospective partner of adsorption and/or reaction. The positive observation of reaction products of the activated complexes **[1(-HCl)]$^+$** and **[2(-HCl)]$^+$** with D_2 let us assume that the activation barrier for D_2 uptake is smaller than that for uptake of isopropanol. Mere physisorption of D_2 seems unlikely when considering that the observed association of D_2 to **[1(-HCl)]$^+$** and **[2(-HCl)]$^+$** takes place under thermal conditions (at 300 K). Instead, we conclude in dissociative D_2 attachment to the Ru center, which might be regarded as a Ru insertion into D_2. The observation that **[1(-HCl)]$^+$** reacts by addition of D_2 is further consistent with its derived structure (see 3.1) as roll-over type isomer (Iso$_1$). Moreover, **1$^+$** is not catalytically active in solution,[35] but its activated form **[1(-HCl)]$^+$** reacts readily in the gas phase as demonstrated here. We refrained from conducting further kinetic analysis of the D_2 uptake which would suffer from considerable uncertainties by the partially overlapping isotopic distributions of reactants and products.

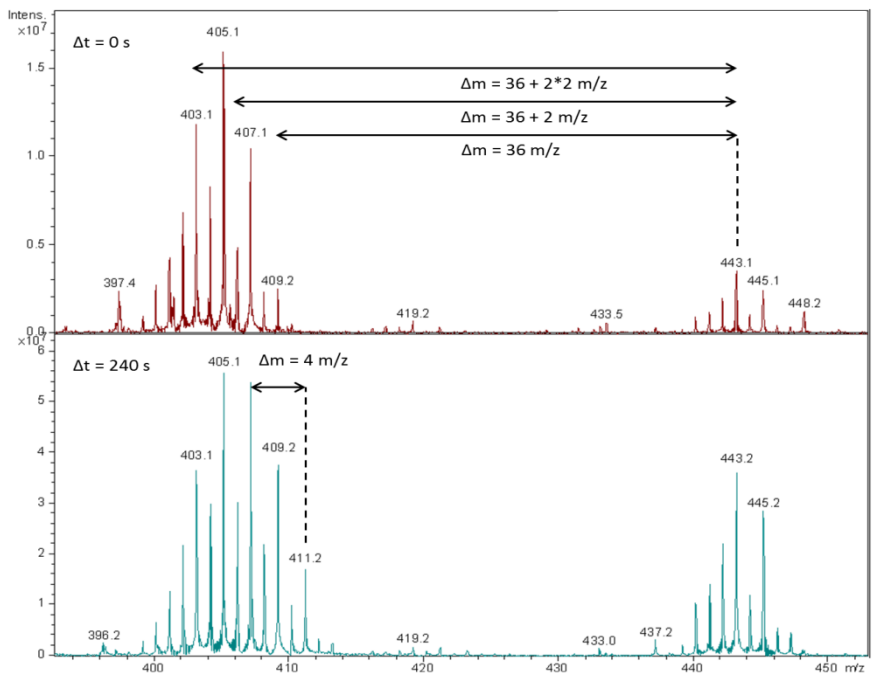

Figure 6: Section of the FT-ICR mass spectra of complexes **1**$^+$ and **[1(-HCl)]**$^+$ at Δt = 0 s (top) and after 240 s reaction time (bottom) with D_2. The isotope pattern at 443.1 m/z (most abundant mass) correlates to complex **1**$^+$, the peak at 407.1 m/z (most abundant mass) to the activated complex **[1(-HCl)]**$^+$, 405.1 and 403.1 m/z to its singly and doubly dehydrogenated products **[1(-HCl-H$_2$)]**$^+$ and **[1(-HCl-2H$_2$)]**$^+$, respectively. 411.2 m/z in the lower spectrum corresponds to the reaction product of complex **[1(-HCl)]**$^+$ with D_2 (p = 5 x 10^{-9} mbar, T = 298 K).

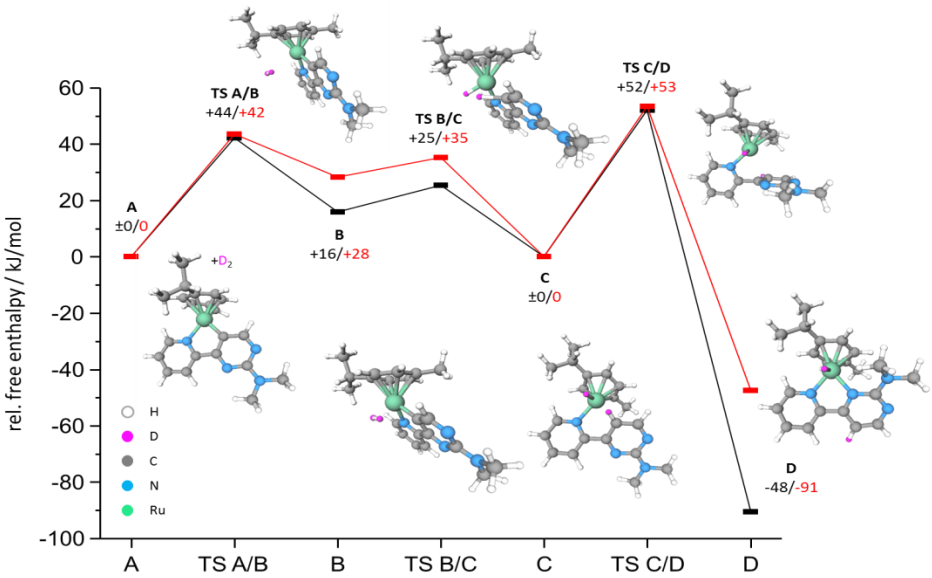

Figure 7: Reaction coordinate of D_2 dissociative attachment at the catalytically active complexes **[1(-HCl)]**$^+$ (–) and **[2(-HCl)]**$^+$ (–). Structures and free enthalpies derived from DFT calculations at the B3LYP/6-311G* (H, D, C, N) and Stuttgart 1997 ECP (Ru) level of theory. Free enthalpies for the separated molecules **[1(-HCl)]**$^+$ and **[2(-HCl)]**$^+$ and D_2 are set to zero. **A**, **B**, **C** and **D** indicate local DFT energy minimum structures, **TS** indicates a transition state between adjacent minima.

DFT modelling of the D_2 uptake: We have conducted a systematic DFT based modeling of the D_2 reaction path with activated catalysts **[1(-HCl)]**$^+$ and **[2(-HCl)]**$^+$, starting from their structures as confirmed by IR-MPD spectroscopy, and DFT based modeling of the HCl loss (cf. Ref.[35] and Fig. 7). The obtained reaction coordinate of D_2 addition shows four local minima (***A***, ***B***, ***C***, and ***D***), and three transition states: an early one (***TS A/B***) while D_2 approaches the complexes, a second one (***TS B/C***) slightly lower in free enthalpy corresponding to the activation of the D-D bond and a late one (***TS C/D***) slightly higher in free enthalpy than the first one (ca. 10 kJ/mol) and corresponding to the reverse rollover isomerization of the pyrimidine ring. The relative free enthalpic barriers for ***TS A/B*** and ***TS C/D*** for D_2 attachment are approximately equal for both complexes with a small influence originating from the side group (-NH_2 in **[1(-HCl)]**$^+$ vs. –$N(CH_3)_2$ in **[2(-HCl)]**$^+$). The third transition state ***TS C/D*** of the reverse rollover is the likely rate determining step on the way to the final products ***D***, which are **[1(-HCl+D$_2$)]**$^+$ and **[2(-HCl+D$_2$)]**$^+$. Their free enthalpies differ by 43 kJ/mol such that we find a conformation of our previous interpretation of the CID experiments: The torsional strain within the pympyr ligand is modulated by the size of the residue R in **[1(-HCl+D$_2$)]**$^+$ and **[2(-HCl+D$_2$)]**$^+$. Note, that the nature of the observed reaction products **[1(-HCl+D$_2$)]**$^+$ and **[2(-HCl+D$_2$)]**$^+$ is hardly in doubt. The complex cannot trap in minimum ***C*** which would react further to ***D*** or back to ***A*** across the given barriers within the timescale of our experiment.

Conclusions and outlook

IR-MPD: We have structurally characterized the archetypal complexes **1**$^+$, **2**$^+$, **[1(-HCl)]**$^+$, and **[2(-HCl)]**$^+$ out of a series of [(η^6-cym)RuCl(pympyr)]$^+$ catalysts by 1- and 2-color IR-MPD spectroscopy. The residues (NH_2 vs. $N(CH_3)_2$) induce structural differences amongst **1**$^+$ and **2**$^+$ by affecting the prevailing torsional strain within the pympyr ligand. The residues modulate the degree of conjugation of the lone-pair of the amine group to the pyridinyl ring, as well as the conjugation of the aromatic rings in the pympyr ligand. The steric requirements of the dimethylamino group lead to a loss of conjugation and therefore a lower activation barrier. Note that the torsional strain vanishes upon HCl elimination and concomitant pympyr intra-ligand roll-over.

Our use of a double resonance scheme allowed for the recording of otherwise 'dark' vibrational IR-MPD bands and we thereby enhanced the validity of our spectral assignments. Thus, the proposed 'roll-over' activation mechanism of [(η^6-cym)RuCl(pympyr)]$^+$ catalysts receives independent confirmation by our spectroscopic data on the isolated species.

CID: The variation of the anion X (X= Cl, Br, I) bound to the ruthenium center in **2(X)**$^+$ modulates its activation barrier partly in line with the HSAB concept and fully according to their gas phase acidities. **2(Br)**$^+$ and **2(I)**$^+$ exhibit higher activation barriers than **2(Cl)**$^+$. We observed the lowest activation barrier in the case of complex **2(SO$_3$CF$_3$)**$^+$. The $CF_3SO_3^-$ anion is an exception in the trend with respect to its higher gas phase acidity but overcompensates this due to an energetically favored six-membered transition state. The activation barriers by CID and DFT correlate well.

Reactivity: We did not observe any gas phase reactions between the catalysts and isopropanol (neither the precursors nor the activated complexes). However, there are gas phase reactions of the activated complexes **[1(-HCl)]**$^+$ and **[2(-HCl)]**$^+$ with D_2. DFT modelling of their reaction pathways suggests a heterolytic cleavage of the D_2 molecule and the formation of a ruthenium hydrido complex via three consecutive transition states.

Outlook: Future spectroscopic IR-MPD characterization might unravel further details of the product conformation ***D*** in **[1(-HCl+D$_2$)]**$^+$ and **[2(-HCl+D$_2$)]**$^+$. It might also help to obtain absolute rate constants in order to evaluate against a quantitative kinetic modelling on the basis of the computed structures and reaction path enthalpies.

Acknowledgements

This work was supported by the German research foundation DFG within the transregional collaborative research center SFB/TRR 88 "Cooperative effects in homo and heterometallic complexes" (3MET).

Supporting Information

Supporting Information is available free of charge on the ACS Publications website at DOI: xxxx. It contains structural data, mass spectra, band assignments and input coordinates of the investigated ruthenium complexes.

References

1. Ikariya, T.; Murata, K.; Noyori, R., Bifunctional Transition Metal-Based Molecular Catalysts for Asymmetric Syntheses. *Org Biomol Chem* **2006,** *4*, 393-406.
2. Zassinovich, G.; Mestroni, G.; Gladiali, S., Asymmetric Hydrogen Transfer Reactions Promoted by Homogeneous Transition Metal Catalysts. *Chem Rev* **1992,** *92*, 1051-1069.
3. Noyori, R.; Hashiguchi, S., Asymmetric Transfer Hydrogenation Catalyzed by Chiral Ruthenium Complexes. *Acc Chem Res* **1997,** *30*, 97-102.
4. Naota, T.; Takaya, H.; Murahashi, S. I., Ruthenium-Catalyzed Reactions for Organic Synthesis. *Chem Rev* **1998,** *98*, 2599-2660.
5. Yamakawa, M.; Ito, H.; Noyori, R., The Metal-Ligand Bifunctional Catalysis: A Theoretical Study on the Ruthenium(II)-Catalyzed Hydrogen Transfer Between Alcohols and Carbonyl Compounds. *J Am Chem Soc* **2000,** *122*, 1466-1478.
6. Clapham, S. E.; Hadzovic, A.; Morris, R. H., Mechanisms of the H_2-Hydrogenation and Transfer Hydrogenation of Polar Bonds Catalyzed by Ruthenium Hydride Complexes. *Coordin Chem Rev* **2004,** *248*, 2201-2237.
7. Gladiali, S.; Alberico, E., Asymmetric Transfer Hydrogenation: Chiral Ligands and Applications. *Chem Soc Rev* **2006,** *35*, 226-236.
8. Azua, A.; Mata, J. A.; Peris, E.; Lamaty, F.; Martinez, J.; Colacino, E., Alternative Energy Input for Transfer Hydrogenation Using Iridium NHC Based Catalysts in Glycerol as Hydrogen Donor and Solvent. *Organometallics* **2012,** *31*, 3911-3919.
9. Han, Y. F.; Jin, G. X., Cyclometalated [Cp*M(C^X)] (M = Ir, Rh; X = N, C, O, P) Complexes. *Chem Soc Rev* **2014,** *43*, 2799-2823.
10. Mirzadeh, N.; Bennett, M. A.; Bhargava, S. K., Cycloaurated Complexes of Aryl Carbanions: Digold(I), Digold(II) and Beyond. *Coordin Chem Rev* **2013,** *257*, 2250-2273.
11. Albrecht, M., Cyclometalation Using d-Block Transition Metals: Fundamental Aspects and Recent Trends. *Chem Rev* **2010,** *110*, 576-623.
12. Omae, I., Intramolecular Five-Membered Ring Compounds and Their Applications. *Coordin Chem Rev* **2004,** *248*, 995-1023.
13. Bruce, M. I., Cyclometalation Reactions. *Angew Chem Int Edit* **1977,** *16*, 73-86.
14. Dehand, J.; Pfeffer, M., Cyclometallated Compounds. *Coordin Chem Rev* **1976,** *18*, 327-352.
15. Foubelo, F.; Najera, C.; Yus, M., Catalytic Asymmetric Transfer Hydrogenation of Ketones: Recent Advances. *Tetrahedron-Asymmetr* **2015,** *26*, 769-790.
16. Vaclavik, J.; Sot, P.; Vilhanova, B.; Pechacek, J.; Kuzma, M.; Kacer, P., Practical Aspects and Mechanism of Asymmetric Hydrogenation with Chiral Half-Sandwich Complexes. *Molecules* **2013,** *18*, 6804-6828.
17. Nixon, T. D.; Whittlesey, M. K.; Williams, J. M. J., Transition Metal Catalysed Reactions of Alcohols Using Borrowing Hydrogen Methodology. *Dalton T* **2009**, 753-762.
18. Dub, P. A.; Gordon, J. C., The Mechanism of Enantioselective Ketone Reduction with Noyori and Noyori-Ikariya Bifunctional Catalysts. *Dalton T* **2016,** *45*, 6756-6781.
19. Morris, R. H., Exploiting Metal-Ligand Bifunctional Reactions in the Design of Iron Asymmetric Hydrogenation Catalysts. *Acc Chem Res* **2015,** *48*, 1494-1502.
20. Warner, M. C.; Casey, C. P.; Backvall, J. E., Shvo's Catalyst in Hydrogen Transfer Reactions. *Top Organometal Chem* **2011,** *37*, 85-125.
21. Ohkuma, T.; Ooka, H.; Hashiguchi, S.; Ikariya, T.; Noyori, R., Practical Enantioselective Hydrogenation of Aromatic Ketones. *J Am Chem Soc* **1995,** *117*, 2675-2676.

22. Fujii, A.; Hashiguchi, S.; Uematsu, N.; Ikariya, T.; Noyori, R., Ruthenium(II)-Catalyzed Asymmetric Transfer Hydrogenation of Ketones Using a Formic Acid-Triethylamine Mixture. *J Am Chem Soc* **1996,** *118*, 2521-2522.
23. Sandoval, C. A.; Ohkuma, T.; Utsumi, N.; Tsutsumi, K.; Murata, K.; Noyori, R., Mechanism of Asymmetric Hydrogenation of Acetophenone Catalyzed by Chiral eta(6)-arene-N-tosylethylenediamine-ruthenium(II) Complexes. *Chem-Asian J* **2006,** *1*, 102-110.
24. Dong, Z. R.; Li, Y. Y.; Chen, J. S.; Li, B. Z.; Xing, Y.; Gao, J. X., Highly Eefficient Iridium Catalyst for Asymmetric Transfer Hydrogenation of Aromatic Ketones Under Base-Free Conditions. *Org Lett* **2005,** *7*, 1043-1045.
25. Clarke, Z. E.; Maragh, P. T.; Dasgupta, T. P.; Gusev, D. G.; Lough, A. J.; Abdur-Rashid, K., A Family of Active Iridium Catalysts for Transfer Hydrogenation of Ketones. *Organometallics* **2006,** *25*, 4113-4117.
26. Corberan, R.; Peris, E., An Unusual Example of Base-Free Catalyzed Reduction of C=O and C=NR Bonds by Transfer Hydrogenation and Some Useful Implications. *Organometallics* **2008,** *27*, 1954-1958.
27. Lagaditis, P. O.; Lough, A. J.; Morris, R. H., Low-Valent ene-Amido Iron Complexes for the Asymmetric Transfer Hydrogenation of Acetophenone without Base. *J Am Chem Soc* **2011,** *133*, 9662-9665.
28. Wienhofer, G.; Sorribes, I.; Boddien, A.; Westerhaus, F.; Junge, K.; Junge, H.; Llusar, R.; Beller, M., General and Selective Iron-Catalyzed Transfer Hydrogenation of Nitroarenes without Base. *J Am Chem Soc* **2011,** *133*, 12875-12879.
29. Castarlenas, R.; Esteruelas, M. A.; Onate, E., Preparation, X-ray Structure, and Reactivity of an Osmium-Hydroxo Complex Stabilized by an N-heterocyclic Carbene Ligand: A Base-Free Catalytic Precursor for Hydrogen Transfer from 2-propanol to Aldehydes. *Organometallics* **2008,** *27*, 3240-3247.
30. Carrion, M. C.; Sepulveda, F.; Jalon, F. A.; Manzano, B. R.; Rodriguez, A. M., Base-Free Transfer Hydrogenation of Ketones Using Arene Ruthenium(II) Complexes. *Organometallics* **2009,** *28*, 3822-3833.
31. Elliott, A. G.; Green, A. G.; Diaconescu, P. L., Transfer Hydrogenation with a Ferrocene Diamide Ruthenium Complex. *Dalton T* **2012,** *41*, 7852-7854.
32. He, L.-P.; Chen, T.; Xue, D.-X.; Eddaoudi, M.; Huang, K.-W., Efficient Transfer Hydrogenation Reaction Catalyzed by a Dearomatized PN^3P Ruthenium Pincer Complex Under Base-Free Conditions. *J Organomet Chem* **2012,** *700*, 202-206.
33. DePasquale, J.; Kumar, M.; Zeller, M.; Papish, E. T., Variations on an NHC Theme: Which Features Enhance Catalytic Transfer Hydrogenation with Ruthenium Complexes? *Organometallics* **2013,** *32*, 966-979.
34. Kumar, M.; DePasquale, J.; White, N. J.; Zeller, M.; Papish, E. T., Ruthenium Complexes of Triazole-Based Scorpionate Ligands Transfer Hydrogen to Substrates under Base-Free Conditions. *Organometallics* **2013,** *32*, 2135-2144.
35. Ghoochany, L. T.; Kerner, C.; Farsadpour, S.; Menges, F.; Sun, Y.; Niedner-Schatteburg, G.; Thiel, W. R., C-H Activation at a Ruthenium(II) Complex - The Key Step for a Base-Free Catalytic Transfer Hydrogenation? *Eur J Inorg Chem* **2013,** *2013*, 4305-4317.
36. Jongbloed, L. S.; de Bruin, B.; Reek, J. N. H.; Lutz, M.; van der Vlugt, J. I., Reversible Cyclometalation at Rh-I as a Motif for Metal-ligand Bifunctional Bond Activation and Base-Free Formic Acid Dehydrogenation. *Catal Sci Technol* **2016,** *6*, 1320-1327.
37. Jazzar, R. F. R.; Macgregor, S. A.; Mahon, M. F.; Richards, S. P.; Whittlesey, M. K., C-C and C-H Bond Activation Reactions in N-heterocyclic Carbene Complexes of Ruthenium. *J Am Chem Soc* **2002,** *124*, 4944-4945.
38. Burling, S.; Paine, B. M.; Nama, D.; Brown, V. S.; Mahon, M. F.; Prior, T. J.; Pregosin, P. S.; Whittlesey, M. K.; Williams, J. M. J., C-H Activation Reactions of Ruthenium N-heterocyclic Carbene Complexes: Application in a Catalytic Tandem Reaction Involving C-C Bond Formation from Alcohols. *J Am Chem Soc* **2007,** *129*, 1987-1995.
39. Choi, G.; Tsurugi, H.; Mashima, K., Hemilabile N-Xylyl-N'-methylperimidine Carbene Iridium Complexes as Catalysts for C-H Activation and Dehydrogenative Silylation: Dual Role of N-Xylyl Moiety for ortho-C-H Bond Activation and Reductive Bond Cleavage. *J Am Chem Soc* **2013,** *135*, 13149-13161.
40. Bhattacharya, P.; Krause, J. A.; Guan, H. R., Mechanistic Studies of Ammonia Borane Dehydrogenation Catalyzed by Iron Pincer Complexes. *J Am Chem Soc* **2014,** *136*, 11153-11161.
41. Boulho, C.; Djukic, J. P., The Dehydrogenation of Ammonia-Borane Catalysed by Dicarbonylruthenacyclic(II) Complexes. *Dalton T* **2010,** *39*, 8893-8905.
42. Ghatak, K.; Mane, M.; Vanka, K., Metal or Nonmetal Cooperation with a Phenyl Group: Route to Catalysis? A Computational Investigation. *Acs Catal* **2013,** *3*, 920-927.
43. Li, B.; Dixneuf, P. H., sp(2) C-H Bond Activation in Water and Catalytic Crosscoupling Reactions. *Chem Soc Rev* **2013,** *42*, 5744-5767.
44. Ackermann, L.; Vicente, R.; Kapdi, A. R., Transition-Metal-Catalyzed Direct Arylation of (Hetero)Arenes by C-H Bond Cleavage. *Angewandte Chemie-International Edition* **2009,** *48*, 9792-9826.

45. Farsadpour, S.; Ghoochany, L. T.; Sun, Y.; Thiel, W. R., Small Substituents Make Large Differences: Aminopyrimidinyl Phosphanes Undergoing C–H Activation. *Eur J Inorg Chem* **2011,** *2011*, 4603-4609.
46. Farsadpour, S.; Ghoochany, L. T.; Shylesh, S.; Dörr, G.; Seifert, A.; Ernst, S.; Thiel, W. R., A Covalently Supported Pyrimidinylphosphane Palladacycle as a Heterogenized Catalyst for the Suzuki–Miyaura Cross Coupling. *ChemCatChem* **2012,** *4*, 401-407.
47. Kerner, C.; Straub, S.-D.; Sun, Y.; Thiel, W. R., A Rapid and Additive-Free Ruthenium-Catalyzed Reductive Amination of Aromatic Aldehydes. *Eur J Org Chem* **2016,** *2016*, 3060-3064.
48. MacAleese, L.; Maitre, P., Infrared Spectroscopy of Organometallic Ions in the Gas Phase: From Model to Real World Complexes. *Mass Spectrom Rev* **2007,** *26*, 583-605.
49. Wu, G. H.; Chapman, D.; Stace, A. J., Trapping and Recording the Collision- and Photo-Induced Fragmentation Patterns of Multiply Charged Metal Complexes in the Gas Phase. *Int J Mass Spectrom* **2007,** *262*, 211-219.
50. Jasikova, L.; Hanikyrova, E.; Schroder, D.; Roithova, J., Aromatic C-H Bond Activation Revealed by Infrared Multiphoton Dissociation Spectroscopy. *J Mass Spectrom* **2012,** *47*, 460-465.
51. Roithova, J., Characterization of Reaction Intermediates by Ion Spectroscopy. *Chem Soc Rev* **2012,** *41*, 547-559.
52. Laskin, J.; Futrell, J. H., Activation of Large Ions in FT-ICR Mass Spectrometry. *Mass Spectrom Rev* **2005,** *24*, 135-167.
53. Polfer, N. C.; Oomens, J., Vibrational Spectroscopy of Bare and Solvated Ionic Complexes of Biological Relevance. *Mass Spectrom Rev* **2009,** *28*, 468-494.
54. Sleno, L.; Volmer, D. A., Ion Activation Methods for Tandem Mass Spectrometry. *J Mass Spectrom* **2004,** *39*, 1091-1112.
55. Škríba, A.; Jašík, J.; Andris, E.; Roithová, J., Interaction of Ruthenium(II) with Terminal Alkynes: Benchmarking DFT Methods with Spectroscopic Data. *Organometallics* **2016,** *35*, 990-994.
56. Janis, J.; Jakonen, M.; Oresmaa, L.; Hirva, P.; Laurila, E.; Vlasova, L.; Vainiotalo, P.; Haukka, M., Fragmentation Pathways of $[MX_2(CO)_2(dcbpy)]$ (M = Ru, Os; X = Cl, Br, I; dcbpy=2,2 '-bipyridine-4,4 '-dicarboxylic acid) Complexes. *Organometallics* **2010,** *29*, 1070-1078.
57. Imanbaew, D.; Nosenko, Y.; Kerner, C.; Chevalier, K.; Rupp, F.; Riehn, C.; Thiel, W. R.; Diller, R., Excited-State Dynamics of a Ruthenium(II) Catalyst Studied by Transient Photofragmentation in Gas Phase and Transient Absorption in Solution. *Chem Phys* **2014,** *442*, 53-61.
58. Nosenko, Y.; Menges, F.; Riehn, C.; Niedner-Schatteburg, G., Investigation by Two-Color IR Dissociation Spectroscopy of Hoogsteen-Type Binding in a Metalated Nucleobase Pair Mimic. *Phys Chem Chem Phys* **2013,** *15*, 8171-8178.
59. Pankewitz, T.; Lagutschenkov, A.; Niedner-Schatteburg, G.; Xantheas, S. S.; Lee, Y.-T., Infrared Spectrum of $NH_4^+(H_2O)$: Evidence for Mode Specific Fragmentation. *J Chem Phys* **2007,** *126*, 074307.
60. Wolke, C. T.; Menges, F. S.; Tötsch, N.; Gorlova, O.; Fournier, J. A.; Weddle, G. H.; Johnson, M. A.; Heine, N.; Esser, T. K.; Knorke, H.; Asmis, K. R.; McCoy, A. B.; Arismendi-Arrieta, D. J.; Prosmiti, R.; Paesani, F., Thermodynamics of Water Dimer Dissociation in the Primary Hydration Shell of the Iodide Ion with Temperature-Dependent Vibrational Predissociation Spectroscopy. *J Phys Chem A* **2015,** *119*, 1859-1866.
61. Pivonka, N. L.; Kaposta, C.; Helden, G. v.; Meijer, G.; Wöste, L.; Neumark, D. M.; Asmis, K. R., Gas Phase Infrared Spectroscopy of Cluster Anions as a Function of Size: The Effect of Solvation on Hydrogen-Bonding in $Br^-(HBr)_{1,2,3}$ Clusters. *J Chem Phys* **2002,** *117*, 6493-6499.
62. Di Tommaso, D.; French, S. A.; Catlow, C. R. A., The H_2-Hydrogenation of Ketones Catalysed by Ruthenium(II) Complexes: A Density Functional Theory Study. *J Mol Struc-Theochem* **2007,** *812*, 39-49.
63. Prokopchuk, D. E.; Morris, R. H., Inner-Sphere Activation, Outer-Sphere Catalysis: Theoretical Study on the Mechanism of Transfer Hydrogenation of Ketones Using Iron(II) PNNP Eneamido Complexes. *Organometallics* **2012,** *31*, 7375-7385.
64. Prokopchuk, D. E.; Sonnenberg, J. F.; Meyer, N.; Iuliis, M. Z. D.; Lough, A. J.; Morris, R. H., Spectroscopic and DFT Study of Ferraaziridine Complexes Formed in the Transfer Hydrogenation of Acetophenone Catalyzed Using trans-$[Fe(CO)(NCMe)(PPh_2C_6H_4CH{=}NCH_2\text{-})_2\text{-}k^4\ P,N,N,P](BF_4)_2$. *Organometallics* **2012,** *31*, 3056-3064.
65. Nakajima, Y.; Sakaki, S.; Nakao, Y.; Suzuki, H., Theoretical Study of Dihydrogen Activation by a Trinuclear Ruthenium m_3-Imido Complex. *Organometallics* **2012,** *31*, 5342-5348.
66. Kerner, C.; Lang, J.; Gaffga, M.; Menges, F. S.; Sun, Y.; Niedner-Schatteburg, G.; Thiel, W. R., Mechanistic Studies on Ruthenium(II)-Catalyzed Base-Free Transfer Hydrogenation Triggered by Roll-Over Cyclometalation. *ChemPlusChem* **2017,** *82*, 212-224.
67. Laskin, J.; Lifshitz, C., Kinetic Energy Release Distributions in Mass Spectrometry. *J Mass Spectrom* **2001,** *36*, 459-478.

68. Armentrout, P. B., Guided Ion Beam Studies of Transition Metal-Ligand Thermochemistry. *Int J Mass Spectrom* **2003,** *227*, 289-302.
69. Zins, E.-L.; Pepe, C.; Schroeder, D., Energy-Dependent Dissociation of Benzylpyridinium Ions in an Ion-Trap Mass Spectrometer. *J Mass Spectrom* **2010,** *45*, 1253-1260.
70. Mcluckey, S. A., Principles of Collisional Activation in Analytical Mass-Spectrometry. *J Am Soc Mass Spectr* **1992,** *3*, 599-614.
71. Becke, A. D., Density-Functional Exchange-Energy Approximation With Correct Asymptotic-Behavior. *Phys Rev A* **1988,** *38*, 3098-3100.
72. Lee, C. T.; Yang, W. T.; Parr, R. G., Development of the Colle-Salvetti Correlation-Energy Formula into a Functional of the Electron-Density. *Phys Rev B* **1988,** *37*, 785-789.
73. Miehlich, B.; Savin, A.; Stoll, H.; Preuss, H., Results Obtained with the Correlation-Energy Density Functionals of Becke and Lee, Yang and Parr. *Chem Phys Lett* **1989,** *157*, 200-206.
74. Becke, A. D., Density-Functional Thermochemistry.3. The Role of Exact Exchange. *J Chem Phys* **1993,** *98*, 5648-5652.
75. Dolg, M.; Stoll, H.; Preuss, H.; Pitzer, R. M., Relativistic and Correlation Effects for Element 105 (Hahnium, Ha): a Comparative Study of M and MO (M = Nb, Ta, Ha) Using Energy-Adjusted ab initio Pseudopotentials. *J Phys Chem* **1993,** *97*, 5852-5859.
76. Frisch, M. J.; Trucks, G. W.; Schlegel, H. B.; Scuseria, G. E.; Robb, M. A.; Cheeseman, J. R.; Scalmani, G.; Barone, V.; Mennucci, B.; Petersson, G. A.; Nakatsuji, H.; Caricato, M.; Li, X.; Hratchian, H. P.; Izmaylov, A. F.; Bloino, J.; Zheng, G.; Sonnenberg, J. L.; Hada, M.; Ehara, M.; Toyota, K.; Fukuda, R.; Hasegawa, J.; Ishida, M.; Nakajima, T.; Honda, Y.; Kitao, O.; Nakai, H.; Vreven, T.; Montgomery, J. A.; Peralta, J. E.; Ogliaro, F.; Bearpark, M.; Heyd, J. J.; Brothers, E.; Kudin, K. N.; Staroverov, V. N.; Kobayashi, R.; Normand, J.; Raghavachari, K.; Rendell, A.; Burant, J. C.; Iyengar, S. S.; Tomasi, J.; Cossi, M.; Rega, N.; Millam, J. M.; Klene, M.; Knox, J. E.; Cross, J. B.; Bakken, V.; Adamo, C.; Jaramillo, J.; Gomperts, R.; Stratmann, R. E.; Yazyev, O.; Austin, A. J.; Cammi, R.; Pomelli, C.; Ochterski, J. W.; Martin, R. L.; Morokuma, K.; Zakrzewski, V. G.; Voth, G. A.; Salvador, P.; Dannenberg, J. J.; Dapprich, S.; Daniels, A. D.; Farkas; Foresman, J. B.; Ortiz, J. V.; Cioslowski, J.; Fox, D. J., Gaussian 09, Revision B.01. Wallingford CT, 2009.
77. Andersson, M. P.; Uvdal, P., New Scale Factors for Harmonic Vibrational Frequencies Using the B3LYP Density Functional Method with the Triple-x Basis Set 6-311+G(d,p). *J Phys Chem A* **2005,** *109*, 2937-2941.
78. Fehrensen, B.; Luckhaus, D.; Quack, M., Inversion Tunneling in Aniline from High Resolution Infrared Spectroscopy and an Adiabatic Reaction Path Hamiltonian Approach. *Z Phys Chem* **1999,** *209*, 1-19.
79. McCarthy, W. J.; Lapinski, L.; Nowak, M. J.; Adamowicz, L., Out-of-plane Vibrations of NH_2 in 2-aminopyrimidine and Formamide. *J Chem Phys* **1998,** *108*, 10116-10128.
80. Pearson, R. G., Hard and Soft Acids and Bases. *J Am Chem Soc* **1963,** *85*, 3533-&.
81. Pearson, R. G., Absolute Electronegativity and Hardness - Application to Inorganic-Chemistry. *Inorg Chem* **1988,** *27*, 734-740.
82. Trummal, A.; Lipping, L.; Kaljurand, I.; Koppel, I. A.; Leito, I., Acidity of Strong Acids in Water and Dimethyl Sulfoxide. *J Phys Chem A* **2016,** *120*, 3663-3669.

11.7 The Dinickelocene [Cp´´´Ni-NiCp´´´]

Ina Schädlich, Frank Zimmer#, Yu Sun, Werner R. Thiel, Harald Kelm, Benjamin Oelkers, Gotthelf Wolmershäuser, Johannes Lang, Gereon Niedner-Schatteburg, Christine Mehlich, Christoph van Wüllen, Helmut Sitzmann

Department of Chemistry and Forschungszentrum OPTIMAS,
Technical University Kaiserslautern,
67663 Kaiserslautern, Germany

Current address: INVISTA Resins & Fibers GmbH,
Ketteler Str. 99, 63075 Offenbach, Germany.

11.7.1 Preamble

The following chapter is formatted as a manuscript for publication. It is prepared for submission as soon as pending crystallographic analytics have been finalized.

The crystal structure of [Cp´´´Ni-NiCp´´´] as presented in this study has yet to be confirmed and distinguished beyond reasonable doubt from its dihydride version [Cp´´´Ni(μ-H)]$_2$. One crystal structure modification of [Cp´´´Ni(μ-H)]$_2$ has been identified. We cannot rule out, that it exhibits a second modification in analogy to [Cp´´´Ni(μ-Br)]$_2$, which does indeed exhibit two modifications. It is a challenging task to differentiate between [Cp´´´Ni-NiCp´´´] and a possible second modification of [Cp´´´Ni(μ-H)]$_2$ in the crystallographic data. [Cp´´´Ni-NiCp´´´] crystals without any contribution of [Cp´´´Ni(μ-H)]$_2$ are currently in preparation to solve this issue (as of Mai 2017).

I. Schädlich and F. Zimmer from the research group of Prof. Dr. H. Sitzmann synthesized the investigated complexes. Y. Sun, and B. Oelkers from the research group provided the crystallographic data. H. Kelm contributed with NMR measurements. C. Mehlich from the research group of Christoph van Wüllen conducted the DFT modelling. I contributed with Electrospray Ionization mass spectrometry (ESI-MS) and Collision Induced Dissociation (CID) experiments. I. Schädlich and H. Sitzmann wrote this manuscript and were supported by C. van Wüllen and myself.

11.7.2 Manuscript

The Dinickelocene [Cp´´´Ni-NiCp´´´]

Authors: Ina Schädlich, Frank Zimmer#, Yu Sun, Werner R. Thiel, Harald Kelm, Benjamin Oelkers, Gotthelf Wolmershäuser, Johannes Lang, Gereon Niedner-Schatteburg, Christine Mehlich, Christoph van Wüllen*, Helmut Sitzmann*

Affiliations:

Department of Chemistry and Forschungszentrum OPTIMAS, Technical University Kaiserslautern, Erwin-Schroedinger-Str. 54, 67663 Kaiserslautern, Germany.

*Correspondence to: vanwullen@chemie.uni-kl.de, sitzmann@chemie.uni-kl.de.
#Current address: INVISTA Resins & Fibers GmbH, Ketteler Str. 99, 63075 Offenbach, Germany.

Abstract

More than a decade after the discovery of decamethyldizincocene the reduction of alkylcyclopentadienylnickel(II) bromides with trisodium heptaantimonide yielded reaction mixtures, from which hexa(*tert*-butyl)dinickelocene could be crystallized. In the paramagnetic dimer with a Ni-Ni distance of 2.2944(3) Å, quantum chemical calculations suggest that this is a Ni-Ni single bond. The paramagnetic dihydride $[Cp´´´Ni(\mu\text{-}H)]_2$ with a 2.2707(5) Å Ni-Ni distance is the main product in pentane solution and even more prominent, if the reaction is carried out in tetrahydrofuran. An intermediate capable of abstracting hydrogen from pentane could be the nickel(I) half sandwich fragment [Cp´´´Ni] or its bromide adduct $[Cp´´´NiBr]^-$.

One Sentence Summary

Reduction of $[Cp´´´Ni(\mu\text{-}Br)]_2$ with Na_3Sb_7 produced $[Cp´´´Ni(\mu\text{-}H)]_2$ and the first dinickelocene $[Cp´´´Ni]_2$ via intermediates capable of attacking the pentane solvent.

Main Text

Although mercury(I) ions had long been known to form strong Hg-Hg bonds (*1*) and the first molecular species with a direct metal-metal bond between two group 12 metal atoms was the cadmium(I)tris(pyrazolyl)borate derivative $[HB(3,5\text{-}Me_2pz)_3Cd\text{-}Cd(3,5\text{-}Me_2pz)_3BH]$ (*2*), it was a zinc(I) compound that became the first dimetallocene: The discovery of the decamethyldizincocene [Cp*Zn-ZnCp*] (*1,3*) stimulated theoretical work on dimetallocenes of zinc (*4-9*), cadmium (*6,8,9*), mercury (*8,9*), copper (*4,5*), nickel (*4,5*) and alkaline earth metals (*5,6,10*). Reactions with (*11*) or without Zn-Zn bond cleavage (*12*) have been carried out with decamethyldizincocene (*13*) and its catalytic properties have been used for intra- and intermolecular hydroamination (*14*). Calculations have also been carried out on dimetallocenes of scandium and titanium (*15*), vanadium and chromium (*16*), osmium, rhenium, tungsten, and tantalum (*17*) as well as thorium, protactinium, uranium, neptunium, and plutonium (*18*).

Apart from treatment as an object of theoretical calculations, dinickelocene has been postulated as an intermediate in reactions of nickelocene with organolithium compounds affording the tri- and tetranuclear nickel clusters $[(CpNi)_3CMe]$ and $[(CpNi)_4(H)_2]$ (*19*). The latter can be viewed as an addition product of the parent dinickelocene $[CpNi]_2$ with its dihydride $[(CpNi)(\mu\text{-}H)]_2$. In electron ionization (ESI) mass spectra of tris(cyclopentadienylnickel)alkylidyne complexes the molecular ion of dinickelocene $[(CpNi)_2]^+$ has been observed with a relative intensity of 50% (*19*) and mass spectra of the cyclopentadiene complex $[CpNi(\mu\text{-}C_5H_6)NiCp]$ (*20*) showed the *m/z*=246 signal for $[(CpNi)_2]^+$ with 98% relative intensity (*21*). The cyclopentadienylnickel(II) cation $[CpNi]^+$ could be reduced to the neutral

[CpNi] fragment in the gas phase by collision with xenon atoms and reionized in a second collision step with oxygen molecules (*22*). The octahedral cyclopentadienylnickel hexamer $[CpNi]_6$ was isolated from the reduction of nickelocene with one equivalent of sodium naphthalenide (*23*) and the heterobimetallic dimetallocene [CpNi-ZnCp] has been postulated as an intermediate of $[Cp_6Zn_4Ni_2]$ cluster formation in the reaction of dicyclopentadienylzinc $[Cp_2Zn]$ with bis(cyclooctadiene)nickel(0) (*24*). The cocondensation of di(*tert*-butyl)cyclopentadiene with nickel atoms produced the trinuclear dihydride $[(Cp''Ni)_3(\mu^3\text{-}H)_2]$ and tri(*tert*-butyl)cyclopentadiene afforded the mononuclear cyclopentadienyl(cyclopentenyl)nickel derivative $[Cp'''Ni(\eta^3\text{-}C_5H_4{}^tBu_3)]$ under similar conditions (*25*). However, a dinickelocene could so far not be characterized as a stable compound.

This work was started by Frank Zimmer in 2002 during reactions of the 1,2,4-tri(tert-butyl)cyclopentadienylnickel(II) bromide dimer $[Cp'''Ni(\mu\text{-}Br)]_2$ (**1**) in tetrahydrofuran with trisodium heptaantimonide, Na_3Sb_7, which yielded a yellow-brown powder of the dihydride $[Cp'''Ni(\mu\text{-}H)]_2$ (**2**) in 58% yield after solvent removal, pentane extraction and storage at -78 °C (*26*). The dihydride **2** is moderately sensitive towards air and moisture, melts with decomposition at 154 °C and shows the broad ^1H NMR signals within a wide spectral window typical for paramagnetic alkylcyclopentadienylnickel(II) complexes (*27*). Single crystals of **2** suitable for X-ray diffraction could be obtained from pentane at -20 °C (*26*). A very reactive nickel complex **3** was obtained by reduction of **1** in pentane and could only be isolated as oily or tarry mixtures with significant amounts of the dihydride $[Cp'''Ni(\mu\text{-}H)]_2$ (**2**) and varying amounts of 1,3,5-tri(tert-butyl)cyclopentadiene (*26*). This complex **3** gave the dihydride **2** with tetrahydrofuran and the known (*28*) binuclear carbonyl complex $[Cp'''Ni(\mu\text{-}CO)]_2$ (**4**) with carbon monoxide (*26*). Regarding **3** as the 1,1′,2,2′,4,4′-hexa(tert-butyl)dinickelocene [Cp′′′Ni-NiCp′′′] and finding ourselves unable to get a hold on it, another attempt more than ten years later went better and revealed intriguing processes in the reaction solutions. The reactions within this tri(tert-butyl)cyclopentadienylnickel system are more straightforward than those of the tetraisopropylcyclopentadienylnickel analogues and will be discussed in this manuscript.

On a search for a more selective reduction process, other reducing agents such as alkali metals, sodium amalgam, or potassium graphite performed less promising than Na_3Sb_7 for the nickel analogue **1**, which parallels previous experience with the reduction of the iron analogue of **1** (*29*). Attempted reduction with magnesium, aluminum, or zinc led to the isolation of unreacted dibromide **1**, which crystallized in a previously unknown monoclinic modification (see supporting information).

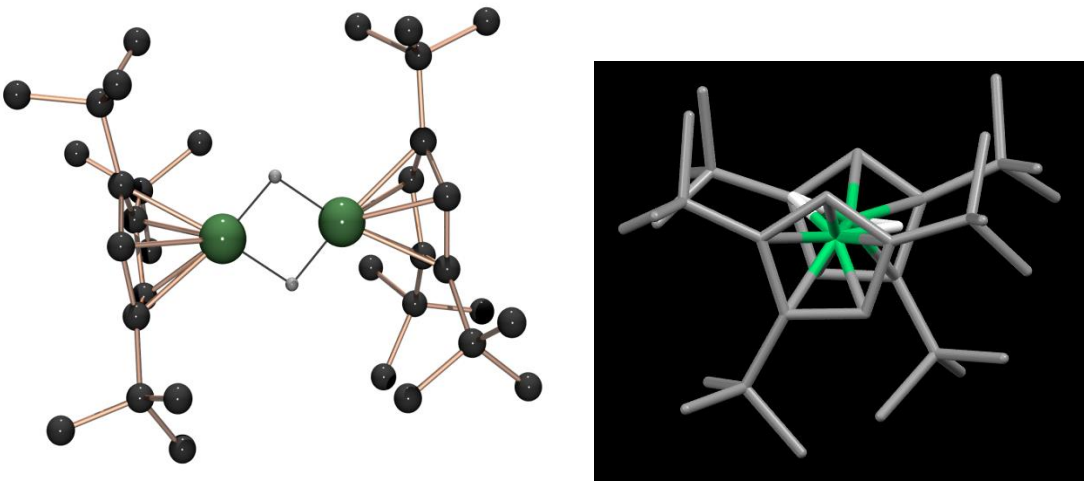

Figure 1: Crystal structure and rotational conformation of the dinickel dihydride **2**.

Distances/Å and angles/°: Ni1-Ni2 2.2707(5), Ni1-H1 1.47(4), Ni1-H2 1.58(3), Ni2-H1 1.53(3), Ni2-H2 1.51(3), Ni1-C1 2.139(3), Ni1-C2 2.111(3), Ni1-C3 2.104(3), Ni1-C4 2.114(3), Ni1-C5 2.120(3), Ni2-C6 2.115(3), Ni2-C7 2.133(3), Ni2-C8 2.094(3), Ni2-C9 2.126(3), Ni2-C10 2.115(3), Ni1-Cp_{cent} 1.738, Ni2-Cp_{cent} 1.737, H-Ni1-H 78.609(4), H-Ni2-H 78.737(4), Ni-H1-Ni 98.499(5), Ni-H2-Ni 94.432(5).

The reduction of the dimeric bromide **1** with 4.24 equivalents of trisodium heptaantimonide in pentane at ambient temperature for one week including 43 h of ultrasound treatment yielded a brown-black tar after solvent evaporation. The crude product mixture in our hands always contained major amounts of the dihydride **2** and either small amounts of the unreacted bromide starting material or – if the reaction was carried out with more reducing agent – with significant amounts of 1,3,5-tri(tert-butyl)cyclopentadiene (HCp´´´). Solutions containing even minor amounts of the dibromide **1** frequently gave very nice crystals of this bromo-bridged dimer, which crystallizes readily. Cooling of a pentane solution of material prepared with an excess of reducing agent and therefore free from **1**, but containing HCp´´´, afforded a crop of green crystals of the dinickelocene **3** in a brown oil at 3 °C. Oily tetraisopropylcyclopentadiene, another $C_{17}H_{30}$ isomer like HCp´´´, has previously been recognized as a well-suited solvent for the growth of single crystals (*30*). The crystals of **3** were suitable for an X-ray crystal structure determination (fig. 2) and could also be used for small scale experiments.

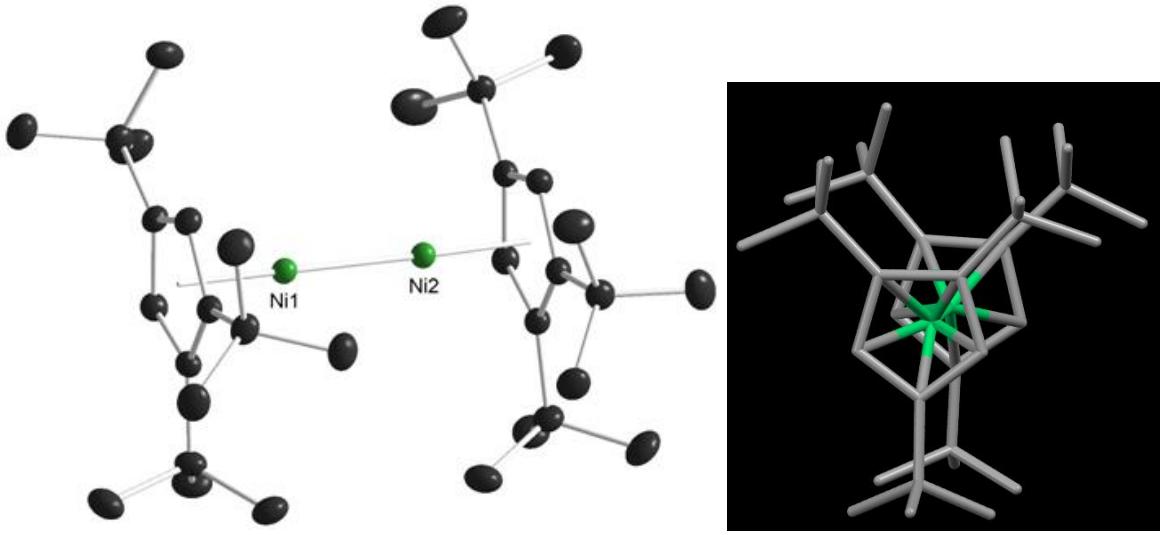

Figure 2: Crystal structure of the dinickelocene **3**.

Although the dinickelocene **3** has no crystallographic symmetry, the two NiCp´´´ moieties display almost identical angles and distances and combine with very small deviations from linearity along a centroid-Ni-Ni-centroid axis in a fully eclipsed conformation (fig. 2) spanning a pentagonal prismatic C_{10} ensemble around the dinickel dumbbell. The Ni-Ni bond length of 2.2944(3) Å is about 1% longer than the 2.2707(5) Å Ni-Ni distance in the dihydride **2**. The ring planes deviate by 1.13° from parallel orientation. With 1.75 Å Ni-centroid distances these planes are about 5.8 Å apart from each other and the Cp´´´ ligands show no signs of steric strain: The tert.-butyl groups are bent out of the ring planes by only 2.78° (average), the maximum bending is below 3.6°. A Cp´´´ complex with steric strain is [Cp´´´Cp´´$ZrCl_2$] with an average bending of the five tert.-butyl substituents of 14.7° with individual bending angles between 9.3° and 22.6° (*31*). The right part of fig. 2 illustrates, how within the $(^tBu)_4$ rectangle in the upper part of the picture every methyl group extending towards an alkyl neighbor is tucked in between two methyl groups. The third tert-butyl group of each ring avoids strain by rotating one methyl group outward and presenting itself as flat as possible towards the opposing alkyl group on the same prism edge. This kind of arrangement with two methyl groups extending to both sides close to the ring plane is possible because these two alkyl groups have two hydrogen neighbors each.

The characterization of the hexa(tert-butyl)dinickelocene **3** has to take into account the possibility of unobserved hydride ligands close to the metal atoms. The diagnostic value of ^{1}H NMR spectra for the characterization of paramagnetic complexes is limited. **3** exhibits the three signals of the Cp´´´ ligand at 16.8 (two ^{t}Bu groups in 1,2 position), 22.2 ppm (one tBu group in 4 position), and 141.3 ppm for the Cp´´´ ring CH groups. Additional signals for **3** have been searched, but not found within a large spectral window in the spectra of many samples containing **3**. In the case of the dihydride **2** there are also only the three signals of the Cp´´´ ligand: 11.2 ppm (two ^{t}Bu), 14.7 ppm (one ^{t}Bu), and 153.4 ppm for the ring protons. All of the paramagnetic Cp´´´Ni complexes observed so far show the ring proton signal at high field and the ^{t}Bu signals can be unambiguously assigned because of their high intensity. In a communication on the very similar tetraisopropylcyclopentadienylnickel hydride $[^4CpNi(\mu\text{-}H)]_2$ (*32*) four isopropyl methyl signals have been mentioned. This nickel hydride dimer was found by magnetic susceptibility measurements to occupy a triplet ground state. In our hands this same tetraisopropylcyclopentadienylnickel hydride dimer shows the alkyl signals as reported (*32*), and the ring proton signal at 154.4 ppm. Hydride signals of transition metal complexes with a paramagnetic ground state apparently have not yet been observed because of extremely short relaxation times (*33*). Nickel hydride has been observed in ^{1}H NMR spectra, however, in a trinickel complex with four hydride bridges possessing a singlet ground state and a triplet excited state 17.6 kJ/mol higher in energy, which is just low enough for about 0.08% thermal population at 300 K (*34*).

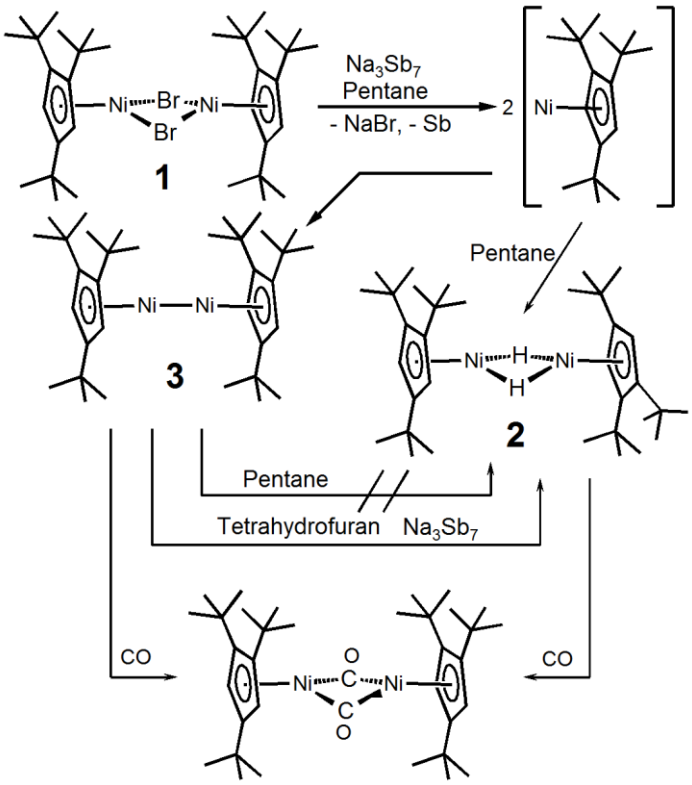

Scheme 1. Formation of the dihydride **2** and the dinickelocene **3** during trisodium heptaantimonide reduction of the dibromide **1** in pentane. A more detailed hypothesis on the course of the observed transformations is outlined in the text.

The reactions of **3** with tetrahydrofuran in the presence of Na_3Sb_7 or carbon monoxide support its dinickelocene identity. The latter reaction is also given by the dihydride **2**, which is also converted to the carbonyl dimer $[Cp´´´Ni(\mu\text{-}CO)]_2$ in a carbon monoxide atmosphere. The strongest argument from chemical reactions for the identity of the dinickelocene **3** is therefore derived from its transformation to the dihydride **2** with tetrahydrofuran and Na_3Sb_7.

Experimental support for the postulated hydrogen abstraction from tetrahydrofuran could be extracted from electrospray ionization mass spectra of hexa(tert.-butyl)dinickelocene **3** in tetrahydrofuran solution: Cations detected at *m/z* 652.1 were isolated in an ion trap and fragmented via collision induced dissociation. We observed the signals of the dinickelocene **3** (main peak at *m/z* 582.2) and of the dihydride **2** (main peak at *m/z* 584.1) as fragment peaks with high intensity (see supporting information). We interpret the mass peak at *m/z* 652.1 as a dihydrofuran adduct of the dinickelocene **3**, which prefers two fragmentation channels: The loss of a mass of 70 u corresponds to the elimination of dihydrofuran (main isotopomer $^{12}C_4{}^{1}H_6{}^{16}O$, m = 70 u) yielding the dinickelocene **3**. The other fragmentation channel proceeds with loss of 68 u and is tentatively assigned to furan elimination (m = 68 u) with formation of the dihydride **2**.

The dinickelocene **3** does not react with pentane, however. Since reactions of the dibromide **1** with Na_3Sb_7 under argon give the dihydride **2** as the main product in pentane solution, there must be a very reactive intermediate. Our hypothesis assumes formation of a mononuclear intermediate, which may be [Cp´´´Ni], possibly stabilized by weak interaction with pentane or by bromide coordination as cyclopentadienyl(bromo) nickelate(I) [Cp´´´NiBr]-. This nickel(I) intermediate probably attacks pentane in an oxidative addition reaction to become a nickel(III) complex such as [Cp´´´Ni(H)C_5H_{11}], which could undergo β hydride elimination to form the nickel(III) dihydride [Cp´´´Ni$(H)_2$] and pentene. Such a Ni(III) half sandwich dihydride could combine with the bromonickelate(I) [Cp´´´NiBr]- with bromide liberation or directly with a [Cp´´´Ni] fragment to the dihydride **2**.

The experimental findings for the tert-butyl-substituted dinickelocene **3** are in marked contrast to theoretical predictions by Xie et al. (*4*) for the unsubstituted dinickelocene parent CpNi≡NiCp (**3^{u}**). Based on their calculations, they describe the dinickelocene as a closed-shell diamagnetic compound with a 206 pm Ni≡Ni triple bond, and more severely, they find a structure with the Ni≡Ni bond perpendicular to the Cp-Cp axis substantially lower (more than 200 kJ/mol) in energy than the coaxial D_{5h} structure. In contrast, our dinickelocene **3** is coaxial, certainly paramagnetic (because of the broad and strongly shifted ^{1}H NMR signals), and has a much longer Ni-Ni bond (229 pm). Therefore we performed density functional calculations on hexa(tert-butyl)dinickelocene **3**.

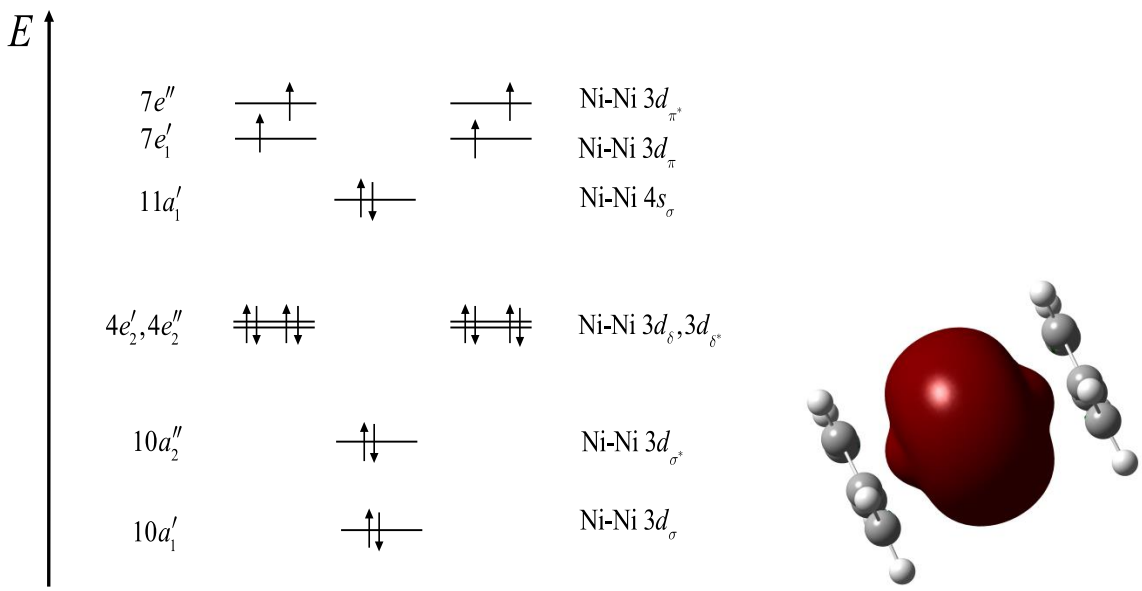

Figure 3: left: Qualitative MO diagram of the highest occupied orbitals in the parent D5h dinickelocene 3u. To the left the symmetry of the MOs is given, to the right their composition and Ni-Ni bonding character. Right: Plot of the Ni-Ni bonding s orbital (from the CASSCF calculation)

TZVP basis sets (35) were used together with the PBE0 exchange-correlation functional (36,37), and the calculations were carried out with the TURBOMOLE package (38,39). We optimized the geometry for a closed-shell singlet, for a triplet with two unpaired electrons and for a quintet with four unpaired electrons. In neither case a collapse to a structure with a Ni-Ni bond perpendicular to the Cp-Cp axis was observed. For the singlet and the quintet, the two cyclopentadienyl ligands show parallel displacement such, that the Ni-Ni bond forms obtuse angles with both Ni-Cp_{cent} vectors (see supporting information). For the triplet, this tilt is even more pronounced such that the Ni_2 unit shows interaction with C-H bonds of the tert-butyl substituents. The optimized triplet structure is only 30 kJ/mol below the quintet but the singlet is much higher in energy (115 kJ/mol above the quintet). The calculated Ni-Ni distances are 212 pm for the singlet and 240 pm both for the triplet and the quintet. This deviates from the crystal structure of **3**, where there is no parallel displacement of the Cp rings and the Ni-Ni distance is 229 pm. The energy difference associated with this geometry shift is small, however: we repeated the geometry optimization for the triplet and the quintet under the constraint that the positions of the Ni and Cp ring atoms match those of the crystal structure. Then, the quintet is lowest (26 kJ/mol below the triplet), and only 34 kJ/mol above the fully optimized quintet structure. So both the deviation from a perfectly coaxial structure and the difference in Ni-Ni bond length involve only small energy differences which could be overcome by crystal packing effects. We note in passing that pentane solutions of **3** display a weak absorption band at 2745 cm^{-1} in the IR spectra, which is not found in IR spectra of solid **3** (KBr pellet). Since other interpretations for an IR signal in this spectral region (apart from covalent bonds of hydrogen to elements not present in this study) are not common, this signal could be explained by a tilted structure in solution, where an agostic interaction could weaken a C-H bond of a tert-butyl group.

To clarify the discrepancy to the theoretical prediction from ref. (*4*) for the parent dinickelocene $\mathbf{3^u}$, we performed a CASSCF calculation (using the MOLPRO (*40*) program) on this compound, with the cc-pVTZ basis set (*41,42*) and an active space with 18 electrons (the Ni valence electrons) in 12 orbitals (the 3d and 4s orbitals of two nickel atoms). We obtained a singlet, a triplet and a quintet very close in energy and well separated from other excited states. All three low-lying states have four singly occupied orbitals, which are two pairs of formally Ni-Ni π-bonding and Ni-Ni π-antibonding orbitals composed of the d_{xy} and d_{xz} atomic orbitals. There is a doubly occupied Ni-Ni σ-bonding orbital with dominant 4s character. There is thus only a Ni-Ni single bond. In the electronic structure described in ref. (*4*), the Ni-Ni π-bonding orbital pair is doubly occupied and the Ni-Ni π-antibonding orbital pair is empty, thus leading to a Ni≡Ni triple bond. Experimental observations and our calculations suggest, that the Ni-Ni π bond is not strong enough to overcompensate the increase in electron repulsion caused by covalent bonding, because in a covalent bond there is a probability to find the shared electrons on one side of the bond. This penalty is much larger for the compact Ni 3d orbitals than for the diffuse Ni 4s orbital. Filling both the bonding and antibonding 3dπ orbitals with unpaired electrons, the two pairs of unpaired electrons on both Ni atoms stay apart from each other and form local (effective) S = 1 spins interacting with each other through the super-exchange mechanism and result in three close-lying S = 0,1,2 states. Since the CASSCF calculations lack dynamical electron correlation, it cannot be decided which of the three states is the ground state of $\mathbf{3^u}$, but all these cases feature four unpaired electrons and a single Ni-Ni bond. On the left side of fig. 3 a qualitative MO energy diagram of D_{5h} $\mathbf{3^u}$ is shown. The MOs with Ni 3d character are Ni-Ni nonbonding and the energetic order mainly depends on their Ni-Cp bonding properties: for example, the $3d_{\pi}$ and $3d_{\pi^*}$ orbitals are Ni-Cp antibonding while the $3d_{\delta}/3d_{\delta^*}$ orbitals are Ni-Cp nonbonding. The Ni 4s orbitals are pushed to quite high energy by the interaction with Cp, but the 11a' orbital formed therefrom comes down in energy because of its Ni-Ni bonding character. A plot of this Ni-Ni bonding orbital is shown in Fig. 3 (right part).

We then performed density functional calculations on the unsubstituted D_{5h} dinickelocene $\mathbf{3^u}$, essentially repeating the calculations of ref. (*4*). It turned out that the authors obviously have not considered the possibility of a quintet ground state: for a closed-shell diamagnetic singlet we also arrived at a structure with a short Ni≡Ni triple bond, but a quintet with singly occupied 7e1' and 7e1'' orbital pairs is more than 250 kJ/mol below the singlet. If the Ni_2 unit is allowed to rotate out of a coaxial position towards an

alignment perpendicular to the Cp-Cp axis, the structure collapses to a perpendicular structure for the singlet (the energy lowers by 315 kJ/mol), while the Ni_2 unit tilts only slightly for the quintet with an energy lowering of 26 kJ/mol. At the end the 'perpendicular' singlet is slightly below the marginally tilted quintet (by 32 kJ/mol), but such a structure is disfavored for Cp ligands with bulky substituents such as the dinickelocene **3**.

To verify that the substituted dinickelocene 3 also carries two pairs of unpaired electrons on each nickel atom, we finally performed a broken symmetry calculation with two spin-up electrons localized on one Ni atom and two spin-down electrons localized on the other. The calculation not only yielded a self-consistent solution for such a configuration, it also displayed virtually the same energy as the high-spin quintet. The quintet and triplet states are so close that no one can be ruled out as the true ground state based on DFT calculations. Since both states gave virtually the same bond length in the DFT calculation on **3**, the assignment of the Ni-Ni bond as a single bond remains valid for both cases.

References and Notes:

1 E. Carmona, A. Galindo, Angew. Chem. Int. Ed. Engl. 47, 6526 – 6536 (2008).
2 D. L. Reger, S. S. Mason, A. L. Rheingold, J. Am. Chem. Soc. 115, 10406 – 10407 (1993).
3 I. Resa, E. Carmona, E. Gutierrez-Puebla, A. Monge, Science 305, 1136 – 1138 (2004).
4 Y. Xie, H. F. Schaefer III, R. B. King, J. Am. Chem. Soc. 127, 2818 – 2819 (2005).
5 X. Li, S. Huo, Y. Zeng, Z. Sun, S. Zheng, L. Meng, Organometallics 32, 1060 – 1066 (2013).
6 Z.-Z. Xie, W.-H. Fang, Chem. Phys. Lett. 404, 212 – 216 (2005).
7 S. L. Richardson, T. Baruah, M. R. Pederson, Chem. Phys. Lett. 415, 141 – 145 (2005).
8 Y.-H. Kan, Theochem. 805, 127 – 132 (2007).
9 M.-R. Philpott, Y. Kawazoe, Chem. Phys. 333, 201 – 207 (2007).
10 Y. Xie, H. F. Schaefer III, E. D. Jemmis, Chem. Phys. Lett. 402, 414 -421 (2013).
11 M. Carrasco, R. Peloso, I. Resa, A. Rodríguez, L. Sánchez, E. Àlvarez, C. Maya, R. Andreu, J. J. Calvente, A. Galindo, E. Carmona, Inorg. Chem. 50, 6361 – 6371 (2011).
12 D. Schuchmann, U. Westphal, S. Schulz, U. Flörke, D. Bläser, R. Boese, Angew. Chem. Int. Ed. Engl. 48, 807 – 810 (2009).
13 T. Li, S. Schulz, P. W. Roesky, Chem. Soc. Rev. 41, 3759 – 3771 (2012)
14 A. Lühl, H. P. Nayek, S. Blechert, P. W. Roesky, Chem. Commun. 8280 – 8282 (2011).
15 H. Zhu, Y. Chen, S. Li, X. Cao, Y. Liu, Chinese J. Chem. 30, 173 - 176 (2012).
16 Y. Meng, Y. Han, H. Zhu, Z. Yang, K. Shen, B. Suo, Y. Lei, G. Zhai, Z. Wen, Int. J. Hydrogen Energy 40, 12047 - 1256 (2015).
17 B. Xu, Q.-S. Li, Y. Xie, R. B. King, H. F. Schaefer III, J. Chem. Theory Comput. 6, 735 - 746 (2015).
18 C.-Z. Wang. J. K. Gibson, J.-H. Lan, Q.-Y. Wu, Y.-L. Zhao, J. Li, Z.-F. Chai, W.-Q. Shi, Dalton Trans. 44, 17045 – 17053 (2015).
19 S. Pasynkiewicz, W. Buchowicz, A. Pietrzykowski, T. Glowiak, J. Organomet. Chem. 536-537, 249 – 256 (1997).
20 S. Pasynkiewicz, W. Buchowicz, J. Poplawska, A. Pietrzykowski, J. Zachara, J. Organomet. Chem. 490, 189 – 195 (1995)
21 S. Pasynkiewicz, A. Pietrzykowski, L. Trojanowska, P. Sobota, L. Jerzykiewicz, J. Organomet. Chem. 550, 111 – 118 (1998)
22 T. Drewello, H. Schwarz, Int. J. Mass Spectrom. Ion Processes 93, 177 - 183 (1989)
23 M. S. Paquette, L. F. Dahl, J. Am. Chem. Soc. 102, 6621 - 6623 (1980)
24 P. H. M. Budzelaar, J. Boersma, G. J. M. van der Kerk, Organometallics 4, 680 – 683 (1985)
25 J. J. Schneider, R, Goddard, C. Krüger, S. Werner, B. Metz, Chem. Ber. 124, 301 – 308 (1991)
26 F. Zimmer, PhD Dissertation, TU Kaiserslautern (2003).
27 M. Schär, D. Saurenz, F. Zimmer, I. Schädlich, G. Wolmershäuser, S. Demeshko, F. Meyer, H. Sitzmann, O. M. Heigl, F. H. Köhler, Organometallics 32, 6298 – 6305 (2011).
28 H. Sitzmann, G. Wolmershäuser, Z. Naturforsch. 50b, 750 – 756 (1995).
29 Guy Y. Vollmer, M. W. Wallasch, D. Saurenz, T. R. Eger, H. Bauer, G. Wolmershäuser, M. H. Prosenc, H. Sitzmann, Organometallics 34, 644 – 652 (2015).
30 F. Baumann, E. Dormann, Y. Ehleiter, W. Kaim, J. Kärcher, M. Kelemen, R. Krammer, D. Saurenz, D. Stalke, C. Wachter, G. Wolmershäuser, H. Sitzmann, J. Organomet. Chem. 587, 267 - 283 (1999).

31 H. Sitzmann, P. Zhou, G. Wolmershäuser, Chem. Ber. 127, 3 – 9 (1994).
32 S. A. Yao, Am. R. Corcos, I. Infante, E. A. Hillard, R. Clérac, J. F. Berry, J. Am. Chem. Soc. 136, 13538 - 13541 (2014).
33 T. R. Dugan, E. Bill, K. C. McLeod, W. W. Brennessel, P. L. Holland, Inorg. Chem. 53, 2370 – 2380 (2014).
34 S. Pfirrmann, C. Limberg, C. Herwig, C. Knispel, B. Braun, E. Bill, R. Stösser, J. Am. Chem. Soc. 132, 13684 - 13691 (2010).
35 A. Schäfer, C. Huber, R. Ahlrichs, J. Chem. Phys. 100, 5829 – 5835 (1994).
36 J. P. Perdew, K. Burke, M. Ernzerhof, Phys. Rev. Lett. 77, 3865 – 3868 (1996).
37 C. Adamo, V. Barone, J. Chem. Phys. 110, 6158 – 6170 (1999).
38 R. Ahlrichs, M. Bär, M. Häser, H. Horn, C. Kölmel, Chem. Phys. Lett. 162, 165 - 169 (1989).
39 C. van Wüllen, Chem. Phys. Lett. 219, 8 – 14 (1994).
40 MOLPRO, version 2010.1, is a quantum chemical program package written by H. J. Werner, P. J. Knowles, G. Knizia, F. R. Manby, M. Schütz and others, see www.molpro.net.
41 T. H. Dunning Jr., J. Chem. Phys. 90, 1007 – 1023 (1989).
42 N. B. Balabanov, K. A. Peterson, J. Chem. Phys. 123, 064107/1 – 064107/15 (2005).
43 Guy Y. Vollmer, M. W. Wallasch, D. Saurenz, T. R. Eger, H. Bauer, G. Wolmershäuser, M. H. Prosenc, H. Sitzmann, Organometallics 34, 644 - 652 (2015).

Acknowledgments: H. S. is grateful to Professor Otto J. Scherer for many years of friendly and encouraging support, the President Professor Helmut Schmidt for his supportive action in 2002 and to the colleagues of the chemistry department of the Technical University of Kaiserslautern for their cooperativity.

The crystallographic data for **1, 2,** and **3** have been deposited with the Cambridge Crystallographic Data Center as entries 1473480, 1473481, and 1473423.

11.8 Gas Phase Reactivity of Cp* Group IX Metal Complexes Bearing Aromatic N,N'-Chelating Ligands

Christian Kerner[a], Jens.P. Neu[a], Maximillian Gaffga[ab], Johannes Lang[ab], Benjamin Oelkers[a], Yu Sun[a], Gereon Niedner-Schatteburg[ab] and Werner R. Thiel[a]

a)Fachbereich Chemie,
Technische Universität Kaiserslautern,
67663 Kaiserslautern, Germany

b) Forschungszentrum Optimas
Technische Universität Kaiserslautern,
67663 Kaiserslautern, Germany

11.8.1 Preamble

The following chapter is a manuscript, which is accepted for publication the New Journal of Chemistry.

C. Kerner and J. P Neu from the research group of Prof. Dr. W. R Thiel synthesized the investigated transition metal complexes. B. Oelkers and Y. Sun provided crystallographic data. W. R. Thiel conducted the quantum chemical calculations. M. Gaffga and I conducted Electrospray Ionization mass spectrometry (ESI-MS) and Collision Induced Dissociation (CID) experiments. I evaluated the CID data. W. R Thiel wrote this manuscript supported by G. Niedner-Schatteburg and myself.

<u>Full Reference:</u>

Gas-phase reactivity of Cp* Group IX metal complexes bearing aromatic N,N'-chelating ligands

C. Kerner, J.P. Neu, M. Gaffga, **J. Lang**, B. Oelkers, Y. Sun, G. Niedner-Schatteburg and W.R. Thiel, *New Journal of Chemistry*, **2017**, published online.

http://dx.doi.org/10.1039/C7NJ01079F

11.8.2 Manuscript

New Journal of Chemistry

ARTICLE

Gas-phase reactivity of Cp* Group IX metal complexes bearing aromatic *N,N'*-chelating ligands

Received 00th January 20xx,
Accepted 00th January 20xx

DOI: 10.1039/x0xx00000x

www.rsc.org/

C. Kerner,[a] J. P. Neu,[a] M. Gaffga,[a,b] J. Lang,[a,b] B. Oelkers,[a] Y. Sun,[a] G. Niedner-Schatteburg[*a,b] and W. R. Thiel[*a]

Dedicated to Prof. Dr. Dieter Fenske on the occasion of his 75th birthday

A set of cationic group IX metal complexes of the type $[(\eta^5\text{-Cp*})M(Cl)(N,N')]^+$ bearing *N,N'*-coordinating ligands structurally related to2,2'-biypyridine were synthesized and characterized by means of elemental analysis, spectroscopy and single crystal x-ray diffraction. These complexes can undergo two different modes of CH activation in the gas-phase, which were examined by CID ESI-MS spectrometry and by DFT calculations. On one hand, a roll-over cyclometallation can occur at one of the aromatic rings of the *N,N'*-coordinated ligands. On the other hand, a deprotonation of one of the Cp* methyl groups can take place, leading to complexes in the oxidation state +I with a tetramethylfulvene ligand coordinated. In both cases, the chlorido ligand acts as an internal base in the ESI-MS CID experiment.

Introduction

Already in 1963 Kleiman and Dubeck synthesized the first transition metal compound possessing an *ortho*-metallated phenyl ring by reacting dicyclopentadienyl nickel(II) with an excess of diazobenzene.[1] Although they postulated the diazo group to coordinate as a π-type ligand, which is not correct, this compound became the starting point of a completely new and fascinating class of metal complexes. Cope and Siekman were the ones who in 1965 addressed the correct N-donation of the *ortho*-metallated diazobenzene in closely related palladium resp. platinum compounds.[2] Trofimenko launched the nowadays generally employed wording "cyclometallation" for the cleavage of a CH bond (CH activation, deprotonation) by a metal in close proximity to a donor site leading to a chelating coordination.[3]

From the early 1970ies on, this field in organometallic chemistry was summarized in a whole bunch of review articles.[4] During the last ten years numerous applications of cyclometallated compounds in catalysis,[5] medicine [6] and especially in photochemistry/photophysics [7] appeared. In a review from 1990 by Ryabov, the mechanisms leading to cyclometallated complexes were explained in detail.[8] Among a series of different possibilities for a metal to attack a CH-bond, the electrophilic substitution of an arene-bound hydrogen atom is most frequently found for late transition metal centres in the oxidation states +II (groups XIII and X) and +III (groups IX and XI). Due to the relevance of these metals in catalytic reactions, the cyclometallation process became matter of theoretical [9] as well as of kinetic [10] investigations.

A variation of the classical cyclometallation of aromatic compounds is the so-called roll-over cyclometallation. Here, a chelating ligand like 2,2'-bipyridine first coordinates the metal centre by its two donor sites, which is the kinetically favoured mode of coordination. However, cleavage of one of the M-donor bonds allows a rotation of one ligand site (roll-over), bringing a carbon atom close to the metal centre, which can result in a CH-activation (deprotonation). In this context a series of N,N'-coordinating ligands [11] including 2,2'-bipyridines [12] have been investigated in the past. For substituted 2,2'-bipyridines, electronic and steric effects have been worked out.[13] In addition a variety of metal centres such as platinum,[14] iridium,[15] and rhodium [16] have been studied concerning their behaviour in roll-over cyclometallations.

We recently found, that chelating ligands containing a 2-(2-aminopyrimidin-4-yl) moiety undergo roll-over cyclometallation at this ring. The activation barrier of the cyclometallation process strongly depends on the substitution pattern in the 2-position of the pyrimidinyl ring. Tertiary amino groups lower this barrier, a feature that has turned out to enhance the activity of such complexes in catalysis. Compared to compounds with "classical" N-donating 2-(2-aminopyrimidin-4-yl) ligands, palladium complexes bearing metallated chelating 2-(2-

[a] Dr.Christian Kerner, Dipl.-Chem. Jens P. Neu, Dr. Benjamin Oelkers, Dr. Yu Sun, Prof. Dr. Werner R. Thiel
Fachbereich Chemie, Technische Universität Kaiserslautern, Erwin-Schrödinger-Straße 54, 67663 Kaiserslautern, Germany
thiel@chemie.uni-kl.de
[b] Dr. Maximilian Gaffga, Dipl.-Chem. Johannes Lang, Prof Dr. Dr. Gereon Niedner-Schatteburg
State Research Centre OPTIMAS, Technische Universität Kaiserslautern, 67663 Kaiserslautern, Germany
† Footnotes relating to the title and/or authors should appear here. Electronic Supplementary Information (ESI) available: [details of any supplementary information available should be included here]. See DOI: 10.1039/x0xx00000x

aminopyrimidin-4-yl) ligands show largely enhanced activities in the Suzuki-Miyaura coupling.[17] Ruthenium complexes with a tertiary 2-(2-aminopyrimidin-4-yl)pyridine) ligand undergo reversible roll-over cyclometallation and allow a base free transfer hydrogenation of ketones and an adduct free reductive amination of benzaldehydes. The latter reaction proceeds via in-situ formed imines.[18] A reversible cyclometallation was found for ruthenium complexes by Constable et al. already in 1996[19] but was not taken into account to be of importance for catalysis. This seems to be changing during the last years.[9i,20]

To the best of our knowledge, there is no study on the trends of the barriers related to the roll-over cyclometallation occurring in one group of transition metals with the same set of ligands. This approach allows to elucidate the intrinsic role of the metal site in this process and to display the changes in reactivity from the first to the third row of this group. We have carried this out for the Group IX elements cobalt, rhodium and iridium, since for all these elements appropriate precursor compounds of the type $[(\eta^5\text{-}C_5Me_5)MCl_2]_2$ (C_5Me_5: 1,2,3,4,5-pentamethylcyclopentadienide) had been reported in the literature.[21]

Results and Discussion

Synthesis of the Group IX metal complexes

To elucidate the influence of the ligand on the energetics of the roll-over cyclometallation, five different N,N'-donor ligands were included in this study (Scheme 1): 2,2'-bipyridine (**1a**), 2-(pyrimidin-4-yl)pyridine (**1b**), 2-(2-aminopyrimidin-4-yl)pyridine (**1c**), 2-(2-methylaminopyrimidin-4-yl)pyridine (**1d**) and 2-(2-dimethylaminopyrimidin-4-yl)pyridine (**1e**).

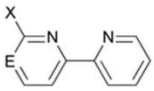

1	a	b	c	d	e
E	CH	N	N	N	N
X	H	H	NH_2	NHMe	NMe_2

Scheme 1 Ligands applied in this study.

With this selection, a general set-up for variations of electronic and steric factors is given. The introduction of heteroatoms reduces the electron density at the donating nitrogen atom of the pyrimidine ring and thus weakens the M-N bond electronically, while the presence of an amino group will facilitate the electrophilic attack of the metal site at the pyrimidine ring. Finally, the steric impact of the amino group is gradually increased by the presence of methyl groups. The ligands shown in Scheme 1 are either commercially available or accessible via a few steps from versatile starting materials.

The corresponding Group IX metal derivatives were obtained by simply stirring the dimeric precursor complexes $[(\eta^5\text{-}C_5Me_5)MCl_2]_2$ (M = Co, Rh, Ir) in the presence of the appropriate ligand and $NaBF_4$ resp. KPF_6 in dichloromethane solution (Scheme 2).

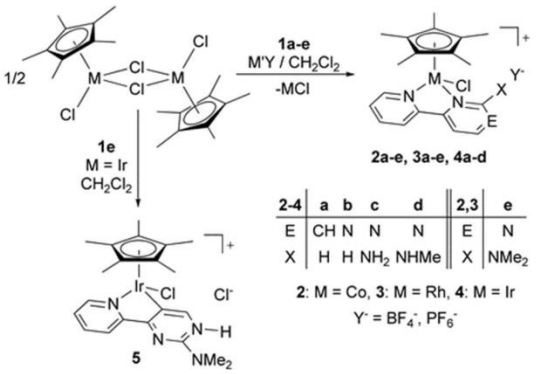

2-4	a	b	c	d	2,3	e
E	CH	N	N	N	E	N
X	H	H	NH_2	NHMe	X	NMe_2

2: M = Co, **3**: M = Rh, **4**: M = Ir
$Y^- = BF_4^-, PF_6^-$

Scheme 2 Syntheses of the Group IX metal complexes.

In contrast to all other combinations of metal precursors and ligands, the reaction of the tertiary amino derivative **1e** with $[(\eta^5\text{-}C_5Me_5)IrCl_2]_2$ exclusively gives the cyclometallated complex **5**. The cyclometallation here occurs independently from the absence or presence of a weakly coordinating anion (BF_4^- resp. PF_6^-).

Structural elucidation and spectroscopy

The molecular structures of the products could unambiguously be proved spectroscopically and by solid-state structure analysis. Figure 1 presents the structures of seven cations from this series. Table 1 summarizes the relevant structural parameters.

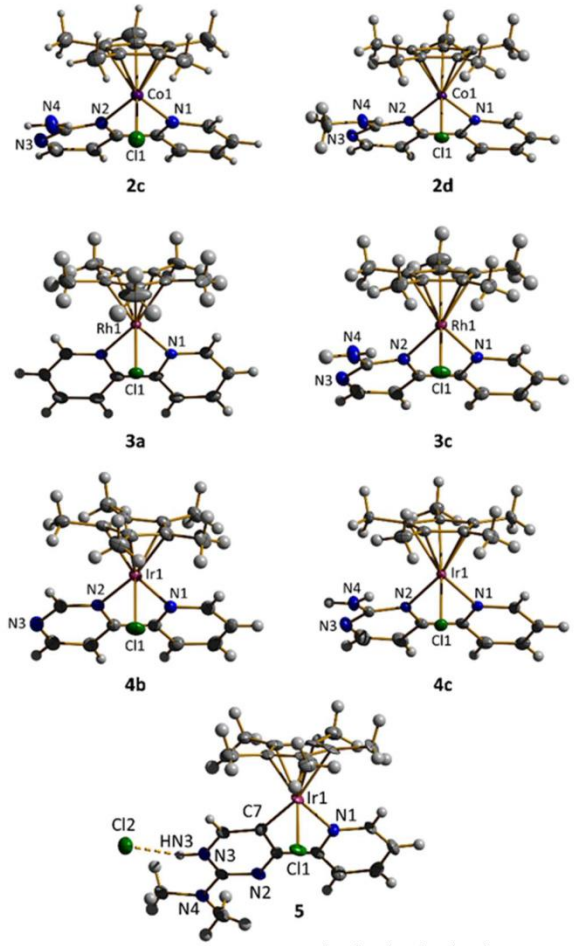

Fig. 1 Molecular structures of compounds **2c**$^+$, **2d**$^+$, **3a**$^+$, **3c**$^+$, **4b**$^+$, **4c**$^+$, and **5** in the solid state.

Table 1 Selected bond distances (Å) and dihedral angles (°) for compounds **2c**, **2d**, **3a**, **3c**, **4b**, **4c**, and **5**.

	M1-N1	M1-N2	M1-Cl1	M1-Cp*[a]	N1-C-C-N2
2c$^+$	1.954(2)	1.968(2)	2.251(1)		0.6(3)
2d$^+$	1.9548(13)	1.9541(13)	2.2515(5)		2.1(2)
3a$^+$	2.108(4)	-	2.3956(2)		0.0(6)
3c$^+$	2.094(2)	2.107(2)	2.3766(6)		1.2(2)
4b$^+$	2.083(3)	2.099(3)	2.394(1)		2.6(4)
4c$^+$	2.083(2)	2.099(2)	2.4008(7)		2.7(3)
	M1-N1	M1-C7	M1-Cl1	M1-Cp*[a]	N1-C-C-C7
5	2.117(8)	2.053(10)	2.403(2)		0.8(12)

[a] M1-Cp*: distance between the metal site and the centroid of the Cp* ring.

The metal-to-ligand distances reflect the positions of the metal sites in Group IX: while the Co1-L distances are by about 0.13-0.15 Å shorter than the corresponding distances found for the rhodium and iridium complexes, there is as expected no large difference between the two heavier metals. Generally, the M1-N2 distances are slightly longer than the M1-N1 distances, independent from the substitution pattern of the pyrimidine ring. This indicates slightly weaker donor potentials of the pyrimidine compared to the pyridine sites. Due to steric interference with the Cp* ligand, the pyrimidine rings are found to be distorted when an amino group is attached to this ring. However, this does not cause a clear elongation of the M1-N2 bond, which was found for ruthenium(II) complexes of the type [(η^6-cymene)Ru(**1a-e**)]$^+$ bearing the same ligands.[18a] We assign this finding to the higher Lewis-acidity of the Group IX metal ions M(+III) compared to Ru(+II). Nevertheless, there must be a destabilization of the M-N2 bond according to steric parameters, since reacting the sterically most demanding ligand **1e** with [(η^5-Cp*)IrCl$_2$]$_2$ does not give compound **4e**. Instead, a spontaneous roll-over cyclometallation leads to compound **5**. The Ir1-C7 bond in **5** is clearly shorter than the Ir1-N1 bond speaking for a strong interaction between the metal site and the carbanion. Since there was no base added to promote this reaction, one of the pyrimidine nitrogen atoms is found protonated. The proton undergoes a hydrogen bond to a chloride anion. According to spectroscopic data and elemental analyses N,N-coordination of ligand **1e** to a [(η^5-Cp*)MCl]$^+$ fragment is possible for cobalt and rhodium. This means on one hand, that the formation of the stable Ir-C7 bond is the driving force for the generation of **5** and on the other hand, that there is probably a dynamic behavior concerning the M1-N2 bond for rhodium and cobalt too. While the rhodium complex **3e** is stable in solution for long times, the analogous cobalt complex **2e** decomposed during the recrystallization, which gave a few crystals of the cobalt(II) complex CoCl$_2$(**1e**) (see Supporting Information).

In addition to single crystal X-ray structure analysis, the cyclometallated structure of **5** is clearly assigned by its NMR spectrum: Instead of two doublets that are observed for the aromatic protons of the pyrimidine ring in the ^{1}H NMR spectra of **1-3e**, only one singlet appears at 8.44 ppm. The ^{13}C NMR resonance of the carbanionic carbon atom C8 is detected at 149.0 ppm. The resonances of all other hydrogen and carbon sites of **5** do not differ very much compared to those of compounds **4a-d**. However, there are differences that are related to the metals: The coordination to cobalt(III) makes the ^{1}H NMR resonances of the aromatic protons next to coordinating nitrogen atoms shift by about 0.5 ppm more to lower field than coordination to rhodium(III) or iridium(II). In contrast, the ^{13}C NMR resonances of the "inner" carbon atoms of the Cp* ligands are found at approx. 96-98 ppm for the cobalt(III) and rhodium(III) complexes, while the according signals for the iridium(III) compounds are found at about 90 ppm. This can be interpreted as an effect of a more covalent M-Cp* bonding being present in the iridium(III) derivatives.

CID ESI mass spectrometry

We chose CID ESI mass spectrometry to elucidate the activation barrier for the roll-over cyclometallation of the complex cations **2a-e**$^+$, **3a-e**$^+$ and **4a-d**$^+$. The recorded fragmentation energies for the splitting of HCl (Scheme 3) can be calibrated by using so-called thermometer ions to obtain real energies.[22]

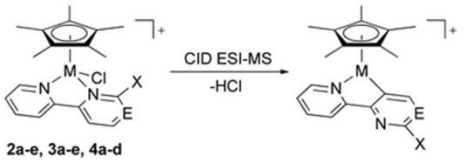

Scheme 3 Proposed fragmentation and roll-over cyclometallation.

The cyclometallation of the pyrimidinyl ring was proposed due to the structural discussion above and our experiences with isostructural ruthenium(II) complexes. Figure 2 shows the CID curves of the rhodium(III) cations **3a-e**$^+$.

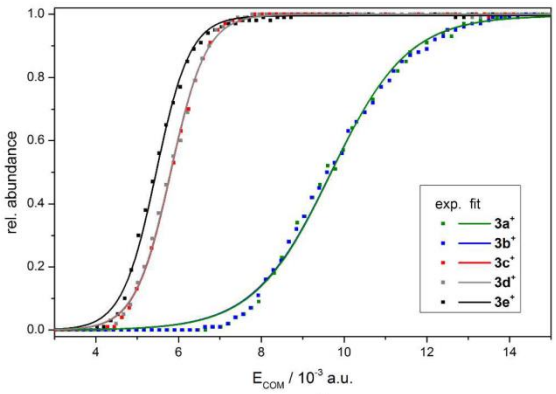

Fig. 2 CID curves for the rhodium cations **2a-e**$^+$.

The sequence of fragmentation energies follows the same series as observed for the ruthenium complexes: **3a**$^+$ ≈ **3b**$^+$ >> **3c**$^+$ ≈ **3d**$^+$ > **3e**$^+$, and can be explained by a combination of steric and electronic influences. Cations **3c**$^+$, **3d**$^+$ and **3e**$^+$ bearing an amino group at the pyrimidine ring undergo the cyclometallation much easier than **3a**$^+$ and **3b**$^+$, which is in agreement with the mechanism of an electrophilic aromatic substitution. Among the amino functionalized cations **3c**$^+$-**e**$^+$, **3e**$^+$ bears the most bulky amino group, which further weakens the Rh-N2 bond sterically. The steric demand of the NH_2 and the NHMe group is almost identical, since the methyl group in **3d**$^+$ can turn to the periphery of the complex as shown in the solid state structure of the according cobalt complex **2d**$^+$ (Figure 1).

The low barrier measured for compound **3e**$^+$ agrees with the spontaneous roll-over cyclometallation occurring by reacting ligand **1e** with $[(\eta^5\text{-Cp*})IrCl_2]_2$, which makes it impossible to isolate **4e**$^+$. Nevertheless, roll-over cyclometallation could be observed by means of CID ESI-MS for the N,N'-coordinated iridium(III) complexes **4a-d**$^+$ (Figure 3). These compounds show a behaviour similar to the rhodium(III) derivatives, but the energy gap between **4a**$^+$ and **4b**$^+$ on one side and **4c**$^+$ ≈ **4d**$^+$ is much less pronounced than for the analogous rhodium(III) complexes, which speaks for a general preference of iridium(III) to undergo binding to a carbon site.

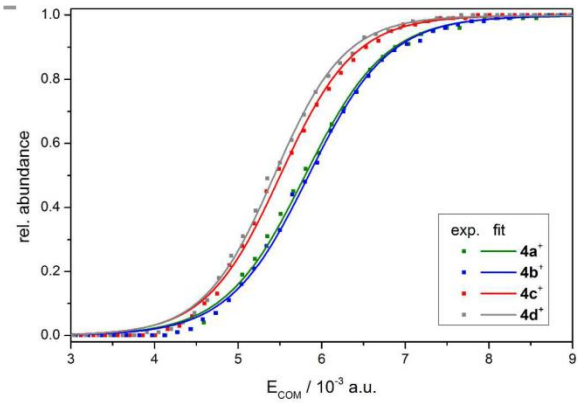

Fig. 3 CID curves for the iridium cations **4a-d**$^+$.

The situation changes completely by switching from rhodium/iridium to cobalt. Figure 4 shows the CID ESI-MS curves recorded for the cobalt(III) cations **2a-e**$^+$. The according fragmentation energies now follow the order **2c**$^+$ ≈ **2d**$^+$ > **2e**$^+$ > **2a**$^+$ ≈ **2b**$^+$, but there are no such large differences as for the rhodium complexes. In contrast to the rhodium complexes, the ordering of the cobalt complexes does not speak for an electrophilic aromatic substitution at the pyrimidine ring.

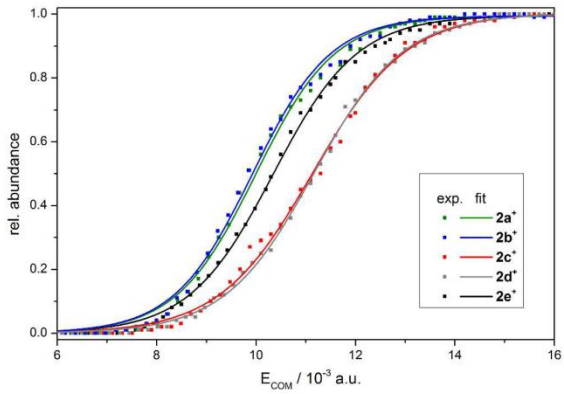

Fig. 4 CID curves for the cobalt cations **2a-e**$^+$.

Although the HCl splitting is the major CID ESI-MS fragmentation pathway for **2c-e**$^+$, the steric pressure induced by the amino groups leads to the loss of Cp*, providing a second fragmentation channel at high fragmentation amplitudes. **2e**$^+$ furthermore shows splitting of a methyl group probably coming from the *N*,*N*-dimethylamino substituent.

DFT calculations

To elucidate the nature of the differences in the HCl splitting between the cobalt(III) complexes on one side and the rhodium(III) resp. iridium(III) complexes on the other side, DFT calculations were carried out. For this, the cyclometallation of the pyrimidine ring and of the pyridine ring was taken into

account as well as a deprotonation of one of the Cp* methyl groups (Scheme 3) to obtain an overview on all possible sites for C-H bond cleavage. The deprotonation of a methyl group at the Cp* ligand accompanied by a loss of the chloride ligand is finally nothing but a reductive elimination of HCl leading to a cationic tetramethylfulvene complex and leaving the metal in the oxidation state +I.

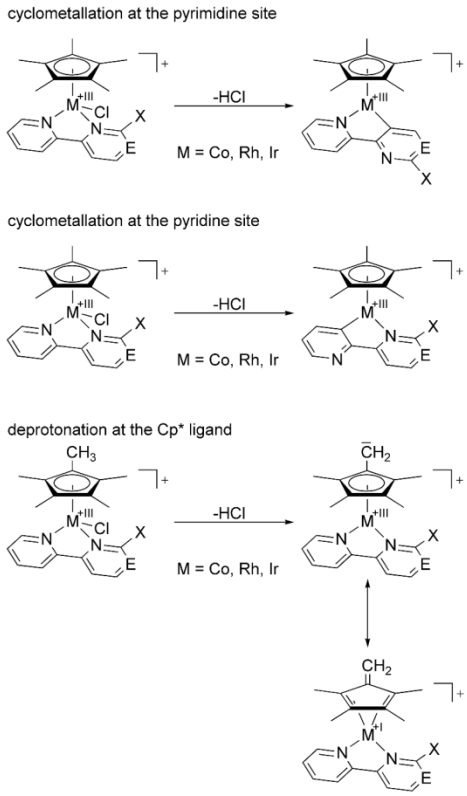

Scheme 4 Possible cyclometallation processes at compounds **2a-e**$^+$, **3a-e**$^+$, and **4a-e**$^+$.

The calculated energies that are requested for the splitting of HCl from the three different positions in compounds **2a-e**$^+$, **3a-e**$^+$, and **4a-e**$^+$ are presented in Figure 5. The energy of the highest transition states for these processes are close to these values (see the Supporting Information).

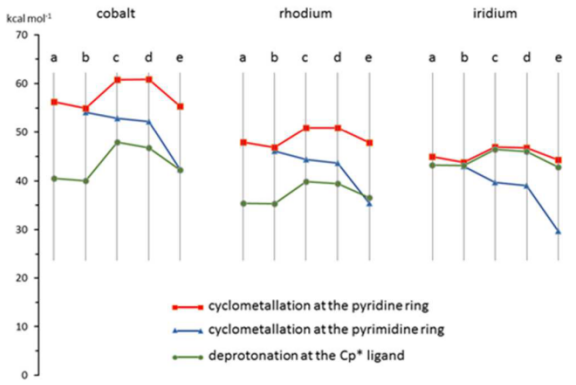

Fig. 5 Calculated energies for the splitting of HCl from different positions in the complexes **2a-e**$^+$ (cobalt), **3a-e**$^+$ (rhodium) and **4a-e**$^+$ (iridium).

From the results presented in Figure 5 some trends can be worked out. Obviously, cyclometallation preferentially occurs at the pyrimidine site (blue lines) and not at the pyridine site (red lines) as long as there is an amino substituent at the pyrimidine ring. The introduction of the amino group at the pyrimidine ring makes this site to be attacked easier, which is in agreement with an electrophilic aromatic substitution mechanism for the cyclometallation. However, the presence of an amino group at the pyrimidine ring also leads to a pronounced increase of the energy that is required for the activation of the pyridine ring. This can be explained by steric considerations: In the resulting 16 VE M(III) complexes, the N,C-ligand is ideally oriented almost perpendicular to the Cp* plane. In case the pyrimidine ring undergoes cyclometallation, the amino group points away from the Cp* ligand, in case the pyridine ring is cyclometallated, it directs towards the Cp* ligand. It then strongly interferes with the Cp* ligand, leading to a severe distortion of the ideal geometry. Figure 6 shows exemplarily the calculated structures for compounds **2a**$^+$ and **2e**$^+$ after HCl elimination from the pyrimidine, the pyridine and the Cp* site The strongest weakening of the M-N2 bonds calculates as expected for the NMe_2 substituted complexes, which means that the presence of a tertiary amino group makes the HCl splitting energies decrease even more compared to those calculated for a primary or secondary amino group. This might be due to weak N-H···Cl hydrogen bonds in compounds **2-4c,d**$^+$ that stabilize these complexes against M-N-bond splitting. The X-ray structure analyses of the cations **2-4c**$^+$ and **2d**$^+$, allow to evaluate this situation: The H4A···Cl1 distances increase from cobalt via rhodium to iridium (H4A···Cl1: **2c**$^+$, 2.56(4); **2d**$^+$, 2.59(2); **3c**$^+$, 2.63(3); **4c**$^+$, 2.88(3) Å) as do the N4···Cl1 distances (N4···Cl1: **2c**$^+$, 3.323(4); **2d**$^+$, 3.3305(2); **3c**$^+$, 3.413(2); **4c**$^+$, 3.524(3), which speaks for a decrease in hydrogen bond strength. However, there is a more pronounced difference between rhodium and iridium than between cobalt and rhodium although the Rh1-Cl1 and Ir-Cl1 distances are almost identical and the distance Co1-Cl1 is much shorter (see table 1). Therefore the hydrogen bonds give a hint, that the electronic situation at rhodium is not the same as at iridium, which is also reflected by the calculated

activation energies as shown in Figure 5 and the CID measurements (Figures 2 and 3).

Concerning the influence of the metal, cyclometallation at one of the N-donors becomes easier by proceeding from cobalt via rhodium to iridium, which explains, why **4e**$^+$ could not be isolated, but instead the cyclometallated compound **5** was obtained. This trend follows the stabilities of the formed metal-carbon bonds.

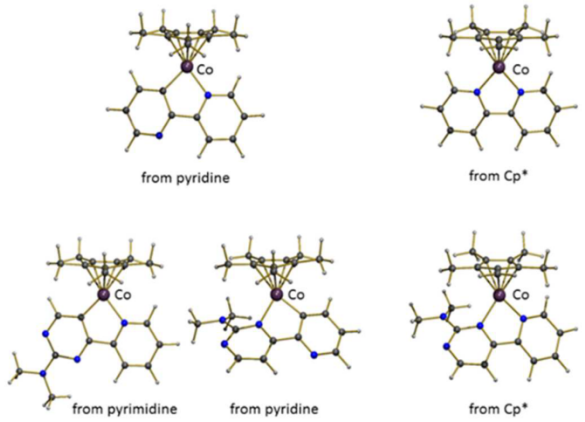

Fig. 6 Calculated structures resulting after the splitting of HCl from **2a**$^+$ (top) and **2e**$^+$ (bottom).

Even more interesting is the behaviour of the three different metals towards the deprotonation at one of the Cp* methyl groups with the chlorido ligand acting as the base. Similar reactions have been reported in the literature for all three metals. In 1994 Maitlis et al. published the deprotonation of $[Cp^*RhCp]^+$ by KO^tBu,[23] one year later Astruc et al. succeeded in deprotonating $[Cp^*CoCp]^+$ with $KN(SiMe)_2)_2$.[24] Tatsumi et al. could prove the stoichiometric deprotonation of $[Cp^*CoCp^*]^+$ with the same external base,[25] a process that was postulated by Astruc to occur in-situ. Bergman et al. could deprotonate Cp*Ir complexes bearing phosphines by applying amido ligands as an internal base.[26] Macchioni et al. postulated the formation of rhodium(I) fulvene complexes as intermediates of the deuteration of Cp* rhodium(III) complexes in aqueous solution and elucidated the according reaction sequence by means of DFT calculations.[27] While the deprotonation of Cp* complexes of group IX metal(III) complexes can be considered as a reductive elimination, Heinekey et al. found that the cleaving of a hydride from one of the Cp* methyl groups of $(Cp^*)Ir(Me)_2(NHC)$ (NHC = dimethylimidazolylidene) gives an iridium(III) cation with the fulvene ligand acting as a 6e-donor. This is structurally characterized by a strong bending of the exocyclic double bond towards the metal site. [28]

In the case of cobalt, splitting of HCl with the proton coming from the Cp* ligand is much easier than cyclometallation of the pyridine as well as of the pyrimidine ring discussed above. The presence of the amino group at the pyrimidine ring again leads to a strong increase of the energy requested for this way of splitting HCl, since the resulting 16VE cobalt(I) tetramethylfulvene complex requires a (distorted) square-pyramidal coordination geometry. The amino group therefore will interfere sterically with the tetramethylfulvene ligand the same way as discussed above for the Cp* ligand (see Figure 6). For rhodium, the energy gap between the cyclometallation at the pyrimidine ring and the deprotonation of the Cp* ligand becomes smaller, for the iridium complexes, cyclometallation was calculated to be the energetically favourable channel of reactivity. The metal influence can be correlated to the relative stabilities of the oxidation states +I and +III.

Deuteration experiments

To finally support the theoretical results experimentally, the deuterated ligand **1b-D** was coordinated to the precursors $[(\eta^5\text{-}C_5Me_5)MCl_2]_2$ (M = Co, Rh, Ir). We chose this ligand, because the calculated energies for the splitting of the proton from the pyridine ring resp. from the pyrimidine ring are almost the same. Therefore deuteration of one of these sites would allow to differ between the two possible cyclometallation sites. **1b-D** was synthesized according to a procedure published earlier,[18a] starting from trideuteromethylpyridinyl ketone.[29] Reacting this precursor with dimethylformamide diemethylacetale gave the corresponding aminopropenone **6** (Scheme 5). Probably, dimethylformamide dimethylacetale is acidic enough to exchange its proton with CH_3OD liberated during the reaction, since we found approx. 75% of deuteration in the α- and 25% of deuteration in the β-position.

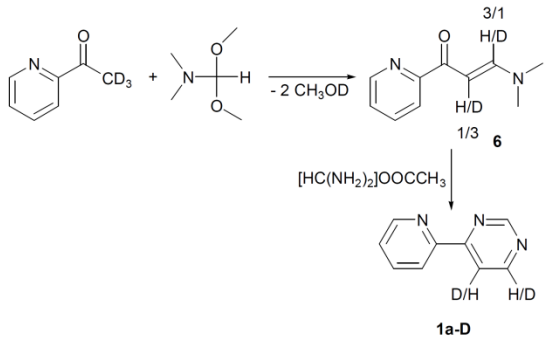

Scheme 5 Synthesis of the deuterated ligand **1b-D**.

Ring closure with formamidinium acetate [30] results in the formation of **1b-D** having the same deuterium pattern as observed for compound **6**. The ESI-MS spectra of the cationic complexes **[2b-D]**$^+$, **[3b-D]**$^+$ and **[4b-D]**$^+$ are given in the Supporting Information. CID ESI-MS experiments were carried out with **[2b-D]**$^+$, **[3b-D]**$^+$ and **[4b-D]**$^+$. Hereby the different isotopomers of each of these compounds were selected in the Pauli trap and were subjected to fragmentation reactions which were followed by mass spectrometry. For **[2b-D]**$^+$ and **[3b-D]**$^+$ solely HCl splitting was observed, proving that there is no cyclometallation at the pyrimidine ring occurring in the gas phase. The proton liberated with the chloride anion can either come from the cyclopentadienyl ligand or the pyridine site of the *N,N'*-chelating ligand. The latter process seems quite unfavourable regarding the large differences in energy

between the cyclometallation reactions and the deprotonation of the cyclopentadienyl ligand. For the iridium complex, HCl splitting as well as DCl splitting was observed, with a larger amount of HCl splitting than predetermined by the amount of deuteration in the *ortho*-position of the pyrimidine ring. This is in complete agreement with the fact that the calculated energies for all three possible processes of HCl splitting from **[4b]**$^+$ are almost identical.

Experimental

General information

Organic precursors were purchased form Sigma-Aldrich, Acros and TCI Chemicals and used without further purification. 2-(Pyrimidin-4-yl)pyridine (**1b**),[30] 2-(2-aminopyrimidin-4-yl)pyridine (**1c**),[18a] 2-(2-methylaminopyrimidin-4-yl)pyridine (**1d**),[31] 2-(2-dimethylaminopyrimidin-4-yl)pyridine (**1e**),[18a] bis[(η^5-1,2,3,4,5-pentamethylcyclopentadienyl)cobalt(II)dichloride],[21] bis[(η^5-1,2,3,4,5-pentamethylcyclopentadienyl)rhodium(II)dichloride],[21] and bis[(η^5-1,2,3,4,5-pentamethylcyclopentadienyl)iridium(II)dichloride] [21] were synthesized according to published procedures. Solvents solvents were purchased from Sigma Aldrich and dried over molecular sieves in a Braun MB SPS solvent dryer. All reactions were carried out under an atmosphere of nitrogen using standard Schlenk-techniques. The NMR spectra were obtained on Bruker Avance 400 and 600 systems. For the assignment of the peaks, see the structures presented in the Supporting Information. The IR spectra were recorded with a Perkin Elmer FT-IR Spectrum 100 device equipped with an ATR sample assembly. For data refining the Perkin Elmer software Spectrum 6.3.5 was used. Elemental analysis measurements were performed with a Hanau Elemental Analyzer Vario Micro cube.

General procedure for the syntheses of the cobalt(III) complexes 2a-e, the rhodium(III) complexes 3a-e and the iridium(III) complexes 4a-d and 5.

[(η^5-Cp*)MCl_2]$_2$, the *N,N'*-chelating ligand and a salt providing the appropriate anion (the salt was left for compound **5**; molar ratios given below) were filled into a Schlenk-tube. CH_2Cl_2 or thf was added and the resulting suspension was stirred at room temperature for 48 h (Rh, Ir) resp. 72 h (Co). The reaction mixture was filtered, the solvent was removed under vacuum. The raw product was recrystallized by slow diffusion of Et_2O in an acetonitrile or CH_2Cl_2 solution.

2,2'-Bipyridine(chlorido)(η^5-1,2,3,4,5-pentamethylcyclopentadienyl)cobalt(III) hexafluorophosphate (2a)

40.0 mg (0.07 mmol) of [(η^5-Cp*)$CoCl_2$]$_2$, 23.6 mg (0.15 mmol) of **1a**, 27.8 mg (0.15 mmol) of KPF_6, 12 mL of CH_2Cl_2. Recrystallized from CH_3CN/Et_2O. Dark violet crystals, yield: 31%. Anal. calcd. for $C_{20}H_{23}ClCoF_6N_2P$ (530.77): C 45.26, H 4.37, N 5.28, found: C 45.56, H 4.23, N 5.55%. ^{1}H NMR (400.1 MHz, CD_3CN): δ 9.42 (d, $^3J_{HH}$ = 5.5 Hz, 2H, H1), 8.30 (d, $^3J_{HH}$ = 7.9 Hz, 2H, H4), 8.22 (t, $^3J_{HH}$ = 7.8 Hz, 2H, H3), 7.87 (t, $^3J_{HH}$ = 6.4 Hz, 2H, H2), 1.23 (s, 15H, C_5Me_5). ^{13}C NMR (100.6 MHz, CD_3CN): δ 156.6 (C5), 155.0 (C1), 141.0 (C3), 129.0 (C2), 124.1 (C4), 96.4(C_5Me_5), 9.5 (C_5Me_5). ^{19}F NMR (376.5 MHz, CD_3CN): δ -72.9 (d, $^1J_{PF}$ = 706 Hz). ^{31}P NMR (162.0 MHz, CD_3CN): δ -144.7 (hept, $^1J_{PF}$ = 706 Hz). IR (ATR, cm^{-1}): 3090w, 2924w, 1607m, 1566w, 828s.

Chlorido(η^5-1,2,3,4,5-pentamethylcyclopentadienyl)(2-pyrimidin-4-ylpyridine)cobalt(III) hexafluorophosphate (2b)

250 mg (0.47 mmol) of [(η^5-Cp*)$CoCl_2$]$_2$, 149 mg (0.94 mmol) of **1b**, 174 mg (0.94 mmol) of KPF_6, 30 mL of thf. Recrystallized from CH_2Cl_2/Et_2O. Violet crystals, yield: 46%. Anal. calcd. for $C_{19}H_{22}ClCoF_6N_3P$ (531.75): C 42.92, H 4.17, N 7.90, found: C 42.62, H 4.29, N 7.72%. ^{1}H NMR (400.1 MHz, CD_3CN): δ 10.13 (s, 1H, H9), 9.47 (d, $^3J_{HH}$ = 5.37, 1H, H1), 9.35 (d, $^3J_{HH}$ = 4.13 Hz, 1H, H8), 8.39 (d, $^3J_{HH}$ = 8.0 Hz, 1H, H7), 8.26 (m, 2H, H3, H4), 7.98 (t, $^3J_{HH}$ = 6.24 Hz, 1H, H2), 1.28 (s, 15H, C_5Me_5). ^{13}C NMR (100.6 MHz, CD_3CN): δ 163.0 (C9), 162.2 (C1), 160.8 (C6), 155.6 (C8), 154.8 (C5), 141.4 (C3), 131.0 (C2), 126.2 (C4), 120.5 (C7), 97.0 (C_5Me_5), 9.8 (C_5Me_5). ^{19}F NMR (376.5 MHz, CD_3CN): δ -72.9 (d, $^1J_{PF}$ = 706 Hz) ppm.^{31}P NMR (162.0 MHz, CD_3CN): δ -144.6 (hept, $^1J_{PF}$ = 706 Hz) ppm. IR (ATR, cm^{-1}): 3076w, 2923w, 1593m, 1545w, 831s.

(2-(2-Aminopyrimidin-4-yl)pyridine)(chlorido)(η^5-1,2,3,4,5-pentamethylcyclopentadienyl)cobalt(III) hexafluorophosphate (2c)

40.0 mg (0.07 mmol) of [(η^5-Cp*)$CoCl_2$]$_2$, 23.6 mg (0.15 mmol) of **1c**, 26.0 mg (0.15 mmol) of KPF_6, 12 mL of CH_2Cl_2. Recrystallized from CH_3CN/Et_2O. Violet crystals, yield: 36%. Anal. calcd. for $C_{19}H_{23}ClCoF_6N_4P$ (546.77): C 41.74, H 4.24, N 10.25, found: C 41.91, H 4.34, N 10.59%. ^{1}H NMR (400.1 MHz, CD_3CN): δ 9.41 (d, $^3J_{HH}$ = 5.3 Hz, 1H, H1), 8.85 (d, $^3J_{HH}$ = 3.9 Hz, 1H, H8), 8.26 (m, 2H, H3, H4), 7.88 (m, 1H, H2), 7.63 (d, $^3J_{HH}$ = 4.5 Hz, 1H, H7), 7.03, 6.83 (2×br, 2H, H10), 1.13 (s, 15H, C_5Me_5). ^{13}C NMR (100.6 MHz, CD_3CN): δ 167.2 (C9), 162.9 (C6), 162.9 (C8), 156.9 (C5), 156.8 (C1), 141.7 (C3), 129.9 (C2), 125.9 (C4), 111.3 (C7), 96.7 (d, C_5Me_5), 9.7 (C_5Me_5). ^{19}F NMR (376.5 MHz, CD_3CN): δ –72.9 (d, $^1J_{PF}$ = 706 Hz). ^{31}P NMR (162.0 MHz, CD_3CN): δ –144.6 (hept, $^1J_{PF}$ = 706 Hz). IR (ATR, cm^{-1}): 3383w, 3291w, 3079w, 2969w, 1586m, 1556w, 829s.

Chlorido(2-(2-methylaminopyrimidin-4-yl)pyridine)(η^5-1,2,3,4,5-pentamethylcyclopentadienyl)cobalt(III) hexafluorophosphate (2d)

40.0 mg (0.07 mmol) of [(η^5-Cp*)$CoCl_2$]$_2$, 28.1 mg (0.15 mmol) of **1d**, 26.0 mg (0.15 mmol) of KPF_6, 12 mL of CH_2Cl_2. Recrystallized from CH_2Cl_2/Et_2O. Dark green crystals, yield: 42%. Anal. calcd. for $C_{20}H_{25}ClCoF_6N_4P$ (546.77): C 42.84, H 4.49, N 9.99, found: C 42.87, H 4.42, N 10.05%. ^{1}H NMR (400.1 MHz, CD_3CN): δ 9.34 (d, $^3J_{HH}$ = 4.9 Hz, 1H, H1), 8.71 (d, $^3J_{HH}$ = 4.3 Hz, 1H, H8), 8.23 (m, 2H, H3, H4), 7.89 (t, $^3J_{HH}$ = 4.6 Hz, 1H, H2), 7.49 (d, $^3J_{HH}$ = 4.3 Hz, 1H, H7), 7.36 (br, 1H, H10), 3.24 (s, 3H, H11), 1.15 (s, 15H, C_5Me_5). ^{13}C NMR (100.6 MHz, CD_3CN): δ 165.5 (C9), 162.6 (C6), 162.4 (C8), 156.7 (C5), 156.1 (C1), 141.5 (C3), 129.5 (C2), 125.4 (C4), 109.4 (C7), 96.3 (d, C_5Me_5), 29.4 (C11), 9.9 (C_5Me_5). ^{19}F NMR (376.5 MHz, CD_3CN): δ –73.0 (d, $^1J_{PF}$ = 710 Hz). ^{31}P NMR (162.0 MHz, CD_3CN): δ –144.5 (hept, $^1J_{PF}$ = 710 Hz). IR (ATR, cm^{-1}): 3343w, 3086w, 2973w, 1600m, 1539w, 828s.

Chlorido(2-(2-dimethylaminopyrimidin-4-yl)pyridine)(η^5-1,2,3,4,5-pentamethylcyclopentadienyl)cobalt(III) hexafluorophosphate (2e)

53.0 mg (0.10 mmol) of $[(\eta^5\text{-Cp*})CoCl_2]_2$, 40.0 mg (0.20 mmol) of **1e**, 36.8 mg (0.20 mmol) of KPF_6, 12 mL of CH_2Cl_2. Recrystallized from CH_2Cl_2/Et_2O. Dark green crystals, yield: 42%. Anal. calcd. for $C_{21}H_{27}ClCoF_6N_4P$ (546.77): C 43.88, H 4.73, N 9.75, found: C 43.98, H 4.94, N 9.66 %. ^{1}H NMR (400.1 MHz, CD_3CN): δ 9.30 (d, $^3J_{HH}$ = 5.5 Hz, 1H, H1), 8.61 (d, $^3J_{HH}$ = 4.2 Hz, 1H, H8), 8.21 (dt, 1H, $^3J_{HH}$ = 7.9 Hz, H3), 8.11 (d, 1H, 1H, $^3J_{HH}$ = 7.86 Hz, H4), 7.90 (t, $^3J_{HH}$ = 6.0 Hz, 1H, H2), 7.55 (d, $^3J_{HH}$ = 4.4 Hz, 1H, H7), 3.59 (s, 3H, H10), 3.44 (s, 3H, H10), 1.00 (s, 15H, C_5Me_5). ^{13}C NMR (100.6 MHz, CD_3CN): δ 167.8 (C9), 164.2 (C6), 159.6 (C8), 156.8 (C5), 155.2 (C1), 141.3 (C3), 129.5 (C2), 124.4 (C4), 110.0 (C7), 95.2 (C_5Me_5), 42.7 (C10), 40.2 (C10), 9.6 (C_5Me_5). ^{19}F NMR (376.5 MHz, CD_3CN): δ –73.2 (d, $^1J_{PF}$ = 710 Hz). ^{31}P NMR (162.0 MHz, CD_3CN): δ –144.6 (hept, $^1J_{PF}$ = 710 Hz). IR (ATR, cm^{-1}): 3069w, 2965w, 1600m, 1546m, 827s.

2,2'-Bipyridine(chlorido)(η^5-1,2,3,4,5-pentamethylcyclopentadienyl)rhodium(III) hexafluorophosphate (3a)

49.4 mg (0.08 mmol) of $[(\eta^5\text{-Cp*})RhCl_2]_2$, 25.0 mg (0.16 mmol) of **1a**, 29.4 mg (0.16 mmol) of KPF_6, 10 mL of CH_2Cl_2. Recrystallized from CH_3CN/Et_2O. Red-orange crystals, yield: 20%. Anal. calcd. for $C_{20}H_{23}ClF_6N_2PRh$ (574.74): C 41.80, H 4.03, N 4.87, found: C 41.27, H 4.01, N 4.78%. ^{1}H NMR (400.1 MHz, CD_3CN): δ 8.88 (d, $^3J_{HH}$ = 5.4 Hz, 2H, H1), 8.38 (d, $^3J_{HH}$ = 8.1 Hz, 2H, H4), 8.22 (m, 2H, H3), 7.80 (m, 2H, H2), 1.66 (s, 15H, C_5Me_5). ^{13}C NMR (100.6 MHz, CD_3CN): δ 155.3 (C1), 152.9 (C5), 141.3 (C3), 129.3 (C2), 124.7 (C4), 98.3 (d, $^1J_{CRh}$ = 8.1 Hz, C_5Me_5), 9.1 (C_5Me_5). ^{19}F NMR (376.5 MHz, CD_3CN): δ –72.9 (d, $^1J_{PF}$ = 706 Hz). ^{31}P NMR (162.0 MHz, CD_3CN): δ –144.7 (hept, $^1J_{PF}$ = 706 Hz). IR (ATR, cm^{-1}): 3084w, 1605m, 1468m, 1438m, 1026m, 826s, 773s.

Chlorido(η^5-1,2,3,4,5-pentamethylcyclopentadienyl)(2-pyrimidin-4-ylpyridine)rhodium(III) hexafluorophosphate (3b)

49.4 mg (0.08 mmol) of $[(\eta^5\text{-Cp*})RhCl_2]_2$, 25.1 mg (0.16 mmol) of **1b**, 29.4 mg (0.16 mmol) of KPF_6, 10 mL of CH_2Cl_2. Orange crystals, yield: 89%. Anal. calcd. for $C_{19}H_{22}ClF_6N_3PRh$ (575.73): C 39.64, H 3.85, N 7.30, found: C 39.41, H 3.77, N 7.10%. ^{1}H NMR (400.1 MHz, CD_3CN): δ 9.47 (s, 1H, H9), 9.17 (d, $^3J_{HH}$ = 5.3 Hz, 1H, H8), 8.95 (d, $^3J_{HH}$ = 5.4 Hz, 1H, H1), 8.51 (d, $^3J_{HH}$ = 7.9 Hz, 1H, H4), 8.35 (dd, $^4J_{HH}$ = 1.2, $^3J_{HH}$ =5.4 Hz, 1H, H7), 8.30 (td, ^{4}JHH = 1.5, $^3J_{HH}$ =7.90 Hz, 1H, H3), 7.93 (ddd, $^4J_{HH}$ = 1.3, $^3J_{HH}$ = 5.5, $^3J_{HH}$ = 7.5 Hz, 1H, H2), 1.71 (s, 15H, C_5Me_5). ^{13}C NMR (100.6 MHz, CD_3CN): δ 161.7 (C6), 161.7 (C9), 160.4 (C8), 153.5 (C1), 153.3 (C5), 141.6 (C3), 131.3 (C2), 126.5 (C4), 120.2 (C7), 98.8 (d, $^1J_{CRh}$ = 8.3 Hz, C_5Me_5), 9.3 (C_5Me_5). ^{19}F NMR (376.5 MHz, CD_3CN): δ –72.9 (d, $^1J_{PF}$ = 706 Hz) ppm.^{31}P NMR (162.0 MHz, CD_3CN): δ –144.6 (hept, $^1J_{PF}$ = 706 Hz) ppm. IR (ATR, cm^{-1}): 2925w, 1592m, 1462m, 1025m, 825vs, 797s, 753s.

(2-(2-Aminopyrimidin-4-yl)pyridine)(chlorido)(η^5-1,2,3,4,5-pentamethylcyclopentadienyl)rhodium(III) hexafluorophosphate (3c)

49.4 mg (0.08 mmol) of $[(\eta^5\text{-Cp*})RhCl_2]_2$, 27.6 mg (0.16 mmol) of **1c**, 29.4 mg (0.16 mmol) of KPF_6, 10 mL of CH_2Cl_2. Red-orange crystals, yield: 90%. Anal. calcd. for $C_{19}H_{23}ClF_6N_4PRh$ (590.74): C 38.63, H 3.92, N 9.48, found: C 38.68, H 3.92, N 9.44%. ^{1}H NMR (400.1 MHz, CD_3CN): δ 8.90 (d, $^3J_{HH}$ = 5.4 Hz, 1H, H1), 8.66 (d, $^3J_{HH}$ = 4.9 Hz, 1H, H8), 8.34 (d, $^3J_{HH}$ = 7.8 Hz, 1H, H4), 8.24 (td, $^4J_{HH}$ = 1.5, $^3J_{HH}$ = 7.87 Hz, 1H, H3), 7.85 (m, 1H, H2), 7.59 (d, $^3J_{HH}$ = 4.2 Hz, 1H, H7), 6.43 (br, 2H, H10), 1.56 (s, 15H, C_5Me_5). ^{13}C NMR (100.6 MHz, CD_3CN): δ 164.3 (C9), 163.3 (C8), 161.6 (C6), 155.0 (C5), 153.8 (C1), 141.1 (C3), 130.5 (C2), 126.2 (C4), 110.3 (C7), 98.5 (d, $^1J_{CRh}$ = 8.3 Hz, C_5Me_5), 9.2 (C_5Me_5). ^{19}F NMR (376.5 MHz, CD_3CN): δ –72.9 (d, $^1J_{PF}$ = 706 Hz). ^{31}P NMR (162.0 MHz, CD_3CN): δ –144.6 (hept, $^1J_{PF}$ = 706 Hz). IR (ATR, cm^{-1}): 3392w, 3299m, 3160m, 1639m, 1556m, 828vs, 796s.

Chlorido(2-(2-methylaminopyrimidin-4-yl)pyridine)(η^5-1,2,3,4,5-pentamethylcyclopentadienyl)rhodium(III) hexafluorophosphate (3d)

49.4 mg (0.08 mmol) of $[(\eta^5\text{-Cp*})RhCl_2]_2$, 29.8 mg (0.16 mmol) of **1d**, 29.4 mg (0.16 mmol) of KPF_6, 10 mL of CH_2Cl_2. Orange crystals, yield: 82%. Anal. calcd. for $C_{20}H_{25}ClF_6N_4PRh$ (604.77): C 39.72, H 4.17, N 9.26, found: C 40.06, H 4.23, N 9.41. ^{1}H NMR (400.1 MHz, CD_3CN): δ 8.90 (d, $^3J_{HH}$ = 5.4 Hz, 1H, H1), 8.72 (d, $^3J_{HH}$ = 4.9 Hz, 1H, H8), 8.34 (d, $^3J_{HH}$ = 7.9 Hz, 1H, H4), 8.24 (td, $^4J_{HH}$ = 1.5, $^3J_{HH}$ = 7.87 Hz, 1H, H3), 7.85 (m, 1H, H2), 7.53 (d, $^3J_{HH}$ = 4.9 Hz, 1H, H7), 6.44 (br, 1H, H10), 3.13 (d, $^3J_{HH}$ = 5.0 Hz, 3H, H11), 1.53 (s, 15H, C_5Me_5). ^{13}C NMR (100.6 MHz, CD_3CN): δ 163.2 (C9), 162.9 (C8), 161.8 (C6), 155.1 (C5), 153.8 (C1), 141.6 (C3), 130.5 (C2), 126.3 (C4), 109.3 (C7), 98.6 (d, $^1J_{CRh}$ = 8.2 Hz, C_5Me_5), 29.5 (C11), 9.2 (C_5Me_5). ^{19}F NMR (376.5 MHz, CD_3CN): δ –72.9 (d, $^1J_{PF}$ = 706 Hz). ^{31}P NMR (162.0 MHz, CD_3CN): δ –144.6 (hept, $^1J_{PF}$ = 706 Hz). IR (ATR, cm^{-1}): 3354w, 3083w, 1597s, 1579s, 832vs, 791s, 775s.

Chlorido(2-(2-dimethylaminopyrimidin-4-yl)pyridine)(η^5-1,2,3,4,5-pentamethylcyclopentadienyl)rhodium(III) tetrafluoroborate (3e)

49.4 mg (0.08 mmol) of $[(\eta^5\text{-Cp*})RhCl_2]_2$, 35.8 mg (0.18 mmol) of **1e**, 24.2 mg (0.22 mmol) of $NaBF_4$, 10 mL of CH_2Cl_2. Orange crystals, yield: 98%. Anal. calcd. for $C_{21}H_{27}BClF_4N_4Rh$ (560.63): C 44.99, H 4.85, N 9.99, found: C 45.18, H 4.89, N 9.95. ^{1}H NMR (400.1 MHz, CD_3CN): δ 8.76 (d, $^3J_{HH}$ = 5.4 Hz, 1H, H1), 8.59 (d, $^3J_{HH}$ = 4.6 Hz, 1H, H8), 8.19 (m, 2H, H3, H4), 7.81 (td, $^4J_{HH}$ = 2.5, $^3J_{HH}$ = 6.0 Hz, 1H, H2), 7.43 (d, $^3J_{HH}$ = 4.6 Hz, 1H, H7), 3.34 (s, 3H, H10), 3.30 (s, 3H, H10), 1.53 (s, 15H, C_5Me_5). ^{13}C NMR (100.6 MHz, CD_3CN): δ 165.7 (C9), 163.8 (C6), 160.3 (C8), 155.4 (C5), 153.9 (C1), 141.7 (C3), 129.9 (C2), 125.3 (C4), 109.9 (C7), 97.8 (d, $^1J_{CRh}$ = 8.3 Hz, C_5Me_5), 42.1 (C10), 39.6 (C10), 8.7 (C_5Me_5). ^{19}F NMR (376.5 MHz, CD_3CN): δ –151.6. ^{11}B NMR (128.4 MHz, CD_3CN): δ –1.2 ppm. IR (ATR, cm^{-1}): 2966w, 2929w, 1557m, 1475m, 1363m, 1044vs, 769s.

2,2'-Bipyridine(chlorido)(η^5-1,2,3,4,5-pentamethylcyclopentadienyl)iridium(III) tetrafluoroborate (4a)

55.8 mg (0.07 mmol) of $[(\eta^5\text{-Cp*})IrCl_2]_2$, 21.9 mg (0.14 mmol) of **1a**, 24.2 mg (0.14 mmol) of $NaBF_4$, 10 mL of CH_2Cl_2. Yellow crystals, yield: 79%. Anal. calcd. for $C_{20}H_{23}BClF_4IrN_2$ (605.89): C

39.65, H 3.83, N 4.62, found: C 39.70, H 3.80, N 4.55%. ^{1}H NMR (400.1 MHz, CD_3CN): δ 8.88 (dd, $^4J_{HH}$ = 0.6, $^3J_{HH}$ = 5.6 Hz, 2H, H1), 8.45 (d, $^3J_{HH}$ = 8.1 Hz, 2H, H4), 8.21 (td, $^4J_{HH}$ = 1.4, $^3J_{HH}$ = 8.0 Hz, 2H, H3), 7.78 (m, 2H, H2), 1.65 (s, 15H, C_5Me_5). ^{13}C NMR (100.6 MHz, CD_3CN): δ 156.3 (C5), 152.7 (C1), 141.2 (C3), 129.8 (C2), 125.0 (C4), 90.5 (C_5Me_5), 8.8 (C_5Me_5). ^{19}F NMR (376.5 MHz, CD_3CN): δ –151.7. ^{11}B NMR (128.4 MHz, CD_3CN): δ –1.2. IR (ATR, cm^{-1}): 2917w, 1606m, 1446m, 1094m, 1049vs, 772s, 727m.

Chlorido(η^5-1,2,3,4,5-pentamethylcyclopentadienyl)(2-pyrimidin-4-ylpyridine)iridium(III) tetrafluoroborate (4b)

47.8 mg (0.06 mmol) of [(η^5-Cp*)IrCl$_2$]$_2$, 22.0 mg (0.14 mmol) of **1b**, 15.9 mg (0.15 mmol) of $NaBF_4$, 10 mL of CH_2Cl_2. Yellow crystals, yield: 95%. Anal. calcd. for $C_{19}H_{22}BClF_4IrN_3$ (606.88): C 37.60, H 3.65, N 6.92, found: C 37.65, H 3.56, N 6.84. ^{1}H NMR (400.1 MHz, CD_3CN): δ 9.45 (s, 1H, H9), 9.13 (d, $^3J_{HH}$ = 5.3 Hz, 1H, H8), 8.95 (dd, $^4J_{HH}$ = 0.7, $^3J_{HH}$ =5.6 Hz, 1H, H1), 8.59 (d, $^3J_{HH}$ = 7.7 Hz, 1H H4), 8.43 (dd, $^4J_{HH}$ = 1.2, $^3J_{HH}$ =5.3 Hz, 1H, H7), 8.29 (td, $^4J_{HH}$ = 1.4, $^3J_{HH}$ =7.9 Hz, 1H, H3), 7.91 (ddd, $^4J_{HH}$ = 1.4, $^3J_{HH}$ = 5.6, $^3J_{HH}$ =7.6 Hz, 1H, H2), 1.70 (s, 15H, C_5Me_5). ^{13}C NMR (100.6 MHz, CD_3CN): δ 163.0 (C6), 161.5 (C9), 160.1 (C8), 154.4 (C5), 153.3 (C1), 141.6 (C3), 131.9 (C2), 126.9 (C4), 120.2 (C7), 91.1 (C_5Me_5), 9.0 (C_5Me_5). ^{19}F NMR (376.5 MHz, CD_3CN): δ –151.8 ppm. ^{11}B NMR (128.4 MHz, CD_3CN): δ–1.2. IR (ATR, cm^{-1}): 3107w, 2917m, 1599m, 1459m, 1392m, 1032vs, 756m.

(2-(2-Aminopyrimidin-4-yl)pyridine)(chlorido)(η^5-1,2,3,4,5-pentamethylcyclopentadienyl)iridium(III) tetrafluoroborate (4c)

63.0 mg (0.08 mmol) of [(η^5-Cp*)IrCl$_2$]$_2$, 29.0 mg (0.17 mmol) of **1c**, 21.0 mg (0.19 mmol) of $NaBF_4$, 10 mL of CH_2Cl_2. Yellow crystals, yield: 92%. Anal. calcd. for $C_{19}H_{23}BClF_4IrN_4$ (621.90.) C 36.70, H 3.73,N 9.01, found: C 37.03, H 3.91, N 9.54%. ^{1}H NMR (400.1 MHz, CD_3CN): δ 8.88 (dd, $^4J_{HH}$ = 0.7, $^3J_{HH}$ = 5.6 Hz, 1H, H1), 8.61 (d, $^3J_{HH}$ = 4.9 Hz, 1H, H8), 8.37 (d, $^3J_{HH}$ = 7.8 Hz, 1H, H4), 8.22 (td, $^4J_{HH}$ = 1.5, $^3J_{HH}$ = 7.9 Hz, 1H, H3), 7.84 (m, 1H, H2), 7.59 (d, $^3J_{HH}$ = 4.9 Hz, 1H, H7), 6.60 (br, 2H, H10), 1.57 (s, 15H, C_5Me_5). ^{13}C NMR (100.6 MHz, CD_3CN): δ 163.4 (C9), 163.2 (C8), 162.0 (C6), 155.8 (C5), 153.4 (C1), 141.5 (C3), 131.0 (C2), 126.3 (C4), 109.9 (C7), 90.6 (C_5Me_5), 9.0 (C_5Me_5). ^{19}F NMR (376.5 MHz, CD_3CN): δ –151.7 ppm. ^{11}B NMR (128.4 MHz, CD_3CN): δ -1.2 ppm. IR (ATR, cm^{-1}): 3412w, 3289w, 3098w, 1636m, 1556m, 1027vs, 771s.

Chlorido(2-(2-methylaminopyrimidin-4-yl)pyridine)(η^5-1,2,3,4,5-pentamethylcyclopentadienyl)iridium(III) tetrafluoroborate (4d)

85.3 mg (0.11 mmol) of [(η^5-Cp*)IrCl$_2$]$_2$, 39.3 mg (0.21 mmol) of **1d**, 28.4 mg (0.26 mmol) of $NaBF_4$, 10 mL of CH_2Cl_2. Orange crystals, yield: 92%. Anal. calcd. for $C_{20}H_{25}BClF_4IrN_4$ (635.92): C 37.78, H 3.96, N 8.81, found: C 38.13, H 4.09,N 9.04%. ^{1}H NMR (400.1 MHz, CD_3CN): δ 8.88 (d, $^3J_{HH}$ = 5.6 Hz, 1H, H1), 8.66 (d, $^3J_{HH}$ =4.9 Hz, 1H, H8), 8.38 (d, $^3J_{HH}$ = 8.1 Hz, 1H, H4), 8.22 (td, $^4J_{HH}$ = 1.4, $^3J_{HH}$ = 7.9 Hz, 1H, H3), 7.84 (m, 1H, H2), 7.54 (d, $^3J_{HH}$ = 4.9 Hz, 1H, H7), 6.28 (s, 1H, H10), 3.14 (d, $^3J_{HH}$ = 5.0 Hz, 3H, H11), 1.55 (s, 15H, C_5Me_5). ^{13}C NMR (100.6 MHz, CD_3CN): δ 162.8 (C8), 162.3 (C9), 162.1 (C6), 156.0 (C5), 153.1 (C1), 141.6 (C3), 131.1 (C2), 126.4 (C4), 108.9 (C7), 90.7 (C_5Me_5), 29.9 (C11), 8.9 (C_5Me_5). ^{19}F NMR (376.5 MHz, CD_3CN): δ –151.6. ^{11}B NMR (128.4 MHz, CD_3CN): δ –1.2. IR (ATR, cm^{-1}): 3379m, 3106w, 3064w, 1579s, 1046vs, 808s, 780s.

Chlorido(2-*N*,*N*-dimethylamino-4-(pyridin-2-yl-κ*N*)pyrimidine-κC5)(η^5-1,2,3,4,5-pentamethylcyclopentadienyl)iridium(III) hydrochloride (5)

55.8 mg (0.07 mmol) of [(η^5-Cp*)IrCl$_2$]$_2$, 28.0 mg (0.14 mmol) of **1e**, 10 mL of CH_2Cl_2. Red crystals, yield: 64%. Anal. calcd. for $C_{21}H_{27}Cl_2IrN_4$ (598.60): C 42.14, H 4.55, N 9.36%, found: C 41.94, H 4.59, N 9.06%. ^{1}H NMR (600.1 MHz, CD_2Cl_2): δ 15.35 (br, 1H, H11), 8.78 (d, $^3J_{HH}$ = 5.0 Hz, 1H, H1), 8.44 (s, 1H, H8), 8.35 (dd, $^4J_{HH}$ = 0.7, $^3J_{HH}$ = 7.8 Hz, 1H, H4), 7.97 (td, $^4J_{HH}$ = 1.4, $^3J_{HH}$ = 7.7 Hz, 1H, H3), 7.56 (ddd, $^4J_{HH}$ = 1.5, $^3J_{HH}$ = 5.6, $^3J_{HH}$ = 7.3 Hz, 1H, H2), 3.45 (s, 6H, H10), 1.72 (s, 15H, C_5Me_5). ^{13}C NMR (150.9 MHz, CD_2Cl_2): δ 178.9 (C7), 160.3 (C5), 153.0 (C9), 152.9 (C1), 149.0 (C8), 138.9 (C3), 131.7 (C6), 129.3 (C2), 125.0 (C4), 89.7 (C_5Me_5), 38.9 (C10), 9.5 (C_5Me_5). IR (ATR, cm^{-1}): 2866w, 2508br, 1617m, 1585m, 866s, 839s, 764vs.

DFT calculations

Quantum chemical calculations on the the HCl splitting from the cations **2-4a-e**$^+$ with the program Gaussian09 [32] using the B3LYP gradient corrected exchange-correlation functional [33] in combination with the 6-311+G* basis set for C, H, N, Cl.[34] For rhodium and iridium, the according Def2-TZVP ECP basis sets were applied,[35] for cobalt Ahlrichs TZV basis set was used.[36] Full geometry optimizations were carried out in C_1 symmetry using analytical gradient techniques and the resulting structures were confirmed to be true minima by diagonalization of the analytical Hessian Matrix. The starting geometries for the calculations were taken from solid-state structures. Not all transition states could be located. In some cases scans along the internal reaction coordinate were carried out to find the transition state. For more details see the Supporting Information.

X-ray structure analyses

Crystal data and refinement parameters for compounds **2c**, **2d**, **3a**, **3c**, **4b**, **4c** and **5** are collected in Table 1. The structures **2c**, **2d**, **3a**, **4b**, **4c** and **5** were solved using direct methods,[37] while **3c** was solved using SUPERFLIP programm,[38] completed by subsequent difference Fourier syntheses, and refined by full-matrix least-squares procedures.[39] For compounds **2d** and **5**, semi-empirical absorption corrections from equivalents (Multiscan) were carried out, while analytical numeric absorption corrections were applied on complexes **2c**, **3a**, **3c**, **4b** and **4c**.[40] All non-hydrogen atoms were refined with anisotropic displacement parameters. In **2c** and **4c** hydrogen atoms which are bound to nitrogen atoms were located in the difference Fourier synthesis, and were refined semi-freely with the help of a distance restraint, while constraining their *U* values to 1.2 times the *U(eq)* values of the corresponding nitrogen atoms. In **2d** and **3c** hydrogen atoms bound to nitrogen atoms were also located in the difference Fourier synthesis, but were then refined freely. In the structure of compound **3a** the hydrogen

atoms H11A and H11B, which are bound to C11, were located in the difference Fourier synthesis, and were refined semi-freely with the help of a distance restraint, while constraining their *U* values to 1.5 times the *U(eq)* values of C11. All the other hydrogen atoms were placed in calculated positions and refined by using a riding model. In the structure of complex **5**, because of the existence of severely disordered and/or partially occupied CH_2Cl_2/H_2O, SQUEEZE process integrated in PLATON was used.[41] Detailed information has been posted in the final CIF file. CCDC 1541493 - 1541499 contain the supplementary crystallographic data for this paper. These data can be obtained free of charge from The Cambridge Crystallographic Data Centre via www.ccdc.cam.ac.uk/data_request/cif.

Mass spectrometry

ESI-MS and CID measurements were performed by a Paul-type quadrupole ion trap instrument (Bruker Esquire 3000plus). The ion source was set to positive and negative electrospray ionization mode. Scan speed was 13000 m/z / s in standard resolution scan mode (0.3 FWHM / m/z) and the scan range was 15 to 1200 m/z. Mass spectra were accumulated for at least two minutes. MS^n spectra were accumulated for at least twenty seconds. Sample solutions were continuously infused into the ESI chamber by a syringe pump at a flow rate of 2 µL min^{-1}. Nitrogen was used as drying gas with a flow rate of 3.0 L min^{-1} at 220 °C. The solutions were sprayed at a nebulizer pressure of 280 mbar (4 psi) and the electrospray needle was held at 4.5 kV.

Collision induced dissociation (CID) appearance curves were recorded with varying excitation amplitudes (0.0 V to 1.0 V), which determine the internal energy scale of the mass spectrometer ($\mathbf{E_{LAB}}$ in V). Relative abundances were calculated according to:

$$I_{tot}^{fr}\cdot(E_{lab}) = \left(\frac{\sum_i I_i^{fr}(E_{lab})}{\sum_i I_i^{fr}(E_{lab}) + \sum_i I_i^{p}(E_{lab})}\right) \quad (1)$$

where I_i^{fr} = intensity of the fragment ions and I_i^{p} = intensity of the parent ions.

Fragmentation amplitude dependent CID spectra were modeled and fitted by sigmoidal functions of the type

$$I_{fit}^{fr}(E_{lab}). = \left(\frac{1}{1 + e^{(E_{lab}^{50} - E_{lab})\,B}}\right) \quad (2)$$

using a least-squares criterion. The E_{lab}^{50} fit parameter is the amplitude at which the sigmoid function is at half maximum value, whereas B describes the rise of the sigmoid curve.main paragraph text follows directly on here.

Conclusions

Cationic complexes of the type $[(\eta^5\text{-Cp*})M(Cl)(N,N')]^+$ (M = Co, Rh, Ir) undergo cleavage of HCl under CIDS conditions in the gas-phase. Although being part of a series of isostructural compounds, they show large differences in activation energies and even more important in the reaction channels. Not only the *N,N'*-coordinating ligands have a strong impact on the site, the proton is coming from. In addition there is a pronounced influence of the metal centre that could be elucidated by a combination of spectroscopic and theoretical tools.

While iridium prefers to go into a cyclometallation of the *N,N'*-coordinating ligand, cobalt exclusively undergoes splitting of a CH-bond at a Cp* methyl group, even for aminopyrimidinylpyridine ligands, which are strongly activated for an electrophilic aromatic substitution (cyclometallation). The reactivity of rhodium is found somewhere in between the two other complexes. This series can be explained by the differences in stabilities of M-C bonds and of the oxidation states +I and +III for the Group IX elements.

Acknowledgements

This work was supported by the German research foundation DFG within the transregional collaborative research centre SFB/TRR 88 “Cooperative effects in homo and heterometallic complexes” (3MET) and by the state research centre OPTIMAS. The authors furthermore gratefully acknowledge the research college MAGNENZ, the state research unit NanoKat and the Carl Zeiss Stiftung for financial support.

Notes and references

1 J. Kleiman and M. Dubeck, *J. Am. Chem. Soc.*, 1990, **85**, 1544.
2 A. C. Cope and R. W. Siekman, *J. Amer. Chem. Soc.*, 1965, **87**, 3272.
3 S. Trofimenko, *Inorg. Chem.*, 1973, **12**, 1215.
4 (a) J. Dehand and M. Pfeffer, Coord. *Chem. Rev.*, 1976, **18**, 327; (b) M. I. Bruce, *Angew. Chem. Int. Ed. Engl.*, 1977, 16, 73; (c) I. Omae, *Coord. Chem. Rev.*, 2004, **248**, 995; (d) M. Albrecht, *Chem. Rev.*, 2010, **110**, 576; (e) N. Mirzadeh, M. A. Bennett and S. K. Bhargava, *Coord. Chem. Rev.*, 2013, **257**, 2250; (f) Y.-F. Han and G.-X. Jin, *Chem. Soc. Rev.*, 2014, 43, 2799.
5 (a) M. E. van der Boom and D. Milstein, *Chem. Rev.*, 2003, **103**, 1759; (b) I. Omae, *Coord. Chem. Rev.*, 2011, **255**, 139; (c) Z. Liu and P. J. Sadler, *Acc. Chem. Res.*, 2014, **47**, 1174; (d) S. Chakraborty, P. Bhattacharya, H. Dai and H. Guan, *Acc. Chem. Res.*, 2015, **48**, 1995.
6 (a) N. Cutillas, G. S. Yellol, C. de Haro, C. Vicente, V. Rodríguez and J. Ruiz, *Coord. Chem. Rev.*, 2013, **257**, 2784; (b) I. Omae, *Coord. Chem. Rev.*, 2014, **280**, 84; (c) D.-L. Ma, D. S.-H. Chan and C.H. Leung, *Acc. Chem. Res.*, 2014, **47**, 3614.
7 (a) A. von Zelewski, P. Belser, P. Hayoza, R. Dux, X. Hua, A. Suckling and H. Stoeckli-Evans, *Coord. Chem. Rev.*, 1994, **132**, 75; (b) K. P. Balashev, M. V. Puzyk, V. S. Kotlyar and M. V. Kulikova, *Coord. Chem. Rev.*, 1997, **159**, 109; (c) B. Ma, P. I. Djurovich and M. E. Thompson, *Coord. Chem. Rev.*, 2005, **249**, 1501; (d) J. A. Gareth Williams, S. Develay, D. L. Rochester and L. Murphy, *Coord. Chem. Rev.*, 2008, **252**, 2596; (e) J. A. Gareth Williams, Chem. Soc. Rev., 2009, **38**, 1783; (f) Y. Chi and P.-T. Chou, *Chem. Soc. Rev.*, 2010, **39**, 638; (g) J. Kalinowski, V. Fattori, M. Cocchi and J. A. Gareth Williams, *Coord. Chem. Rev.*, 2011, **255**, 2401; (h) V. Guerchais and J.-L. Fillaut, *Coord. Chem. Rev.*, 2011, **255**, 2448; (i) P. G. Bomben, K. C. D. Robson, B. D. Koivisto and C. P. Berlinguette, *Coord. Chem. Rev.*, 2012, **256**, 1438; (j) R. D. Costa, E. Ortí, H. J. Bolink, F. Monti, G. Accorsi and N. Armaroli, *Angew. Chem. Int. Ed.*, 2012, **51**, 8178; (k) Y. You and W. Nam, *Chem. Soc. Rev.*, 2012, **41**, 7061; (l) O. S.

Wenger, *Acc. Chem. Res.*, 2013, **46**, 1517; (m) B. J. Powell, *Coord. Chem. Rev.*, 2015, **295**, 46; (n) K. K.-W. Lo, *Acc. Chem. Res.*, 2015, **48**, 2985; (o) Y.-W. Zhong, Z.-L. Gong, J.-Y. Shao and J. Yao, *Coord. Chem. Rev.*, 2016, **312**, 22.
8 A. D. Ryabov, *Chem. Rev.*, 1990, **90**, 403.
9 (a) J. Kwak, Y. Ohk, Y. Jung and S. Chang, *J. Am. Chem. Soc.*, 2012, **134**, 17778; (b) W. B. Cross, E. G. Hope, Y.-H. Lin, S. A. Macgregor, K. Singh, G. A. Solan and N. Yahya, *Chem. Commun.*, 2013, **49**, 1918; (c) K. J. T. Carr, D. L. Davies, S. A. Macgregor, K. Singh and B. Villa-Marcos, *Chem. Sci.*, 2014, **5**, 2340; (d) J. Li, W. Hu, Y. Peng, Y. Zhang, J. Li and W. Zheng, *Organometallics*, 2014, **33**, 2150; (e) D. L. Davies, C. E. Ellul, S. A. Macgregor, C. L. McMullin and K. Singh, *J. Am. Chem. Soc.*, 2015, **137**, 9659; (f) K. F. Donnelly, R. Lalrempuia, H. Müller-Bunz, E. Clot, and M. Albrecht, *Organometallics*, 2015, **34**, 858; (g) S. Stoccoro, L. Maidich, T. Ruiu, M. A. Cinellu, G. J. Clarkson and A. Zucca, *Dalton Trans.*, 2015, **44**, 18001; (h) L. Maidich, G. Dettori, S. Stoccoro, M. A. Cinellu, J. P. Rourke and A. Zucca, *Organometallics*, 2015, **34**, 817; (i) L. S. Jongbloed, B. de Bruin, J. N. H. Reek, M. Lutz and J. I. van der Vlugt, *Catal. Sci. Technol.*, 2016, **6**, 1320.
10 J. Granell, M. Martínez, *Dalton Trans.*, 2012, **41**, 11243.
11 (a) S.-B. Zhao, R.-Y. Wang and S. Wang, *J. Am. Chem. Soc.*, 2007, **129**, 3092; (b) A. Zucca, D. Cordeschi, L. Maidich, M. I. Pilo, E. Masolo, S. Stoccoro, M. A. Cinellu and S. Galli, *Inorg. Chem.*, 2013, **52**, 7717.
12 A. Zucca, D. Cordeschi, S. Stoccoro, M. A. Cinellu, G. Minghetti, G. Chelucci and M. Manassero, *Organometallics*, 2011, **30**, 3064.
13 L. Maidich, G. Dettori, S. Stoccoro, M. A. Cinellu, J. P. Rourke, A. Zucca, *Organometallics*, 2015, **34**, 817.
14 (a) B. Butschke, M. Schlangen, D. Schröder and H. Schwarz, *Chem. Eur. J.*, 2008, **14**, 11050; (b) A. Zucca, G. L. Petretto, S. Stoccoro, M. A. Cinellu, M. Manassero, C. Manassero and G. Minghetti, *Organometallics*, 2009, **28**, 2150; (c) G. Minghetti, S. Stoccoro, M. A. Cinellu, B. Soro and A. Zucca, *Organometallics*, 2003, **22**, 4770; d) S. Stoccoro, L. Maidich, T. Ruiu, M. A. Cinellu, G. J. Clarkson and A. Zucca, *Dalton Trans.*, 2015, **44**, 18001.
15 (a) K. J. H. Young, M. Yousufuddin, D. H. Ess and R. A. Periana, *Organometallics*, 2009, **28**, 3395; (b) W. A. Wickramasinghe, P. H. Bird and N. Serpone, *J. Chem. Soc. Chem. Commun.*, 1981, 1284.
16 A. A. Danopoulos, S. Winston and M. B. Hursthouse, *J. Chem. Soc., Dalton Trans.*, 2002, 3090.
17 (a) S. Farsadpour, L. Taghizadeh Ghoochany, Y. Sun and W. R. Thiel, *Eur. J. Inorg. Chem.*, 2011, 4603; (b) S. Farsadpour, L. Taghizadeh Ghoochany, S. Shylesh, G. Dörr, A. Seifert, S. Ernst and W. R. Thiel, *ChemCatChem*, 2012, **4**, 395.
18 (a) L. Taghizadeh Ghoochany, C. Kerner, S. Farsadpour, Y. Sun, F. Menges, G. Niedner-Schatteburg and W. R. Thiel, *Eur. J. Inorg. Chem.*, 2013, 4305; (b) D. Imanbaew, Y. Nosenko, C. Kerner, K. Chevalier, F. Rupp, C. Riehn, W.R. Thiel and R. Diller, *Chem. Phys.*, 2014, **442**, 53; (c) C. Kerner, S.-D. Straub, Y. Sun, W. R. Thiel, *Eur. J. Org. Chem.*, 2016, 3060.
19 E. C. Constable, S. J. Dunne, D. G. F. Rees and C. X. Schmitt, *Chem. Commun.*, 1996, **10**, 1169.
20 (a) R. F. R. Jazzar, S. A. Macgregor, M. F. Mahon, S. P. Richards and M. K. Whittlesey, *J. Am. Chem. Soc.*, 2002, **124**, 4944; (b) S. Burling, B. M. Paine, D. Nama, V. S. Brown, M. F. Mahon, T. J. Prior, P. S. Pregosin, M. K. Whittlesey and J. M. J. Williams, *J. Am. Chem. Soc.*, 2007, **129**, 1987; (c) G. Choi, H. Tsurugi and K. Mashima, *J. Am. Chem. Soc.*, 2013, **135**, 13149; (d) P. Bhattacharya, J. A. Krause and H. Guan, *J. Am. Chem. Soc.*, 2014, **136**, 11153; (e) C. Boulho and J.-P. Djukic, *Dalton Trans.*, 2010, 8893. (f) K. Ghatak, M. Mane and K. Vanka, *ACS Catal.*, 2013, **3**, 920.
21 (a) U. Kölle, F. Khouzami and B. Fuss, *Angew. Chem Int. Ed. Engl.*, 1982, **21**, 131; (b) U. Kölle and B. Fuss, *Chem. Ber.*, 1984, **117**, 743; (c) C. White, A. Yates, P. M. Maitlis and D. M. Heinekey, *Inorg. Synth.*, 1992, **29**, 228.
22 (a) V. Gabelica and E. De Pauw, *Mass Spectrom. Rev.,* 2005, **24**, 566; (b) E.-L. Zins, C. Pepe, D. Rondeau, S. Rochut, N. Galland and J.-C. Tabet, *J. Mass. Spectrom.,* 2009, **44**, 12; (c) E.-L. Zins, D. Rondeau, P. Karoyan, C. Fosse, S. Rochut and C. Pepe, *J. Mass. Spectrom.,* 2009, **44**, 1668; (d) E.-L.; Zins, C. Pepe and D. Schröder, *J. Mass Spectrom.,* 2010, **45**, 1253; (e) K. V. Barylyuk, K. Chingin, R. M. Balabin and R. Zenobi, *J. Am. Soc. Mass Spectrom.,* 2010, **21**, 172. (f) C. Collette and E. De Pauw, *Rapid Commun. Mass Spectrom.,* 1998, **12**, 165. (g) L. Drahos, R. M. Heeren, C. Collette, E. De Pauw and K. Ve´key, *J. Mass Spectrom.,* 1999, **34**, 1673.
23 O. V. Gusev, S. Sergeev, I. M. Saez and P. M. Maitlis, *Organometallics,* 1994, **13**, 2059.
24 D. Buchholz, B. Gloaguen, J.-L. Fillaut, M. Cotrait and D. Astruc, *Chem. Eur. J., 1*995, **1**, 374.
25 Y. Ohki, A. Murata, M. Imada and K. Tatsumi, *Inorg. Chem.,* 2009, **48**, 4271.
26 (a) D. S. Glück and R. G. Bergman, *Organometallics*, 1990, **9**, 2862; (b) D. Rais and R. G. Bergman, *Chem. Eur. J.*, 2004, **10**, 3970.
27 G. Ciancaleoni, S. Bolaño, J. Bravo, M. Peruzzini, L. Gonsalvi and A. Macchioni, *Dalton Trans.*, 2010, **39**, 3366.
28 J. M. Meredith, K. I. Goldberg, W. Kaminsky and D. Michael Heinekey, *Organometallics*, 2012, **31**, 8459.
29 C. Sabot, K. A. Kumar, C. Antheaume and C. Mioskowski, J. Org. Chem., 2007, **72**, 5001.
30 (a) D. A. Beauchamp and S. J. Loeb, Chem. Commun., 2002, 2484; (b) E. Bejan, H. A. Haddou, J. C. Daran and G. G. A. Balavoine, Synthesis, 1996, 1012; c) E. Ioachim, E. A. Medlycott, M. I. J. Polson and G. S. Hanan, Eur. J. Org. Chem., 2005, 3775.
31 C. Kerner, J. Lang, M. Gaffga, Y. Sun, G. Niedner-Schatteburg and W. R. Thiel, Chempluschem, 2016, **82**, 212.
32 M. J. Frisch, G. W. Trucks, H. B. Schlegel, G. E. Scuseria, M. A. Robb, J. R. Cheeseman, G. Scalmani, V. Barone, B. Mennucci, G. A. Petersson, H. Nakatsuji, M. Caricato, X. Li, H. P. Hratchian, A. F. Izmaylov, J. Bloino, G. Zheng, J. L. Sonnenberg, M. Hada, M. Ehara, K. Toyota, R. Fukuda, J. Hasegawa, M. Ishida, T. Nakajima, Y. Honda, O. Kitao, H. Nakai, T. Vreven, J. A. Montgomery, Jr., J. E. Peralta, F. Ogliaro, M. Bearpark, J. J. Heyd, E. Brothers, K. N. Kudin, V. N. Staroverov, T. Keith, R. Kobayashi, J. Normand, K. Raghavachari, A. Rendell, J. C. Burant, S. S. Iyengar, J. Tomasi, M. Cossi, N. Rega, J. M. Millam, M. Klene, J. E. Knox, J. B. Cross, V. Bakken, C. Adamo, J. Jaramillo, R. Gomperts, R. E. Stratmann, O. Yazyev, A. J. Austin, R. Cammi, C. Pomelli, J. W. Ochterski, R. L. Martin, K. Morokuma, V. G. Zakrzewski, G. A. Voth, P. Salvador, J. J. Dannenberg, S. Dapprich, A. D. Daniels, O. Farkas, J. B. Foresman, J. V. Ortiz, J. Cioslowski and D. J. Fox, Gaussian, Inc., Wallingford CT, 2013.
33 (a) P. J. Stephens, F. J. Devlin, C. F. Chabalowski and M. J. Frisch, J. Phys. Chem., 1994, **98**, 11623; (b) A. D. Becke, J. Chem. Phys., 1993, **98**, 5648; (c) A. D. Becke, Phys. Rev. A, 1988, **38**, 3098; d) C. Lee, W. Yang and R. G. Parr, Phys. Rev. B, 1988, **37**, 785.
34 (a) R. Krishnan, J. S. Binkley, R. Seeger and J. A. Pople, J. Chem. Phys., 1980, **72**, 650; (b) A. D. McLean and G. S. Chandler, J. Chem. Phys. 1980, **72**, 5639.
35 F. Weigend and R. Ahlrichs, PhysChemChemPhys., 2005, **7**, 3297.
36 A. Schäfer, C. Huber and R. Ahlrichs, J. Chem. Phys., 1994, **100**, 5829.

37 A. Altomare, G. Cascarano, C. Giacovazzo, A. Guagliardi, M. C. Burla, G. Polidori and M. Camalli, J. Appl. Cryst., 1994, **27**, 435.
38 L. Palatinus and G. Chapuis, J. Appl. Cryst., 2007, **40**, 786.
39 G. M. Sheldrick, Acta Cryst., 2008, **A64**, 112.
40 CrysAlisPro, Agilent Technologies, Version 1.171.36.32, 2013 and Version 1.171.37.35, 2014; CrysAlisPro, Rigaku Oxford Diffraction, Version 1.171.38.41, 2015.
41 A. L. Spek, Acta Cryst., 2009, **D65**, 148.

12 Appendix II: Modification of the Laser Induced Liquid Bead Ion Desorption (LILBID) Apparatus

Laser Induced Liquid Bead Ion Desorption[1-6] (LILBID) is a very gentle method to transfer large molecular ions from solution into the gas phase. A micro droplet dispenser is used to generate free-flying micro droplets of an analyte solution (10 Hz duty cycle). Aliphatic alcohols or water are used as solvents. The droplets are transferred into high vacuum and subsequently irradiated by intensive infrared (IR) laser radiation. The frequency of the laser radiation is tuned to an absorption band of the solvent. A custom optical parametric oscillator[7] (OPO) unit converts the fundamental radiation of a Nd:YAG laser (1064 nm) into MID IR radiation. The solvent absorbs the radiation, which causes a temperature increase and the formation of a supercritical state. In the subsequent explosion, the dissolved ions are released from the droplet into the gas phase. The ions can guided into a mass spectrometer for further investigations. The LILBID technology was developed in the research group of Prof. Dr. Brutschy in Frankfurt and is rebuilt, modified and tested in the research group of Prof. Dr. G. Niedner-Schatteburg. A part of my doctoral studies was associated with this project. The following chapter provides some material illustrating the current state of development of the LILBID apparatus.

<u>Overview of the LILBID apparatus:</u>

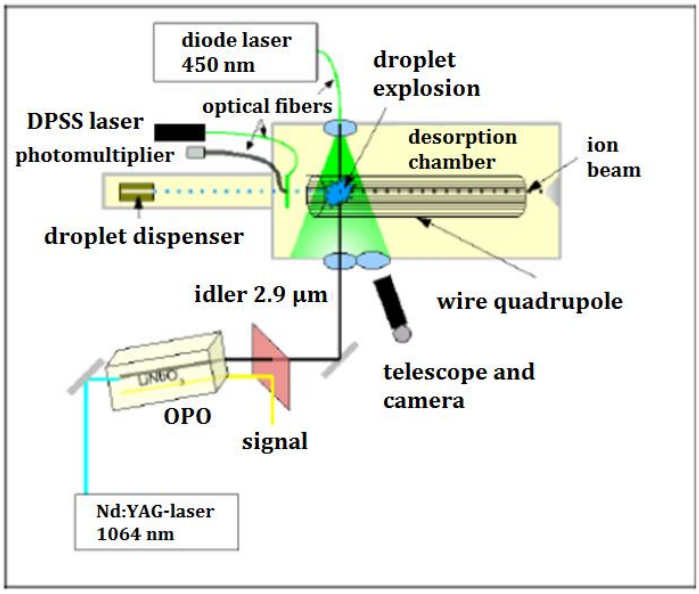

Figure 1: Schematic representation of the experimental setup of the current LILBID apparatus in Kaiserslautern.

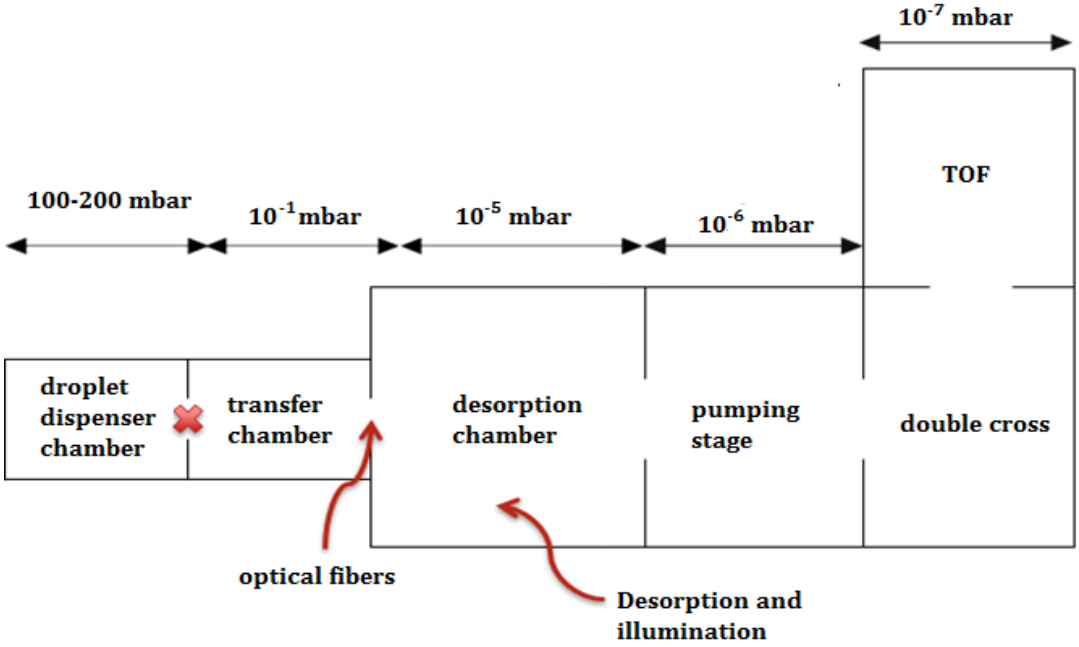

Figure 2: Schematic representation of the vacuum system of the current LILBID apparatus in Kaiserslautern.

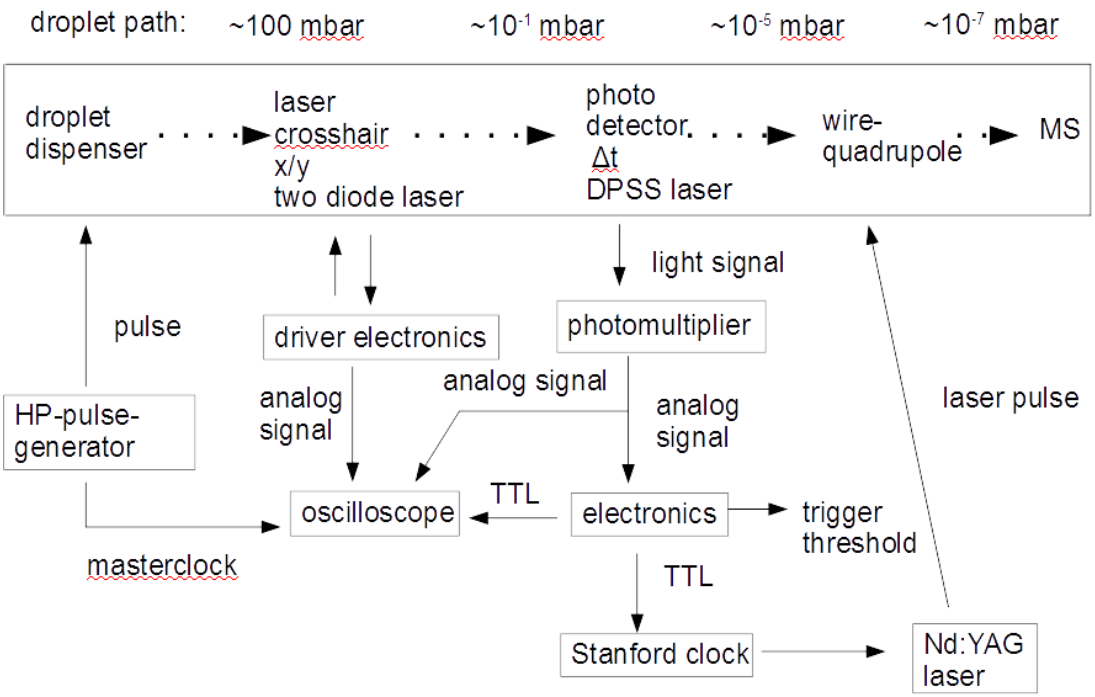

Figure 3: Overview over the instruments contributing to the current LILBID apparatus in Kaiserslautern.

Detection of the micro droplets in the low pressure region

A custom build X/Y aim unit (cf. Fig. 4a) serves to detect and align the micro droplets in the low pressure region to the entrance of to the high vacuum region of the LILBID apparatus. Two of diodes with associated detectors form a crosshair. Dips of the constant light signal indicate the presence of the mircodoplets (cf. Fig. 4).

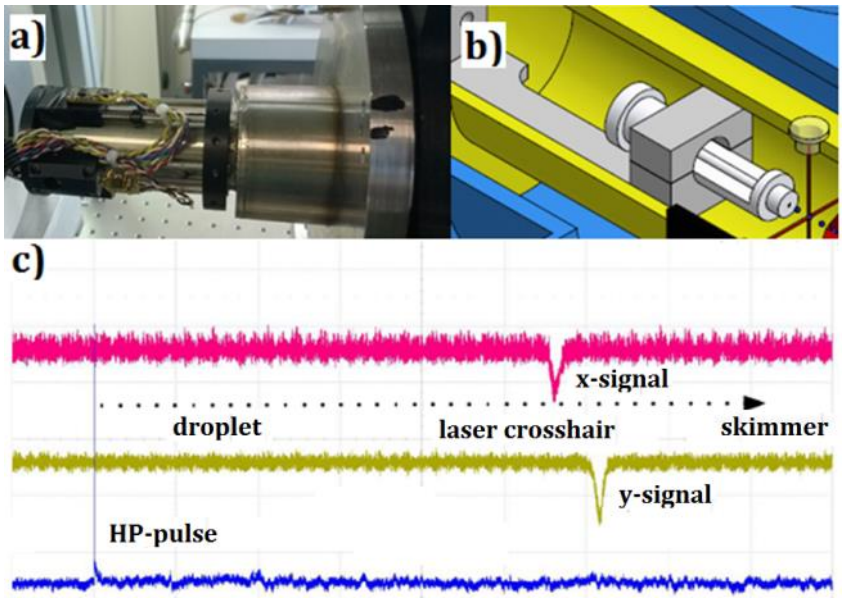

Figure 4: a) A photograph of the X/Y unit. **b)** 3D model of the interior of the X/Y unit. **c)** Dip signals of the X/Y unit indicate the presence of the micro droplets in the vicinity to the entrance to the high vacuum region of the LILBID apparatus.

Detection of the micro droplets in the high vacuum region

The entrance of the high vacuum chamber is illuminated by green light of solid state DPSS Laser (100mW), which is guided into the chamber by optical fibres (CeramOptec, Nylon 600/660 N; cf. Fig. 5a). Arriving droplets scatter the light. An additional optical fiber guides the scattered light to a photomultiplier (cf. Fig. 5b). A signal of the photo multiplier (Hamamatsu R7400U, cf. Fig. 5c) indicates the presence of a microdroplet in the high vacuum region of the apparatus.

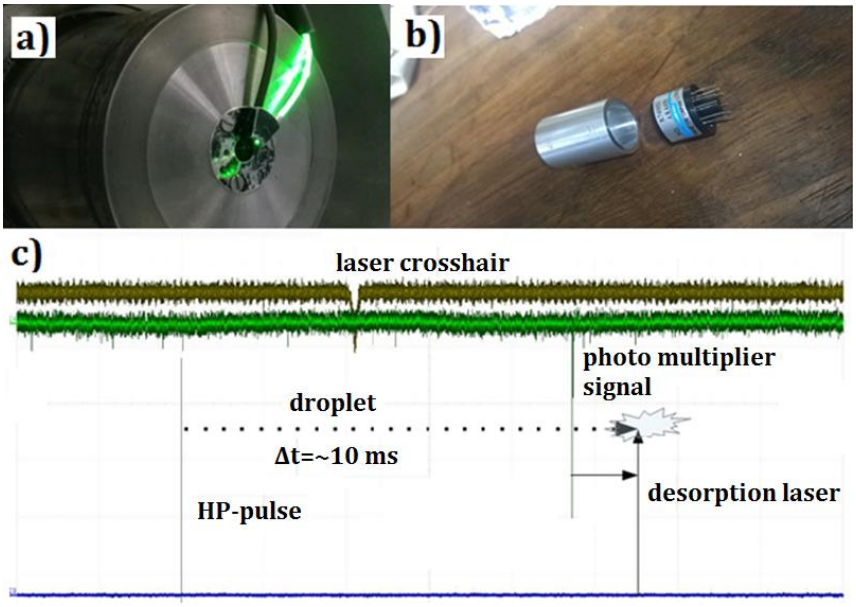

Figure 5: a) Optical fibers illuminate the entrance of the high vacuum chamber. **b)** A photomultiplier (Hamamatsu R7400U) serves to detect light scattered by arriving micro droplets. **c)** The photomultiplier signal indicates the presence of a microdroplet in the vacuum chamber.

Visualization of micro droplets within the high vacuum chamber

The micro droplets are visualized on a screen by a combination of a telescope and a high speed CMOS camera (PhotonFocus, MV-D2048x1088, cf. Fig. 6).

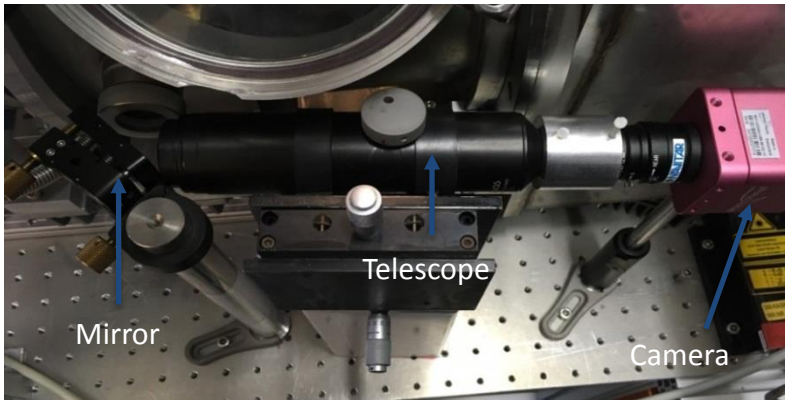

Figure 6: Photograph of the experimental setup to visualize micro droplets on a screen.

Short pulses of blue light serve to illuminate the droplets for visualization on a screen. Optical fibers (cf. Fig. 7a) guide blue light of a pulsed diode laser (mpc - Laser Power Supplies DLM 40450 with a VFM 5-25 driver; cf. Fig. 7b) into the high vacuum chamber. The resulting images (cf. Fig. 7c and d) crucially depend on the pulse length of the illumination light.

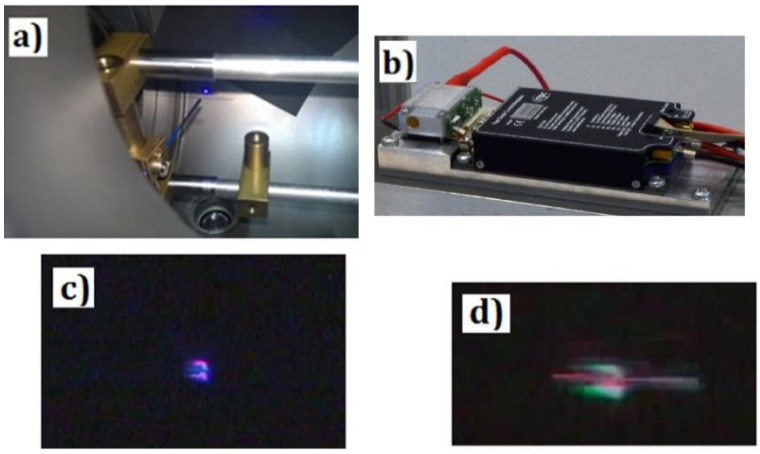

Figure 7: Optical fibers **(a)** guide blue light pulses of a pulsed diode laser **(b)** into the high vacuum chamber. In combination with a telescope and a camera we gain enlarged images of the droplet.

12.1 References

1. M. Cernescu, T. Stark, E. Kalden, C. Kurz, K. Leuner, T. Deller, M. Göbel, G. P. Eckert and B. Brutschy, *Laser-Induced Liquid Bead Ion Desorption Mass Spectrometry: An Approach to Precisely Monitor the Oligomerization of the β-Amyloid Peptide*, Anal. Chem., 2012, **84**, 5276-5284.
2. N. Morgner, T. Kleinschroth, H. D. Barth, B. Ludwig and B. Brutschy, *A novel approach to analyze membrane proteins by laser mass spectrometry: From protein subunits to the integral complex*, J. Am. Soc. Mass. Spectrom., 2007, **18**, 1429-1438.
3. J. Hoffmann, L. Sokolova, L. Preiss, D. B. Hicks, T. A. Krulwich, N. Morgner, I. Wittig, H. Schagger, T. Meier and B. Brutschy, *ATP synthases: cellular nanomotors characterized by LILBID mass spectrometry*, PCCP, 2010, **12**, 13375-13382.
4. F. Sobott, S. A. Schunk, F. Schüth and B. Brutschy, *Examination of Condensation Products of Group 4 Alkoxides with Laser-Induced Liquid Beam Ionization/Desorption Mass Spectrometry*, Chem.-Eur. J., 1998, **4**, 2353-2359.
5. W. Kleinekofort, J. Avdiev and B. Brutschy, *A new method of laser desorption mass spectrometry for the study of biological macromolecules*, Int. J. Mass Spectrom. Ion Processes, 1996, **152**, 135-142.
6. N. Morgner, H.-D. Barth and B. Brutschy, *A New Way To Detect Noncovalently Bonded Complexes of Biomolecules from Liquid Micro-Droplets by Laser Mass Spectrometry*, Aust. J. Chem., 2006, **59**, 109-114.
7. D. W. Michael, K. Kolenbrander and J. M. Lisy, *New cavity design for a LiNbO3 optical parametric oscillator*, Review of Scientific Instruments, 1986, **57**, 1210-1212.

Lebenslauf

Persönliche Angaben

Vor- und Zuname	Johannes Lang

Schulbildung

12/1996 -07/2000	Grundschule Birkenfeld
09/2000 -03/2009	Gymnasium Birkenfeld Abschluss: Allgemeine Hochschulreife, Note 2,0

Studium

04/2009 – 12/2013	Chemiestudium an der Technischen Universität Kaiserslautern Vertiefungsrichtung: Physikalische Chemie Abschluss als Diplom-Chemiker, Note 1,0 Titel der Diplomarbeit: „Charakterisierung kationischer mono- und dinuklearer Silber(I)-Komplexe mittels Stoßinduzierter Dissoziation (CID) sowie Infrarot-Multiphotonen-Dissoziation (IRMPD)“
Seit 01/2014	Wissenschaftlicher Mitarbeiter an der TU-Kaiserslautern im Arbeitskreis Prof. Dr. Niedner-Schatteburg (Physikalische Chemie) Titel der Doktorarbeit: „ Characterization of Structures, Fragmentation Pathways and Magnetism of Mononuclear and Oligonuclear Transition Metal Complexes in Isolation “

Fremdsprachen

Englisch: gut in Wort und Schrift
Russisch: gut in Wort

Auszeichnungen

OPTIMAS **Hiwi Program** for young researchers

Steinhofer Preis (1. Platz) der Prof. Dr. Drs. H.c. A. Steinhofer Stiftung für herausragende Leistungen während der Diplomarbeit

PCCP Posterpreis der Bunsentagung in Hamburg, 2014

Curriculum Vitae

Personal Information

Name	Johannes Lang

School Education

12/1996 -07/2000	Elementary School Birkenfeld
09/2000 -03/2009	Gymnasium Birkenfeld German Abitur, Grade: 2.0

University Education

	Studies in Chemistry at the University of Kaiserslautern Specialization: Physical Chemistry
04/2009 – 12/2013	Diploma in the group of Prof. Dr. Niedner-Schatteburg, Grade: 1.0 Title of the thesis „Characterization of Mononuclear and Binuclear silver(I) Complexes via Collision Induced Dissociation (CID) and InfraRed Multiple Photon Dissociation (IR-MPD)" (translated from German)
01/2014- today	PhD student in the group of Prof. Dr. Niedner-Schatteburg Titel of the thesis: „ Characterization of Structures, Fragmentation Pathways and Magnetism of Mononuclear and Oligonuclear Transition Metal Complexes in Isolation"

Foreign Languages

English
Russian

Awards

OPTIMAS **Hiwi Program** for young researchers

Steinhofer Prize 2015 of the Prof. Dr. Drs. hack A. Steinhofer foundation for outstanding achievements during the diploma thesis work

PCCP Poster Prize, 113th General Assembly of the German Bunsen Society for Physical Chemistry, Hamburg, 2014

List of Publications

1. *Two-color delay dependent IR probing of torsional isomerization in a $AgL_1L_2^+$ complex*
   J. Lang, M. Gaffga, F. Menges and G. Niedner-Schatteburg, *Physical Chemistry Chemical Physics* **2014**, *16*, 17417-17421.
   http://dx.doi.org/10.1039/c4cp02045f

2. *P,C-bond cleavage in the ligand sphere of a nickel(II) complex*
   S. P. Walg, A. D. Schmidt, M. Schmitz, S. Farsadpour, **J. Lang**, M. Niebergall, Y. Sun, P. W. Roesky, G. Niedner-Schatteburg and W. R. Thiel, *Dalton Transactions* **2015**, *44*, 1317-1322.
   http://dx.doi.org/10.1039/C4DT02158D

3. *Multistate-Mediated Rearrangements and $FeCl_2$ Elimination in Dinuclear FePd Complexes*
   M. Gaffga, I. Munstein, P. Müller, **J. Lang**, W. R. Thiel and G. Niedner-Schatteburg, *The Journal of Physical Chemistry A* **2015**, *119*, 12587-12598.
   http://dx.doi.org/10.1021/acs.jpca.5b06952

4. *Intermetallic Competition in the Fragmentation of Trimetallic Au–Zn–Alkali Complexes*
   J. Lang, M. Cayir, S. P. Walg, P. Di Martino-Fumo, W. R. Thiel and G. Niedner-Schatteburg, *Chemistry – A European Journal* **2016**, 22, 2345-2355.
   http://dx.doi.org/10.1002/chem.201504093

5. *Mechanistic Studies on the Ruthenium(II) Catalyzed Base-Free Transfer Hydrogenation Triggered by a Roll-Over Cyclometallation*
   C. Kerner, **J. Lang**, M. Gaffga, F. S. Menges, Yu Sun, G. Niedner-Schatteburg and W. R. Thiel, *ChemPlusChem*, **2017**, 82, 212-224.
   http://dx.doi.org/10.1002/cplu.201600526

6. *Vibrational fingerprints of a tetranuclear cobalt carbonyl cluster within an ion trap*
   J. Mohrbach, **J. Lang**, S. Dillinger, M. H. Prosenc, P. Braunstein and G. Niedner-Schatteburg, *Journal of Molecular Spectroscopy*, **2017**, 332, 103-108.
   http://dx.doi.org/10.1016/j.jms.2016.11.008

7. *Vibrational Blue Shift of coordinated N_2 in $[Fe_3O(OAc)_6(N_2)_n]^+$: "Non Classical" Dinitrogen Complexes*
   J. Lang, J. Mohrbach, S. Dillinger, J. M. Hewer and G. Niedner-Schatteburg, *Chemical Communications,* **2017**, 53, 420-423.
   http://dx.doi.org/10.1039/C6CC07481B

8. *Pump-probe fragmentation action spectroscopy: a powerful tool to unravel light-induced processes in molecular photocatalysts*
*D. Imanbaew, **J. Lang**, M. F. Gelin, S. Kaufhold, M. G. Pfeffer, S. Rau, and C. Riehn, Angewandte Chemie – International Edition,* **2017**, 56, 5471-5474.
http://dx.doi.org/10.1002/anie.201612302

9. *Exploring the gas phase activation and reactivity of a Ru transfer hydrogenation catalyst by experiment and theory in concert*
F. S. Menges, **J. Lang**, Y. Nosenko, C. Kerner, M. Gaffga, L. Taghizadeh Ghoochany, W. R. Thiel, C. Riehn, and G. Niedner-Schatteburg, *Journal of Physical Chemistry A*, **2017**, published online.
http://dx.doi.org/10.1021/acs.jpca.7b02459

10. *Gas-phase reactivity of Cp* Group IX metal complexes bearing aromatic N,N'-chelating ligands*
C. Kerner, J.P. Neu, M. Gaffga, **J. Lang**, B. Oelkers, Y. Sun, G. Niedner-Schatteburg and W.R. Thiel, New Journal of Chemistry, **2017**, published online.
http://dx.doi.org/10.1039/C7NJ01079F

11. *Magnetostructural Correlations in isolated trinuclear iron(III) oxo acetate complexes*
J. Lang, J. M. Hewer, M. Klein, T. J. Lau, C. van Wüllen and G. Niedner-Schatteburg, **in preparation**.

12. *Structural characterization of mono and binuclear palladium complexes in isolation*
J. Lang, D. Hackenberger, Saeid Farsadpour, W. R. Thiel, L. Goossen and G. Niedner-Schatteburg, **in preparation**.

13. *The Dinickelocene [Cp´´Ni-NiCp´´]*
I. Schädlich, F. Zimmer, Y. Sun, W. R. Thiel, H. Kelm, B. Oelkers, G. Wolmershäuser, **J. Lang**, G. Niedner-Schatteburg, C. Mehlich, C. van Wüllen and H. Sitzmann, **in preparation**.

Contribution to Conferences: Oral Presentations

2014

Johannes Lang, Maximilian Gaffga, Fabian Menges, Kevin Muller, Werner Thiel and Gereon Niedner-Schatteburg, "Elucidating the Building and Breaking of Hydrogen Bonds: Two color delay dependent IR probing of torsional isomerization in a $[AgL_1L_2]^+$ complex", Frühjahrstagung der Deutschen Physikalischen Gesellschaft, Berlin, 17.-21.03.2014.

Johannes Lang, Maximilian Gaffga, Fabian Menges and Gereon Niedner-Schatteburg, "Elucidating the Building and Breaking of Hydrogen Bonds: Two color delay dependent IR probing of torsional isomerization in a $[AgL_1L_2]^+$ complex", 3MET PhD - Meeting, Karlsruhe, 28.03.2014.

2015

Johannes Lang, Patrick Di Martino-Fumo, Merve Cayir, Werner R. Thiel and Gereon Niedner-Schatteburg, "Alkali effect on bimetallic hydroamination catalysts the gas phase", Frühjahrstagung der Deutschen Physikalischen Gesellschaft, Heidelberg, 23-27.03.2015.

Johannes Lang, "Charakterisierung kationischer mono-und dinuklearer Ag(I)-Komplexe mittels Stoßinduzierter Dissoziation sowie Infrarot-Multiphotonen Dissoziation (IRMPD) ", Steinhofer Preis 2014, 20.03.2015

2016

Johannes Lang, Jennifer Mohrbach, Sebastian Dillinger, Joachim M. Hewer, and Gereon Niedner-Schatteburg, Oxo-centered trinuclear Iron(III) carboxylate complexes as model systems for the interplay of molecular geometry and magnetism, 3MET.de Gas Phase Meeting 2016, Karlsruhe, 20.05.2016.

2017

Johannes Lang, Jennifer Mohrbach, Sebastian Dillinger, Joachim M. Hewer and Gereon Niedner-Schatteburg, Non Classical Dinitrogen Bonding and Magnetostructural Correlations in Trinuclear Iron – Oxo Acetate Complexes, Frühjahrstagung der Deutschen Physikalischen Gesellschaft 2017, Mainz, 06-10.03.2017.

Contribution to Conferences: Poster Presentations

2014

Johannes Lang, Maximilian Gaffga, Fabian Menges and Gereon Niedner-Schatteburg, " Two color delay dependent IR probing of torsional isomerization in a $[AgL_1L_2]^+$ complex", Bunsentagung 2014, Hamburg, 29.-31.05.2014.

2015

Johannes Lang, Patrick Di Martino-Fumo, Merve Cayir, Werner R. Thiel and Gereon Niedner-Schatteburg, "Alkali effect on bimetallic homogenous catalysts", Gordon Research Conference 2015: Gaseous Ions, Galveston, TX, 22-27.02.2015.

Johannes Lang, Joachim Hewer, Maximilian Gaffga, and Gereon Niedner-Schatteburg, "Two color IR spectroscopy: Enhancing fragmentation efficiency and changing isomer populations ", Bunsentagung 2015, Bochum, 14.-16.05.2015.

2016

Johannes. Lang, Jennifer. Mohrbach, Sebastian. Dillinger, Joachim M. Hewer and Gereon. Niedner-Schatteburg, "Vibrational Blue Shift of coordinated N_2 in $[Fe_3O(OAc)_6(N_2)_n]^+$: Non Classical Dinitrogen Complexes", International Symposium on Small Particles and Inorganic Clusters XVIII, Jyväskylä, Finnland, 14.08.2016 - 19.08.2016.

Johannes. Lang, Jennifer. Mohrbach, Sebastian. Dillinger, Joachim M. Hewer and Gereon. Niedner-Schatteburg, "Vibrational Blue Shift of coordinated N2 in $[Fe_3O(OAc)_6(N_2)_n]^+$: Non Classical Dinitrogen Complexes", European Conference on Trapped Ions 2016, Arosa, Schweiz, 29.08.2016 - 02.09.2016

2017

Johannes Lang, Jennifer Mohrbach, Sebastian Dillinger, Joachim M. Hewer and Gereon Niedner-Schatteburg, “Non Classical Dinitrogen Bonding and Magnetostructural Correlations in Trinuclear Iron – Oxo Acetate Complexes”, Gordon Research Seminar 2017: Gaseous Ions, Ventura, CA, 11-12.02.2017.

Johannes Lang, Jennifer Mohrbach, Sebastian Dillinger, Joachim M. Hewer and Gereon Niedner-Schatteburg, “Non Classical Dinitrogen Bonding and Magnetostructural Correlations in Trinuclear Iron – Oxo Acetate Complexes”, Gordon Research Conference 2017: Gaseous Ions, Ventura, CA, 12-17.02.2017.

Danksagung

Ich danke Prof. Dr. Gereon Niedner-Schatteburg für die Betreuung, die gute Zusammenarbeit und vorallem für den mir eingeräumten Freiraum in meiner wissenschatflichen Arbeit. Auch für die Diskussionen und Ratschläge abseits der eigentlichen Promotion bin ich sehr dankbar.

Herrn Prof. Dr. Gerhards danke ich für die Übernahme des Zweitgutachtens und die unterhaltsamen Gespräche und Diskussionen auf dem PC Flur und auf Tagungen. Hernn Prof. Dr. Thiel danke ich für die Übernahme des Prüfungsvorsitzes und für die Offenheit für Kooperationsprojekte

Der „vorhergehenden Generation“ an GNS´lern, Fabian Menges, Lars Barzen, Christine Merkert, Jennifer Meyer, Matthias Tombers und Maximillian Gaffga möchte ich für die Hilfe beim Einstieg in den Arbeitskreis und den Wissenstransfer in meine Richtung danken.

Meiner „Generation“ an GNS´lern, Jennifer Mohrbach, Joachim Hewer, Dimitri Imanbaew, Sebastian Dillinger möchte ich für den unglaublichen Zusammenhalt, die Kollegialität und vorallem für die Freundschaft danken. In diesem Zusammenhang danke ich YoπShi für die beste Erdnuss-Soße der Welt ;)

Für die Unterstützung meiner Arbeit danke ich allen Vertiefungspraktikanten, Diplomanden und Bacheloranden, die ich betreuen dürfte: Patrick Müller, Lukas Burkhardt, Björn Kwasigroch, Yannick Mees, Patrick Di Martino-Fumo, Daniela Fries und Robert Schellenberg.

Der „nächsten Generation“ an GNS´lern, Matthias Klein, Michael Lembach, Björn Kwasigroch und Annika Steiner danke ich für die Fortführung unserer Projekte und das engagierte Einbringen in unseren Arbeitskreis.

Thomas Kolling und Yevgeniy Nosenko danke ich für die Unterstützung, die Geduld und die stete Hilfsbereitschaft bei Problemem jeglicher Art während meiner Doktorarbeit.

Herrn PD Dr. Christoph Riehn danke ich für die stete Diskussionsbereitschaft und die Zusammenarbeit bei den Anfägerpraktika. Auch für die unvergessene Dartrunde in der „Studentenkneipe“ und das Bekanntmachen mit Dr. Sam Buca möchte ich mich bedanken ;).

Ich danke allen PC´lern, Theroretikern und dem AK Patureau für den berühmten Flurfunk im 5. Stock, die super Zusammenarbeit bei den Anfängerpraktika und die tolle Atmosphäre im Kaffezimmer.

Tobias Lau, Vicente Zamundio-Bayer und allen Mitarbeitern der Lau-Gruppe danke ich für die gute Zusammenarbeit und die Unterstützung während der Messungen an der NanoclusterTrap am BESSY II Sychrotron in Berlin.

Meinen Kollegen Matthias Tombers, Jochen Hewer und Jonathan Meyer danke ich für die Einarbeitung und die Zusammenabeit während der vielen Nachtschichten in Berlin. Ich hoffe, dass der AK GNS noch oft beim Inder und im Görlitzer Park in Berlin anzutreffen sein wird ;).

Ich danke den vielen Kollegen/innen in den Arbeitskreisen Thiel, Sitzmann und Gooßen, mit denen ich viele Kooperations-Projekte erfogreich bearbeiten konnte. Kommt weiterhin zum ESI-Messen!

Ein besonderer Dank geht an Hilde Seelos, Sybille Heieck, Petra Wetzel und Birgit Harrison-Weber für das Managen und Abarbeiten der Papierberge.

Den Handballern des TV Birkenfeld danke ich für den mannschaftlichen Zusammenhalt und die spannenden, lustigen und auch ärgerlichen Stunden abseits der Uni, die mir die notwendige Ablenkung vom Promotionsstreß geboten haben. In diesem Zusammenhang danke ich auch all meinen Freunden, die ich teilweise noch aus der Schulzeit wertschätze.

Ein unbeschreiblich großer Dank geht an meine Familie, im Besonderen an meine Eltern Peter und Elena, meinen Bruder Alex und meine Schwägerin Galina für die Unterstützung und den Rückhalt während meines ganzen Studiums. Вы это сделали возможным!

Eine solche Dankesliste ist sicherlich niemals allumfassend. Ich bitte daher alle, die ich übersehen oder nicht namentlich erwähnt habe, es mir nicht krumm zu nehmen. Ihr wisst, dass ich euch sehr dankbar bin!

Eidesstattliche Erklärung

Hiermit bestätige ich, Johannes Lang, dass die vorliegende Arbeit mit dem Titel „*Characterization of Structures, Fragmentation Pathways and Magnetism of Mononuclear and Oligonuclear Transition Metal Complexes in Isolation*“ gemäß der Promotionssordnung des Fachbereichs Chemie der Technischen Universität Kaiserslautern selbstständig und mit keinen anderen als den hier angegebenen Quellen und Hilfsmitteln erstellt wurde.

Kaiserslautern, im Mai 2017 Johannes Lang